

University of South Bohemia in České Budějovice
Faculty of Science

Plasma-Assisted Deposition of Functional Bioactive Nanostructured Films

Ph.D. Thesis

Mgr. Petr Sezemský

Supervisor: **doc. RNDr. Vítězslav Straňák, Ph.D.**

Faculty of Science, University of South Bohemia in České Budějovice

České Budějovice

2021

This thesis should be cited as:

Sezemský, P., 2021: Plasma-Assisted Deposition of Functional Bioactive Nanostructured Films. Ph.D Thesis Series, No. 19. University of South Bohemia, Faculty of Science, České Budějovice, Czech Republic, 375 pp.

Annotation

The Ph.D. thesis focuses on the interdisciplinary research of advanced materials for the development of biosensors with multiple domain interrogation capabilities for the detection of biomolecules and pathogens, namely, Lyme borreliosis spirochetes, *Borrelia burgdorferi s.l.* The strategy for biosensor fabrication is based on an optical fiber whose surface is coated by precisely tailored nanostructured thin films by means of low-temperature plasma. The thesis demonstrates that an indium tin oxide (ITO) thin film, deposited by magnetron sputtering onto the optical fiber surface, can serve as an effective transducer for electrochemical and optical measurements. The optical interrogation is based on the measurement of the refractive index utilizing lossy-mode resonance (LMR) phenomena, while the electrochemical interrogation is performed mostly by cyclic voltammetry. It is shown that the optimal design of the active surface on an optical fiber enables simultaneous (in time and in situ) optical and electrochemical interrogation of liquids and detection of biological complexes, including markers of Lyme borreliosis pathogens.

Declaration:

I hereby declare that I am the author of this dissertation and that I have used only those sources and literature detailed in the list of references.

České Budějovice, October 24, 2021

.....
Petr Sezemský



Přírodovědecká
fakulta
Faculty
of Science

Financial support

The research was partially supported by the following grants:

Ministry of Education, Youth and Sports:

MŠMT 8JPL19012 (2019-2020)

North Atlantic Treaty Organization:

NATO SPS G5147 (2017-2020)

Grant Agency of Czech Republic:

GAČR 16-14024S (2016-2018)

GAČR 21-05030K (2021-2023)

Grant Agency of University of South Bohemia:

110/2020/P (2020)

Acknowledgements

It is hard to list all the people to whom I am grateful for their support, not because there are so few of them, but because there are so many.

I am grateful to my wife and parents, my loving family, for giving me the essential support throughout my whole study and life. Without you, none of it would have been possible, none of it would make sense.

Vit'ò, your hard work and dedication to the development of the laboratory taught me a lot. Thank you for the opportunity to be part of it, for sharing your valuable experience, and for your guidance.

I also want to thank all my colleagues, local and foreign. It was great fun working with you, yet I have also learned a lot.

*The noblest pleasure is the joy of understanding.
Learning is the only thing the mind never
exhausts, never fears, and never regrets.*

Leonardo da Vinci

List of publications and author's contributions

The following 17 publications are ordered chronologically and serve as a base for this thesis:

Magdalena Dominik, Katarzyna Siuzdak, Paweł Niedziałkowski, Vitezslav Stranak, **Petr Sezemsky**, Michał Sobaszek, Robert Bogdanowicz, Tadeusz Ossowski, Mateusz Smietana, Annealing of indium tin oxide (ITO) coated optical fibers for optical and electrochemical sensing purposes, Proceedings of SPIE 1075, (2016), UNSP 1017515.

<https://doi.org/10.1117/12.2263289>

(IF = 0.56)

PS built the deposition setup, optimized the procedure, and prepared the samples; 5 %.

Michał Sobaszek, Magdalena Dominik, Dariusz Burnat, Robert Bogdanowicz, Vitezslav Stranak, **Petr Sezemsky**, Mateusz Smietana, Optical monitoring of thin film electro-polymerization on surface of ITO-coated lossy-mode resonance sensor, 2017 25TH INTERNATIONAL CONFERENCE ON OPTICAL FIBER SENSORS (OFS), Proceedings of SPIE 10323, (2017), UNSP 103234W.

<https://doi.org/10.1117/12.2265932>

(IF = 0.56)

PS built the deposition setup, optimized the procedure, and prepared the samples; 5 %.

Vitezslav Stranak, Robert Bogdanowicz, **Petr Sezemsky**, Harm Wulff, Angela Kruth, Mateusz Smietana, Jiri Kratochvil, Martin Cada, Zdenek Hubicka, Towards high quality ITO coatings: The impact of nitrogen admixture in HiPIMS discharges, Surface and Coatings Technology 335, (2018), 126-133.

<https://doi.org/10.1016/j.surfcoat.2017.12.030>

(IF = 4.158)

PS built the deposition setup, optimized the procedure, performed all experiments in the range from sample preparation to electrical and optical investigation of their properties, executed all data analysis, and participated in the writing and revision of the manuscript; 35 %.

Robert Bogdanowicz, Paweł Niedziałkowski, Michał Sobaszek, Dariusz Burnat, Wioleta Białobrzaska, Zofia Cebula, **Petr Sezemsky**, Marcin Koba, Vitezslav Stranak, Tadeusz Ossowski, Mateusz Smietana, Optical Detection of Ketoprofen by Its Electropolymerization on an Indium Tin Oxide-Coated Optical Fiber Probe, Sensors (Basel) 18(5), (2018), pii: E1361.

<https://doi.org/10.3390/s18051361>

(IF = 3.576)

PS built the deposition setup, optimized the procedure, prepared the samples, and participated in writing of the manuscript; 15 %.

Mateusz Smietana, Michał Sobaszek, Bartosz Michalak, Paweł Niedziałkowski, Wioleta Białobrzaska, Marcin Koba, **Petr Sezemsky**, Vitezslav Stranak, Jakub Karczewski, Tadeusz Ossowski, Robert Bogdanowicz, Optical Monitoring of Electrochemical Processes With ITO-Based Lossy-Mode Resonance Optical Fiber Sensor Applied as an Electrode, *Journal of Lightwave Technology* 36, (2018), 954 - 960.

<https://doi.org/10.1109/jlt.2018.2797083>

(IF = 4.288)

PS built the deposition setup, optimized the procedure, prepared the samples, and participated in writing of the manuscript; 10 %.

Marta Janczuk-Richter, Monika Piestrzyńska, Dariusz Burnat, Katarzyna Szot-Karpińska, **Petr Sezemsky**, Vitezslav Stranak, Wojtek J. Bock, Robert Bogdanowicz, Joanna Niedziółka-Jönsson, and Mateusz Smietana, Optical monitoring of electrochemical processes with ITO-coated long-period fiber grating, 26th International Conference on Optical Fiber Sensors, September 24-28 2018, Lausanne, Switzerland, OSA Technical Digest (Optical Society of America, 2018), paper ThE54.

<https://doi.org/10.1364/OFS.2018.ThE54>

(IF = 2.180)

PS built the deposition setup, optimized the procedure, and prepared the samples; 15 %.

Marta Janczuk-Richter, Monika Piestrzynska, Dariusz Burnat, **Petr Sezemsky**, Vitezslav Stranak, Wojtek J Bock, Robert Bogdanowicz, Joanna Niedziółka-Jönsson, Mateusz Smietana, Optical investigations of electrochemical processes using a long-period fiber grating functionalized by indium tin oxide, *Sensors and Actuators: B Chemical* 279, (2019), 223–229.

<https://doi.org/10.1016/j.snb.2018.10.001>

(IF = 7.46)

PS built the deposition setup, optimized the procedure, prepared the samples, and participated in writing the manuscript; 15 %.

Mateusz Smietana, Paweł Niedziałkowski, Wioleta Białobrzaska, Dariusz Burnat, **Petr Sezemsky**, Marcin Koba, Vitezslav Stranak, Katarzyna Siuzdak, Tadeusz Ossowski, Robert Bogdanowicz, Study on Combined Optical and Electrochemical Analysis Using Indium-tin-oxide-coated Optical Fiber Sensor, *Electroanalysis* 31, (2019), 398.

<https://doi.org/10.1002/elan.201800638>

(IF = 2.544)

PS built the deposition setup, optimized the procedure, prepared the samples, and participated in writing of the manuscript; 10 %.

Michał Sobaszek, Dariusz Burnat, **Petr Sezemsky**, Vitezslav Stranak, Robert Bogdanowicz, Marcin Koba, Katarzyna Siuzdak, Mateusz Smietana, Enhancing electrochemical properties of an ITO-coated lossy-mode resonance optical fiber sensor by electrodeposition of PEDOT:PSS, *Optical Materials Express* 9(7), (2019), 3069-3078.

<https://doi.org/10.1364/OME.9.003069>

(IF = 3.442)

PS built the deposition setup, optimized the procedure, prepared the samples, and participated in writing of the manuscript; 15 %.

Paweł Niedziałkowski, Wioleta Białobrzaska, Dariusz Burnat, **Petr Sezemsky**, Vitezslav Stranak, Harm Wulff, Tadeusz Ossowski, Robert Bogdanowicz, Marcin Koba, Mateusz Smietana, Electrochemical performance of indium-tin-oxide-coated lossy-mode resonance optical fiber sensor, *Sensors and Actuators B: Chemical* 301, (2019), 127043.

<https://doi.org/10.1016/j.snb.2019.127043>

(IF = 7.46)

PS built the deposition setup, optimized the procedure, prepared the samples, and participated in writing of the manuscript; 10 %.

Marcin Koba, Dariusz Burnat, Katarzyna Szot-Karpińska, **Petr Sezemsky**, Vitezslav Stranak, Robert Bogdanowicz, Joanna Niedziółka-Jönsson, Mateusz Smietana, Combined optical and electrochemical analysis of protein binding with ITO-coated lossy-mode resonance sensor, *Proceedings SPIE* 11199, Seventh European Workshop on Optical Fibre Sensors, (2019), 111991E.

<https://doi.org/10.1117/12.2540849>

(IF = 0.56)

PS built the deposition setup, optimized the procedure, and prepared the samples; 10 %.

Dariusz Burnat, Marta Janczuk-Richter, Paweł Niedziałkowski, Wioleta Białobrzaska, **Petr Sezemsky**, Marcin Koba, Vitezslav Stranak, Robert Bogdanowicz, Tadeusz Ossowski, Joanna Niedziółka-Jönsson, Mateusz Smietana, Optical fiber lossy-mode resonance sensors with doped tin oxides for optical working electrode monitoring in electrochemical systems, *Proceedings SPIE* 11199, Seventh European Workshop on Optical Fibre Sensors, (2019), 111991O.

<https://doi.org/10.1117/12.2541354>

(IF = 0.56)

PS built the deposition setup, optimized the procedure, and prepared the samples; 10 %.

Petr Sezemsky, Vitezslav Stranak, Jiri Kratochvil, Martin Cada, Rainer Hippler, Miroslav Hrabovsky, Zdenek Hubicka, Modified high frequency probe approach for diagnostics of highly reactive plasma, *Plasma Sources Science and Technology*, 28, (2019), 115009.

<https://doi.org/10.1088/1361-6595/ab506c>

(IF = 3.193)

PS built the experimental setup, optimized the procedure, performed all experiments, developed the data evaluation procedures, prepared the scripts for large dataset evaluation, and participated in the writing and revision of the manuscript; 55 %.

Mateusz Smietana, Marcin Koba, **Petr Sezemsky**, Katarzyna Szot-Karpinska, Dariusz Burnat, Vitezslav Stranak, Joanna Niedziółka-Jönsson, Robert Bogdanowicz, Simultaneous optical and electrochemical label-free biosensing with ITO-coated lossy-mode resonance sensor, *Biosensors and Bioelectronics*, 154, (2020), 112050.

<https://doi.org/10.1016/j.bios.2020.112050>

(IF = 10.618)

PS built the deposition setup, optimized the procedure, prepared the samples, and participated in writing of the manuscript; 15 %.

Monika Janik, Paweł Niedziałkowski, Katarzyna Lechowicz, Marcin Koba, **Petr Sezemsky**, Vitezslav Stranak, Tadeusz Ossowski, Mateusz Smietana, Electrochemically directed biofunctionalization of lossy-mode resonance optical fiber sensor, *Optics Express* 28(11), (2020), 15934.

<https://doi.org/10.1364/OE.390780>

(IF = 3.894)

PS built the deposition setup, optimized the procedure, prepared the samples, and participated in writing of the manuscript; 15 %.

Bartosz Michalak, **Petr Sezemsky**, Vitezslav Stranak, Mateusz Smietana, Effect of thermal annealing on sensing properties of optical fiber sensors coated with indium tin oxide nano-overlays, *Photonics Letters of Poland* 12(2), (2020), 58-60.

<https://doi.org/10.4302/plp.v12i2.1024>

(IF = 0.67)

PS built the deposition setup, optimized the procedure, prepared the samples, and participated in writing of the manuscript; 20 %.

Petr Sezemsky, Dariusz Burnat, Jiri Kratochvil, Harm Wulff, Angela Kruth, Katarzyna Lechowicz, Monika Janik, Robert Bogdanowicz, Martin Cada, Zdenek Hubicka, Pawel Niedzialkowski, Wioleta Bialobrzaska, Vitezslav Stranak, Mateusz Smietana, Tailoring properties of indium tin oxide thin films for their work in both electrochemical and optical label-free sensing systems, *Sensors and Actuators B: Chemical* 343, (2021), 130173.

<https://doi.org/10.1016/j.snb.2021.130173>

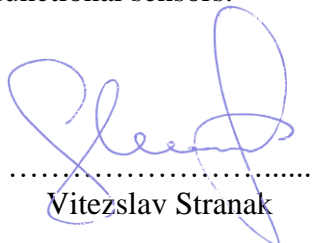
(IF = 7.46)

PS built the deposition setup, optimized the procedure, performed all experiments in the range from sample preparation to electrical and optical investigation of their properties, executed the data analysis, and participated in the writing and revision of the manuscript; 55 %.


Note that, for the sake of clarity, the publications are organized thematically in the Research section, where they use a unique reference system [A1] to [C5], see the Research section.

Co-author agreement

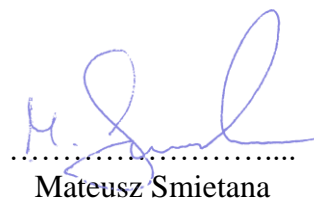
Vitezslav Stranak, Robert Bogdanowicz, and Mateusz Smietana, the first or corresponding authors of the listed publications, fully acknowledge the stated contribution of Petr Sezemsky. They all confirm a significant and key contribution of Petr Sezemsky to the carried research that was, namely, oriented toward advanced material research with the possibility to fabricate functional sensors.



.....
Vitezslav Stranak



.....
Robert Bogdanowicz



.....
Mateusz Smietana

CONTENTS

PREFACE	1
THEORETICAL SECTION	3
I. NANOSTRUCTURED SURFACE SCIENCE FOR LIFE AND HEALTH CARE	4
NANOSTRUCTURES FOR (BIO)DETECTORS	5
II. LOW-TEMPERATURE PLASMA-ASSISTED DEPOSITION OF FUNCTIONAL FILMS	9
MAGNETRON SPUTTERING FOR DEPOSITION OF NANOSTRUCTURED SURFACES	11
ADVANCED PULSED MAGNETRON SPUTTERING FOR TAILORING OF FILM PROPERTIES	13
III. NANOSTRUCTURED FUNCTIONAL SURFACES FOR BIOSENSING APPLICATIONS	19
OPTICAL INTERROGATION: REFRACTOMETRY FOR DETECTION	19
Surface Plasmon Resonance	19
Localized Surface Plasmon Resonance	20
Lossy-Mode Resonance	23
LMR Based Sensing: Principles and Practice	29
ITO for the Fabrication of LMR Sensor	32
Introduction to Theoretical Modeling of LMR	36
INTRODUCTION OF ELECTROCHEMISTRY FOR ITO-LMR-BASED SENSORS	40
Cyclic Voltammetry for Electrochemical Domain of Interrogation	42
RESEARCH SECTION	51
LMR FIBER AS AN ACTIVE ELECTRODE – MULTI-DOMAIN (BIO)SENSOR	52
A. SENSOR FABRICATION: TECHNOLOGY AND PROCEDURE	55
List of the publications in the subsection	61
B. COMBINED ELECTROCHEMICAL AND LMR INTERROGATION OF LIQUIDS	62
List of the publications in the subsection	67
C. BIOACTIVATION OF SENSORS FOR SELECTIVE DETECTION	68
List of the publications in the subsection	74
SUMMARY AND CONCLUSION	75
REFERENCES	77

A1. ANNEALING OF INDIUM TIN OXIDE (ITO) COATED OPTICAL FIBERS FOR OPTICAL AND ELECTROCHEMICAL SENSING PURPOSES	92
A2. TOWARDS HIGH QUALITY ITO COATINGS: THE IMPACT OF NITROGEN ADMIXTURE IN HIPIMS DISCHARGES	102
A3. MODIFIED HIGH FREQUENCY PROBE APPROACH FOR DIAGNOSTICS OF HIGHLY REACTIVE PLASMA	126
A4. ELECTROCHEMICAL PERFORMANCE OF INDIUM-TIN-OXIDE-COATED LOSSY-MODE RESONANCE OPTICAL FIBER SENSOR	148
A5. EFFECT OF THERMAL ANNEALING ON SENSING PROPERTIES OF OPTICAL FIBER SENSORS COATED WITH INDIUM TIN OXIDE NANO-OVERLAYS	174
A6. TAILORING PROPERTIES OF INDIUM TIN OXIDE THIN FILMS FOR THEIR WORK IN BOTH ELECTROCHEMICAL AND OPTICAL LABEL-FREE SENSING SYSTEMS	182
B1. OPTICAL MONITORING OF ELECTROCHEMICAL PROCESSES WITH ITO-COATED LONG-PERIOD FIBER GRATING	212
B2. OPTICAL INVESTIGATIONS OF ELECTROCHEMICAL PROCESSES USING A LONG-PERIOD FIBER GRATING FUNCTIONALIZED BY INDIUM TIN OXIDE	220
B3. OPTICAL MONITORING OF ELECTROCHEMICAL PROCESSES WITH ITO-BASED LOSSY-MODE RESONANCE OPTICAL FIBER SENSOR APPLIED AS AN ELECTRODE	238
B4. STUDY ON COMBINED OPTICAL AND ELECTROCHEMICAL ANALYSIS USING INDIUM-TIN-OXIDE-COATED OPTICAL FIBER SENSOR	256
B5. ENHANCING ELECTROCHEMICAL PROPERTIES OF AN ITO-COATED LOSSY-MODE RESONANCE OPTICAL FIBER SENSOR BY ELECTRODEPOSITION OF PEDOT:PSS	274
B6. OPTICAL FIBER LOSSY-MODE RESONANCE SENSORS WITH DOPED TIN OXIDES FOR OPTICAL WORKING ELECTRODE MONITORING IN ELECTROCHEMICAL SYSTEMS	290
C1. OPTICAL MONITORING OF THIN FILM ELECTRO-POLYMERIZATION ON SURFACE OF ITO-COATED LOSSY-MODE RESONANCE SENSOR	298
C2. OPTICAL DETECTION OF KETOPROFEN BY ITS ELECTROPOLYMERIZATION ON AN INDIUM TIN OXIDE-COATED OPTICAL FIBER PROBE	306
C3. COMBINED OPTICAL AND ELECTROCHEMICAL ANALYSIS OF PROTEIN BINDING WITH ITO-COATED LOSSY-MODE RESONANCE SENSOR	330
C4. SIMULTANEOUS OPTICAL AND ELECTROCHEMICAL LABEL-FREE BIOSENSING WITH ITO-COATED LOSSY-MODE RESONANCE SENSOR	338
C5. ELECTROCHEMICALLY DIRECTED BIOFUNCTIONALIZATION OF A LOSSY-MODE RESONANCE OPTICAL FIBER SENSOR	356

PREFACE

This Ph.D. thesis deals with the research of new and advanced materials that have application potential in the biosensor area with the motivation to develop nanostructured coatings that might be suitable for fast, cheap, and label-free detection of pathogens. Especially for the prevention of epidemic outbreaks, novel approaches are sought that enable the detection and monitoring of pathogens. Fast screening tests, with easy manipulation and quick response, are highly appreciated nowadays. In addition to this, sensor sensitivity and selectivity are the most critical properties in the effort to eliminate false results, errors, and inaccuracies. For that reason, current research focuses on sensors with multiple interrogations that combine different domains of sensing; for example, sensors that combine electrochemical detection with surface plasmon resonance [1] or UV/VIS [2] have been reported.

The ultimate challenge of this thesis is to develop a dual-domain electrochemically and optically active sensor for the detection of biomolecules and pathogens. For example, Lyme borreliosis, caused by *Borrelia burgdorferi* *sl.* spirochetes, is one of the most widespread infectious zoonotic diseases in the Czech Republic as well as worldwide [3]. Chronic disabling symptoms, caused often by rather expensive and complex diagnostics, are a typical complication of treatment resulting in permanent harm or even life-threatening emergencies for the patient. Hence, the development of fast and inexpensive biosensors for Lyme borreliosis or other neglected or (re)emerging diseases such as tick-borne encephalitis virus, dengue virus, Zika virus, or pathogens causing onchocerciasis represents the main objective of this thesis. It presents interdisciplinary research on the frontier of material and biomedical science that has been carried out over the past four years.

The practical approach of the thesis is the development of the strategy for the fabrication of optical fiber-based sensors with simultaneous electrochemical and optical interrogation of an analyte. It is shown in the thesis that the deposition of a highly tailored, nanostructured, and functionalized thin film onto the surface of the optical fiber results in an active transducer that enables in situ and in time electrochemical and optical detection with possible cross-verification of the achieved results. Cross sensitivity eliminates false results that can be caused by many factors (temperature, impurities, limited sensitivity and range, nonspecific bindings, and many others). The indium tin

oxide (ITO) film, deposited by a low-temperature plasma on the optical fiber, serves as a thin electrically conductive ‘coat’ that enables propagation of optical phenomena known as lossy mode resonance (LMR). The fiber equipped with a functional ITO-LMR coat serves as a working electrode in a cyclic voltammetry compartment (electrochemical detection domain) and simultaneously allows measurement of the modulation of the LMR shift (optical detection domain). The thesis demonstrates that careful tailoring of the ITO properties (its physical and chemical features) determines both the electrochemical and optical interrogation that is needed for the detection.

The thesis is logically divided into two parts. The first part of the thesis is in the form of a literary review that aims at the introduction of nanostructured surfaces and their application in bioscience, the justification of PVD methods for sensor fabrication, and the introduction to the physics of LMR and electrochemistry as analytical tools for the investigation of liquids. This introduction reviews the current state of research with projection to the topic of the Ph.D. thesis; fabrication of multi-interrogation sensors for the detection of biocomplexes.

The second part of the thesis is devoted to actual research and consists of published results that were achieved in the framework of the Ph.D. thesis. For the sake of clarity, there are three sections: (i) research devoted to sensor fabrication technology and procedure and characterization of thin functional films, (ii) investigation of nanostructured ITO for simultaneous LMR and electrochemical interrogation of an analyte, and (iii) bioactivation of the fabricated sensors for the selective detection of biomolecules, e.g., drugs and proteins, or pathogens, where *Borrelia burgdorferi* was selected as an exemplary organism to be detected. These main research results are presented in articles that have already been published in journals with an impact factor; see the list of publications and the author’s contributions shown previously.

THEORETICAL SECTION

I. Nanostructured Surface Science for Life and Health Care

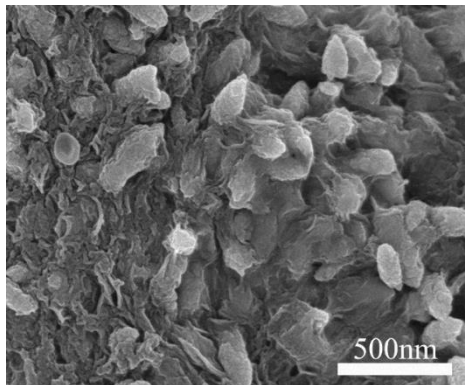


Fig. 1. Reduced nanostructured graphene oxide and Fe_2O_3 compound used as an active electrode [4].

With advances in the field of material physics in recent decades, new methods for the modification of material properties have emerged. Nanostructured surfaces with dimensions in the range of 100 nm are highly interesting for science and industry, as they reveal novel properties of the matter. Nanostructured surfaces can typically be produced as laterally homogeneous films, ultrathin 2D atom aggregates called (nano)islands and/or nanoparticles (of 10 to 100 nm size) incorporated into the material matrix or

deposited directly on a flat substrate [5]. The most fundamental characteristics of nanostructures are represented by (i) a high surface area to volume ratio and (ii) unique physical and chemical features. The ability to tailor surface parameters such as surface geometry, building block size, chemical or physical properties, e.g., optical and electrical properties [6], opens new ways for various and unique applications in many areas of human activity [7], for example, optics, electronics, catalysis, medicine, etc.

The major profit of nanostructured surfaces is attributed to their large effective area, for a particular example see Fig. 1, which can be exceptionally valuable for surface functionalization by, e.g., graft-rich amine ($-NH_2$), hydroxyl ($-OH$), or carboxyl ($-COOH$) functional groups [8]. Such chemically or physically active surfaces enable reactions with surrounding media. For example, the mentioned functional groups allow immobilization of, for example, biomolecules on the surface [9], which is often the key principle for detection. Therefore, the possibility of modifying the surface in these ways provides an opportunity for the development of new sensors, biocell separation methods, biochips, and many other goals [10]. Although there are numerous advantages of nanostructured surfaces [7], the following theoretical introduction will focus primarily on physical and chemical surface

modifications with the possibility of subsequent immobilization of biomolecules, which have application potential in biosensor technology.

Nanostructures for (Bio)Detectors

Nanostructured surfaces that serve as sensor transducers are highly appreciated because of (i) the large effective area, which can significantly increase their sensitivity, and (ii) the possibility of variable functionalization by active chemical grafts (natural, linkers, antibodies, etc.) that improve the sensor selectivity. The following examples of successfully detectable substances illustrate the versatility and great detection potential of nanostructured transducers:

- metabolites and signaling molecules [11],
- proteins [12, 13],
- pathogens [14].

Advances in the research of nanostructured surfaces have led to the development and production of sensors for label-free detection. Such biosensors are highly valuable for fast detection of pathogens during outbreaks or even bioweapon attacks [15] and bring advances in the so-called point of care testing (POCT). For example, a form of electrochemical immunoassay was developed, which can be used as cheap one-use detectors [16]. Another great example is a cheap electrochemical detector for the estimation of glucose concentration in blood [17]. The advantages of such POCT detectors are their usually low cost together with the possibility of being operated by staff without higher professional education, e.g., nurses, laboratory assistants, or even patients themselves. This is another reason to seek new easy-to-use detectors. More attention is also paid to the development of quick diagnostic tools for emergency departments, biodefense, sensors for bacteria resistant to antibiotics, quick diagnostics of central nervous system infections, emerging infections, etc. [18]. The development of simply operable sensors designated for POCT is especially important when it comes to the detection of metabolites and signaling molecules that have low stability and degrade over time [19].

Recently developed polymer materials with active chemical grafts are gaining popularity as promising materials for biosensors, too. Some synthetic antibodies are also polymer-based, for example, iBodies, where polymers serve as a base support to which specific inhibitors together with an affinity

anchor and an imaging probe are attached [20]. As an example of a backbone, N-(2-hydroxypropyl)methacrylamide (HPMA) can be mentioned [21], see Fig. 2. The advantage of HPMA lies in the possibility to be attached to the sensor surface with another material by, for instance, the polyelectrolyte multilayer method [22].

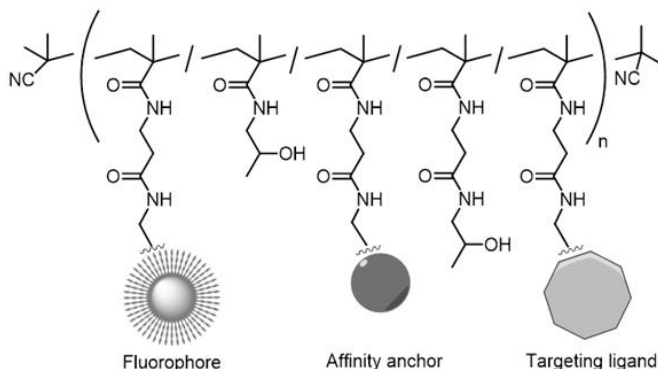


Fig. 2. Schematic structure of iBody [21].

Another approach to sensor development is the usage of optical detection methods, for example, modification of ELISA [23]. This implements an optical fiber with a sensing area covered by an immobilized aptamer or antibody, as shown in Fig. 3. The antibody is immobilized onto the functionalized surface, leading to the formation of a sensing biolayer. Once the specific biomolecule is interacting with the antibody, modulation of the optical signal traveling through the fiber is induced. Any other nonspecific biomolecules presented in the complex matrix will not bind to the receptor of the sensing layer, and thus will not generate any change in the optical signal. It was reported that it is possible to detect the corresponding antigen precisely and quickly, for instance, *Bacillus anthracis* spores [24]. However, a wide range of other applications are available for detection, including pathogens [25] or pesticides [26].

Immobilization of larger macromolecules, such as proteins and enzymes, is also possible and used in sensor techniques [27]. For example, a recombinant cholinesterase for detection and also decontamination of organophosphorous compounds which include chemical warfare agents [28] or microbial enzymes haloalkane dehalogenases (HLDs) can be utilized as a biosensor for the detection of halogenated hydrocarbons (known dangerous pollutants) [29].

Fig. 4 illustrates a concept of biosensors for the monitoring of halogenated hydrocarbons. It is based on an optical fiber with the tip covered by immobilized HLD and a fluorescence pH indicator. The conversion of halogenated hydrocarbons modifies the pH in the vicinity of the sensor, causing a change in the intensity of the detected fluorescence signal [29]. Such a biosensor was successfully applied for the detection of several important halogenated pollutants under laboratory conditions as well as in field trials [30].

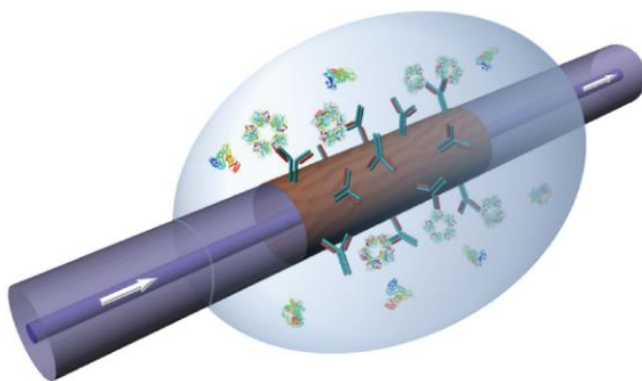


Fig. 3. Schematic illustration of the detection by an optical fiber coated with a functionalized nanostructured overlay [23].

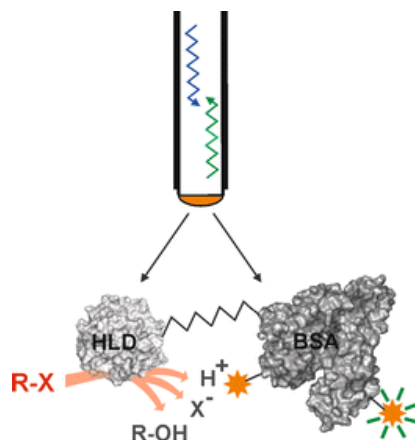


Fig. 4. Fiber-optic biosensor composed of purified enzyme haloalkane dehalogenase (HLD) and fluorescence pH indicator 5(6)-carboxyfluorescein conjugated with bovine serum albumin (BSA) [29].

In addition to a well-adjusted transducer, it is also important to attain efficient binding and grafting of the detected complexes onto the transducer surface.

There are numerous concepts for biocomplex grafting, e.g., covalent bonding, cross-linking, entrapment, microencapsulation, and adsorption [31]. Covalent bonding represents the strongest and most frequently used immobilization method for biosensors. It involves a suitable bond between the attached biomolecule and the functional group at the surface of the sensor. Such functional groups can be present on the surface naturally or can be introduced to the surface using chemical methods. For example, 3-triethoxysilylpropyl succinic anhydride (TESPSA) and aminopropyl-triethoxysilane (APTES) can be used for the introduction of carboxyl (-COOH) and amine (-NH₂) groups, respectively [31-33]. However, as shown in the following chapters, plasma-assisted deposition and plasma surface treatment provide the possibility of producing graft-rich surfaces that might serve as sensor transducers that convert biochemical signals to signals that can be processed by a corresponding measurement device, i.e., optical or electric/electronic signals.

This very brief resume demonstrates that tailoring of functional surfaces opens a large field of possibilities that might be utilized for various detecting and sensing applications. Mentioned literature references confirmed that chemical grafts created on the surfaces, together with their optimized morphology and chemical composition, enable efficient immobilization of biosubstances. This thesis focuses primarily on the development of a complex strategy for the fabrication of highly tailored sensor transducers with multiple interrogation capabilities, sufficient sensitivity, and selectivity for the detection of biomolecules and, e.g., Lyme borreliosis pathogens. The concept of the developed sensor is based on an optical fiber, covered by novel functionalized surfaces, resulting in an advanced type of opto-electrochemical sensor. Practically, the sensor is made of a conventional and commercially available optical fiber, which is coated by a suitable functional thin film by means of low-temperature plasma-assisted deposition.

II. Low-Temperature Plasma-Assisted Deposition of Functional Films

There exists a wide spectrum of methods suitable for the fabrication of nanostructured surfaces. Among wet chemistry, electrochemical deposition, and lithography, plasma-assisted deposition is a promising tool [7]. The low-temperature plasma is an ionized gas that contains charged particles, i.e., electrons, positive and negative ions, and neutral atoms [34]. Due to the unique properties of ionized gases, the low-temperature plasma enables the deposition of novel materials, advanced thin films, and nanostructures [34]. Hence, low-temperature plasma is a well-suited candidate for the deposition of highly tailored and functionalized films serving as sensor transducers.

Despite being in a gaseous state, due to the presence of free charge carriers, the plasma is electrically conductive. For plasma with ion density n_i significantly lower than the density of neutrals n_n , the conductivity σ greatly depends on the plasma ionization degree $\alpha = n_i/(n_i + n_n)$ and is given by equation (1) where e is the elementary charge, $n_e \approx n_i$ is the electron density, τ_e denotes the mean free time of flight of electrons between collisions with atoms, and m_e represents the electron mass [34].

$$\sigma = \frac{e^2 n_e \tau_e}{m_e} \quad (1)$$

The already mentioned equilibria criterion $n_e \approx n_i$ defines another important feature of plasma state: its electrical quasi-neutrality, i.e., the fact that the plasma is electrically neutral in spite of containing free and energetic positive and negative particles. If an external electric field is applied, e.g., stationary charge Q is inserted, the quasi-neutrality of the plasma is disturbed so that particles carrying the opposite charge are attracted to the inserted charge while the particle with the opposite polarity are repelled.

Such behavior results in the shielding effect of the inserted charge and exponential decay of the inserted potential φ with distance r [34] according to equation (2), where φ_0 is the unshielded potential of the inserted charge Q , ϵ_0 is the vacuum permittivity.

$$\varphi(r) = \varphi_0 e^{-\frac{r}{\lambda_D}} = \frac{Q}{4\pi\epsilon_0 r} e^{-\frac{r}{\lambda_D}} \quad (2)$$

The parameter λ_D is called Debye length [34] and is given by equation (3) where k_B is Boltzmann constant, T_e and T_i are the electron and ion temperatures, respectively and Z is the oxidation number of ions.

$$\lambda_D = \sqrt{\frac{\epsilon_0 k_B T_e}{e^2 n_e \left(1 + Z \frac{T_e}{T_i}\right)}} \quad (3)$$

Low-temperature plasma discharges generated in a laboratory are typically electrically driven. Here, a mean kinetic energy E_k of the charged particles is conveniently controlled by an electric field applied between the electrodes, i.e., is determined by an accelerating voltage U , as expressed by equation (4).

$$E_k = \frac{3}{2} k_B T_e = eU \quad (4)$$

It is common to express T_e in eV units (1 eV \cong 11600 K given by the ratio of e/k_B [34]). Charged particles, namely, fast electrons, can carry rather high energies (up to 10 eV per particle) while the total energy of the plasma bulk is low (sometimes characterized by room temperature) [34, 35]. Since the ionization coefficient is rather low ($\alpha < 1$), the majority of particles in the plasma bulk are low-energetic. For this reason, these discharges are called as low-temperature.

However, the energetic species presented in the discharge (electrons, ions, excited species, metastables, radicals, photons, etc.) can initiate physical changes or chemical reactions that can occur only with difficulty or not at all in ordinary chemical processes. Given these benefits, low-temperature plasma is frequently used in different ways for the deposition of thin films or to support the modification of bulk surfaces. Current research has clearly proved that low-temperature plasma is a promising tool for the fabrication of nanostructured surfaces, as well as the introduction of surface functional

groups, such as amine ($-\text{NH}_2$), hydroxyl ($-\text{OH}$), or carboxyl ($-\text{COOH}$) groups [34].

Fig. 5 schematically shows a simple capacitively coupled electrical discharge. It consists of two parallel conducting plates or electrodes placed in a low-pressure environment. Upon applying a breakdown voltage between the electrodes, the gas becomes ionized and forms plasma through the collisions of neutral particles with free electrons accelerated by the electric field. As pointed above, the density of the created plasma is usually small, and only a fraction of the neutral gas atoms/molecules is ionized, i.e., weakly ionized plasma [36, 37].

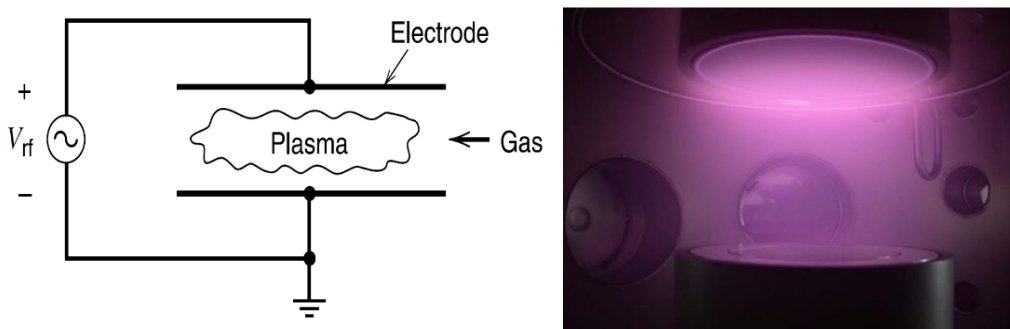


Fig. 5. Left: a simplified discharge scheme [36]. Right: a photo of RF discharge.

Magnetron Sputtering for Deposition of Nanostructured Surfaces

Physical Vapour Deposition (PVD) is the most common plasma-assisted deposition technique. PVD processes typically employ a planar magnetron or hollow cathode sputtering [37]. These sputtering concepts dominate in the PVD of thin films [38]. The magnetron sputtering was used in the frame of this thesis for the deposition of thin films, which, once coated onto an optical fiber core, serves as sensor transducers. For that reason, a detailed description of the magnetron sputtering phenomena follows. Other sputtering techniques can be found elsewhere [34, 36].

The magnetron is a versatile device for the production of plasma and the deposition of thin films. Compared to the former method of diode sputtering, magnetron can be operated at reduced pressure (0.1 – 10 Pa), mitigates film contamination, reduces unwanted substrate heating, and is able to provide higher deposition rates in a typical range of 1-100 nm/min [34]. The basic

principle is sputtering of the cathode made of the material to be deposited (later will be explained that in our case the compound target of ITO was used). The ejected cathode atoms subsequently condense on a substrate, forming a thin film. The magnetron sputtering is used in many fields of application for the preparation of a wide variety of thin films including metal (Ti, Cu, Ag, Au, etc.), metal oxides (TiO_x, ZnO_x, etc.), metal nitrides (TiN_x, ZrN_x, etc.), or even polymers (PFTE, C:H:N:O) [34, 37, 39, 40].

From a technical point of view, the magnetron is a diode sputtering source that implements additional magnets installed behind the sputtering target, see Fig. 6. The magnetic circuit forms a magnetic field (at least locally) parallel to the cathode to form an electron trap $\vec{E} \times \vec{B}$ [34], as shown in Fig. 6. Any particle with charge q and mass m moving with velocity \vec{v} in an electric \vec{E} and a magnetic \vec{B} fields is influenced by Lorentz force according to equation (5).

$$m \frac{d\vec{v}}{dt} = q(\vec{E} + \vec{v} \times \vec{B}) \quad (5)$$

In the case of the magnetron, the electric and magnetic fields are locally perpendicular, which results in drifting of the charged particles in a direction perpendicular to both fields with drifting velocity \vec{v}_D given by equation (6).

$$\vec{v}_D = \frac{\vec{E} \times \vec{B}}{B^2} \quad (6)$$

It is worth noting that drift velocity is charge- and mass-independent and is given solely by electric and magnetic fields. As a result, electrons and ions drift with the same speed and direction. This, together with electron gyration, prolongs the total electron trajectory and therefore increases the probability of ionization [34], see Fig. 6 (left). Hence, the magnetic field enhances the density of electrons in front of the target surface. The enhanced electron density increases the probability of their inelastic collisions with neutral gas atoms (typically Ar), triggering the following reaction $e + \text{Ar} \rightarrow \text{Ar}^+ + e + e$.

Positive ions (Ar⁺), not affected by a rather weak magnetic field, are accelerated toward the cathode, impinging it with the energy gained by the cathode potential fall. The acceleration of impacting ions in the cathodic region is usually sufficient enough to initiate a sputtering of the target atoms.

The production of the Ar^+ is the most intensive in $\vec{E} \perp \vec{B}$ area, which well corresponds with the well-pronounced target erosion area, see Fig. 6. Sputtered atoms condensate on the substrate forming a thin film.

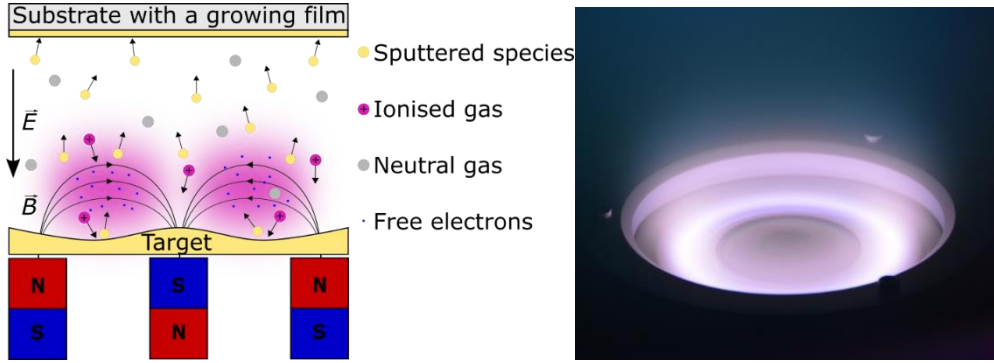


Fig. 6. Left: scheme of a circular planar magnetron. Lines with arrows represent the magnetic field. Right: photo of a magnetron discharge with a visible torus of intensive plasma indicating $\vec{E} \perp \vec{B}$ trap where Ar^+ ions are produced.

Advanced Pulsed Magnetron Sputtering for Tailoring of Film Properties

Magnetrons can be driven by Direct Current (DC), pulsed DC, or Radio Frequency (RF) power which together with the installed magnet assembly makes the $\vec{E} \times \vec{B}$ fields necessary for efficient sputtering [34]. Lately, High-Power Impulse Magnetron Sputtering (HiPIMS), which belongs to the family of High Power Pulsed techniques (HiPPS), has been introduced [41]. This new trend has been widely and intensively explored in the last decade. HiPPS systems are driven in a DC pulse modulated regime operated at low repetition frequency ($f \approx 100$ Hz) and small duty cycle ($T_a/T \approx 1-5$ %) to achieve high power density within a pulse [42]. Here it is worth reminding that very high instantaneous energy is attained in the pulse, while the mean power averaged over a period is about two orders of magnitude lower and comparable to conventional DC sputtering discharges [43]. The HiPIMS discharge typically operates with current densities of up to $3 - 4$ A/cm², a cathode voltage of up to 2000 V, peak power densities in the range of $0.5 - 10$ kW/cm², and the duty cycle in a range of $0.5 - 5$ % [41, 43].

From the experimental point of view, the HiPIMS arrangement is identical to conventional DC magnetron sputtering except for the power supply unit. The

basic scheme of the HiPPS circuit is shown in Fig. 7. Here the DC power supply V_Z feeds the capacity serving as an energy storage. The energy is described by equation (7), where C is the storage capacitance and V_C is the peak voltage on the capacitors [42].

$$E_C = \frac{1}{2}CV_C^2 \quad (7)$$

For this reason, HiPIMS unit requires a large bank of capacitors to store a greater amount of energy that can be released into the discharge once the transistor switch S opens the path for exciting the plasma pulse. The transistor switch is typically controlled by the external TTL trigger signal feeding the transistor base, see Fig. 7. The inductance L is placed in the circuit between the switch S and the cathode to protect the transistor from high current surge, and it also helps to reduce the occurrence of unwanted arcs in the discharge. This is given by the fact that the current I_D , growing at the beginning of the pulse, induces a voltage V_i across the inductor that has orientation opposing the current change, see equation (8) [42].

$$V_i = -\frac{dI_D}{dt}L \quad (8)$$

With this arrangement, the peak power reaches up to several kW within the pulses with frequencies in the range of 50 – 5000 Hz and must be generated by the power supply with average powers around 100 W – 1 kW, having arc suppression [41, 43]. High instantaneous power results in the production of dense plasma with a large fraction of ionized sputtered material [44], significantly higher than in conventional DC magnetron sputtering where the particles sputtered from the target are mostly neutral [43]. For that reason, the HiPPS has become an established technique for ionized physical vapor deposition and has begun to be implemented in industrial applications [43].

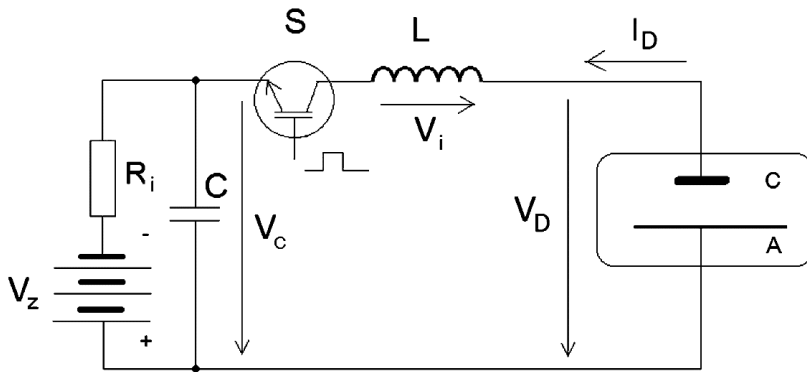


Fig. 7. The very basic schematic of the HiPPS circuit. C – a large bank of capacitors; V_z – DC power supply; V_c – the peak voltage on the capacitors; S – switching transistor; L – inductance; V_i – induced voltage; I_D – discharge current; V_D – voltage in the pulse; C – cathode; A – anode. The opening and closing of the switch are usually controlled by a TTL generator [42].

The high fraction of ionized sputtered species is proportional to the electron density and the electron temperature, as both factors increase the probability of ionization [42]. In other words, the intensive HiPIMS discharges with high electron density can reach a high fraction of sputtered atom ionization. The level of sputtered atom ionization was reported to be in the range of about 10 – 90 % with higher values for pressures < 2.0 Pa and higher discharge peak current densities, only weakly depending on the sputtered material. It is worth reminding that in DC magnetron discharges the ionization fraction is usually < 1 % [42]. An enhanced ionization degree of the sputtered vapor is desirable because the ion flux to the substrate usually improves the quality of the growing film. Therefore, the ionization fraction is another parameter that enables control of the properties of the deposition process and the thin film properties. Depending on the sputtered material, HiPIMS can bring several advantages to the growth and formation of the thin film:

- surface roughness [43, 45],
- higher density [43, 45, 46],
- controllable crystallography [43, 47],
- changes in phase composition [46, 47],
- improvements in microstructural properties [43, 45, 46],
- higher hardness [43],
- improved adhesion [43, 45, 46].

In summary, the HiPIMS deposition system provides a wider spectrum of tunable control parameters compared to conventional DC and RF modes, e.g., pulse frequency, pulse width, and duty cycle, which play a role in the formation of the growing film. This represents significant advantages for the deposition of highly tailored thin films that need to be optimized for particular applications, e.g., for sensing and detection.

However, PVD methods allow the deposition of not only metal-based films but also plasma polymers. Typically, RF sputtering of polymeric materials in inert gas or its own fragmented polymer vapors is used [48]. An example of the polymer prepared by magnetron sputtering is depicted in Fig. 8. Furthermore, amino-rich coatings were prepared by sputtering of nylon in reactive Ar/N₂ and N₂/H₂ atmosphere [40].

Optimized input parameters and experimental conditions of the PVD process allow tailoring of film properties and surface morphology. For example, it has been reported that HiPIMS preferentially produces dense and homogeneous films [43, 45, 46]. Additionally, in the case of plasma polymers, smooth or nanostructured surfaces may both be produced depending on the actual process parameters [49]. Since surface morphology influences biological processes, including protein adsorption, cell behavior, blood-contacting properties, and bacterial adhesion, the possibility of depositing nanostructured films is of great importance for biosensing [50].

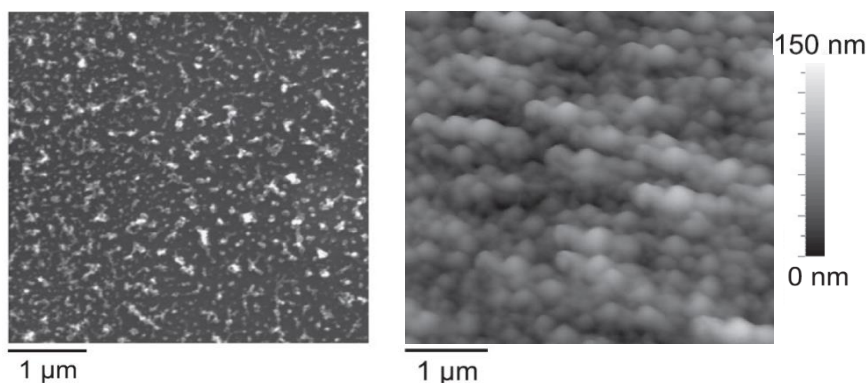


Fig. 8. SEM image (left) and AFM image (right) of superhydrophobic nanostructured fluorocarbon plasma polymer film prepared by RF sputtering of PTFE target at high pressure [39].

An alternative to continuous films is metal nanoparticles, that is, aggregates of atoms on the size scale of 10–100 nm. The plasma-based technologies allow

the formation of different metal nanoparticles (e.g., Cu, Ti, Pt, Si, Ag, Co, Au [51, 52]) and nanocomposites consisting of metal nanoparticles [5]. Besides it, plasma polymerization of nanoparticles produced by gas aggregation in the Ar/n-hexane atmosphere was presented [53]. By input process parameters, the amount of the metal in a film, i.e., the filling factor, can be controlled to tailor its electrical and optical properties [54].

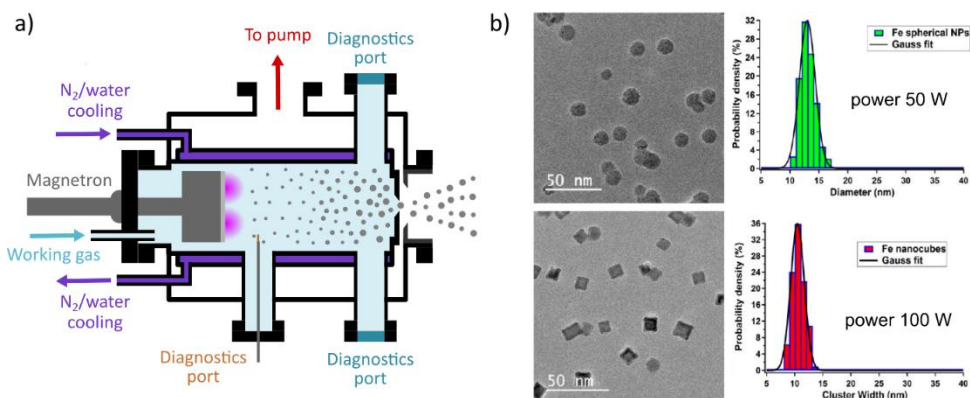


Fig. 9. a) Scheme of nanoparticle source, b) example of deposition Fe nanoparticles with different shapes in dependence on deposition conditions [55].

Fig. 9 shows a scheme of nanoparticle source and examples of the production of Fe nanoparticles with different shapes depending on deposition conditions [55]. It has already been reported that the size of formed nanoparticles can be effectively controlled by pulsed sputtering [51] or by pulsed gas delivery [56]. Isolated nanoparticles deposited onto the substrate can further serve as pre-seeds of nanostructured surfaces such as columnar or spiral structures or helical nanorods [57, 58].

In conclusion, low-temperature plasma offers a variety of methods suitable for the preparation of nanostructured surfaces. Such surfaces have great potential for biosensing applications. However, the development of any surface with optimal properties is a challenging process because of a great variety of deposition parameters that play a role in the final properties of the prepared film. Therefore, the key factor for the production of any nanostructured material is a detailed understanding of the film formation process. For the

above reasons, PVD methods were used within the frame of this thesis for the fabrication of nanostructured surfaces for biosensing applications.

III. Nanostructured Functional Surfaces for Biosensing Applications

Nanostructured films can be utilized as active surfaces for sensor transducers. This thesis pays attention primarily to applications for biosensors whose efficiency (sensitivity, selectivity, and cross-verification of the detection) can be boosted by properly tailored nanodesigned surfaces.

This chapter explains the basic concept of the sensor which enables simultaneous optical and electrochemical interrogation of an analyte and which was developed in the framework of the thesis. The attention is focused on detection methods based on optical signal modulation that occurs upon the interaction of electromagnetic waves with a properly tailored functional nanostructure; the mechanism of a transducer for analyte interrogation.

The concept of surface plasmon resonance (SPR) and its more advanced derivative localized surface plasmon resonance (LSPR) are discussed. However, the core topic is a recently discovered optical phenomenon of lossy mode resonance (LMR) that resembles the previous two from the practical point of view, even though it is different principally.

Furthermore, the electrochemical domain of interrogation will be introduced, followed by its integration into lossy-mode resonance measurements. The merging of the two principles results in the opto-electrochemical sensor for the detection of biomolecules and pathogens.

Optical Interrogation: Refractometry for Detection

Surface Plasmon Resonance

Surface plasmon resonance (SPR) is a well-known phenomenon for the detection of a wide family of compounds, including biocomplexes [59]. SPR was first introduced as a detection method in the late 70s of the last century. This technique is based on the detection of changes in the refractive index (RI) in the vicinity of the sensor surface [59]. The sensor body needs to be made of an optically transparent substrate which is covered by a thin metal film (typically silver or gold) that serves as a reflection film for the light passing through the substrate. At specific angles of incidence, a part of the light power couples through the conductive film, where it creates a surface plasmon wave

(SPW) propagating at the boundary between the external medium and the metallic film [59]. The SPW must be TM polarized (Transverse Magnetic; the magnetic vector is perpendicular to the direction of the surface plasma wave propagation and parallel to the plane of the interface) [60]. The incident light angle at which the SPW is generated is strongly influenced by the surrounding refractive index.

Since the refractive index depends on the chemical composition of the analyte, the association of biomolecules at the sensor surface induces substantial local changes in the refractive index, and therefore it can be easily detected. Since the 80s, SPR-based sensors have become familiar in science and are widely used for gas detection and biosensing [61, 62]. This brief overview of the physical principle of the SPR measurement represents a short but necessary introduction to more advanced light modulation techniques and detection concepts, namely, localized surface plasmon resonance (LSPR) and more importantly lossy mode resonance (LMR) that represents the optical detection domain of the sensor developed in the frame of this thesis.

Localized Surface Plasmon Resonance

Although SPR is an effective detection method, its efficiency can be improved by implementing a nanostructured metal film instead of a homogeneous film. The employment of metal nanostructures, such as nanoparticles or nanoislands, leads to a phenomenon known as Localized Surface Plasmon Resonance (LSPR). LSPR is based on the interaction of light with plasmons of separated conductive nanoparticles, with a size smaller than the light wavelength, immersed in a matrix of a dielectric material [63, 64]. Because of nanoparticle separation, the continuous electron bands, which are typical for regular homogeneous conductors, become discrete, and the usual SPR effect starts to be strongly influenced by the nanoparticle size. The electric field of light shifts the conductive electrons in the nanoparticles against the positively charged core, which causes repulsive interaction. This principal effect results in electron cloud oscillations at a specified resonance frequency. Conducting oscillating electrons induces a surface wave (see Fig. 10 a) that leads to accumulation of polarization charges on the nanoparticle surface [64-67]. This phenomenon causes anomalous optical absorption [68]. Nanoparticles proved to be very effective and sensitive transducers for even small changes in the

local refractive index because of their enormously strong and highly localized electromagnetic fields stimulated by LSPR. This is also the main advantage of LSPR when compared to standard SPR. It is also important that the sensitivity of the sensor can be tuned by the shape or size of the nanoparticles.

From a general point of view, there are two families of LSPR-based sensors [69]:

1. refractive index sensors,
2. aggregation sensors.

The refractive index-based LSPR sensors have been briefly explained above. The redshift of the LSPR spectrum is induced by a change in the refractive index in the vicinity of the metal nanoparticles. Local refractive index changes can result from, e.g., the presence of biomolecules or their specific interaction with the surrounding media. The shift in the LSPR spectrum, caused by the immobilization of biomolecules on the active surface of the sensor, can be measured by UV-VIS spectrophotometry; see Fig. 10 b) and c) [68].

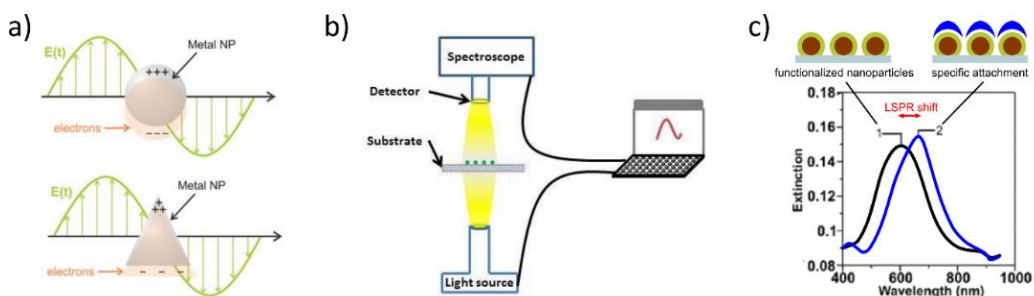


Fig. 10. a) Scheme of LSPR in nanoparticles with different shapes [68]. b) One of the possible experimental settings for the measurement of LSPR optical spectroscopy [70]. c) Example of LSPR spectra before and after specific binding of biomolecules [71].

The aggregation LSPR sensors are based on the fact that the LSPR spectrum is also influenced by the shape and size of the nanoparticles and their relative distance. When some of these parameters are altered, the color change of the film can be induced. For instance, when the distance between two particles of the film can be induced. For instance, when the distance between two particles of the metal decreases below the particle diameter, their resonance peak redshifts because of the interaction of their electric fields. Thus, through biochemical interactions, properly biofunctionalized nanoparticles can aggregate, resulting in a color change that indicates the presence of the interaction [69].

It could be deduced from the previous part that, for applicable LSPR sensors, it is crucial to have functionalized nanoparticles for their ability to respond to the presence of searched substances [69]. However, the situation can be more complicated in the case of nanoparticles than in the case of continuous film. For instance, amino groups may negatively affect the colloidal stability of some nanoparticles because of induced oxidation [72]. The spectrum of biomolecules that can be detected in a label-free approach is determined by the choice of a suitable binding strategy of the transducer. For example, LSPR was used in bioassays for the detection of heparin [73], glucose [74], dipicolinic acid [75], lactate [76], pathogenic bacteria *Salmonella typhimurium* and *Escherichia coli* [77], etc.

As shown in the previous part, plasma provides the possibility to deposit nanostructured surfaces suitable for both SPR-based and LSPR-based biosensors. In addition to the deposition of a sensor nanostructure onto a flat prism, it is also possible to coat different shapes and objects such as optical fibers. Generally, compared with the prism-based detection systems, the optical fiber-based sensor provides many benefits: simplified and flexible design, possibility of remote sensing, continuous analysis, in situ monitoring, etc. [78, 79], see Fig. 11. The optical fiber-based LSPR sensors were already used for the detection of more than a dozen proteins and a similar amount of toxins [80]. It was theoretically [78] and experimentally [81] shown that for the Indium Tin Oxide (ITO) matrix with metallic nanoparticles (Au, Ag, Cu), the maximum sensitivity occurs for a 60 nm thick layer with fixed 20 nm particle size. These properties of films and nanoparticles match well with the deposition capabilities of low temperature plasma deposition techniques [34, 51, 82]. Another reason to use plasma coating methods is their capability to deposit structures with grafts, e.g., amine and carboxyl groups [83, 40], for immobilization of biomolecules, e.g., antibodies that consequently react with the searched antigens.

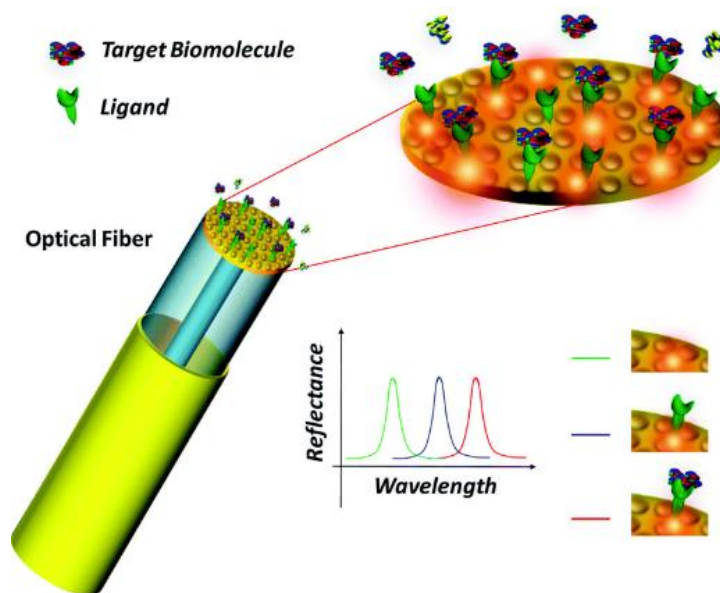


Fig. 11. Schematic of a possible approach for the optical fiber-based biosensor demonstrating the utility of optical fibers for detection [84].

Lossy-Mode Resonance

Another principle based on the nanostructured and functionalized surface is Lossy-Mode Resonance (LMR). This recently developed method can be considered, together with SPR and LSPR, as highly sensitive refractometry. However, LMR-based sensors avoid the basic limitations typical for SPR and LSPR sensors:

- utilization of plasmonic and usually noble metals (Au, Ag),
- necessity of optical polarizers to observe the resonance effect [85].

The LMR is based on attenuation of particular wavelengths of the incident light propagated in the high-refractive-index layer of a certain thickness deposited onto a transparent substrate. This phenomenon is caused by a coupling between waveguide modes in the substrate and specific lossy modes propagated in the thin film [59]. This effect was observed for a wide number of thin film materials, e.g., ITO, TiO₂, In₂O₃ [86], poly(allylamine hydrochloride) (PAH) and poly(acrylic acid) (PAA) [87] ZnO, etc. [88].

For the first time, Del Villar et al. [89] proposed the LMR phenomenon for optical fiber-based sensing applications in 2010. In the design of a sensing probe, the substrate, i.e., the optical fiber core, and deposited thin film material

are the main factors that determine LMR. The optical fiber can be considered as a suitable substrate primarily for its small size, wide range of operating temperature, remote sensing capability, multiplexing capability, and immunity to electromagnetic interference [59]. Although LMR is similar to the phenomenon of SPR, the generation of surface plasmon waves leading to SPR and lossy modes leading to LMR requires the fulfillment of completely different material conditions of the thin film [59].

The necessary condition to guide lossy modes lies in the real part of the electric permittivity of the coated film, which practically serves as a sensor transducer. The permittivity of any material is expressed by equation (9) where ε' and ε'' are its real and imaginary parts, respectively [59].

$$\varepsilon = \varepsilon' + i\varepsilon'' \quad (9)$$

Depending on the generated resonance phenomena, the materials for the thin film, i.e., transducer, can be classified into two categories. LMR can occur if the real part of permittivity ε' is positive, while the SPR can occur if the real part of thin film permittivity is negative. In both cases, ε' of the film have to be higher in magnitude than both its own imaginary part ε'' and the permittivity of the external medium ε_s [86].

Complex refractive index N is often a more convenient parameter for the description of key material conditions for LMR. It can be estimated using equation (10) where n and k denote the real and imaginary parts of the refractive index, respectively, $\varepsilon_r = \varepsilon/\varepsilon_0$ and $\mu_r = \mu/\mu_0$ are relative permittivity and relative permeability, respectively, μ represents permeability, and ε_0 and μ_0 are vacuum permittivity and vacuum permeability, respectively [90, 91].

$$N = n + ik = \sqrt{\varepsilon_r \mu_r} = \sqrt{\frac{\varepsilon}{\varepsilon_0} \frac{\mu}{\mu_0}} \quad (10)$$

For materials that are nonmagnetic at optical frequencies, i.e., $\mu_r = 1$ and $N = \sqrt{\varepsilon_r}$, real and imaginary parts of permittivity can be obtained through equations (11) and (12) [91].

$$\varepsilon' = (n^2 + k^2)\varepsilon_0 \quad (11)$$

$$\varepsilon'' = 2nk\varepsilon_0 \quad (12)$$

From the permittivity values ε' and ε'' the values of n and k can be retrospectively determined by equations (13) and (14).

$$n = \sqrt{\frac{|\varepsilon| + \varepsilon'}{2\varepsilon_0}} \quad (13)$$

$$k = \sqrt{\frac{|\varepsilon| - \varepsilon'}{2\varepsilon_0}} \quad (14)$$

In the above equations, $|\varepsilon| = \sqrt{\varepsilon'^2 + \varepsilon''^2}$ is a complex modulus of ε . Relations (13) and (14) enable formulation of the material conditions for the generation of SPR and LMR in terms of refractive index. Essentially, n has to be relatively high, and k needs to be relatively low compared to n for LMR generation.

Table 1 defines the different material conditions needed for the generation of SPR and LMR in terms of permittivity ε and refractive index N for any surrounding medium characterized by its permittivity ε_s or refractive index N_s . To highlight the principal differences, see Fig. 12, where the LMR and SPR corresponding regions k vs. n are shown. Note that the graph considers a film deposited on silica substrate with $n_s = 1.45$ for its stable value across a wide range of optical spectra, and that the film was surrounded by air [85].

Table 1. LMR and SPR generating conditions [59, 85].

Resonance type	Resonance conditions in terms of permittivity $\epsilon = \epsilon' + i\epsilon''$	Resonance conditions in terms of refractive index $N = n + ik$	Suitable materials for thin film
SPR	$\epsilon' < 0$ $ \epsilon' > \epsilon'' $ $ \epsilon' > \epsilon'_s $	$k > n$ $k > (\sqrt{2} + 1)n$ $k^2 - n^2 > n_s^2$	metals, semiconductors
LMR	$\epsilon' > 0$ $ \epsilon' > \epsilon'' $ $ \epsilon' > \epsilon'_s $	$k < n$ $k < (\sqrt{2} - 1)n$ $n^2 - k^2 > n_s^2$	polymers, semiconductors, dielectrics, etc.

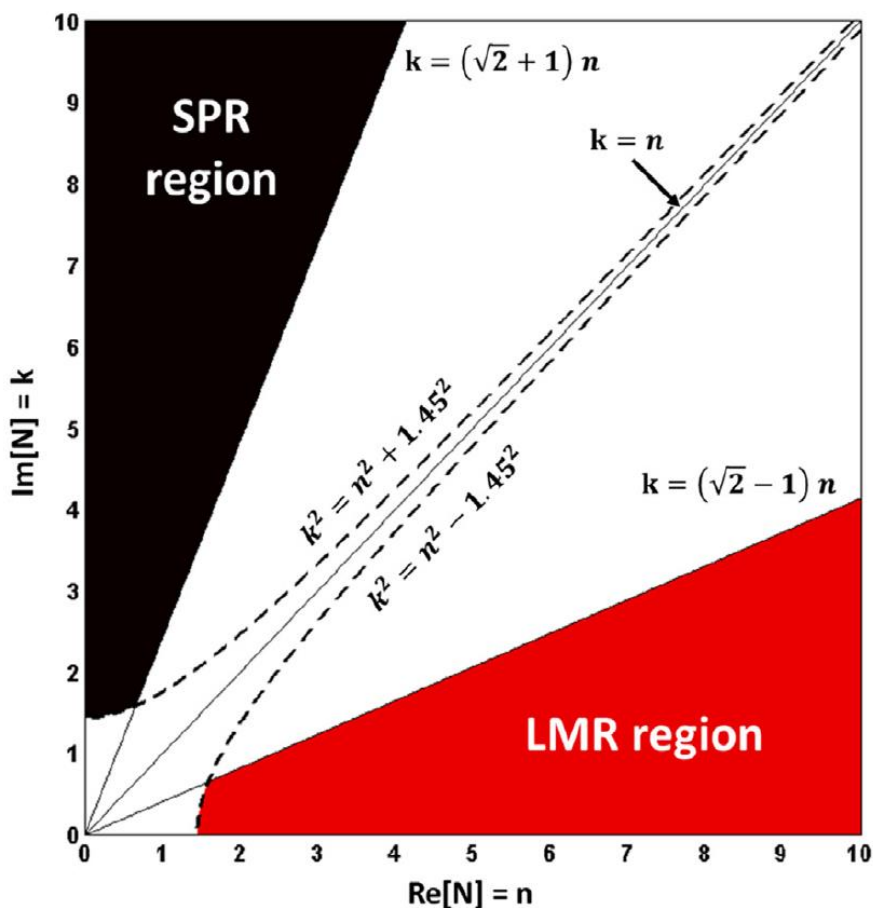


Fig. 12. Visualisation of LMR and SPR conditions in terms of refractive index for substrate with $n_s = 1.45$ [85].

Similarly to the SPR, the phenomenon of LMR emerges as a substrate coated by a thin film made of suitable materials is immersed in dielectric media of higher refractive index (RI). Such conditions can induce a number of modes called ‘lossy modes’ or ‘long-range guided modes’, which are channeled in the thin film. Such lossy modes can be produced with both TE and TM polarized light [59, 86, 92, 93].

A detailed mode analysis was reported and showed that if the thickness of the thin film is increased, lossy modes cross the cutoff condition and start guiding in the thin film, leaving the core of the fiber [94-96]. The coupling between a specific lossy mode guided within the thin film and a waveguide mode is determined by the film thickness. The coupling requires to fulfill two conditions: (i) overlapping of mode fields and (ii) phase matching. To achieve these conditions, the real parts of the waveguide mode and lossy-mode propagation constants need to be equal.

To deeper understand the LMR phenomenon, the evolution of modal effective index can be analyzed in the form of an evanescent wave given by equation (15), where n_s is the refractive index of the glass substrate (e.g., the optical fiber core) and θ_i is the incidence angle of the light [59].

$$n_{\text{eff}} = n_s \sin\theta_i \quad (15)$$

As the evanescent field propagates through a low refractive index medium in the direction of the y-axis, it is subjected to an exponential decay, as shown by equation (16), where ω is the angular frequency of the light, $k_{iz} = k_i \sin\theta$ is an interface plane projection of the wave vector k_i of the reflected wave, see also Fig. 13 [90].

$$E(y, z, t) \propto e^{-\alpha y} e^{i(\omega t - k_{iz} z)} \quad (16)$$

The parameter α is an attenuation coefficient given by equation (17) with condition that $n_1 > n_2$ where n_1 and n_2 represent the refractive indices of the materials forming the interface in Fig. 13 [90].

$$\alpha = \frac{2\pi n_2}{\lambda} \sqrt{\left(\frac{n_1}{n_2}\right)^2 \sin^2 \theta_i - 1} \quad (17)$$

The reverse value of the attenuation coefficient is the penetration depth $\delta = 1/\alpha$ at which the field of the evanescent wave is decreased by a factor of e. The penetration depth is then described by equation (18).

$$\delta = \frac{\lambda}{2\pi\sqrt{n_{1\text{eff}}^2 - n_2^2}} \quad (18)$$

Equations (15) to (18) show that the effective index and the evanescent wave can be modified by changing either the incident light wavelength or its incidence angle. At particular wavelengths and incidence angles, the effective index of lossy modes and the evanescent wave match. As a consequence, the coupling between the lossy modes and the evanescent wave reaches a maximum, enabling effective power transfer between the two materials. For a particular thickness of the thin film, the LMR phenomenon is generated as a consequence of this coupling, causing attenuation dips in the transmission spectra [59].

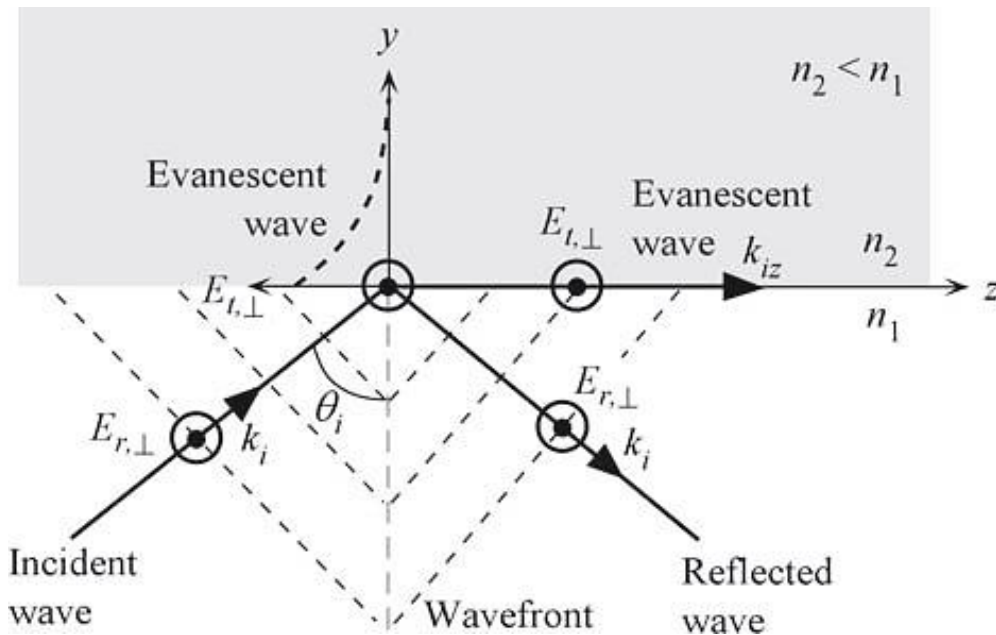


Fig. 13. Evanescent wave propagation through the low-refractive-index material upon reflection of a plane wave with an incidence angle exceeding the critical angle [90].

The basic principle of LMR can also be illustrated by the well-known *Kretschmann-Reather configuration*, as shown in Fig. 14. The Kretschmann configuration is the most prevalent attenuated total reflection (ATR) method for coupling of the modes guided in the thin film coated on a prism surface and the waveguide mode [97]. A light entering into the prism bulk, incident with an angle greater than the ATR angle, causes a generation of the evanescent wave at the interface between the prism and the film.

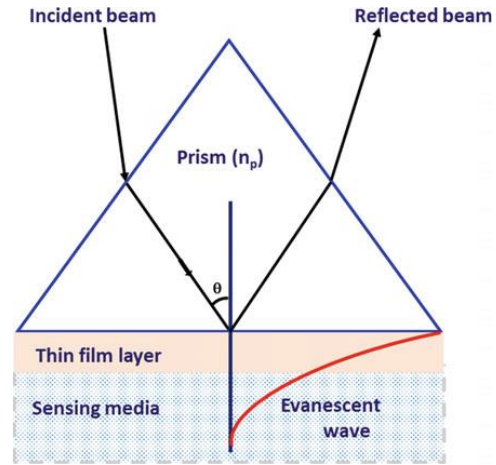


Fig. 14. Kretschmann configuration [59].

The coupling between the lossy modes in the thin film and the evanescent wave occurs under phase matching and mode field overlapping conditions, resulting in the LMR phenomenon. If sufficient coupling between the thin film modes and an evanescent wave exists, the energy from the waveguide modes can be transferred to the lossy modes, leading to an intensity dip of the reflected light. This dip in the normalized reflected power occurs at a particular light wavelength or angle of incidence, see Fig. 15. These specific wavelength and angle values are termed resonance wavelength (λ_{res}) and resonance angle (θ_{res}), respectively [59].

LMR Based Sensing: Principles and Practice

The lossy mode resonance sensing can be in principle based on either angular or wavelength interrogation. The angular interrogation is performed by reflectance measurement of the prism-film interface utilizing various incidence angles of the light with a fixed wavelength. In this configuration, the reflectance reaches the minimum at the resonance angle (θ_{res}). The resonance angle is generally sensitive to the surrounding medium refractive index changes. Vice-versa, knowing the thickness and dielectric constant of the film, the dielectric constant of the surrounding medium can be estimated [59]. Alternatively, wavelength interrogation is performed by

measuring the reflectance of prism-film interface utilizing various incidence light wavelengths with the angle of incidence fixed. For wavelength interrogation, a broadband light source is typically used for the production of the incidence light beam. The specific wavelength, at which the minimum reflectance is measured, is the lossy mode resonance wavelength (λ_{res}) [59].

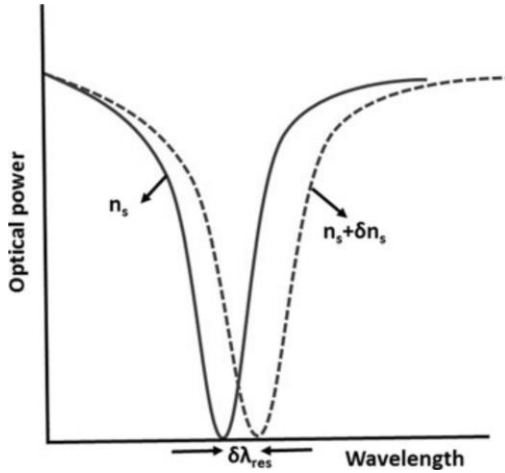


Fig. 15. Shift of the reflection spectra caused by a change of the surrounding medium refractive index from n_s to $n_s + \delta n_s$ [59].

The detection usability of an LMR-based sensor is determined by its sensitivity and detection accuracy. In an ideal case, the LMR sensor would have both high sensitivity as well as high detection accuracy. The shift of the resonance dip with the refractive index change of the surrounding media determines the sensitivity of the LMR sensor. It means that the larger shift in the resonance angle or wavelength, the better sensitivity the LMR sensor provides.

The reflectance curves for two surrounding medium refractive indices, n_s and $n_s + \delta n_s$ are shown in Fig. 15. These curves can be used to determine the θ_{res} or λ_{res} . The sensitivity can be then determined for the two techniques by formulas (19) and (20) [59].

$$S_{\theta} = \frac{\delta \theta_{\text{res}}}{\delta n_s} \quad (\text{angular interrogation sensitivity}) \quad (19)$$

$$S_{\lambda} = \frac{\delta \lambda_{\text{res}}}{\delta n_s} \quad (\text{wavelength interrogation sensitivity}) \quad (20)$$

The detection accuracy (DA) of an LMR sensor is defined by its ability to determine the value of the resonance position precisely. Therefore, higher accuracy enables the determination of the unknown surrounding medium refractive index more precisely. Accuracy of detection is inversely proportional to the full width at half maximum ($FWHM$) of the LMR dip. For

that reason, a narrower resonance dip provides a higher level of measurement precision [59].

From the sensitivity and detection accuracy, a figure of merit (*FOM*) can be determined by equation (21), where *S* is the sensitivity of the interrogation described by equations (19) and (20). The higher is the value of *FOM*, the better is the performance of the sensor [98].

$$FOM = \frac{S}{FWHM} = S \cdot DA \quad (21)$$

These two parameters of an LMR-based sensor, i.e., sensitivity S_θ , S_λ and accuracy *DA*, is highly influenced by properties of the deposited thin film in which the lossy modes are guided. For example, as shown by Del Villar et al. [86], the sensitivity to changes in the surrounding refractive index can be greatly increased by tuning the thickness of the film or its refractive index. Although the higher orders of resonance are less affected by these changes, they are still substantial, see Fig. 16. Hence, the proper selection and design of thin-film material, its thickness, and optimization of the deposition procedure seem to be crucial in the fabrication of the LMR sensor.

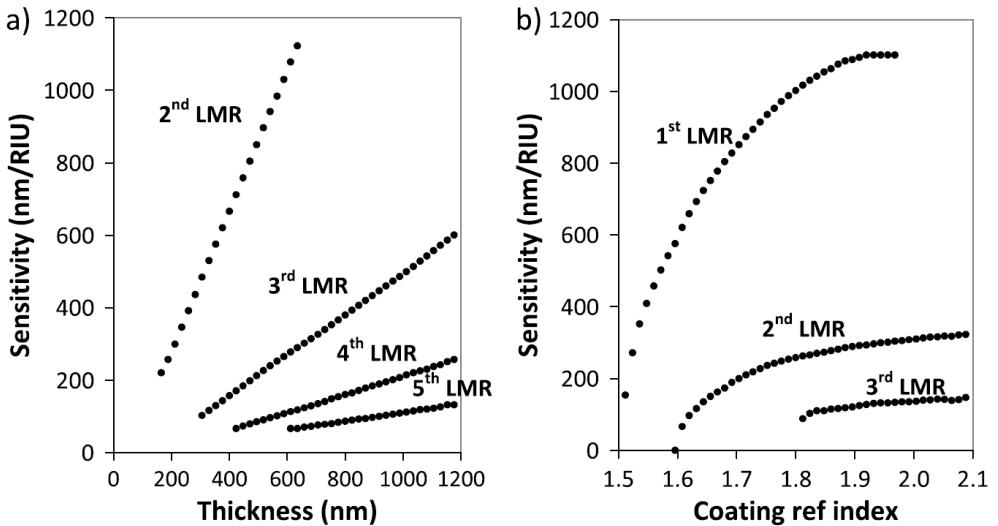


Fig. 16. Variation of sensitivity to changes of the surrounding refractive index depending on (a) thickness and (b) refractive index of the thin film [86].

Major advantages of LMR against the SPR/LSPR based devices are:

1. LMR does not require a specific polarization of light and can be generated with both transverse electric (TE) and transverse magnetic (TM) polarized light, though, the LMR spectra of the two light polarizations may differ, depending on the sensor geometry [99]. SPR phenomenon can be generated only by TM polarized light [59, 86, 92, 93].
2. LMR is supported by a significantly wider variety of materials that fulfill the conditions mentioned in Table 1. Hence, expensive plasmonic metals such as silver and gold in the case of SPR are not required [87, 100-102].
3. Multiple LMR attenuation dips can be generated in the transmittance spectra by increasing the film thickness. In the same manner, LMR sensor sensitivity is optimizable by tailoring the properties of the transducer, i.e., the film [59, 86, 103, 104].

From the practical point of view, the fabrication of the LMR sensor is less complicated; the core of the optical fiber is coated with a thin film made of LMR suitable material. Practically, there exist families of polymers, semiconductors, and dielectrics that are promising candidates for LMR-responding materials. Typically, TiO_2 [100] is one of the most frequently used plasma deposited materials [105] that fulfills the criteria for the LMR propagation. Other suitable materials are indium oxide (In_2O_3) [101] or polymers, e.g., poly(allylamine hydrochloride) (PAH) and poly(acrylic acid) (PAA) [87, 102]. Indium Tin Oxide (ITO) is another LMR-suitable material that was first used for LMR sensors [59] and is still used. ITO-based LMR sensors have been already employed for successful detection of different biosubstances such as isatin [106], immunoglobulin [107], thrombin [108]. Because of its advantages, ITO was employed also for the investigation carried out in this thesis.

ITO for the Fabrication of LMR Sensor

The tailoring of the properties of the coating film, which serves as a transducer for efficient detection of biomolecules and pathogens such as Lyme borreliosis, is the main motivation and objective of this thesis. It will be shown later that low-temperature plasma-assisted deposition has been employed for

the preparation of a highly tailored indium tin oxide (ITO) thin film onto an optical fiber core to fabricate the ITO-LMR sensor. The ITO-LMR provides the optical domain of interrogation.

Indium doped tin oxide (ITO) is an optically transparent, chemically stable, and electrically conductive oxide. It is a ternary compound, with varying stoichiometry, with the contribution of indium, tin, and oxygen. It can either be considered as a ceramic or alloy, depending on the oxygen content. ITO with ratio $\text{In}_2\text{O}_3/\text{SnO}_2$ 90/10 is one of the most widely used compounds in the thin film industry, having a melting point at 1800 °C and a density of 7.14 g/cm³ [109]. Depending on the chemical composition and physical properties, the color of ITO ranges from dark green or dark gray to pale yellow with different levels of transparency [109].

Besides promising LMR properties, a large application potential of ITO is determined by its electrical conductivity and optical transparency in the visible range; for these properties, ITO belongs to a family of transparent conductive oxides together with, e.g., F-doped SnO_2 (FTO) [110], ZnO [111], Al-doped ZnO (AZO) [112], etc. The unique optical properties of ITO are given by its relatively large band gap of about 3.5 - 4.3 eV [113] which well corresponds to the energy of visible light. Therefore, it is mostly transparent in a range of wavelengths from about 400 to 1000 nm with extinction coefficient k values close to zero [114]. On the other hand, the ITO is opaque for the ultraviolet (UV) spectral range of the light and for the near-infrared (NIR) and infrared (IR) range of spectra, so the extinction coefficient $k \neq 0$ in the UV, NIR, and IR [114]. The opacity in the UV range is a result of band-to-band absorption when electrons in the valence band are excited to the conduction band. NIR and IR absorption is caused by the presence of free charge carriers (electrons in lower energetic states within the conduction band) which can be excited to higher energetic states. The behavior of ITO is similar to that of metals in the NIR and IR wavelength range where the absorption coefficient reaches its maximum value [114].

Electrically, ITO is an n-type semiconductor. The low resistivity of ITO is associated with two effects: (i) presence of donors or impurities providing energetic states close to the conduction band of the host matrix (In_2O_3) formed by chemical doping of Sn^{4+} into In^{3+} [115], (ii) vacancies caused by the

absence of oxygen. Such oxygen vacancies, if present in the lattice, act as doubly charged donors. On the other hand, it should be noted that oxygen vacancies increase optical absorption [115].

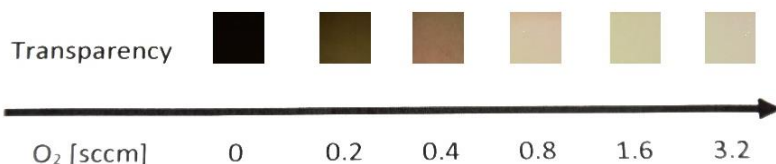


Fig. 17. Influence of O_2 on the optical transparency and color of ITO films with identical thickness 350 nm against a white background. Ar flow was 100 sccm, pressure 0.5 Pa, RF sputtering (done in a frame of the Ph.D. thesis).

For sensing applications, the ITO thin film can be prepared by reactive magnetron sputtering [116]. Then the ITO properties can be easily modified by optimization of deposition conditions such as process gas flow rates and composition (see Fig. 17), sputtering power, energy flux toward the substrate, annealing, deposition forwarded power, etc. [85, 86]. ITO was the first LMR-promoting material investigated by *Del Villar* and his group [59]. An example of the ITO dispersion curves is shown in Fig. 18 [89, 117]. It demonstrates that ITO is a suitable material for LMR generation in the visible range, while it is also suitable for SPR generation in the IR range; compare with the conditions in Table 1. Moreover, it has already been proved that ITO-based humidity [102] and pH [87] LMR sensors display sensitivity similar to that of SPR-based devices.

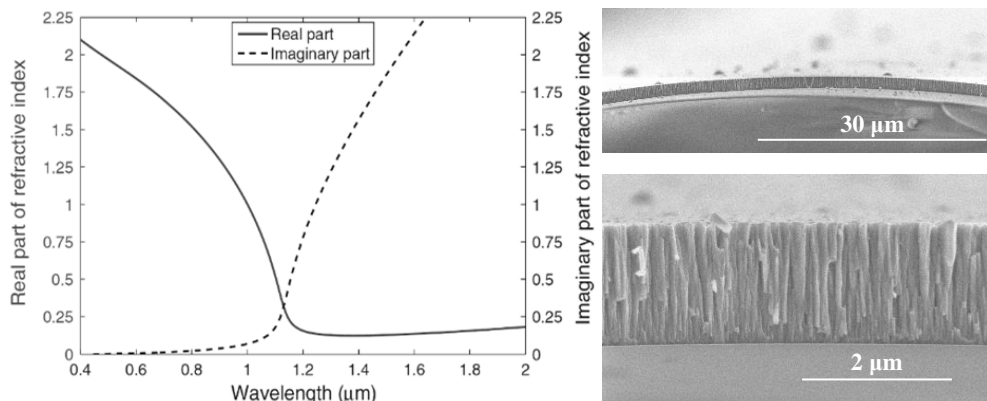


Fig. 18. Left: ITO dispersion curves [59]. Right: SEM cross-section image of an optical fiber with ITO film deposited by magnetron sputtering (done in a frame of the Ph.D. thesis).

The wavelength interrogation is the most commonly used method in LMR fiber sensing because multiple reflections occur from the fiber core. All light rays undergo total internal reflection at the fiber-cladding interface if their corresponding incidence angles are greater than the critical angle. Consequently, the evanescent wave is generated and, under the previously mentioned conditions, enables the coupling of the transition modes with the modes in the thin (ITO) film. The critical angle θ_{cr} is determined by the wavelength of light and by the numerical aperture (NA) of the fiber or by the light acceptance angle γ_{max} as given by equation (22), where n_{air} , n_{core} , and $n_{cladding}$, are refractive indices of air, fiber core, and fiber cladding, respectively [59].

$$NA = n_{air} \sin \gamma_{max} = n_{core} \cos \theta_{cr} = \sqrt{n_{core}^2 - n_{cladding}^2} \quad (22)$$

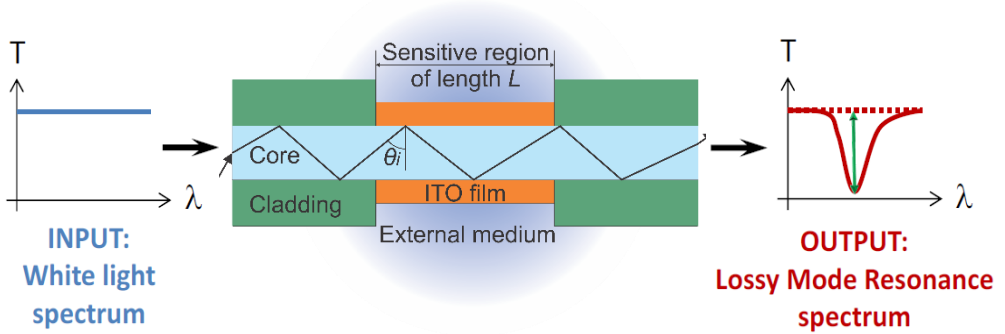


Fig. 19. Scheme of an optical fiber-based LMR sensor. Part of the cladding is removed and replaced by a thin ITO film with tailored properties. The light ray propagates along the fiber core axis by the total reflection principle. The LMR phenomenon results in the modulation of the signal and the presence of the attenuation band in the output spectrum.

There exist cutoff conditions at which the attenuation reaches maximum. It was shown in some previous studies [118] that the cutoff effect is determined by the film thickness and can be tailored in this way. However, the generation of LMR is also possible by introducing broadband spectra into the optical fiber and observing the cutoff at a specific wavelength. The basic principle of this sensor is illustrated in Fig. 19. Practically, a broadband light source is connected at one end of the fiber. The light passes through the fiber core without any noteworthy attenuation up to the detection region where the thin

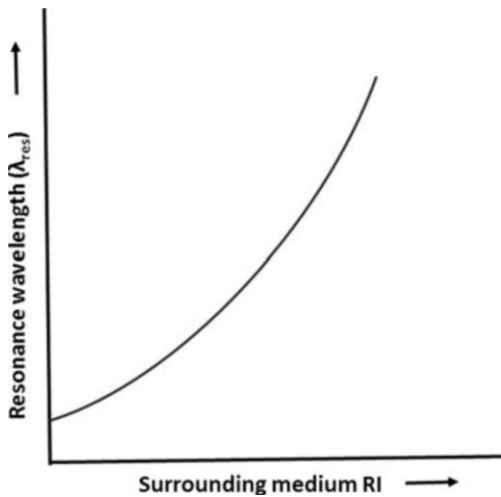


Fig. 20. The LMR calibration curve illustrates the shift of the resonance wavelength with the change of the surrounding medium RI, i.e., of the analyte [59].

LMR-supporting film is deposited onto the uncladded core, see Fig. 19. At the detection region, the passing light is modulated, as part of the transmitted power is transferred into the thin film, where it is propagated in the form of the lossy modes. The LMR modulated signal then exits the optical fiber and enters the detector, i.e., spectrograph. The LMR phenomenon is expressed by attenuation dip in the detected spectrum at a specific resonance wavelength (λ_{res}). Because the value of λ_{res} is sensitive to the variations of the surrounding medium refractive

index, the LMR phenomenon can be utilized in RI sensors [59]. Fig. 20 shows the shift of the resonance wavelengths with a change in the refractive index of the surrounding media, which provides the calibration curve for LMR sensors.

Introduction to Theoretical Modeling of LMR

Theoretical modeling of the LMR phenomenon utilizes the equation (23) that enables calculation of the normalized transmitted power T of the LMR based structure [59].

$$T(\lambda) = \frac{\int_0^{\alpha_{max}} \int_{\theta_c}^{\pi/2} p(\theta) R^{N_{ref}(\theta, \alpha)}(\theta, \lambda) d\theta d\alpha}{\int_0^{\alpha_{max}} \int_{\theta_c}^{\pi/2} p(\theta) d\theta d\alpha} \quad (23)$$

In the above equation, α and α_{max} are skewness angle and its maximum value, respectively, $\theta_c = \sin^{-1} n_{cl}/n_0$ is a critical angle with n_{cl} and n_0 being refractive indices of the fiber cladding and core, respectively, $p(\theta)$ states for optical power distribution of the light source, and $R(\theta, \lambda)$ is the reflectance. In the case of an optical fiber, the light is unpolarized, i.e., it consists of both TE and TM polarizations, and R is given as an average of both $R_{TE}(\theta, \lambda)$ and $R_{TM}(\theta, \lambda)$ according to equation (24) [59].

$$R^{N_{\text{ref}}(\theta, \alpha)}(\theta, \lambda) = \frac{R_{\text{TE}}^{N_{\text{ref}}(\theta, \alpha)}(\theta, \lambda) + R_{\text{TM}}^{N_{\text{ref}}(\theta, \alpha)}(\theta, \lambda)}{2} \quad (24)$$

To determine the effective power transmitted through the fiber, the reflectance $R(\theta, \lambda)$ for a single reflection has to be raised to the power of $N_{\text{ref}}(\theta, \alpha)$ which represents the number of reflections of the specific ray propagating undergoes at the core-cladding interface. This number of reflections $N_{\text{ref}}(\theta, \alpha)$ is given by equation (25) where L represents the active sensor length (the fiber core part where cladding was removed and coated by ITO film, see Fig. 19), i.e., the sensing region, d is the fiber core diameter [59].

$$N_{\text{ref}}(\theta, \alpha) = \frac{L}{d \tan \theta \cos \alpha} \quad (25)$$

Table 2. Formulas typically used for the estimation of the optical power distribution.

$p(\theta) \propto k_0^2 n_0^2 \sin \theta \cos \theta$	for diffuse or Lambertian light sources such as LED [59, 89, 100, 104, 119]
$p(\theta) \propto \frac{n_0^2 \sin \theta \cos \theta}{(1 - n_0^2 \cos^2 \theta)^2}$	for collimated sources such as laser focused onto the end face of optical fiber [119-121]
$p(\theta) \propto e^{-\frac{(\theta - \frac{\pi}{2})^2}{2W^2}}$	for Gaussian distribution in case of remote sensing application [86, 87, 101, 121]

Table 2 presents formulas commonly used for the estimation of the optical power distribution $p(\theta)$ in the equation (23), here $k_0 = 2\pi/\lambda$ is the propagation constant and W indicates the width of the Gaussian function.

Once the geometric properties (L , d , and film thickness) and material properties (permittivities ε and refractive indices N) of the sensing structure are measured or modeled, the reflectance $R(\theta, \lambda)$ of the multilayer system can be calculated and used to determine the transmitted power [86, 100], employing the Fresnel equations. However, for multilayer geometries, it is very difficult to calculate the overall reflection due to the sum of a large number of reflections at multiple interfaces. Hence, the N-layer reflection matrix method (or Transfer matrix method for a multilayer system) should be used preferentially [104]. For more details on this method and LMR modeling, see references [59, 89, 92, 100, 104, 119-122].

Fig. 21 highlights the differences in the contributions of TE, TM, and TE+TM modes for generated SPR and LMR illustrated on the transmission curves for a thin ITO film [59, 89]. Fig. 21a) shows that the TE polarized light produces only a single attenuation dip in the transmission spectrum localized in the LMR's spectral region. Yet, as shown in panel b) in the same figure, TM-polarized light produces two attenuation dips appearing in two different spectral regions [93]. Here, the first dip occurs in the visible part of the spectrum and is attributed to LMR, while the second appears in the infrared region and is attributed to the SPR effect. The results for the unpolarized light, i.e., the combination of both TE and TM modes, are shown in Fig. 21c). Hence, both TE and TM polarizations, as well as unpolarized light, can generate the LMR phenomenon [59, 92, 101].

Another important feature of LMR is the possibility to shift and to generate multiple LMR attenuations with increasing thickness of the thin film, as shown in Fig. 22 a) and b). This is caused by the fact that the thicker film allows propagation of additional modes in the film, resulting in the appearance of multiple LMR dips without the need for any geometry or material modification [89, 104].

In conclusion, the LMR phenomenon provides a novel expandable platform for sensing and detection. Potential applications can range from industry through environment monitoring to medicine, as in many fields, changes in the investigated quantities are closely tied to the change in RI detectable by the LMR-based refractometers. For example, as shown in [88], LMR-based sensors were successfully implemented for the measurement of quantities such as voltage, temperature, relative humidity, pH, or for the detection and concentration determination of H₂S, H₂, and volatile organic compounds in a gaseous environment. Moreover, LMR-based biosensors were successfully implemented for the detection of anti-gliadin antibodies marking celiac disease [123], C-reactive protein marking inflammation [124], thrombin [108], H₂O₂ [125], etc. In summary, the advantages of LMR-based sensors are inexpensivity, tunable performance, variable geometries, and simpler complementary setup.

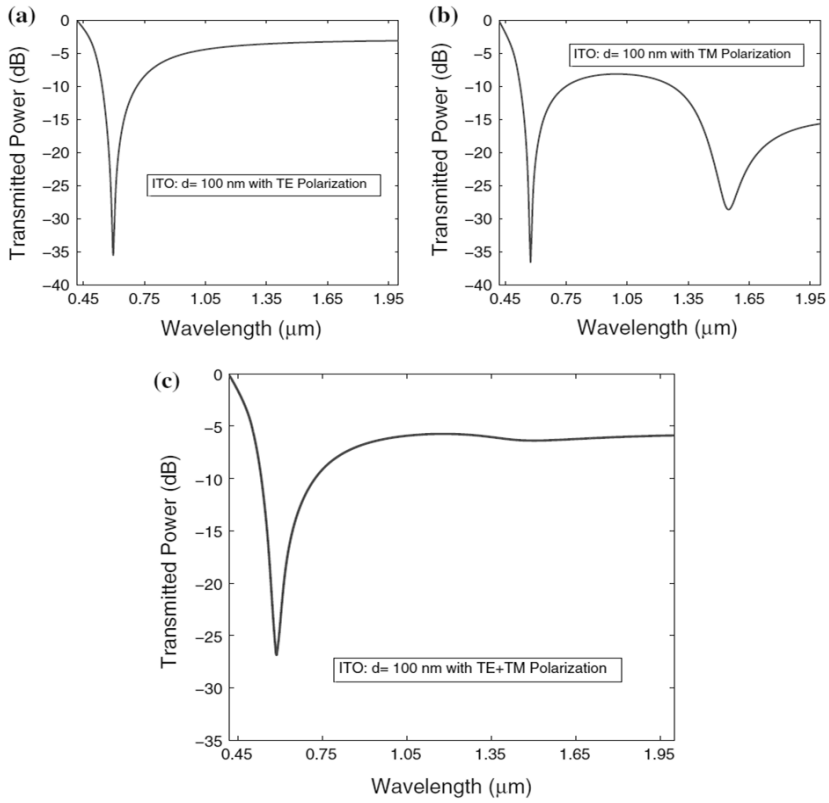


Fig. 21. Transmission spectra of light of a) TE, b) TM, and c) TE+TM polarization. The modelled length of sensing region = 3 cm, core diameter = 200 μm , NA = 0.22, thickness of ITO layer $d = 100$ nm, and surrounding medium refractive index = 1.33 [59].

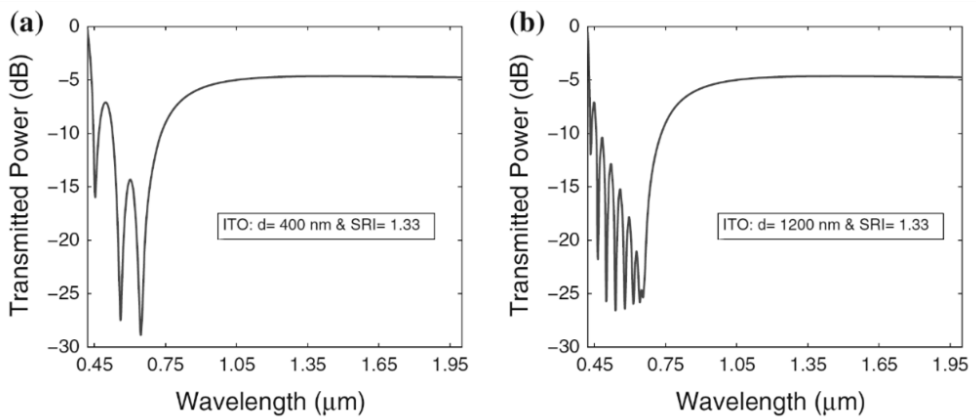


Fig. 22. Multiple LMR generation by unpolarized light with ITO layer thickness of a) $d = 400$ nm, b) $d = 1200$ nm. The modelled length of the sensing region = 3 cm, core diameter = 200 μm , numerical aperture NA = 0.22, and surrounding medium refractive index SRI = 1.33 [59].

Introduction of Electrochemistry for ITO-LMR-Based Sensors

Electrochemistry studies the interchange of chemical and electrical energy and the transfer of electrons in oxidation-reduction (redox) reactions [126]. It represents a family of methods with a wide variety of applications, such as batteries, electrodeposition [127], electroplating [128] or electropolishing [129], etc. However, in the framework of this thesis, the primal interest is that electroanalytical chemistry provides powerful tools for the qualitative as well as quantitative detection and analysis of compounds from both inorganic and organic chemistry. Utilizing its electrical conductivity, the ITO film deposited on optical fiber could work not only as an LMR sensor for refractometry but also as an active electrochemical electrode.

Usually, electrochemical methods are based on the interaction of electrodes immersed in an analyte, i.e., a solution with an investigated compound. The transfer of electrons between the electrode surface and molecules in the electrode surrounding is an essential process in electrochemical reactions. This transfer may be accompanied by other events, e.g., atom or ion transfer, but the net result is the electron transfer and hence a change in the oxidation number of an element present in the solution [130]. The transfer of electrons is governed by the Nernst equation (26), where E is the instantaneous potential of the analyte, i.e., cell potential, E° is standard potential of the redox couple (which contains qualitative information about reaction and analyte), R denotes the gas constant, T represents solution temperature, n states the number of electrons transferred in the reaction, F is Faraday's constant and Q is the reaction quotient given by the ratio of activities of products and reactants [130].

$$E = E^{\circ} - \frac{RT}{nF} \ln Q \quad (26)$$

The activities of products and reactants, with the corresponding activity coefficients γ_p and γ_r , are in the reaction quotient usually approximated by concentrations, in which case the standard potential E° is replaced by formal potential E_f° given by equation (27) [131]. Whenever the potential of the electrode and the potential of the analyte are different, electron transfer occurs; electron transfer can occur between the electrode and the analyte in a direction

leading to reduction of the occurred potential difference and change of the reaction quotient, i.e. the chemical composition of the analyte, in order to equalize the electrode and cell potential [132].

$$E_f^o = E^o - \frac{RT}{F} \ln \frac{\gamma_p}{\gamma_r}. \quad (27)$$

The kinetics of electrochemical processes can be significantly altered not only by the analyte but also by the material and surface properties of the electrode (grain size, crystal texture, presence of lattice defects and impurities, surface roughness, and in the case of thin-film electrodes also film thickness, presence of adsorbed material or functional groups and their chemical character) [133]. The electrode surface optimization represents the main aim of this thesis, i.e., preparation an ITO-coated optical fiber that can be employed as a working electrode in the electrochemical compartment for simultaneous optical (LMR) and electrochemical characterization of the analyte. From a practical point of view, it brings the necessity of tailoring both the electrical and optical properties of the ITO.

Electroanalytical methods usually employ two or three electrodes (working, reference, and auxiliary electrodes) immersed in an analyte, together forming an electrochemical cell, and a potentiostat that controls the electrical interaction between the electrodes and the solution [134], see Fig. 23. Although there are several different electrochemical methods used in electroanalytical detection, linear sweep voltammetry and cyclic voltammetry (CV) are the most widely used [135]. They are popular because of a relatively simple underlying theory combined with robustness and a wide range of data accessed [135]. The electrochemical methods are already well developed with an accurate theory, and their common features are the usage of an electrochemical cell, excellent sensitivity, and high accuracy. However, they generally suffer from poor resolution and selectivity [136]. For that reason, the multi-domain interrogation of electrochemical measurements integrated with, e.g., optical methods, is highly appreciated in analytical chemistry.

Generally, in the voltammetry methods, the varying potential of a working electrode (ITO-LMR structure in our case) immersed in a solution is controlled by the potentiostat to induce a redox reaction at the electrode surface. The rate of the redox reaction is proportional to the electrical current

flowing through the electrode. The output of the measurement is a voltammogram – a plot of the current flowing through the electrode versus the potential of the electrode [136], see Fig. 23. In the case of the linear sweep voltammetry, the measurement proceeds in a manner that the potential of the electrode is swept between two potentials at a fixed rate. The current measured in a solution can reach several local peaks whose positions provide qualitative information about the reactants in the solution. Yet, at the same time, the current amplitudes are directly proportional to the concentration of the electroactive species, thus providing quantitative information [136].

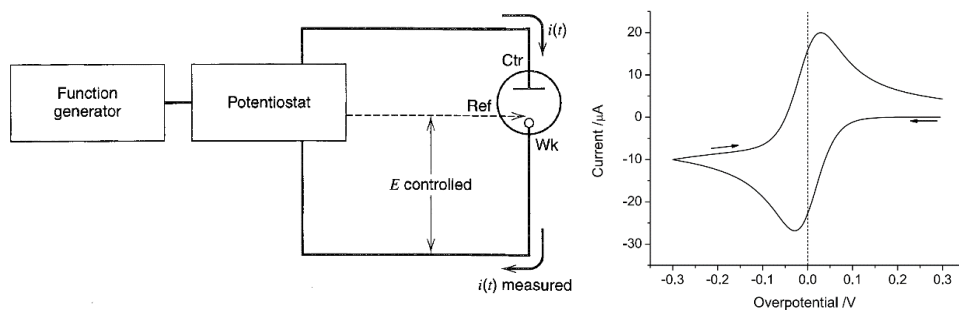


Fig. 23. Scheme of the typical arrangement of cyclic voltammetry. Left: scheme of the three electrode compartment [134]. Right: the output voltammogram from cyclic voltammetry with the arrows indicating the direction of the voltage sweep [137].

Cyclic Voltammetry for Electrochemical Domain of Interrogation

This chapter deals mostly with cyclic voltammetry (CV), which is more relevant for the purpose of this thesis, the development and fabrication of a multi-domain interrogating sensor simultaneously combining approaches of LMR and electrochemistry, especially CV. Generally, cyclic voltammetry is a method for investigating the electrochemical behavior of a system. The main difference of CV from linear sweep voltammetry is that the potential progression is inverted after reaching the maximum value of the potential, so it returns to its initial value with a possibility of repeating the procedure in multiple cycles. An example of the voltammogram produced by CV is shown in Fig. 23. Consequently, the procedure includes both oxidation and reduction processes on the electrode [138]. The cyclic voltammetry is considered to be a nondestructive analytical method, since the monitored changes of the analyte are closely localized at the electrode surface while the bulk of the analyte

remains at its original state [139]. As shown in Fig. 23, the potential of the working electrode is controlled versus a reference electrode using a potentiostat, which allows the current flow between the working and auxiliary (counter) electrodes. The current of the reference electrode is negligible. With this arrangement, the measured potential of the working electrode is not affected by the voltage drop caused by the current flowing through the solution [134, 135].

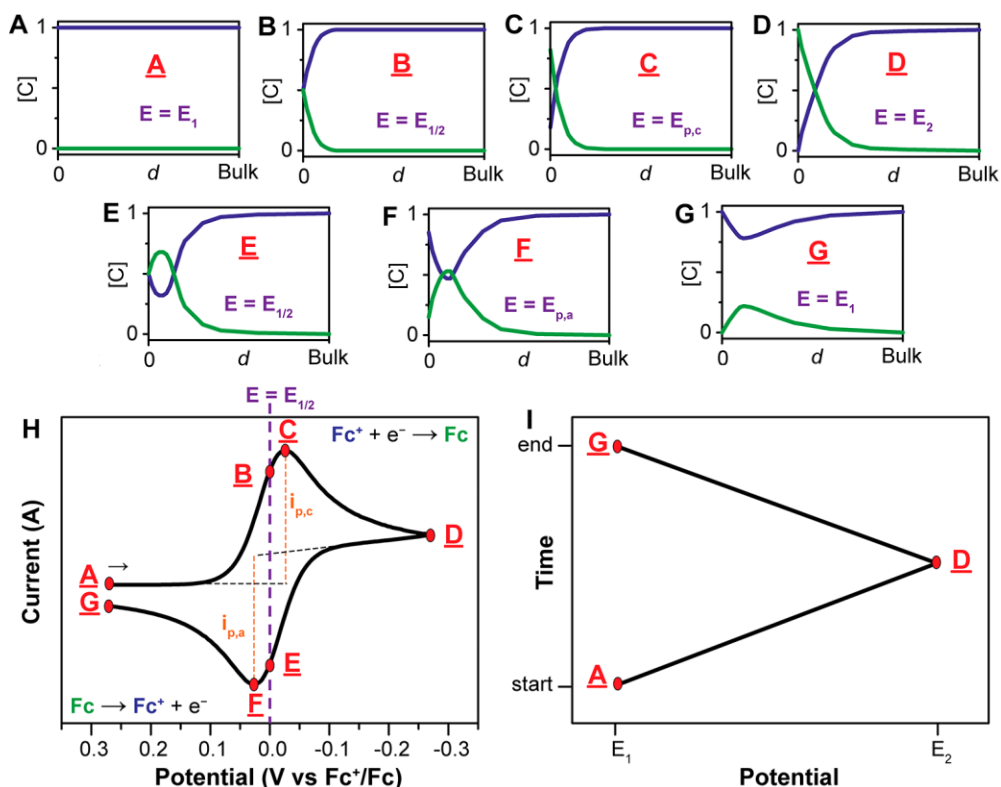


Fig. 24. Changes in the concentrations of redox couple during CV measurements. Panels A-G: Evolution of concentration profiles of Fc^+ (blue) and Fc (green) as a function of distance from the electrode surface. Panel H: Cyclic voltammogram of the reversible reduction of Fc^+ to Fc . Panel I: Time development of the potential applied to the electrode. Panels A-G correspond to points A-G in panels H and I [132].

To understand the voltammogram, the diffusion of the species present in the analyte and contributing to the redox reactions has to be considered, see Fig. 24 panels A to G. Fig. 24H shows a typical cyclic voltammogram of a solution containing ferrocenium (Fc^+) which is reduced to ferrocene (Fc). Marking points A to G in the voltammogram correspond to accompanying

panels (Fig. 24A-G) illustrating the spatial distributions of the reactant and product concentrations surrounding the working electrode. Working electrode potential E is changed in time t during the measurement [131]:

$$0 \leq t \leq t_r : E = E_i - vt$$

$$E_f = E_i - vt_r$$

$$t_r \leq t \leq 2t_r : E = E_f + v(t - t_r) = 2E_f - E_i + vt$$

where t_r is the time at which the direction of scanning is reversed (corresponds to point D), v is a scan rate, E_i and E_f are initial and final potentials, respectively. In this particular example, the initial potential is also the highest potential reached during the measurement, $E_i = E_{\max}$, and the final potential is the lowest, $E_f = E_{\min}$ (note that depending on the procedure, the initial scanning direction and therefore also E_i and E_f can be inverted); all related to Fig. 24. The trend of electrode potential is depicted in Fig. 24I.

At the beginning of the measurement (point A), the solution contains only the oxidized species Fc^+ , and the starting potential is set to a value positive enough so that no redox reaction occurs at the electrode surface, i.e., the current is infinitesimal. When the electrode potential is scanned during the CV, the concentrations c_{Fc^+} and c_{Fc} in the vicinity of the electrode change in time according to the Nernst law (equation (28)) [131].

$$c_{\text{Fc}^+} = c_{\text{Fc}} e^{\frac{nF}{RT}(E - E_f^0)} \quad (28)$$

When the solution is scanned in a negative direction from point A to point D, Fc^+ molecules accept one electron from the electrode and are reduced to Fc . This exchange gives rise to the measured current and simultaneously causes a decrease of Fc^+ concentration c_{Fc^+} , and an increase of Fc concentration c_{Fc} , in the vicinity of the electrode. For reversible processes where the diffusion coefficients of the reactants and products are equal, the formal potential E_f^0 is often estimated with the experimentally determined cell half potential $E_{1/2} \approx E_f^0$ [132, 138]. As the electrode potential approaches the value of $E_{1/2}$ at point B, the solution around the electrode achieves equilibrium with $c_{\text{Fc}^+} \approx c_{\text{Fc}}$, see panel B. At point C, where the electrode reaches cathodic peak potential $E_{p,c}$, the measured cathodic current attains maximum value $I_{p,c}$. At

that point, the electron transfer from the electrode to the solution is favorable and, at the same time, there is still an abundance of electron-accepting Fc^+ molecules in the vicinity of the electrode surface, see panel C. The value of the peak current for reversible processes is given by Randles–Sevcik equation (29), where I_p is the peak current, n denotes the number of electrons transferred per species, A represents the electrode area (in cm^2), D is the diffusion coefficient of the electroactive species (in cm^2/s), and C is the concentration of the analyte in the bulk solution (in mol/cm^3) which provides quantitative information about the analyte [132].

$$I_p = 0.446nFAC \sqrt{\frac{nFvD}{RT}} \quad (29)$$

The current is limited by the transport of additional Fc^+ molecules from the bulk solution to the electrode. After crossing the cathodic peak potential, i.e., $E < E_{p,c}$, the electron transfer is still favorable, but the diffusion of additional Fc^+ molecules from the bulk solution is severely limited by the growing diffusion layer, i.e., the volume of solution around the electrode containing a high concentration of reduced Fc molecules, see panel D. This results in a decrease in current as E becomes more negative. After reaching E_{\min} at point D, the scan direction is reversed and the solution is scanned in an anodic direction. The Fc molecules produced during the cathodic scan are still present at the electrode surface and are reoxidized back to Fc^+ as the electrode potential grows and the electrode accepts electrons from the solution. At point E, where $E = E_{1/2}$, the direction of the current is opposite compared to point B because the composition of the diffusion layer is now richer in electron-donating Fc molecules, although the solution in direct contact with the electrode is again in equilibrium with $c_{\text{Fc}^+} \approx c_{\text{Fc}}$, see panel E. This fact emphasizes the importance of the diffusion of the species during the measurement. At point F, where the electrode reaches an anodic peak potential $E_{p,a}$, the anodic current value attains local extreme $I_{p,a}$, which is again given by the combination of the favorable electron transfer from the solution to the electrode and the sufficient supply by oxidizable Fc molecules, see panel F.

Peak-to-peak separation $\Delta E_p = E_{p,a} - E_{p,c}$ is another important parameter investigated during cyclic voltammetry measurement. For ideal reversible processes, ΔE_p is given by equation (30) [132].

$$\Delta E_p = 2.22 \frac{RT}{nF} = \frac{57}{n} \text{ mV at } 25 \text{ }^\circ\text{C.} \quad (30)$$

By reaching E_{\max} at point G, the electrolyte at the electrode approaches its original state of composition, yet not completely in the bulk solution, see panel G [131, 132].

An important feature of the CV measurements is an estimation of the reversibility of the studied system, which alters the measured shape in the voltammogram. In the case of the ideal reversible process, the voltammogram is governed exclusively by the Nernst equation and the diffusion of the species [138]. To accomplish that, the process must be both electrochemically as well as chemically reversible.

Electrochemical reversibility is attained when the electron transfer between the electrode and analyte is fast enough for the electrode and analyte to remain at equilibrium [131]; in other words, a barrier to electron transfer has to be low enough that any change of applied electrode potential immediately results in the change of the surrounding analyte according to Nernst law. For example, for a high barrier to electron transfer, the reactions are hindered and require more positive/negative potentials to cause oxidation/reduction of the analyte, i.e., $\Delta E_p > \frac{57}{n} \text{ mV at } 25 \text{ }^\circ\text{C}$, [132].

Chemical reversibility is attained when the products of the electron transfer are stable, i.e., no parallel reactions in the solution and no surface effects occur. Practically, it means that processes such as gas release, adsorption, desorption, formation, or dissolution of solid deposits, cannot occur [138]. For example, if the products of the forward scan are unstable, the current peak in the reverse scan is smaller in magnitude than for the forward scan, i.e., $I_{p,c}/I_{p,a} \neq -1$ [131].

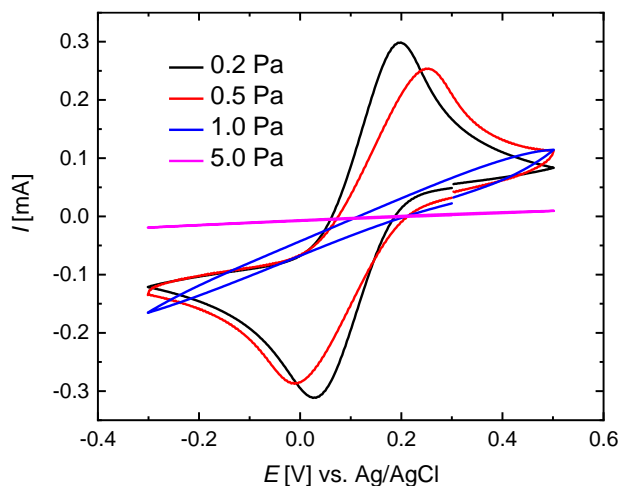


Fig. 25. Voltammograms obtained by ITO working electrodes prepared by plasma-assisted deposition at different pressures. Voltammograms were measured in a solution of 0.5 M Na_2SO_4 + 5 mM $\text{K}_3\text{Fe}(\text{CN})_6$ at a scan rate $v = 100$ mV/s. The different shapes of the voltammograms indicate the need for optimization of the deposition process. (Data achieved in the frame of the thesis).

If the above-mentioned conditions are not satisfied, the system is losing its reversibility. This is indicated in the measured voltammogram by changes of E_p as redox peaks shift and by changes of I_p according to equations (31) and (32), respectively; here α is a transfer coefficient, k^0 denotes the standard rate constant of electron transfer reaction, and n_a represents the number of electrons in the rate-determining step of the electrode process [138].

$$E_p = E_f^0 - \frac{RT}{\alpha n F} \left[0.78 - \ln \frac{k^0}{\sqrt{D}} + \ln \sqrt{\frac{\alpha n F v}{RT}} \right] \quad (31)$$

$$I_p = 2.99 \times 10^5 n A C \sqrt{\alpha n_a D v} \quad (32)$$

Finally, Table 3 summarizes the behavior of systems with different degrees of reversibility. In some cases, the reactants and/or products of the reaction can be intentionally or unintentionally attached to the electrode surface (by chemical bonds, immobilization matrix, or adsorption) providing an electrochemical response instead of surface shielding. Since diffusion does not play a major role, the cathodic and anodic peaks are closer to each other, i.e.,

$\Delta E_p < \frac{57}{n}$ mV at 25 °C, and $\Delta E_p = 0$ mV for reversible surface processes. Peak current for cases with electrode surface concentration Γ (in mol/cm²) is then given by equation (33) [138].

$$I_p = \frac{n^2 F^2 v A \Gamma}{4RT} \quad (33)$$

It is worth reminding that the previously listed equations related to peak current (29), (32), and (33) show a linear increase of I_p with the electrode area A . The effective surface area can be significantly enlarged by a properly tailored nanostructured electrode [140]. The plasma-assisted deposition techniques enable such tailoring of nanostructured ITO electrodes for enhanced electrochemical response together with the optimization of the optical properties. As already shown in the previous chapters, the electrical conductivity of ITO provides a possibility to use the ITO-covered fiber as an electrochemical electrode. However, the electrochemical activity of the thin film needs to be optimized by the deposition process. Fig. 25 presents voltammograms of ITO films prepared in the frame of this Ph.D. thesis, at different argon pressures. It can be clearly seen that through the optimization of the plasma process conditions, it is possible to reach a sufficient current signal and enhance the reversibility of the electrochemical reactions.

Table 3. Main differences between systems with different degrees of reversibility measured by cyclic voltammetry. Based on [132] and [138].*

Reaction	Conditions
Reversible CV	<p>The reaction is fully controlled by the diffusion of the analyte.</p> <p>I_p is linearly proportional to \sqrt{v}</p> <p>I_p is linearly proportional to C</p> <p>$I_{p,c}/I_{p,a} = 1$</p> <p>E_p is independent of v</p> <p>$\Delta E_p = E_{p,a} - E_{p,c} = 57/n$ mV at 25 °C</p>
Quasi-reversible CV	<p>The change in electrode potential is not instantly accompanied by the electron transfer reaction. The current is controlled by charge transfer and mass transport.</p> <p>I_p depends on \sqrt{v} non-linearly</p> <p>I_p is linearly proportional to C</p> <p>E_p depends on v</p> <p>$\Delta E_p > 57/n$ mV at 25 °C and increases with v</p>
Irreversible CV	<p>Electron transfer is significantly slower compared to mass transport; the current peaks become wider and are reduced in height. Additional reactions in the solution may occur.</p> <p>I_p is proportional to \sqrt{v}</p> <p>I_p is linearly proportional to C</p> <p>E_p depends on v</p> <p>ΔE_p may be non-defined as the reverse reaction may not occur</p>

* I_p - peak current; $I_{p,c}$ and $I_{p,a}$ - maximum value of cathodic and anodic currents, respectively; v - scan rate; C - concentration of the analyte in the bulk solution; E_p - peak potential; $E_{p,c}$ and $E_{p,a}$ - cathodic and anodic peak potential, respectively; n - the number of electrons transferred per species.

RESEARCH SECTION

LMR Fiber as an Active Electrode – Multi-Domain (Bio)Sensor

As already mentioned in the theoretical section of the thesis, there is a seek for multi-domain sensors that are capable of simultaneous or independent detection of the required substances. Interest for such sensors is coming from a wide spectrum of fields including medicine and health protection, biology, environmental protection (water, air pollutants, etc.), civil protection (explosives, hazardous substances), and many others. The multi-domain interrogation significantly enlarges the application potential of the sensor because of its improved selectivity and sensitivity.

The main motivation and aim of this thesis is the development and fabrication of a two-domain sensor based on optical fiber, which enables simultaneous optical (LMR) and electrochemical interrogation. The ultimate goal was the two-domain detection of various biomolecules and pathogens, such as *Borrelia burgdorferi s.l.*, which is an exemplary microorganism suitable to prove the viability of the sensor concept. The experimental research was mostly focused on the material research of ITO film deposited onto the optical fiber for the fabrication of electrochemically active LMR sensors. The possible configuration of the measuring setup is illustrated in Fig. 26. The scheme shows an optical fiber operating in a transmission mode covered by a properly tailored nanostructure, which is electrochemically active and fulfills the conditions for LMR. Such a configuration simultaneously enables:

- Optical LMR interrogation of the analyte – the mechanically flexible optical fiber coated by optically tailored ITO thin films is immersed into the analyte. The broad-spectrum wavelength light source is connected to one end of the optical fiber. The light passes through the fiber, the LMR effect occurs in the sensing area, and the LMR-modulated light signal is processed by an optical spectrum analyzer connected to the other end of the fiber. The LMR modulation and the LMR shift enable detection of the searched substance as it interacts, e.g., with the receptor molecules covalently attached to the surface of the sensor.
- Electrochemical interrogation of the analyte – the optical fiber coated by ITO film is electrically conductive and can serve as a working electrode of the electrochemical compartment. The electrode potential

is controlled by the potentiostat, and voltammograms can be measured. If the surface of the sensing area is functionalized by receptor molecules, the attachment of the target substance blocks the surface, resulting in a decrease in the current amplitude.

- Moreover, electrochemical processes on the surface of the fiber can lead to a change in the refractive index in the sensor vicinity, which can initiate changes in the LMR spectrum. Hence, the electrochemical processes in the sensor vicinity could be observed by an independent non-electrochemical method.

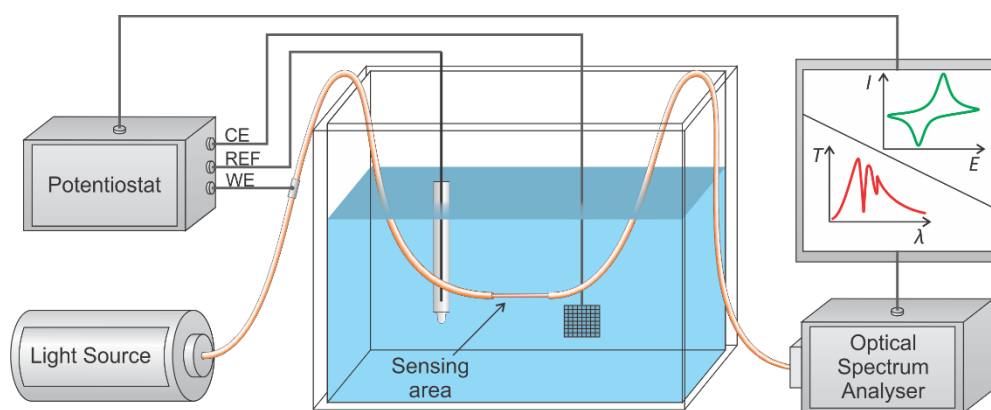


Fig. 26. Scheme of the combined electrochemical and optical setup; CE: counter electrode, REF: reference electrode, WE: working electrode. The work was done in the framework of the Ph.D. thesis.

The proposed configuration allows simultaneous utilization of the two independent interrogation methods in ‘one’ device and during ‘one’ measurement. Such a mutual effect has the potential to extend the range of sensor use. This approach reduces the need for excessive manipulation of the sample (analyte) as well as reduces the necessary volume of the analyzed liquid. Sensors based on optical fiber allow miniaturization of the device, easy implementation into the measuring set, high flexibility, low-cost production, and resistance to electromagnetic noise/smog.

The main experimental and theoretical achievements attained during the Ph.D. study were disseminated in the form of publications in international WoS-recognized journals, conference contributions, and seminar presentations. The most significant papers are attached to this thesis; see the list of publications.

Besides it, copies of already published papers directly connected with the thesis aims are included in the thesis, too. The research includes plasma diagnostics as well as analysis of prepared films and tests of optical fibers covered by these films as necessary steps in the sensor development. Due to the multidisciplinary character of the research, publications within this research section are divided into three groups, although some of them may fit into more than one of the following sections:

- A. Sensor Fabrication: Technology and Procedure [A1-A6]
- B. Combined Electrochemical and LMR Interrogation of Liquids [B1-B6]
- C. Bioactivation of Sensors for Selective Detection [C1-C5]

Therefore, in the following three sections, a brief summary of the most important outcomes is provided which correspond to the main milestones of the carried research. The summary is then followed by the corresponding articles. The content of the presented publications is preserved, although the style, layout, and format may be slightly different from the original.

A. Sensor Fabrication: Technology and Procedure

Initial research was focused primarily on the optimization of the sensor fabrication procedure that utilizes magnetron sputtering and other low-temperature plasma techniques. The experimental setup developed for the deposition of most of the indium tin oxide (ITO) films and for the fabrication of lossy-mode resonance (LMR) sensors is shown in Fig. 27, though in [A1, A5] two perpendicular magnetrons were used. The ITO thin film deposition was carried out in a high-vacuum chamber capable of reaching the back-down pressure of 10^{-5} Pa to ensure the high purity of the deposition. A commercial planar magnetron was installed in the upper part of the vacuum chamber or a side wall depending on the type of the substrate and other conditions, see the scheme in Fig. 27. The sputtering gun was equipped with a compound ITO target ($\text{In}_2\text{O}_3/\text{SnO}_2$ of composition 90/10 wt% and a purity of 99.99 %). For more details on the deposition conditions, see the individual publications.

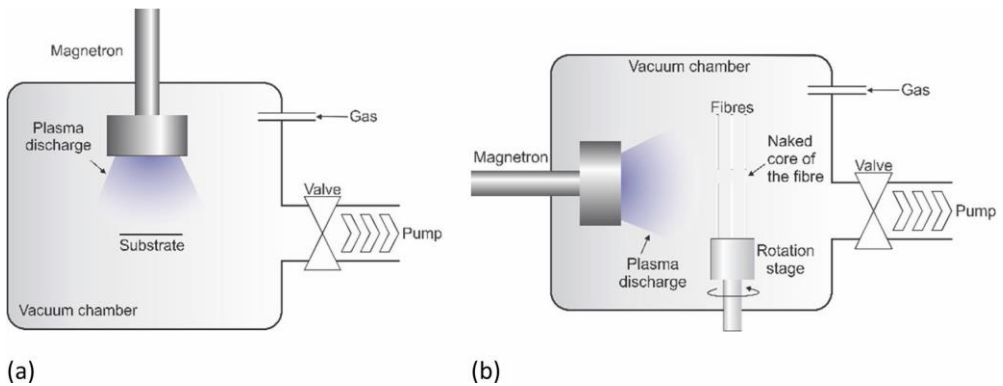


Fig. 27. Experimental setup used for deposition on (a) flat substrates and (b) on optical fibers [A6].

The Theoretical Section clearly demonstrates that the precise controlling of the deposition process is the key for tailoring of the thin films. For that reason, the deposition process, namely, the energy influx toward the substrate, needs to be carefully controlled and in situ monitored. However, it is rather complicated in reactive discharges because the film, unintentionally growing on the diagnostic tool immersed in the plasma, increases the error of the measurement.

In the frame of the thesis, a new type of electrical probe for advanced diagnostics in reactive and dusty plasmas was developed. It enables in situ

monitoring of the parameters during the deposition of transparent conductive oxides (TCOs); the method is described in publication [A3] in detail. Reactive or dusty plasma typically creates an insulating film of unknown impedance on inserted diagnostic tools, resulting in distortion of the measured data and their unreliable processing. To avoid this complication, the new approach proposed in [A3] utilizes a so-called radiofrequency (rf) Sobolewski probe for ion flux measurement, which is further modified to also obtain the electron temperature and the ion density. It introduces the procedure where, by subtracting the capacitive current, the measured rf probe characteristics are transformed toward I–V curves typical for the standard Langmuir probe but undistorted by undesirable surface modifications of the probe, see Fig. 28. This processing enables not only the monitoring of plasma sheath impedance and the ion flux toward the substrate but also allows for an estimation of other parameters of the reactive plasma such as the plasma density or electron temperature, respectively. For more details on the procedure and comparison of results from the modified Sobolewski and Langmuir probe, see [A3].

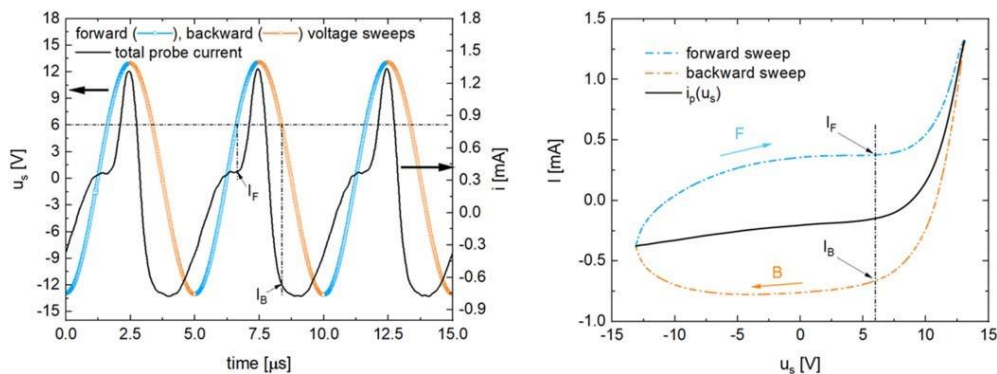


Fig. 28. The transformation of the rf measured waveforms toward the I–V curve. Left: the rf probe voltage $u_s(t)$ considered as the forward and backward voltage sweep of the measured total probe current $i(t)$. Right: the graph $i(u_s)$ results in a typical Lissajous-like pattern from which, after proper processing, the I–V curve is obtained. The I_F and I_B in both panels represent the currents measured for the same voltage value during the forward and backward sweep, respectively [A3].

However, in this subsection, attention is mainly given to the development and fabrication of the electrochemically active ITO films supporting LMR from the point of view of film properties and optimization of the deposition procedure. Careful in situ plasma monitoring provided the possibility to optimize the deposition process and subsequent tailoring of ITO thin-film

properties. It revealed that it is the energy influx to the substrate that influences the ITO crystallinity and related parameters such as electrical and optical properties.

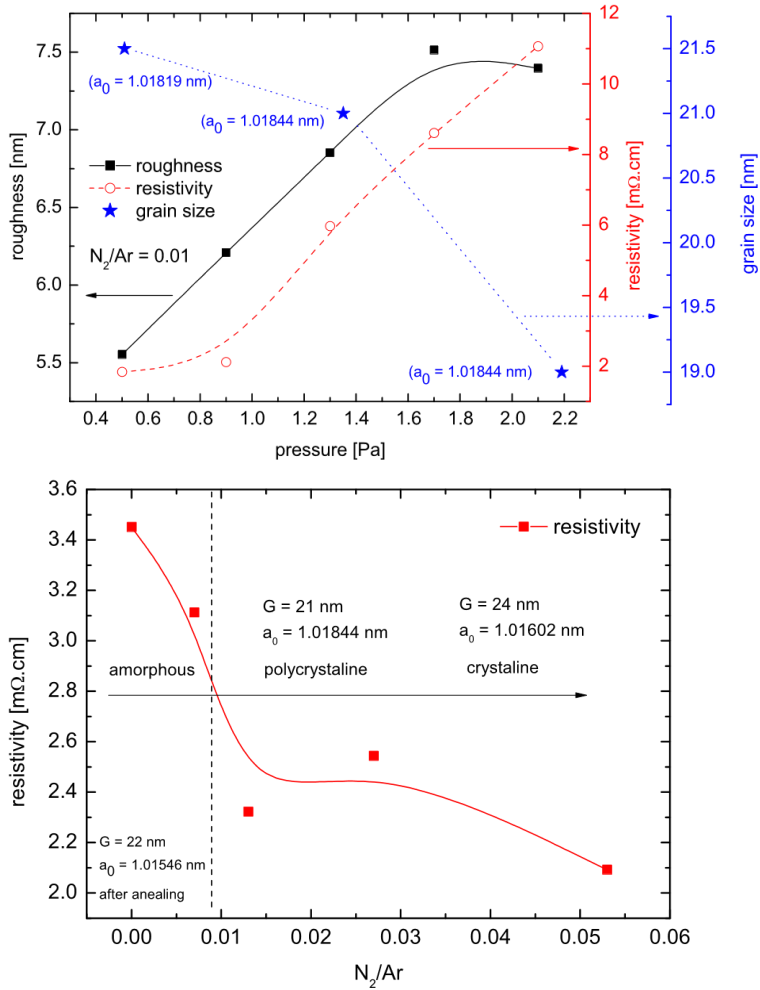


Fig. 29. Dependence of the ITO resistivity on its crystallinity which was controlled by the pressure of the working gas (top) and gas composition (bottom). The crystalline films regularly exhibit lower resistivity [A2].

The crystallinity of the ITO films proved to be a crucial parameter determining the electrical properties, particularly. Fig. 29 illustrates that the improved crystallinity of the ITO films usually exhibits a lower resistivity, as larger crystals in the film minimize scattering of charge carriers (electrons in this case) at grain boundaries, impurities, or lattice dislocations, and thus the electrical conductivity is improved, see papers [A2, A4].

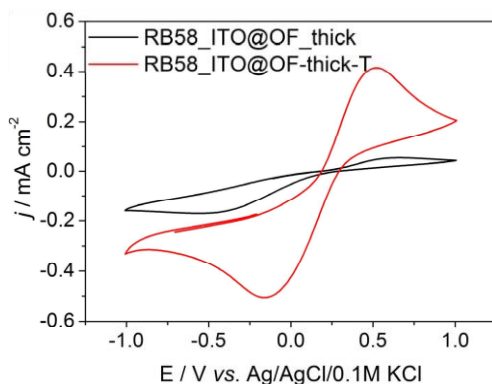


Fig. 30. Effect of thermal annealing (200°C, 2 h) on CV measurements of ITO-coated PCS fibers. The result for the annealed sample is plotted in red [A1].

At the same time, the well-crystalline films exclusively exhibited a better electrochemical response than amorphous films which usually were not electrochemically active at all. The crystallinity can be enhanced by supplying energy into the layers, e.g., by post-deposition annealing [A1, A5], or by reducing the working gas pressure during the deposition [A4]. Fig. 30 shows this effect on the change in the voltammogram recorded before (black) and after (red) annealing of the ITO-fiber electrode (in a solution of 5 mM $K_3[Fe(CN)_6]$ in 0.5 M K_2SO_4 at a scan rate of 0.05 Vs^{-1}). The improvement of the electrochemical response follows the improved crystallinity. This could suggest that high charge carrier mobility is more decisive for the optimal electrochemical performance of highly crystalline ITO films than a high charge carrier concentration in the case of amorphous ITO films [A4]. At the same time, the LMR sensitivity of the prepared films is not significantly affected by the change in crystallinity after annealing [A5].

The research in this subsection revealed that utilization of the HiPIMS discharges provides a possibility to deliver and to control the energy influx toward the growing ITO film, due to the presence of highly energetic species, typical for the method. HiPIMS deposited ITO films are crystalline, which excludes the need for any post-deposition annealing. This is advantageous for the fabrication of optical fiber-based LMR sensors as they have a rather low thermal load tolerance. The typical HiPIMS deposition procedure can be considered a room-temperature process safe for optical fibers.

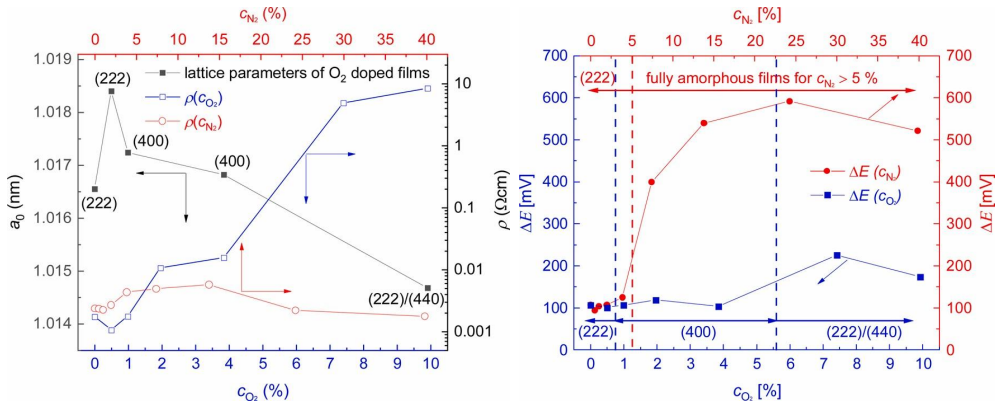


Fig. 31. Left: Evolution of the lattice parameter a_0 (left axis) and resistivity ρ_{N_2, O_2} (right axis) with concentrations of reactive process gases c_{O_2} and c_{N_2} . Right: Evolution of the current peak separation with the concentration of the reactive gases $\Delta E(c_{O_2}, c_{N_2})$ [A6].

A detailed study of HiPIMS based ITO depositions shows a great possibility to tune the electrochemical as well as optical (LMR) response of the sensor [A6]. In the study, the ITO crystallinity was controlled by the composition of the working gas, namely, the content of reactive oxygen and nitrogen. As shown in Fig. 31, the conductivity of ITO films prepared by HiPIMS is again determined by crystallinity which also determines the electrochemical response of the sensor. The right panel of Fig. 31 shows that peak-to-peak separation ΔE_p in voltammograms grows rapidly for the films that do not exhibit any XRD pattern, i.e., amorphous films.

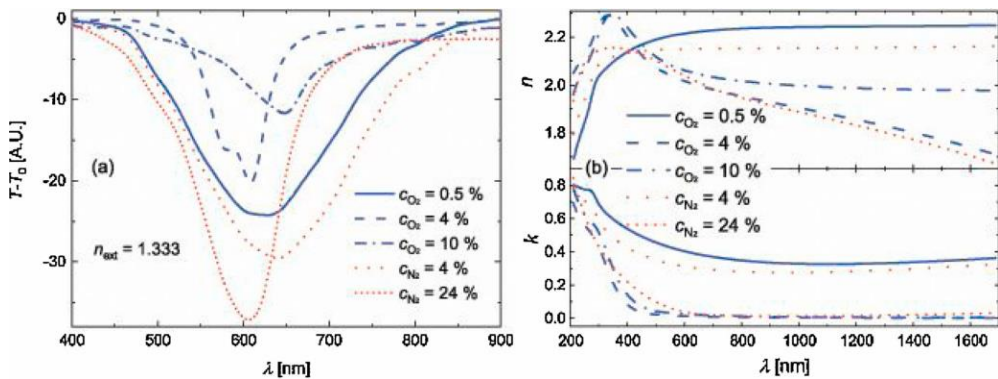


Fig. 32. (a) LMR spectrum for optical fiber sensors coated at different gas compositions when immersed in water, and (b) corresponding refractive indices and extinction coefficients of the ITO films deposited at the same conditions on flat substrates [A6].

The content of the reactive gases in the deposition environment also strongly influences the optical properties and consequently, the LMR response of the ITO films as well, see Fig. 32. Moreover, the study demonstrate that doping

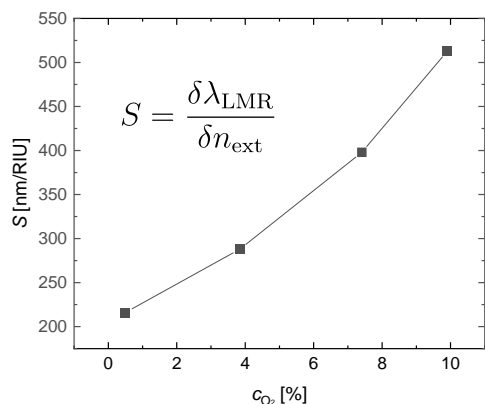


Fig. 33. RI sensitivity for sensors received at different c_{O_2} [A6].

of the films by oxygen during HiPIMS increases the sensitivity in the LMR domain while keeping lower values of the ΔE_p , compare Fig. 31 and Fig. 33. Moreover, in both electrochemical and optical domains, the response of the sensor showed improvement when compared to standard RF sputtering proving the superiority of reactive HiPIMS for the preparation of ITO-based dual-domain sensors [A6].

Summary: The research presented above was generally oriented toward the deposition of ITO thin films and tailoring of their properties. The results in this subsection show that plasma-based techniques provide means to increase the detection possibilities of the ITO-based dual-domain sensors through modifications of the deposition procedure. Namely, HiPIMS techniques are suitable for the fabrication of the electrochemically active ITO-LMR sensors. It is caused specifically by the advanced ability to control the energy flux to the substrate where the ITO film is formed. Due to the high versatility of HiPIMS, it is possible to tune the internal properties of ITO, which results in possible dual domain interrogation (optical and electrochemical) of liquids. As shown in Subsections B and C, these adjustments of the deposition procedure are necessary for the fabrication of sensors for the detection of biomolecules and pathogens. However, it is worth noting that the research presented in the following subsections was conducted simultaneously with the research presented in this subsection, not after it. Naturally, it means that not all the presented results were obtained from the sensors that underwent such tuning during their fabrication. Yet, their performance was sufficient to prove the concepts the individual publications were aimed at.

List of the publications in the subsection

- A1. Magdalena Dominik, Katarzyna Siuzdak, Paweł Niedziałkowski, Vitezslav Stranak, **Petr Sezemsky**, Michał Sobaszek, Robert Bogdanowicz, Tadeusz Ossowski, Mateusz Smietana, Annealing of indium tin oxide (ITO) coated optical fibers for optical and electrochemical sensing purposes, *Proceedings of SPIE 1075*, (2016), UNSP 1017515. (<https://doi.org/10.1117/12.2263289>)
- A2. Vitezslav Stranak, Robert Bogdanowicz, **Petr Sezemsky**, Harm Wulff, Angela Kruth, Mateusz Smietana, Jiri Kratochvil, Martin Cada, Zdenek Hubicka, Towards high quality ITO coatings: The impact of nitrogen admixture in HiPIMS discharges, *Surface and Coatings Technology 335*, (2018), 126-133. (<https://doi.org/10.1016/j.surfcoat.2017.12.030>)
- A3. **Petr Sezemsky**, Vitezslav Stranak, Jiri Kratochvil, Martin Cada, Rainer Hippler, Miroslav Hrabovsky, Zdenek Hubicka, Modified high frequency probe approach for diagnostics of highly reactive plasma, *Plasma Sources Science and Technology*, 28, (2019), 115009. (<https://doi.org/10.1088/1361-6595/ab506c>)
- A4. Paweł Niedziałkowski, Wioleta Białobrzeska, Dariusz Burnat, **Petr Sezemsky**, Vitezslav Stranak, Harm Wulff, Tadeusz Ossowski, Robert Bogdanowicz, Marcin Koba, Mateusz Smietana, Electrochemical performance of indium-tin-oxide-coated lossy-mode resonance optical fiber sensor, *Sensors and Actuators B: Chemical 301*, (2019), 127043. (<https://doi.org/10.1016/j.snb.2019.127043>)
- A5. Bartosz Michalak, **Petr Sezemsky**, Vitezslav Stranak, Mateusz Smietana, Effect of thermal annealing on sensing properties of optical fiber sensors coated with indium tin oxide nano-overlays, *Photonics Letters of Poland 12(2)*, (2020), 58-60. (<https://doi.org/10.4302/plp.v12i2.1024>)
- A6. **Petr Sezemsky**, Dariusz Burnat, Jiri Kratochvil, Harm Wulff, Angela Kruth, Katarzyna Lechowicz, Monika Janik, Robert Bogdanowicz, Martin Cada, Zdenek Hubicka, Paweł Niedziałkowski, Wioleta Białobrzeska, Vitezslav Stranak, Mateusz Smietana, Tailoring properties of indium tin oxide thin films for their work in both electrochemical and optical label-free sensing systems, *Sensors and Actuators B: Chemical 343*, (2021), 130173. (<https://doi.org/10.1016/j.snb.2021.130173>)

B. Combined Electrochemical and LMR Interrogation of Liquids

The research in this section focuses primarily on the performance of optical fibers covered by optimized ITO thin films, acting as sensors simultaneously working in both the electrochemical and optical domains. Given the fact that the ITO is electrically conductive, the sensing LMR region of the optical fiber can be connected to a potentiostat as a working electrode and perform electrochemical interrogation of an analyte. At the same time, the optical properties of the ITO film provide a possibility for the optical LMR interrogation of the analyte, representing the proposed concept of simultaneous interrogation.

The investigation of the refractive index (RI) of the media surrounding the sensing region can be done through the LMR phenomenon or long-period gratings (LPG) induced in the optical fiber as shown in [B1] and [B2]. LPG is a periodic RI modulation (period in the order of hundreds of micrometers) of the core of single-mode optical fiber. The modulation induces coupling of the fundamental core mode and forward propagating cladding modes, resulting in a series of resonances appearing in the LPG transmission spectrum. The coupling conditions corresponding to the resonance wavelengths are highly dependent on the external RI [B2]. The scheme of an exemplary experimental setup for such a dual analysis of liquids is shown in Fig. 34, where the optical fiber with the ITO film tuned for LMR is connected as a working electrode in a three-electrode arrangement for cyclic voltammetry. Given the character of the experimental setup, the electrochemical and optical measurements can be performed simultaneously as well as separately.

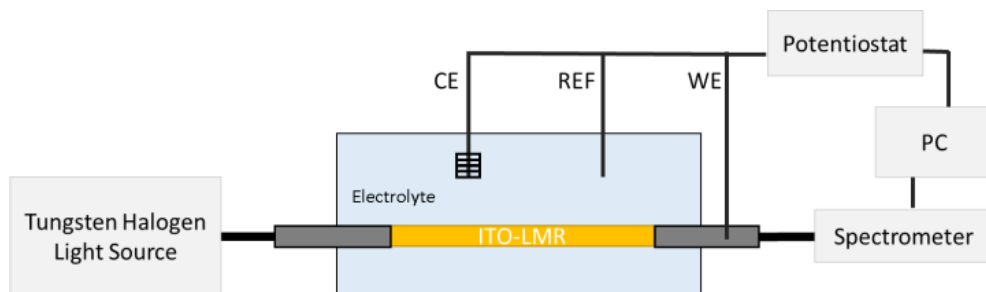


Fig. 34. Scheme of an experimental setup. (CE – counter electrode, REF – reference electrode, WE – working electrode, PC – personal computer) [C3].

An important feature revealed during the research was that the electrochemical and optical domains are not completely independent, as the resonance position observed in the spectrum responds to an applied potential during simultaneous measurements. The first reason is that the concentration of the free charges in the film depends on the applied potential. As the change in the concentration of the free charges results in variation of the optical properties, namely, the refractive index of the film, the LMR conditions are changed as well, resulting in a shift of the resonance. The second reason is more connected with the processes in the solution around the sensor (e.g., chemical changes, oxidation, and reduction of the reacting agents and their corresponding concentration variations in the sensor vicinity) and processes occurring in the outer layer of the ITO film (e.g., electrode oxidation, or dissolution) [B1, B2, B3, B4].

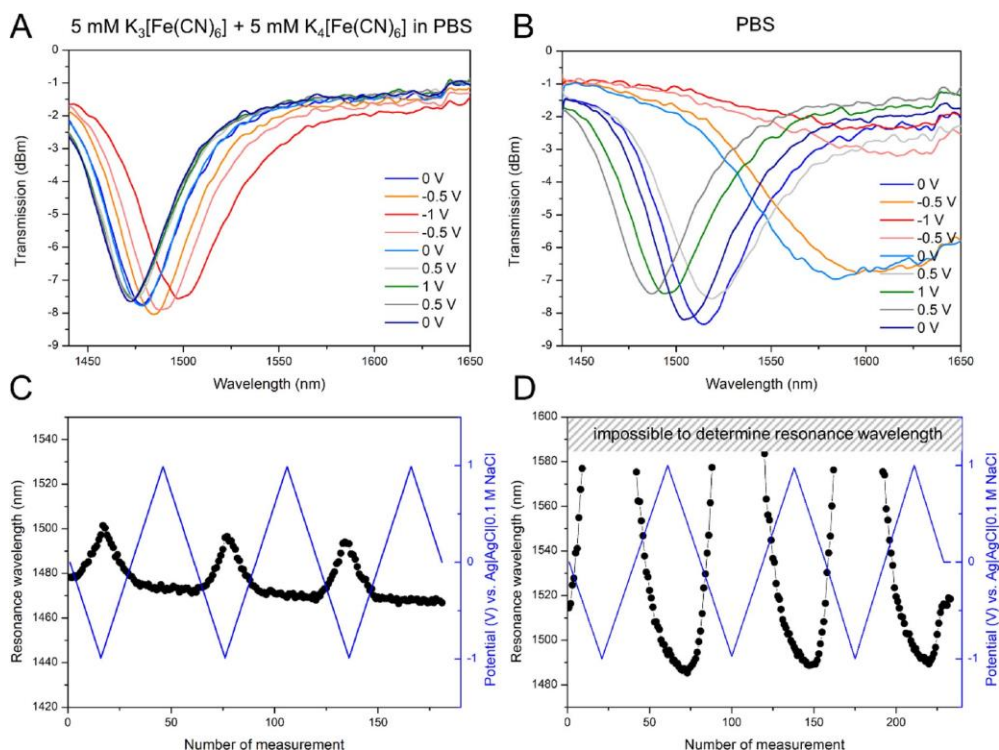


Fig. 35. Optical response of LPG during EC stimulation (three CV scans) in different electrolytes, where transmission spectra for selected potentials are shown for the first scan in PBS with redox probe (A) and in PBS only (B), and the corresponding resonance wavelength vs. potential applied during measurements in PBS with redox probe (C) and in PBS only (D) [B2].

These changes are induced by the electrochemical processes which are governed by the applied potential. This phenomenon, originating from the above-mentioned effects, provides a unique possibility to optically monitor electrochemical processes in the close vicinity of the electrode as well as the chemical changes of the electrode surface. Moreover, the effect depends on the composition of the investigated solution and therefore has the potential as a detection technique by itself [B2]. Fig. 35 shows the optical response of the LPG fiber covered by a thin ITO film to the changes in applied potential during cyclic voltammetry in PBS (phosphate buffered saline). A similar effect was also observed for PCS fibers with ITO-LMR film [B3], see Fig. 36.

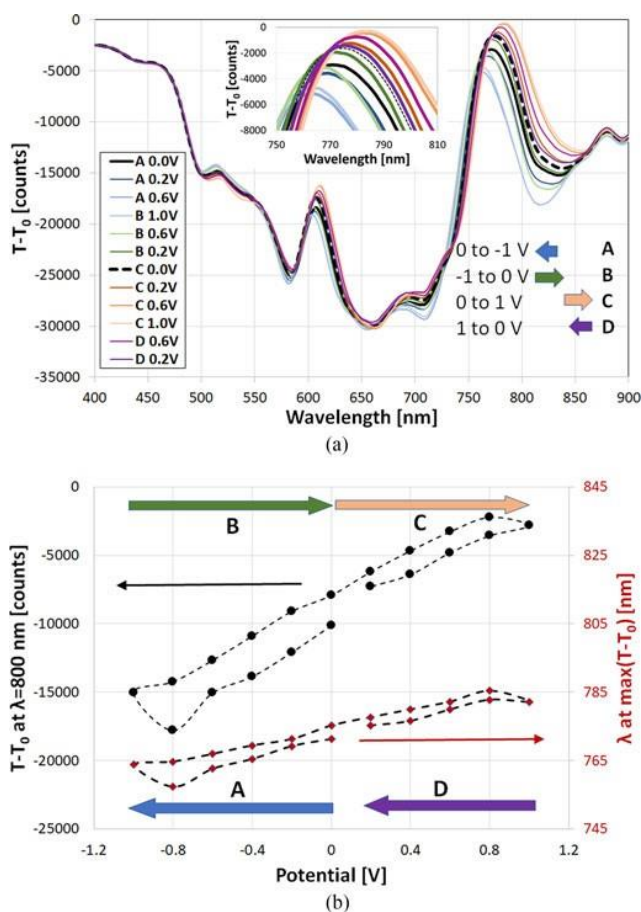


Fig. 36. Response of the ITO-LMR sensor to a cycling potential between -1 and 1 V with a scan rate 10 mV/s in 0.5 M Na_2SO_4 solution containing 5 mM $[\text{Fe}(\text{CN})_6]^{3-/4-}$ where (a) shows the sensor's spectral response and (b) compares corresponding transmission changes at $\lambda = 800$ nm and transmission maximum's wavelength shift. The inset in (a) shows the investigated spectral range [B3].

It has also been shown in [B4] that both the electrochemical and optical responses of the sensor to the applied potential are similar in character. However, the optical readout may deliver supplementary information about the investigated liquid, i.e., molecules adsorbed to the surface of the electrode, or clear optical response at low scan rates when the recorded currents tend to be low. Fig. 37 shows the effect of the scan rate on the electrochemical and optical response – while the measured current is proportional to the scan rate, the LMR shift behaves in an opposite manner, i.e., is greater for lower scan rates. When the electrochemical response depends solely on the charge transfer at the ITO/electrolyte interface, the optical response on top of charge-induced changes in the optical properties of ITO also depends on the composition of the electrolyte and its admixtures.

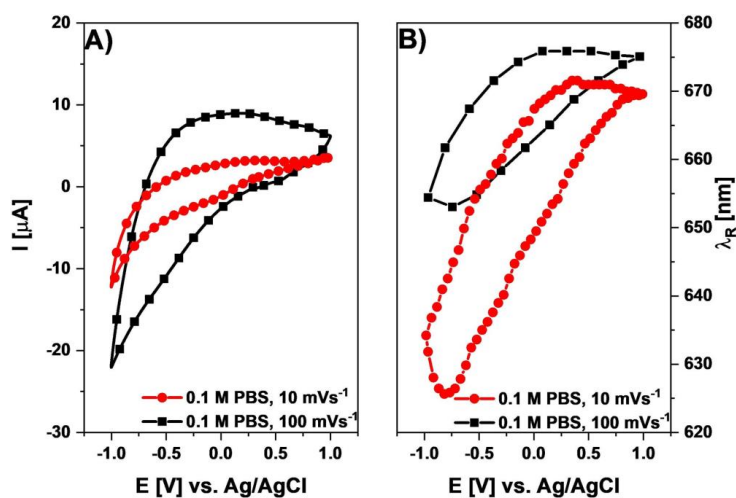


Fig. 37. Electrochemical (A) and optical (B) response of the ITO-LMR sensor when investigated in 0.1 M PBS with a scan rate of 10 and 100 mV/s [B4].

It must be noted that not only multi-domain interrogations are possible with the proposed approach, but it also gives a capability to initiate a specific process in one domain and monitor its progress in the other domain (e.g. measure sub-nanometer changes in the layer deposited by electropolymerization) [B2]. For example, in [B3], the LMR interrogation enabled observation of electrode oxidation in PBS solution through 10 consecutive scans in the positive potential region. This phenomenon, on top of the potential cycling effect, is visible in Fig. 38(a) as a gradual build-up of the mean transmission $T-T_0$ along with the number of scans. As a result of

subsequent CV scans, a clear decrease in current is observed for the ITO-LMR electrode/sensor, see Fig. 38(b).

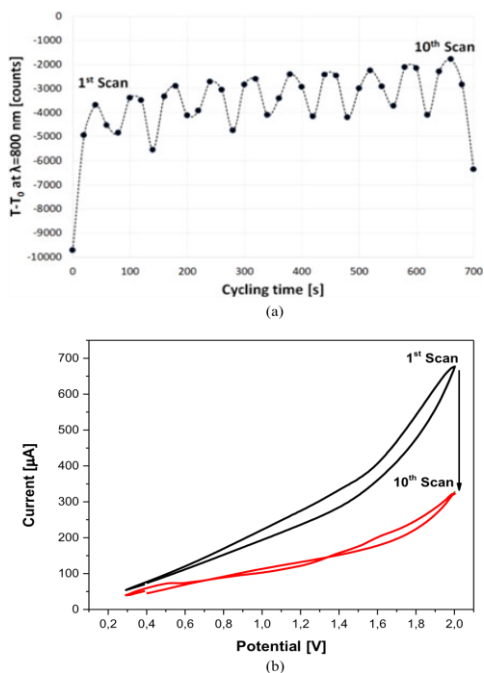


Fig. 38. The effect scanning process in 0.1 M PBS (pH = 7.02), where (a) shows the change in transmission at $\lambda = 800$ nm acquired on average every 20 s and (b) the change in current peaks during the cyclic voltammetry scans from 1 to 10 scans. The scan rate 10 mV/s and the first measurement in (a) corresponds to 0.4 V [B3].

Among the studies in this subsection, attention was also paid to the further enhancement of the sensor electrochemical response by electropolymerization of poly(3,4-ethylenedioxythiophene)-poly(4-styrenesulfonate) (PEDOT:PSS) on the ITO surface. As shown in [B5], the PEDOT:PSS film enhances the transfer of electric charges between the electrolyte and ITO, leading to an enhancement of the electrochemical response – improved reversibility of the reaction while maintaining the optical response. Moreover, the usage of fluorine-doped tin oxide (FTO) instead of ITO leads to a better performance in the electrochemical domain, while only slightly worse performance in the optical domain. Hence, FTO is a promising candidate for replacing ITO, as FTO is less expensive and also more mechanically and chemically durable [B6].

Summary: The research presented in this subsection verified and highlighted the great utility of the TCO materials for the dual-domain interrogation of an analyte. This approach is valuable, especially in cases where the detection possibilities in one domain are severely limited. This can be crucial for the monitoring of various processes on the surface of the sensor that can occur during biological experiments. Furthermore, the concept of dual-domain interrogation of liquids introduced above demonstrates great potential for the detection of biomolecules and pathogens.

List of the publications in the subsection

- B1. Marta Janczuk-Richter, Monika Piestrzyńska, Dariusz Burnat, Katarzyna Szot-Karpińska, **Petr Sezemsky**, Vitezslav Stranak, Wojtek J. Bock, Robert Bogdanowicz, Joanna Niedziółka-Jönsson, and Mateusz Smietana, Optical monitoring of electrochemical processes with ITO-coated long-period fiber grating, 26th International Conference on Optical Fiber Sensors, September 24-28 2018, Lausanne, Switzerland, OSA Technical Digest (Optical Society of America, 2018), paper ThE54. (<https://doi.org/10.1364/OFS.2018.ThE54>)
- B2. Marta Janczuk-Richter, Monika Piestrzynska, Dariusz Burnat, **Petr Sezemsky**, Vitezslav Stranak, Wojtek J Bock, Robert Bogdanowicz, Joanna Niedziółka-Jönsson, Mateusz Smietana, Optical investigations of electrochemical processes using a long-period fiber grating functionalized by indium tin oxide, *Sensors & Actuators: B Chemical* 279, (2019), 223–229. (<https://doi.org/10.1016/j.snb.2018.10.001>)
- B3. Mateusz Smietana, Michał Sobaszek, Bartosz Michalak, Paweł Niedziałkowski, Wioleta Białobrzeska, Marcin Koba, **Petr Sezemsky**, Vitezslav Stranak, Jakub Karczewski, Tadeusz Ossowski, Robert Bogdanowicz, Optical Monitoring of Electrochemical Processes With ITO-Based Lossy-Mode Resonance Optical Fiber Sensor Applied as an Electrode, *Journal of Lightwave Technology* 36, (2018), 954 - 960. (<https://doi.org/10.1109/jlt.2018.2797083>)
- B4. Mateusz Smietana, Paweł Niedziałkowski, Wioleta Białobrzeska, Dariusz Burnat, **Petr Sezemsky**, Marcin Koba, Vitezslav Stranak, Katarzyna Siuzdak, Tadeusz Ossowski, Robert Bogdanowicz, Study on Combined Optical and Electrochemical Analysis Using Indium-tin-oxide-coated Optical Fiber Sensor, *Electroanalysis* 31, (2019), 398. (<https://doi.org/10.1002/elan.201800638>)
- B5. Michał Sobaszek, Dariusz Burnat, **Petr Sezemsky**, Vitezslav Stranak, Robert Bogdanowicz, Marcin Koba, Katarzyna Siuzdak, Mateusz Smietana, Enhancing electrochemical properties of an ITO-coated lossy-mode resonance optical fiber sensor by electrodeposition of PEDOT:PSS, *Optical Materials Express* 9(7), (2019), 3069-3078. (<https://doi.org/10.1364/OME.9.003069>)
- B6. Dariusz Burnat, Marta Janczuk-Richter, Paweł Niedziałkowski, Wioleta Białobrzeska, **Petr Sezemsky**, Marcin Koba, Vitezslav Stranak, Robert Bogdanowicz, Tadeusz Ossowski, Joanna Niedziółka-Jönsson, Mateusz Smietana, Optical fiber lossy-mode resonance sensors with doped tin oxides for optical working electrode monitoring in electrochemical systems, *Proceedings SPIE* 11199, Seventh European Workshop on Optical Fibre Sensors, (2019), 111991O. (<https://doi.org/10.1117/12.2541354>)

C. Bioactivation of Sensors for Selective Detection

The final subsection summarizes the research that utilized electrochemically active LMR optical fiber-based sensors for selective label-free detection of biochemical complexes. Sensors without any further functionalization, as presented in the previous subsection, could be utilized for electrochemical measurements combined with optical refractometry but without selective detection. For selective label-free detection of biomolecules or microorganisms, the sensor transducer needs to be functionalized. Primarily, two methods of functionalization were carried out in the frame of this thesis to obtain biologically active surfaces: (i) silanization and (ii) electropolymerization.

The first one employs standard silanization procedures on the sensor's active area, i.e., on the ITO surface of the transducer, for the introduction of grafting functional groups; see the attached works [C3, C4]. These functional groups provide possible covalent binding of biologically active molecules, i.e., receptor molecules, responsible for the selective detection of the required complexes. For example, work [C4] describes the standard biotin-avidin complex to verify sensor functional properties. Here, the biotin served as the receptor agent and was attached to the ITO surface through APTES (3-aminopropyltriethoxysilane) introducing NH_2 groups. The sensor was then exposed to solutions with different concentrations of avidin. Throughout the whole process of functionalization by biotin and detection of avidin, the LMR was monitored. After each step of the procedure, the electrochemical response of the sensor in PBS was measured as well. Fig. 39 shows a clear correlation of the electrochemical and optical responses to the progress of the experiment.

It was demonstrated on the example of the biotin-avidin detection system that when avidin concentration increases, a decrease in current and an increase in LMR wavelength shift were recorded in EC and optical domains, respectively. Hence, the simultaneous dual-domain EC and optical detection was achieved. Both optical and EC responses follow the protein interaction process and thus can be used as cross-verification of the readouts. Moreover, extensive information has been achieved compared to solely EC interrogation, i.e., the biotin and avidin grafting process was directly monitored optically, displaying individual steps of an incubation procedure [C4].

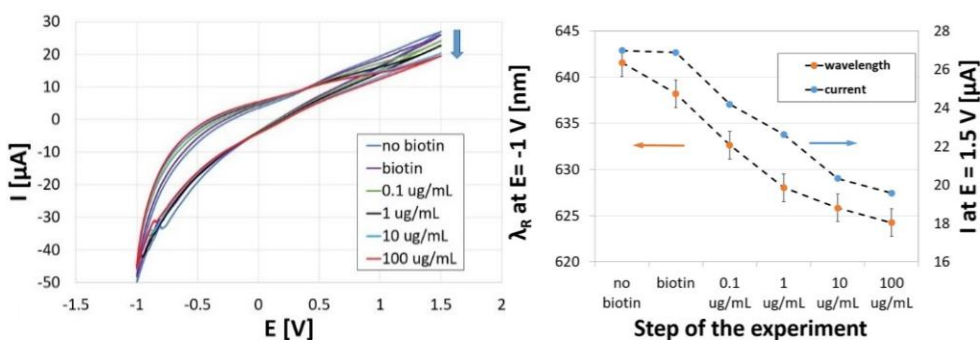


Fig. 39. Left: CV curves recorded in PBS for all steps of the experiment. The arrow at $E = 1.5 \text{ V}$ indicates the drop in current (I). The scan rate was set to 20 mV/s . Right: Comparison of optical (λ_R at $E = -1 \text{ V}$) and electrochemical (I at $E = 1.5 \text{ V}$) readouts for each step of the experiment [C4].

The second method utilizes the electrochemical activity of the sensor body to induce direct electropolymerization of molecules directly on the surface of the sensor active area. At first, this inherent property of the sensor was used for direct observation of the electropolymerization of isatin [C1] and ketoprofen [C2] on the sensor surface. However, this effect was later utilized for direct binding of the receptor molecules, too. The advantage of such an approach is that it skips the time-consuming procedure of the silanization step in the sensor fabrication process.

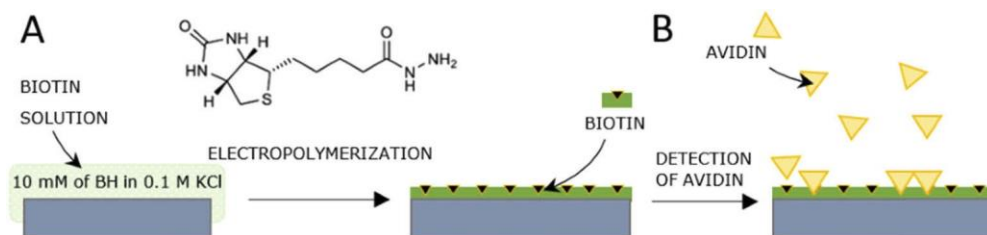


Fig. 40. Schematic representation of A) biotin hydrazide electropolymerization process, B) binding of avidin to the biotinylated ITO-LMR surface [C5].

Also, in this case, the standard biotin-avidin biochemical system was tested to verify the efficiency of sensor functionalization; the procedure is shown in Fig. 40. CV curves recorded in $1 \text{ mM Fc}-(\text{CH}_2\text{OH})_2^{+/0}$ solution containing 0.1 M KCl after incubation in bovine serum albumin (BSA), 0.01 and 0.1 mg/mL of avidin are depicted in Fig. 41(a). Right after electropolymerization, the ITO-LMR electrode was immersed in a 1% BSA

solution to block any nonspecific interactions on the surface. This caused a decrease in the current peak and increased ΔE_p from 220 to 270 mV. In the next step, the functionalized ITO-LMR electrode was submerged for 30 minutes in 0.1 mg/mL solution of avidin. Although the current peak decreased after avidin incubation, the shapes of the obtained voltammograms were very similar to those after BSA. Additionally, the calculated value of ΔE_p was at the same level ~ 270 mV as for the previous stage of the experiment. In contrast, the immersion of the ITO-LMR in the second concentration of avidin caused noticeable changes in CV, decreasing the peak current and increasing ΔE_p to the value of ~ 250 mV [C5].

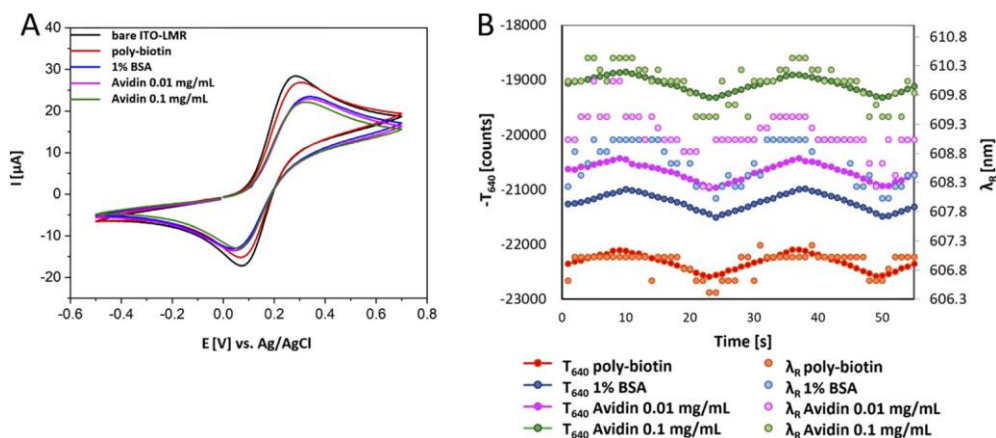


Fig. 41. A) CVs after each step of avidin detection in the presence of 1 mM $Fe-(CH_2OH)_2$ in 0.1 M KCl, scan rate: 50 mV/s; (B) Corresponding change in ITO-LMR λ_R and T_{640} after each step of the avidin detection experiment [C5].

Fig. 41(b) shows the evolution of the corresponding optical parameters, namely, the resonance position λ_R and transmittance at 640 nm T_{640} after each step of the experiment. The apparent shift to longer wavelengths and decrease in transmission corresponds to an increase in the thickness and/or RI of the surface of the biological layer on the biotin-functionalized ITO-LMR surface. Starting from the formation of the BSA layer, the ~ 1 nm shift of λ_R can be observed. Next, for the avidin molecule, we can observe further changes. It can be seen that the higher the concentration of avidin, the greater the LMR shift to longer wavelengths is obtained. The most significant change of $\lambda_R \sim 2$ nm was observed for the 0.1 mg/mL concentration of avidin. The

obtained results confirm the detection of avidin on the ITO-LMR sensor using both electrochemical and optical methods at a level of 0.01 to 0.1 mg/mL [C5].

Regardless of the chosen surface bioactivation method, i.e., electropolymerization or silanization, each step of the preparation process is observable in the LMR spectrum as well as in the electrochemical response of the sensor. The molecules attached to the surface cause changes in the refractive index of the surrounding media, but also block the surface for passage of the electroactive species and change the measured current upon applying a potential to the electrode. Once the sensor surface is covered by receptor molecules that selectively interact with the target species, the detection principle and procedure lie in observing the changes in LMR upon the interaction and in the changed electrochemical behavior of the probe.

It is important to note that, while the electrochemical response to the low concentration of avidin was rather poor, the LMR response was clearly observable. At the same time, during the biotin incubation, the situation was the opposite, i.e., the LMR response was relatively weak while the electrochemical response was strong. This feature highlights the advantages of dual-domain monitoring [B4, C5].

Finally, further research has shown the viability of the simultaneous dual-domain sensor concept for the detection of pathogens, *Borrelia burgdorferi*, specifically [A6]. Regarding the detection of pathogens, it is possible indirectly through the presence of antibodies synthesized by the immune system of an organism during an infection. In this case, sandwich immunoassays are one of the most frequently applied. Two antibodies (primary and secondary) synthesized against *Borrelia burgdorferi* have been utilized as a receptor and specific target, respectively. The LMR sensor with an ITO film surface has been biofunctionalized to facilitate the specific binding of an analyte. First, surface silanization with TESPSA (3-triethoxysilylpropyl succinic anhydride) was performed. In the next step, the sensor was submerged in a solution of the primary antibodies to covalently bond them to the surface. For the sensitivity analysis, the sensor was immersed in increasing concentrations (1, 5, and 10 $\mu\text{g/mL}$) of the secondary antibody. During each step, the optical signal of the LMR sensor was monitored. At each step of the experiment, after binding and washing, the samples have been

placed consecutively in PBS and 1 mM ferrocenedimethanol (in PBS) and underwent 3 CV cycles with simultaneous optical monitoring.

Fig. 42 shows the evolution of the EC and optical response of the sensor after each step of the experiment recorded in 1,1'-Ferrocenedimethanol and PBS, respectively. At first, the rapid decrease of anodic and cathodic peak currents indicates successful silanization, see Fig. 42 (a). The shift to longer wavelengths (indicated by the black arrow in Fig. 42 (b)) corresponds to an increase in the thickness of the surface of the biological layer on the functionalized ITO-LMR's surface, which additionally confirms the electrochemical results. Next, both optical and EC responses followed the antibody-antibody interaction. When the target antibody concentration increases, a decrease in current and an increase in LMR wavelength shift were recorded in the EC and optical domain, respectively, proving the binding of antibodies to the sensor surface. It can also be noted that measurements in the EC domain are effective when interactions occur at the sensor surface, while optical measurements may deliver information about events taking place slightly away from the surface. However, the changes after further steps of the experiment, such as increasing ΔE , are still clear and indicate binding of the receptor and different concentrations of the target [A6].

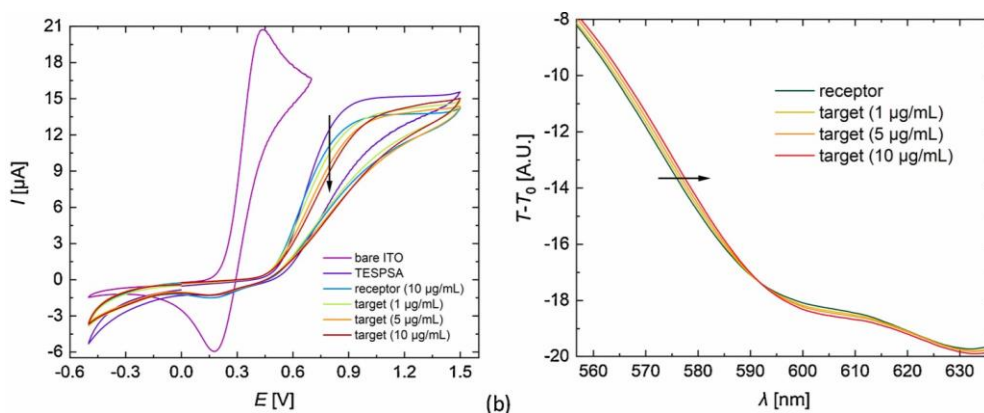


Fig. 42. EC and optical responses of ITO-LMR sensors recorded after each incubation step during the process of *Borrelia burgdorferi* receptor-target interactions, (a) shows CV recorded at scan rate 20 mV/s in 1,1'-Ferrocenedimethanol and (b) optical spectra acquired in PBS [A6].

Fig. 43(a) presents the evolution of λ_{LMR} during the entire experiment. A clear shift of the LMR wavelength to longer wavelengths can be seen at the functionalisation stages and for an increase in the target concentration. It can

also be seen in Fig. 43(b) that the trend for both electrochemical and optical measurements is very similar, providing cross-verification of biosensing experiments [A6].

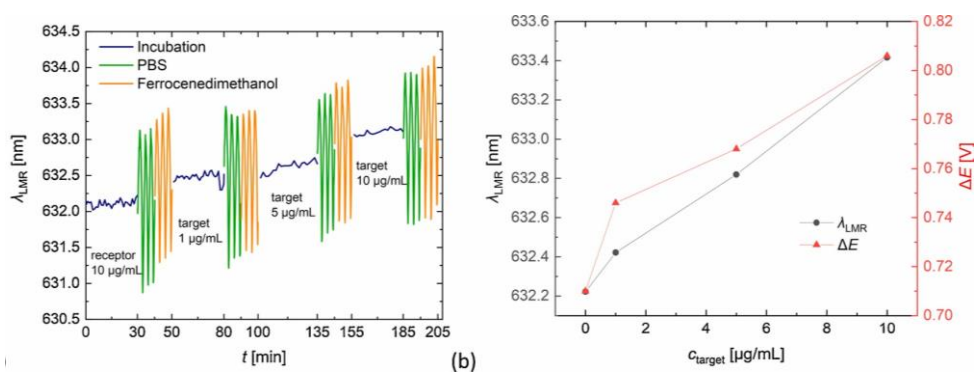


Fig. 43. (a) Sensogram for the ITO-LMR biosensing experiment and (b) comparison of the ITO-LMR wavelength and ΔE shift at each step of the *Borrelia burgdorferi* receptor-target interaction experiment. The oscillations seen in (a) correspond to the cycling potential [A6].

Summary: Here, a novel concept of a sensor simultaneously interrogating in two independent domains was presented: (i) the optical lossy mode resonance (LMR) domain and (ii) the electrochemical domain. The dual-domain sensor, based on the optical fiber with an ITO transducer deposited by magnetron sputtering, was successful in the detection of various biocomplexes with the potential to reveal and recognize Lyme Borreliosis infection in the human body. Dual-domain sensing design increases the reliability of the detection and extends the measurement range. The reported dual-domain system allows to gather considerably more information on the investigated samples with cross-verification of the obtained results possible within one experiment. Since the sensitivity and range for the two domains may be different, they can serve as a complement to each other, leading to a significant improvement in sensor performance. What is more, it also gives the capability to conduct a functionalization process (namely, electropolymerization) in one domain and to monitor its progress in the other one. All of these features can be especially valuable in biochemical and biomedical applications and the interrogation of low-volume samples.

List of the publications in the subsection

- C1. Michał Sobaszek, Magdalena Dominik, Dariusz Burnat, Robert Bogdanowicz, Vitezslav Stranak, **Petr Sezemsky**, Mateusz Smietana, Optical monitoring of thin film electro-polymerization on surface of ITO-coated lossy-mode resonance sensor, 2017 25TH INTERNATIONAL CONFERENCE ON OPTICAL FIBER SENSORS (OFS), Proceedings of SPIE 10323, (2017), UNSP 103234W. (<https://doi.org/10.1117/12.2265932>)
- C2. Robert Bogdanowicz, Paweł Niedziałkowski, Michał Sobaszek, Dariusz Burnat, Wioleta Białobrzaska, Zofia Cebula, **Petr Sezemsky**, Marcin Koba, Vitezslav Stranak, Tadeusz Ossowski, Mateusz Smietana, Optical Detection of Ketoprofen by Its Electropolymerization on an Indium Tin Oxide-Coated Optical Fiber Probe, Sensors (Basel) 18(5), (2018), pii: E1361. (<https://doi.org/10.3390/s18051361>)
- C3. Marcin Koba, Dariusz Burnat, Katarzyna Szot-Karpińska, **Petr Sezemsky**, Vitezslav Stranak, Robert Bogdanowicz, Joanna Niedziółka-Jönsson, Mateusz Smietana, Combined optical and electrochemical analysis of protein binding with ITO-coated lossy-mode resonance sensor, Proceedings SPIE 11199, Seventh European Workshop on Optical Fibre Sensors, (2019), 111991E. (<https://doi.org/10.1117/12.2540849>)
- C4. Mateusz Smietana, Marcin Koba, **Petr Sezemsky**, Katarzyna Szot-Karpinska, Dariusz Burnat, Vitezslav Stranak, Joanna Niedziółka-Jönsson, Robert Bogdanowicz, Simultaneous optical and electrochemical label-free biosensing with ITO-coated lossy-mode resonance sensor, Biosensors and Bioelectronics, 154, (2020), 112050. (<https://doi.org/10.1016/j.bios.2020.112050>)
- C5. Monika Janik, Paweł Niedziałkowski, Katarzyna Lechowicz, Marcin Koba, **Petr Sezemsky**, Vitezslav Stranak, Tadeusz Ossowski, Mateusz Smietana, Electrochemically directed biofunctionalization of lossy-mode resonance optical fiber sensor, Optics Express 28(11), (2020), 15934. (<https://doi.org/10.1364/OE.390780>)

SUMMARY AND CONCLUSION

The ultimate motivation and purpose of this thesis was the development and fabrication of a two-domain sensor based on the optical fiber which enables simultaneous optical (LMR) and electrochemical interrogation of liquid analytes. For that reason, multidisciplinary research on the borders of plasma physics, material science, optics, electrochemistry, and biochemistry was carried out.

The strategy for dual-domain interrogation sensor fabrication was developed and investigated in detail. The challenge of a simultaneous and dual-domain sensor was approached by coating the optical fiber with a highly tailored indium tin oxide (ITO) thin film. Precisely optimized and nanostructured ITO film, acting as a sensor transducer, was deposited by plasma-assisted techniques. As shown in Part A of the Research Section, low-temperature plasma deposition enables tuning of the process for optimization of the ITO structure for both the LMR and electrochemical detection. Namely, the utilization of HiPIMS enabled the production of highly crystalline films with proper optical and electrochemical properties while keeping the fabrication procedure at room temperature without post-deposition annealing.

As shown in part B of the Research Section, sensors with sufficient performance in both domains simultaneously enabled a new opto-electrochemical interrogation of an analyte. In general, the material properties and physical principles of the proposed sensing concept are explained in detail. Carefully conducted research showed that the readouts in the two domains are not completely independent, as the potential applied to the electrode (sensor) induces changes in the surrounding media as well as in the film itself. These changes, in turn, lead to alterations in the LMR spectra, enabling a more detailed study of the electrochemical processes. Particularly interesting results showed that by applying a negative potential to the electrode, the LMR sensitivity could be increased. Moreover, the presented results show that the detection range of the sensor is extended, as, in some particular experimental conditions, one of the domains could not provide sufficient information about the surface events while the other could.

In part C of the Research Section, it is shown that the optimal design of the active surface on an optical fiber enables simultaneous (in time and in situ)

optical and electrochemical interrogation of liquids and detection of biomolecules and biocomplexes. Ultimately, the sensor concept was able to verify the presence of Lyme borreliosis pathogens. Moreover, utilizing the electrochemical activity of the ITO film enabled direct electropolymerization of the receptor molecules on the sensor, which significantly simplifies the transducer functionalization and subsequently reduces the duration of the sensor fabrication procedure and its cost. Although the group of molecules and pathogens tested so far is limited, the character of the developed sensor enables its relatively simple modification to also enable the detection of many other substances from the family of biomolecules and microorganisms.

The results achieved within my Ph.D. study have been published in 20 papers in scientific journals and presented 6 times as oral contributions (1 of them invited) at international conferences. In two papers, published in *Plasma Sources Science Technology* (IF 3.193) and *Sensors and Actuators B* (IF 7.46), I am the first author. In the rest of the papers, I am a coauthor with a contribution to the fabrication of sensors, material research, and optimization of detecting capabilities.

Finally, it can be concluded that all the objectives of the thesis were met successfully. We have developed a concept for novel detection from the idea up to the final product, from the sensing concept up to the sensor capable of revealing the presence of selected biomolecules and pathogens. Despite advancements in its development, the presented sensor can be even further improved and optimized. Hopefully, in the future, the developed biosensor will provide aid in the field of analytical chemistry and in controlling and prevention of disease outbreaks as well as in the overall improvement of worldwide medical care due to its low-cost character and fast and reliable detection.

REFERENCES

- [1] Y. Yuan, T. Guo, X. Qiu, J. Tang, Y. Huang, L. Zhuang, S. Zhou, Z. Li, B.-O. Guan, X. Zhang and J. Albert, "Electrochemical Surface Plasmon Resonance Fiber-Optic Sensor: In Situ Detection of Electroactive Biofilms," *Analytical Chemistry*, vol. 88, pp. 7609-7616, 2016.
- [2] J. F. Cerda, C. X. Guzman, H. Zhang, E. J. Amendola, J. D. Castorino, N. Millet, A. L. Fritz, D. N. Houchins and M. H. Roeder, "Spectroelectrochemical measurements of redox proteins by using a simple UV/visible cell," *Electrochemistry Communications*, vol. 33, pp. 76-79, 2013.
- [3] E. Lindgren and T. G. Jaenson, Lyme borreliosis in Europe: influences of climate and climate change, epidemiology, ecology and adaptation measures, Copenhagen: World Health Organization, 2006.
- [4] L. Penggao, W. Dongling, G. Yang, W. Y. Tao, "Reduced graphene oxide-coated mulberry-shaped α -Fe₂O₃ nanoparticles composite as high performance electrode material for supercapacitors," *Journal of Alloys and Compounds*, pp. 89-96, 25 MAR 2018.
- [5] O. Polonskyi, P. Solar, O. Kylian, M. Drabik, A. Artemenko, J. Kousal, J. Hanus, J. Pesicka, I. Matolinova, E. Kolibalova, D. Slavinska and H. Biederman, "Nanocomposite metal/plasma polymer films prepared by means of gas aggregation cluster source," *Thin Solid Films*, vol. 520, p. 4155–4162, 2012.
- [6] F. Flory, L. Escoubas and G. Berginc, "Optical properties of nanostructured materials: a review," *Journal of Nanophotonics*, vol. 5, p. 1 – 21, 2011.
- [7] F. Rosei, "Nanostructured surfaces: challenges and frontiers in nanotechnology," *Journal of Physics: Condensed Matter*, vol. 16, p. S1373–S1436, April 2004.
- [8] L. Dai, H. A. W. StJohn, J. Bi, P. Zientek, R. C. Chatelier and H. J. Griesser, "Biomedical coatings by the covalent immobilization of polysaccharides onto gas-plasma-activated polymer surfaces," *Surface and Interface Analysis*, vol. 29, pp. 46-55, 2000.
- [9] K. Vasilev, S. S. Griesser and H. J. Griesser, "Antibacterial Surfaces and Coatings Produced by Plasma Techniques," *Plasma Processes and Polymers*, vol. 8, pp. 1010-1023, 2011.
- [10] C. Chouquet, J. Gavillet, C. Ducros and F. Sanchette, "Effect of DLC surface texturing on friction and wear during lubricated sliding," *Materials Chemistry and Physics*, vol. 123, pp. 367-371, 2010.

-
- [11] Y.-B. Choi, W.-Y. Jeon and H.-H. Kim, "A Simple Interfacial Platform for Homogeneous Electrochemical Immunoassays Using a Poly(Vinylimidazole)-Modified Electrode," *Sensors*, vol. 17, 2017.
- [12] V. Kunduru, M. Bothara, J. Grosch, S. Sengupta, P. K. Patra and S. Prasad, "Nanostructured surfaces for enhanced protein detection toward clinical diagnostics," *Nanomedicine: Nanotechnology, Biology and Medicine*, vol. 6, pp. 642-650, 2010.
- [13] K. Liang, H. Wu and Y. Li, "Immune-enrichment of insulin in biofluids on gold-nanoparticle decorated target plate and in situ detection by MALDI MS," *Clinical Proteomics*, vol. 14, p. 5, 2017.
- [14] D. T. N. Tram, H. Wang, S. Sugiarto, T. Li, W. H. Ang, C. Lee and G. Pastorin, "Advances in nanomaterials and their applications in point of care (POC) devices for the diagnosis of infectious diseases," *Biotechnology Advances*, vol. 34, pp. 1275-1288, 2016.
- [15] B. Pejcic, R. De Marco and G. Parkinson, "The role of biosensors in the detection of emerging infectious diseases," *Analyst*, vol. 131, pp. 1079-1090, 2006.
- [16] F. Pires, H. Silva, O. Domínguez-Renedo, M. A. Alonso-Lomillo, M. J. Arcos-Martínez and A. C. Dias-Cabral, "Disposable immunosensor for human cytomegalovirus glycoprotein B detection," *Talanta*, vol. 136, pp. 42-46, 2015.
- [17] A. Heller and B. Feldman, "Electrochemical glucose sensors and their applications in diabetes management," *Chemical Reviews*, vol. 108, pp. 2482-2505, 2008.
- [18] A. M. Caliendo, D. N. Gilbert, C. C. Ginocchio, K. E. Hanson, L. May, T. C. Quinn, F. C. Tenover, D. Alland, A. J. Blaschke, R. A. Bonomo, K. C. Carroll, M. J. Ferraro, L. R. Hirschhorn, W. P. Joseph, T. Karchmer, A. T. MacIntyre, L. B. Reller, A. F. Jackson and for the Infectious Diseases Society of America (IDSA), "Better Tests, Better Care: Improved Diagnostics for Infectious Diseases," *Clinical Infectious Diseases*, vol. 57, pp. S139-S170, December 2013.
- [19] N. Dale and B. G. Frenguelli, "Measurement of purine release with microelectrode biosensors," *Purinergic Signalling*, vol. 8, p. 27-40, 2012.
- [20] P. Šácha, T. Knedlík, J. Schimer, J. Tykvart, J. Parolek, V. Navrátil, P. Dvořáková, F. Sedlák, K. Ulbrich, J. Strohalm, P. Majer, V. Šubr and J. Konvalinka, "iBodies: Modular Synthetic Antibody Mimetics Based on Hydrophilic Polymers Decorated with Functional Moieties," *Angewandte Chemie International Edition*, vol. 55, pp. 2356-2360, 2016.

-
- [21] "iBodies.eu," iBodies project, 2021. [Online]. Available: <https://www.ibodies.eu/#about>. [Accessed 1 10 2021].
- [22] D. Oupický, C. Konák and K. Ulbrich, "DNA complexes with block and graft copolymers of N-(2-hydroxypropyl)methacrylamide and 2-(trimethylammonio)ethyl methacrylate," *Journal of Biomaterials Science, Polymer Edition*, vol. 10, pp. 573-590, 1999.
- [23] F. Chiavaioli, F. Baldini, S. Tombelli, C. Trono and A. Giannetti, "Biosensing with optical fiber gratings," *Nanophotonics*, vol. 6, p. 663–679, 2017.
- [24] T. B. Tims and D. V. Lim, "Rapid detection of Bacillus anthracis spores directly from powders with an evanescent wave fiber-optic biosensor," *Journal of Microbiological Methods*, vol. 59, pp. 127-130, 2004.
- [25] S. M. Yoo and S. Y. Lee, "Optical Biosensors for the Detection of Pathogenic Microorganisms," *Trends in Biotechnology*, vol. 34, pp. 7-25, 2016.
- [26] S. Liu, Z. Zheng and X. Li, "Advances in pesticide biosensors: current status, challenges, and future perspectives," *Analytical and Bioanalytical Chemistry*, vol. 405, p. 63–90, 2013.
- [27] V. K. Nigam and P. Shukla, "Enzyme Based Biosensors for Detection of Environmental Pollutants-A Review," *Journal of Microbiology and Biotechnology*, vol. 25, pp. 1773-1781, 2015.
- [28] Y. Rosenberg, "Production of highly thermally stable recombinant cholinesterases for the detection, detoxification and decontamination of organophosphorus compounds". Patent WO2015142679A1, 24 9 2015.
- [29] S. Bidmanova, R. Chaloupkova, J. Damborsky and Z. Prokop, "Development of an enzymatic fiber-optic biosensor for detection of halogenated hydrocarbons," *Analytical and Bioanalytical Chemistry*, vol. 398, p. 1891–1898, 2010.
- [30] R. Chaloupkova, T. Prudnikova, P. Rezacova, Z. Prokop, T. Koudelakova, L. Daniel, J. Brezovsky, W. Ikeda-Ohtsubo, Y. Sato, M. Kutý, Y. Nagata, I. K. Smatanova and J. Damborsky, "Structural and functional analysis of a novel haloalkane dehalogenase with two halide-binding sites," *Acta Crystallographica Section D Biological Crystallography*, vol. 70, pp. 1884-1897, 2014.
- [31] B. R. Eggins, *Biosensors: An introduction*, Stuttgart: Wiley Teubner, 1996.

-
- [32] A. Ebner, P. Hinterdorfer and H. J. Gruber, "Comparison of different aminofunctionalization strategies for attachment of single antibodies to AFM cantilevers," *Ultramicroscopy*, vol. 107, no. 10-11, pp. 922-927, 2007.
- [33] A. Gang, G. Gabernet, L. D. Renner, L. Baraban and G. Cuniberti, "A simple two-step silane-based (bio-) receptor molecule immobilization without additional binding site passivation," *RSC ADVANCES*, vol. 5, pp. 35631-35634, 2015.
- [34] R. Hippler, H. Kersten, M. Schmidt and K. Schoenba, *Low Temperature Plasmas: Fundamentals, Technologies and Techniques*, Berlin: WILEY-VCH Verlag, 2007.
- [35] J. R. Roth, *Industrial Plasma Engineering: Principles*, Bristol: Institute of Physics Publishing, 2001.
- [36] M. A. Lieberman and A. J. Lichtenberg, *Principles of Plasma Discharges and Materials Processing*, Hoboken, Hoboken (New Jersey): John Wiley & Sons, Inc., 2005.
- [37] D. M. Mattox, *Handbook of Physical Vapor Deposition Processing*, Oxford: Elsevier Inc., 2010.
- [38] J. Musil, J. Vlcek and P. Baroch, "Magnetron discharges for thin films plasma processing," in *Materials Surface Processing by Direct Energy Techniques*, Y. Pauleau, Ed., Oxford, Elsevier Inc., 2006, pp. 67-110.
- [39] O. Kylián, M. Drábik, O. Polonskyi, J. Čechvala, A. Artemenko, I. Gordeev, A. Choukourov, I. Matolínová, D. Slavínská and H. Biederman, "Deposition of nanostructured fluorocarbon plasma polymer films by RF magnetron sputtering of polytetrafluoroethylene," *Thin Solid Films*, vol. 519, pp. 6426-6431, 2011.
- [40] O. Kylián, J. Kousal, A. Artemenko, A. Choukourov, M. Petr, O. Polonskyi, D. Slavinska and H. Biederman, "Deposition of amino-rich coatings by RF magnetron sputtering of Nylon: In-situ characterization of the deposition process," *Surface and Coatings Technology*, vol. 205, pp. S558-S561, 2011.
- [41] P. M. Martin, *Handbook of Deposition Technologies for Films and Coatings*, Oxford: Elsevier Inc., 2005.
- [42] D. Lundin, J. T. Gudmundsson and T. Minea, *High power impulse magnetron sputtering: fundamentals, technologies, challenges and applications*, Elsevier, 2020.
- [43] J. T. Gudmundsson, N. Brenning, D. Lundin and U. Helmersson, "High power impulse magnetron sputtering discharge," *Journal of Vacuum Science & Technology A*, vol. 30, p. 030801, 2012.

-
- [44] K. Sarakinos, J. Alami and S. Konstantinidis, "High power pulsed magnetron sputtering: A review on scientific and engineering state of the art," *Surface and Coatings Technology*, vol. 204, pp. 1661-1684, 2010.
- [45] M. Samuelsson, D. Lundin, J. Jensen, M. A. Raadu, J. T. Gudmundsson and U. Helmersson, "On the film density using high power impulse magnetron sputtering," *Surface and Coatings Technology*, vol. 205, pp. 591-596, 2010.
- [46] A. P. Ehiasarian, J. G. Wen and I. Petrov, "Interface microstructure engineering by high power impulse magnetron sputtering for the enhancement of adhesion," *Journal of Applied Physics*, vol. 101, p. 054301, 2007.
- [47] S. Konstantinidis, J. P. Dauchot and M. Hecq, "Titanium oxide thin films deposited by high-power impulse magnetron sputtering," *Thin Solid Films*, vol. 515, pp. 1182-1186, 2006.
- [48] H. Biederman, "RF sputtering of polymers and its potential application," *Vacuum*, vol. 59, pp. 594-599, 2000.
- [49] P. Solař, O. Kylián, O. Polonskyi, A. Artemenko, D. Arzhakov, M. Drábik, D. Slavínská, M. Vandrovcová, L. Bačáková and H. Biederman, "Nanocomposite coatings of Ti/C:H plasma polymer particles providing a surface with variable nanoroughness," *Surface and Coatings Technology*, vol. 206, pp. 4335-4342, 2012.
- [50] E. Luong-Van, I. Rodriguez, H. Y. Low, N. Elmouelhi, B. Lowenhaupt, S. Natarajan, C. T. Lim, R. Prajapati, M. Vyakarnam, K. Cooper and et al., "Review: Micro- and nanostructured surface engineering for biomedical applications," *Journal of Materials Research*, vol. 28, p. 165-174, 2013.
- [51] V. Straňák, S. Block, S. Drache, Z. Hubička, C. A. Helm, L. Jastrabík, M. Tichý and R. Hippler, "Size-controlled formation of Cu nanoclusters in pulsed magnetron sputtering system," *Surface and Coatings Technology*, vol. 205, pp. 2755-2762, 2011.
- [52] O. Kylián, V. Valeš, O. Polonskyi, J. Pešička, J. Čechvala, P. Solař, A. Choukourov, D. Slavínská and H. Biederman, "Deposition of Pt nanoclusters by means of gas aggregation cluster source," *Materials Letters*, vol. 79, pp. 229-231, 2012.
- [53] P. Solař, O. Polonskyi, A. Choukourov, A. Artemenko, J. Hanuš, H. Biederman and D. Slavínská, "Nanostructured thin films prepared from cluster beams," *Surface and Coatings Technology*, vol. 205, pp. S42-S47, 2011.
-

-
- [54] H. Biederman and L. Martinu, "Plasma Polymer-Metal Composite Films," in *Plasma deposition, treatment, and etching of polymers*, Boston, Academic Press, 1990, pp. 269-317.
- [55] J. Zhao, E. Baibuz, J. Vernieres, P. Grammatikopoulos, V. Jansson, M. Nagel, S. Steinhauer, M. Sowwan, A. Kuronen, K. Nordlund and F. Djurabekova, "Formation Mechanism of Fe Nanocubes by Magnetron Sputtering Inert Gas Condensation," *ACS Nano*, vol. 10, p. 4684–4694, April 2016.
- [56] S. Drache, V. Stranak, Z. Hubicka, F. Berg, M. Tichy, C. A. Helm and R. Hippler, "Study of mass and cluster flux in a pulsed gas system with enhanced nanoparticle aggregation," *Journal of Applied Physics*, vol. 116, p. 143303, 2014.
- [57] R. Alvarez, J. M. García-Martín, M. Macías-Montero, L. Gonzalez-Garcia, J. C. González, V. Rico, J. Perlich, J. Cotrino, A. R. González-Elipe and A. Palmero, "Growth regimes of porous gold thin films deposited by magnetron sputtering at oblique incidence: from compact to columnar microstructures," *Nanotechnology*, vol. 24, p. 045604, January 2013.
- [58] Y. Zhao, D. Ye, G.-C. Wang and T.-M. Lu, "Designing nanostructures by glancing angle deposition," in *Nanotubes and Nanowires*, 2003.
- [59] I. R. Matias, S. Ikezawa and J. Corres, *Fiber Optics Sensors*, vol. 21, Springer International Publishing Switzerland, 2017.
- [60] J. Homola, S. S. Yee and G. Gauglitz, "Surface plasmon resonance sensors: review," *Sensors and Actuators B: Chemical*, vol. 54, pp. 3-15, 1999.
- [61] C. Nylander, B. Liedberg and T. Lind, "Gas detection by means of surface plasmon resonance," *Sensors and Actuators*, vol. 3, pp. 79-88, 1982.
- [62] B. Liedberg, C. Nylander and I. Lunström, "Surface plasmon resonance for gas detection and biosensing," *Sensors and Actuators*, vol. 4, pp. 299-304, 1983.
- [63] A. D. Pomogailo and V. N. Kestelman, "Physical Methods of Incorporating Nanoparticles into Polymers," in *Metallopolymer Nanocomposites*, Berlin, Heidelberg: Springer Berlin Heidelberg, 2005, p. 117–134.
- [64] E. Petryayeva and U. J. Krull, "Localized surface plasmon resonance: Nanostructures, bioassays and biosensing—A review," *Analytica Chimica Acta*, vol. 706, pp. 8-24, 2011.

-
- [65] K. A. Willets and R. P. Van Duyne, "Localized Surface Plasmon Resonance Spectroscopy and Sensing," *Annual Review of Physical Chemistry*, vol. 58, pp. 267-297, 2007.
- [66] A. J. Haes and R. P. Van Duyne, "A unified view of propagating and localized surface plasmon resonance biosensors," *Analytical and Bioanalytical Chemistry*, vol. 379, p. 920-930, 2004.
- [67] S. A. Maier and H. A. Atwater, "Plasmonics: Localization and guiding of electromagnetic energy in metal/dielectric structures," *Journal of Applied Physics*, vol. 98, p. 011101, 2005.
- [68] E. A. Coronado, E. R. Encina and F. D. Stefani, "Optical properties of metallic nanoparticles: manipulating light, heat and forces at the nanoscale," *Nanoscale*, vol. 3, no. 10, pp. 4042-4059, 2011.
- [69] B. Sepúlveda, P. C. Angelomé, L. M. Lechuga and L. M. Liz-Marzán, "LSPR-based nanobiosensors," *Nano Today*, vol. 4, pp. 244-251, 2009.
- [70] J. L. Hammond, N. Bhalla, S. D. Rafiee and P. Estrela, "Localized Surface Plasmon Resonance as a Biosensing Platform for Developing Countries," *Biosensors*, vol. 4, p. 172-188, 2014.
- [71] A. J. Haes, S. Zou, J. Zhao, G. C. Schatz and R. P. Van Duyne, "Localized Surface Plasmon Resonance Spectroscopy near Molecular Resonances," *Journal of the American Chemical Society*, vol. 128, p. 10905-10914, August 2006.
- [72] Y. Kobayashi, H. Katakami, E. Mine, D. Nagao, M. Konno and L. M. Liz-Marzán, "Silica coating of silver nanoparticles using a modified Stöber method," *Journal of Colloid and Interface Science*, vol. 283, pp. 392-396, 2005.
- [73] P. Anna Rita Bizzarri and P. Salvatore Cannistraro, "SERS detection of thrombin by protein recognition using functionalized gold nanoparticles," *Nanomedicine: Nanotechnology, Biology and Medicine*, vol. 3, pp. 306-310, 2007.
- [74] O. Lyandres, N. C. Shah, C. R. Yonzon, J. T. Walsh, M. R. Glucksberg and R. P. Van Duyne, "Real-Time Glucose Sensing by Surface-Enhanced Raman Spectroscopy in Bovine Plasma Facilitated by a Mixed Decanethiol/Mercaptohexanol Partition Layer," *Analytical Chemistry*, vol. 77, p. 6134-6139, October 2005.
- [75] X. Zhang, M. A. Young, O. Lyandres and R. P. Van Duyne, "Rapid Detection of an Anthrax Biomarker by Surface-Enhanced Raman Spectroscopy," *Journal of the American Chemical Society*, vol. 127, p. 4484-4489, March 2005.
-

-
- [76] N. C. Shah, O. Lyandres, J. T. Walsh, M. R. Glucksberg and R. P. Van Duyne, "Lactate and Sequential Lactate–Glucose Sensing Using Surface-Enhanced Raman Spectroscopy," *Analytical Chemistry*, vol. 79, p. 6927–6932, September 2007.
- [77] C. Wang and J. Irudayaraj, "Gold Nanorod Probes for the Detection of Multiple Pathogens," *Small*, vol. 4, pp. 2204–2208, 2008.
- [78] M. Rani, N. K. Sharma and V. Sajal, "Localized surface plasmon resonance based fiber optic sensor with nanoparticles," *Optics Communications*, vol. 292, pp. 92–100, 2013.
- [79] W. B. Lin, N. Jaffrezic-Renault, A. Gagnaire and H. Gagnaire, "The effects of polarization of the incident light-modeling and analysis of a SPR multimode optical fiber sensor," *Sensors and Actuators A: Physical*, vol. 84, pp. 198–204, 2000.
- [80] A. Leung, P. M. Shankar and R. Mutharasan, "A review of fiber-optic biosensors," *Sensors and Actuators B: Chemical*, vol. 125, pp. 688–703, 2007.
- [81] Y. Shao, S. Xu, X. Zheng, Y. Wang and W. Xu, "Optical Fiber LSPR Biosensor Prepared by Gold Nanoparticle Assembly on Polyelectrolyte Multilayer," *Sensors*, vol. 10, p. 3585–3596, 2010.
- [82] V. Stranak, S. Drache, H. Wulff, Z. Hubicka, M. Tichy, A. Kruth, C. A. Helm and R. Hippler, "Oxidation behavior of Cu nanoparticles embedded into semiconductive TiO₂ matrix," *Thin Solid Films*, vol. 589, pp. 864–871, 2015.
- [83] O. Kylián, A. Choukourov and H. Biederman, "Nanostructured plasma polymers," *Thin Solid Films*, vol. 548, pp. 1–17, 2013.
- [84] A. Ricciardi, A. Crescitelli, P. Vaiano, G. Quero, M. Consales, M. Pisco, E. Esposito and A. Cusano, "Lab-on-fiber technology: a new vision for chemical and biological sensing," *Analyst*, vol. 140, no. 24, pp. 8068–8079, 2015.
- [85] I. D. Villar, F. J. Arregui, C. R. Zamarreño, J. M. Corres, C. Bariain, J. Goicoechea, C. Elosua, M. Hernaez, P. J. Rivero, A. B. Socorro, A. Urrutia, P. Sanchez, P. Zubiate, D. Lopez, N. D. Acha, J. Ascorbe and I. R. Matias, "Optical sensors based on lossy-mode resonances," *Sensors and Actuators B: Chemical*, vol. 240, pp. 174–185, 2017.
- [86] I. D. Villar, M. Hernaez, C. R. Zamarreño, P. Sánchez, C. Fernández-Valdivielso, F. J. Arregui and I. R. Matias, "Design rules for lossy mode resonance based sensors," *Applied Optics*, vol. 51, p. 4298–4307, July 2012.

-
- [87] C. R. Zamarreño, M. Hernáez, I. D. Villar, I. R. Matías and F. J. Arregui, "Optical fiber pH sensor based on lossy-mode resonances by means of thin polymeric coatings," *Sensors and Actuators B: Chemical*, vol. 155, pp. 290-297, 2011.
- [88] Q. Wang and W.-M. Zhao, "A comprehensive review of lossy mode resonance-based fiber optic sensors," *Optics and Lasers in Engineering*, vol. 100, pp. 47-60, 2018.
- [89] I. Del Villar, C. R. Zamarreno, M. Hernaez, F. J. Arregui and I. R. Matias, "Lossy Mode Resonance Generation With Indium-Tin-Oxide-Coated Optical Fibers for Sensing Applications," *Journal of Lightwave Technology*, vol. 28, pp. 111-117, 2010.
- [90] S. O. Kasap, *Optoelectronics and Photonics: Principles and Practices*, 2nd ed., Boston: Pearson, 2013.
- [91] F. Wooten, *Optical Properties of Solids*, London: Academic Press Inc., 1972.
- [92] I. Del Villar, C. R. Zamarreño, M. Hernaez, F. J. Arregui and I. R. Matias, "Generation of Lossy Mode Resonances With Absorbing Thin-Films," *Journal of Lightwave Technology*, vol. 28, pp. 3351-3357, 2010.
- [93] C. R. Zamarreño, P. Zubiate, M. Sagües, I. R. Matias and F. J. Arregui, "Experimental demonstration of lossy mode resonance generation for transverse-magnetic and transverse-electric polarizations," *Optics Letters*, vol. 38, no. 14, p. 2481–2483, July 2013.
- [94] T. E. Batchman and G. M. McWright, "Mode Coupling Between Dielectric and Semiconductor Planar Waveguides," *IEEE Transactions on Microwave Theory and Techniques*, vol. 30, pp. 628-634, 1982.
- [95] R. F. Carson and T. E. Batchman, "Multimode phenomena in semiconductor-clad dielectric opticalwaveguide structures," *Applied Optics*, vol. 29, no. 18, p. 2769–2780, June 1990.
- [96] I. D. Villar, I. R. Matias, F. J. Arregui and M. Achaerandio, "Nanodeposition of Materials With Complex Refractive Index in Long-Period Fiber Gratings," *J. Lightwave Technol.*, vol. 23, p. 4192, December 2005.
- [97] E. Kretschmann and H. Raether, "Notizen: Radiative Decay of Non Radiative Surface Plasmons Excited by Light," *Zeitschrift für Naturforschung A*, vol. 23, p. 2135–2136, 1968.
- [98] S. P. Usha, A. M. Shrivastav and B. D. Gupta, "Semiconductor metal oxide/polymer based fiber optic lossy mode resonance sensors: A contemporary study," *Optical Fiber Technology*, vol. 45, pp. 146-166, 2018.

-
- [99] O. Fuentes, I. Del Villar, J. M. Corres and I. R. Matias, "Lossy mode resonance sensors based on lateral light incidence in nanocoated planar waveguides," *Scientific Reports*, vol. 9, p. 8882, 2019.
- [100] N. Paliwal and J. John, "Theoretical modeling of lossy mode resonance based refractive index sensors with ITO/TiO₂ bilayers," *Applied Optics*, vol. 53, no. 15, p. 3241–3246, May 2014.
- [101] I. D. Villar, C. R. Zamarreño, P. Sanchez, M. Hernaez, C. F. Valdivielso, F. J. Arregui and I. R. Matias, "Generation of lossy mode resonances by deposition of high-refractive-index coatings on uncladded multimode optical fibers," *Journal of Optics*, vol. 12, p. 095503, September 2010.
- [102] C. R. Zamarreño, M. Hernaez, I. D. Villar, I. R. Matias and F. J. Arregui, "Tunable humidity sensor based on ITO-coated optical fiber," *Sensors and Actuators B: Chemical*, vol. 146, pp. 414-417, 2010.
- [103] M. Śmietana, M. Sobaszek, B. Michalak, P. Niedziałkowski, W. Białobrzeska, M. Koba, P. Sezemsky, V. Stranak, J. Karczewski, T. Ossowski and R. Bogdanowicz, "Optical Monitoring of Electrochemical Processes With ITO-Based Lossy-Mode Resonance Optical Fiber Sensor Applied as an Electrode," *Journal of Lightwave Technology*, vol. 36, no. 4, p. 954–960, February 2018.
- [104] N. Paliwal and J. John, "Lossy Mode Resonance (LMR) Based Fiber Optic Sensors: A Review," *IEEE Sensors Journal*, vol. 15, pp. 5361-5371, 2015.
- [105] V. Straňák, M. Quaas, H. Wulff, Z. Hubička, S. Wrehde, M. Tichý and R. Hippler, "Formation of TiO_x films produced by high-power pulsed magnetron sputtering," *Journal of Physics D: Applied Physics*, vol. 41, p. 055202, February 2008.
- [106] M. Sobaszek, M. Dominik, D. Burnat, R. Bogdanowicz, V. Stranak, P. Sezemsky and M. Śmietana, "Optical monitoring of thin film electropolymerization on surface of ITO-coated lossy-mode resonance sensor," in *25th International Conference on Optical Fiber Sensors*, 2017.
- [107] A. B. Socorro, I. D. Villar, J. M. Corres, F. J. Arregui and I. R. Matias, "Spectral width reduction in lossy mode resonance-based sensors by means of tapered optical fibre structures," *Sensors and Actuators B: Chemical*, vol. 200, pp. 53-60, 2014.
- [108] L. Razquin, C. R. Zamarreño, F. J. Muñoz, I. R. Matias and F. J. Arregui, "Thrombin detection by means of an aptamer based sensitive coating fabricated onto LMR-based optical fiber refractometer," in *SENSORS, 2012 IEEE*, 2012.

-
- [109] "Indium Tin Oxide, ITO In₂O₃/SnO₂ 90/10 wt % Sputtering Targets," Kurt J. Lesker Company, [Online]. Available: https://www.lesker.com/newweb/deposition_materials/depositionmaterials_sputtertargets_1.cfm?pgid=in3. [Accessed 1 10 2021].
- [110] J. E. N. Swallow, B. A. D. Williamson, T. J. Whittles, M. Birkett, T. J. Featherstone, N. Peng, A. Abbott, M. Farnworth, K. J. Cheetham, P. Warren, D. O. Scanlon, V. R. Dhanak and T. D. Veal, "Self-Compensation in Transparent Conducting F-Doped SnO₂," *Advanced Functional Materials*, vol. 28, p. 1701900, 2018.
- [111] Ü. Özgür, Y. I. Alivov, C. Liu, A. Teke, M. A. Reshchikov, S. Doğan, V. Avrutin, S.-J. Cho and H. Morkoç, "A comprehensive review of ZnO materials and devices," *Journal of Applied Physics*, vol. 98, p. 041301, 2005.
- [112] A. Suzuki, T. Matsushita, N. Wada, Y. Sakamoto and M. Okuda, "Transparent Conducting Al-Doped ZnO Thin Films Prepared by Pulsed Laser Deposition," *Japanese Journal of Applied Physics*, vol. 35, p. L56–L59, January 1996.
- [113] J. Du, X.-l. Chen, C.-c. Liu, J. Ni, G.-f. Hou, Y. Zhao and X.-d. Zhang, "Highly transparent and conductive indium tin oxide thin films for solar cells grown by reactive thermal evaporation at low temperature," *Applied Physics A*, vol. 117, p. 815–822, 2014.
- [114] H. Kim, C. M. Gilmore, A. Piqué, J. S. Horwitz, H. Mattoussi, H. Murata, Z. H. Kafafi and D. B. Chrisey, "Electrical, optical, and structural properties of indium–tin–oxide thin films for organic light-emitting devices," *Journal of Applied Physics*, vol. 86, pp. 6451–6461, 1999.
- [115] P. P. Edwards, A. Porch, M. O. Jones, D. V. Morgan and R. M. Perks, "Basic materials physics of transparent conducting oxides," *Dalton Transactions*, no. 19, pp. 2995–3002, 2004.
- [116] M. Mazur, M. Szymańska, M. Kalisz, D. Kaczmarek and J. Domaradzki, "Surface and mechanical characterization of ITO coatings prepared by microwave-assisted magnetron sputtering process," *Surface and Interface Analysis*, vol. 46, pp. 827–831, 2014.
- [117] I. D. Villar, C. R. Zamarreño, M. Hernaez, P. Sanchez, F. J. Arregui and I. R. Matias, "Generation of Surface Plasmon Resonance and Lossy Mode Resonance by thermal treatment of ITO thin-films," *Optics & Laser Technology*, vol. 69, pp. 1–7, 2015.
-

-
- [118] M. Marciniak, J. Grzegorzewski and M. Szustakowski, "Analysis of lossy mode cut-off conditions in planar waveguides with semiconductor guiding layer," *IEE Proceedings J (Optoelectronics)*, vol. 140, no. 4, pp. 247-252(5), August 1993.
- [119] Y. Xu, N. B. Jones, J. C. Fothergill and C. D. Hanning, "Analytical estimates of the characteristics of surface plasmon resonance fibre-optic sensors," *Journal of Modern Optics*, vol. 47, pp. 1099-1110, 2000.
- [120] Y. S. Dwivedi, A. K. Sharma and B. D. Gupta, "Influence of skew rays on the sensitivity and signal-to-noise ratio of a fiber-optic surface-plasmon-resonance sensor: a theoretical study," *Applied Optics*, vol. 46, p. 4563–4569, July 2007.
- [121] A. K. Sharma and B. D. Gupta, "On the sensitivity and signal to noise ratio of a step-index fiber optic surface plasmon resonance sensor with bimetallic layers," *Optics Communications*, vol. 245, pp. 159-169, 2005.
- [122] J. Chilwell and I. Hodgkinson, "Thin-films field-transfer matrix theory of planar multilayer waveguides and reflection from prism-loaded waveguides," *Journal of the Optical Society of America A*, vol. 1, no. 7, p. 742–753, July 1984.
- [123] A. B. Socorro, J. M. Corres, I. D. Villar, I. R. Matias and F. J. Arregui, "Celiac disease biodetection using lossy-mode resonances generated in tapered single-mode optical fibers," in *23rd International Conference on Optical Fibre Sensors*, 2014.
- [124] C. R. Zamarreño, I. Ardaiz, L. Ruete, F. J. Muñoz, I. R. Matias and F. J. Arregui, "C-reactive protein aptasensor for early sepsis diagnosis by means of an optical fiber device," in *SENSORS, 2013 IEEE*, 2013.
- [125] S. P. Usha, A. M. Shrivastav and B. D. Gupta, "Silver nanoparticle nodule ZnO nanowedge fetched novel FO-LMR based H₂O₂ biosensor: A twin regime sensor for in-vivo applications and H₂O₂ generation analysis from polyphenolic daily devouring beverages," *Sensors and Actuators B: Chemical*, vol. 241, pp. 129-145, 2017.
- [126] D. Harvey, "Analytical Chemistry 2.0," DePauw University, 2019.
- [127] A. Amirudin and D. Thieny, "Application of electrochemical impedance spectroscopy to study the degradation of polymer-coated metals," *Progress in Organic Coatings*, vol. 26, pp. 1-28, 1995.
- [128] N. Kanani, *Electroplating - Basic Principles, Processes and Practice*, Oxford: Elsevier Advanced Technology, 2005.
- [129] G. F. Vander Voort, *ASM Handbook, Vol. 9: Metallography and Microstructures*, ASM International, 2004.

-
- [130] P. Atkins and J. de Paula, *Atkins' Physical chemistry*, Eighth Edition ed., New York: W.H. Freeman, 2006.
- [131] J.-M. Savéant and C. Costentin, *Elements of Molecular and Biomolecular Electrochemistry*, Second edition ed., Hoboken, N.J.: JohnWiley & sons Inc., 2019.
- [132] N. Elgrishi, K. J. Rountree, B. D. McCarthy, E. S. Rountree, T. T. Eisenhart and J. L. Dempsey, "A Practical Beginner's Guide to Cyclic Voltammetry," *Journal of Chemical Education*, vol. 95, no. 2, p. 197–206, February 2018.
- [133] W. R. Heineman and P. T. Kissinger, *Laboratory Techniques in Electroanalytical Chemistry*, New York: Marcel Dekker, 1996.
- [134] A. J. Bard and L. R. Faulkner, *Electrochemical Methods Fundamentals and Applications*, New York: Wiley-Interscience, 2000.
- [135] Y. Saito and T. Kikuchi, *Voltammetry - Theory, Types and Applications (Chemical Engineering Methods and Technology)*, New York: Nova Science Pub Inc, 2013.
- [136] F. A. Settle, *Handbook of Instrumental Techniques for Analytical Chemistry*, Prentice Hall PTR, 1997.
- [137] R. G. Compton and C. E. Banks, *Understanding voltammetry - problems and solutions*, WORLD SCIENTIFIC EUROPE L, 2018.
- [138] S. A. Ozkan, J.-M. Kauffmann and P. Zuman, *Electroanalysis in Biomedical and Pharmaceutical Sciences: Voltammetry, Amperometry, Biosensors, Applications*, Springer-Verlag Berlin Heidelberg, 2015.
- [139] D. J. Graham, *Standard Operating Procedures for Cyclic Voltammetry*, LULU Press, 2017.
- [140] M. Sobaszek, M. Dominik, D. Burnat, R. Bogdanowicz, V. Stranak, P. Sezemsky and M. Śmietana, "Optical monitoring of thin film electropolymerization on surface of ITO-coated lossy-mode resonance sensor," in *2017 25th Optical Fiber Sensors Conference (OFS)*, 2017.

APPENDICES

A1. Annealing of indium tin oxide (ITO) coated optical fibers for optical and electrochemical sensing purposes

Magdalena Dominik, Katarzyna Siuzdak, Paweł Niedziałkowski, Vitezslav Stranak, Petr Sezemsky, Michał Sobaszek, Robert Bogdanowicz, Tadeusz Ossowski, Mateusz Smietana, Annealing of indium tin oxide (ITO) coated optical fibers for optical and electrochemical sensing purposes, Proceedings of SPIE 1075, (2016), UNSP 1017515.

Abstract

Glass and fiber structures with Indium Tin Oxide (ITO) coating were subjected to annealing in order to identify impact of the thermal treatment on their optical and electrochemical properties. It is shown that the annealing process significantly modifies optical properties and thickness of the films, which are crucial for performance of optical fiber sensors. Moreover, it visibly improves electrochemical activity of ITO on glass slides and thicker ($\varnothing = 400 \mu\text{m}$) ITOcoated fibers, whereas in the case of thinner fibers ($\varnothing = 125 \mu\text{m}$) it could lead to a loss of their electrochemical activity. Depending on the applied substrate and the annealing process, the investigated structures with ITO coating can be further used as fiber-based sensors with integrated opto-electrochemical readout.

1. INTRODUCTION

Indium Tin Oxide (ITO, $\text{In}_2\text{O}_3\text{-SnO}_2$) is one of the most widely used in optics and electronics optically transparent and electrically conductive metal oxide. ITO has found applications in many different fields, e.g., as transparent electrodes for solar cells, liquid crystal displays or touch panels, as well as active film for gas sensors.¹ Due to ability to control its optical properties in a wide range it is also used as a coating for optical fiber sensors.² Sensing effect of these devices is based on a lossy mode resonance (LMR) phenomenon, which takes place when real part of the thin-film electrical permittivity is positive and higher in magnitude than both its own imaginary part and the material surrounding the thinfilm (e.g. external medium). On the other hand, ITO has also been successively applied as a transparent electrode for spectro-electrochemical studies.³

In this work we present preliminary results obtained for optical structures with ITO coating that can play both the roles, i.e., a film deposited on optical fibers sensors and an electrochemical electrode. We mainly investigate the influence of ITO annealing, since the process has a great influence on the properties of those thin films, such as their electrical conductivity and electrochemical activity. The post-deposition annealing usually takes place in oxidizing atmosphere and the effects of the process are investigated by measuring decrease in resistivity of the films. During the thermal treatment, oxygen vacancies are filled and redistributed into ITO with a corresponding change in the Sn(IV)/Sn(II) ratio.³

ITO film can be deposited with various chemical techniques, i.e., spray pyrolysis⁴ and sol-gel⁵, or by physical deposition, namely electron beam evaporation⁶ and reactive magnetron sputtering (RMS)¹. Chemical methods are relatively simple and low-cost, but usually require high-temperature post processing (annealing) and do not provide efficient control over properties of the thin films, which are critical for their performance as a part of optical sensors. To overcome some of the disadvantages of the chemical deposition methods, alternatively RMS can be used. The RMS, which belongs to group of physical vapor deposition method, gives precise control over the thin films properties, is highly repeatable and can be used for deposition of a wide selection of metal alloy or compound with excellent adhesion and uniformity.

Properties of ITO can be easily modified by changing flow rates of O₂ or Ar during sputtering, thus such ITO films can be used as an effective and useful coating for optical fiber sensors, where its optical properties as well as thickness are crucial parameters for sensor performance.^{2,7-10}

In this work we have applied RMS for deposition ITO on flat surface (glass slides, silicon) and circular in shape samples (fused silica glass fibers with various diameters). Deposition of uniform films on curved surfaces, such as optical fibers, was possible thanks to rotation of the fiber between deposition processes. We have investigated optical and electrochemical properties of the films which underwent the annealing process. The effects of the process on ITO properties are discussed from a point of view of applied substrate (glass, single- and multimode fibers) and foreseen opto-electrochemical sensing capabilities.

2. EXPERIMENTAL DETAILS

2.1. Technology

ITO coatings were deposited with RMS method on reference silicon wafers and fused silica glass slides (sample RB61), as well as on fused silica cladding of single-mode fibers (SMF, $\Phi_{\text{cladding}} = 125 \mu\text{m}$, sample RB59) and fused silica core of multimode polymer-clad silica (PCS) optical fibers ($\Phi_{\text{core}} = 400 \mu\text{m}$, sample RB58) prepared as in ⁷.

ITO films were deposited using standard planar magnetrons with unbalanced magnetic field. The deposition system, arranged for deposition of fibers, combines two perpendicularly oriented sputtering guns. The magnetron from side, magnetron axis perpendicular to the deposited fiber, was operated in mode of high power impulse magnetron sputtering (HiPIMS) running in pulsed mode with repetition frequency of 1 kHz and duty 10%, keeping mean discharge current at 350 mA. The magnetron mounted parallel with the fibers was running with continuous RF power 300 W (13.56 MHz).

Both magnetron cathodes were equipped with ITO targets with composition In₂O₃-SnO₂ 90-10 wt% and 99.99% purity. Such arrangement allowed to produce energetic species for ITO film deposition (mainly contributed by

HiPIMS) and to reduce the working pressure to 0.3 Pa (due to RF discharge support). It was empirically proved that described configuration enables to produce ITO films with relevant properties needed for opto-electrochemical purposes. The fibers were placed on the rotational substrate holder which guarantees a homogeneous coating during the deposition. Next, the ITO samples were annealed in air for 2 h in 200 °C.

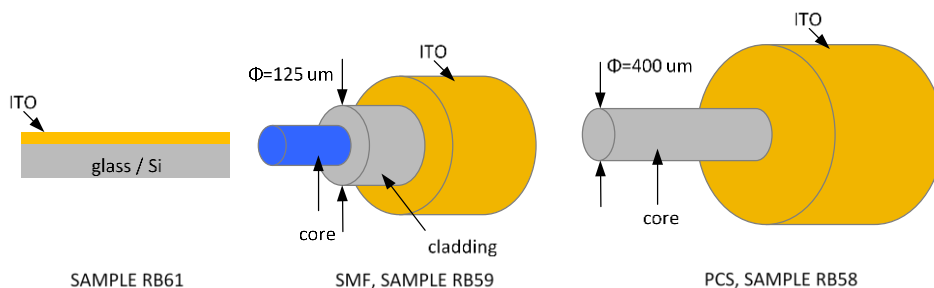


Fig. 1. Schematically shown structure of the investigated samples coated with ITO.

2.2. Measurements

The properties of the ITO films deposited on the reference silicon wafers, such as their thickness (d), refractive index (n) and extinction coefficient (k) were determined with a Horiba Jobin-Yvon UVISSEL spectroscopic ellipsometer. Measurements were performed over the spectral range 260-820 nm at an angle of incidence of 70°. The ellipsometric model for ITO analysis was described by combination of a Drude oscillator (to model the absorption in the NIR range) and a double New Amorphous Formula.

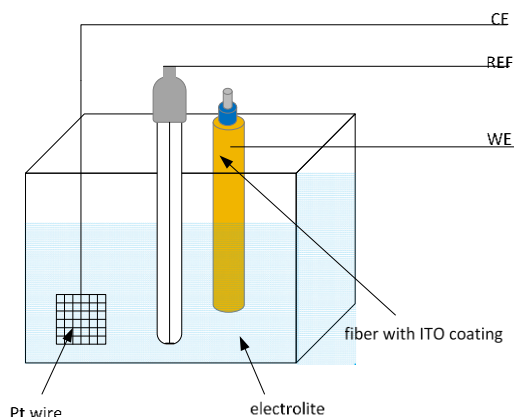


Fig. 2. Scheme of the electrochemical measuring system, where CE – platinum wire, counting electrode, REF - Ag/AgCl/0.1 KCl, reference electrode, WE – ITO, working electrode.

The resistivity values at room temperature were measured by four-point probe placed in a straight line with equal interprobe spacing ($s = 1.5$ mm). The needle-like probes with a radius of $100 \mu\text{m}$ were utilized. The correction factor of 0.86 was taken into account during resistivity estimation due to the finite sample size.¹¹ A source meter (Keithley 2400, UK) was used as a current source applied to the external probes. The current was gradually increased from 0 up to $100 \mu\text{A}$ with a step of $1 \mu\text{A}$. Voltage on the internal probes was measured with a VA multimeter (Appa 207, Taiwan). Each sample was measured at four surface points and the mean resistivity was calculated.

Cyclic voltammetry (CV) measurements (Fig. 2) were carried out in aqueous media consisting of $5 \text{ mM K}_3[\text{Fe}(\text{CN})_6]$ in $0.5 \text{ M K}_2\text{SO}_4$ at a scan rate of 0.05 Vs^{-1} . Electrochemical cell consisted of a three electrode system. ITO, platinum wire and $\text{Ag}/\text{AgCl}/0.1 \text{ KCl}$ were used as working (WE), counter (CE) and reference (REF) electrodes, respectively. The electrochemical experiment was performed using an Autolab potentiostat/galvanostat (302N).

3. RESULTS

3.1. Optical and electrical properties of ITO

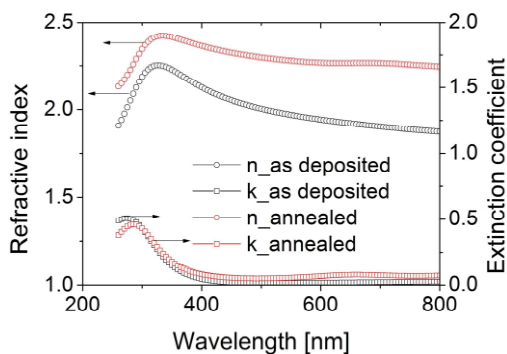


Fig. 3. Effect of thermal annealing ($200 \text{ }^\circ\text{C}$, 2 h) on optical properties of ITO-coated samples. Annealed samples are plotted in red.

The thin films of ITO deposited on Si wafers had thickness of 162, 222 and 258 nm for RB58, RB59 and RB61 sample, respectively (Table 1). It has been found that after annealing d slightly decreased (1%). In Fig. 1. Evolution of optical properties for RB61 sample is shown. It can be seen that annealing resulted in significant increase of n . It is well known that annealing of ITO increases its density as well as transparency due a structural relaxation and crystallization.¹² These processes also had an impact on k , which increased in visible and infrared spectral range.

The lowest resistivity of the as deposited films was achieved for sample RB58 equal to $11.99 \cdot 10^{-4} \Omega \text{ cm}$. Resistivity increased with thickness of ITO films up to $21.7 \cdot 10^{-4} \Omega \text{ cm}$ for RB61. After annealing the sample RB59 deposited on SMF optical fiber became nonconductive. It should be noted that annealing process might induce cracking in the ITO coating due to difference thermal coefficient between ITO coating and optical fiber core cladding and induce internal stress in it. The sample RB59 and 61 have shown reduction in their resistivity after the annealing process.

Table 1. Properties of the ITO films before and after annealing

Sample	Resistivity [$\Omega \text{ cm}$]		Thickness [nm]		$n @ 640 \text{ nm}$ [RIU]		$k @ 640 \text{ nm}$	
	as deposited	after annealing	as deposited	after annealing	as deposited	after annealing	as deposited	after annealing
RB58	$11.99 \cdot 10^{-4}$	$2.95 \cdot 10^{-4}$	162.0	160.2	1.97	2.23	0.013	0.072
RB59	$14.42 \cdot 10^{-4}$	nonconductive	221.9	220.1	1.97	2.22	0.006	0.012
RB61	$21.70 \cdot 10^{-4}$	$6.72 \cdot 10^{-4}$	258.3	257.4	1.99	2.25	0.005	0.010

3.2. Electrochemical measurements

Fig. 4 shows cyclic voltammograms of ITO deposited on various substrates before and after annealing. As mentioned above, the sample RB59 due to loss its conductivity after annealing show non electrochemical response (Fig 2a). The thermal process of sample deposited on quartz glass (RB61) has a slightly effect on their electrochemical performance, introducing change of ΔE equal to 30 mV (for as deposited layer $\Delta E = 670 \text{ mV}$ and the annealed $\Delta E = 700 \text{ mV}$). The largest increase of electrochemical response was noticed for sample deposited directly on the PCS fiber core RB58 (Fig 2b). Before the annealing the ΔE value was 1180 mV and after the thermal process the ΔE decreased to 680 mV. The obtained value is similar as for sample RB61. This change in ΔE can be explained by change in the internal structure of ITO. After the deposition process the samples are rich in amorphous phase which after annealing transforms more into crystals.^{13,14} Moreover, the grain size is increased with temperature and an internal stress is released.¹⁴ What is more, tin atoms are activated after the annealing process and behave as effective donors.^{15,16} That is why the electrical resistivity decreases as shown in Table 1.

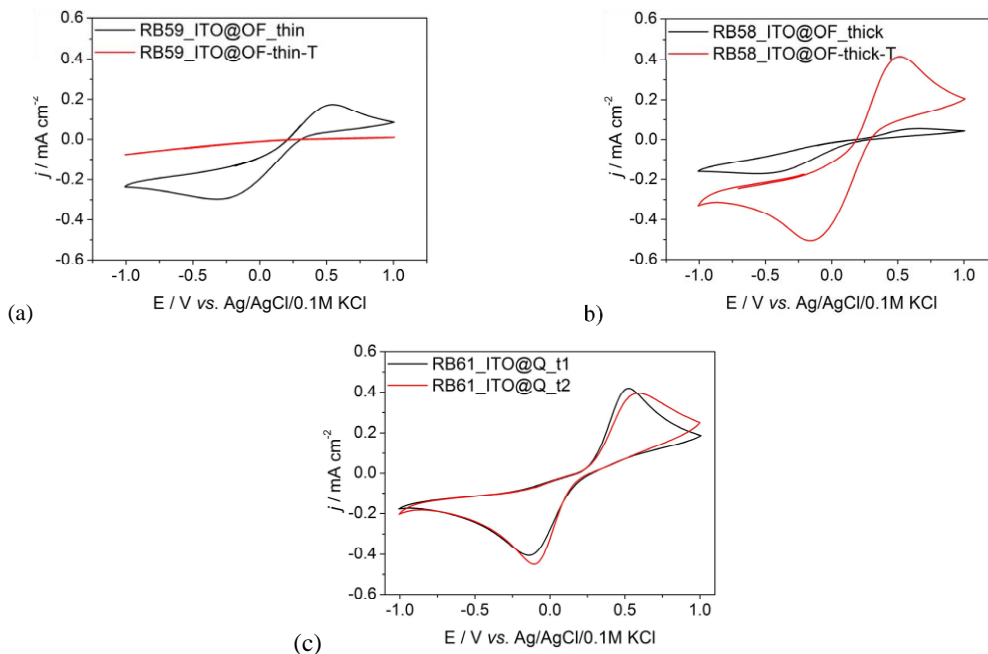


Fig. 4. Effect of thermal annealing (200 °C, 2 h) on CV measurements of ITO-coated (a) SMF optical fibers (RB59), (b) PCS (RB58) and (c) glass slide (RB61). Results for annealed samples are plotted in red.

4. CONCLUSIONS

Glass and fiber structures with ITO coating were subjected to annealing in order to identify impact of the thermal treatment on their optical and electrochemical properties. The annealing process results in increase of refractive index and extinction coefficient of the films. The process also improves electrochemical activity of the films deposited on glass and thicker fibers, whereas in the case of thinner fibers it can lead to a loss of electrochemical activity. Depending on the applied substrate and the annealing conditions the investigated structures with ITO coating can be further applied as a fiber-based sensor with integrated opto-electrochemical readout.

Acknowledgements

This work was supported by the Polish National Science Centre (NCN) under grant No. 2014/14/E/ST7/00104.

References

- [1] Mazur, M; Szymańska, M; Kalisz, M; Kaczmarek, D; Domaradzki, J., “Surface and mechanical characterization of ITO coatings prepared by microwave-assisted magnetron sputtering process,” *Surf. Interface Anal.* **46**, 827– 831 (2014).
- [2] Hernaez, M., Villar, I. Del., Matias, I. R., Arregui, F. J., Zamarre, C. R., “Sensors and Actuators B: Chemical Tunable humidity sensor based on ITO-coated optical fiber,” *Sensor. Actuator. B Chem.* **146**, 414–417 (2010).
- [3] Matveeva, E., “Electrochemistry of the Indium-Tin Oxide Electrode in 1 M NaOH Electrolyte,” *J. Electrochem. Soc.* **152**(9), 138–145 (2005).
- [4] Marikkannu, S., Sanjeeviraja, C., Piraman, S., Ayeshamariam, A., “Studies on the structural , optical , and electrical properties of jet-nebulized spray pyrolysis ITO thin films,” *J Mater Sci Mater Electron* **26**, 2531–2537 (2015).
- [5] Kim, S., Choi, S., Park, C., Jin, H., “Transparent conductive ITO thin films through the sol-gel process using metal salts,” *Thin Solid Films* **347**, 155–160 (1999).
- [6] Yamaguchi, M., Ide-ektessabi, A., Nomura, H., Yasui, N., “Characteristics of indium tin oxide thin films prepared using electron beam evaporation,” *Thin Solid Films* **447-448**, 115–118 (2004).
- [7] Dudek, M., Koba, M., Michalak, B., “Influence of diamond-like carbon overlay properties on refractive index sensitivity of nano-coated optical fibres,” *Phys. Status Solidi A* **2105**(10), 2100–2105 (2013).
- [8] Smietana, M., Koba, M., Brzozowska, E., Krogulski, K., Nakonieczny, J., Wachnicki, L., Mikulic, P., Godlewski, M., Bock, W. J., “Label-free sensitivity of long-period gratings enhanced by atomic layer deposited TiO₂ nano-overlays,” *Opt. Express* **23**(7), 8441 (2015).
- [9] Śmietana, M., Myśliwiec, M., Mikulic, P., Witkowski, B. S., Bock, W. J., “Capability for fine tuning of the refractive index sensing properties of long-period gratings by atomic layer deposited Al₂O₃ overlays,” *Sensors* **13**(12), 16372–16383 (2013).
- [10] Smietana, M., Dominik, M., Mysliwiec, M., Kwietniewski, N., Mikulic, P., Witkowski, B. S., Bock, W. J., “Properties of silicon nitride thin overlays deposited on optical fibers - Effect of fiber suspension in radio frequency plasma-enhanced chemical vapor deposition reactor,” *Thin Solid Films* **603**, 8–13 (2016).
- [11] Smits, F. M., “Measurement of Sheet Resistivities with the Four-Point Probe,” *Bell Syst. Tech. J.* **37**(3), 711–718 (1958).

- [12] Paine, D. C., Whitson, T., Janiac, D., Beresford, R., Yang, C. O., Lewis, B., Paine, D. C., Whitson, T., Janiac, D., et al., “A study of low temperature crystallization of amorphous thin film indium – tin – oxide A study of low temperature crystallization of amorphous thin film indium – tin – oxide,” *J. Appl. Phys.* **85**(12), 8445–8450 (1999).
- [13] Raoufi, D., Kiasatpour, A., Fallah, H. R., Rozatian, A. S. H., “Surface characterization and microstructure of ITO thin films at different annealing temperatures,” *Appl. Surf. Sci.* **253**(23), 9085–9090 (2007).
- [14] Kerkache, L., Layadi, A., Dogheche, E., Rémiens, D., “Physical properties of RF sputtered ITO thin films and annealing effect,” *J. Phys. D. Appl. Phys.* **39**(1), 184 (2006).
- [15] Wu, W.-F., Chiou, B.-S., “Effect of annealing on electrical and optical properties of RF magnetron sputtered indium tin oxide films,” *Appl. Surf. Sci.* **68**(4), 497–504 (1993).
- [16] Fallah, H. R., Ghasemi, M., Hassanzadeh, A., Steki, H., “The effect of annealing on structural, electrical and optical properties of nanostructured ITO films prepared by e-beam evaporation,” *Mater. Res. Bull.* **42**(3), 487–496 (2007).

A2. Towards high quality ITO coatings: The impact of nitrogen admixture in HiPIMS discharges

Vitezslav Stranak, Robert Bogdanowicz, Petr Sezemsky, Harm Wulff, Angela Kruth, Mateusz Smietana, Jiri Kratochvil, Martin Cada, Zdenek Hubicka, Towards high quality ITO coatings: The impact of nitrogen admixture in HiPIMS discharges, Surface and Coatings Technology 335, (2018), 126-133.

Republished with permission of Elsevier Science & Technology Journals; permission conveyed through Copyright Clearance Center, Inc.

Abstract

The paper reports controlled deposition of optically transparent and electrically conductive ITO films prepared by a combination of rf (13.56 MHz) and High Power Impulse Magnetron Sputtering (HiPIMS) systems without any post deposition thermal treatment/annealing. It is shown that (i) reactive admixture of N₂ gas to the process and (ii) pressure in the deposition chamber enable to optimize optical properties of ITO films. Furthermore, the changes of electrical resistivity were observed, too. The variation of these ITO properties is attributed to change of crystalline structure measured by XRD methods.

INTRODUCTION

Optically transparent and electrically conductive oxide (TCO) semiconductors are widely known and used in numerous applications, e.g. for liquid crystal displays (LCD), working electrodes in electrochemistry, electrodes in solar cells [1]. Generally, there is a search for the materials, highly transparent in wide optical spectral range, as well as highly conductive. An important family of TCO is represented by ZnO, SnO₂, In₂O₃ and also includes some ternary compound existing systems. Among them, In₂O₃ doped with Sn, also called Indium Tin Oxide (ITO), belongs to most favorable material that is well explored and appreciated TCO material [2]. Despite current TCO material, research is still being carried out for other suitable and efficient candidates (e.g. Al and/or Ga doped ZnO [3]), because of expensive and scarce indium, ITO is still a highly promising material for some particular applications. For example, we could mention nano and/or micro-sized devices where the added value is significantly higher than the cost of production.

Our research, performed of this study, is focused on the development of functional ITO films for lossy-mode resonance sensors based on the optical fiber [4]. Lossy-mode resonance (LMR) sensors emerged a few years ago and represent a hot topic in the field of fast, small and smart sensors. From a practical point of view, an LMR sensor is the optical fiber coated with a proper thin film. Very briefly, the LMR phenomenon is based on attenuation of a certain wavelength of the incident light propagated in the high-refractive-index overlay of suitable thickness deposited onto an optical fiber. This effect is caused by a coupling between the waveguide modes and a specific lossy mode propagated in the thin film [5]. ITO was the first, and still widely used, material explored for LMR sensors. Sensors of such types have been successfully applied for detection of various bio-substances as isatin [6], immunoglobulin [7], thrombin [8], etc. The main advantage of ITO-LMR is the possibility to combine optical (the conventional) and electrical way of sensing. The electrically conductive surface can be used, e.g. for initiation of electrochemical reactions onto the surface [6].

However, the efficient sensor structure needs optimization of ITO properties that allows to tailor the optical and electrical properties of the film. Plasma assisted deposition is often used for production of ITO films [9, 10]. Plasma

deposition of ITO films is typically followed by post-processing thermal annealing at enhanced temperatures to achieve required film resistivity. For example, in works [11-15] the temperature of the substrate was enhanced by about a few hundred degrees Celsius. Such a high annealing temperature immediately disqualifies this technique for coating of heat-sensitive samples, e.g. optical fibers in our case. Another way of film tailoring was introduced in [16] where the direct current magnetron sputtering was operated at powers from 0.4 to 2.0 kW. In the same work it is shown that high power load provides a similar effect like annealing at temperatures of about 200 °C. Ellmer and Welzel attribute this behavior to energetic ions occurring in plasma discharges [17]. Another technique for tailoring the ITO properties utilizes optimization of reactive gas (O₂) flow during the deposition [18] or during the post-deposition thermal annealing at ambient atmosphere [19].

Reactive high power impulse magnetron sputtering (R-HiPIMS) was beneficially used in the study [18]. R-HiPIMS is an ionized physical vapor deposition (IPVD) method used for synthesis of metal oxide and/or metal nitride films. High ionization level of the sputtered metal species is achieved by operating the magnetron discharge in a low duty-cycle and low-frequency mode [20-22]. A high degree of ionization [23, 24] of the sputtered material is one of the main benefits of HiPIMS discharges that usually improves the film quality [25-28]. Once the sputtered species are ionized, their energy can be influenced by the potential applied onto the substrate or by input discharge parameters [29]. Furthermore, localized ionization zones [30], often called as spokes, have been observed in HiPIMS discharges [31, 32] as well as lately also in dc magnetrons [33]. Most probably they influence not only the discharge but also properties of the films.

In this work we carried out a research focused on optimization of the ITO deposition without any post-processing treatment. ITO films were prepared by means of reactive HiPIMS of ITO target in Ar/N₂ atmosphere. Pressure in the chamber p and reactive nitrogen admixture to the deposition process were chosen as variable parameters to control the transparency and electrical resistivity of the film. The effects of spokes on the film properties are neglected in this study and can represent a future research challenge.

5. EXPERIMENTAL SETUP AND METHODS

Electrically conductive and optically transparent ITO films were deposited by R-HiPIMS. The experiments were carried out in a UHV chamber (reaching background pressure 10^{-7} mbar) using a combination of two perpendicularly oriented sputtering guns equipped by commercial ITO targets ($\text{In}_2\text{O}_3/\text{SnO}_2$ of composition 90/10) of 3 in. in diameter, see Fig. 1. The position of the planar substrate is shown in Fig. 1, as well. The HiPIMS magnetron, whose axis is parallel to the substrate, was driven with dc-pulse modulated HiPIMS, with repetition frequency $f = 1$ kHz, duty cycle 10% and the pulse width 100 μs . The home-made pulsed power supply combines a commercial dc voltage source Heinzinger PNC1500 and high-power insulated gate bipolar transistors (IGBT) based switch with a large capacitor bank [34]. The mean discharge current was kept constant at $I_m = 780$ mA; if other values were used, this is mentioned in text. The magnetron, whose axis is perpendicular to the substrate, was supplied by an RF source COMET Cito1310 (13.56 MHz, 300 W). The RF driven magnetron was mostly used for (i) stabilization of HiPIMS discharge and its operation at lower pressure which was impossible without the secondary discharge and (ii) for increasing of the environment to enhance film crystallization. Voltage and current waveforms were simultaneously measured using voltage and current probes, respectively, and recorded with a digital oscilloscope (Tektronix TDS1012). Optical emission spectroscopy measurements were performed using a Shamrock SR500D spectrometer (focal length 500 mm) equipped with an iCCD detector (iStar DH740I, Andor Technology, Belfast, Northern Ireland). The optical cable, connected with the spectrometer, was built directly into the vacuum chamber. The collimator at the end of the cable faced the substrate position, in parallel with the target surface. The exposure time for emission images was 500 ns with a resolution step of 1 μs .

The experiments were carried out typically in reactive N_2/Ar atmosphere. Argon and nitrogen gas flows of 15 sccm for the pure argon and 0.1–1.0 sccm for the N_2 , respectively, were utilized. Argon and nitrogen flow rates were separately controlled by two independent mass flow controllers. The working pressure p was adjusted by a gate valve installed between the vacuum chamber and the high vacuum pump in the range of $p = 0.5$ – 2.1 Pa. The films were deposited onto the Si(100) and glass substrates.

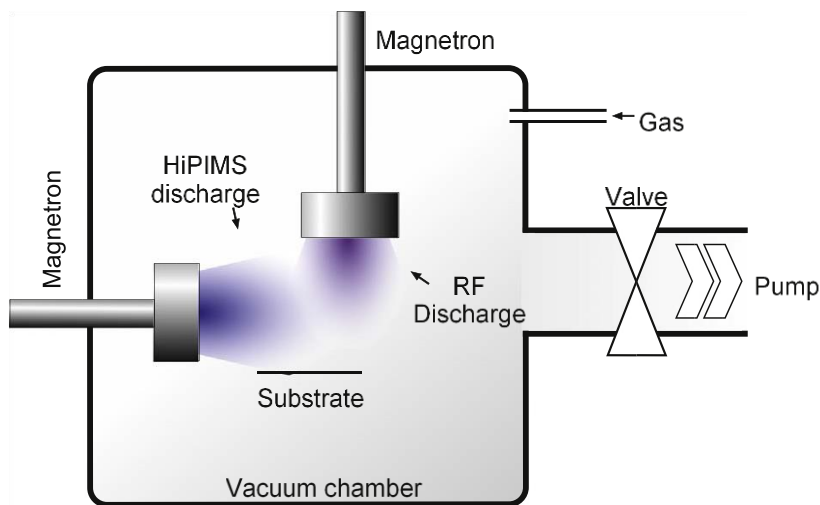


Fig. 1. Scheme of the experimental arrangement utilizing two perpendicular sputtering guns powered by rf (13.56 MHz) and HiPIMS (1000 Hz) discharges, respectively.

The deposited ITO films were characterized by grazing incidence X-ray diffractometry (GIXD) with regard to line position, intensity, and line profile of the observed Bragg reflections. The employed methods have been described elsewhere [35]. GIXD was performed on a D8 ADVANCE diffractometer (Bruker AXS). Cu $K\alpha$ radiation (40 kV, 40 mA) was used. The scanned 2θ range was from 20° to 80° at an incidence angle $\omega = 0.5^\circ$. The film surface morphology was measured by atomic force microscopy (AFM), recorded with the tapping mode. The AFM measurements were performed with the scanning area of $500 \times 500 \text{ nm}^2$ neglecting all inhomogeneities.

Ellipsometric investigations were carried out using a phase modulated ellipsometer Jobin-Yvon UVISSEL (HORIBA Jobin-Yvon Inc, Edison, NJ) in the 1.8–4.8 eV photon energy range at an angle of 70° , due to Brewster's angle of Si wafer substrate. Angles Δ and Ψ were simulated using three-layer base consisting of surface roughness layer (SRL), ITO film and Si substrate. The SRL was simulated using the Bruggeman Effective Medium Approximation [36] including 50% of void and 50% of ITO film. The optical indices of Si were obtained from a known database [37]. The complex dielectric function of ITO was assumed to be described by a Lorentz oscillator to obtain the dispersion due to the interband absorption and a Drude oscillator to include the free electron contribution in the NIR range. Finally,

the optical model was fitted to the experimental data using Levenberg–Marquardt nonlinear least-squares algorithm [38]. The fitting measure, mean square error (MSE), was used to verify the ability of the applied model to fit the experimental data. The ellipsometric data analysis allows us to estimate the film thickness and the optical constants with an accuracy of ± 0.2 nm and ± 0.005 , respectively. DeltaPsi software (v.2.4.3) was employed to determine the spectral distributions of refractive index $n(\lambda)$ and the extinction coefficient $k(\lambda)$ of the ITO films.

The room temperature resistivity of ITO samples was measured by a four-point probe placed in a straight line with equal inter-probe spacing ($s = 1.5$ mm). The needle-like probes with a radius of $100 \mu\text{m}$ were utilized. The size of samples was $1 \times 1 \text{ cm}^2$. A source meter (Keithley 2400, UK) was used as a current source, applied to the external probes, and a voltage meter recording on the internal probes.

6. RESULTS AND DISCUSSION

6.1. Properties of plasma discharges used for deposition of ITO thin films

In this chapter we want to show the effect of pressure p and the process gas composition on properties of generated discharge and subsequently the effect on deposited film. Fig. 2 shows HiPIMS current density waveforms and their dependence on process pressure p . It should be reminded that the same mean discharge current was preferentially set as $I_m = 780$ mA with some small deviations which we neglected in the discussion, see Fig. 2. It is evident that the current starts to rise with a small delay of $10 \mu\text{s}$ after the pulse onset. Furthermore, we observe that the pressure in the deposition chamber significantly influences the shape of the waveforms. The current density for low pressure $p \approx 0.5$ Pa rises quite quickly and reaches its maximum $j_p = 700$ mA/cm² at roughly $20 \mu\text{s}$. Such peak discharge current corresponds with peak power density of about 280 W/cm^2 . The current drop, observed after reaching its maximum, is typical for HiPIMS metallic discharges and is usually explained by a gas rarefaction effect, i.e. by the decrease of the gas density in front of the target [39-41]. Gas rarefaction in the target vicinity is caused by the so-called sputtering wind (i.e. process when sputtered particles push away gas atoms in close neighborhood of the target)

and by thermal heating of the cathode/target. None of these effects should be neglected in our case because of high mean discharge current $I_m = 780$ mA.

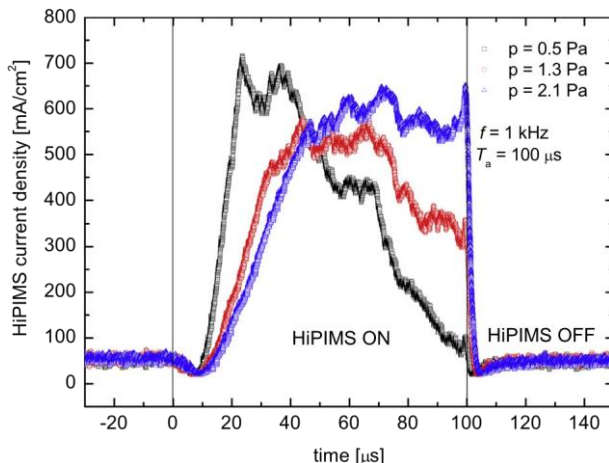


Fig. 2. HiPIMS discharge current density waveforms for different pressures. HiPIMS parameters: frequency $f = 1$ kHz, duty cycle 10% and mean discharge current $I_m = 780$ mA (for 0.5 Pa), $I_m = 760$ mA (for 1.3 Pa) and $I_m = 775$ mA (for 2.1 Pa), respectively.

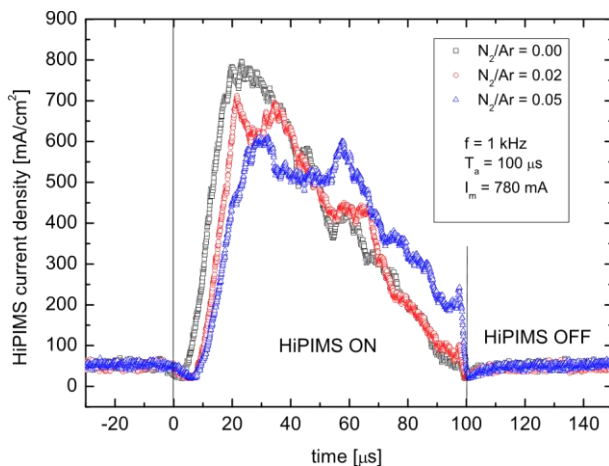


Fig. 3. HiPIMS current density waveforms for different gas composition. Process pressure $p = 0.5$ Pa.

At higher pressure, the rarefaction effect vanishes and the current fall is not so obvious. It is well pronounced for waveform measured at $p = 2.1$ Pa in Fig. 2 where a current plateau is distinguishable. The reduction of gas rarefaction effect is attributed to the larger number of species in the discharge volume, the number of species being proportional to pressure. This shape of discharge current is usually observed during reactive HiPIMS of e.g. metal

oxide films. The current rise with increased compound fraction on the target has been investigated by Gudmundsson et al. [42]. They show that the working gas recycling is actually the dominant mechanism behind the observed current increase determined by small self-sputtering yield in the poisoned mode. In principle, this process has no upper limit and results in a triangular shape of the current waveform.

Fig. 3 demonstrates that the gas composition does not significantly influence the current density. Hence, it seems that the gas rarefaction is the main mechanism which determines waveform shape. This is not so surprising because of compound $\text{In}_2\text{O}_3/\text{SnO}_2$ target on the one hand and very small ratio of reactive gas $\text{N}_2/\text{Ar} \leq 0.06$ on the other. The waveforms presented in Fig. 3 were recorded during experiments driven at low pressure $p = 0.5$ Pa; this explains the shape of the waveforms determined by the gas rarefaction effect.

Properties of the produced discharge, namely its chemical (elemental) composition, were studied by means of optical emission spectroscopy. The plasma properties were revealed in the substrate vicinity, i.e. the optical fiber was inserted inside the vacuum chamber and faced towards the substrate, to study the deposition condition. The overview spectra, not presented here as a graph, show dominant metallic lines In (450.9 nm), In^+ (591.0 nm), Sn (283.6 nm) and Sn^+ (607.5 nm) followed by gas lines Ar (420.1 nm), Ar^+ (610.5 nm), respectively. In case of reactive discharges with N_2 admixture a line of N (650.6) was observable as well. It is worth mentioning that no evident nor a strong line related to impurities was observed.

First of all, there is a question whether the RF discharge contributes to the deposition process. Our effort was to minimize RF discharge contribution to the deposition process despite the geometrical arrangement shown in Fig. 1. To verify this expectation, a time-resolved measurement of metal species (In, In^+ , Sn, Sn^+) was performed; time-resolved emission intensities for In (450.9 nm) are compared for pure HiPIMS (top panel) and HiPIMS+RF (middle panel) discharges in Fig. 4. Here, in 3D graphs, axis x represents the wavelength, y denotes time and z is the emission intensity. The same figure also shows a panel with comparison of intensities for a particular wavelength In (450.9 nm) to make comparison easier.

The emission intensity maximum is reached at about 50–75 μs after the pulse onset followed by its drop. This corresponds well with the behavior of the discharge current, see Fig. 2. Hence, it is assumed that the fall of the discharge current, explained by gas rarefaction, might also be responsible for reduced sputtering effect in the second half of the HiPIMS pulse. This behavior is unwanted, because reduced sputtering decreases the deposition rate. Slightly enhanced emission intensity, which can be considered to be proportional to the sputtering rate, was observed for HiPIMS+RF discharge. Furthermore, a culmination and also a fall of the intensity seems to be postponed by RF support. However, the most pronounced difference between these two sputtering modes appears after the HiPIMS pulse end, i.e. in time $\tau \geq 100 \mu\text{s}$. Here the emission is significantly lower, but still easily recognizable, at the same wavelength produced by RF discharge, which is continuously running during the HiPIMS idle time.

To consider the effect of RF discharge, we can subtract and compare the relative intensities from the bottom panel of Fig. 4. The intensity maxima measured for HiPIMS and HiPIMS+RF discharges at time $\tau \approx 75 \mu\text{s}$ are denoted as $I_{\tau_1}^{\text{H}}$ and $I_{\tau_1}^{\text{H+R}}$, respectively. In the same manner denoted intensities are measured in the idle time ($\tau > 100 \mu\text{s}$) of the pulse $I_{\tau_2}^{\text{H}}$, $I_{\tau_2}^{\text{H+R}}$, see Fig. 4. Then the ratio $I_{\tau_1}^{\text{H+R}}/I_{\tau_1}^{\text{H}} \approx 1.2$ while $I_{\tau_2}^{\text{H+R}}/I_{\tau_2}^{\text{H}} \approx 8$. Hence, this indicates that the RF discharge enhances the HiPIMS pulse, i.e. sputtering of the target, but this factor is not significant; it attained the value of about 1.2 in the pulse. Such an intensity increase is lower than the rise observed in the idle time of the pulse. On the other hand, the ratio $I_{\tau_1}^{\text{H+R}}/I_{\tau_2}^{\text{H+R}} > 55$ demonstrates a rather low deposition contribution during the HiPIMS pulse. In other words, we assume further in this work that the RF discharge: (i) enables us to stabilize the discharge and to reduce the pressure during deposition, (ii) has a somewhat small but measurable effect on HiPIMS discharge and (iii) has a rather lower effect on deposition process/rate than one would expect.

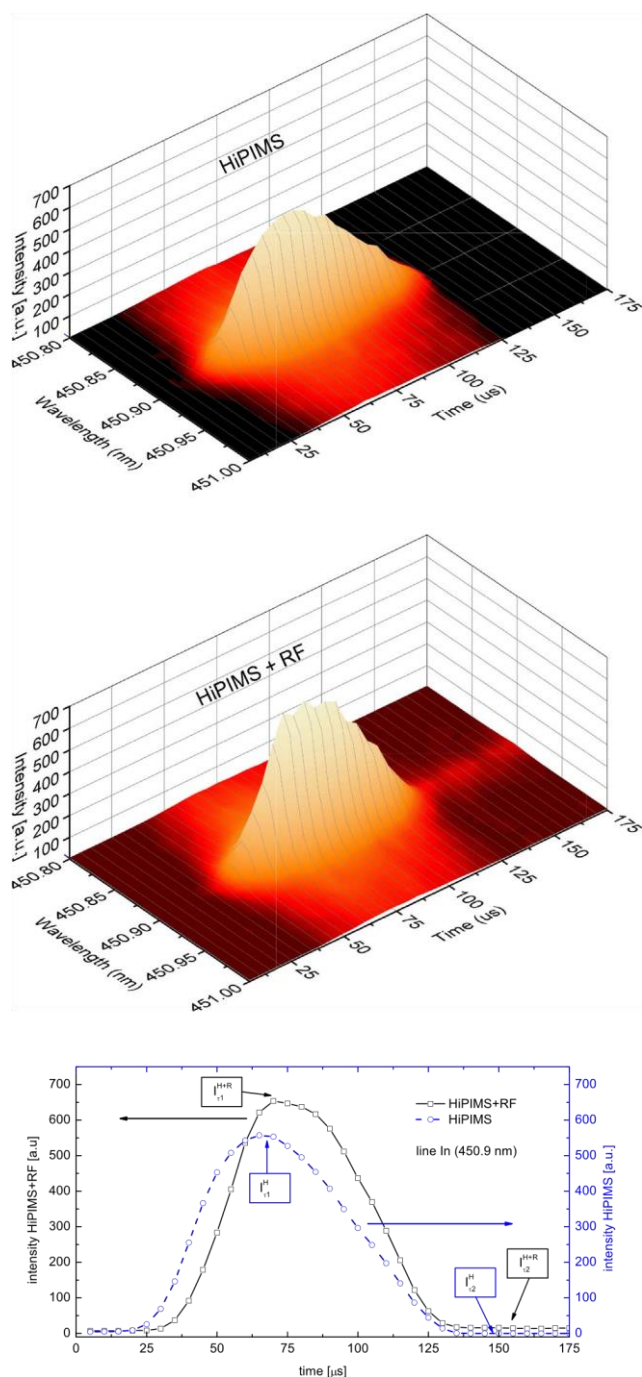


Fig. 4. Time-evolution of relative intensity emission of In (450.9 nm) spectral line measured by OES: (i) top panel - time evolution of In in pure HiPIMS discharge, (ii) middle panel - time evolution for HiPIMS+RF discharge and (iii) bottom panel - comparison for particular wavelength 450.9 nm. HiPIMS repetition frequency 1 kHz, $N_2/Ar = 0.06$, $p = 0.5$ Pa.

Averaged intensities over the pulse, estimated from the integral below the pulse intensity waveform, of selected metal and metal ion lines were measured at the time $\tau = 75 \mu\text{s}$ when the signal used to reach its maximum, see Fig. 4. These values are presented in Fig. 5 as functions of the process pressure p . Intensities of metal species increase more or less proportionally with pressure. It is assumed that the emission intensity depends on the number of excited species which are subsequently proportional to the number of sputtered species. In other words, dependences in Fig. 5 indicate a rise in the number of deposited species with increasing pressure. This is rather surprising because the number of species, arriving to the substrate region, should decrease at higher pressure due to elastic collisions and diffusion inside the discharge volume. This unexpected behavior might be related to the reduced gas rarefaction effect observed at higher pressure, see Fig. 2. It has been already mentioned above that the emission intensity corresponds with discharge current waveforms (compare Figs. 2 and 4). Gas rarefaction, indicated by a fall in the discharge current, prevents (mainly) working gas Ar^+ ions from bombarding the target surface and from providing efficient sputtering and production of the deposited species. Hence, the total number of the sputtered species is reduced at lower pressures, which also results in weaker emission intensity. Such explanation is supported by the fact that the rise in intensities was observed for metal atoms (In, Sn) as well as for metal ions (In^+ , Sn^+) due to low ionization potentials In^+ 5.78 eV and Sn^+ 7.34 eV, respectively. On the other hand, the intensity of Ar^+ (376.6 nm) behaves in opposite, i.e. decreases with increasing pressure. The behavior of Ar line is not included in the graph but the mentioned trend was observed regularly. The preferential ionization of metal species causes a lack of energetic species (electrons and/or metastable Ar^*) suitable for Ar excitation/ionization.

Reactive gas N_2 added to the discharge decreases the emission intensity of metal species In and Sn, see Fig. 6. A decrease in emission intensity of the sputtered species in reactive discharges is usually attributed to the formation of a compound layer on the target surface which reduces the sputtering rate, so-called target poisoning [43]. However, the target poisoning may not be the main actor in our case, because measurements of mass flux to the substrate do not vary significantly with the rise $\text{N}_2/\text{Ar} \leq 0.05$. However, the intensity drop is recognizable even with a small amount of added N_2 , $\text{N}_2/\text{Ar} \leq 0.03$. Such an

amount is nearly negligible, especially if a compound target $\text{In}_2\text{O}_3/\text{SnO}_2 = 90/10$ is used. This is obvious for In (450.9 nm) when the intensity is reduced about 50%. On the other hand, a decrease in Sn (285.6 nm) intensity is slower and less significant (about 15%). Because the discharge waveforms do not significantly suffer from reactive gas admixture (Fig. 3), it is assumed that sputtering is rather influenced by species impinging onto the target than by its surface state. It should be remembered that the bond dissociation energy of N_2 molecule is 9.79 eV and the ionization potential of nitrogen atom is 14.54 eV. These energies are higher than the ionization potentials of metals (In 5.78 eV and Sn 7.34 eV, respectively) but still lower than the ionization potential of Ar 15.76 eV. In other words, preferentially ionized N^+ can contribute to the sputtering process which is less effective because of lower momentum transfer. In the same graph, the dependence of emission intensity of N^{2+} (336.7 nm) is shown, as well. It is not so surprising that the intensity rises with increasing N_2/Ar ratio. Hence, the observed fall in metal emission intensities is also influenced by different sputtering yields that are reported $Y_{\text{In}} = 2.12$ and $Y_{\text{Sn}} = 1.57$ for Ar^+ bombardment at 600 eV [44].

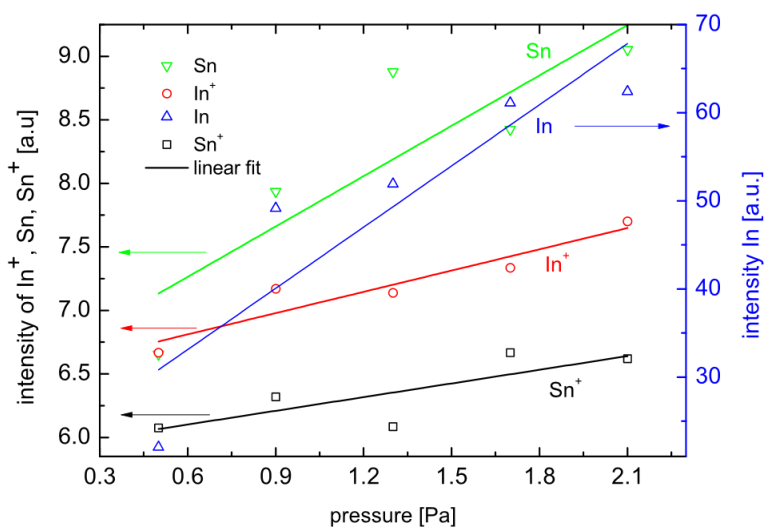


Fig. 5. Dependence of emission intensities for selected spectral lines for metal and metal ion species In 450.9 nm, In^+ 591.0 nm, Sn 283.6 nm and Sn^+ 607.5 nm. $\text{N}_2/\text{Ar} = 0.06$, $p = 0.5$ Pa.

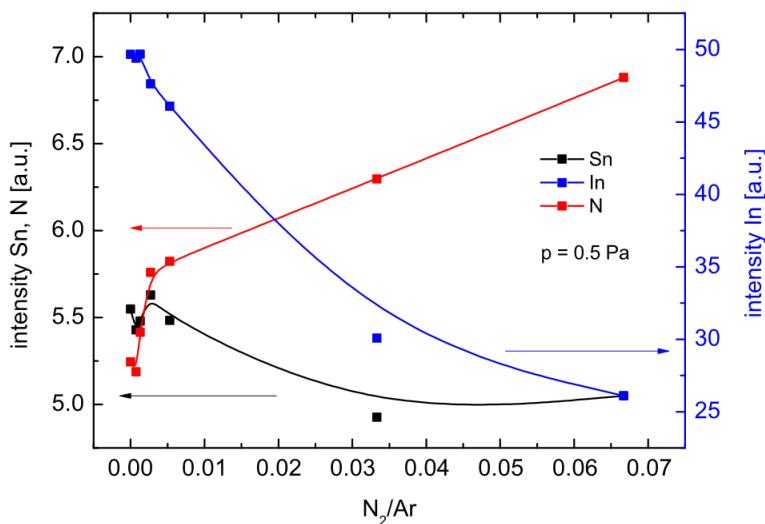


Fig. 6. Dependence of emission intensities for In (450.9 nm), Sn (285.6 nm) and N^{2+} (336.7 nm) as a function of N_2/Ar ratio.

6.2. Effect of pressure and a gas composition on ITO film formation

The research of discharge properties has been performed in order to optimize the deposition process of electrically conductive and transparent ITO films. The main idea is to use two easily controllable deposition parameters (pressure p and reactive gas N_2/Ar composition) to optimize ITO properties. For this reason we focused our attention on the investigation of physical parameters which determine optical and electrical properties of ITO films. The films were primarily deposited onto glass and Si substrates. No post-deposition thermal annealing was performed. However, the substrates were non-intentionally heated during the deposition. In fact, measurements using a thermocouple have shown that their temperature was enhanced about of 100 °C.

The effect of total pressure p , varied in range $p = 0.5$ – 2.1 Pa, on the layer properties was investigated first. The XRD patterns measured for film prepared at $p = 0.5$ Pa and $p = 2.1$ Pa are compared in Fig. 7. For both cases, well crystalline In_2O_3/SnO_2 was observed, however with preferred orientation along [h00]. As shown in Fig. 7, films prepared at higher pressure indicate more pronounced [h00] preferred orientation and the complete diminishing of the x-ray amorphous parts (28–30°) in comparison to the low-pressure grown film.

AFM images, see Fig. 8, illustrate the surface morphology of deposited films; the identical films measured by XRD are shown in Fig. 7. The surface roughness σ_{rms} as a function of pressure p is shown in Fig. 9. Standard deviation of σ_{rms} was calculated ± 0.5 nm from five independent images measured in the corners and in the center of the square of 1 cm size. A small rise in the surface roughness was observed with increased operation pressure. It seems to be nearly proportional to the pressure with an observable plateau for $p > 1.5$ Pa. Rather smooth surfaces $\sigma_{\text{rms}} \approx 5.6$ nm measured for $p = 0.5$ Pa are attributed to the bombarding effect of the deposited species which arrive onto the substrate with higher

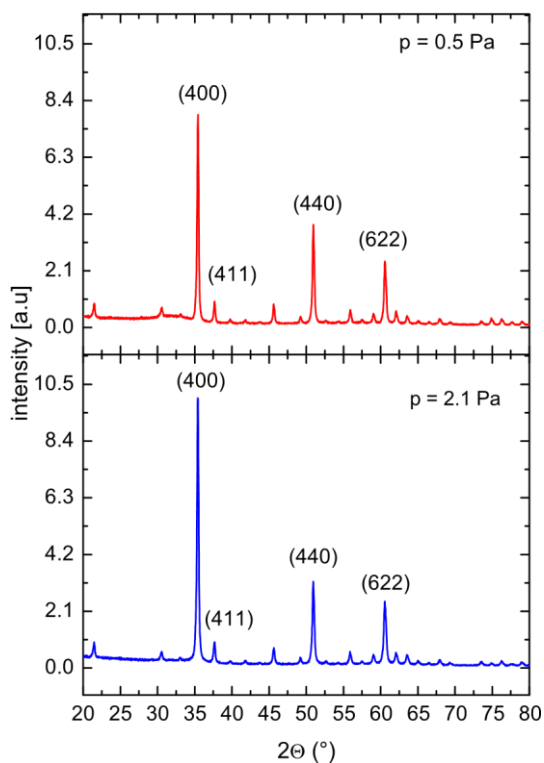


Fig. 7. XRD patterns of ITO films deposited at different pressures: upper panel $p = 0.5$ Pa, lower panel $p = 2.1$ Pa. Gas mixture $N_2/A = 0.01$ was used. Despite only the most intensive peaks are denoted, all of them indicate ITO structure.

energy. The mean free path is about $\lambda \geq 5$ cm at pressures 0.5 Pa and corresponds with the target vs. substrate distance. Hence, sputtered particles impinging the substrate without collision have a Thompson energy distribution [45]. Sputtered particles start to collide with neutral gas at pressure $p > 0.5$ Pa in the discharge volume and their kinetic energy is decreased, resulting in the formation of surfaces with higher roughness. This corresponds well with a zone structure model for PVD presented by [46] and with a modified version that includes energetic particles [47].

It is evident from Fig. 9 that the pressure, i.e. the energy of particles bombarding the substrate, influences also the crystallography of ITO film. The energy, delivered to the growth process at low pressures, enhances the

crystallization process, which is indicated by increased intensity of diffraction peaks. The size of the crystallite grain was estimated by XRD profile to be about 22 nm with the lattice constant $a_0 = 1.01819$ nm, see Fig. 9. Higher deposition pressure seems to be responsible for reduced size of grains as it is corresponding well with the zone structure mode [47]. It is worth reminding that the opposite behavior was observed for the film resistivity; the growth of resistivity is proportional to the growth pressure. Films with large crystallites are typical by their lower electrical resistivity since the electron mobility of TCO is limited by scattering at grain boundaries in polycrystalline films and at ionized impurities (Sn-ions in ITO) [48, 49]. The influence of grain boundary scattering decreases with increasing grain size due to the lower grain boundary.

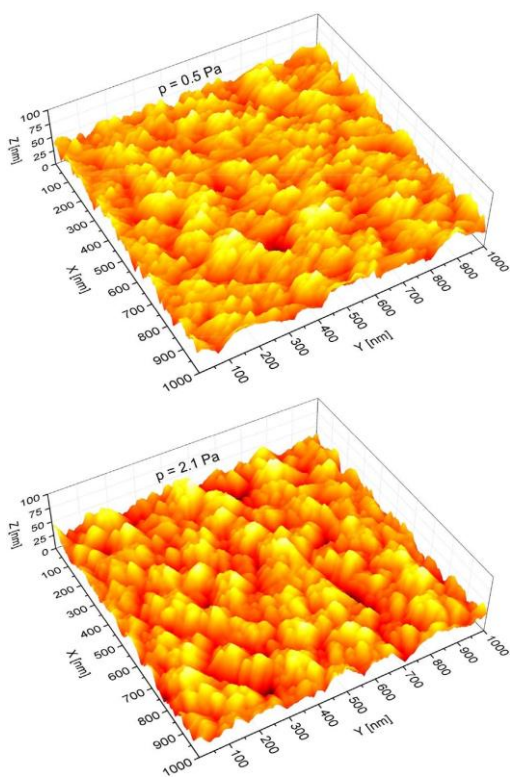


Fig. 8. Comparison of AFM images for: upper panel - film prepared at pressure $p = 0.5$ Pa, bottom panel - film prepared at pressure $p = 2.1$ Pa. The AFM images were measured on identical samples as in Fig. 7.

Another parameter that influences the film crystallinity is the gas environment during the deposition. The dependence of the electrical resistivity on the reactive gas N_2/Ar composition is shown in Fig. 10, as well. The highest resistivity was measured for amorphous films and was found to decrease with rising amount of nitrogen. This behavior is somewhat expected and can be explained by previously observed effect of larger domains. Furthermore, the presence of nitrogen probably results in possible preferential occupation of proper lattice sites by nitrogen instead of oxygen. Such effect might result in enhanced electron density and subsequently improved electrical conductivity. Similar phenomena were already

observed in recent works [50, 51] where the grain size also decreased with addition of nitrogen [50], which is contrary with our observation.

We suppose that the presence of nitrogen in the plasma will increase a stored energy in vibrational and rotational states of nitrogen molecules. This accumulated energy can be released by interaction of the nitrogen plasma with the substrates during the growth process. Thus the nitrogen plasma will cause a higher energy flux to the substrate promoting a better crystallization of the deposited films. A similar effect was already observed in the reactive sputtering of TiO₂ anatase films in Ar/O₂/N₂ reactive gasses [52]. In this work, films crystallization was unambiguously promoted by the presence of nitrogen plasma. We believe that our case is very similar. Unfortunately, as confirmed by Tian et al. [50], ITO films are probably doped by nitrogen creating acceptor levels above the valence band. This phenomenon will probably increase the concentration of carriers in ITO films and the conductivity will further increase in this way. The effect of doping is supported also by the fact that we observed atomic nitrogen in emission spectra Fig. 6. Excited nitrogen atoms in plasma will probably react with growing ITO films.

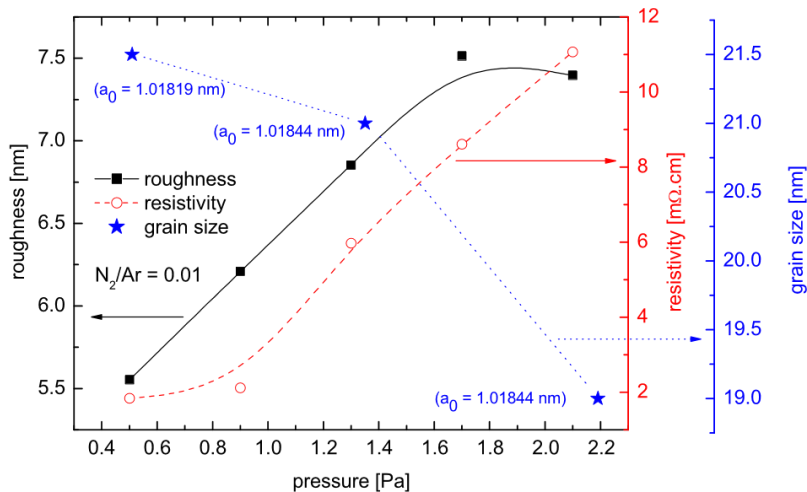


Fig. 9. Dependence of ITO surface roughness, electrical resistivity and the size of crystal grains on pressure. Films were prepared at gas mixture $N_2/Ar = 0.01$, $p = 0.5$ Pa. Furthermore, the lattice constants for ITO structures, denoted as a_2 are shown in the figure, as well.

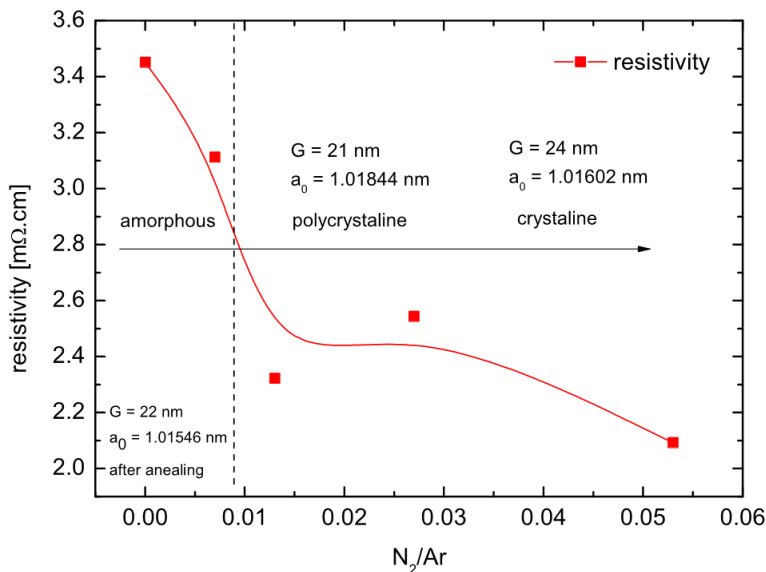


Fig. 10. Dependence of ITO electrical resistivity on gas mixture N_2/Ar at pressure $p = 0.5$ Pa. Furthermore, the lattice constants for ITO structures, denoted as a_0 , and grain sizes G are shown in the figure, as well.

6.3. Optical and electrical properties of deposited ITO films

High transparency and relatively low electrical resistivity represent the main benefits of ITO films. Fig. 12 illustrates optical constants of ITO samples estimated by means of spectroscopic ellipsometry. The different nitrogen admixture and pressure values lead to considerable shifts of $n(\lambda)$ and $k(\lambda)$ functions ($\lambda = 200 - 800$ nm). The dispersions of dielectric constants clearly show typical ITO behavior. It can be observed that the optical constant is similar for no or low nitrogen admixtures ($N_2/Ar = 0.00$ or 0.01). As shown in Fig. 12 (upper panel), the refractive index of the deposited ITO films rises to a peak value at a wavelength of around 310 nm and next shows normal dispersion for longer wavelengths [53, 54, 55]. Higher nitrogen admixture (0.05) causes a downshift of the dispersion maxima to the wavelengths of ca. 200 nm, suggesting significant ITO structural changes providing increase in band gap value. The extinction coefficient of ITOs deposited using various N_2/Ar ratios exhibits minor changes for the wavelength in the visible region (around 400–800 nm) in Fig. 12, bottom panel.

In addition, it was observed that maxima of the refractive index shift to higher wavelengths with increasing process pressure, revealing significant downshift of the energy band gap. In that condition, refractive index increases with

higher process pressures (Fig. 12). Since the refractive index is proportional to physical density, it is slightly increased by nitrogen, while the pressure provides significant film densification [17, 18, 56].

The transmittance estimated from the $k(\lambda)$ reached in average 70%, i.e. for wavelengths > 400 nm (not shown here) in all the samples. A decrease in the extinction coefficient, i.e. a decrease in absorbance, with a rise in wavelength is a well-known phenomenon, which is related to the behavior of a heavily-doped n-type semiconductor with a large band gap about of 4 eV [48, 54, 57]. UV photons excite an electron from the valence band to the conduction band, which leads to non-zero extinction coefficient. The presented values are consistent with those of other studies [16, 56, 58] but no additional post-deposition thermal annealing was needed to achieve them. As reported by other groups [19, 59, 60], the thermal treatment improves the ITO properties but induces material stresses and causes oxidization of surface.

Fig. 13 presents dependence of refractive index (for $\lambda = 550$ nm) on process gas composition and process pressure. In general, the value of refractive index about $n \approx 2.2$ was measured for crystalline films and its decrease was observed when the crystallinity, estimated from XRD pattern, was reduced. The pressure shows significant influence on the refractive index, while it seems that the film crystallography does not play so important role, compare with Fig. 7. The higher refractive index of the ITO films grown at higher pressures is attributed to the higher density caused by bombarding of energetic species [13, 18]. As shown in Fig. 12, the lower extinction coefficient occurs

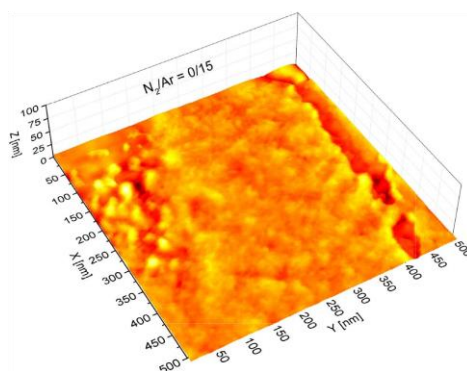
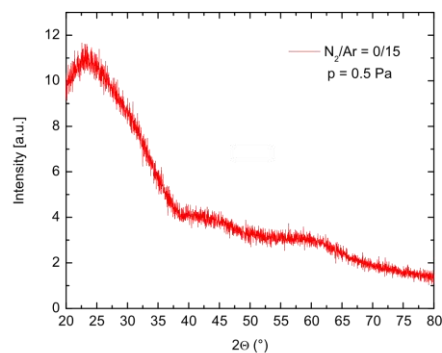


Fig. 11. X-ray pattern of ITO film deposited in pure Ar atmosphere at $p = 0.5$ Pa. Below is shown AFM image of the identical surface.

at pressure of 2.1 Pa, but only in the range below 400 nm. Previous studies of Jung et al. [57] showed that the higher extinction coefficient can be attributed to sub-oxide phases such as InO_x or SnO_x . Moreover, the nitrogen admixture causes the co-doping of ITO films shifting band gap and thus reduces refractive index of films.

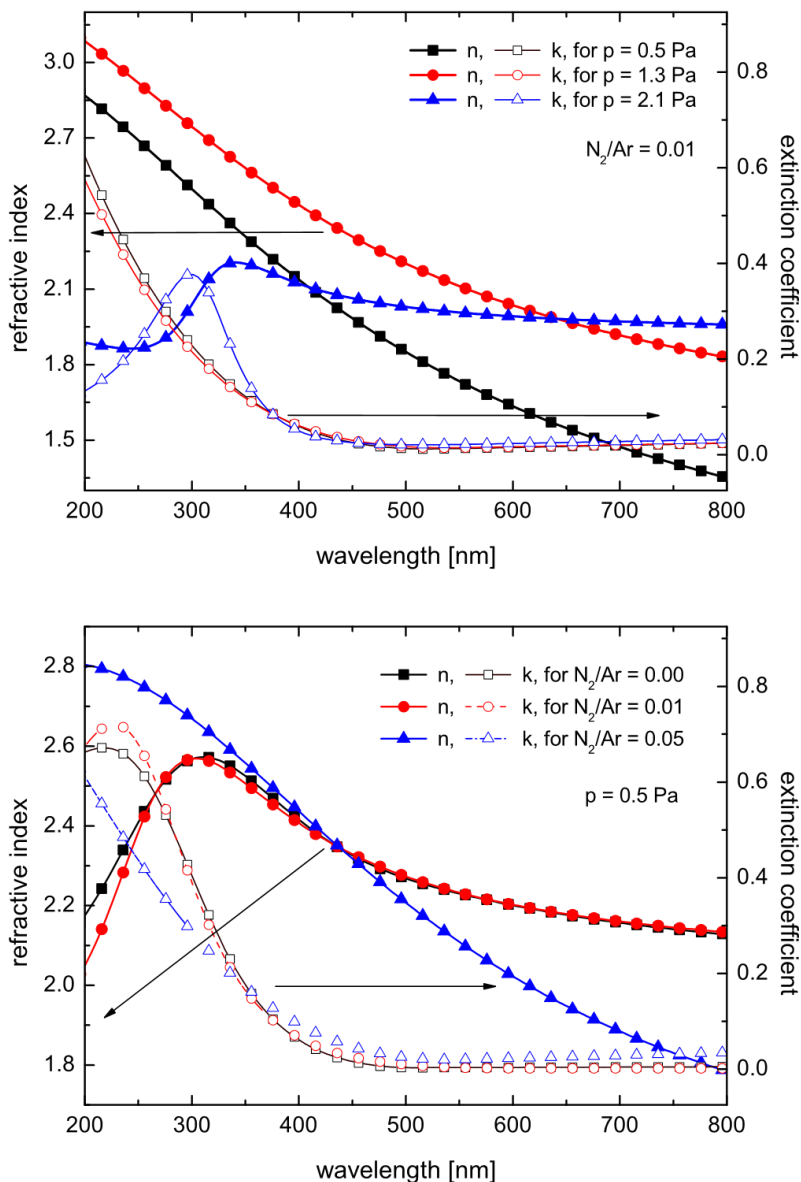


Fig. 12. Refractive index $n(\lambda)$ and extinction coefficient $k(\lambda)$ for different pressures at $N_2/Ar = 0.01$ (upper panel) and for different gas ratio at $p = 0.5$ Pa (bottom panel). Here the solid symbols are used for the refractive index n while open symbols denote extinction coefficient $k(\lambda)$.

In general, nitrogen admixture shows minor influence on the optical constants, while it leads to a substantial decrease in the electrical resistivity ρ . The dependence of the ITO film electrical resistivity is shown in Fig. 9. This can be attributed to the increase in carrier concentration induced by nitrogen co-doping and also to higher carriers mobility in the crystalline rich phase [61]. Oppositely, the pressure induces a decreasing trend of the electrical resistivity of the film, while its effect on film crystallography and surface morphology is not significant. The $\rho(p)$ predicates the method for tunable deposition of ITO films with ρ in a wider range.

The highest resistivity corresponds with the X-ray amorphous pattern of ITO deposited without nitrogen and is shown in Fig. 11. Presence of nitrogen probably results in possible preferential occupation of proper places of the lattice by nitrogen instead of oxygen. Such effect might result in enhanced electron density and subsequently improved electrical conductivity, i.e. reduced resistivity. The saturation point corresponds to $N_2/Ar = 0.02$ and the resistivity is not significantly influenced and remains constant. The higher electrical conductivity is enhanced by improvement of crystallinity: films with large crystals are typical for lower electrical resistivity since the electron mobility of TCO is limited by scattering at grain boundaries in polycrystalline films and at ionized impurities (Sn-ions in ITO) [48, 49]. The influence of grain boundary scattering decreases with increasing grain size due to the lower grain boundary density. In case of larger domains formed due to incorporated nitrogen to the discharge the electron movement is in accordance with the theory.

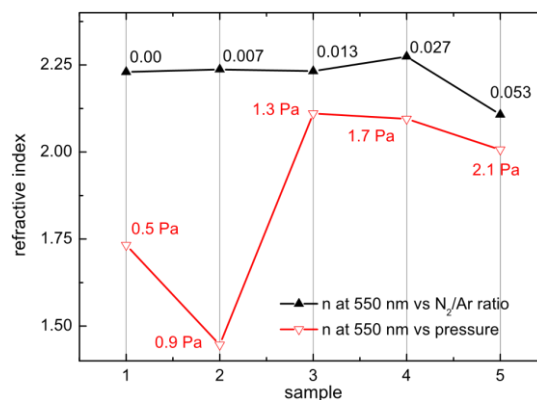


Fig. 13. Dependence of refractive index n on different gas ratio (full triangles, $p = 0.5$ Pa) and process pressure (opened triangles, $N_2/Ar = 0.01$) estimated for particular wavelength 550 nm. The values for gas ratio and pressure are written inside the graph describing each point.

7. CONCLUSION

In summary, the electrically conductive and optically transparent ITO films were deposited by the R-HiPIMS technique. The nitrogen addition during the HiPIMS process to the argon carrying gas has been particularly studied. Reactive gas N₂ added into the discharge decreases the emission intensity of metal species In and Sn. It could be concluded that ionized N⁺ can contribute to the sputtering process, which is less effective because of lower momentum transfer. Moreover, the nitrogen admixture causes the co-doping of ITO films to shift the band gap and thus reduce the refractive index of the films. In general, nitrogen admixture shows minor influence on the optical constants, while it leads to a substantial decrease in the electrical resistivity. It was shown that ITO film resistivity can be tuned in range of an order of magnitude by nitrogen admixture.

It should be noted that the parameters were achieved without additional thermal annealing, while that work was done by energy enhanced HiPIMS process. The reported films could be applied for temperature-sensitive materials, such as polymers or organics e.g., 3D printouts, flexible and printed electronics or optical fiber sensors.

Acknowledgments

This work was financially supported by the Czech Science Foundation (GACR) through project 16-14024S and research NATO grant SPS G5147. The authors gratefully acknowledge the financial support from the Polish National Science Centre (NCN) under the grant nos. 2016/21/B/ST7/01430, 2014/14/M/ST5/00715 and 2014/14/E/ST7/00104. The DS funds of the Faculty of Electronics, Telecommunications and Informatics of the Gdansk University of Technology are also acknowledged.

References

- [1] T. Minami, *Semicond. Sci. Technol.* 20 (2005) S35.
- [2] K. Ellmer, *Nat. Photonics* 6 (2012) 808.
- [3] P. Banerjee, W.J. Lee, K.R. Bae, S.B. Lee, G.W. Rubloff, *J. Appl. Phys.* 108 (2010) 043504.
- [4] I. Del Villar, F.J. Arregui, C.R. Zamarreno, J.M. Corres, et al., *Sensors Actuators B* 240 (2017) 174.
- [5] N. Paliwal, J. John, *Fiber Optics Sensors*, Springer International Publishing, Switzerland, 2017.

-
- [6] M. Sobaszek, M. Dominik, D. Burnat, R. Bogdanowicz, et al., *Proc. of SPIE* 10233 (2017).
- [7] A.B. Socorro, I. Del Villar, J.M. Corres, F.J. Arregui, I.R. Matias, *Sens. Actuators B Chem.* 200 (2014) 53.
- [8] L. Razquin, C.R. Zamarreno, F.J. Munoz, I.R. Matias, F.J. Arregui, *Proc. IEEE, Sens.* 2012 (2012) 6411186.
- [9] M. Quass, H. Steffen, R. Hippler, H. Wulff, *Surf. Sci.* 454 (2000) 790.
- [10] B. Szyszka, W. Dewald, S.K. Gurram, A. Pflug, C. Schulz, M. Siemers, V. Sittinger, S. Ulrich, *Curr. Appl. Phys.* 12 (2012) S2.
- [11] R. Latz, K. Michael, M. Scherer, *Jpn. J. Appl. Phys.* 30 (1991) L149.
- [12] M.S. Hwang, H.J. Lee, H.S. Jeong, Y.W. Seo, S.J. Kwon, *Surf. Coat. Technol.* 171 (2003) 29.
- [13] S. Ohno, Y. Kawaguchi, A. Miyamura, Y. Sato, P.K. Song, et al., *Sci. Technol. Adv. Mater.* 7 (2006) 56.
- [14] F.C. Carreri, A. Sabelfeld, H. Gerdes, R. Bandorf, M. Vergöhl, G. Bräuer, *Surf. Coat. Technol.* 290 (2016) 65.
- [15] C. David, B.P. Tinkham, P. Prunici, A. Panckow, *Surf. Coat. Technol.* 314 (2017) 113.
- [16] M. Huang, Z. Hameiri, A.G. Aberle, T. Mueller, *Vacuum* 121 (2015) 187.
- [17] K. Ellmer, T. Welzel, *J. Mater. Res.* 27 (2012) 765.
- [18] V. Sittinger, F. Ruske, W. Werner, C. Jacobs, B. Szyszka, D.J. Christie, *Thin Solid Films* 516 (2008) 5847.
- [19] F. Horstmann, V. Sittinger, B. Szyszka, *Thin Solid Films.* 517 (2009) 3178.
- [20] K. Sarakinos, J. Alami, S. Konstantinidis, *Surf. Coat. Technol.* 204 (2010) 1661.
- [21] J.T. Gudmundsson, N. Brenning, D. Lundin, U. Helmersson, *J. Vac. Sci. Technol.* A30 (3) (2012) 030801.
- [22] N. Britun, T. Minea, S. Konstantinidis, R. Snyders, *J. Phys. D: Appl. Phys.* 47 (2014) 224001.
- [23] V. Stranak, A.P. Herendorf, S. Drache, M. Cada, Z. Hubicka, et al., *Appl. Phys. Lett.* 100 (2012) 141604.
- [24] U. Helmersson, M. Lattemann, J. Bohlmark, A.P. Ehiasarian, J.T. Gudmundsson, *Thin Solid Films* 513 (2006) 1.
- [25] A.P. Ehiasarian, J.G. Wen, I. Petrov, *J. Appl. Phys.* 101 (2007) 054301.
- [26] V. Stranak, Z. Hubicka, M. Cada, S. Drache, M. Tichy, R. Hippler, *J. Appl. Phys.* 115 (2014) 153301.
- [27] S. Konstantinidis, J.P. Dauchot, M. Hecq, *Thin Solid Films* 515 (2006) 1182.
- [28] J. Rezek, J. Vlcek, J. Houska, R. Cersty, *Thin Solid Films* 566 (2014) 70.
-

- [29] V. Stranak, S. Drache, M. Cada, Z. Hubicka, et al., *Contrib. Plasma Phys.* 51 (2011) 237.
- [30] P.A. Ni, C. Hornschuch, M. Panajan, A. Anders, *Appl. Phys. Lett.* 101 (2012) 224102.
- [31] A. Hecimovic, M. Boeke, J. Winter, *J. Phys. D.: Appl. Phys.* 47 (2014) 102003.
- [32] A. Anders, Y. Yang, *Appl. Phys. Lett.* 111 (2017) 064103.
- [33] M. Panjan, R. Franz, A. Anders, *Plasma Sour. Sci. Technol.* 23 (2014) 025007.
- [34] V. Stranak, P. Adamek, J. Blazek, M. Tichy, P. Spatenka, *Contrib. Plasma Phys.* 46 (2006) 439.
- [35] H. Wulff, H. Steffen, *Characterization of Thin Films, in Low Temperature Plasmas*, Wiley-VCH, Berlin, 2008, p. 329.
- [36] D.A.G. Bruggeman, *Ann. Phys.* 24 (1935) 636.
- [37] E.D. Palik, *Handbook of Optical Constants of Solids*, Academic, New York, 1985.
- [38] H.G. Tomkins, *Spectroscopic Ellipsometry and Reflectometry*, Wiley, New York, 1999.
- [39] M. Aiempnanakit, A. Aijaz, D. Lundin, U. Helmersson, T. Kubart, J. *Appl. Phys.* 113 (2013) 133302.
- [40] D. Lundin, N. Brenning, D. Jadernas, P. Larsson, E. Wallin, M. Lattemann, M.A. Raadu, U. Helmersson, *Plasma Sources Sci. Technol.* 18 (2009) 045008.
- [41] C. Huo, M.A. Raadu, D. Lundin, J.T. Gudmundsson, A. Anders, N. Brenning, *Plasma Sources Sci. Technol.* 21 (2012) 045004.
- [42] J.T. Gudmundsson, D. Lundin, N. Brenning, M.A. Raadu, C. Huo, T.M. Minea, *Plasma Sources Sci. Technol.* 25 (2016) 65004.
- [43] V. Stranak, J. Kratochvil, J. Olenicek, et al., *J. Appl. Phys.* 121 (2017) 171914.
- [44] Y. Yamamura, H. Tawara, *At. Data Nucl. Data Tables* 62 (1996) 149; *NIFS-DATA* 23 (1995).
- [45] M.W. Thompson, *Philos. Mag.* 18:152 (1968) 377.
- [46] J.A. Thornton, *J.V.a.c. Sci, Technol.* 11 (1974) 666.
- [47] A. Anders, *Thin Solid Films* 518 (2010) 4087.
- [48] K.S. Tseng, Y.L. Lo, *Appl. Surf. Sci.* 285 (2013) 157.
- [49] O. Tuna, Y. Selamet, G. Aygun, L. Ozyuzer, *J. Phys. Appl. Phys.* 43 (2010) 055402.
- [50] L. Tian, G. Cheng, H. Wang, Y. Wu, R. Zheng, P. Ding, *Superlattice. Microst.* 101 (2017) 261.
- [51] E. Aperathitis, *J. Appl. Phys.* 94 (2003) 1258.
- [52] S. Kment, P. Kluson, Z. Hubicka, J. Krysa, et al., *Electrochim. Acta* 55 (2010) 1548.
- [53] J. Bartella, J. Schroeder, K. Witting, *Appl. Surf. Sci.* 179 (2001) 181.

-
- [54] Y.S. Jung, *Thin Solid Films* 467 (2004) 36.
- [55] R.A. Synowicki, *Thin Solid Films* 313-314 (1998) 394.
- [56] A. Sytchkova, D. Zola, L.R. Bailey, B. Mackenzie, et al., *Mater. Sci. Eng. B.* 178 (2013) 586.
- [57] Y.S. Jung, Y.W. Choi, H.C. Lee, D.W. Lee, *Thin Solid Films* 440 (2003) 278.
- [58] H. Stroescu, M. Anastasescu, S. Preda, et al., *Thin Solid Films* 541 (2013) 121.
- [59] L.J. Meng, F. Placido, *Surf. Coat. Technol.* 166 (2003) 44.
- [60] M. Noh, Y.S. Lee, J. Park, J.S. Chung, et al., *Curr. Appl. Phys.* 16 (2016) 1576.
- [61] M. Gartner, H. Stroescu, A. Marin, P. Osiceanu, et al., *Appl. Surf. Sci.* 313 (2014) 311.

A3. Modified high frequency probe approach for diagnostics of highly reactive plasma

Petr Sezemsky, Vitezslav Stranak, Jiri Kratochvil, Martin Cada, Rainer Hippler, Miroslav Hrabovsky, Zdenek Hubicka, Modified high frequency probe approach for diagnostics of highly reactive plasma, Plasma Sources Science and Technology, 28, (2019), 115009.

Republished with permission of IOP Publishing, Ltd; permission conveyed through Copyright Clearance Center, Inc.

Abstract

The paper introduces a modified approach of time resolved in situ diagnostics of highly reactive discharges (C_2H_2 in our case) usually used for a deposition process of various non-conductive thin films. Reactive plasma could create an insulating film onto inserted diagnostic tools, which distorts measured data and makes their processing unreliable; a typical problem of Langmuir probe measurements. The proposed approach utilizes a so-called radiofrequency (rf) Sobolewski probe for ion flux measurement which is further modified to also obtain the electron temperature in some cases and the ion density. In this work, we introduce the procedure where measured rf probe characteristics are transformed towards I-V curves of the plasma sheath with subtracted capacitive current. This processing enables not only the monitoring of plasma sheath impedance and the ion flux towards the substrate but also allows for an estimation of other parameters as the plasma density or electron temperature, respectively. We demonstrate that the substrate used for thin film deposition can act as an active probe itself. The relevance of the proposed method was verified in pure Ar discharge where the results correspond with conventional Langmuir probe diagnostics. Furthermore, internal plasma parameters of highly reactive Ar/ C_2H_2 plasma, formed from acetylene, were evaluated, too.

1. INTRODUCTION

Nanostructured surfaces, often prepared by plasma deposition methods, have gained an enormous interest in last years because of their wide range of applications. However, modern technology (sensor industry, solar cells, catalysts, nanosemiconductors, biofunctional surfaces and many others [1–6]) seeks for rather complex and multicomponent thin films which cannot be prepared straightforward and needs more sophisticated plasma deposition processes in a reactive environment. Namely, we can point out reactive plasma physical vapor deposition and/or plasma enhanced chemical vapor deposition processes [7]. The plasma deposition processing is rather complex and offers many parameters that have to be adjusted [8]. All these parameters need to be known, understood, optimized and controlled to obtain reproducible deposition process of films with desired properties. Hence, the careful diagnostics of plasma properties and their feedback-wise control is essential.

Unfortunately, any diagnostics tools inserted into the process chamber are also coated. Hence, for the diagnostics of highly reactive and harsh discharges non-invasive techniques are preferentially used; typically based on optical emission spectroscopy providing information about chemical composition [9, 10] or microwave plasma analysis [11]. However, other unwanted information, especially about energetic properties, is often received during invasive measurements when a biased electrode or mesh is immersed directly into the plasma bulk [9]. Then the deposited film changes the active diagnostic surface which alters the measured signal. This is the typical limitation of the oldest diagnostic approach by the Langmuir probe [12–14] because altering its surface changes the electrical conductivity and subsequently the I - V characteristics becomes distorted [12] and unreliable. To overcome this problem pulsed and superposed voltage bias [14, 15], fast scanning [14, 16], probe shielding [16], periodic cleaning of the probe surface by ion bombardment [17], or by heating [18] have been developed. However, these methods usually bring only a partial solution.

The most promising methods, for invasive diagnostics based on current collection, are probe methods operated with altering bias with frequency in a range from kHz up to MHz. The method introduced by Braithwaite et al. [19] utilize the probe self-bias effect when the pulsed modulated radiofrequency

(rf) voltage is applied on a planar probe divided from the external circuit by a defined capacitor. Here the applied voltage has to be large enough in respect to the electron temperature. This method was further studied and optimized in [20, 21]. Sobolewski [22, 23] extended this approach by applying a defined rf voltage and determined the ion flux from current and voltage waveforms measured on the probe. It can be used in the reactive plasma because the insulating film, growing onto the probe surface, does not affect the electrical reactance of the probe significantly [24]. The ion flux to the probe represents the probe current when the applied voltage reaches a minimum value. The presented technique is very suitable for ion flux estimation and was further developed and improved [22–24]. The RF current and voltage waveforms measured in the plasma in order to get information about plasma impedance or other plasma parameters were already developed on very high level and described in [25–30]. The information about plasma impedance was used in some papers for determination of electron concentration as it was described in [31–36]. The plasma was usually supplied by the RF frequency 13.56 MHz or low frequency 100 kHz with superimposed RF (13.56 MHz) in this case and the plasma impedance of all the discharge volume was obtained. The method provided some average values of plasma parameters over all the discharge volume.

Recently, various modifications of fast sweep Langmuir probes were developed [37–39] and used in reactive plasma for plasma parameters determination. The voltage applied on the probe was swept with very high frequency up to 400 kHz. In this case, the parasitic capacitive current flowing through the probe, was subtracted by the specific circuit and a dummy probe and suitable current and voltage characteristics were obtained for electron temperature and concentration calculations.

In this work, we present a modified Sobolewski probe method where the measured rf waveforms are transformed towards Langmuir I – V curve with a subtracted capacitive current. This approach enables an estimation of plasma density and electron temperature assuming a Maxwellian distribution function. The proof of concept is verified during diagnostic of Ar plasma where we observe a good agreement between results obtained by the conventional slowly swept Langmuir probe and the modified Sobolewski approach. After that, highly reactive dusty plasma discharge (driven by rf

13.56 MHz power) formed from acetylene was investigated and the internal plasma parameters were estimated. The results are discussed in the context of previously published work [40] which confirm hydrocarbon nanoparticle (dust) formation.

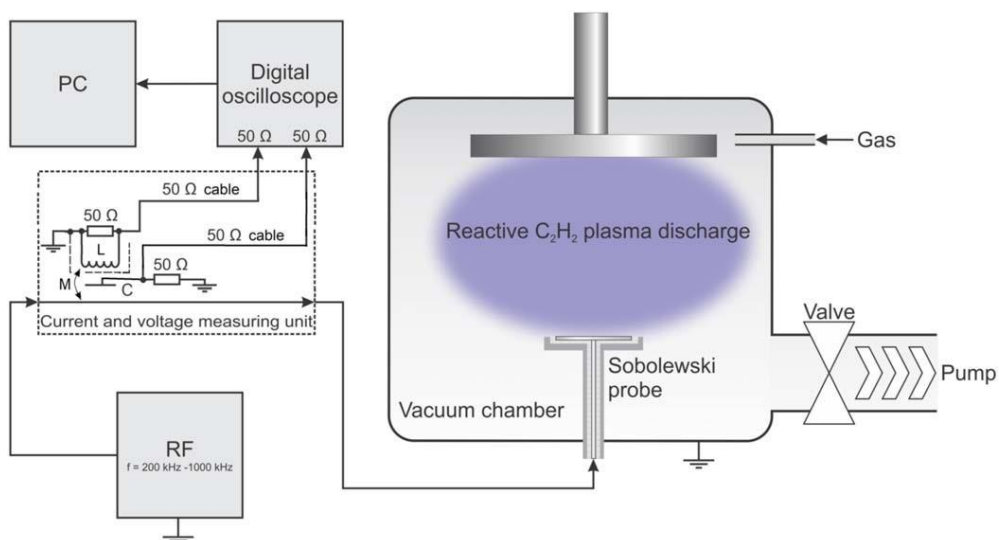


Figure 1. Simplified scheme of the experimental and measuring setup. C denotes a capacitive probe for voltage sensing, L is the Rogowski coil for current sensing. The capacitively coupled plasma was driven with an rf power of 100 W (13.56 MHz) in a vacuum vessel.

2. EXPERIMENTAL SETUP

2.1. Vacuum and Ar/C₂H₂ plasma production

Figure 1 schematically depicts the used experimental setup. The stainless steel vacuum chamber was evacuated using an oil diffusion pump. The capacitively coupled rf discharge was generated by a planar electrode (200 mm in diameter) fed by a rf power supply with a frequency of 13.56 MHz; the absorbed rf power of 100 W and the electrode self-bias voltage of about -400 V was kept constant during the experiments. The pressure in the chamber was 5 Pa attained by an Ar mass flow rate of 50 sccm for the non-reactive environment. The mixture Ar/C₂H₂ = 50/5 was used for generation of the reactive dusty plasma.

2.2. Sobolewski rf probe

A planar, circular rf Sobolewski probe [22–24], with defined active area 1 cm^2 , was inserted into the plasma to measure substrate ion flux and plasma sheath impedance, see figure 1. The probe body was shielded by a PTFE cover, to define the active probe area. The probe was distanced 5 cm from the discharge rf electrode. The active rf probe was powered by Tabor Electronics 9100 high-voltage wideband amplifier controlled by an Agilent 33250A function waveform generator. The function generator was set to deliver a sinusoidal signal with a frequency in the range of 200–1000 kHz. After amplification, the signal had a peak-to-peak value of 80 V. A 4.7 nF high-voltage ceramic capacitor was connected between the probe and the amplifier and served as a blocking capacitor for the dc self-bias voltage. The rf current through the probe was measured by a current transformer. The scheme of all the circuit can be seen in figure 1. The current transformer was wound on a Teflon core which guaranteed excellent linearity of this current transformer. This one was implemented as a toroid with a rectangular cross-section with inner and outer radii of 8 and 30 mm, respectively. The induced current in the coil, proportional to the RF probe current, was measured as a voltage drop on a sensing resistor, $R = 50 \Omega$, placed between the two leads of the windings. The current transformer was further connected with 50Ω coaxial cable to 50Ω input of digital sampling oscilloscope. The current transformer had a calculated self-inductance $L = 12.7 \mu\text{H}$ and a mutual inductance $M = 0.32 \mu\text{H}$ between the sensing winding and conductor. A capacitive shielding was placed between the main probe conductor and current transformer in order to eliminate undesired capacitive pick up of current sensor. A voltage sensor based on capacitive probe was placed directly below the current transformer in order to measure RF current and voltage exactly at the same point. The voltage sensor has capacitance $C = 1.5 \text{ pF}$ relative to main probe conductor and measured signal related to RF voltage on this conductor relative to ground. The voltage and current waveforms were acquired by a Tektronix MDO3034 oscilloscope and saved on the flash memory. The plasma probe was connected with this current and voltage sensor via a coaxial cable with impedance 50Ω and length 100 mm. Since the maximum detected frequency is only 3 MHz we can consider this short cable as a pure capacitor. This sensor was able to provide two voltage signals in

dependence on time which were related to the RF current and RF voltage on the probe conductor, respectively. A proper calibration was needed to get correct values of the RF current and voltage waveforms on the plasma probe. The presented RF current/voltage sensor can be considered as fully linear circuit. The only nonlinear element is the measured plasma in this experiment.

Although the pure harmonic voltage signal is applied on the probe due to the nonlinearity of plasma load higher harmonics will be detected with the current and voltage sensor. For this reason, the calibration of the current–voltage sensor has to be done also for these higher harmonics.

3. CALIBRATION OF THE RF CURRENT AND RF VOLTAGE SENSOR

In order to get correct values of current and voltage on the probe, the sensor has to be calibrated on wide frequency range from 200 kHz up to 3 MHz. For the calibration procedure, the accurate calibration carbon resistor with frequency independent resistance $R_{zc} = 50 \Omega \pm 1 \Omega$ in this frequency range was placed behind the RF current/voltage sensor. This calibration resistor was further connected in parallel with other input of the digital sampling oscilloscope with input resistance $1 \text{ M}\Omega$ and capacity 14 pF . The scope input impedance was considered much higher than calibration resistance and was omitted. The output of current and voltage sensors were connected to two channels of the scope with input impedance set up on 50Ω . This measured voltage waveform on the calibrating resistor provided information about RF voltage on this resistor and RF current which have the same phase angle as the RF voltage and RF current amplitude

$$I_{azc} = \frac{U_{azc}}{50 \Omega} \quad (1)$$

This knowledge of current and voltage amplitudes on the calibrating resistor can provide information about amplitude and phase correction coefficients for sensors of current and voltage signals on particular frequencies in the range 200 kHz–4 MHz. The plots of amplitude and phase correction coefficients for voltage and current signals in dependence on the frequency can be seen in figures 2(a) and (b), respectively.

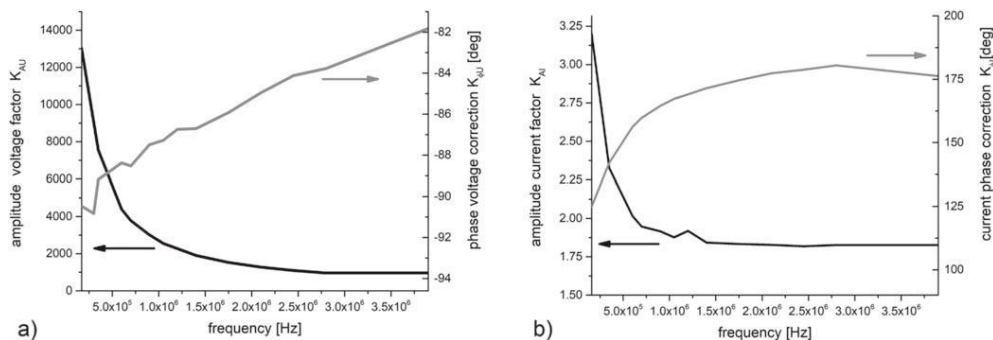


Figure 2. Voltage and current amplitude and phase correction factors of calibrated IV sensor in the frequency range 150 kHz–4 MHz.

$$C = 220 \text{ pF} \pm 10\%$$

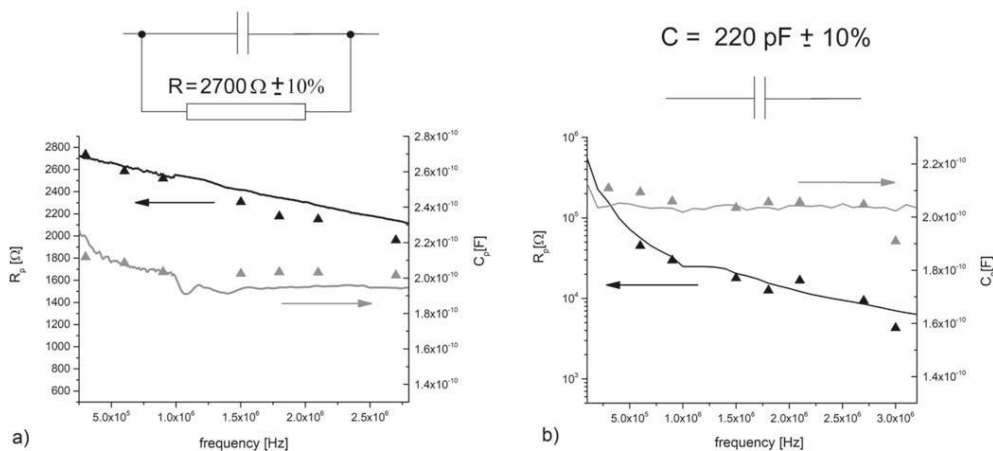


Figure 3. Impedances of (a) parallel connection of carbon resistor $R = 2700 \Omega$ and capacitor 220 pF (b) only ceramic capacitor 220 pF placed instead of planar probe and measured by calibrated RF current and voltage sensors (black and gray triangles) and for comparison measured by calibrated impedance spectrometer (black and gray solid line) in spectral range 200 kHz–3.5 MHz.

The practical procedure of calculation of RF current and voltage from the measured signal waveforms is the use of DFT (discrete Fourier transformation) of measured signals. The DFT spectrum is then corrected with amplitude and phase factors presented in figure 2 and the corrected DFT spectra were transformed back by the inverse DFT. The correct RF voltage and current waveforms were determined in this way. This procedure provided a realistic information about the RF current and voltage and their relative phase in the position of the RF current/voltage sensor.

In order to verify that the described calibration procedure was correct we placed behind the RF current/voltage sensor (i) a parallel connection of resistor 2700Ω and capacitor 220 pF (figure 3(a)) and (ii) only capacitor 220 pF (figure 3(b)). Impedance of these elements were measured with the RF current/voltage sensor in the frequency range up to 3 MHz at selected discrete frequencies. The measured impedance was converted in an admittance and values of the parallel resistor and capacitor were calculated from this admittance model. For comparison, these circuit elements were measured in the same frequency range by calibrated impedance spectrometer. We can see very good agreement of parallel resistance and capacitance determination by both devices with the difference lower than 5% .

4. MODIFIED RF PROBE METHOD AND ITS VERIFICATION

In principle, the Sobolewski probe method is based on a precise simultaneous measurement of the rf voltage and current waveforms measured by the RF current/voltage probes [41]. The above described calibrated RF current/voltage sensor was used to determine j between the probe voltage $u_s(t)$ and probe current $i_s(t)$, here the index s denotes the probe related parameters as ‘Sobolewski’ voltage and current. The probe calibration was performed at a wide range of rf frequencies with fast Fourier transformation post-processing; a more detailed description of the calibration procedure can be found elsewhere [24]. From these measurements, plasma parameters such as ion flux towards the probe Γ_i and sheath impedance Z_{pl} can be estimated more or less directly.

The left panel of figure 4 shows the measured data after calibration procedure and fast Fourier transformation. The probe voltage is shown with subtracted dc self-bias. The right panel indicates the estimation of the ion flux to the probe surface. The voltage applied to the probe needs to have a sufficiently high amplitude ($>10 \text{ V}$) to repel most of the electrons. In the case of amplitude $U_s^{\min} \approx -40 \text{ V}$, it is assumed that electron contribution to the probe current is close to zero. Hence, the total probe current measured at U_s^{\min} is attributed only to positive ions hitting the probe. According to Sobolewski, the ion flux to the probe surface Γ_i is equal to the probe current divided by the probe surface A at the same time when the simultaneously measured probe voltage reaches its minimum [42], as shown in right panel of figure 4. Here we should

remind that this simplest Sobolewski analytical method for the ion flux determination is properly valid only for rf frequencies significantly lower than the ion plasma frequency, $\omega_s \ll \omega_{pl}$ [22].

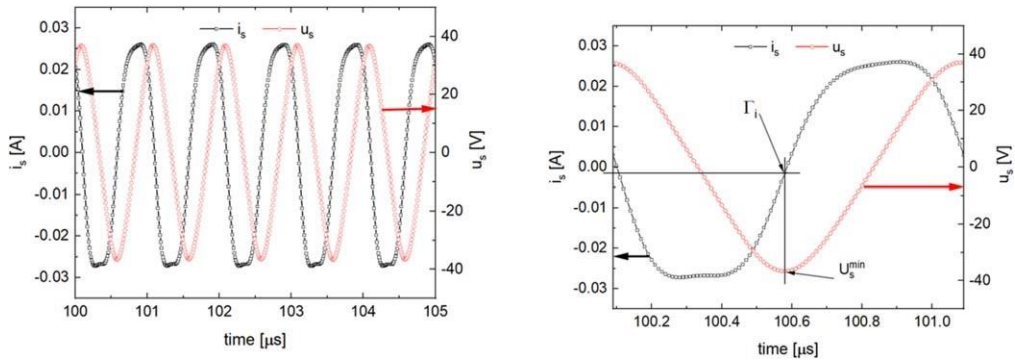


Figure 4. Left: filtered waveforms of voltage $u_s(t)$ and probe current $i_s(t)$, respectively, measured with the calibrated probe. Right: estimation of the ion flux Γ_i from the U_s^{min} value.

Another parameter available from the voltage and current waveforms is the plasma sheath impedance Z_{pl} which determines the current flowing through the sheath. Equations (2) and (3) were used to estimate the real part Z_s^{Re} and the imaginary part Z_s^{Im} (reactance) of the total impedance Z_{pl} [24]:

$$Z_s^{Im} = |Z_s| \cdot \sqrt{1 - \cos^2 \varphi_s}, \quad (2)$$

$$Z_s^{Re} = |Z_s| \cdot \cos \varphi_s, \quad (3)$$

where $|Z_s| = \frac{U_s}{I_s}, \quad (4)$

and $\cos \varphi_s(t) = \frac{\frac{2}{T} \int_0^T u_s(t) \cdot i_s(t) \cdot dt}{U_s \cdot I_s}. \quad (5)$

Here U_s and I_s denote peak values of the measured rf probe voltage and current, respectively, $j_s(t)$ is the phase shift between $u_s(t)$ and $i_s(t)$, and T is the period of the rf probe signal.

However, the important fact is that the measured signal is not given solely by the sheath impedance Z_{pl} but also by the impedance of the probe itself and the

power feed line between the probe and the measurement unit. This background impedance Z_{bc} has a capacitive character and causes a displacement current that is also included in the current signal $i_s(t)$. Therefore the background impedance needs to be measured and subtracted from the calculated impedance Z_s in order to obtain correct plasma sheath impedance. The problem can be approached using a theoretical model of two in parallel connected impedances. The first one represents the background impedance Z_{bc} , while the second is the desired plasma sheath impedance Z_{pl} , both contributing to Z_s :

$$\frac{1}{Z_s} = \frac{1}{Z_{bc}} + \frac{1}{Z_{pl}} \quad (6)$$

Turning to corresponding admittances the solution simplifies:

$$Y_{pl} = Y_s - Y_{bc}, \quad (7)$$

$$Y_{pl} = \frac{1}{|Z_s|} [\cos \varphi_s - i \sin \varphi_s] - \frac{1}{|Z_{bc}|} [\cos \varphi_{bc} - i \sin \varphi_{bc}], \quad (8)$$

where Y_{pl} is the plasma sheath admittance, Y_s is the admittance of the measured signal and Y_{bc} is the admittance of the background, respectively. Furthermore, the j_{bc} represents the phase shift of the background signal. The right side of equation (8) can be separated into real and imaginary part giving values of Y_{pl}^{Re} and Y_{pl}^{Im} . From there the plasma sheath impedance Z_{pl} , its real and imaginary parts Z_{pl}^{Re} and Z_{pl}^{Im} , and the phase shift j_{pl} can be easily estimated as:

$$Z_{pl} = \frac{1}{Y_{pl}} = \frac{1}{|Y_{pl}|^2} (Y_{pl}^{Re} + Y_{pl}^{Im}), \quad (9)$$

$$Z_{pl}^{Re} = \frac{Y_{pl}^{Re}}{|Y_{pl}|^2}, \quad (10)$$

$$Z_{pl}^{Im} = \frac{Y_{pl}^{Im}}{|Y_{pl}|^2}, \quad (11)$$

$$\varphi_{pl} = \text{atan} \left(\frac{Z_{pl}^{Im}}{Z_{pl}^{Re}} \right). \quad (12)$$

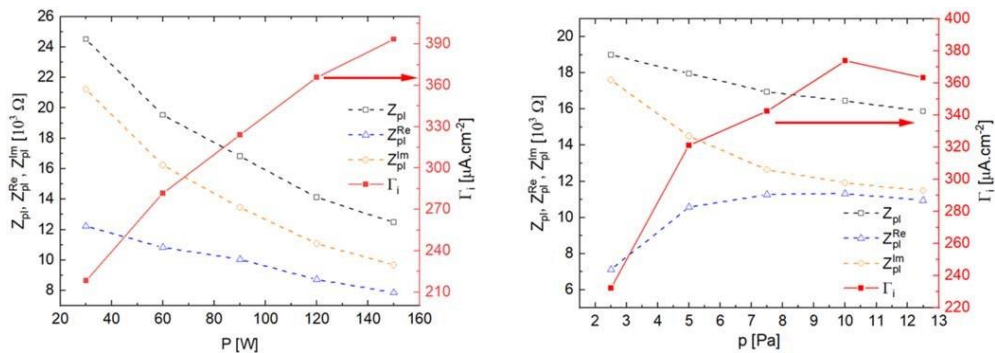


Figure 5. The dependence of plasma sheath impedances (Z_{pl} , Z_{pl}^{Re} , Z_{pl}^{Im}) and the ion flux Γ_i as a function of discharge absorbed power (on the left, pressure kept constant 5 Pa) and process pressure (on the right, power kept constant 100 W). Estimated by the Sobolewski method in pure Ar discharge.

Figure 5 shows the dependence of the ion flux Γ_i and plasma sheath impedance Z_{pl} on the absorbed power (left panel) and gas pressure (right panel), respectively. These data were measured with a signal frequency on the probe of 200 kHz. It can be clearly seen that the ion flux is more or less proportional to the power due to enhanced production of ions in the plasma bulk. The higher density of ions and subsequently of their flux towards the substrate with increasing power is as expected. Once the plasma density increases the plasma sheath impedance is decreased by the presence of energetic free electrons in the sheath; in fact the Debye length will be shorter for higher plasma density. Furthermore, both contributions of plasma impedances Z_{pl}^{Re} , Z_{pl}^{Im} have a similar qualitative behavior with an indication that the reactance is the dominant part of the total plasma sheath impedance at this signal frequency (200 kHz). Furthermore, Γ_i and Z_{pl} are also pressure-dependent, see figure 5 (right panel). We observe a rising ion flux with increasing gas pressure within the measured pressure range (2.5–12.5 Pa). It predicts an increasing number density of plasma species, and also higher ionization fraction at higher pressures. The error estimated from a larger amount of measurement is about 20%. Here, we want to namely show that the Sobolewski method is capable for the estimation of plasma impedance and the ion flux with their reasonable values of about 20 k Ω and 300 $\mu\text{A cm}^{-2}$.

Once these characteristics are known, the estimation of other inner plasma parameters is wanted. For example, Sobolewski [41] and Sprott [43] proposed

a semi-empirical relation between the electron temperature T_e , the ion current I_i and the real part of the plasma sheath admittance:

$$\frac{1}{Y_{\text{pl}}^{\text{Re}}} = \frac{k_B T_e}{q_e I_i} \quad (13)$$

where k_B is the Boltzmann constant and q_e is the elementary charge. However, the validity of this relation is strictly limited; the derived equation agrees with the experimental data, obtained in [41], only for low sheath voltages < 3 V. On the other hand, we could not use such a low voltage for the current and voltage waveforms due to the small sensitivity of our current and voltage sensors in our experimental set up.

For that reason, we propose a novel approach to the evaluation of data obtained by the rf probe with sufficiently high voltage amplitudes (> 10 V). The method utilizes the approach from [44] where high-frequency voltage sweeps were used during Langmuir probe diagnostics. The method is based on the transformation of data measured by RF current/voltage sensor to Langmuir-like I - V characteristics by conversion of the rf probe curves to the $i_p(u_s)$ function. This method can be used only in the case the used probe voltage frequency is well below ion plasma frequency ω_{pi} . In this case ions can follow the applied high frequency field. This can be considered as a limitation of this method and the same limitation appeared also for the fast sweep probe presented in [37]. Each period of the rf probe voltage $u_s(t)$ can be considered as sweeping probe voltage with a forward and backward part, see figure 6 (left panel). It is not a linear sweep but rather a sinusoidal sweep. Besides the voltage $u_s(t)$, the figure also shows total probe current $i(t)$, obtained by subtraction of the displacement current from the measured signal $i_s(t)$ between the probe and the measurement unit. The subtracted displacement current was obtained by RF current measurement through this probe without plasma. On the other hand the total current $i(t)$ still contains some capacitive part because in case of plasma presence this parasitic capacitance is slightly different and sheath capacitance appears.

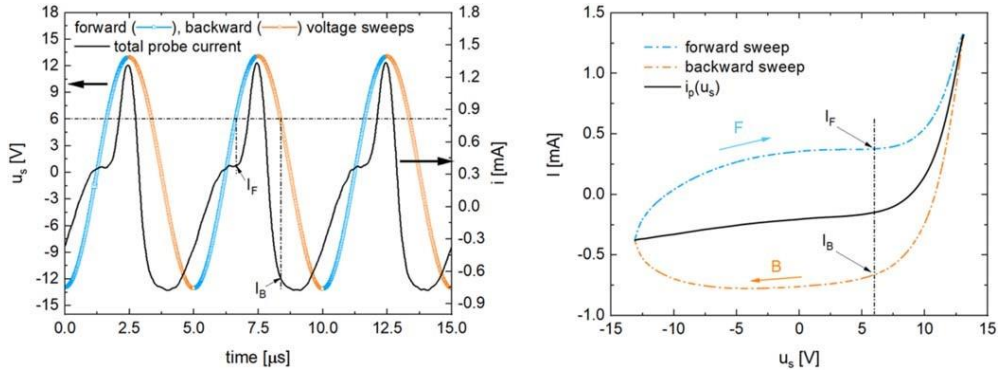


Figure 6. The transformation of the rf measured waveforms towards the I - V curve. Left: the rf probe voltage $u_s(t)$ considered as forward and backward voltage sweep of measured total probe current $i(t)$. Right: graph $i(u_s)$ results in a typical Lissajous-like pattern from which, after proper processing, the I - V curve is obtained. The I_F and I_B in both panels represent the currents measured for the same value of voltage during forwards and backward sweep, respectively.

The right panel of figure 6 shows the plot of the total current $i(t)$ as a function of probe voltage u_s averaged over several periods. This transformation leads to a Lissajous-like pattern where, in case of a single period, each value of the voltage corresponds with two total current values: the current obtained during (i) forward and (ii) backward voltage sweeps of the probe. Hence, for $n = 100$ measured periods, each value of the voltage $u_s(t)$ corresponds to $2n$ values of the current. Proper averaging enables to relate each voltage value with only 2 currents; current I_F corresponding to the forward voltage sweep and the current I_B corresponding to the backward voltage sweep, see figure 4 (right panel).

The difference between these two current values is:

$$I_F - I_B = \left[\left(\frac{du_s(t)}{dt} \right)_F - \left(\frac{du_s(t)}{dt} \right)_B \right] C_{sh}(u_s) \quad (14)$$

$C_{sh}(u_s)$ denotes a differential sheath capacity together with the rest of parasitic capacity of the probe relative to the ground. The capacity of the short coaxial cable between the RF current/voltage sensor can be included to this parasitic capacity as well. In addition, we can write following formula for the total probe current $i(t)$:

$$i(t) = i_p(t) + C_{sh} \frac{du_s(t)}{dt} \quad (15)$$

where $i_p(t)$ is the Ohmic current through the sheath which is the proper one for plasma parameters determination. The plasma sheath behaves like a nonlinear resistor shunted by a parallel capacity. Validity of equation to (14) for the probe current was discussed in [41, 45] for the probe voltage frequency below ω_{ip} and it was justified the use of $C_{sh}(u_s)$ as a function of voltage.

In case the used voltage signal is symmetric, the derivation $\frac{du_s(t)}{dt}$ for both the forward and backward sweeps results in the same value but with an opposite sign. Hence, equation (14) simplifies to:

$$I_F - I_B = 2 \left| \frac{du_s(t)}{dt} \right| C_{sh}(u_s) \quad (16)$$

Equations (16) or (14) enable to obtain the capacity $C_{sh}(u_s)$ and subsequently also the capacitive current $i_c(u_s)$. The capacitive current $i_c(u_s)$ is obtained as:

$$i_c(u_s) = \frac{du_s}{dt} C_{sh}(u_s) \quad (17)$$

The desired probe current $i_p(u_s)$ for plasma parameters calculation is then:

$$i_p(u_s) = i(u_s) - i_c(u_s) \quad (18)$$

Calculation of i_p as the function of u_s provides the single I - V characteristics, see figure 6 (right panel). Such an I - V curve represents the voltage span corresponding to the rf probe voltage amplitude. The I - V curve can be further processed in a similar manner as the Langmuir probe data [46].

The electron temperature T_e (in eV) can be determined from the first derivative of the electron current I_e at floating potential U_f in the semi-logarithmic plot:

$$T_e = \left(\frac{d(\ln I_e(U))}{dU} \right)_{U \approx U_f}^{-1} \quad (19)$$

Once the electron temperature is known, the electron density n_e can be estimated according to the Bohm criterion

$$j_{i0} = 0.61 q_e n_e \sqrt{\frac{k_B T_e}{M_i}} \tag{20}$$

where j_{i0} is ion current density $j_{i0} = \frac{I_{i0}}{A}$; here I_{i0} is the ion current at floating potential U_f obtained by extrapolation of the ion current part in the I - V curve, see figure 7, and A represents the probe area. Other quantities are: q_e elementary charge, M_i mass of Ar ions, k_B Boltzmann constant, T_e electron temperature in Kelvin, and n_e electron density. We should state here that this electron temperature T_e calculation is correct only in case of a Maxwellian distribution function for electrons. Otherwise, this method will give us only electron temperature of faster electrons with energy around floating potential and the body of the electron distribution function would not contribute significantly. The other limitation of this method is the fact that it is obtained only a small part of Langmuir probe characteristics with missing part approaching to plasma potential and electron saturation current. Generally, the presented method contains only a relatively simple hardware and can be easily implemented in industrial machines.

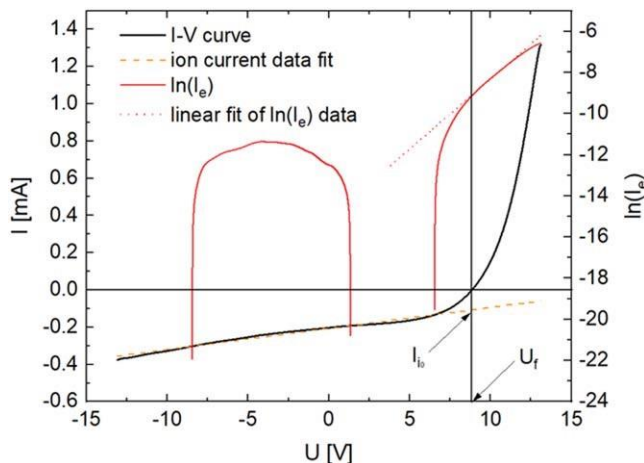


Figure 7. Processing of the obtained I - V curve by the Langmuir approach. The I - V curve is identical with the one shown in figure 4 (right panel). I_{i0} is the ion current at floating potential U_f obtained by the extrapolation of the ion current. The T_e is estimated from the first derivative of the electron current in the semi-logarithmic plot.

The method described above was verified during a conventional capacitive rf discharge in pure Ar. The discharge was investigated for different absorbed powers and pressures by the method described above and by the classical Langmuir method [46]. It is worth noting that the same planar probe, at the same experimental condition was used.

The obtained data for electron temperature T_e and ion density n_i at the edge of the sheath and the bulk plasma are shown and compared in figure 8. The most important finding is the fact that results obtained by the rf and Langmuir probe have similar qualitative trend and also somewhat correspond quantitatively with each other for both T_e and n_i . T_e measured by rf probe is about 2 eV smaller compared to Langmuir one, but still it is in reasonable agreement with previous measurements reported in [40, 47]. Similar for n_i where rf shows about 2×10^{15} smaller values (right panel). While the n_i rises with the pressure up to a certain value where it remains more or less constant, T_e exhibits the opposite trend. This trend has been already observed several times and is attributed to the number of particles in the system, their collision frequency which influences a number of ionized species as well as ionization energy losses [48].

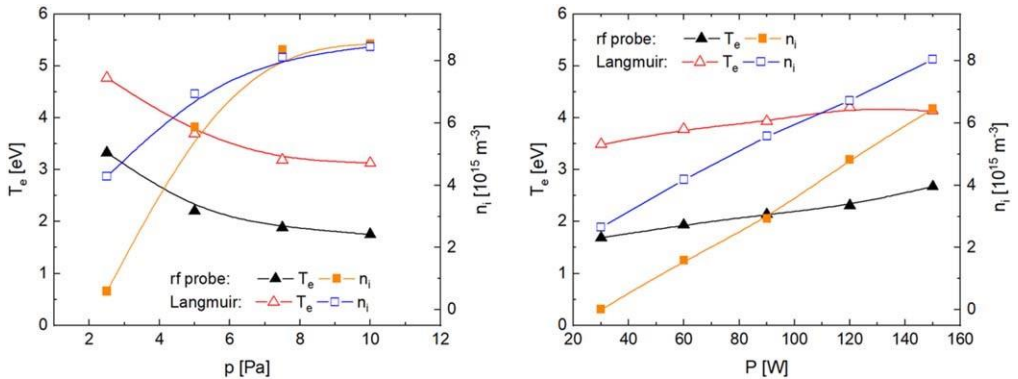


Figure 8. Comparison of plasma parameters measured by rf and Langmuir probe methods. The measurements were performed at the same condition and parameters were processed by equation (19)—electron temperature and (17)—ion density, respectively, for rf probe. The left panel shows the pressure dependence at 100 W while the right panel shows the power dependence at a constant pressure of 5 Pa.

5. PROBE DIAGNOSTICS OF HIGHLY REACTIVE DISCHARGES

Corresponding results obtained by the two different approaches (the modified rf probe versus Langmuir probe) proved the reliability of the method with the possibility to employ the rf probe in highly reactive and harsh discharges. As we already mentioned, probes driven at higher frequencies overcome the problem of the capacitive reactance of the deposited parasitic film [19, 22]. In our case, the diagnostics of rf excited Ar/C₂H₂ plasma was performed in a timeresolved mode within a total experiment time 850 s. The power delivered into the system was kept at 100 W. At first, the discharge was stabilized by operation in pure Ar for 150 s. After that, reactive C₂H₂ was added to the discharge for the next 350 s; i.e. up to time 500 s from the beginning of the experiment. After this time, $t > 500$ s, the C₂H₂ flow was switched off and only pure Ar was delivered to the chamber again. The results are shown in figure 9 where the experiment window with the reactive plasma is highlighted. Former work [40], performed at similar experimental conditions, reports the formation of dusty carbonaceous nanoparticles in the volume of C₂H₂ plasma. It is assumed that dust particles are formed in several steps; after nucleation at the initial stage, the growth is determined by absorption of neutral and charged species in the later stage. A linear dependence of the particle size d with the time is usually expected $d(t) \propto t$. Furthermore, during the growth of nanoparticles, they can be charged, preferentially negatively up to the floating potential.

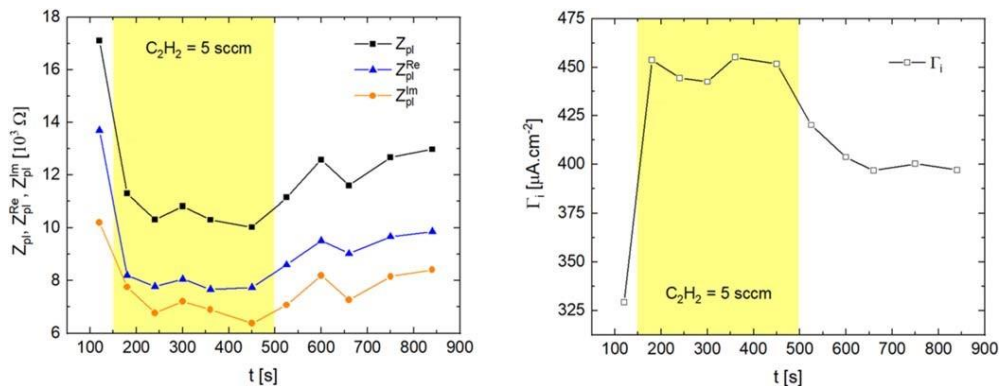


Figure 9. The time dependence of the plasma sheath impedances (left) and ion flux (right). The highlighted area represents the experimental window when C₂H₂ was delivered to the plasma.

Plasma sheath impedances Z_{pl} , Z_{pl}^{Re} , Z_{pl}^{Im} were estimated in Ar/C₂H₂ plasma, using equations (9)–(11), at first, see the left panel in figure 9. The data were obtained from measurements performed at rf probe amplitude $U_s = 12.5$ V and signal frequency 200 kHz. It is apparent that the total impedance Z_{pl} is determined by its reactance (capacitive) contribution. The same trend was also observed in pure Ar discharge where the Z_{pl}^{Im} is the main player. Furthermore, the absolute values of impedances in reactive and in pure Ar discharge are somewhat similar (≈ 18 k Ω); compare figures 5 and 9 in the process without C₂H₂ presence. C₂H₂ causes the steep fall of Z_{pl} and Z_{pl}^{Re} ; the Z_{pl}^{Im} also decreases but it is less apparent. The plasma impedances become more or less constant during the reactive discharge (of about ~ 10 k Ω) and start to rise after the reactive gas delivery has ceased. The behaviour of the ion flux Γ_i is exactly the opposite: it increases in reactive plasma by about 1/3. The effect is attributed to the formation of dust nanoparticles which can be preferentially charged by an accumulation of fast negative electrons. Since the lifetime of nanoparticles is significantly longer than the electron diffusion time and related sideward wall losses, the increased volume charge decreasing the plasma impedance. However, the nanoparticle existence in the discharge volume is also influenced by their mass; after a certain time the nanoparticles are large and expelled out of the plasma volume, for example by ion and neutral drag forces.

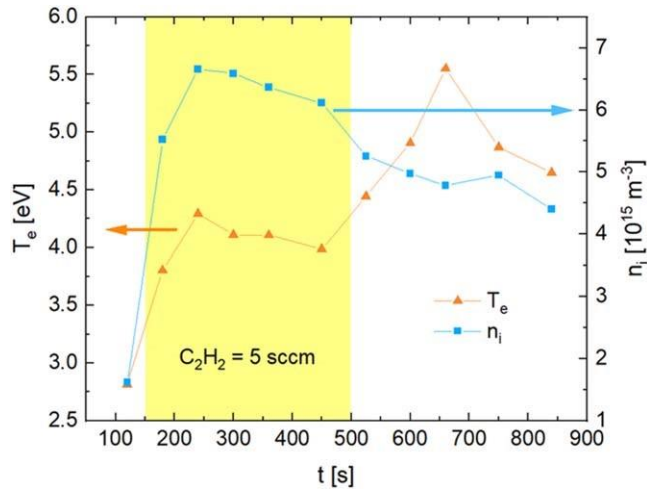


Figure 10. Time evolution of electron temperature T_e and ion density n_i . Quasineutrality $n_i \approx n_e$ was assumed.

The electron temperature T_e and the ion density n_i , respectively the electron density n_e assuming plasma electrical quasineutrality $n_i \approx n_e$, were obtained from equations (19) and (20). These parameters were measured by the described rf probe with the signal frequency 200 kHz. The electron density enhances, being multiplied nearly by factor 2, in reactive acetylene discharge. The growth of electron density has the same trend as the electron temperature; enhanced T_e results in dissociative and ionization collision processes. It seems that the electron density culminates rather soon after the C_2H_2 delivery and starts to decrease. This can be explained by the nanoparticle formation, their negative charging and the reduced density of free electrons in the volume. This $n_i(t)$ behavior corresponds well with the $\Gamma_i(t)$; compare figures 9 and 10. However, after the C_2H_2 gas pulse, we observe the contrary behavior of $T_e(t > 500 \text{ s})$ versus $n_i(t > 500 \text{ s})$. The density falls while the temperature rises. This mechanism has not been fully understood yet but it indicates a strong relation with (i) the carbonaceous dust and/ or (ii) long-live Ar metastables.

6. CONCLUSION

A modified Sobolewski rf probe method for diagnostic of internal plasma parameters is proposed. The main approach is based on the assumption that each period of the measured rf signal acts as a forward and backward part of the $I-V$ curve during Langmuir probe measurements. The transformation of total probe current $i(t)$, measured as a function of rf probe voltage u_s , results in a Lissajous-like pattern from which the $I-V$ characteristics can be obtained by the tailored data processing. The obtained $I-V$ can be processed in a similar way to Langmuir probe theory. Hence, besides the plasma impedance and the ion flux, the parameters typically obtained from Sobolewski probe, the plasma density and electron temperature can be measured as well. On the other hand, the method measures only electron temperature of faster electrons with an energy around the floating potential and requires the existence of a Maxwellian distribution function for determination of the electron temperature.

The method was verified by measurement in a pure Ar discharge. Satisfactory agreement was observed between the results obtained from the slow classical Langmuir and modified rf probe. After that, the rf probe was successfully

employed for diagnostics in highly reactive acetylene Ar/C₂H₂ plasma. The rf probe provides reasonable results indicating wide versatility of proposed rf probe approach for in-time and in situ monitoring of reactive discharges.

Acknowledgments

This work was financially supported by the project GACR 1920168S by Czech Science Foundation, by project MPO TRIO II no. FV20580 and by the Operational Programme Research, Development and Education financed by European Structural and Investment Funds and the Czech Ministry of Education, Youth and Sports, partner network CZ.02.1.01/0.0/0.0/17 049/0008422.

References

- [1] Rath J K 2003 *Solar Energy Mater. Solar Cells* 76 431–87
- [2] Guerrero de Leon J A et al. 2018 *Mater. Res. Express* 5 066417
- [3] Gudmundsson J T et al. 2012 *J. Vac. Sci. Technol. A* 30 030801
- [4] Colligon J S 1995 *J. Vac. Sci. Technol. A* 13 1649–57
- [5] Rossnagel S M and Cuomo J J 1988 *Vacuum* 38 73–81
- [6] Patenge N et al. 2012 *Biofouling* 28 267
- [7] Rooth J R 2001 *Industrial Plasma Engineering I and II* (Bristol: IOP Publishing Ltd)
- [8] Mattox D M 2010 *Handbook of Physical Vapor Deposition Processing* (Oxford: Elsevier)
- [9] Shul R J and Pearton S J 2000 *Handbook of Advanced Plasma Processing Techniques* (New York, Berlin Heidelberg: Springer-Verlag, GmbH)
- [10] Marcus R K 1993 *Glow Discharge Spectroscopies* (New York: Springer Science+Business Media, LLC)
- [11] Lapke M, Mussenbrock T and Brinkmann R P 2008 *Appl. Phys. Lett.* 93 051502
- [12] Thomas T L and Battle E L 1970 *J. Appl. Phys.* 41 3428
- [13] Han S M and Aydil E S 1996 *Thin Solid Films* 290 427–34 [14] Bose S, Kaur M and Chattopadhyay P K 2017 *J. Plasma Phys.* 83 615830201
- [15] Szuszczewicz E P and Holmes J C 1975 *J. Appl. Phys.* 46 5134–9
- [16] Bilik N et al. 2015 *J. Phys. D: Appl. Phys.* 48 105204
- [17] Klindworth M, Arp O and Piel A 2007 *Rev. Sci. Instrum.* 78 033502
- [18] Annaratone B M, Jacob W and Arnas C 2009 *IEEE Trans. Plasma Sci.* 37 270–80
- [19] Braithwaite N S J, Booth J P and Cunge G 1996 *Plasma Sources Sci. Technol.* 5 677

- [20] Braithwaite N S J, Sheridan T E and Boswell R W 2003 *J. Phys. D: Appl. Phys.* 36 2837–44
- [21] Darnon M, Cunge G and Braithwaite N J 2014 *Plasma Sources Sci. Technol.* 23 025002
- [22] Sobolewski M A 1998 *Appl. Phys. Lett.* 72 1146–8 [23] Sobolewski M A 2001 *J. Appl. Phys.* 90 2660
- [24] Lundin D, Cada M and Hubicka Z 2016 *J. Vac. Sci. Technol. A* 34 041305
- [25] Braithwaite N S J 1997 *Plasma Sources Sci. Technol.* 6 133–9 [26] Sobolewski M A J 1992 *Vac. Sci. Technol. A* 10 3550
- [27] Sobolewski M A and Lahr D L 2012 *J. Vac. Sci. Technol. A* 30 051303
- [28] Gahan D and Hopkins M B 2005 *Rev. Sci. Instrum.* 76 106107
- [29] Gahan D and Hopkins M B 2007 *Rev. Sci. Instrum.* 78 016102 [30] Sobolewski M A 1995 *J. Res. Natl Inst. Stand. Technol.* 100 341
- [31] Thompson B E and Jaiprakash V C 1993 *Plasma Sources Sci. Technol.* 2 112–8
- [32] Thompson E, Utagir A and Avona P 1991 *J. Vac. Sci. Technol. A* 9 675
- [33] van Roosmalen A J 1983 *Appl. Phys. Lett.* 42 416 [34] Raufa S and Kushner M J 1998 *Appl. Phys. Lett.* 73 2730 [35] Henault M, Wattieaux G, Lecas T, Renouard J P and Boufendi L 2016 *Phys. Plasmas* 23 023504
- [36] Bakker L P, Kroesen G M W and de Hoog F J 1999 *IEEE Trans. Plasma Sci.* 27 759
- [37] Chiodini G, Riccardi C and Fontanesi M 1999 *Rev. Sci. Instrum.* 70 2681–8
- [38] Giannone L, Balbín R, Niedermeyer H, Endler M, Herre G, Hidalgo C, Rudyj A, Theimer G, Verplanke P and the W7AS Team 1994 *Phys. Plasmas* 1 3614–21
- [39] Skoutnev V, Dourbal P, Rodríguez E and Raitses Y 2018 *Rev. Sci. Instrum.* 89 123501
- [40] Sushkov V, Herrendorf A and Hippler R 2016 *J. Phys. D: Appl. Phys.* 49 425201
- [41] Sobolewski M A 1999 *Phys. Rev. E* 59 1059–72
- [42] Virostko P et al. 2008 *AIP Conf. Proc.* 993 427
- [43] Sprott J 1968 *Rev. Sci. Instrum.* 39 1569 [44] Müller H, Adamek J, Horacek J, Ionita C, Mehlmann F, Rohde V, Schrittwieser R and ASDEX Upgrade Team 2010 *Contrib. Plasma Phys.* 50 847–53
- [45] Crawford F W and Grard R 1966 *J. Appl. Phys.* 37 180
- [46] Hippler R, Pfau S, Schmidt M and Schoenbach K H 2001 *Low Temperature Plasma Physics: Fundamental Aspects and Applications* (Berlin: Wiley-VCH)

- [47] Ussenov Y A, von Wahl E, Marvi Z, Ramazanov T S and Kersten H 2019
Vacuum 166 15–25
- [48] Stranak V et al. 2014 J. Appl. Phys. 115 153301

A4. Electrochemical performance of indium-tin-oxide-coated lossy-mode resonance optical fiber sensor

Paweł Niedziałkowski, Wioleta Białobrzaska, Dariusz Burnat, Petr Sezemsky, Vitezslav Stranak, Harm Wulff, Tadeusz Ossowski, Robert Bogdanowicz, Marcin Koba, Mateusz Smietana, Electrochemical performance of indium-tin-oxide-coated lossy-mode resonance optical fiber sensor, Sensors and Actuators B: Chemical 301, (2019), 127043.

Republished with permission of Elsevier Science & Technology Journals; permission conveyed through Copyright Clearance Center, Inc.

Abstract

Analysis of liquids performed in multiple domain, e.g., optical and electrochemical (EC), has recently focus significant attention. Our previous works have shown that a simple device based on indium-tin-oxide (ITO) coated optical fiber core may be used for optical monitoring of EC processes. At satisfying optical properties and thickness of ITO a lossy-mode resonance (LMR) effect can be obtained and used for monitoring of optical properties of an analyte in proximity of the ITO surface. However, EC response of the ITO-LMR device to a redox probe has not been achieved for ITO-LMR sensor whereas it is generally observed for commercially available ITO electrodes. The changes in the response to a redox probe are typically used as a sensing parameter when EC label-free sensing is considered, so it is crucial for further development of combined LMR-EC sensing concept. In this work, we focus on enhancing the EC activity of the device by tuning ITO magnetron sputtering deposition parameters. Influence of the deposition pressure on the ITO properties has been the main consideration. Both optical and EC readouts in 0.1 M KCl containing such redox probes as 1 mM of $K_3[Fe(CN)_6]$ or 1 mM 1,1'-Ferrocenedimethanol were discussed at different scan rate. The performed studies confirm that for optimized ITO properties the ITO-LMR sensor used as the EC electrode may also show excellent EC performance. The observed EC processes are quasi-reversible and diffusion-controlled. Moreover, for the devices, which offer improved EC response, an optical monitoring of the EC process is also possible. According to our best knowledge, fully functional combined optical and EC sensor, where optical effect is resonance-based and other than well-known surface plasmon resonance, is presented for the first time.

1. INTRODUCTION

Novel spectroelectrochemical sensing systems focus significant attention due to their enhanced, comparing to solely electrochemical (EC) or optical systems, sensitivity to physical, chemical, and biological interactions at micro and nanoscale [1]. When using label-free sensing mechanism, these systems are universal, i.e., detected target depends on sensor functionalization, and thus may find many applications in health, security and environmental analysis [2]. Moreover, the approach allows for investigating process kinetics at molecular level without affecting functionality of the analyzed target [3].

The cross-correlation of data achieved simultaneously from EC and optical readout allows for obtaining unique synergy in sensing devices. Up to date several dual-domain optical and EC systems have been reported. For majority of the systems optical data is represented as absorption spectrum of the analyte at a transparent EC electrode. When interactions at the electrode surface are of interest the systems are typically based on surface plasmon resonance (SPR) effect [4] achieved in different planar [5] or optical-fiber-based [6] sensing configuration, where thin gold film is simultaneously used for optical sensing and as an EC electrode. Some other electrically conductive materials can be also used as an electrode, such as different electrically conductive carbon-based materials [7], including boron-doped diamond [8], as well as platinum [9] or silicon [1], but their deposition is often very demanding and expensive. On top of the technological issues, these materials do not satisfy SPR conditions and thus other optical sensing phenomena need to be employed [5].

When thin film is optically transparent, conditions for obtaining lossy-mode resonance (LMR) can be satisfied and it can be applied for sensing in the optical domain [10]. Sensors based on LMR effect were reported for detection of changes in external refractive index (RI) and based on them an optical detection of e.g., organic compound [11], humidity [12] or biomolecules [13] was presented. For obtaining LMR it is required to satisfy certain conditions between electrical permittivity of a substrate, the thin film, and an external medium [14]. A variety of thin films can be applied for achieving LMR. They include polymers [2], diamond-like carbon [15], as well as various metal oxides and nitrides [16, 17]. When on top of LMR satisfying optical properties also high electrical conductivity is required, as it is the case for combined

optical and EC measurements, indium-tin-oxide (ITO) thin films may be considered as a choice for LMR-supporting material [18]. ITO deposition can be relatively inexpensive when done by magnetron sputtering, both in direct current (DC) [19] or radio frequency (RF) [20] configuration, chemical vapor deposition [21], spray pyrolysis [22] and/or other methods involving wet chemistry. A series of optical sensors employing ITO has already been reported. ITO thin film is typically applied as a transparent electrode, where no response to redox probe is required [23]. When EC activity was expected from ITO films working as an electrode on optical fibers, they showed relatively poor response to redox probes [10, 24-27]. Reported up to date ITO films deposited on optical fibers showed narrow bandgap. This resulted in weak or lack of EC response to standard redox probes. To enhance the EC response, the surface of ITO requires post-processing, including typically applied high-temperature annealing, which in turn may damage optical fiber sensors [28].

In our previous works we have shown that ITO-coated optical fiber can be used for LMR-based optical monitoring of EC processes through tracking of changes in optical properties of both ITO and its surrounding medium [18, 29]. These films were prepared by Reactive High Power Impulse Magnetron Sputtering deposition [18]. Low level of ITO crystallinity is most probably the reason why these ITO-coated optical fiber devices have not manifested standard response to redox probes, which is required when label-free sensing concept is considered, in a way as is in case of commercially available flat ITO electrodes. It has already been shown in our earlier work [33] that the film crystallinity has significant influence on ITO properties. These results motivated us to improve the experimental setup, optimize the deposition geometry and better control the deposition conditions [25, 43]. Hence, in this work we report investigation performed on ITO-coated optical fibers coated by a novel deposition approach using only one RF sputtering gun operating in broad pressure range. As an output, we achieved simultaneous LMR readout and standard response to redox probe at the ITO-coated optical fiber for the first time. The EC processes in 0.1 M KCl solvent containing such redox probes as 1 mM of $K_3[Fe(CN)_6]$ or 1 mM 1,1'-Ferrocenedimethanol were quasi-reversible and diffusion-controlled. The performed studies reveal that for optimized ITO coating at the ITO-LMR sensor the EC performance can be

comparable to those for other EC electrode materials, such as glassy carbon or gold. Optical sensor with simultaneous EC interrogation based on resonance effect other than SPR is shown for the first time.

2. MATERIALS AND METHODS

2.1. ITO-LMR sensor fabrication

The LMR structures were fabricated using approx. 15 cm long polymer-clad silica optical fiber of 400/730 μm core/cladding diameter, where 2.5 cm length of polymer cladding was removed from the fiber central section [18]. Next, the electrically conductive and optically transparent ITO films were deposited by RF magnetron sputtering of 3" ITO target ($\text{In}_2\text{O}_3\text{-SnO}_2$ - 90/10 wt% and purity of 99.99%) in a vacuum chamber with base pressure 2×10^{-5} Pa. The magnetron was fed by RF power of 150 W at frequency 13.56 MHz, delivered by COMET Cito 1310 supply. The fiber structures were coated in Ar atmosphere with purity 99.999% to avoid contamination of the deposition process. The fibers were located about 20 cm away from the sputtered target as shown in Fig. 1 and they were rotated with angular speed of 4 rpm. In this work the pressure (p) was chosen as a variable parameter of the deposition process and it varied from 0.05 Pa to 1 Pa. The p was set at Ar mass flow controller from 12 to 100 sccm for the lowest and the highest p , respectively. Reference Si wafers were also coated with ITO in the same deposition conditions and used for further measurements.

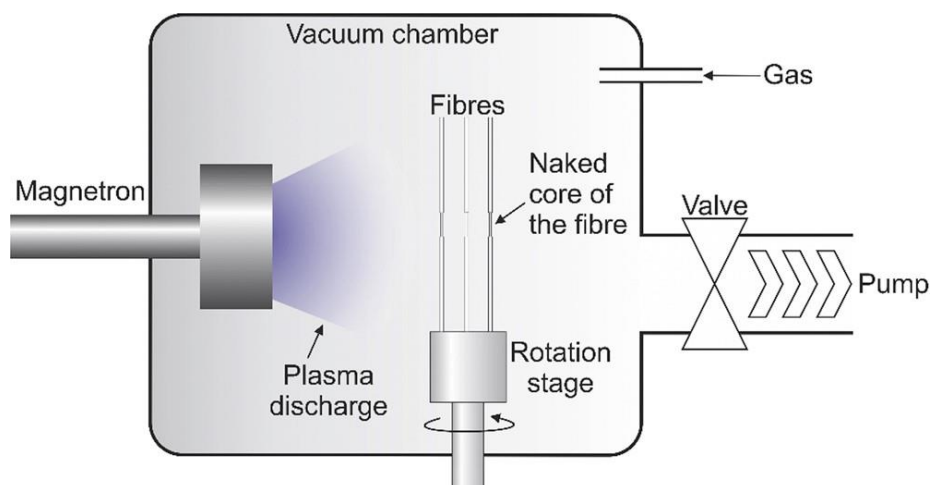


Fig. 1. Simplified scheme of the magnetron sputtering deposition system used in this experiment.

2.2. Thin ITO film measurements

The ITO films were characterized by grazing incidence X-ray diffractometry (GIXD) analysing line position, intensity, and line profile of the observed Bragg reflections. The employed methods have been described elsewhere [30]. We used a D8 ADVANCE diffractometer (Bruker AXS, USA) and Cu K α radiation (40 kV, 40 mA). The scanned 2θ range was from 20° to 80° at an incidence angle $\omega = 0.5^\circ$.

Optical properties, i.e., RI (n) and extinction coefficient (k) of the ITO films deposited on reference Si wafers were measured with Jobin Yvon UVISEL spectroscopic ellipsometer (Horiba, France) according to the procedure described in [31].

The deposition rate was estimated as $a_d = d/t$, where d is the film thickness measured by a profilometry and t denotes the deposition time. NexView NX2 profilometer (Zygo, USA) was used for measurement of the step achieved by a mechanical mask installed on the substrate before the deposition. Furthermore, the d was also estimated from the cross-sectional Scanning Electron Microscope (SEM, Ultra-high Resolution S-4800, Hitachi) image of cleaved ITO-coated fiber.

Electrical resistivity (ρ) was measured at a room temperature using 4-point probe with in-line and equal interspacing ($s = 1.5$ mm) probes. Probes with a radius of $100\ \mu\text{m}$ were used. A current source (Keithley 2400, UK) was applied to external probes while voltage was measured at internal probes. The current was gradually increased up to 100 mA with a step of 1 mA. ITO-coated samples 1×1 cm in size were investigated. Due to finite sample size the correction factor of 0.86 was taken into account for ρ estimation [32]. Each sample was measured 10 times at four various surface points and averaged ρ was calculated.

2.3. Optical ITO-LMR sensor measurements

Both the fiber sample end-faces were mechanically polished before optical testing. Next, the ITO-based optical fiber was mounted in a dedicated setup containing Ocean Optics HL-2000 white light source and Ocean Optics USB4000 spectrometer, and investigated in a wavelength range of

345–1040 nm [18]. The sensitivity of prepared device to external RI was determined using water/glycerin solutions with $n_D = 1.33$ – 1.45 RIU. Reichert AR200 refractometer was used to measure the RI of the solutions. The optical transmission (T) was recorded as counts within a specified integration time (up to 100 ms).

2.4. Electrochemical ITO-LMR sensor measurements

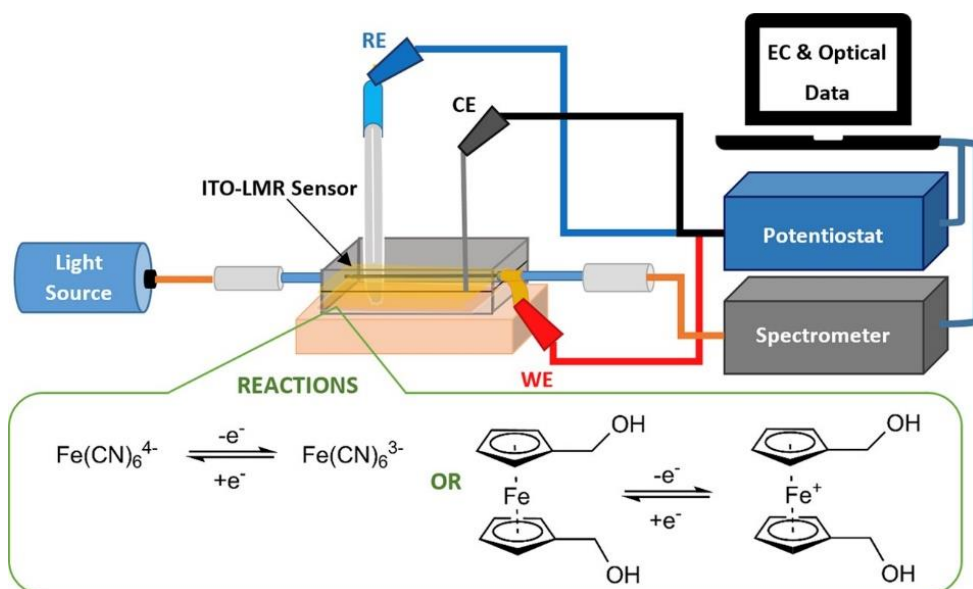


Fig. 2. Schematic representation of combined optical and EC measurement setup where ITO-LMR sensor was used as a working electrode (WE). Chemical reactions for the two redox probes analyzed with the system are also given.

All the voltammetric measurements were performed with a potentiostat PalmSens Emstat3+ equipped with a PStTrace 5.4 software (PalmSens BV, The Netherlands) and using a custom-made cell supported by a three-electrode system at room temperature (Fig. 2). The ITO-LMR sensor, an Ag/AgCl 0.1 M NaCl and a platinum wire were used as a working (WE), reference (RE) and counter electrode (CE), respectively. In the cell the ITO-LMR sensor was placed between two silicone gasket in a way that the active part of the fiber was in the solution and the electrical connection to the potentiostat was maintained by conductive copper adhesive tape. This tape was placed between two silicone gasket to keep the contact with ITO, but had no electrical contact with the test solution. Next, the tape was connected outside the cell using a crocodile clip and in this way the ITO-coated fiber was used as the WE. The

cyclic voltammograms (CVs) were recorded at a various scan rate from 10 mV/s to 500 mV/s. All the measurements were carried in 0.1 M potassium chloride (KCl) solutions containing 1 mM potassium ferrocyanide ($K_3[Fe(CN)_6]$) or 1 mM 1,1'-Ferrocenedimethanol as redox probes. All reagents were analytical grade and used without further purification. $K_3[Fe(CN)_6]$ and KCl were purchased from POCh, Poland while 1,1'-Ferrocenedimethanol was purchased from Acros Organics. The ultrapure water was used in all of the experiments.

3. RESULTS AND DISCUSSION

3.1. Properties of ITO

Plasma-based deposition methods, which include magnetron sputtering, enable to tailor properties of ITO films up to requirements of their applications. The film properties can be attributed to the film crystallographic structure that is determined by the energy delivered to the growing film [33]. In this study both optical and electrical/EC properties of the films must be satisfied. The p was used as a variable parameter tuned between 0.05 and 1.0 Pa. This parameter can be easily fixed during the deposition process and it enables the control of the energy flux to the deposition process by changing the collision rates between particles [34]. In other words, by increasing p the mean free path of particles reduces causing energy depletion by elastic or inelastic collisions. The mean free path at pressure 0.05 Pa is in order of tens of centimeters and is comparable to the distance between the target surface and the substrate. At these conditions the number of collisions in the plasma can be neglected and particles impinging onto the substrate have the Thompson distribution [35]. As reported elsewhere [36], at low pressure RF discharges the energy of sputtered species impinging the substrate can reach 30–40 eV. Such energy delivered by deposited species is significantly higher than reported activation energy for crystallization of ITO (1.3 eV) [37].

XRD patterns shown in Fig. 3 reveal well-crystalline In_2O_3/SnO_2 film with preferential orientation (h00). For deposition at lower p the domain size reaches 19 nm and the lattice constant is 1.01844 nm. The XRD patterns vanish with increasing p what corresponds to decrease of both the domain sizes and the lattice constant. In other words, the films deposited at higher p become polycrystalline and transform towards amorphous. This effect stays in

agreement with zone diagrams proposed in [38, 39]. The transition between crystalline, polycrystalline and amorphous structure is rather fast with an edge between $p = 0.2$ and 0.3 Pa. Above this edge no XRD patterns were observed at all, what indicated amorphous structure of the ITO film.

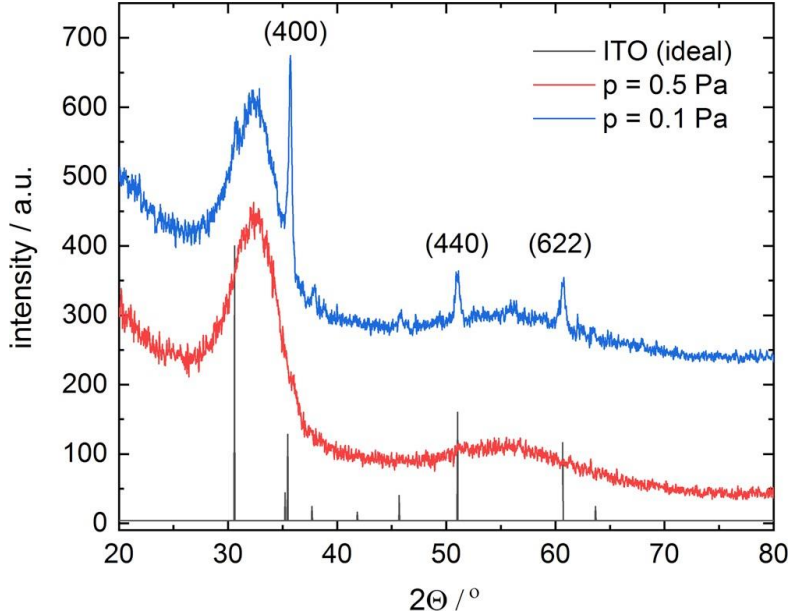


Fig. 3. XRD patterns of ITO deposited at $p = 0.1$ Pa and 0.5 Pa. A theoretical, reference pattern for ITO is shown for comparison.

Table 1. Deposition rates and resistivity of ITO films deposited on reference Si wafers at various p tuned in range from 0.05 to 1 Pa.

p [Pa]	0.05	0.1	0.5	1
t [min]	50	55	60	65
d [nm]	282 ± 18	271 ± 13	258 ± 14	229 ± 11
a_d [nm min ⁻¹]	5.6	4.9	4.3	3.52
ρ [mΩ·cm]	1.02 ± 0.04	1.50 ± 0.1	4.72 ± 0.14	146.87 ± 2.01

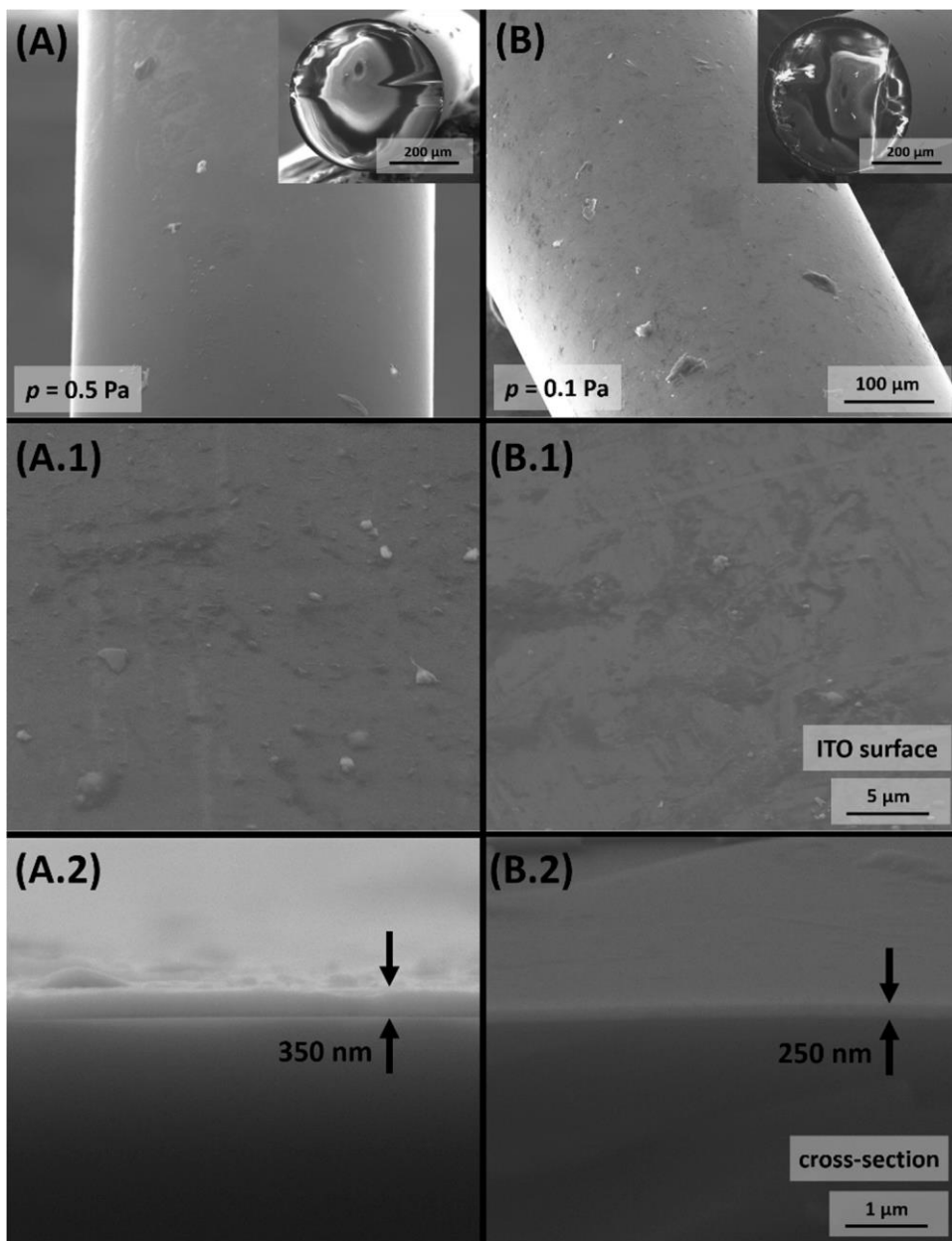


Fig. 4. The SEM images of ITO deposited on optical fiber at $p = 0.5$ Pa (A) and $p = 0.1$ Pa (B). (X.1– side view; X.2- cross-section).

Improvement of film crystallinity is followed by improvement of its electrical properties. As shown in Table 1 a decrease in p results in significant drop of ρ . Higher ρ is caused by reduced crystal size [40]. Larger crystals in the film minimize scattering of charge carriers (electrons in this case) at grain boundaries, impurities, or lattice dislocations, and thus the electrical

conductivity is improved. It is worth noting that the ITO thin films were prepared without any post-deposition treatment nor thermal annealing. It is questionable whether the additional treatment may further improve crystallinity and film properties. No additional treatment has been performed due to rather low tolerable thermal load of the fibers used later as a substrate. As an alternative, deposition techniques with high energy of sputtered species can be employed [41].

On top of electrical properties, also d of the film influences both optical as well as EC response. Here, d was estimated by: (i) profilometry measurements on Si substrates as shown above in Table 1, and (ii) by the cross-section SEM images of the ITO-coated fibers (Fig. 4). It should be noted that some film properties can be measured using planar samples only, while the other by investigating the fibers. Hence, to keep d constant on reference samples in the range of 250–300 nm for different p , t varied from 50 to 65 min. Beside the d , also a_d and ρ are shown in the Table 1 together with corresponding p and t .

It is obvious that a_d significantly decreases with p , what is caused by increase in number of elastic collisions between the particles and shortening of the mean free path. Hence, not only crystallography, but also the a_d is influenced by the p . Fig. 4 presents estimated d of ITO on optical fibers for $p = 0.1$ and 0.5 Pa, where the deposition time was 60 and 120 min-long, respectively. In both cases coating distribution around the fiber is homogeneous due to constant fiber axial rotation during the deposition. The cross-sections of both ITO-coated fibers also show low roughness and high uniformity of the film with nanocrystalline structure as revealed by XRD. Also, on fibers d changes significantly with p . The d on the fiber reaches 250 and 350 nm for 0.1 Pa and 0.5 Pa, respectively (Fig. 4A.2 and B.2). In other words, d increases with p which is contradictory to the trend observed for the planar samples (Table 1). For the $p = 0.1$ Pa the a_d on fiber is approx. half of that on reference Si wafers. For $p = 0.5$ Pa, the a_d on fiber is, in turn, approx. 30% higher than that on Si wafers. We may attribute these differences to particle transport mechanism in discharges at both the p and shape of the coated substrates. The mean free path is shortened to millimeters at 0.5 Pa and the diffusive character of the particle motion prevails. This enables also the back-side deposition which seems to be more dominant for cylindrical shaped substrates (the fibers) than for the planar ones (Si substrates). For $p = 0.1$ Pa the diffusion process is

very limited and both planar substrates as well as fibers are faced only to straight-coming particles. The fibers surfaces are smaller and in the same way exposed to deposition during rotation what limits the a_d . In this discussion we neglect influence of substrate properties (Si and fused silica glass) on the a_d . According to our previous experiments, ITO films deposited simultaneously with no rotation on different inert and solid substrates such as Si and fused silica glass, do not show differences in properties for sufficiently thick films, i.e. $d > 100$ nm. The intensity of the XRD patterns differs in range of a few per-cent as well as thickness measured by profilometry.

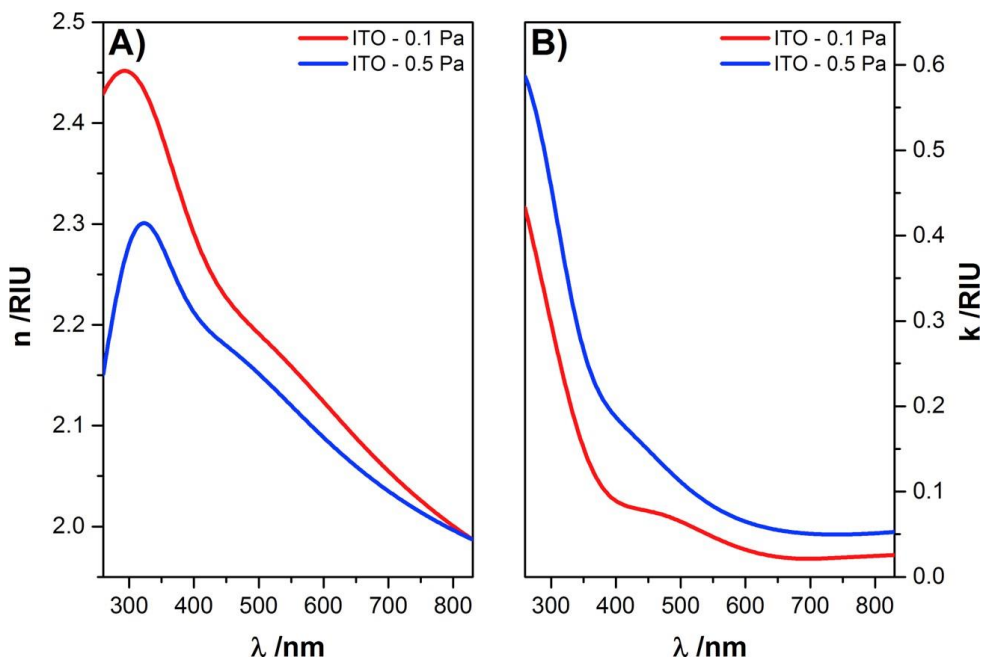


Fig. 5. Optical properties, i.e., n (A) and k (B) of ITO deposited on reference Si wafers at $p = 0.1$ Pa and 0.5 Pa with deposition time as given in Table 1.

The curves of n and k of ITO films deposited on reference Si wafers at p where the crystallographic structure changes the most, i.e., $p = 0.1$ and 0.5 Pa, are shown in Fig. 5. The plots show that when p is lower n and k on the films increases and decreases, respectively. Higher n corresponds to higher density achieved by improved crystallinity, while lower k indicates lower absorption. Increase in n and decrease in k is often observed for ITO that underwent post-annealing [42]. However, it must be noted that both n and k of ITO film, as well as its thickness determine LMR conditions what is shown in next section.

3.2. Optical analysis of ITO-LMR sensor

Due to different a_d and optical properties of the films, to satisfy LMR conditions at each p the t had to be set differently too. The LMR for $p = 0.5$ Pa could be well seen for $t = 60$ min (Fig. 6A). However, when the p has been reduced to 0.1 Pa the t had to be extended up to 120 min in order to observe the LMR effect (Fig. 6B). The LMR was obtained in either case, however the attenuation at the resonance wavelength is distinctly higher for the sensor, where the ITO thin film was deposited at higher p . It is mainly induced by differences in the k – Fig. 4B. An increase in k results in deeper LMR [14]. For $p = 0.1$ Pa the LMR is shallow, but still distinguishable when external RI changes. However, as already reported in [18, 25, 43] the sensors obtained at $p = 0.5$ Pa or higher did not show well-pronounced and characteristic for commercial ITO substrates redox response when investigated in the EC setup. That is why the EC response of ITO-LMR sensor when p has been reduces to 0.1 Pa is discussed in detail in Section 3.3.

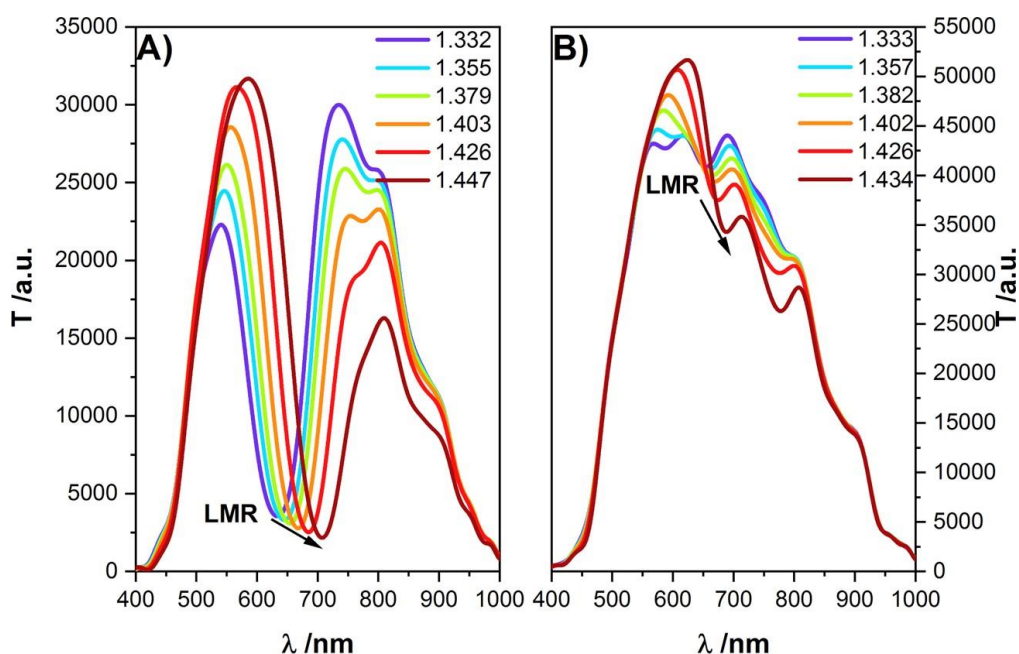


Fig. 6. Spectral response of the ITO-LMR sensor to RI for ITO deposition at (A) $p = 0.5$ Pa, and (B) $p = 0.1$ Pa with t reaching 60 and 120 min, respectively. Integration time of spectrometer was set to 50 ms and 5 ms for (A) and (B), respectively.

3.3. EC and optical analysis of ITO-LMR sensor

Since EC response to redox probe of ITO-LMR sensor with ITO deposited at higher p was not satisfactory [18, 43], here we have tailored parameters of the sputtering process focusing on the EC reaction of the sensors. Decrease of p down to 0.1 Pa revealed considerably improved crystallinity in XRD of as-deposited ITO surfaces and allowed to avoid typically applied thermal annealing post-processing. EC performance of the ITO coated optical sensors was explored using 0.1 M KCl based solvent with two redox probes, i.e., 1 mM $[\text{Fe}(\text{CN})_6]^{3-/4-}$ and 1 mM 1,1'-Ferrocenedimethanol, which are negatively [44] and neutrally [45] charged, respectively. The probes were applied for deeper understanding of ITO surface - solvent charge mediation. Both undergo one electron reversible oxidation and are highly soluble in water what meets conditions of biosensing experiments.

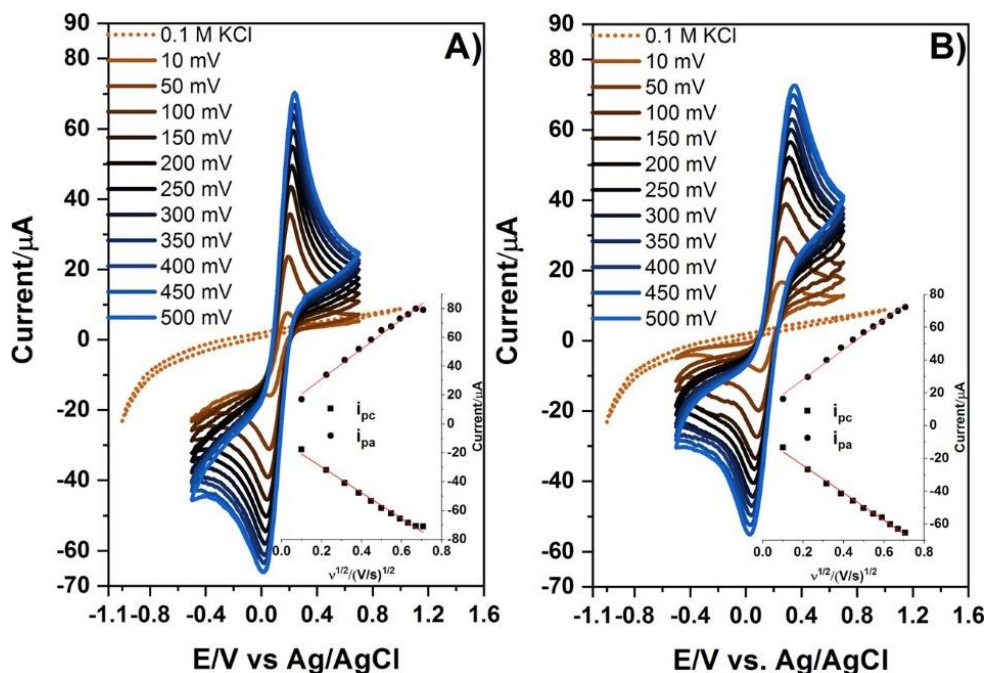


Fig. 7. EC response recorded with ITO-LMR sensor in 0.1 M KCl containing redox probes (A) 1 mM $[\text{Fe}(\text{CN})_6]^{3-/4-}$ and (B) 1 mM 1,1'-Ferrocenedimethanol at scan rate 10 to 500 mVs^{-1} . Response in 0.1 M KCl has been shown for comparison. Insets show relations between i_{pa} and i_{pc} peak currents versus the square root of the scan rates.

The CVs were recorded at the scan rates from 10 to 500 mVs^{-1} , and based on them for both the redox probes the following parameters were estimated:

formal reduction potential (E°), the peak potentials for the cathodic (E_{pc}) and anodic (E_{pa}) processes, potential peak splitting ($\Delta E_p = E_{pa} - E_{pc}$), and diffusion coefficients (D). In Fig. 7 the effect of scan rate on the EC response is shown, the current peaks shifts are given in the insets. The potential window curves studied in 0.1 M KCl (dotted line) were shown for comparison. The windows extend from +1 down to -1 V revealing low background currents. The ΔE_p increases from 140 to 300 mV for the investigated scan rates and for lower scan rates is slightly higher for 1,1'-Ferrocenedimethanol than for $[\text{Fe}(\text{CN})_6]^{3-/4-}$. On the other hand, for higher scan rates the ΔE_p is lower for $[\text{Fe}(\text{CN})_6]^{3-/4-}$. Such an effect was also observed by Branch et al. for non-annealed sputtered ITO electrode [46].

In the case of quasi-reversibility, the rate of electron transfer becomes comparable to the mass transport rate. Taking into account the interaction between the electrode and the solution, it can be assumed that diffusion is the most significant mass transport process in the movement of material above migration, and convection contributions can be neglected [38, 47]. This fact can be attributed to larger mass of the redox probe molecule. Nevertheless, recorded values of ΔE_p are much greater than ~ 60 mV, which is reached for an ideal diffusion controlled reversible redox reaction at ITO substrate. The difference may result from other EC side reactions as revealed by Martínez et al. [48]. Conversion of electron transfer from reversible to heterogeneous quasi-reversible mechanism can be attributed to weak crystallinity of ITO and possible non-stoichiometric composition of sputtered electrodes as suggested by Popovich et al. [49]. The insets in Fig. 7 illustrate cathodic (i_{pc}) and anodic (i_{pa}) peak currents increasing with the scan rate. Thus, the $E_{1/2}$ potential at which the half current is recorded, increases at higher rates. In summary, ITO-coated optical probe electrodes reveal ΔE_p and current peaks shifts which can correspond to twice slower charge transfer processes induced by some charge blocking regions or surface energy barrier requiring larger potentials for tunneling [48].

For further studies and comparisons, peak shifts of i_{pc} and i_{pa} recorded in $[\text{Fe}(\text{CN})_6]^{3-/4-}$ were approximated by Eq. (1), where correlation coefficient of 0.986 was reached for both the currents. The linear fit was also derived for i_{pc} and i_{pa} obtained in ferrocenedimethanol expressed by Eq. (2), where correlation coefficient reached 0.991 and 0.994 for i_{pa} and i_{pc} , respectively.

$$i_{pa} [\mu A] = 104.17 v^{1/2} + 10.23 \text{ and } i_{pc} [\mu A] = -89.44 v^{1/2} - 11.89 \quad (1)$$

$$i_{pa} [\mu A] = 91.04 v^{1/2} + 9.92 \text{ and } i_{pc} [\mu A] = -83.29 v^{1/2} - 7.67 \quad (2)$$

High correlation coefficients indicate clearly that the studied EC processes are diffusion-controlled. The rate of diffusion is controlled by the concentration gradient, while the electroactive electrode area can be estimated for quasi-reversible mechanisms based on Eq. (3), where A_{eff} is an electrode area, D is a diffusion coefficient, n is a number of electrons, C is a concentration of redox probe, and v is a scan rate.

$$i_{pa} = (2.69 \times 105)A_{\text{eff}}D^{1/2}n^{3/2}Cv^{1/2} \quad (3)$$

For the case shown in Fig. 7A the i_{pa} and i_{pc} result from the ferricyanide $[\text{Fe}(\text{CN})_6]^{3-}$ and ferrocyanide $[\text{Fe}(\text{CN})_6]^{4-}$ undergoing reduction and oxidation reactions, respectively [50]. The magnitude of the voltammetric current observed for the electrode is proportional to the applied voltammetric scan rate. Different D for potassium ferricyanide ($7.6 \times 10^{-6} \text{ cm}^2\text{s}^{-1}$) and potassium ferrocyanide ($6.3 \times 10^{-6} \text{ cm}^2\text{s}^{-1}$) in 0.1 M KCl [51, 52], were used for determination of the electroactive surface area of the ITO-LMR sensor. Considering both the EC process and active area of the sensor, the electroactive area of studied electrode is smaller by factor of 2.23 and 2.37 than calculated geometrical surface area for oxidation and reduction reaction, respectively. Using the same approach and assuming D for 1,1'-Ferrocenedimethanol reaching $6.4 \times 10^{-6} \text{ cm}^2\text{s}^{-1}$ [45, 53, 54], the factors reach 2.3 and 2.5 of the geometric surface area for oxidation and reduction reaction, respectively. These results indicate that EC process in both the redox probes employ comparable electroactive surface area. Effect of twice lower electroactive than geometrical area can be attributed to local drops of conductivity induced by defects [55] or to the presence of heterogeneous conductive regions/pathways [56, 57].

The ratio of the oxidation to reduction current peaks (i_{pa}/i_{pc}) versus investigated scan rates reaches values close to unity (Fig. 8A & C). Further analysis of peak current ratio in 0.1 M KCl with 1 mM $[\text{Fe}(\text{CN})_6]^{3-/4-}$ show that only at scan rate of 10 mV/s the value goes below 1 (Fig. 8A). Also, for 0.1 M KCl with 1 mM 1,1'-Ferrocenedimethanol at the lowest applied scan rate the i_{pa}/i_{pc} reaches 1.21, where for scan rates the ratio is close to 1.1

(Fig. 8C). This result indicates that the observed reaction corresponds to a quasi-free reversible process, where electron transfer occurs by tunneling through the space charge barrier of these highly doped oxide electrodes [51].

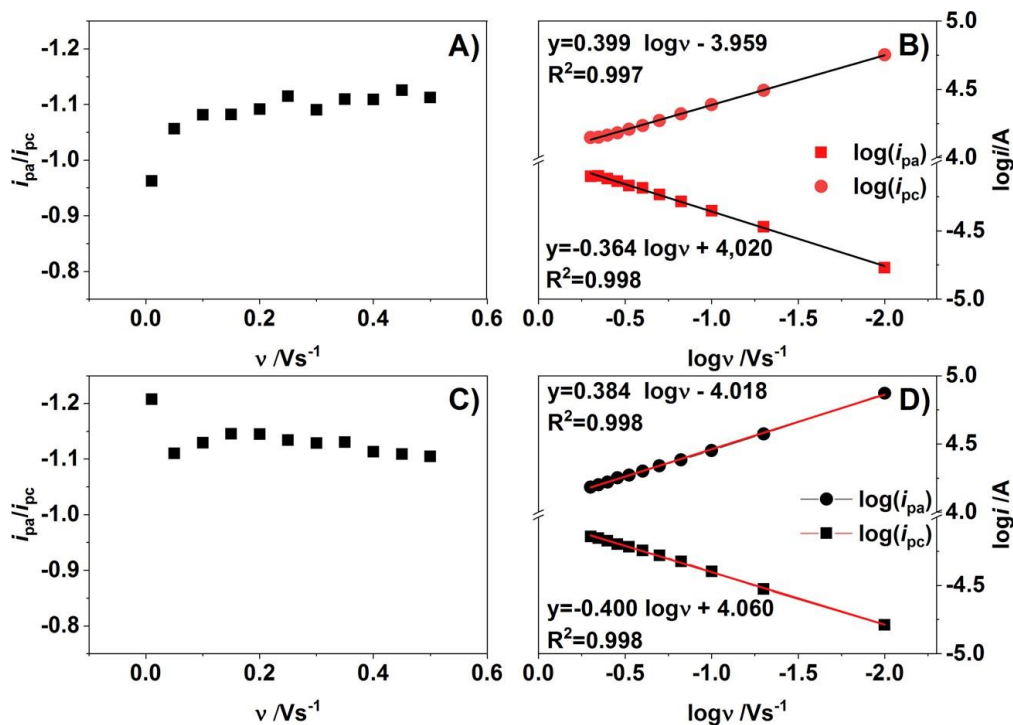


Fig. 8. Peak current ratio versus different scan rate and logarithm of anodic and cathodic peak current versus logarithm of scan rate obtained in 1 mM $[Fe(CN)_6]^{3-/4-}$ in 0.1 M KCl (A) and (B), and in 1 mM 1,1'-Ferrocenedimethanol in 0.1 M KCl solution (C) and (D), respectively.

Next, the logarithm of i_{pa} and i_{pc} were plotted versus logarithm of the scan rate to determine the slope value. For the 0.1 M KCl with 1 mM $[Fe(CN)_6]^{3-/4-}$ it reaches 0.4 for i_{pa} and 0.36 for i_{pc} with correlation coefficient of 0.997 and 0.998, respectively (Fig. 8B). These values are close to 0.5 which is a theoretical value [58], what indicates that diffusion controlled process occurs at the ITO-LMR sensor. In theory, the value of slope of 0.5 corresponds to pure diffusion, while 1 is for adsorption process, a slope between 0.5 and 1 is attributed to mixed adsorption–diffusion controlled mechanism [59–62]. Similar dependence was plotted for solution containing 1 mM 1,1'-Ferrocenedimethanol where for i_{pa} and i_{pc} the slope reaches 0.384 and 0.4, respectively, with correlation coefficient of 0.999 (Fig. 8D). This result

confirms that these EC reactions are also diffusion controlled as reported previously by Senthilkumar et al. [63].

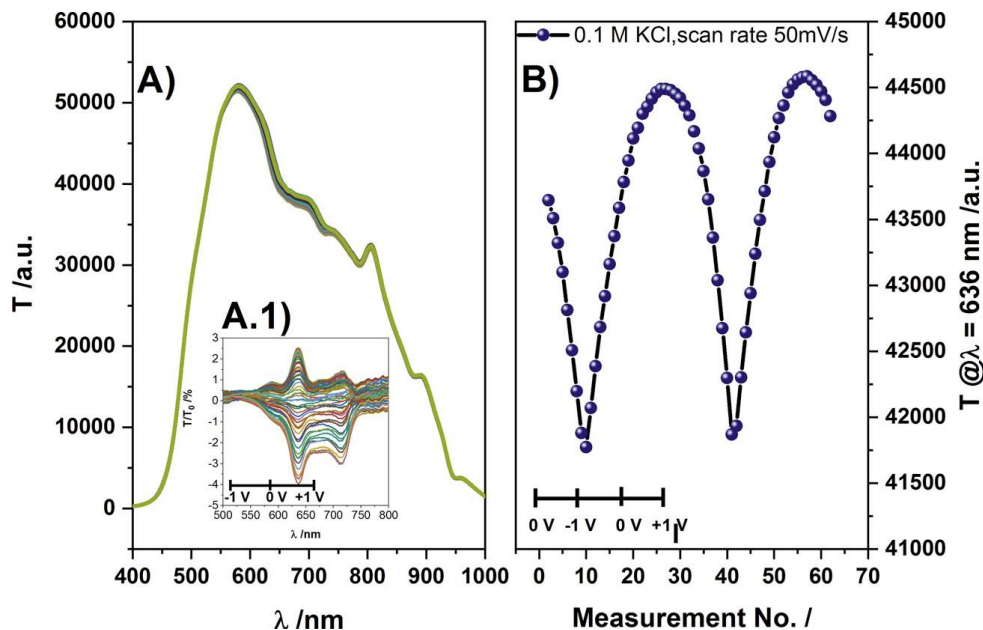


Fig. 9. Optical response of the ITO-LMR probe to potential cycling in 0.1 M KCl at scan rate 50 mV/s, where (A) shows transmitted spectrum (A.1) the spectrum normalized vs initial spectrum and (B) transmission value at $\lambda = 636$ nm for measurements taken every 2 s.

Optical responses of the ITO-LMR sensor to applied potential and solution containing the redox probes were investigated next. The spectral changes are less pronounced than those observed with changes in external RI. Thus, to determine the most valuable set of data, i.e., wavelength range where T changes the most, initial cycling has been performed in 0.1 M KCl only. In Fig. 9A and A.1 it is shown that changing potential influences T the most in wavelength range 550–750 nm, but in particular at $\lambda = 636$ nm corresponding to the LMR. The T at this wavelength was plotted for each of the measurement acquired approx. every 2 s (Fig. 9B). As an optical response can be clearly seen two periods corresponding to two potential scans. What is more, sensitivity in positive potential range is lower than in the negative range. The difference in sensitivity for positive and negative potentials has been discussed in [43] and is a result of ITO bandgap configuration. Next, the response to the solutions with addition of two redox probes at scan rate of 10 and 50 mV/s has been analyzed at the same wavelength as for 0.1 M KCl. It

can be seen in Fig. 10 that at lower scan rate not only more measurements can be done, but also response corresponding to redox probe (for measurement no. 60 and 120 shown in Fig. 10A and C) is more pronounced. Both the redox probes manifest their presence in optical response, even when for $[\text{Fe}(\text{CN})_6]^{3-/4-}$ the distortion is more significant than for 1,1'-Ferrocenedimethanol. Thus in the proposed system, the optical outcome may be used for cross-correlation, i.e., control and reference for the EC processes or probe usage indication. In these terms, different electrode condition will be designated by e.g., the change of the peak spacing or their magnitude, as in Fig. 10. Additionally, at the same time the exact same process is monitored in two domains, but the two domains may be interrogated with e.g., different scan rate or dynamics, giving more insightful information in the complementary domain.

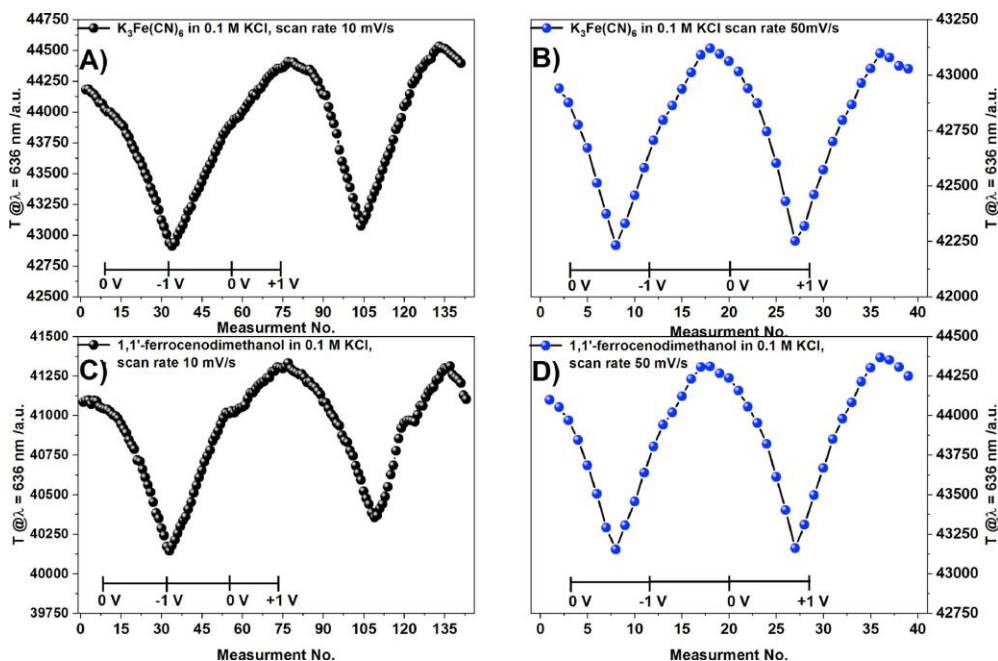


Fig. 10. Transmission changes at $\lambda = 636 \text{ nm}$ for measurements in $[\text{Fe}(\text{CN})_6]^{3-/4-}$ at the scan rate of (A) 10 mV/s and (B) 50 mV/s. The corresponding changes in ferrocenedimethanol at scan rate of 10 mV/s and 50 mV/s are shown in (C) and (D), respectively.

4. CONCLUSIONS

Analysis of liquids done simultaneously in multiple domain may deliver enhanced set of data about an analyte, also those containing biological species, when compared to a single domain investigation. In this work we have shown that optical-fiber-based devices coated with ITO thin films that are interrogated optically and electrochemically can be considered as dual-domain sensors. Performance of these sensors in both the domains mostly depend on the properties of ITO. We focused here on the improvement of electrochemical response of lossy-mode resonance optical sensors to redox probes, such as $K_3[Fe(CN)_6]$ or 1,1'-Ferrocenedimethanol, by tuning conditions of ITO sputtering. It has been found that when deposition pressure is as low as 0.1 Pa, the electrochemical processes at the optical-fiber-based device surface are quasi-reversible and diffusion-controlled. The devices offer electrochemical activity as good as the commercially available ITO-coated electrodes. Low deposition pressure results in increased crystallinity of the films and their improved conductivity. However, improved electrochemical response is followed by change in optical properties of ITO what slightly disturbs lossy-mode resonance conditions, but still makes the optical monitoring of the electrode surface possible. Any changes in the optical or electrochemical response to the redox probe may be further used as a parameter for label-free sensing. The enhanced lossy-mode resonance sensing concept can be further developed towards the biosensing solution, where the results are cross-verified by optical and electrochemical readouts to better control the experiment, or deliver supplementary information about properties of the sensor surface. According to our best knowledge fully functional combined optical and electrochemical sensor, where optical effect is resonance-based and other than well-known surface plasmon resonance, has been shown here for the first time.

Acknowledgements

This work was financially supported in Poland by the National Science Centre (NCN), grant No. 2014/14/E/ST7/00104 and the National Centre for Research and Development (NCBiR), Techmatstrateg program, grant No.347324/12/NCBR/2017. Authors are thankful to Ms. Katarzyna Lechowicz for her support in preparation of Fig. 2.

References

- [1] L. León, J.D. Mozo, Designing spectroelectrochemical cells: a review, *Trac Trends Anal. Chem.* 102 (2018) 147–169, <https://doi.org/10.1016/j.trac.2018.02.002>.
- [2] M. Odijk, A. van den Berg, Nanoscale electrochemical sensing and processing in Microreactors, *Annu. Rev. Anal. Chem. Palo Alto Calif (Palo Alto Calif)* 11 (1) (2018) 421–440, <https://doi.org/10.1146/annurev-anchem-061417-125642>.
- [3] X. Wang, O.S. Wolfbeis, Fiber-optic chemical sensors and biosensors (2013–2015), *Anal. Chem.* 88 (1) (2016) 203–227, <https://doi.org/10.1021/acs.analchem.5b04298>.
- [4] C. Caucheteur, T. Guo, J. Albert, Review of plasmonic Fiber optic biochemical sensors: improving the limit of detection, *Anal. Bioanal. Chem.* 407 (14) (2015) 3883–3897, <https://doi.org/10.1007/s00216-014-8411-6>.
- [5] J. Juan-Colás, S. Johnson, T.F. Krauss, Dual-mode electro-optical techniques for biosensing applications: a review, *Sensors* 17 (9) (2017) 2047, <https://doi.org/10.3390/s17092047>.
- [6] T. Guo, Fiber grating-assisted surface plasmon resonance for biochemical and electrochemical sensing, *J. Lightwave Technol., JLT* 35 (16) (2017) 3323–3333.
- [7] W. Hu, Y. Huang, C. Chen, Y. Liu, T. Guo, B.-O. Guan, Highly sensitive detection of dopamine using a graphene functionalized plasmonic fiber-optic sensor with aptamer conformational amplification, *Sens. Actuators B Chem.* 264 (2018) 440–447, <https://doi.org/10.1016/j.snb.2018.03.005>.
- [8] P. Niedziałkowski, Z. Cebula, N. Malinowska, W. Białobrzeska, M. Sobaszek, M. Ficek, R. Bogdanowicz, J.S. Anand, T. Ossowski, Comparison of the paracetamol electrochemical determination using boron-doped diamond electrode and borondoped carbon nanowalls, *Biosens. Bioelectron.* 126 (2019) 308–314, <https://doi.org/10.1016/j.bios.2018.10.063>.
- [9] N. Elhalawany, H. Elmelegy, M. Nayfeh, Synthesis, Characterization and Electrical Properties of Highly Conductive Polyaniline/gold And/or Platinum Nanocomposites, *Synth. Met.* 205 (2015) 145–152, <https://doi.org/10.1016/j.synthmet.2015.04.004>.
- [10] T. Okazaki, E. Shiokawa, T. Orii, T. Yamamoto, N. Hata, A. Taguchi, K. Sugawara, H. Kuramitz, Simultaneous multiselective spectroelectrochemical fiber-optic sensor: sensing with an optically transparent electrode, *Anal. Chem.* 90 (4) (2018) 2440–2445, <https://doi.org/10.1021/acs.analchem.7b03957>.

- [11] C.R. Zamarreno, P. Sanchez, M. Hernaez, I.D. Villar, C. Fernandez-Valdivielso, I.R. Matias, F.J. Arregui, Sensing Properties of Indium Oxide Coated Optical Fiber Devices Based on Lossy Mode Resonances, *IEEE Sens. J.* 12 (1) (2012) 151–155, <https://doi.org/10.1109/JSEN.2011.2142181>.
- [12] J. Ascorbe, J.M. Corres, F.J. Arregui, I.R. Matias, Optical fiber humidity sensor based on a tapered fiber asymmetrically coated with indium Tin oxide, 2014 IEEE SENSORS (2014) 1916–1919, <https://doi.org/10.1109/ICSENS.2014.6985405>.
- [13] F. Chiavaioli, P. Zubiato, I. Del Villar, C.R. Zamarreño, A. Giannetti, S. Tombelli, C. Trono, F.J. Arregui, I.R. Matias, F. Baldini, Femtomolar detection by nanocoated Fiber label-Free biosensors, *ACS Sens.* 3 (5) (2018) 936–943, <https://doi.org/10.1021/acssensors.7b00918>.
- [14] I.D. Villar, M. Hernaez, C.R. Zamarreño, P. Sánchez, C. Fernández-Valdivielso, F.J. Arregui, I.R. Matias, Design rules for lossy mode resonance based sensors, *Appl. Opt.*, AO 51 (19) (2012) 4298–4307, <https://doi.org/10.1364/AO.51.004298>.
- [15] M. Śmietana, M. Dudek, M. Koba, B. Michalak, Influence of diamond-like carbon overlay properties on refractive index sensitivity of nano-coated optical fibres, *Phys. Status Solidi* 210 (10) (2013) 2100–2105, <https://doi.org/10.1002/pssa.201300059>.
- [16] D. Burnat, M. Koba, Ł. Wachnicki, S. Gieratowska, M. Godlewski, M. Śmietana, Refractive index sensitivity of optical fiber lossy-Mode resonance sensors based on atomic layer deposited TiOx thin overlay, *Sixth European Workshop on Optical Fibre Sensors; International Society for Optics and Photonics* (2016) 99161G, <https://doi.org/10.1117/12.2236908> Vol. 9916.
- [17] K. Kosiel, M. Koba, M. Masiewicz, M. Śmietana, Tailoring Properties of Lossy-Mode Resonance Optical Fiber Sensors with Atomic Layer Deposition Technique, *Opt. Laser Technol.* 102 (2018) 213–221, <https://doi.org/10.1016/j.optlastec.2018.01.002>.
- [18] M. Śmietana, M. Sobaszek, B. Michalak, P. Niedziałkowski, W. Białobrzeska, M. Koba, P. Sezemsky, V. Stranak, J. Karczewski, T. Ossowski, et al., Optical monitoring of electrochemical processes with ITO-Based lossy-mode resonance optical Fiber sensor applied as an electrode, *J. Light. Technol.* 36 (4) (2018) 954–960, <https://doi.org/10.1109/JLT.2018.2797083>.
- [19] B.-S. Chiou, J.-H. Tsai, Antireflective coating for ITO films deposited on glass substrate, *J. Mater. Sci. Mater. Electron.* 10 (7) (1999) 491–495, <https://doi.org/10.1023/A:1008924018328>.

-
- [20] M. Higuchi, S. Uekusa, R. Nakano, K. Yokogawa, Postdeposition annealing influence on sputtered indium tin oxide film characteristics, *J. Appl. Phys.* 33 (1R) (1994) 302, <https://doi.org/10.1143/JJAP.33.302>.
- [21] T. Maruyama, K. Fukui, Indium-tin oxide thin films prepared by chemical vapor deposition, *J. Appl. Phys.* 70 (7) (1991) 3848–3851, <https://doi.org/10.1063/1.349189>.
- [22] H. Bisht, Comparison of spray pyrolyzed FTO, ATO and ITO coatings for flat and bent glass substrates, *Thin Solid Films* 351 (1999) 109–114, [https://doi.org/10.1016/S0040-6090\(99\)00254-0](https://doi.org/10.1016/S0040-6090(99)00254-0).
- [23] E. Eltzov, S. Cosnier, R.S. Marks, Biosensors based on combined optical and electrochemical transduction for molecular diagnostics, *Expert Rev. Mol. Diagn.* 11 (5) (2011) 533–546, <https://doi.org/10.1586/erm.11.38>.
- [24] T. Konry, A. Novoa, S. Cosnier, R.S. Marks, Development of an “Electroptode” immunosensor: indium tin oxide-coated optical Fiber tips conjugated with an electropolymerized thin film with conjugated cholera toxin B subunit, *Anal. Chem.* 75 (11) (2003) 2633–2639, <https://doi.org/10.1021/ac026444q>.
- [25] M. Janczuk-Richter, M. Piestrzyńska, D. Burnat, P. Sezemsky, V. Stranak, W.J. Bock, R. Bogdanowicz, J. Niedziółka-Jönsson, M. Śmietana, Optical investigations of electrochemical processes using a long-period Fiber grating functionalized by indium tin oxide, *Sens. Actuators B Chem.* 279 (2019) 223–229, <https://doi.org/10.1016/j.snb.2018.10.001>.
- [26] K. Imai, T. Okazaki, N. Hata, S. Taguchi, K. Sugawara, H. Kuramitz, Simultaneous multiselective spectroelectrochemical fiber-optic sensor: demonstration of the concept using methylene blue and ferrocyanide, *Anal. Chem.* 87 (4) (2015) 2375–2382, <https://doi.org/10.1021/ac504321u>.
- [27] B.M. Beam, N.R. Armstrong, S.B. Mendes, An electroactive Fiber optic chip for spectroelectrochemical characterization of ultra-thin redox-active films, *Analyst* 134 (3) (2009) 454–459, <https://doi.org/10.1039/B814338B>.
- [28] M. Smietana, W.J. Bock, P. Mikulic, Effect of high-temperature plasma-deposited nano-overlays on the properties of long-period gratings written with UV and electric arc in non-hydrogenated fibers, *Meas. Sci. Technol.* 24 (9) (2013) 94016, <https://doi.org/10.1088/0957-0233/24/9/094016>.

- [29] R. Bogdanowicz, P. Niedziałkowski, M. Sobaszek, D. Burnat, W. Białobrzeska, Z. Cebula, P. Sezemsky, M. Koba, V. Stranak, T. Ossowski, et al., Optical Detection of Ketoprofen by Its Electropolymerization on an Indium Tin Oxide-Coated Optical Fiber Probe, *Sensors* 18 (5) (2018) 1361, <https://doi.org/10.3390/s18051361>.
- [30] R. Hippler, H. Kersten, M. Schmidt, K.H. Schoenbach (Eds.), *Low Temperature Plasmas: Fundamentals, Technologies and Techniques*, 2 edition, Wiley-VCH, Weinheim, 2008.
- [31] M. Lyons, G. Keeley, M.E.G. Lyons, G.P. Keeley, The redox behaviour of randomly dispersed single walled carbon nanotubes both in the absence and in the presence of adsorbed glucose oxidase, *Sensors* 6 (12) (2006) 1791–1826, <https://doi.org/10.3390/s6121791>.
- [32] F.M. Smits, Measurement of sheet resistivities with the four-point probe, *Bell Syst. Tech. J.* 37 (3) (1958) 711–718, <https://doi.org/10.1002/j.1538-7305.1958.tb03883.x>.
- [33] V. Stranak, R. Bogdanowicz, P. Sezemsky, H. Wulff, A. Kruth, M. Smietana, J. Kratochvil, M. Cada, Z. Hubicka, Towards high quality ITO coatings: the impact of nitrogen admixture in HiPIMS discharges, *Surf. Coat. Technol.* 335 (2018) 126–133, <https://doi.org/10.1016/j.surfcoat.2017.12.030>.
- [34] V. Stranak, Z. Hubicka, M. Cada, S. Drache, M. Tichy, R. Hippler, Investigation of ionized metal flux in enhanced high power impulse magnetron sputtering discharges, *J. Appl. Phys.* 115 (15) (2014) 153301, <https://doi.org/10.1063/1.4871635>.
- [35] M.W. Thompson II, The energy Spectrum of ejected atoms during the high energy sputtering of gold, *Philos. Mag.* 18 (152) (1968) 377–414, <https://doi.org/10.1080/14786436808227358>.
- [36] P. Pokorný, J. Musil, J. Lančok, P. Fitl, M. Novotný, J. Bulíř, J. Vlček, Mass spectrometry investigation of magnetron sputtering discharges, *Vacuum* 143 (2017) 438–443, <https://doi.org/10.1016/j.vacuum.2017.06.032>.
- [37] D.C. Paine, T. Whitson, D. Janiac, R. Beresford, C.O. Yang, B. Lewis, A study of low temperature crystallization of amorphous thin film indium–tin–oxide, *J. Appl. Phys.* 85 (12) (1999) 8445–8450, <https://doi.org/10.1063/1.370695>.
- [38] J.A. Thornton, Influence of apparatus geometry and deposition conditions on the structure and topography of thick sputtered coatings, *J. Vac. Sci. Technol.* 11 (4) (1974) 666–670, <https://doi.org/10.1116/1.1312732>.

-
- [39] A.A. Anders, Structure zone diagram including plasma-based deposition and ion etching, *Thin Solid Films* 518 (2010) 4087–4090, <https://doi.org/10.1016/j.tsf.2009.10.145>.
- [40] K.-S. Tseng, Y.-L. Lo, Effect of sputtering parameters on optical and electrical properties of ITO films on PET substrates, *Appl. Surf. Sci.* 285 (2013) 157–166, <https://doi.org/10.1016/j.apsusc.2013.08.024>.
- [41] M. Scampicchio, A. Arecchi, S. Mannino, Optical nanoprobe based on gold nanoparticles for sugar sensing, *Nanotechnology* 20 (13) (2009) 135501, <https://doi.org/10.1088/0957-4484/20/13/135501>.
- [42] I. Del Villar, C.R. Zamarreño, M. Hernaez, P. Sanchez, F.J. Arregui, I.R. Matias, Generation of surface plasmon resonance and lossy mode resonance by thermal treatment of ITO thin-films, *Opt. Laser Technol.* 69 (2015) 1–7, <https://doi.org/10.1016/j.optlastec.2014.12.012>.
- [43] M. Śmietana, P. Niedziałkowski, W. Białobrzaska, D. Burnat, P. Sezemsky, M. Koba, V. Stranak, K. Siuzdak, T. Ossowski, R. Bogdanowicz, Study on combined optical and electrochemical analysis using indium-tin-Oxide-Coated optical Fiber sensor, *Electroanalysis* 31 (2) (2018) 392–404, <https://doi.org/10.1002/elan.201800638>.
- [44] M.B. Rooney, D.C. Coomber, A.M. Bond, Achievement of near-reversible behavior for the $[\text{Fe}(\text{CN})_6]^{3-}/4-$ redox couple using cyclic voltammetry at glassy carbon, gold, and platinum macrodisk electrodes in the absence of added supporting electrolyte, *Anal. Chem.* 72 (15) (2000) 3486–3491, <https://doi.org/10.1021/ac991464m>.
- [45] R.W. French, A.M. Collins, F. Marken, Growth and application of paired gold electrode junctions: evidence for nitrosonium phosphate during nitric oxide oxidation, *Electroanalysis* 20 (22) (2008) 2403–2409, <https://doi.org/10.1002/elan.200804354>.
- [46] S.D. Branch, A.M. Lines, J. Lynch, J.M. Bello, W.R. Heineman, S.A. Bryan, Optically transparent thin-film electrode chip for spectroelectrochemical sensing, *Anal. Chem.* 89 (14) (2017) 7324–7332, <https://doi.org/10.1021/acs.analchem.7b00258>.
- [47] N.R. Armstrong, A.W.C. Lin, M. Fujihira, T. Kuwana, Electrochemical and surface characteristics of tin oxide and indium oxide electrodes, *Anal. Chem.* 48 (4) (1976) 741–750, <https://doi.org/10.1021/ac60368a035>.
- [48] M.A. Martínez, J. Herrero, M.T. Gutiérrez, Electrochemical stability of indium tin oxide thin films, *Electrochim. Acta* 37 (14) (1992) 2565–2571, [https://doi.org/10.1016/0013-4686\(92\)87053-3](https://doi.org/10.1016/0013-4686(92)87053-3).
-

- [49] N.D. Popovich, S.-S. Wong, B.K.H. Yen, H.-Y. Yeom, D.C. Paine, Influence of microstructure on the electrochemical performance of tin-doped indium oxide film electrodes, *Anal. Chem.* 74 (13) (2002) 3127–3133, <https://doi.org/10.1021/ac011168l>.
- [50] M. Lyons, G. Keeley, M.E.G. Lyons, G.P. Keeley, The redox behaviour of randomly dispersed single walled carbon nanotubes both in the absence and in the presence of adsorbed glucose oxidase, *Sensors* 6 (12) (2006) 1791–1826, <https://doi.org/10.3390/s6121791>.
- [51] A.J. Bard, L.R. Faulkner, *Electrochemical Methods: Fundamentals and Applications*, 2 edition, Wiley, New York, 2000.
- [52] I. M. Apetrei; C. Apetrei, Voltammetric determination of melatonin using a graphene-based sensor in pharmaceutical products <https://www.dovepress.com/voltammetric-determination-of-melatonin-using-a-graphene-based-sensor-peerreviewed-article-IJN> (accessed Sep 25, 2018).
- [53] W. Zhang, I. Gaberman, M. Ciszowska, Diffusion and concentration of molecular probes in Thermo-responsive Poly(N-Isopropylacrylamide) hydrogels: effect of the volume phase transition, *Anal. Chem.* 74 (6) (2002) 1343–1348, <https://doi.org/10.1021/ac0107857>.
- [54] C.E. Hotchen, I.J. Maybury, G.W. Nelson, J.S. Foord, P. Holdway, F. Marken, Amplified Electron transfer at poly-ethylene-Glycol (PEG) grafted electrodes, *Phys. Chem. Chem. Phys.* 17 (17) (2015) 11260–11268, <https://doi.org/10.1039/C5CP01244A>.
- [55] J. Stotter, Y. Show, S. Wang, G. Swain, Comparison of the electrical, optical, and electrochemical properties of diamond and indium tin oxide thin-film electrodes, *Chem. Mater.* 17 (19) (2005) 4880–4888, <https://doi.org/10.1021/cm050762z>.
- [56] G. Frank, H. Köstlin, Electrical properties and defect model of tin-doped indium oxide layers, *Appl. Phys. A* 27 (4) (1982) 197–206, <https://doi.org/10.1007/BF00619080>.
- [57] R. Bel Hadj Tahar, T. Ban, Y. Ohya, Y. Takahashi, Tin doped indium oxide thin films: electrical properties, *J. Appl. Phys.* 83 (5) (1998) 2631–2645, <https://doi.org/10.1063/1.367025>.
- [58] K. Siuzdak, M. Ficek, M. Sobaszek, J. Ryl, M. Gnyba, P. Niedziałkowski, N. Malinowska, J. Karczewski, R. Bogdanowicz, Boron-enhanced growth of micronscale carbon-based nanowalls: a route toward high rates of electrochemical biosensing, *ACS Appl. Mater. Interfaces* 9 (15) (2017) 12982–12992, <https://doi.org/10.1021/acsami.6b16860>.

-
- [59] I. Tiwari, M. Gupta, P. Sinha, S.K. Aggarwal, Electro-Oxidation of Phenyl Hydrazine on a Modified Electrode Constructed Using Nanocomposite of Ruthenium Terpyridyl Complex, Multiwalled Carbon Nanotubes and Nafion, *Electrochim. Acta* 76 (2012) 106–111, <https://doi.org/10.1016/j.electacta.2012.04.053>.
- [60] R. Gupta, S.K. Guin, S.K. Aggarwal, A mechanistic study on the electrocatalysis of the Pu(IV)/Pu(III) redox reaction at a platinum electrode modified with singlewalled carbon nanotubes (SWCNTs) and polyaniline (PANI), *RSC Adv.* 2 (5) (2012) 1810–1819, <https://doi.org/10.1039/C1RA01010G>.
- [61] C. Batchelor-McAuley, L.M. Gonçalves, L. Xiong, A.A. Barros, R.G. Compton, Controlling Voltammetric Responses by Electrode Modification; Using Adsorbed Acetone to Switch Graphite Surfaces between Adsorptive and Diffusive Modes, *Chem. Commun. (Camb.)* 46 (47) (2010) 9037–9039, <https://doi.org/10.1039/C0CC03961F>.
- [62] E. Laviron, L. Roullier, C. Degrand, A multilayer model for the study of space distributed redox modified electrodes: part II. Theory and application of linear potential sweep voltammetry for a simple reaction, *J. Electroanal. Chem. Interfacial Electrochem.* 112 (1) (1980) 11–23, [https://doi.org/10.1016/S0022-0728\(80\)80003-9](https://doi.org/10.1016/S0022-0728(80)80003-9).
- [63] M. Senthilkumar, J. Mathiyarasu, J. Joseph, K.L.N. Phani, V. Yegnaraman, Electrochemical instability of indium tin oxide (ITO) glass in acidic pH range during cathodic polarization, *Mater. Chem. Phys.* 108 (2) (2008) 403–407, <https://doi.org/10.1016/j.matchemphys.2007.10.030>.

A5. Effect of thermal annealing on sensing properties of optical fiber sensors coated with indium tin oxide nano-overlays

Bartosz Michalak, Petr Sezemsky, Vitezslav Stranak, Mateusz Smietana, Effect of thermal annealing on sensing properties of optical fiber sensors coated with indium tin oxide nano-overlays, Photonics Letters of Poland 12(2), (2020), 58-60.

Abstract

In this work we discuss an effect of thermal annealing on optical and electrical properties of indium tin oxide (ITO) thin films deposited on a short section of the multimode polymer-clad silica (PCS) optical fiber core. ITO films were deposited using a different configuration of high-power impulse magnetron sputtering (HiPIMS) and radio frequency magnetron sputtering (RF MS) cathodes. Due to tuned ITO film thickness it was possible to observe for these structures a lossy-mode resonance (LMR) and trace changes in the properties of films. Electrical resistance of the ITO overlays was also measured. Both optical and electrical measurements were repeated after annealing at 200 °C in a tube furnace and nitrogen atmosphere. The measurements have shown that thermal annealing changes an optical response to the external refractive index (RI) of the fiber sensor and also changes the ITO layer resistivity. As an effect of thermal annealing, we observed a shift of the LMR towards longer wavelengths. In addition, as a result of annealing, the resistivity of the ITO layer was reduced.

In rising need for body fluid analysis, optical fiber sensors are considered as a suitable solution [1]. Systems based on optical fibers are modular and can be connected in series, which allows for simultaneous measurements of several parameters. Due to low fabrication cost, they can be disposed after contact with a patient's body fluids and replaced with new ones. To increase the reliability of measurements, an optical readout from sensors needs to be verified, most likely by the same setup but different sensing mechanism. One of the solutions is simultaneous optical and electrochemical analysis.

An optical effect employed in this work is lossy-mode resonance (LMR). It occurs when optical properties of the fiber core, deposited thin overlay and surrounding liquid are in a certain relation [2]. This relation is fulfilled when tuned-in-properties indium tin oxide (ITO) is deposited as an overlay. Tracing LMR also makes quick measurement of the refractive index (RI) of surrounding liquid possible. Due to high RI sensitivity, ITO-coated optical fiber structures can be used to measure, for example, the composition of a solution, and also the growth of a biological film on the sensor's surface [3]. Thanks to electrochemical activity of ITO, it can be also used for LMR simultaneous electrochemical measurement, which makes the cross-verification of results possible [1]. However, there is a need for postdeposition optimization of ITO properties for these simultaneous measurements, e.g., towards the reduction in resistivity of the overlays. As one of the postprocessing solutions can be considered thermal annealing.

In this work we discuss the effect of thermal annealing on optical and electrical properties of ITO overlays deposited, by using different magnetron sputtering configurations, on a short section of the multimode polymer-clad silica (PCS) optical fiber core. The annealing effect is analysed by comparing the optical response of the sensor, in particular when submerged in liquids of different RI, as well as by comparing the resistivity of the ITO-coated section.

The sensors were based on PCS optical fiber (150 mm in length, $\varnothing = 400 \mu\text{m}$ fused silica core) where the central section had been chemically exposed to methylene chloride and then some of the cladding was mechanically removed to a length of 25 mm. Next, ITO overlays were deposited on the exposed core section using a different configuration of high-power impulse magnetron sputtering (HiPIMS) and radio frequency magnetron sputtering (RF MS)

cathodes [4]. HiPIMS provides high density plasma with pulses of high energy output which shortens the PCS samples exposure time to high temperature during the deposition process. The introduction of RF MS decreases the process time even further by speeding up the development of HiPIMS pulses and reducing the working pressure [5].

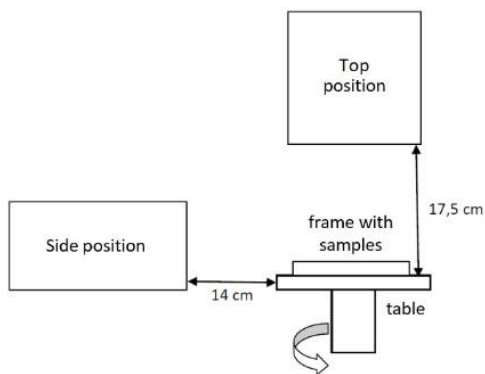


Fig. 1. Schematic representation of elements in the process chamber.

One run of deposition was done on three fiber samples called as A, B and C, installed in a metal frame that was placed on a rotating stage in the process chamber, and after a half of the process time the frame was flipped to the other side. At the top and on the side of the substrate, sputtering targets were installed in the process chamber (Fig. 1) in a different configuration of cathodes.

The configuration for the sample

series is summarized in Table 1. It was done to find the most suitable deposition process parameters.

Optical transmission of the ITO-LMR samples was measured using an Ocean Optics USB4000 spectrometer and Ocean Optics HL-2000 white light source. To identify RI sensitivity, the samples were submerged in liquids with RI in the range $n_D = 1.334 \div 1.466$. The n_D of the liquid was measured using a Rudolph's Digital J57 refractometer. Obtained transmission spectra were normalized using the data set for a sample with no overlay measured in air.

Electrical resistance of the ITO layers was also measured on a 25 mm length of the sensor area using a digital multimeter.

After both optical and electrical measurements, the samples were annealed at 200 °C in a tube furnace in a nitrogen atmosphere for 2 hours. Next, the measurements were repeated. In particular, we analysed the LMR shift observed in the spectrum as an effect of thermal annealing.

Table 1. Magnetron sputtering configurations used in the experiment.

	01	02	03
Top position	RF MS 3" ITO target	-	HiPIMS 2" ITO target
Side position	HiPIMS 2" ITO target	RF MS 3" ITO target	RF MS 3" ITO target
Pressure [Pa]	0.7	0.5	0.5
Argon flow [sccm]	15	15	15
Time [min]	40	120	48

Analysis of the obtained transmission spectra confirms that the position of the sputtered target led to a different thickness of overlays. The number of resonances, shown by black arrows (Fig. 2), indicates the deposited layer thickness – the more resonances, the thicker is the overlay [6]. When RF MS was at the top position and HiPIMS was on the side position, the configuration and 40 min long process led to the deposition of relatively thin overlays - two main resonances can be seen (Fig. 2a). When RF MS was only on the side, it led to an even thinner overlay deposition - only one resonance occurred, even after the process time was tripled (Fig. 2b). Using HiPIMS in the top position and RF MS on the side, thicker ITO overlays were achieved - four resonances can be seen (Fig. 2c).

The samples were submerged in liquids with RI in the range $n_D = 1.334 \div 1.466$, where the brighter plots represent the lower RIs of a used liquid. In all cases, the observed resonances shifted towards longer wavelengths with external RI, shown by the orange arrow (Fig. 2).

Resistance measurements were made on three samples A, B and C, which were present during the same deposition process, except for series 01, which was not considered for resistivity measurement. We have observed differences in the resistance of samples made in the same process (Tab. 2). It may be caused by the spatial heterogeneity of plasma and its different interactions with the samples. Further analysis indicates that thicker layers show lower resistivity, while thermal annealing lowers it even more. Lower resistance helps in conducting efficient electrochemical measurements, and for this reason the contribution of HiPIMS is preferable.

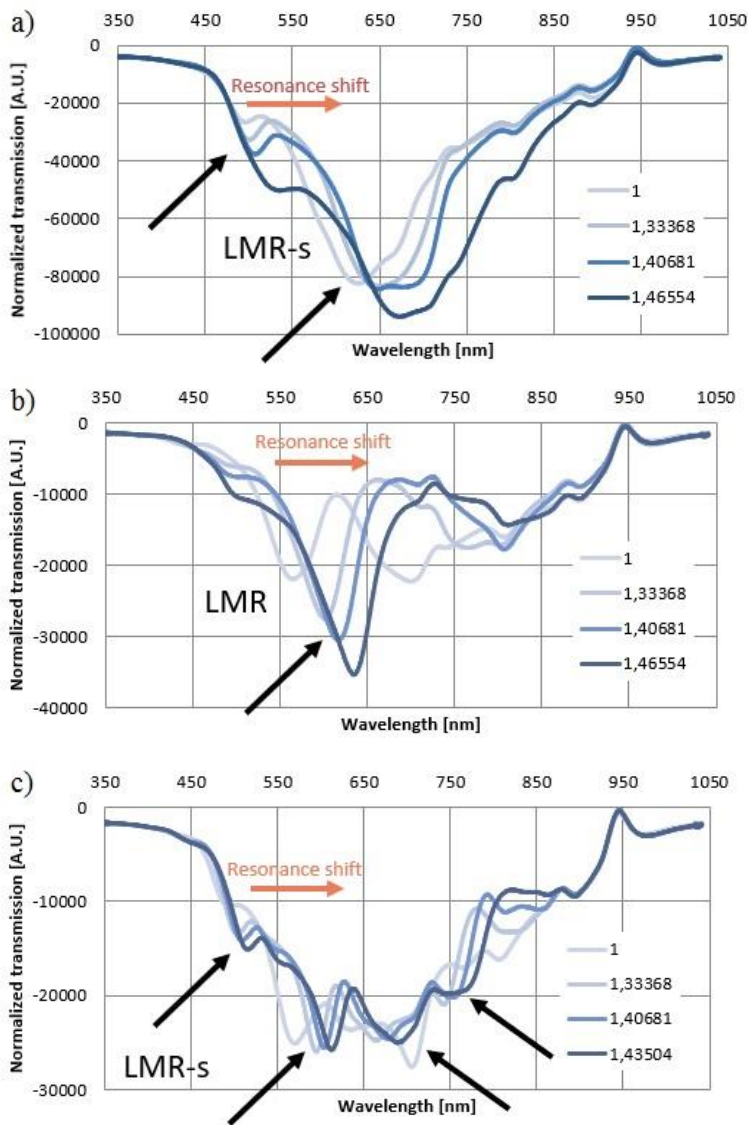


Fig. 2. Optical transmission spectra of a) 01, b) 02, c) 03, sample series and the LMR shift before thermal annealing when immersed in liquids of different RI.

Thermal annealing also affects optical transmission of optical fiber samples, the LMR shift towards longer wavelengths (Fig. 3). We can still observe the LMR shift towards longer wavelengths with an increase of RI. Due to the thermal annealing of optical fiber structure, the RI sensitivity decreased for all cases (Tab. 3.). This is an effect of ordering the crystallographic structure of

the ITO layer, which leads to an increase of ITO overlay RI [7]. It is an undesirable effect from an optical sensing point of view. The effect of annealing is less pronounced for samples received with the HiPIMS contribution due to higher energy already delivered to sputtered particles in this process, compared to RF MS applied solely.

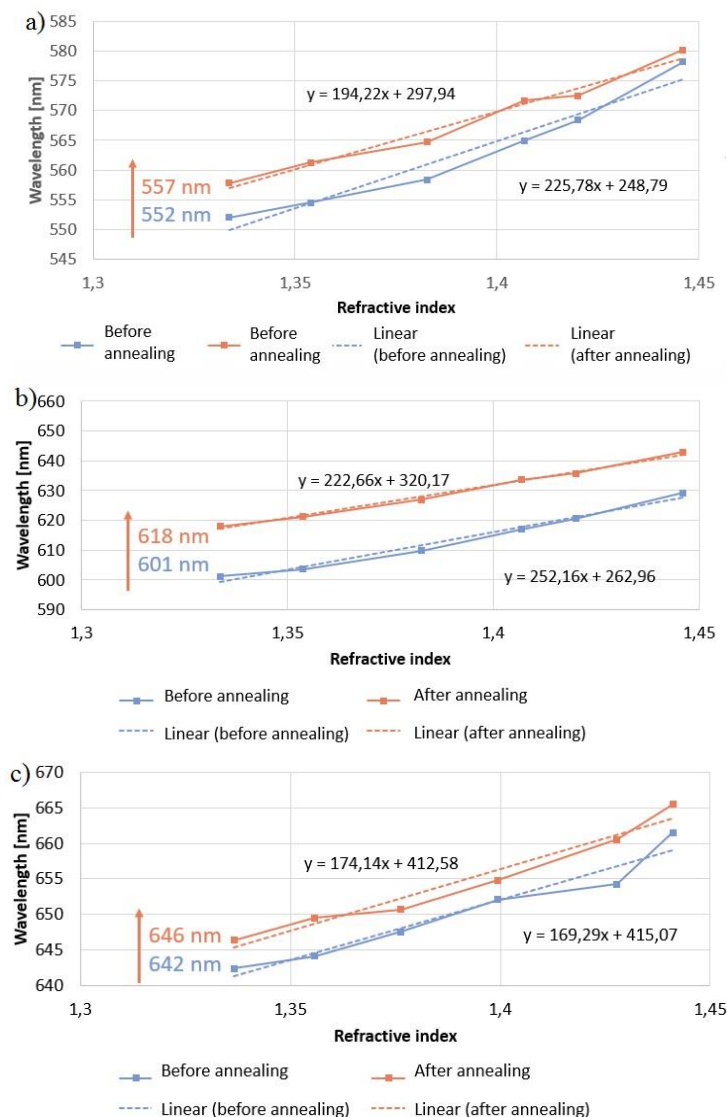


Fig. 3. Resonance shift of a) 01, b) 02, c) 03 sample series with linear approximation before and after thermal annealing when immersed in liquids of different RI.

Table 2. Resistance of three samples A, B and C from 02 and 03 series before and after annealing.

	Resistance before annealing [Ω]	Resistance after annealing [Ω]
02A	-	157 000
02B	-	250 000
02C	-	270 000
03A	360	250
03B	320	300
03C	500	270

Table 3. RI sensitivity for 01, 02 and 03 series before and after annealing

	Sensitivity before annealing [nm/RIU]	Sensitivity after annealing [nm/RIU]
01	232.05	199.22
02	249.49	221.55
03	183.30	183.11

In conclusions, obtained data indicates that ITO films obtained with a contribution of HiPIMS are more resistant to thermal annealing than those deposited using RF MS only. Optical fibers with an ITO layer are sensitive to changes in external RI and respond as an LMR shift towards longer wavelengths. When LMR sensors are considered, thermal annealing changes the optical response of the ITO-coated sensor and, in general, lowers its optical sensitivity. Observed was an LMRs shift with annealing towards longer wavelengths. However, annealing also decreased electrical resistance of the deposited ITO. Understanding both effects can lead to finding optimal ITO deposition parameters and also optimal annealing temperature for optical fiber sensors used in simultaneous optical and electrochemical measurements [8-9]. For these applications, a contribution of HiPIMS is expected.

The authors gratefully acknowledge the support for this work from the National Science Centre of Poland within the research project

2014/14/E/ST7/00104 and The National Centre for Research and Development of Poland within the research project TECHMATSTRATEG1/347324/12/NCBR/2017

References

- [1] M. Sobaszek et al., Proc. SPIE 10323, 103234W (2017).
- [2] I. Del Villar et al., J. Opt. 12(9), 95503 (2010).
- [3] M. Śmietana et al., Biosensors and Bioelectronics 154, 112050 (2020).
- [4] P. Niedziałkowski et al., Sensors and Actuators B: Chemical 301(12), 1 (2019).
- [5] V. Stranak et al., Surface & Coatings Technology 206(11-12), 2801 (2012).
- [6] I. Del Villar et al., Appl. Opt. 51(19), 4298 (2012).
- [7] W.F. Wu, B.S. Chiou, Appl. Surf. Sci. 68(4), 497 (1993).
- [8] M. Smietana et al., J. Light. Technol. 36(4), 954 (2018). [9] M. Śmietana et al., Electroanalysis 31(2), 398 (2019).

A6. Tailoring properties of indium tin oxide thin films for their work in both electrochemical and optical label-free sensing systems

Petr Sezemsky, Dariusz Burnat, Jiri Kratochvil, Harm Wulff, Angela Kruth, Katarzyna Lechowicz, Monika Janik, Robert Bogdanowicz, Martin Cada, Zdenek Hubicka, Pawel Niedzialkowski, Wioleta Bialobrzaska, Vitezslav Stranak, Mateusz Smietana, Tailoring properties of indium tin oxide thin films for their work in both electrochemical and optical label-free sensing systems, Sensors and Actuators B: Chemical 343, (2021), 130173.

Abstract

This work is devoted to the identification properties of indium tin oxide (ITO) thin films responsible for their possible application in combined optical and electrochemical label-free sensing systems offering enhanced functionalities. Since any post-processing would make it difficult to identify direct relation between deposition parameters and properties of the ITO films, especially when deposition on temperature-sensitive substrates is considered, the films were deposited using reactive high power impulse magnetron sputtering (HiPIMS) at low temperature and with no post-deposition annealing. We focused mainly on the impact of reactive gases, such as oxygen or nitrogen introduced to the process chamber, on control over plasma parameters and subsequently properties of the films. The properties of the films were investigated using X-ray diffractometry, spectroscopic ellipsometry, four-point probe, and cyclic voltammetry. For presenting optical sensing capabilities, the tailored ITO films in addition to silicon and glass wafers were also deposited on the core of optical fibers to induce the lossy-mode resonance (LMR) phenomenon. The existence of specific deposition conditions resulting in ITO film properties offering both high-quality electrochemical and LMR responses has been experimentally proven. It has been found that the crystalline structure of ITO plays a key role in the determination of both the sensing capabilities. Finally, label-free sensing of antibody-antibody interactions in both optical and electrochemical domains for the sensor with tailored ITO film has been shown.

1. INTRODUCTION

Optical sensors, especially those based on optical fibers, have been under intensive development for the last 30 years [1]. Significant progress has been made for the sensors used in medicine, defense and security, aerospace application, as well as many others [2]. They are small in size, offer rapid response, make low-cost fabrication possible, as well as are resistant to electromagnetic interference. There is a large variety of optical fiber sensing concepts [1], where those based on the devices coated with thin films are of particular interest due to their capability for large-scale fabrication. Among other thin-film-based optical phenomena, a lossy-mode resonance (LMR) can be found [3]. The LMR sensors may offer exceptionally high sensitivity to change in optical properties at their surface what next to surface plasmon resonance (SPR) sensors, makes them very promising for label-free chemical and biological sensing [4]. To obtain the LMR, the film must be thick enough and the real part of the electrical permittivity of the film must be positive and higher in magnitude than both its imaginary part and the permittivity of the surrounding medium [5, 6]. Since electrical permittivity is correlated with refractive index (RI), the properties of the LMR depend on optical properties of the thin film and these mainly influence the RI sensitivity of the devices [5]. Changes in properties of the films, as well as properties of the external medium, modify the resonant conditions resulting in the shift of the LMR wavelength observed in transmission spectrum $T(\lambda)$ of the optical fiber device. It has been clearly shown that the sensitivity, quality of the LMR, and the RI of the film are strongly correlated [3, 7]. Thus, when fabricating optical sensors, especially those based on the LMR effect, real (n) as well as the imaginary part of RI (k) are crucial parameters determining their performance.

The LMR effect, described for the first time in 1993 [8], was implemented for sensing purposes in 2005 when silicon was used as a thin film material for coating of the optical fiber core [9]. Later on, also an application of other materials such as SnO_2 [10], ZnO [11, 12], TiO_2 [13, 14], DLC [15], SiN_x [16], HfO_2 , ZrO_2 , Ta_xO_y [17], as well as various polymers [5, 18, 19] for receiving LMR has been reported. It must be noted that deposition of these films is significantly more cost-effective than deposition of gold, which is typically required of achieving the SPR effect. Among other LMR structures can be also found those based on indium tin oxide (ITO) thin films deposited on fused

silica glass [20]. ITO has been used as a perspective coating for LMR-based optical fiber sensors where it provides high RI sensitivity [21]. Due to the sensitivity, especially to RI changes in the proximity of the thin film surface, when biofunctionalized ITO-coated optical fiber LMR label-free biosensors of immunoglobulin [22] and thrombin [23] have been reported. Furthermore, ITO may also offer low electrical resistivity [24, 25] and suitable bandgap for application as an active electrode for initiating electrochemical processes [26, 27]. In this case, changes in charge transfer at the sensor surface are monitored and widely used for label-free sensing purposes too [28]. Hence, optical fiber structures coated with tailored in properties ITO thin film offer a great opportunity to combine optical, in particular LMR, and electrochemical sensing techniques [29, 30], i.e. it offers a possibility of application two independent sensor interrogation methods in the same place and time [31]. Such an approach may offer cross-verification of the readouts and an extended sensing range. Moreover, the combined technique makes possible electrochemical processing of surface, such as electrochemical biofunctionalization that can be followed by optical detection [32]. The concept of electrochemically-enhanced optical sensing has already been reported in our former works for successful detection of ketoprofen [33], isatin [31], and also label-free biosensing [34, 32]. Moreover, we have also shown that properties of ITO highly depend on deposition conditions what makes them suitable for LMR-based or electrochemical sensing, but rarely for the combined approach [29].

There are various techniques already applied for ITO thin film deposition, such as e.g., pulsed laser deposition [35], vacuum thermal evaporation [36], dip-coating wet chemistry [37], and layer-by-layer deposition [13]. Among them, an application of magnetron sputtering is of particular interest due to the possibility of precise tailoring of the film properties as demonstrated for highly sensitive SnO₂-LMR sensors [38]. However, in cases of ITO deposition on thermally sensitive substrates, where the post-deposition annealing step cannot be performed, a conventional direct current (DC) and radio frequency (RF) magnetron sputtering produce films with a limited range of properties available for tuning [29, 39–43]. A significantly wider range of the properties with no need for post-deposition annealing can be offered by high power impulse magnetron sputtering discharges (HiPIMS), where a high fraction of

ionized and field accelerated energetic species impinging the surface of the film [43–47].

In this work, we report a comprehensive study on the properties of ITO films responsible for their effective application in both optical and electrochemical sensing systems. We have analyzed the effect of reactive gas composition during HiPIMS discharges on tailoring crystallography of the ITO film, which subsequently determines the LMR conditions, as well as the electrochemical response. We have focused on the identification of deposition conditions, at which both electrochemical and optical interrogations are effectively and simultaneously possible. Finally, for the LMR optical fiber probe with tailored ITO coating, we discuss antibody detection in both electrochemical and optical domains.

2. EXPERIMENTAL DETAILS

2.1. Deposition setup

Reactive HiPIMS deposition of ITO thin film was carried out in a high-vacuum chamber capable for reaching the back-down pressure of 10^{-5} Pa and assure the high purity of the deposition. A commercial planar 3-inch in diameter magnetron was installed in configurations depending on the type of the applied substrates as shown in Fig. 1, i.e., in the upper part of the vacuum chamber or its sidewall. The magnetron was equipped with a compound ITO target ($\text{In}_2\text{O}_3/\text{SnO}_2$ of composition 90/10 wt% and a purity of 99.99 %). The sputtering was driven using pulsed power supply described elsewhere [48] with repetition frequency 1.5 kHz, duty cycle 10 %, and pulse width 66.7 μs . The experiments were carried out at constant mean power $P_m = 150$ W. The pressure was kept constant for all the experiments at $p = 0.5$ Pa. Inert argon (flow $f_{\text{Ar}} = 100$ sccm), reactive oxygen and nitrogen (flow f_{O_2} and f_{N_2} varied in the range 0 – 55 sccm), all with a purity of 99.999 %, were used. The reactive gas concentration in the gas mixture c_R was estimated as $c_R = \frac{f_R}{f_{\text{Ar}} + f_R}$, where R denotes concentrations of O_2 or N_2 .

The ITO films were deposited on Si(100) and glass substrates, both placed 15 cm away from the sputtering target. These flat substrates were used to analyze such ITO film properties as crystallography, electrical resistivity, optical properties (n and k), electrochemical performance, thickness etc.

Furthermore, for LMR measurements, the optical fiber samples were coated too in the same deposition conditions except the magnetron installation (Fig. 1). We used approx. 15 cm long multimode polymer-clad silica fibers with 400/730 μm (core/cladding) diameter, where out of a central part (25 mm) of the fiber the cladding was removed and after ITO deposition it served as an active sensing area. The fiber was rotated during the deposition to receive a uniform ITO coating around it.

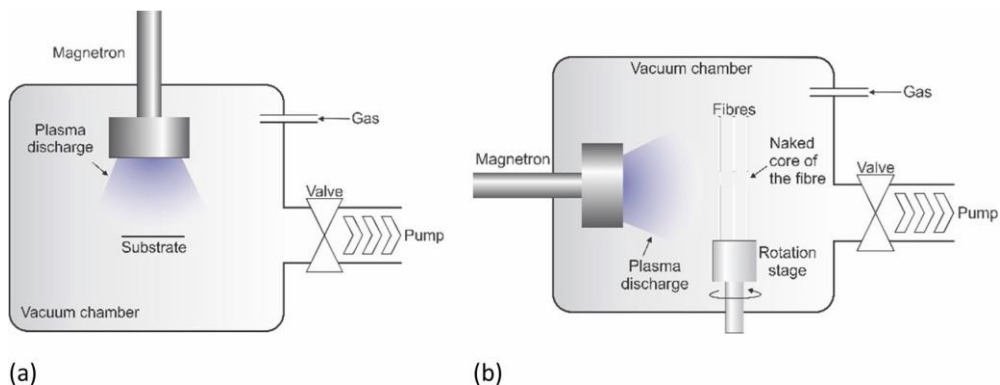


Fig. 1. The experimental setup used for deposition on (a) flat substrates and (b) on optical fibers.

2.2. Analytical methods

The surface morphology of flat reference substrates was investigated using atomic force microscopy (AFM Pico SPM, Agilent Technologies) operating in tapping mode. Film crystal phase analyses were performed by grazing incidence X-ray diffractometry (XRD) described elsewhere [49]. We used a D8 ADVANCE diffractometer (Bruker AXS) with Cu $K\alpha$ radiation (40 kV, 40 mA). The quantitative phase analyses were based on Rietveld calculations (Topas 5, Bruker). Scanned 2θ range was from 15° to 80° at an incidence angle $\omega = 1^\circ$. The resistivity of ITO samples was measured by a four-point probe supported by a Keithley 2400 current source meter, where needle-like probes with 100 μm radius were placed in a straight line with equal inter-probe spacing ($s = 1.5$ mm). Due to the finite sample size (10×25 mm), a correction factor 0.867 was taken into account for resistivity (ρ) estimation [50].

Optical properties of the deposited ITO film were investigated using Woollam M-2000XI variable angle spectroscopic ellipsometer working in range $\lambda = 210 - 1690$ nm and angles of incidence 55° , 65° , and 75° .

Measurement data were fitted to a layer model of the investigated structure, where ITO with a roughness layer was placed on the Si substrate. Dielectric function of the ITO film was modeled by the Tauc-Lorentz oscillator. In the case of samples with added oxygen, the Tauc-Lorentz oscillator was supplemented by the Gaussian oscillator. Thicknesses of the films were almost the same for all the samples. Thickness-independent attenuation coefficient μ was estimated according to relation $\mu = 4\pi k/\lambda$, where k and λ are extinction coefficient of the film measured by the ellipsometry and corresponding wavelength, respectively [51]. The transmittance T of the films for $\lambda = 200 - 1100$ nm was investigated using a double-beam UV-vis spectrophotometer (Shimadzu UV-1800).

The electrochemical performance of the films was tested in cyclic voltammetry (CV) configuration using an Autolab, Metrohm Autolab PGSTAT128 N potentiostat/galvanostat controlled by GPES software. The ITO films deposited together with Si also on glass slides (8 mm diameter) were used as working electrodes (WE), where a platinum wire and an Ag/AgCl 0.1 M KCl were used as a counter electrode (CE) and a reference electrode (REF), respectively. All the measurements were performed at room temperature in a solution of 0.1 M KCl (POCh, Poland) containing 1 mM 1,1'-Ferrocenedimethanol (Acros Organics) as a redox system. All cyclic voltammograms were obtained in the potential range from -0.25 to 0.6 V vs. Ag/AgCl electrode at a scan rate of 100 mV/s.

The optical transmission of the ITO-LMR structure on an optical fiber was interrogated in the range $\lambda = 350 - 1050$ nm using Ocean Optics HL-2000 white light source and Ocean Optics USB4000 spectrometer [29]. The spectra were obtained by subtracting the reference spectrum of the used light source T_0 from the optical transmission spectrum T_{LMR} of the sample. The sensitivity of the samples to changes of external RI (n_{ext}) was determined by immersing the sample in water/glycerin solutions of different concentrations ($n_{\text{D}} = 1.357 - 1.404$ RIU). Reichert AR200 refractometer was used to verify n_{ext} of the solutions.

To identify both electrochemical and optical performance for label-free sensing, the LMR sensor with ITO film surface has been biofunctionalized towards the specific binding of an analyte. First, the ITO-LMR sensor was

consecutively cleaned in isopropanol and water and dried under a stream of argon. Next, surface silanization with 3-triethoxysilylpropyl succinic anhydride (TESPSA) was performed according to the procedure described by Gang et al. [52] The reaction was carried out for 4 h. Primary and secondary antibodies targeted *Borrelia burgdorferi* have been used as receptor and target, respectively. The succinic anhydride reacts with amines in the ring-opening reaction to form amide bonds. In the next step, the sensor was incubated for 30 min in a solution of the primary antibodies (10 $\mu\text{g}/\text{mL}$) to covalently bond them to the surface. This step was followed by extensive washing with PBS. The concentration of the receptor at the ITO-LMR surface was determined by means of the procedure described elsewhere [53]. The incubation buffer concentration of antibodies (*Borrelia burgdorferi* receptors) was 10 $\mu\text{g}/\text{mL}$, therefore $\sim 4 \times 10^{13}$ of antibodies were available for the functionalization process. As the area of the cylindrical LMR sensor is $\sim 25 \text{ mm}^2$, and the area of an antibody is ca. 10 nm^2 , we assume that the optical fiber's surface is covered with up to 2.5×10^{12} interaction units. Next, the sensor surface was immersed in a BSA solution (0.5 mg/mL in PBS) for 30 min to block any remaining unspecific sites. The washing procedure was repeated as described earlier. For the sensitivity analysis, the sensor was immersed in increasing concentrations (1, 5, and 10 $\mu\text{g}/\text{mL}$) of the secondary antibody for 30 min in each solution. Incubation in every concentration was followed by extensive washing with PBS. During each incubation step, the optical signal of the LMR sensor was monitored in the range of $\lambda = 350 - 1040 \text{ nm}$ every 1 min. At each step of the experiment after the incubation and washing the samples have been placed consecutively in PBS and 1 mM Ferrocenedimethanol (in PBS) and underwent CV at scan rate of 20 mV/s for 3 cycles in the potential ranging from -0.5 to 1.5 V with simultaneous optical monitoring.

3. RESULTS AND DISCUSSION

Our previous works [29, 43] indicated contradictory deposition parameters for obtaining ITO films suitable for LMR and those showing electrochemical activity. To broaden the range of properties, we investigate here the effect of oxygen and/or nitrogen doping as the agents for tailoring the ITO properties.

3.1. Crystalline structure of ITO

The presence of reactive gases strongly influences phase formation of deposited ITO films. In the case of pure Ar discharge, i.e., without any reactive admixture, the XRD reveals two crystalline phases - 92.2 wt% ITO and 7.8 wt% metallic indium (Fig. 2(a)). The lattice parameter of ITO in these conditions is $a_{\text{ITO}} = 1.01655$ nm, while metal indium crystalizes with lattices $a_{\text{In}} = 0.32510$ nm and $c_{\text{In}} = 0.49502$ nm. Sub-stoichiometric, i.e., not sufficiently oxidized ITO films were reported in other works when employing RF sputtering. Terzini et al. [54] have shown that an increase of RF power density promotes oxygen vacancies and deposition of metal-like ITO films. This was observed for power densities exceeding 0.75 W/cm². In our case, the peak power density reaches over 60 W/cm². Hence, the formation of metallic In fraction in pure Ar discharge is not surprising. It is worth mentioning that in work by Senol et al. the preference of (222) crystal plane orientation was attributed to the presence of the oxygen vacancies that resulted in lower resistivity of the films [55].

When reactive O₂ was added, despite the peak power increase (by up to 25 % for $c_{\text{O}_2} = 10$ %), the vacancies were occupied and resulted in crystalline ITO deposition (Fig. 2(b)). Slight doping of the discharge by oxygen ($c_{\text{O}_2} = 0.5$ %) is sufficient for formation of crystalline ITO with no XRD peak related to metallic In observed, and even more increased lattice parameter $a_{\text{ITO}} = 1.0184$ nm. For further increase of c_{O_2} , the formation of crystalline ITO structure is significantly disturbed. For these films, smaller lattice sizes were found indicating their over-stoichiometry (Fig. 3). Such an effect indicates that sputtering in pure Ar atmosphere results in sub-stoichiometric films and some oxygen needs to be incorporated to attain pure crystalline ITO films. This effect becomes pronounced specifically for HiPIMS discharges, where the target is loaded by high peak power, and sputtered species are not fully saturated by oxygen.

Change of crystallization was observed also, when N₂ was employed as a reactive gas. In this case, we observed a higher intensity of the dominant (222) peak that was attributed to the sub-stoichiometric character of ITO (Fig. 2(c)). An effect of the increased peak was observed also in our earlier work [43], where it was corresponding to energy stored in vibrational and rotational states

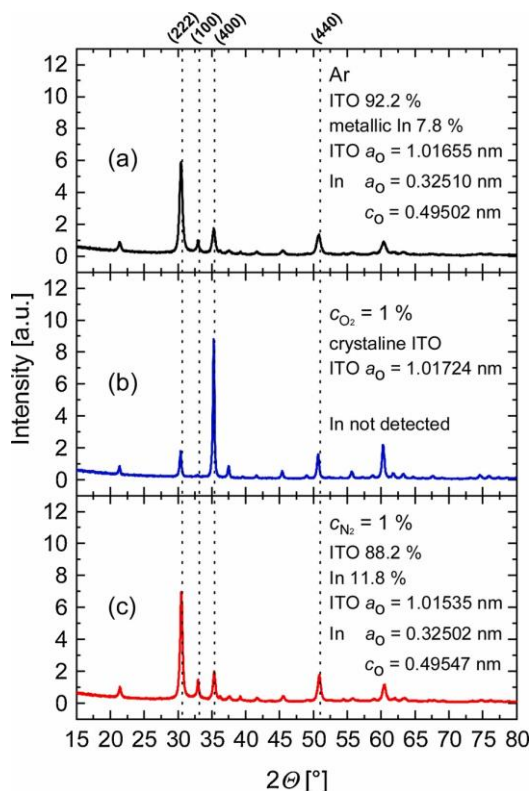


Fig. 2. Selected XRD patterns of ITO films deposited at different concentrations of the reactive gas, (a) corresponds to pure Ar, (b) $c_{O_2} = 1\%$, and (c) $c_{N_2} = 1\%$. The deposited film has to be slightly doped with oxygen to form crystalline ITO. Without oxygen doping, a fraction of metallic In appears in the films what is indicated by peak (100).

of nitrogen molecules. This energy is delivered to the growing film and it affects the crystallization process. The same mechanism was indicated to be responsible for the improved growth of TiO_2 films [56] and it is expected to be responsible for the growth of ITO films with metallic In too. It is important to note that ITO crystallization is improved only up to a certain level of N_2 doping, i.e., for $c_{N_2} < 4\%$ the film is polycrystalline with dominant (222) peak and the further increase of nitrogen flow promotes amorphous film. Films deposited at $c_{N_2} = 1\%$ reveal again a phase mixture of ITO and metallic In. The mass fraction of metallic In is 11.8 % and it is higher than in films deposited in a pure Ar atmosphere. The In lattice parameters are $a_0 = 0.32502$ nm and $c_0 = 0.49547$ nm. The lattice

parameter, the same as properties of the films deposited in the pure Ar, are practically identical as for pure In ($a_0 = 0.3252$ nm and $c_0 = 0.49466$ nm) [57]. However, higher nitrogen flows prevent not only from the formation of the crystalline ITO, but also crystalline metallic In. The patterns for films deposited at $c_{N_2} > 4\%$ indicate their amorphous state. Nevertheless, the detection limit of the employed method is about 3 nm particle size, what makes it difficult to clearly confirm the fully amorphous structure of the films and impact of metallic In on their physical properties.

As it is shown in Fig. 3, for all the deposited ITO films phases show lattice parameter higher than for pure In_2O_3 ($a_0 = 1.0117 \text{ nm}$) [58] and $\text{In}_{0.9}\text{Sn}_{0.1}\text{O}_{3.02}$ ($a_0 = 1.0124 \text{ nm}$ and $a_0 = 1.0126 \text{ nm}$ reported by Quaas et al. [58] and by Gonzales et al. [59], respectively). When compared to metallic In, all the investigated ITO films show a defect structure. Changes in the structure of ITO films could be caused by non-equilibrium HiPIMS deposition conditions. The repulsion forces arising from the extra positive charge of the Sn cations cannot explain changes in the lattice parameters [59]. We propose an explanation based on the impact of (i) large compressive stress produced by atoms irregularly built in the hosting structure and (ii) a mechanical interaction between regions (nanocrystals) with different lattice parameters.

Moreover, the $a_0(c_{\text{O}_2})$ shown in Fig. 3 indicates the preferred orientation (the most intensive XRD patterns) in the film. We can observe the evolution of the preferential planes, i.e., (222) for $c_{\text{O}_2} < 0.5 \%$, (400) for $1.0 \% < c_{\text{O}_2} < 7 \%$ and again dominant (222) peak, but highly competing with (440) as the c_{O_2} ratio further increases.

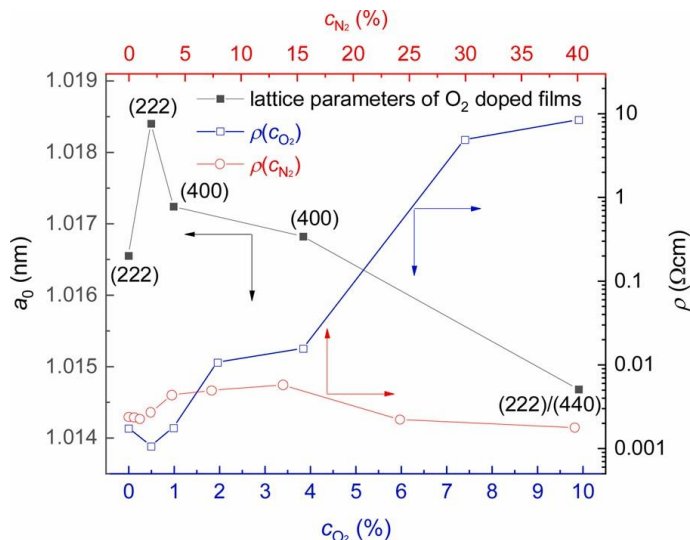


Fig. 3. Evolution of lattice parameter a_0 (left axis) and resistivity $\rho_{\text{N}_2\text{O}_2}$ (right axis) with concentrations of reactive process gases c_{O_2} and c_{N_2} . Different scales for horizontal x-axis related to c_{O_2} (the lower x-axis) and c_{N_2} (the upper x-axis) has been applied. The lattice parameters for films prepared in N_2/Ar are not shown due to their amorphous nature.

The fact that ITO crystallizes in different preferred orientations has not been fully understood yet. However, since the other deposition factors, i.e., substrate temperature, pressure, distance from the magnetron, etc., were kept constant, the observed behavior is attributed to plasma parameters and plasma-substrate interaction. Zhao et al. [60] have shown that (222) orientation is deposited at lower power density while the (400) peak becomes dominant for films deposited at higher power. It could be caused by (i) re-sputtering of the deposited ITO film by impinging energetic species and (ii) mobility of the adatoms on the surface since mobility is strongly influenced by energy delivered to the substrate. At the very beginning of the film formation, nucleation centers with different orientations grow on the substrate surface. Although the (400) orientation is reported as the most resistant against re-sputtering [54] and is more thermodynamically favorable [61] when compared to (222) orientation. Adatoms need to have higher mobility, i.e., energy, to form (400)-oriented nucleus. The (222) orientation of the grains is reported to be dominant at the initial stage of the growth for any deposition conditions. This might be attributed to In metal adatoms aggregating into (111) planes of face-centered tetragonal structure which are very close to (222) planes of ITO bixbite structure [61]. Experiments with low or zero oxygen concentration exhibited lower peak power density, which might reduce the mobility of the adatoms on the surface needed for (400)-oriented growth. However, due to lower incoming energy, the re-sputtering process of (222)-oriented nuclei was limited too. On the contrary, their development was stimulated by the presence of metallic In structures mentioned above. The peak power rises with increasing oxygen concentration what causes: (i) re-sputtering of (222)-oriented grains together with (ii) increased mobility of the adatoms enabling their attachment with thermodynamically favorable (400)-nuclei [60].

Nevertheless, over-saturated oxygen gas mixtures in the deposition process can enhance the oxidation of the metal species impinging the substrate with reduced surface mobility. These deposition conditions were done with increased peak sputtering power - reduced accelerating voltage decreases average kinetic energy of incoming particles, what suppresses the re-sputtering of (222)-oriented crystallization centers and their preferential growth. It can be also expected that a smaller fraction of the delivered oxygen was transformed into reactive form and therefore vibrational states of the

remaining O₂ molecules can contribute significantly to the transfer of heat to the substrate. This assumption is supported by observed both (222) and (440) plane reflections that are typical for annealed ITO films [55]. In this regime, the O₂ molecules may have a similar role as N₂ molecules in the experiments where a small amount of nitrogen was added to the discharge. Finally, the experiments prove that HiPIMS deposition provides a possibility to achieve well-crystalline ITO films without the need for any annealing.

3.2. Electrical and optical properties of ITO films

As shown in Fig. 3, ρ of O₂/Ar prepared films strongly depends on oxygen partial pressure and the profile of the lattice constant. The lowest resistivity ($\rho_{\text{O}_2} = 10^{-3} \Omega\cdot\text{cm}$) was measured for the largest lattices and domains. It is well known that films with large domains exhibit improved conductivity because electron mobility is limited by scattering at the grain boundaries and ionized impurities (Sn-ions in ITO) [62], while increasing oxygen concentration increases ρ due to the formation of stable Sn-O complexes [63]. The same effect was observed for films prepared in the N₂/Ar atmosphere. The lowest ρ was achieved for films deposited in a slightly oxygen-containing atmosphere ($c_{\text{O}_2} = 0.5\%$). However, while ρ is rather gas-composition-independent for low concentrations ($c_{\text{O}_2, \text{N}_2} < 1\%$), it becomes dependent on the composition for higher concentrations of reactive gases. While ρ_{N_2} is more or less constant with the concentration, ρ_{O_2} rises by several orders of magnitude. Lower ITO resistivity of samples prepared at higher nitrogen concentration could be caused by nitrogen creating acceptor levels above the valence band, which increases the concentration of carriers and subsequently also reduces. Low ρ of films deposited in the pure Ar atmosphere, nitrogen admixtures, and low oxygen admixtures (for $c_{\text{O}_2} < 1\%$) can be also influenced by the content of metallic In. It is worth to remind that ρ was measured on as-deposited samples without any post-processing.

For optical sensing purposes of ITO, its optical properties play a crucial role. Hence, n , attenuation coefficient (μ), and transmittance (T) were studied for different c_{O_2} and c_{N_2} . It is well known that the ITO absorbs UV radiation for $\lambda < 350$ nm and it is confirmed by our experiment. The effect corresponds to a fact that ITO is a heavily-doped n-type semiconductor with a rather large

bandgap of about 4.5 eV [64, 65]. Based on ellipsometric data we investigated $\mu(\lambda)$ calculated as $\mu = 4\pi k/\lambda$. The μ at $\lambda = 530$ nm for different gas concentrations was shown in Fig. 4. It must be noted that different scales were applied in the x-axis for c_{O_2} and c_{N_2} . The wavelength was selected specifically for cross-correlation purposes, as it is positioned far enough from the ITO absorption edge and represents the film properties in visible spectral range, where a variety of optical sensors operate. A similar relation between the optical properties of ITO could be observed across the entire useful for optical sensing applications spectral range with minor changes in magnitude. The highest μ values were measured for $c_{N_2} = 2\%$, when ITO is well-crystallized. Generally, the highest decrease in μ was achieved by slight oxygen doping of the process gas ($c_{O_2} = 2\%$). We attribute this effect to more effective crystallization at these conditions. From the point of view of optical properties, sub-stoichiometric films deposited in pure Ar discharge can be significantly improved by slight oxygen doping. In general, a higher concentration of oxygen or nitrogen further improves μ . This finding also corresponds to ρ measurement. The reason behind the absorption drop in the case of the nitrogen addition could be caused by a reduced release of oxygen species from the sputtered material.

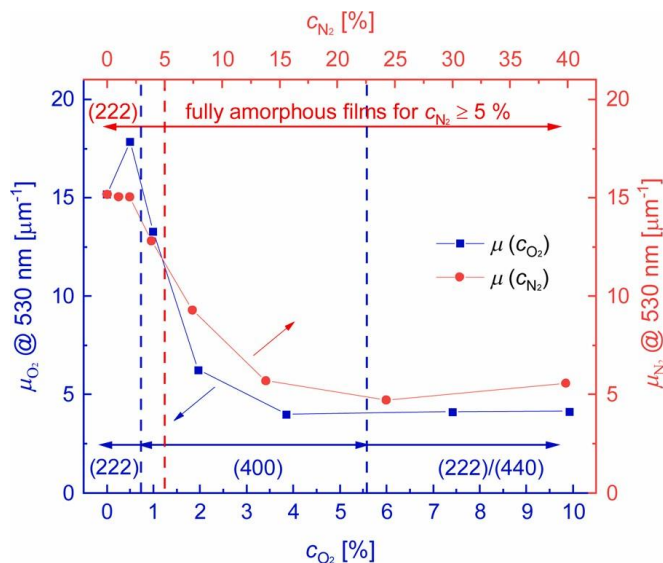


Fig. 4. The dependence of the attenuation coefficient μ on reactive gas concentrations c_{O_2} and c_{N_2} . Different scales for horizontal x-axis related to c_{O_2} (the lower x-axis) and c_{N_2} (the upper x-axis) were applied for comparison. The brackets denote dominant crystal orientation.

3.3. Tailoring ITO film properties for electrochemical sensing

The electrochemical response of ITO films deposited on glass slides is discussed in this section. In all the electrochemical measurements, 1,1'-Ferrocenedimethanol was used as an outer-sphere redox system due to the solubility in aqua solution and lack of its adsorption to the electrode during the electrochemical process [66, 67]. Additionally, these redox species undergoes fast reactions at the ITO electrode [68].

The CVs for selected ITO films prepared at c_{O_2} up to 10 % and used as a working electrode are shown in Fig. 5. The redox reactions of 1,1'-Ferrocenedimethanol are observed in all the measurements as two well-defined current peaks. The shapes of the CVs prove that all the electrodes exhibited high reversibility of the redox reaction. The potential separation between anodic (I_{pa}) and cathodic peak current (I_{pc}) noted as ΔE for the ITO electrode prepared at $c_{O_2} = 0\%$ is equal to 149 mV and the current ratio (I_{pa}/I_{pc}) is near to 1. These results suggest a single electron quasi-reversible electrochemical redox process [69]. It is worth noting that the ΔE initially slightly decreases and further increases with c_{O_2} , i.e., ΔE is equal to 119 mV, 103 mV, and 173 mV for $c_{O_2} = 1\%$, 4%, and 10%, respectively. This phenomenon indicates that electron transfer is disturbed less for the films obtained at c_{O_2} reaching 1–4%. Subsequently, for the samples prepared in the O_2 enriched atmosphere $c_{O_2} > 4\%$, the noticeable changes are observed in the shapes of the obtained voltammograms for the negative potential, what is probably associated with increased capacity of the electrode and its worse electrochemical sensing performance.

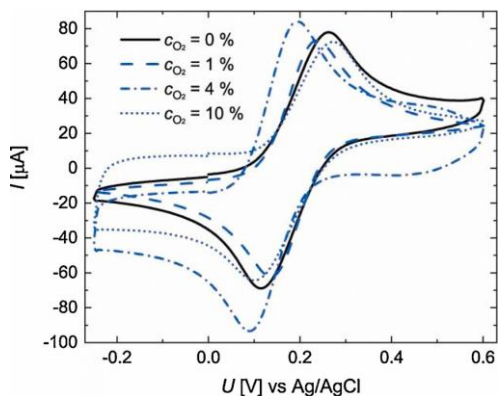


Fig. 5. Cyclic voltammograms at scan rate 100 mV/s for measurements in 1 mM 1,1'-Ferrocenedimethanol in 0.1 M KCl for ITO-coated glass slides received at different gas concentrations.

The effect of the reactive gas doping, i.e., c_{O_2} and c_{N_2} , on the electrochemical response has been compared in Fig. 6. A similar trend as for c_{O_2} has also been observed in the case of nitrogen doping. For small c_{N_2} a slight improvement of ΔE occurs, most probably due to improved crystallinity, was observed that was followed by an increase of $\Delta E \approx 600$ mV for $c_{N_2} > 5\%$ when the ITO structure becomes amorphous. The obtained data indicate a strong correlation of the ΔE and the crystallinity, i.e., films with well-pronounced crystallinity reach $\Delta E \approx 100 - 200$ mV for both the gases, what is comparable or lower than values obtained for ITO electrodes prepared at similar conditions, but using RF sputtering instead of HiPIMS [29]. In the case of the oxygen doping, a slight increase of ΔE apparently follows the trend for ρ (Fig. 3). However, ρ shows a minor impact, when compared with the effect of the crystallinity. Hence, the results revealed that rather the crystallography than ρ determines $\Delta E(c_{O_2}, c_{N_2})$. Since for electrochemical sensing applications, ΔE should be as low as possible, the selection of low concentration of the doping gases (up to 4%) is preferred.

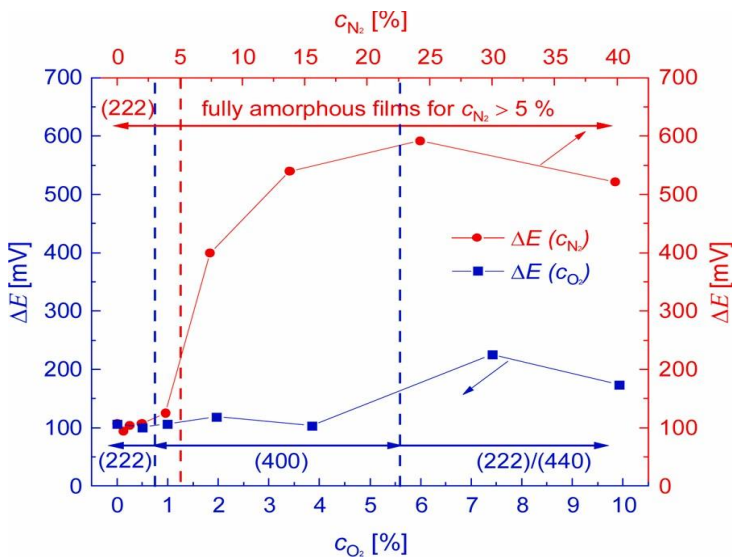


Fig. 6. Evolution of the current peak separation with the concentration of the reactive gases $\Delta E(c_{O_2}, c_{N_2})$. Different scales for horizontal x-axis related to c_{O_2} (the lower x-axis) and c_{N_2} (the upper x-axis) were applied for comparison. The brackets denote crystalline orientation.

3.4. Tailoring ITO film properties towards applications in optical sensing

In this section, we discuss the impact of optical properties of the films on the optical response of an optical sensor using a LMR optical fiber device. For receiving LMR and its sensing applications both optical properties of the film, as well as its thickness, are crucial. Thus, the selected sensing platform can be treated as suitable for discussing general optical sensing applications of the ITO films, especially where those for RI or biosensing are concerned. In the previous section, the ITO film characterization was carried out on planar Si or glass samples where the films for comparison purposes had nearly the same thickness regardless on the deposition conditions. The LMR response was measured for optical fiber devices coated exactly in the same deposition conditions as planar samples, but with a different thickness that is required for receiving LMR response in a specific spectral range. Fiber rotational assembly, as shown in Fig. 1(b), allowed for depositing homogeneous ITO films on a fused silica fiber core. Since the deposition conditions were kept the same, we assume here similar properties of the films on a planar substrate and the fiber surface.

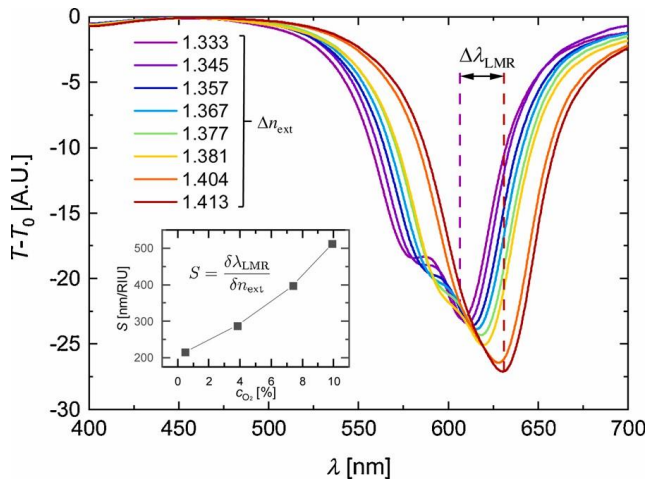


Fig. 7. Evolution of LMR response caused by a change of the external RI for the ITO-LMR sensor prepared at $c_{O_2} = 4\%$. Inset shows RI sensitivity for sensors received at different c_{O_2} .

The thickness of the films on each fiber was optimized to observe a well-pronounced LMR in the wavelength range between 550 and 600 nm when the sensor was surrounded by air. We are aware that the sensors would be more

sensitive when the resonance was positioned at longer wavelengths. The reason behind the resonance positioning in this range was to keep the response in the operation range of the applied spectrometer and light source for the whole range of the n_{ext} . Moreover, to maintain the high sensitivity of the sensor, the lower order of LMR should be traced, and those appear for lower thicknesses of the overlays [5]. For this reason, we continued the deposition only up to the point when the LMR was well pronounced. The RI sensitivity was estimated as $S = \delta\lambda_{\text{LMR}}/\delta n_{\text{ext}}$, where λ_{LMR} denotes as resonance wavelength corresponding to a minimum in the T (Fig. 7). The method of measurement has been described elsewhere [70, 34]. For the purpose of this work, the sensitivity was determined in the n_{ext} range of 1.357–1.404 RIU.

In Fig. 7 is shown the shift of LMR response with n_{ext} for the fiber coated with ITO at $c_{\text{O}_2} = 4\%$. It is worth noting that for sensors prepared in pure Ar or N_2/Ar with low c_{N_2} no LMR effect was observed and for those sensors prepared at high c_{N_2} relatively low sensitivity (193 to 314 nm/RIU for $c_{\text{N}_2} = 4\%$ and $c_{\text{N}_2} = 24\%$, respectively) was reached when compared to those achieved for ITO deposited at higher c_{O_2} . Such sensitivity is comparable to that measured for RF sputtered ITO [70]. That is why in this discussion we will focus more on oxygen- than nitrogen-doped films. The inset in Fig. 7 shows the RI sensitivity of the ITO-LMR sensor received for different c_{O_2} . The sensitivity increases with the concentration of oxygen in the discharge up to 513 nm/RIU (for $c_{\text{O}_2} = 10\%$), which is noticeably higher than in the case of applied conventional RF sputtering [70], where the films are typically amorphous if not annealed [41].

In Fig. 8(a) can be seen that the resonance depth is the highest for discharges with a low amount of oxygen, and becomes lower with increasing oxygen concentration in the discharge. Hence, the LMR depth is inversely proportional to the oxygen concentration. The depth can be mostly correlated with k of the film. Fig. 8(b) presents the dispersion relation for n and k measured on flat substrates corresponding by their deposition conditions to the sensors presented in Fig. 8(a). The comparison indicates that higher oxygen flows induce a reduction in k (comparable to relation for μ in Fig. 4) what makes the resonance shallower [5]. In other words, for the formation of deep LMR only slightly absorbing film with a high n are expected. A different

character of the LMRs in the case of samples prepared at $c_{O_2} > 0.5\%$ is caused also by different n and k . Both the optical parameters tend to decrease with c_{O_2} , while the RI sensitivity increases from 216 nm/RIU to 513 nm/RIU for $c_{O_2} = 0.5\%$ to $c_{O_2} = 10\%$, respectively (see inset in Fig. 7). To identify the reasons for the increase in the sensitivity, profilometry and in situ quartz crystal microbalance measurements were used to estimate the deposition rates. These were roughly the same regardless on the oxygen concentration in the discharge. However, due to a decrease in n with c_{O_2} , to obtain the well-visible LMR the deposition time had to be gradually increased, so that it was almost two times longer for deposition at $c_{O_2} = 10\%$ than at $c_{O_2} = 0.5\%$. Therefore, we attribute the increasing RI sensitivity of the sensors prepared in the oxygen-enriched atmosphere to the increasing thickness of the ITO films [5]. It must be noted that the nitrogen-enriched mixtures result in very well-pronounced LMR too, but for the concentration significantly higher than for doping with oxygen (Fig. 8). However, their sensitivity is rather low (193 nm/RIU for $c_{N_2} = 4\%$) comparing to those shown in Fig. 7, where the one for c_{O_2} is concerned. The fact that for samples prepared without oxygen or with a low concentration of nitrogen no LMR is observed suggests that the obtained samples with higher k are close to the edge of the properties acceptable for LMR at these experimental conditions (Fig. 4) [71]. For this reason, even a small change of deposition parameters can influence the LMR properties dramatically.

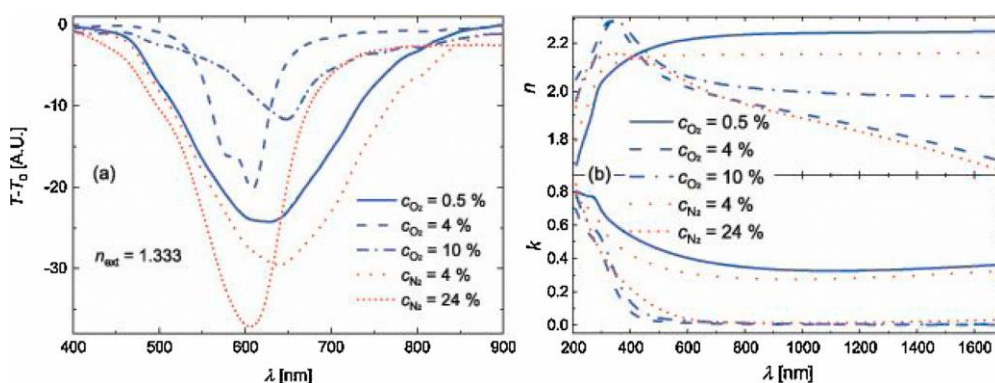


Fig. 8. (a) LMR spectrum for optical fiber sensors coated at different gas composition when immersed in water, and (b) corresponding refractive indices and extinction coefficients of the ITO films deposited at the same conditions on flat substrates.

3.5. ITO for optical and electrochemical label-free biosensing

Detection of the pathogen (*Borrelia burgdorferi*) was carried out to demonstrate the advantages of detailed material research of electrochemically-active LMR sensor surfaces. Simultaneous, dual-domain optical and electrochemical measurements were conducted in the same analytes to prove the concept of cross-verification in the detection procedure. For this part of the experiment, we prepared a batch of ITO-LMR sensors with ITO properties tailored by plasma procedure to obtain well-pronounced electrochemical activity and optical response corresponding the results received at $c_{O_2} = 4 \%$.

When it comes to detection of, e.g., pathogens, it is possible inter alia, indirectly through the presence of antibodies synthesized in a body during an infection. In this case, sandwich immunoassays are one of the most frequently applied. Two antibodies (primary and secondary) synthesized against *Borrelia burgdorferi* have been utilized as a receptor and specific target, respectively. Primary antibodies were covalently immobilized to the ITO-LMR surface (see Section 2.2) through the silanization process. Next, they were captured/recognized by secondary antibodies in the following step of the experiments. These, in turn, allowed to verify the ability of the ITO-LMR for label-free sensing and to estimate the sensitivity of the platform. Thanks to the optimized ITO properties, during the experiment both EC and optical measurements were performed.

First, it must be noted that the ITO-LMR sensors investigated here reveal slightly different EC performance versus that achieved for flat reference samples shown in Fig. 5. Only investigated in Section 3.3 flat substrates allowed for correlating EC and optical properties of ITO, where later were measured using spectroscopic ellipsometry, which is not suitable for analysis of the thin film properties on other than flat substrates. Possible differences between properties of ITO films deposited on the flat and circular substrate at the same deposition conditions have already been reported in [29] for ITO electrodes deposited using RF sputtering. The differences were attributed to the sample shape disturbing discharge resulting in a partially non-stoichiometric composition of deposited films [72]. For such ITO, charge transfer caused by local charge blocking barriers is less effective [73].

However, the difference between the EC performance is not crucial for the ITO biofunctionalization and the final detection of pathogens. For the fiber sample a decrease of anodic and cathodic peak currents that indicate successful silanization of the surface but also a partial limitation of its electrochemical activity (Fig. 9(a)). It must be noted that the applied surface modification offers important advantages – it is an easy, one-step reaction, thus does not need any additional activation. However, the shortage of the reaction time (4 h), thus, control over the thickness of the silane layer, is always at the expense of its quality and stability. Therefore, it is recommended to carry out the reaction for 4 h [52].

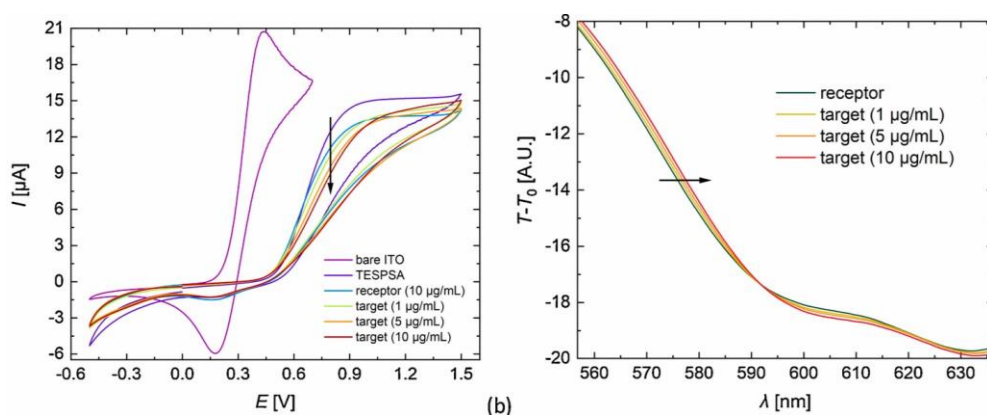


Fig. 9. EC and optical responses of ITO-LMR sensors recorded after each incubation step during process of *Borrelia burgdorferi* receptor-target interactions, (a) shows CV recorded at scan rate 20 mV/s in 1,1'-Ferrocenedimethanol and (b) optical spectra acquired in PBS.

Fig. 9(b) shows, in turn, the evolution of the optical spectra at each step of the experiment. The shift towards longer wavelengths (indicated by the black arrow) corresponds to an increase of the thickness of the biological layer on the functionalized ITO-LMR's surface, additionally confirming the electrochemical results. Next, both optical and EC responses followed the antibody-antibody interaction. When target antibody concentration increases, a decrease in current and increase in LMR wavelength shift were recorded in the EC and optical domain, respectively, proving binding of the antibodies to the sensor's surface. It can be also noted that measurements in the EC domain are effective when interactions at the sensor surface take place, while optical measurements may deliver information about events taking place slightly away from the surface. Notwithstanding, the changes after further steps of the

experiment, such as increasing ΔE , are still clear and indicate binding of the receptor and different concentrations of the target. It is worth to mention that the difference between the initial ΔE described in the paper and here is a result of lower scan rate (20 vs. 100 mV/s). The rate has to be reduced due to time required for simultaneous acquisition of the optical data.

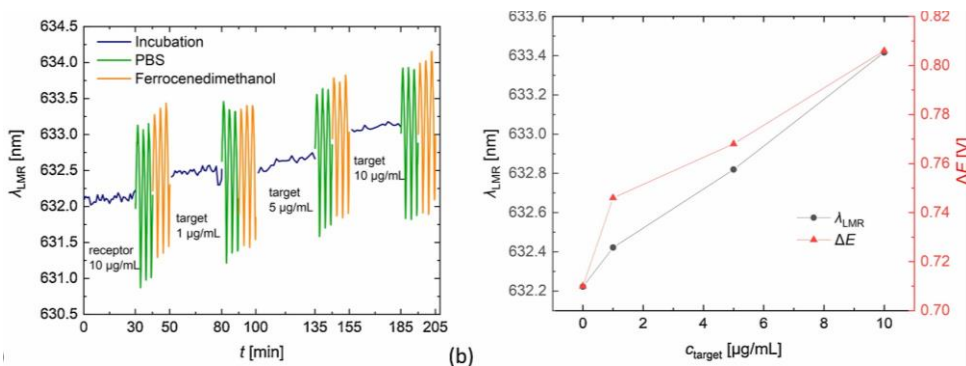


Fig. 10. (a) Sensogram for the ITO-LMR biosensing experiment and (b) comparison of ITO-LMR wavelength and ΔE shift at each step of *Borrelia burgdorferi* receptor-target interaction experiment. Oscillations seen in (a) correspond to the cycling potential.

Fig. 10(a) presents the evolution of λ_{LMR} during the whole experiment. Oscillations observed in PBS and 1,1'-Ferrocenedimethanol at the stages corresponding to CV measurements are low in magnitude when compared to reported previously in [34]. The limited influence of the applied E corresponds to higher doping of ITO investigated in this work. When the material is highly doped, a shallow charge accumulation layer is formed, and the modulation of the RI of ITO is low comparing to materials with low carriers concentration [29]. Moreover, a clear shift of the LMR wavelength towards longer wavelengths at the incubation stages and for an increase in target concentration can be seen. It can be seen in Fig. 10(b) that the trend for both electrochemical and optical measurements is very similar, thus we cross-verify the biosensing experiments. This is evidence that the tuning of the properties makes the verification possible.

In general, dual-domain sensing designs allow to increase the reliability of the measurements or/and extend the measurement range, as revealed in other works reporting protein detection achieved by means of electrochemical surface plasmon resonance [74], electrochemical optical waveguide [75], or electrophotonic silicon biosensing [76]. None of these dual-domain sensors

have used the same receptor-target scheme, which is an immunoassay sandwich for antibody-antibody interactions detection. Thus, the direct comparison of these detection approaches is limited. Moreover, it must be emphasized that both high-performance EC [29] along with LMR [34] responses have not been achieved for non-optimized/un-doped ITO-based structures. Presented here results prove that crucial role of tailoring ITO properties for simultaneous optical and EC biosensing.

4. CONCLUSION

In this work, we have shown a comprehensive study on ITO film properties crucial for their application in combined optical and electrochemical sensing systems. For ITO deposition, we used high power pulse magnetron sputtering (HiPIMS) where high-quality films can be deposited in a single-step process. The applied approach does not require any post-processing, such as high-temperature annealing, which is typically needed when other deposition techniques are used. Application of other deposition methods requiring post-processing would possibly make it difficult to draw direct conclusions on the relation between deposition process parameters and properties of the films. Our experiments have shown that by tuning gas composition in the sputtering chamber it is possible to control the preferred crystal orientation of the films and both their electrical and optical properties. We have found that it is necessary to slightly enrich the deposition atmosphere by oxygen to reach fully oxidized and stoichiometric ITO. Moreover, on top of ITO resistivity, crystallinity mainly influences the electrochemical activity of ITO. We have observed that well-crystalline films exhibit excellent electrochemical properties. The optical properties of ITO are highly influenced by gas composition too. Low concentration of oxygen or nitrogen results in receiving films showing high refractive index and extinction coefficient in the visible and near-infrared spectral range. Both the parameters decrease with the concentration of the gases (investigated up to 10 % and 40 % for oxygen and nitrogen, respectively), where for the concentration of oxygen reaching 4% the extinction coefficient is low as it is expected by the majority of optical applications. Later, we have shown one of the applications - a lossy-mode resonance (LMR) obtained using the ITO-coated optical fibers. The most suitable LMR conditions were found for the relatively low extinction coefficient where the resonances are well-defined as expected for sensing

applications of the device. The refractive index sensitivity, which is crucial for chemical and biochemical label-free sensing applications of the sensors, increases with the concentration of the two gases, but the application of oxygen was found to be more effective than nitrogen.

To summarize, both electrochemical and optical interrogations of ITO-coated sensors can be simultaneously achieved when HiPIMS deposition is applied. Highly crystalline films are expected for electrochemical applications, and those can be obtained at low concentrations (below 5 %) of oxygen or nitrogen in the sputtering atmosphere. However, properties expected for optical applications get more attractive with an increase in the concentration of the gasses. For these conditions optical absorption of the films decreases, especially in the case of oxygen admixtures, when the structure becomes amorphous. Thus, as identified in this work there is a narrow range of ITO film properties, where the films can be simultaneously applied in a wide selection of combined label-free optical and electrochemical sensors, including biosensors with enhanced functionalities.

Acknowledgment

The work was financially supported in the Czech Republic through the project of Czech Science Foundation GACR19-21068S and by Operational Programme Research, Development and Education financed by European Structural and Investment Funds and the Czech Ministry of Education, Youth and Sports, partner network CZ.02.1.01/0.0/0.0/17049/0008422, as well as in Poland partly by the National Center for Research and Development (NCBiR) under grant No. 347324/12/NCBR/2017, Materials Technologies project granted by Warsaw University of Technology under the program Excellence Initiative: Research University (ID-UB), and the National Agency for Academic Exchange (NAWA) under grant No. PPN/BIL/2018/1/00126. P. Sezemsky acknowledges the support of University of South Bohemia grant agency by GAJU 110/2020/P project. Authors acknowledge prof. Jan Sterba and his research group for delivering biological material for the biosensing experiment.

References

- [1] D. Krohn, T. MacDouglas, A. Mendez, *Fibre Optics Sensor: Fundamentals and Applications*, 4th ed., SPIE PRESS, Washington, USA, 2014.
- [2] S. Yin, P.B. Ruffin, F.T.S. Yu (Eds.), *Fiber Optic Sensors*, 2nd ed., CRC press, New York, USA, 2008.
- [3] S.P. Usha, A.M. Shrivastav, B.D. Gupta, Semiconductor metal oxide/polymer based Fiber optic lossy mode resonance sensors: a contemporary study, *Opt. Fib. Technol.* 45 (2018) 146–166.
- [4] F. Chiavaioli, P. Zubiato, I. Del Villar, C.R. Zamarreno, A. Giannetti, S. Tombelli, C. Trono, F.J. Arregui, I.R. Matias, F. Baldini, Femtomolar detection by nanocoated fiber label-free biosensors, *ACS Sens.* 3 (5) (2018) 936–943.
- [5] I. Del Villar, M. Hernaez, C.R. Zamarreno, P. Sanchez, C. Fernandez-Valdivielso, F. J. Arregui, I.R. Matias, Design rules for lossy mode resonance based sensors, *Appl. Opt.* 51 (19) (2012) 4298–4307.
- [6] N. Paliwal, J. John, Lossy mode resonance based fiber optic sensors, in: I.R. Matias, S. Ikezawa, J. Corres (Eds.), *Fiber Optic Sensors: Current Status and Future Possibilities*, Vol. 21, Springer International Publishing, Switzerland, 2017.
- [7] F. Arregui, I. J.; Del Villar, C.R. Zamarreno, P. Zubiato, I.R. Matias, Giant sensitivity of optical Fiber sensors by means of lossy mode resonance, *Sens. Actuat. B* 232 (2016) 660–665.
- [8] M. Marciniak, J. Grzegorzewski, M. Szustakowski, Analysis of lossy mode cutoff conditions in Planar Wave-Guides with semiconductor guiding layer, *IEE Pro.-J. Optoelectron.* 140 (4) (1993) 247–252.
- [9] A. Andreev, B. Pantchev, P. Danesh, B. Zafirova, E. Karakoleva, E. Vlaikova, E. Alipieva, A refractometric sensor using index-sensitive mode resonance between single-mode Fiber and thin film amorphous silicon waveguide, *Sens. Actuat. B* 106 (1) (2005) 484–488.
- [10] J. Ascorbe, J.M. Corres, I.R. Matias, F.J. Arregui, High sensitivity humidity sensor based on cladding-etched optical Fiber and lossy mode resonances, *Sens. Actuat. B* 233 (2016) 7–16.
- [11] G. Korotcenkov, Metal oxides for solid-state gas sensors: what determines our choice? *Mater. Sci. Eng. B* 139 (1) (2007) 1–23.
- [12] S.P. Usha, B.D. Gupta, Performance analysis of zinc oxide-implemented lossy mode resonance-based optical Fiber refractive index sensor utilizing thin Film/ Nanostructure, *Appl. Opt.* 56 (20) (2017) 5716–5725.
- [13] M. Hernaez, I. Del Villar, C.R. Zamarr̃eo, F.J. Arregui, I.R. Matias, Optical Fiber refractometers based on lossy mode resonances supported by TiO₂ coatings, *Appl. Opt.* 49 (20) (2010) 3980–3985.

- [14] D. Burnat, M. Koba, Ł. Wachnicki, S. Gierałowska, M. Godlewski, M. Smietana, Refractive index sensitivity of optical fiber lossy-mode resonance sensors based on atomic layer deposited TiO_x thin overlay, in: E. Lewis (Ed.), Sixth European Workshop on Optical Fibre Sensors, Proceedings of 6th European Workshop on Optical Fibre Sensors, Univ. Limerick, Limerick, Ireland, May 31-Jun 03, SPIE-INT SOC Optical Engineering: Bellingham, USA, 2016; 99161G, 2016.
- [15] M. Smietana, M. Dudek, M. Koba, B. Michalak, Influence of diamond-like carbon overlay properties on refractive index sensitivity of nano-coated optical fibres, *Phys. Status Solidi A* 210 (10) (2013) 2100–2105.
- [16] B. Michalak, M. Koba, M. Smietana, Silicon nitride overlays deposited on optical fibers with RF PECVD method for sensing applications: overlay uniformity aspects, *Acta Phys. Pol. A* 127 (6) (2015) 1587–1590.
- [17] K. Kosiol, M. Koba, M. Masiewicz, M. Smietana, Tailoring properties of lossy-mode resonance optical Fiber sensors with atomic layer deposition technique, *Opt. Laser Technol.* 102 (2018) 213–221.
- [18] C.R. Zamarreno, P. Zubiarte, M. Sagües, I.R. Matias, F.J. Arregui, Experimental demonstration of lossy mode resonance generation for transverse-magnetic and transverse-electric polarizations, *Opt. Lett.* 38 (14) (2013) 2481–2483.
- [19] P.J. Rivero, A. Urrutia, J. Goicoechea, F.J. Arregui, Optical Fiber humidity sensors based on localized surface plasmon resonance (LSPR) and lossy-mode resonance (LMR) in overlays loaded with silver nanoparticles, *Sens. Actuat. B* 173 (2012) 244–249.
- [20] I. Del Villar, C.R. Zamarreno, M. Hernaez, F.J. Arregui, I.R. Matias, Lossy mode resonance generation with indium-tin-Oxide-Coated optical fibers for sensing applications, *J. Light. Technol.* 28 (1) (2010) 111–117.
- [21] T. Minami, Transparent conducting oxide semiconductors for transparent electrodes, *Semicond. Sci. Technol.* 20 (4) (2005) S35–S44.
- [22] A. Socorro, I. B.; Del Villar, J.M. Corres, F.J. Arregui, I.R. Matias, Spectral width reduction in lossy mode resonance-based sensors by means of tapered optical fibre structures, *Sens. Actuators B Chem.* 200 (2014) 53–60.
- [23] L. Razquin, C.R. Zamarreno, F.J. Munoz, I.R. Matias, F.J. Arregui, Thrombin detection by means of an aptamer based sensitive coating fabricated onto LMR-based optical fiber refractometer, in: 2012 IEEE Sens. Proc., Proceedings of the 11th IEEE Sensors Conference, Taipei, TAIWAN, OCT 28-31, IEEE: New York, USA, 2012, 2012, pp. 1104–1107.

-
- [24] J. George, C.S. Menon, Electrical and optical properties of Electron beam evaporated ITO thin films, *Surf. Coat. Technol.* 132 (1) (2000) 45–48.
- [25] J.H. Kim, T.Y. Seong, K.J. Ahn, K.B. Chung, H.J. Seok, H.J. Seo, H.K. Kim, The effects of film thickness on the electrical, optical, and structural properties of cylindrical, rotating, magnetron-sputtered ITO films, *App. Surf. Sci.* 440 (2018) 1211–1218.
- [26] H. Hillebrandt, M. Tanaka, Electrochemical characterization of self-assembled alkylsiloxane monolayers on indium-tin oxide (ITO) semiconductor electrodes, *J. Phys. Chem. B* 105 (19) (2001) 4270–4276.
- [27] X. Jiang, L. Zhang, S.J. Dong, Assemble of poly(Aniline-Co-O-Aminobenzenesulfonic acid) three-dimensional tubal net-works onto ITO electrode and its application for the direct electrochemistry and electrocatalytic behavior of cytochrome C, *Electrochem. Commun.* 8 (7) (2006) 1137–1141.
- [28] S.D. Branch, A.M. Lines, J. Lynch, J.M. Bello, W.R. Heineman, S.A. Bryan, Optically transparent thin-film electrode chip for spectroelectrochemical sensing, *Anal. Chem.* 89 (14) (2017) 7324–7332.
- [29] P. Niedziałkowski, W. Białobrzaska, D. Burnat, P. Sezemsky, V. Stranak, H. Wulff, T. Ossowski, R. Bogdanowicz, M. Koba, M. Smietana, Electrochemical performance of indium-tin-oxide-coated lossy-mode resonance optical fiber sensor, *Sens. Actuators B* 301 (2019), 127043.
- [30] M. Sobaszek, D. Burnat, P. Sezemsky, V. Stranak, R. Bogdanowicz, M. Koba, K. Siuzdak, M. Smietana, Enhancing electrochemical properties of an ITO-Coated lossy-mode resonance optical Fiber sensor by electrodeposition of PEDOT:PSS, *Opt. Mat. Express* 9 (7) (2019) 3069–3078.
- [31] M. Smietana, M. Sobaszek, B. Michalak, P. Niedziałkowski, W. Białobrzaska, M. Koba, P. Sezemsky, V. Stranak, J. Karczewski, T. Ossowski, et al., Optical monitoring of electrochemical processes with ITO-Based lossy-mode resonance optical Fiber sensor applied as an electrode, *J. Lightwave Technol.* 36 (4) (2018) 954–960.
- [32] M. Janik, P. Niedziałkowski, K. Lechowicz, M. Koba, P. Sezemsky, V. Stranak, T. Ossowski, M. Smietana, Electrochemically directed biofunctionalization of lossy-mode resonance optical fiber sensor, *Opt. Express* 28 (11) (2020) 15934–15942. [33] R. Bogdanowicz, P. Niedziałkowski, M. Sobaszek, D. Burnat, W. Białobrzaska, Z. Cebula, P. Sezemsky, M. Koba, V. Stranak, T. Ossowski, et al., Optical detection of ketoprofen by its electropolymerization on an indium tin oxide-coated optical Fiber probe, *Sensors* 18 (5) (2018) 1361.
-

- [34] M. Smietana, M. Koba, P. Sezemsky, K. Szot-Karpinska, D. Burnat, V. Stranak, J. Niedziolka-Jonsson, R. Bogdanowicz, Simultaneous optical and electrochemical label-free biosensing with ITO-Coated lossy-mode resonance sensor, *Biosens. Bioelectron.* 154 (2020), 112050.
- [35] A.T. Andreev, B.S. Zafirova, E.I. Karakoleva, A.O. Dikovska, P.A. Atanasov, Highly sensitive refractometers based on a side-polished single-mode fibre coupled with a metal oxide thin-film planar waveguide, *J. Opt. A Pure Appl. Opt.* 10 (3) (2008), 035303.
- [36] S.P. Usha, A.M. Shrivastav, B.D. Gupta, A contemporary approach for design and characterization of fiber-optic-Cortisol sensor tailoring LMR and ZnO/PPY molecularly imprinted film, *Biosens. Bioelectron.* 87 (2017) 178–186.
- [37] I. Del Villar, C.R. Zamarreno, P. Sanchez, M. Hernaez, C.F. Valdivielso, F. J. Arregui, I.R. Matias, Generation of lossy mode resonances by deposition of High- Refractive-Index Coatings on Uncladded Multimode Optical Fibers, *J. Opt.* 12 (9) (2010), 095503.
- [38] A. Ozcariz, C.R. Zamarreno, P. Zubiate, F.J. Arregui, Is there a frontier in sensitivity with lossy mode resonance (LMR) based refractometers? *Sci. Rep.* 7 (2017) 10280. [39] I. Del Villar, C.R. Zamarreno, M. Hernaez, P. Sanchez, F.J. Arregui, I.R. Matias, Generation of surface plasmon resonance and lossy mode resonance by thermal treatment of ITO thin-films, *Opt. Laser Technol.* 69 (2015) 1–7.
- [40] X.S. Yin, W. Tang, X.L. Weng, L.J. Deng, Surface morphology modelling for the resistivity analysis of low temperature sputtered indium tin oxide thin films on polymer substrates, *J. Phys. D-Appl. Phys.* 42 (22) (2009), 225304.
- [41] D. Kim, Improvement of structural and optoelectrical properties by post-deposition Electron beam annealing of ITO thin films, *Renew. Energy* 36 (2) (2011) 525–528.
- [42] B. He, H.Z. Wang, Y.G. Li, Z.Q. Ma, J. Xu, Q.H. Zhang, C.R. Wang, H.Z. Xing, L. Zhao, D.D. Wang, Fabrication and characterization of amorphous ITO/p-Si heterojunction solar cell, *Sci. China-Technol. Sci.* 56 (8) (2013) 1870–1876. [43] V. Stranak, R. Bogdanowicz, P. Sezemsky, H. Wulff, A. Kruth, M. Smietana, J. Kratochvil, M. Cada, Z. Hubicka, Towards high quality ITO coatings: the impact of nitrogen admixture in HiPIMS discharges, *Surf. Coat. Technol.* 335 (2018) 126–133.
- [44] K. Ellmer, T. Welzel, Reactive magnetron sputtering of transparent conductive oxide thin films: role of energetic particle (Ion) bombardment, *J. Mater. Res.* 27 (5) (2012) 765–779.

-
- [45] J.T. Gudmundsson, N. Brenning, D. Lundin, U. Helmersson, High power impulse magnetron sputtering discharge, *J. Vac. Sci. Technol. A* 30 (3) (2012), 030801.
- [46] N. Britun, T. Minea, S. Konstantinidis, R. Snyders, Plasma diagnostics for understanding the plasma-surface interaction in HiPIMS discharges: a review, *J. Phys. D Appl. Phys.* 47 (22) (2014), 224001.
- [47] V. Stranak, A.P. Herrendorf, S. Drache, M. Cada, Z. Hubicka, M. Tichy, R. Hippler, Highly ionized physical vapor deposition plasma source working at very low pressure, *Appl. Phys. Lett.* 100 (14) (2012), 141604.
- [48] B. Finke, M. Polak, F. Hempel, H. Rebl, C. Zietz, V. Stranak, G. Lukowski, R. Hippler, R. Bader, J.B. Nebe, et al., Antimicrobial potential of copper-containing titanium surfaces generated by ion implantation and dual high power impulse magnetron sputtering, *Adv. Eng. Mat.* 14 (5) (2012) B224–B230.
- [49] H. Wulff, H. Steffen, Characterization of thin films, in: 2nd, in: R. Hippler, H. Kersten, M. Schmidt, K.H. Schoenbach (Eds.), *Low Temperature Plasmas*, Vol. 1, Wiley-VCH, Berlin, Germany, 2008, pp. 375–408.
- [50] F.M. Smits, Measurement of sheet resistivities with the 4-Point probe, *Bell Syst. Tech. J.* 37 (3) (1958) 711–718.
- [51] E. Hecht, *Optics*, 4th ed., Addison Wesley, San Francisco, USA, 2002.
- [52] A. Gang, G. Gabernet, L.D. Renner, L. Baraban, G. Cuniberti, A simple two-step silane-based (bio-) receptor molecule immobilization without additional binding site passivation, *RSC Adv.* 5 (2015) 35631–35634.
- [53] M. Janczuk-Richter, B. Gromadzka, Ł. Richter, M. Panasiuk, K. Zimmer, P. Mikulic, W.J. Bock, S. Maćkowski, M. Smietana, J. Niedźwiedź, "Immuno-sensor" based on long-period Fiber gratings for detection of viruses causing gastroenteritis, *Sensors* 20 (2020) 813.
- [54] E. Terzini, P. Thilakan, C. Minarini, Properties of ITO thin films deposited by RF magnetron sputtering at elevated substrate temperature, *Mat. Sci. Engin. B* 77 (1) (2000) 110–114.
- [55] S.D. Senol, A. Senol, O. Ozturk, M. Erdem, Effect of annealing time on the structural, optical and electrical characteristics of DC sputtered ITO thin films, *J. Mat. Sci.: Mat. in Elect.* 25 (11) (2014) 4992–4999.
- [56] S. Kment, P. Kluson, Z. Hubicka, J. Krysa, M. Cada, I. Gregora, A. Deyneka, Z. Remes, H. Zabova, L. Jastrabik, Double hollow cathode plasma jet-low temperature method for the TiO₂-xN_x photoresponding films, *Electrochim. Acta* 55 (5) (2010) 1548–1556.
-

- [57] M. Wolcyrz, R. Kubiak, S. Maciejewski, X-ray-Investigation of thermal-expansion and atomic thermal vibrations of tin, indium, and their alloys, *Physica Status Solidi B-Basic Res.* 107 (1) (1981) 245–253.
- [58] M. Quaas, C. Eggs, H. Wulff, Structural studies of ITO thin films with the rietveld method, *Thin Solid Films* 332 (1–2) (1998) 277–281.
- [59] G.B. Gonzalez, J.B. Cohen, J.H. Hwang, T.O. Mason, J.P. Hodges, J.D. Jorgensen, Neutron diffraction study on the defect structure of indium-tin-Oxide, *J. Appl. Phys.* 89 (5) (2001) 2550–2555.
- [60] L. Zhao, Z. Zhou, H. Peng, R. Cui, Indium tin oxide thin films by Bias magnetron RF sputtering for heterojunction solar cells application, *Appl. Surf. Sci.* 252 (2) (2005) 385–392.
- [61] Y.S. Jung, S.S. Lee, Development of indium tin oxide film texture during DC magnetron sputtering deposition, *J. Cryst. Growth* 259 (4) (2003) 343–351.
- [62] K.S. Tseng, Y.L. Lo, Effect of sputtering parameters on optical and electrical properties of ITO films on PET substrates, *Appl. Surf. Sci.* 285 (2013) 157–166.
- [63] G. Frank, H. Kostlin, Electrical-properties and defect model of tin-doped indium oxide layers, *Appl. Phys. A Mat. Sci. Proc.* 27 (4) (1982) 197–206.
- [64] M. Huang, Z. Hameiri, A.G. Aberle, T. Mueller, Influence of discharge power and annealing temperature on the properties of indium tin oxide thin films prepared by Pulsed-DC magnetron sputtering, *Vacuum* 121 (2015) 187–193.
- [65] A. Sytchkova, D. Zola, L.R. Bailey, B. Mackenzie, G. Proudfoot, M. Tian, A. Ulyashin, Depth dependent properties of ITO thin films grown by pulsed DC sputtering, *Mater. Sci. Eng. B.* 178 (9) (2013) 586–592.
- [66] R.L. McCreery, Advanced carbon electrode materials for molecular electrochemistry, *Chem. Rev.* 108 (7) (2008) 2646–2687.
- [67] N. Kurapati, P. Pathirathna, Ch.J. Ziegler, S. Amemiya, Adsorption and electron-transfer mechanisms of ferrocene carboxylates and sulfonates at highly oriented pyrolytic graphite, *ChemElectroChem* 6 (22) (2019) 5651–5660.
- [68] C.S. Fang, K.H. Oh, A. Oh, K. Lee, S. Park, S. Kim, J.K. Park, H. Yang, An Ultrasensitive and Incubation-Free Electrochemical Immunosensor Using a Gold- Nanocatalyst Label Mediating Outer-Sphere-Reaction-Philic and Inner-Sphere-Reaction-Philic Species, *Chem. Commun.* 52 (34) (2016) 5884–5887.

-
- [69] R.W. French, A.M. Collins, F. Marken, Growth and application of paired gold electrode junctions: evidence for nitrosonium phosphate during nitric oxide oxidation, *Electroanalysis* 20 (22) (2008) 2403–2409.
- [70] M. Smietana, P. Niedzi'alkowski, W. Białobrzaska, D. Burnat, P. Sezemsky, M. Koba, V. Stranak, K. Siuzdak, T. Ossowski, R. Bogdanowicz, Study on combined optical and electrochemical analysis using indium-tin-Oxide-Coated optical Fiber, *Electroanalysis* 31 (2) (2019) 398–404.
- [71] I. Del Villar, F.J. Arregui, C.R. Zamarreno, J.M. Corres, C. Barriain, J. Goicoechea, C. Elosua, M. Hernaez, P.J. Rivero, A.B. Socorro, et al., Optical sensors based on lossy-mode resonances, *Sens. Actua. B Chemical* 240 (2017) 174–185.
- [72] N.D. Popovich, S.-S. Wong, B.K.H. Yen, H.-Y. Yeom, D.C. Paine, Influence of microstructure on the electrochemical performance of tin-doped indium oxide film electrodes, *Anal. Chem.* 74 (13) (2002) 3127–3133.
- [73] M.A. Martínez, J. Herrero, M.T. Gutiérrez, Electrochemical stability of indium tin oxide thin films, *Electrochim. Acta* 37 (14) (1992) 2565–2571.
- [74] T. Sannomiya, H. Dermutz, C. Hafner, J. Voros, A.B. Dahlin, Electrochemistry on a localized surface plasmon resonance sensor, *Langmuir* 26 (10) (2010) 7619–7626. [75] J.H. Ghithan, M. Moreno, G. Sombrio, R. Chauhan, M.G. O'Toole, S.B. Mendes, Influenza virus immunosensor with an electro-active optical waveguide under potential modulation, *Opt. Lett.* 42 (7) (2017) 1205–1208.
- [76] J. Juan-Colas, A. Parkin, K.E. Dunn, M.G. Scullion, T.F. Krauss, S.D. Johnson, The electrophotonic silicon biosensor, *Nat. Commun.* 7 (2016) 12769.

B1. Optical monitoring of electrochemical processes with ITO-coated long-period fiber grating

Marta Janczuk-Richter, Monika Piestrzyńska, Dariusz Burnat, Katarzyna Szot-Karpińska, Petr Sezemsky, Vitezslav Stranak, Wojtek J. Bock, Robert Bogdanowicz, Joanna Niedziółka-Jönsson, and Mateusz Smietana, Optical monitoring of electrochemical processes with ITO-coated long-period fiber grating, 26th International Conference on Optical Fiber Sensors, September 24-28 2018, Lausanne, Switzerland, OSA Technical Digest (Optical Society of America, 2018), paper ThE54.

Abstract

Indium-tin-oxide-coated long-period fiber grating was used simultaneously as a working electrode and an optical probe sensitive to refractive index changes in combined optoelectrochemical setup. The optical response of the sensor was strongly dependent on the applied potential.

1. INTRODUCTION

In recent years, the development of chemical and biological sensors is one of the most active areas of research. Among the sensing strategies, electrochemical sensors are the most popular on the market and new technological solution for them are still under development. Conventional electrochemistry (EC) provides methods for fast and reliable analysis of chemical reactions, typically oxidation and reduction that take place at the electrode surface. However, received data is often insufficient to provide complete information about reaction mechanisms or undergoing biomolecular interactions. For this reason, dual-mode techniques that can monitor reactions in two measurement domains and give more information about the studied system, are becoming popular these days. EC has already been combined with a number of different techniques, e.g., optical waveguide lightmode spectroscopy [1], quartz crystal microbalance [2], and surface plasmon resonance (SPR) [3–6]. Recently, EC techniques were also combined with SPR-based or lossy-mode resonance-based optical fiber sensors [7, 8]. Application of fibers have some advantages over use of planar substrates, e.g., possibility of miniaturization and remote control, lack of bulky prism configuration, and capability of conducting measurements in hardly accessible places.

Among optical fiber sensors and biosensors, those based on long-period gratings (LPGs) are gaining particular attention because of their high refractive index (RI) sensitivity and thus capability for label-free biosensing applications. LPG is a periodic modulation of the RI of the core of a single-mode optical fiber with a period in the order of hundreds of micrometers [9]. Under certain conditions the modulation induces coupling of the fundamental core mode with cladding modes resulting in appearance of series of resonances in the LPG transmission spectrum. Since the LPG couples light into the cladding, the resonance wavelength depends on the RI of external medium [10], as well as the optical properties of the coating formed on the LPG surface. Thus, LPGs were applied for physical parameters sensing [11] and as biosensors capable for detection of bacteria [12], viruses [13], proteins [14], and DNA [15]. The sensitivity of the LPG sensors can be improved by wet or dry etching of the fiber cladding [16, 17] or deposition of thin high-RI coatings [18, 19]. Out of the coatings for possible dual-mode

applications, indium tin oxide (ITO) is a preferred choice, due to high RI, low electrical resistivity, and EC activity of these films. Therefore, ITO can be used as an electrode material and sensitivity enhancing coating in combined opto-EC technique.

In this work ITO-coated LPG was used for simultaneous optical and electrochemical measurements performed in combined setup containing supercontinuum white light laser source, optical spectrum analyzer, and potentiostat (three-electrode electrochemical setup with ITO-coated LPG as a working electrode). This configuration enabled monitoring of the optical and EC properties at the ITO/electrolyte interface under potential modulation.

2. MATERIALS AND METHODS

2.1. LPG fabrication

The LPGs were written in hydrogen-loaded Corning SMF28 fiber using a Pulse Master 840 high-power KrF excimer laser ($\lambda = 248$ nm) from Light Machinery. The UV exposure was performed through a chromium amplitude mask ($A = 226.8$ μm) for a couple of minutes. The LPGs were monitored in the spectral range from 1100 to 1700 nm, and had a single resonance at about $\lambda = 1245$ nm. Yokogawa AQ6370B spectrum analyzer and a Leukos SM30 supercontinuum white light laser source were used in the experiments.

2.2. ITO deposition on LPG

ITO films were deposited directly on the surface of the LPG using reactive magnetron sputtering method. The process was conducted in a vacuum chamber equipped with sputtering gun using 3-inch ITO target (the composition of $\text{In}_2\text{O}_3:\text{SnO}_2$ was 9:1 by weight). The COMET Cito1310 RF source was applied, with power of 150 W at frequency 13.56 MHz, under a pressure of 0.1 Pa and 100 sccm Ar flow. The samples placed in the holder were rotated during the deposition to provide homogeneity of the thin film. Based on the test processes, the ITO deposition time was adjusted to obtain 60 to 80 nm film in thickness.

2.3. Optical and electrochemical measurements

The sensitivity of the LPG to changes in external RI (n_{ext}) was measured by immersing the fiber structures in air and glycerol/water solutions with RIs in

the range $n_D = 1.333$ -1.443 RIU. The RI of the solutions was determined using a Rudolph J57 automatic refractometer.

All the measurements were conducted in a dedicated setup containing customized cell, optical spectrum analyzer and light source (mentioned above), and Autolab 302N potentiostat. ITO-coated LPG, platinum net and Ag|AgCl|0.1 M NaCl were used as working (WE), counter (CE) and reference (RE) electrodes, respectively (Fig. 1A). Cycling voltammetry (CV) measurements were conducted in solution consisting of 1 mM ferrocenedimethanol (Sigma Aldrich, Fc(OH)₂) in phosphate buffer saline (PBS) or solely in PBS. PBS (Sigma Aldrich, pH 7.4 at 25 °C) consists of 0.01 M phosphate buffer, 0.0027 M potassium chloride and 0.137 M sodium chloride. Potential 0 V → 1 V → -1 V → 0 V was applied, and 3 cycles were measured at a scan rate of 10 mVs⁻¹. Simultaneously with EC measurements, optical transmission of the ITO-coated LPG was monitored.

3. RESULTS AND DISCUSSION

After deposition a series of optical measurements was done for various n_{ext} to verify the RI sensitivity of the obtained sensor (Fig. 1B). As can be seen, the resonance shifted towards shorter wavelengths with increasing n_{ext} reaching over 1500 nm/RIU for $n_{\text{ext}} > 1.41$.

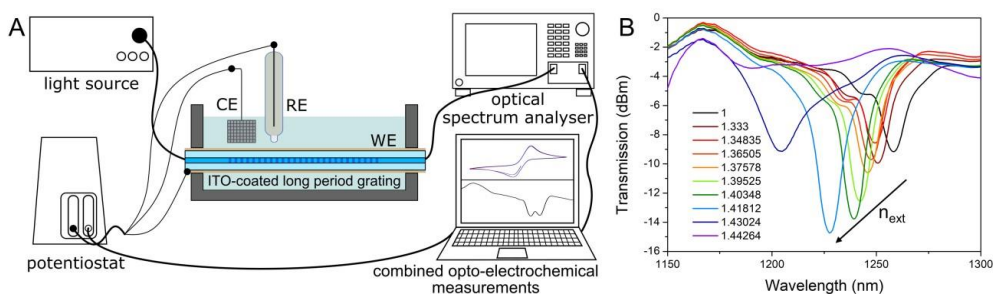


Fig. 1. (A) Scheme of used combined opto-EC setup. The electrodes were described as WE, CE and RE for working, counter and reference electrodes, respectively. (B) Optical response of the ITO-coated LPG to changes in n_{ext} .

Next, to check the influence of the applied potential on the optical response of ITO-coated LPG, the sensing structure was placed in customized EC cell serving as a working electrode in the three-electrode EC setup (Fig. 1A). CV technique was used to apply potential to the ITO surface and the optical transmission spectra were recorded in real time. The potential was changing

from 0 V to 1 V then to -1 V and back to 0 V. The measurements were conducted in PBS with 1 mM $\text{Fc}(\text{OH})_2$ (redox probe) or solely in PBS. Due to relatively high resistivity of thin ITO layer no oxidation or reduction of redox probe was observed in voltammogram (results not shown). In the optical response we observed the changes in the transmission of the resonance peak depending on the applied potential. The same dependence was observed for measurements made in PBS with redox probe and PBS only (Fig. 2A & 2B). We were tracing the changes in transmission at $\lambda = 1262$ nm (located at the slope of the resonance) for three CV scans (Fig. 2C & 2D). For both the studied solutions significant changes were observed for negative potential, while for positive potentials the change was smaller.

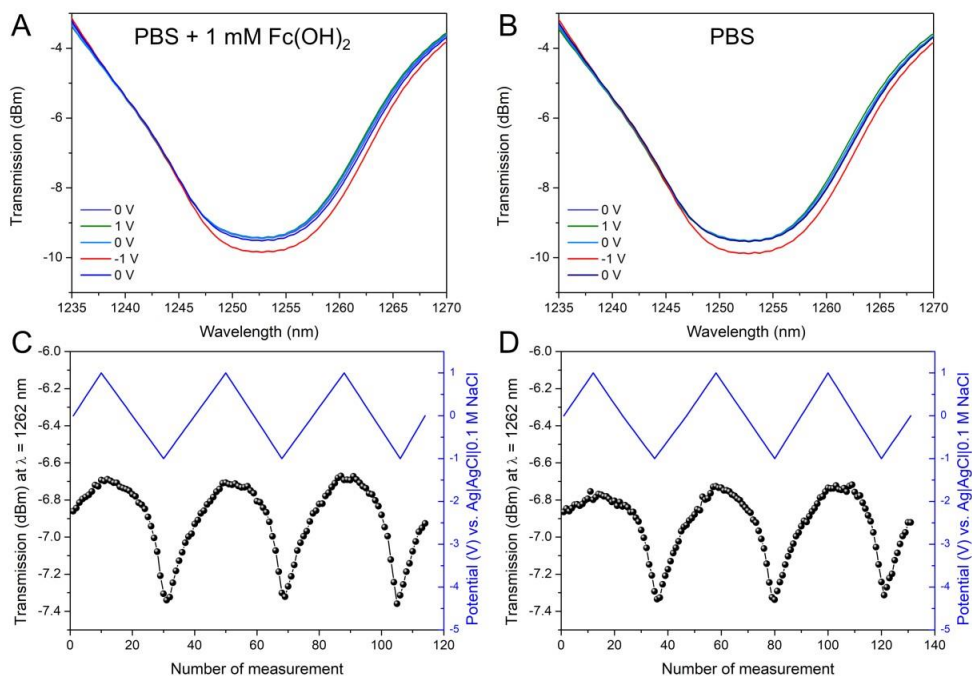


Fig. 2. Optical response of ITO-coated LPG during applied potential sweeping (3 CV scans). Transmission spectra is shown for selected potentials from first scan in PBS with 1 mM $\text{Fc}(\text{OH})_2$ (A) and PBS only (B), as well as transmission at $\lambda = 1262$ nm versus potential applied in PBS with 1 mM $\text{Fc}(\text{OH})_2$ (C) and PBS only (D).

The possible explanation of the changes observed in optical response can be induced by two factors. First, during potential modulation the optical properties of the ITO layer can be altered. According to the Drude model, the real part of RI of metal (or semiconductor) depends on the concentration of

free carriers in the material [20]. For ITO, which is an n-type semiconductor, electrons are majority carriers. For negative potentials the number of electrons near the ITO surface is higher which causes that the real part of RI is decreased. Second, the changes in the applied potential influences also the properties of the electrolyte in the vicinity of electrode due to the Helmholtz double layer formation and rearrangements [21]. Charged electrode immersed in the electrolyte repels co-ions and attract counterions present in the solution. That causes changes in ion concentrations near the electrode surface that modifies local n_{ext} and thus has an influence on optical response of the sensor. For positive potentials the changes were smaller, because two given above factors, i.e., changes in real part of ITO's RI and local changes in n_{ext} of electrolyte, may have smaller total influence on the optical response. For negative potentials one factor enhances the other causing significant changes in the optical response. In the studied case the addition of the redox probe to the electrolyte solution had no effect on the response. The changes in optical response during potential modulations were also demonstrated previously for SPR-based and lossy-mode resonance-based sensors [7, 8, 22], but in our approach thanks to application of LPG the sensitivity to RI changes caused by electrochemical processes could be better.

4. CONCLUSIONS

We have demonstrated novel dual-mode sensing technique with the ITO-coated LPG serving as a working electrode and optical structure sensitive to refractive index changes in combined opto-EC setup. The results for simultaneous optical and electrochemical measurements showed that the optical response of presented device is strongly dependent on the potential applied. Changes observed in optical transmission spectra are much higher for negative potentials and may be a result of alterations in optical properties of ITO and electrolyte in the vicinity of the electrode-electrolyte interface. ITO-coated LPG structures can be further used for sensing and biosensing experiments with enhanced data received from measurements.

Acknowledgements

This work was supported by the Polish National Science Centre (NCN) as a part of 2014/14/E/ST7/00104 project. MJR and JNJ work was supported by the project 3/DOT/2016 funded by the City of Gdynia, Poland.

References

- [1] J. P. Bearinger, J. Vörös, J. A. Hubbell, and M. Textor, “Electrochemical optical waveguide lightmode spectroscopy (EC-OWLS): A pilot study using evanescent-field optical sensing under voltage control to monitor polycationic polymer adsorption onto indium tin oxide (ITO)-coated waveguide chips,” *Biotechnol. Bioeng.* **82**, 465–473 (2003).
- [2] S. Nilsson and N. D. Robinson, “On the anodic deposition of poly-L-lysine on indium tin oxide,” *Electrochim. Acta* **196**, 629–633 (2016).
- [3] S. Sriwichai, A. Baba, S. Deng, C. Huang, S. Phanichphant, and R. C. Advincula, “Nanostructured Ultrathin Films of Alternating Sexithiophenes and Electropolymerizable Polycarbazole Precursor Layers Investigated by Electrochemical Surface Plasmon Resonance (EC-SPR) Spectroscopy,” *Langmuir* **24**, 9017–9023 (2008).
- [4] A. Baba, W. Knoll, and R. Advincula, “Simultaneous in situ electrochemical, surface plasmon optical, and atomic force microscopy measurements: Investigation of conjugated polymer electropolymerization,” *Rev. Sci. Instrum.* **77** (2006).
- [5] C. Wu, F. ur Rehman, J. Li, J. Ye, Y. Zhang, M. Su, H. Jiang, and X. Wang, “Real-Time Evaluation of Live Cancer Cells by an *in Situ* Surface Plasmon Resonance and Electrochemical Study,” *ACS Appl. Mater. Interfaces* **7**, 24848–24854 (2015).
- [6] S. E. Salamifar and R. Y. Lai, “Application of electrochemical surface plasmon resonance spectroscopy for characterization of electrochemical DNA sensors,” *Colloids Surfaces B Biointerfaces* **122**, 835–839 (2014).
- [7] Y. Yuan, T. Guo, X. Qiu, J. Tang, Y. Huang, L. Zhuang, S. Zhou, Z. Li, B. O. Guan, et al., “Electrochemical Surface Plasmon Resonance Fiber-Optic Sensor: In Situ Detection of Electroactive Biofilms,” *Anal. Chem.* **88**, 7609–7616 (2016).
- [8] M. Smietana, M. Sobaszek, B. Michalak, P. Niedzialkowski, W. Bialobrzaska, M. Koba, P. Sezemsky, V. Stranak, J. Karczewski, et al., “Optical Monitoring of Electrochemical Processes With ITO-Based Lossy-Mode Resonance Optical Fiber Sensor Applied as an Electrode,” *J. Light. Technol.* **36**, 954–960 (2018).
- [9] A. M. Vengsarkar, P. J. Lemaire, J. B. Judkins, V. Bhatia, T. Erdogan, and J. E. Sipe, “Long-period fiber gratings as band-rejection filters,” *J. Light. Technol.* **14**, 58–65 (1996).
- [10] V. Bhatia and A. M. Vengsarkar, “Optical fiber long-period grating sensors.,” *Opt. Lett.* **21**, 692–694 (1996).
- [11] J. Hromadka, S. Korposh, M. C. Partridge, S. W. James, F. Davis, D. Crump, and R. P. Tatam, “Multi-parameter measurements using

- optical fibre long period gratings for indoor air quality monitoring,” *Sensors Actuators B Chem.* **244**, 217–225 (2017).
- [12] E. Brzozowska, M. Koba, M. Śmietana, S. Górka, M. Janik, A. Gamian, and W. J. Bock, “Label-free Gram-negative bacteria detection using bacteriophage-adhesin-coated long-period gratings,” *Biomed. Opt. Express* **7**, 829 (2016).
- [13] M. Janczuk-Richter, M. Dominik, E. Roźniecka, M. Koba, P. Mikulic, W. J. Bock, M. Łoś, M. Śmietana, and J. Niedziółka-Jönsson, “Long-period fiber grating sensor for detection of viruses,” *Sensors Actuators B Chem.* **250**, 32–38 (2017).
- [14] P. Pilla, A. Sandomenico, V. Malachovská, A. Borriello, M. Giordano, A. Cutolo, M. Ruvo, and A. Cusano, “A protein-based biointerfacing route toward label-free immunoassays with long period gratings in transition mode,” *Biosens. Bioelectron.* **31**, 486–491 (2012).
- [15] K. H. K. H. Czarnecka, M. Dominik, M. Janczuk-Richter, J. Niedziółka-Jönsson, W. J. Bock, M. Śmietana, and M. Śmietana, “Specific detection of very low concentrations of DNA oligonucleotides with DNA-coated long-period grating biosensor,” *Proc. SPIE - Int. Soc. Opt. Eng.* **10323**, Y. Chung, W. Jin, B. Lee, J. Canning, K. Nakamura, and L. Yuan, Eds., 1032313 (2017).
- [16] S. A. Vasiliev, D. Varelas, H. G. Limberger, E. M. Dianov, and R. P. Salathé, “Postfabrication resonance peak positioning of longperiod cladding-mode-coupled gratings,” *Opt. Lett.* **21**, 1830 (1996).
- [17] M. Śmietana, M. Koba, P. Mikulic, and W. J. Bock, “Measurements of reactive ion etching process effect using long-period fiber gratings,” *Opt. Express* **22**, 5986–5994 (2014).
- [18] P. Pilla, C. Trono, F. Baldini, F. Chiavaioli, M. Giordano, and A. Cusano, “Giant sensitivity of long period gratings in transition mode near the dispersion turning point: an integrated design approach,” *Opt. Lett.* **37**, 4152 (2012).
- [19] M. Dominik, A. Leśniewski, M. Janczuk, J. Niedziółka-Jönsson, M. Hołdyński, Ł. Wachnicki, M. Godlewski, W. J. Bock, and M. Śmietana, “Titanium oxide thin films obtained with physical and chemical vapour deposition methods for optical biosensing purposes,” *Biosens. Bioelectron.* **93**, 102–109 (2017).
- [20] G. T. Reed and C. E. Jason Png, “Silicon optical modulators,” *Mater. Today* **8**, 40–50 (2005).
- [21] S. Grimnes, Ø. G. Martinsen, S. Grimnes, and Ø. G. Martinsen, “Electrodes,” in *Bioimpedance Bioelectr. Basics* (2015).
- [22] V. Lioubimov, A. Kolomenskii, A. Mershin, D. V Nanopoulos, and H. a Schuessler, “Effect of varying electric potential on surfaceplasmon resonance sensing,” *Appl. Opt.* **43**, 3426–3432 (2004)

B2. Optical investigations of electrochemical processes using a long-period fiber grating functionalized by indium tin oxide

Marta Janczuk-Richter, Monika Piestrzynska, Dariusz Burnat, Petr Sezemsky, Vitezslav Stranak, Wojtek J Bock, Robert Bogdanowicz, Joanna Niedziolka-Jönsson, Mateusz Śmietana, Optical investigations of electrochemical processes using a long-period fiber grating functionalized by indium tin oxide, Sensors & Actuators: B Chemical 279, (2019), 223–229.

Republished with permission of Elsevier Science & Technology Journals; permission conveyed through Copyright Clearance Center, Inc.

Abstract

The growing needs for fast and reliable sensing devices stimulate development of new technological solutions. In this work a new multi-domain sensing method is demonstrated where optical sensing device has been applied to enhance amount of data received during electrochemical analysis. Thin, optically transparent, high-refractive-index, and electrically conductive indium tin oxide (ITO) film was deposited using magnetron sputtering on the surface of the long-period gratings (LPG) induced in optical fiber. ITO serves as working electrode in electrochemical setup and as a coating that enhances sensitivity of a LPG to changes of external refractive index. All the measurements were conducted in a combined optical and electrochemical setup. Obtained results show capability of this approach for optical monitoring of both electrochemical processes and changes in optical properties at the ITO surface. The optical response of the sensor was strongly dependent on the voltage applied to the ITO-LPG working electrode and on composition of the electrolyte. Changes observed in optical spectra may be attributed to the alterations in optical properties of both ITO layer (refractive index changes) and electrolyte in the vicinity of electrode (double layer formation). The developed structures can be further used as a fiber-based sensors and biosensors with integrated opto-electrochemical readout.

1. INTRODUCTION

Electrochemistry (EC) is a scientific discipline that covers e.g., conversion and storage of energy, electrosynthesis, and corrosion research. Moreover, conventional EC provides methods for quantitative measurements that find applications in e.g., commonly used glucose sensing. EC techniques have demonstrated capability for fast and reliable analysis of chemical reactions, typically oxidation or reduction, taking place at the sensor surface. However, the data gathered from these measurements alone are often not sufficient to give complete information about investigated compounds or species and details on undergoing molecular and biomolecular processes. For that reason, techniques that can monitor such events in more than one measurement domain (multi-domain or dual-mode techniques) gain attention of scientific community [1]. EC techniques have already been combined with e.g., quartz crystal microgravimetry [2] and optical waveguide lightmode spectroscopy [3]. However, one of the most developed multi-domain techniques is a combination of surface plasmon resonance (SPR) and EC analysis. SPR is stimulated by incident light resonant oscillation of delocalized electrons (plasmon) along a metal-dielectric interface. Resonance conditions are dependent on optical properties at the metal-external medium interface, thus SPR makes possible label-free and real-time monitoring of sensor surface properties that include selective biomolecules binding process. Changes in the refractive index (RI) in the vicinity of the surface that correspond to biomolecule binding are measured by tracing the shift of the resonance. SPR evolved significantly since it was first applied and became one of the most commonly used techniques to monitor binding events at the solid/liquid interface [4]. Since the SPR substrates are usually made of thin gold deposited on glass, they can be also used as electrodes in EC setups. EC-SPR can provide simultaneous information about EC and optical properties of films formed on the sensor surface and makes possible deeper insights into the studied chemical or biological system. EC-SPR has been used for characterization of various conducting and electroactive polymer films [5, 6], evaluation of live cancer cells behavior [7], studying DNA hybridization [8], or enzyme activity [9, 10]. However, traditional SPR (and EC-SPR) requires complex prism-coupling instrumentation, which make the system difficult to miniaturize. Therefore, a new solution was recently

demonstrated by Yuan et al. [11] where EC-SPR sensor for monitoring of electroactive biofilms was based on optical fiber. Such a sensor shows some advantages over planar solution, i.e., small size, lack of bulky prism system, possibility for remote control and capability for measurements in readily available places. These advantages caused that different configurations of optical fiber sensors have been also intensively investigated for physical parameters sensing, as well as chemical and biochemical sensing [12, 13].

Optical fiber sensors based on gratings have been recently widely under development. Long-period grating (LPG) induced in optical fibers has in particular attracted attention due to their high RI sensitivity that can be applied for label-free biosensing. LPG is a periodic modulation (period in the order of hundreds of micrometers) of the RI of the core of single-mode optical fiber [14]. The modulation induces coupling of the fundamental core mode and forward propagating cladding modes resulting in series of resonances centered at discrete wavelengths appearing in the LPG transmission spectrum. Since the LPG makes possible light guiding in fiber cladding, the coupling conditions corresponding to resonance wavelengths are highly dependent on the external RI [15], as well as the properties of a coating formed on the LPG surface. Therefore, LPGs has already been applied as a label-free biosensors for detection of bacteria [16, 17], viruses [18], proteins [19, 20], or DNA [21, 22]. It must be noted that the RI sensitivity may be highly improved by tuning the working conditions of the device towards dispersion turning point (DTP) of the cladding modes. The tuning is possible by wet or dry etching of the fiber cladding [23, 24] and/or deposition of thin and high-RI coatings [25-28]. Application of the coatings of certain thickness makes possible modes transitions in the cladding, what on top of DTP allows for boosting the RI sensitivity [28]. Out of the coating materials for possible multi-domain applications, ITO is an interesting choice, since beside high RI it also shows high optical transparency, low electrical resistivity, and EC activity. Thus, it can be than used as both RI sensitivity enhancing coating and an electrode material for multi-domain opto-EC technique. Thanks to application of the LPG both properties of the external medium and the coating can be monitored with a great sensitivity [29].

Although opto-EC techniques are gaining attention, the studied solutions are still less advanced than in case of singe-domain methods. In this work we

show a new multi-domain configuration for simultaneous measurements of optical and EC properties at the ITO coating/electrolyte interface. The optical response of the ITO-LPG sensor during EC measurements was investigated for various electrolytes.

2. MATERIALS AND METHODS

2.1. Chemicals and materials

Acetone, ethanol, methanol, and phosphate buffered saline (PBS) tablets were purchased from Sigma Aldrich. PBS (pH 7.4 at 25 °C) consists of 0.01 M phosphate buffer, 0.0027 M potassium chloride and 0.137 M sodium chloride. Potassium hexacyanoferrate(III) and potassium hexacyanoferrate(II) trihydrate were purchased from Sigma Aldrich and POCH (Poland), respectively.

2.2. LPG fabrication

The long-period gratings were written in hydrogen-loaded Corning SMF28 fiber using a Pulse Master 840 high-power KrF excimer laser ($\lambda = 248$ nm) from Light Machinery. The UV exposure was done on the 5-cm-long fiber section through a chromium amplitude mask ($A = 226.8$ μm) for about 7 min. The LPGs fabricated this way were monitored in the spectral range from 1100 to 1700 nm, and had a single resonance at $\lambda = 1245$ nm. We used a Yokogawa AQ6370B spectrum analyzer and a Leukos SM30 supercontinuum white light laser source. Before ITO deposition gratings were etched in HF acid towards DTP observed for LPG immersed in deionized water.

2.3. ITO deposition on LPG

Thin, optically transparent, high-RI, and electrically conductive ITO films were deposited directly on the surface of the LPG using magnetron sputtering method. The LPG samples were 5 cm in length and 125 μm in diameter. The only difference between the samples was slightly different working conditions resulted from etching process preceding the deposition. According to our previous work [24], the difference in diameter may reach up to 500 nm. The deposition process was conducted in a UHV chamber with the sputtering gun equipped with 3-inch ITO target (the composition of $\text{In}_2\text{O}_3:\text{SnO}_2$ was 9:1 by weight). The COMET Cito1310 RF source was applied, with power of 150 W at frequency 13.56 MHz, under a pressure of 1 Pa and 100 sccm Ar

flow. The LPGs were exposed to sputtering guns for 11 min. The samples placed in the holder were rotated during the deposition to provide homogeneity of the thin film. SEM images of the ITO films were obtained using FEI Nova NanoSEM 450 with Through the Lens Detector and Circular Backscatter Detector.

2.4. ITO-LPG optical and electrochemical measurements

The sensitivity of the LPG to changes in external RI (n_{ext}) that also corresponds to its label-free sensing capability, was measured by immersing the fiber structures in glycerol/water solutions with RIs in the range $n_D = 1.333$ – 1.423 RIU. The RI of the solutions was determined using a Rudolph J57 automatic refractometer.

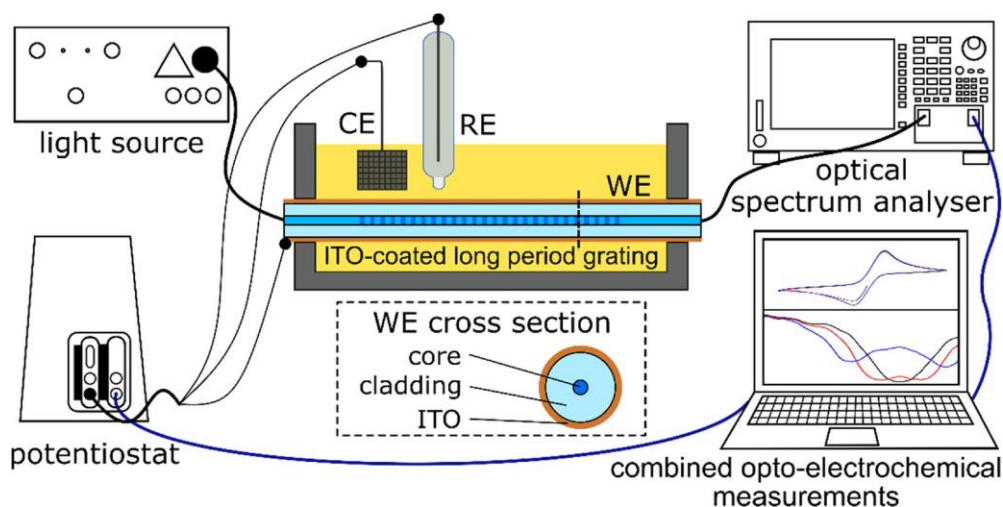


Fig. 1. Schematic representation of the combined setup used for simultaneous optical and EC measurements, where the electrodes were marked as WE, RE and CE for working, reference and counter electrodes, respectively. Additionally, a cross section of the working electrode was shown.

All the measurements were conducted in a dedicated setup containing specially designed cell allowing for maintaining LPG strain, mentioned above optical spectrum analyzer and light source, as well as Autolab 302 N potentiostat. ITO-LPG, platinum net and Ag|AgCl|0.1 M NaCl were used as working (WE), counter (CE), and reference (RE) electrodes, respectively (Fig. 1). Electrical contact with WE was achieved by attaching copper tape directly to the ITO-coated cladding away from the LPG section and outside the measurement cell. Cycling voltammetry (CV) measurements

were carried out in aqueous media consisting of 5 mM $\text{K}_3[\text{Fe}(\text{CN})_6]$ and 5 mM $\text{K}_4[\text{Fe}(\text{CN})_6]$ in PBS or solely in PBS at a scan rate of 10 mVs^{-1} . Potential $0 \text{ V} \rightarrow -1 \text{ V} \rightarrow 1 \text{ V} \rightarrow 0 \text{ V}$ was applied, and 3 continuous cycles were measured. Chronoamperometry measurements were also done in 5 mM $\text{K}_3[\text{Fe}(\text{CN})_6]$ and 5 mM $\text{K}_4[\text{Fe}(\text{CN})_6]$ in PBS, where the each potential (0 V, -1 V, 0 V, 1 V, and 0 V) was applied for 60 s. Simultaneously with EC measurements, optical transmission of the ITO-LPG was monitored. Wavelength range and sensitivity were chosen according to dynamics of changes observed each time in the spectrum.

3. RESULTS AND DISCUSSION

3.1. Characterization of ITO-coated LPGs

LPGs are sensitive to n_{ext} , as well as optical properties and thickness of the overlay formed on their surface. Any changes at the surface manifest themselves as a shift of the resonance wavelength observed in the transmission spectrum. To reach the highest sensitivity it is required to optimize of the LPG working point towards DTP where dual resonance regime is observed and the resonances shift into opposite directions. However, when thin film is deposited on LPG it shifts the working point away from DTP, and even very thin films can induce decrease of the RI sensitivity [27]. Thus, to observe the resonances after deposition it is required to over-etch the fiber cladding [25]. To check the influence of the ITO deposition on the RI sensitivity, a series of optical measurements was conducted for various n_{ext} . In particular, two samples were chosen and called as Sample_A and Sample_B. They differ only in the HF etching time (longer for Sample_A than for Sample_B) before the ITO deposition, while the deposition parameters were the same for both the samples. Based on trial processes, the deposition conditions were adjusted to get about 40 nm of the ITO coating. It can be seen in Fig. 2 that Sample_A operates in close proximity of the DTP and the resonances separate for $n_{\text{ext}} \approx 1.36$ RIU, while for Sample_B the resonance are already separated and shifted away from the DTP for all the applied n_{ext} . In case of Sample_A the resonance first gets dipper with the increase of RI and then it splits into pair of resonances. The highest sensitivity can be obtained there, but the resonance wavelength for lower n_{ext} cannot be determined. For n_{ext} in range 1.36 to 1.39 RIU the sensitivity exceeds 5000 nm/RIU. When Sample_B is concerned

blue-shifting (left) resonance is clearly visible during all the measurements and it shifts towards shorter wavelengths with RI. In this case the RI sensitivity can be determined almost in whole n_{ext} range and reaches about 2200 nm/RIU for $n_{ext} > 1.341$ RIU. Sensitivities obtained for ITO-LPGs are comparable with fiber-optic SPR sensors that reach up to a few thousands nm/RIU [30]. For example, it was shown that fiber-optic SPR sensor coated with Au metal film (39 nm) reached the sensitivity of about 4000 nm/RIU [31].

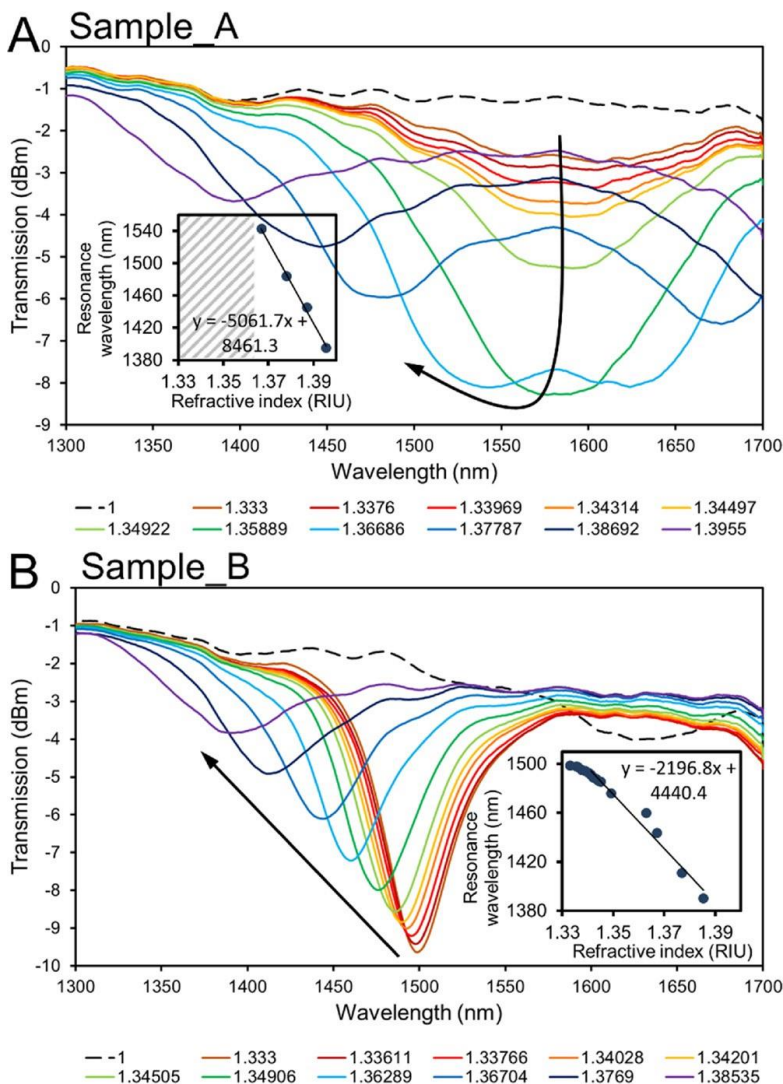


Fig. 2. Spectral response of the ITO-LPG to changes in n_{ext} for Sample_A (A) and Sample_B (B). Arrows show the direction of changes for increasing n_{ext} . Insets show dependence of resonance wavelength on n_{ext} for each sample. For Sample_A it was impossible to determine resonance wavelength for most n_{ext} s due to vicinity of the DTP.

Additionally, SEM images were done to verify thickness of the ITO film and its uniformity on the fiber (Fig. 3). The images were done with two detectors involved, i.e., Through the Lens and Circular Backscatter, and merged together in Fig. 3A. Analyzes of the ITO thickness were done on series of SEM images showing different fragments of the fiber cross-section and measured thickness was 74.6 ± 2.6 nm as marked in Fig. 3B. Thickness observed in the images was higher than this measured on reference Si samples used for trial processes (40 nm), the most probably due to different geometrical configuration of these samples. Moreover, the ITO surface was found to be smooth and homogeneous (Fig. 3C).

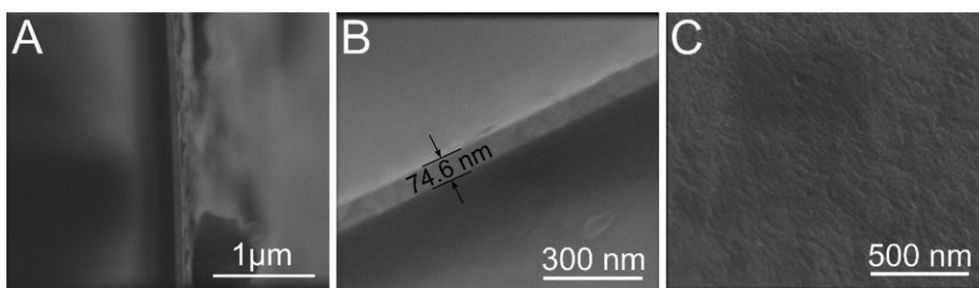


Fig. 3. SEM images of the cross section of the fiber in lower magnification (A) and in higher magnification with indicated ITO thickness (B), and ITO surface (C).

3.2. Simultaneous EC and optical measurements

The experimental validation of the possibility to perform simultaneous EC and optical measurements was conducted with ITO-LPG serving as both working electrode and a structure optically sensitive to phenomena taking place on the ITO surface. Cyclic voltammetry was used to apply the potential to the ITO surface. In this configuration the potential was sweeping between 0 V to -1 V then to 1 V and back to 0 V with the scanning rate of 10 mV/s. The rate enabled gathering between 60 to 80 spectra per CV cycle depending on the chosen wavelength range. PBS solution containing 5 mM $K_3[Fe(CN)_6]$ and 5 mM $K_4[Fe(CN)_6]$ was used first to check both the EC and optical response. No EC reaction related to oxidation and reduction of the redox probes was observed in the voltammogram, probably due to very low thickness of ITO and thus relatively high resistivity [32] (Fig. 4A). As well as current, also transmission spectra recorded during the experiment changed significantly when the potential was applied. Decrease and increase in potential induces shift of the

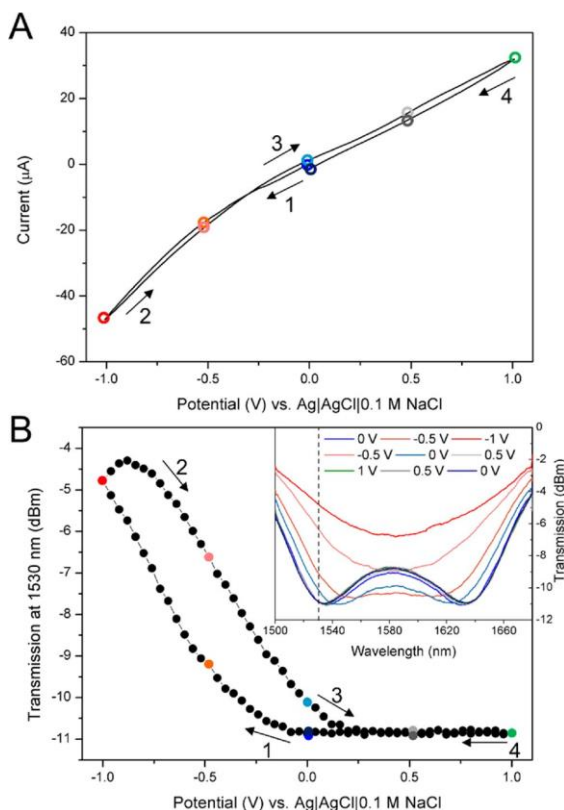


Fig. 4. Response of Sample_A to applied potential during simultaneous EC and optical measurements in 5 mM $K_3[Fe(CN)_6]$ and 5 mM $K_4[Fe(CN)_6]$ in PBS, where (A) is a CV response and (B) shows transmission measured at $\lambda = 1530$ nm. Inset: Transmission spectra at selected potentials. Points corresponding to certain spectra are marked with the same color in (A) and (B).

resonances towards and away from DTP, respectively. Because the working point of Sample_A was optimized to DTP, it was impossible for most of the applied negative potentials to determine the resonance wavelength. Therefore, we were tracing changes in transmission at fixed wavelength ($\lambda = 1530$ nm that is on the left slope of the resonance) and summarized the results in Fig. 4B. As can be seen, significant changes reaching up to 9 dBm/V were observed for negative potentials, while for positive potentials almost no changes in optical response were recorded. Moreover, there is a hysteresis observed for negative potentials. High resistivity of the ITO film may cause the potential distribution generated on the surface along the fiber. However, if the differences in potential in different fragments

of the fiber were large, the optical response would be influenced and generation of characteristic fringes in the transmission spectra would be observed as demonstrated in [33]. This effect did not happen in studied case.

Next, we investigated the optical response time to the applied potential. The potential has been changed stepwise (rather than gradually as applied earlier) in the following order: 0 V, -1 V, 0 V, 1 V, 0 V. It was kept at each state for one minute. As can be seen in Fig. 5, after rapid change from 0 V to -1 V the

transmission went up immediately, i.e., the resonance shifted towards DTP, and then stabilized after about 30 s. The change from -1 V to 0 V caused sudden decrease in the transmission (shift away from DTP) followed by its stabilization. Potential increase to 1 V cause only a slight increase in transmission and no change after another potential switch to 0 V was observed.

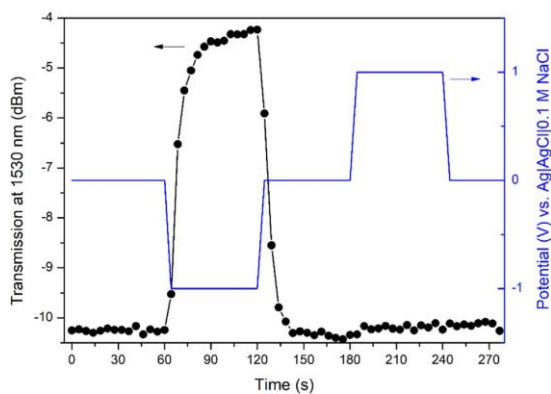


Fig. 5. Dynamic optical response of Sample_A during electrochemical stimulation in 5 mM $K_3[Fe(CN)_6]$ and 5 mM $K_4[Fe(CN)_6]$ in PBS. Chronoamperometry was used to apply the potentials.

Changes in optical response, especially those observed for negative potentials in the experiments (sweeping and switching of the potential), correspond to changes in external RI and can be attributed to two factors, i.e., changes in optical properties of ITO overlay and external medium, especially in close vicinity of the electrode surface. ITO is a n-type semiconductor, what means that electrons are majority carriers. According to the Drude-Lorentz model real part of RI (n) of a metal or semiconductor is dependent on the number of free carriers in the material [34]. Thus, changes in electron density induced by applied potential affect the optical properties of ITO. In negative potentials concentration of charge carriers (electrons) is higher near the surface, so its n is decreased [35]. For thin ITO films it was also shown that the changes with potential modulation may be followed by changes of the imaginary part of ITO's RI (k) [36]. These carrier-density-dependent changes in optical properties of ITO, especially at surface-electrolyte interface, induce evolution of LPG optical response, in similar way as shown for external RI – when increased the resonances shift apart. The optical properties of the external medium (electrolyte) in the vicinity of the electrode are in turn affected by the formation and rearrangements in the Helmholtz double layer [37]. This layer is formed when a charged electrode is immersed in electrolyte, what is followed by attraction of counterions to the surface and repelling of co-ions. The layer can be modeled as a capacitor where potential change is followed

by a change in charge, i.e., concentration and type of ions. The alteration in double layer properties has an impact on external RI in vicinity of ITO surface what is observed in optical response of the LPG in a way as shown in Fig. 2. Changes in the layer properties are likely responsible for presence of a hysteresis in the optical response (Fig. 4B) and limitation in optical response dynamics (Fig. 5). The similar changes in the optical response during potential modulations were previously shown in case of SPR-based measurements on gold [11, 38, 39] and ITO-based lossy-mode resonance sensor [40].

It was also shown previously in case of the SPR effect that the changes of the optical response with the applied potential depend on the composition of the solution (electrolyte) that stays in contact with the electrode [38]. Optical response to applied potential of Sample_B solely in PBS and in PBS with redox probes (5 mM $K_3[Fe(CN)_6]$ and 5 mM $K_4[Fe(CN)_6]$) added were compared in Fig. 6. During three consecutive CV scans (each the scan followed the scheme $0\text{ V} \rightarrow -1\text{ V} \rightarrow 1\text{ V} \rightarrow 0\text{ V}$ with scan rate 10 mV/s) the optical response was analyzed this time by tracing shift of the resonance wavelength (Fig. 6C & D). Response in solution with the redox probe is similar to the one shown for Sample_A, i.e., significant and small changes observed for negative and positive potentials, respectively (Fig. 6A & C). Interestingly, when there was no redox probe in the solution the observed shifts were over 3 times higher. Moreover, in the absence of the redox probes resonance wavelength shift was also observed for positive potentials, but it was still less significant than for negative potentials (Fig. 6B & D). Current response for those experiments was similar to that measured for Sample_A (Fig. 4A).

The difference in optical response between electrolytes with and without redox probe on top of Helmholtz double layer formation can be attributed to presence of big negatively charged ions $[Fe(CN)_3]^{3-/4-}$ (redox couple) [41]. The decrease in the wavelength shift when the probe was added may be caused by the interactions of $[Fe(CN)_3]^{3-/4-}$ ions with the ITO surface. The accumulation of these ions near the surface causes that the migration of other ions present in the electrolyte under the influence of applied potential are less visible in the optical response. It is also worth noticing that the optical response observed in PBS without redox probe in negative potentials for this sample corresponds to external RI change between water and air (Fig. 2B). In addition to the double

layer formation and the RI changes, this response may be influenced by hydrogen evolution that occurs for negative potentials [42] and formation of a gas-like external RI at the ITO surface.

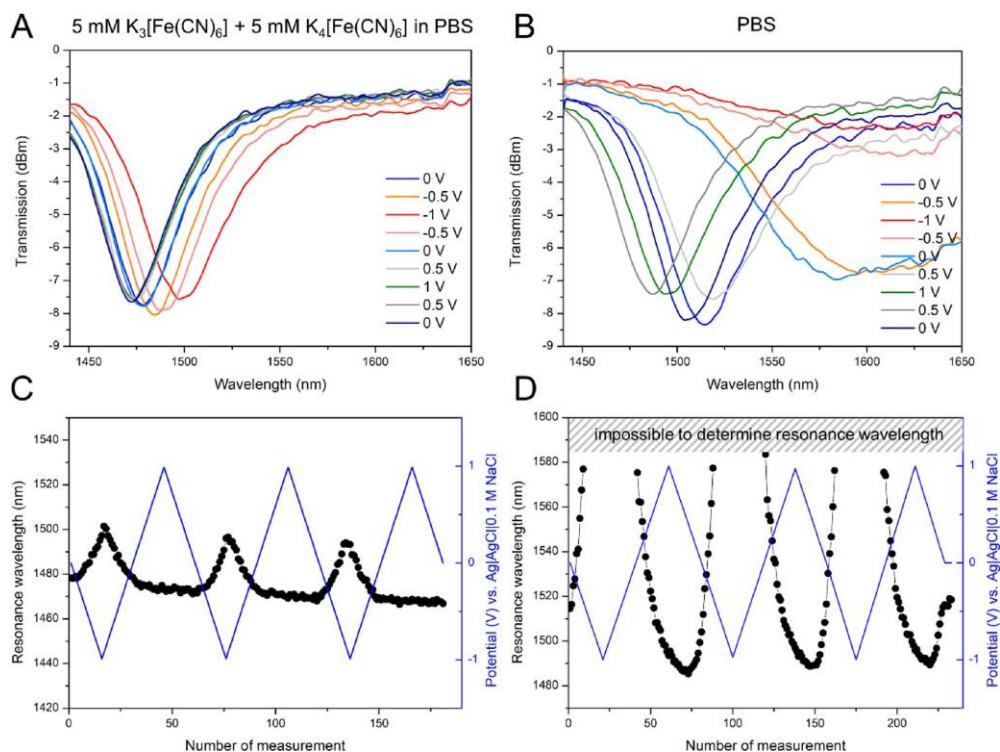


Fig. 6. Optical response of Sample_B during EC stimulation (three CV scans) in different electrolytes, where transmission spectra for selected potentials are shown for first scan in PBS with redox probe (A) and in PBS only (B), and corresponding resonance wavelength vs. potential applied during measurements PBS with redox probe (C) and in PBS only (D). For some measurements performed in PBS only it was impossible to determine resonance wavelength, due to vicinity of the DTP.

4. CONCLUSIONS

The possibility of performing simultaneous electrochemical and optical measurements with ITO-coated LPG serving as both working electrode in electrochemical setup and as highly sensitive to refractive index optical sensor was reported. The optical response of the device is strongly dependent on the applied potential, especially for negative potentials. Changes observed in optical spectra during cycling or switching of the potential may be attributed to the alterations in optical properties of both ITO overlay and the electrolyte in the vicinity of electrode surface (double layer formation). Combined optical

and electrochemical measurements allow for gathering significantly more information on the investigated medium than the methods applied separately. Further investigations of the combined approach based on ITO-coated LPG, due to high surface sensitivity of the device, will allow for performing label-free biosensing experiments with enhanced data received. It must be noted that not only multi-domain measurements are possible with the proposed approach, but it also gives a capability to initiate a specific process in one domain and monitor its progress in other domain (e.g. measure sub-nanometer changes in the layer deposited by electropolymerization). The developed ITO-LPG structures can be further used as fiber-based sensors and biosensors with integrated opto-electrochemical readout.

Declaration of interest

The authors declare no competing financial or personal interests.

Acknowledgements

This work was partially supported by the National Science Centre, Poland as a part of 2014/14/E/ST7/00104 project and National Centre for Research and Development, Poland through project TECHMATSTRATEG1/347324/12/NCBR/2017. MJR and JNJ work was supported by the project 3/DOT/2016 funded by the City of Gdynia, Poland. The DS funds of Faculty of Electronics, Telecommunications and Informatics of the Gdansk University of Technology are also acknowledged. The authors thank Dr. M. Jönsson-Niedziółka for assistance with SEM imaging.

References

- [1] J. Juan-Colás, S. Johnson, T. Krauss, Dual-mode electro-optical techniques for biosensing applications: a review, *Sensors* 17 (2017) 2047, <https://doi.org/10.3390/s17092047>.
- [2] S. Nilsson, N.D. Robinson, On the anodic deposition of poly-L-lysine on indium tin oxide, *Electrochim. Acta* 196 (2016) 629–633, <https://doi.org/10.1016/J.ELECTACTA.2016.02.177>.
- [3] J.P. Bearinger, J. Vörös, J.A. Hubbell, M. Textor, Electrochemical optical waveguide lightmode spectroscopy (EC-OWLS): a pilot study using evanescent-field optical sensing under voltage control to monitor polycationic polymer adsorption onto indium tin oxide (ITO)-coated waveguide chips, *Biotechnol. Bioeng.* 82 (2003) 465–473, <https://doi.org/10.1002/bit.10591>.

-
- [4] D.C. Melo Ferreira, R.K. Mendes, L.T. Kubota, Electrochemical-surface plasmon resonance: concept and bioanalytical applications, in: F.N. Crespilho (Ed.), *Nanobioelectrochemistry From Implant. Biosens. to Green Power Gener.* Springer, Berlin Heidelberg, Berlin, Heidelberg, 2013, pp. 127–137, https://doi.org/10.1007/978-3-642-29250-7_7.
- [5] S. Sriwichai, A. Baba, S. Deng, C. Huang, S. Phanichphant, R.C. Advincula, Nanostructured ultrathin films of alternating sexithiophenes and electropolymerizable polycarbazole precursor layers investigated by electrochemical surface plasmon resonance (EC-SPR) spectroscopy, *Langmuir* 24 (2008) 9017–9023, <https://doi.org/10.1021/la800307u>.
- [6] A. Baba, W. Knoll, R. Advincula, Simultaneous in situ electrochemical, surface plasmon optical, and atomic force microscopy measurements: investigation of conjugated polymer electropolymerization, *Rev. Sci. Instrum.* 77 (2006), <https://doi.org/10.1063/1.2204587>.
- [7] C. Wu, F. ur Rehman, J. Li, J. Ye, Y. Zhang, M. Su, H. Jiang, X. Wang, Real-time evaluation of live cancer cells by an in situ surface plasmon resonance and electrochemical study, *ACS Appl. Mater. Interfaces* 7 (2015) 24848–24854, <https://doi.org/10.1021/acsami.5b08066>.
- [8] S.E. Salamifar, R.Y. Lai, Application of electrochemical surface plasmon resonance spectroscopy for characterization of electrochemical DNA sensors, *Colloids Surf. B Biointerfaces* 122 (2014) 835–839, <https://doi.org/10.1016/j.colsurfb.2014.07.028>.
- [9] Y. Iwasaki, T. Tobita, K. Kurihara, T. Horiuchi, K. Suzuki, O. Niwa, Imaging of electrochemical enzyme sensor on gold electrode using surface plasmon resonance, *Biosens. Bioelectron.* 17 (2002) 783–788, [https://doi.org/10.1016/S09565663\(02\)00054-4](https://doi.org/10.1016/S09565663(02)00054-4).
- [10] A. Baba, P. Taranekar, R.R. Ponnampati, W. Knoll, R.C. Advincula, Electrochemical surface plasmon resonance and waveguide-enhanced glucose biosensing with Nalkylaminated polypyrrole/glucose oxidase multilayers, *ACS Appl. Mater. Interfaces* 2 (2010) 2347–2354, <https://doi.org/10.1021/am100373v>.
- [11] Y. Yuan, T. Guo, X. Qiu, J. Tang, Y. Huang, L. Zhuang, S. Zhou, Z. Li, B.O. Guan, X. Zhang, J. Albert, Electrochemical surface plasmon resonance fiber-optic sensor: in situ detection of electroactive biofilms, *Anal. Chem.* 88 (2016) 7609–7616, <https://doi.org/10.1021/acs.analchem.6b01314>.
- [12] F. Chiavaioli, F. Baldini, S. Tombelli, C. Trono, A. Giannetti, Biosensing with optical fiber gratings, *Nanophotonics* 6 (2017) 663–679, <https://doi.org/10.1515/nanoph2016-0178>.
- [13] X.-D. Wang, O.S. Wolfbeis, Fiber-optic chemical sensors and biosensors (2013–2015), *Anal. Chem.* 88 (2016) 203–227, <https://doi.org/10.1021/acs.analchem.5b04298>.
-

- [14] A.M. Vengsarkar, P.J. Lemaire, J.B. Judkins, V. Bhatia, T. Erdogan, J.E. Sipe, Longperiod fiber gratings as band-rejection filters, *J. Lightwave Technol.* 14 (1996) 58–65, <https://doi.org/10.1109/50.476137>.
- [15] V. Bhatia, A.M. Vengsarkar, Optical fiber long-period grating sensors, *Opt. Lett.* 21 (1996) 692–694, <https://doi.org/10.1364/OL.21.000692>.
- [16] S.M. Tripathi, W.J. Bock, P. Mikulic, R. Chinnappan, A. Ng, M. Tolba, M. Zourob, Long period grating based biosensor for the detection of Escherichia coli bacteria, *Biosens. Bioelectron.* 35 (2012) 308–312, <https://doi.org/10.1016/j.bios.2012.03.006>.
- [17] E. Brzozowska, M. Koba, M. Śmietana, S. Górska, M. Janik, A. Gamian, W.J. Bock, Label-free Gram-negative bacteria detection using bacteriophage-adhesin-coated long-period gratings, *Biomed. Opt. Express* 7 (2016) 829, <https://doi.org/10.1364/BOE.7.000829>.
- [18] M. Janczuk-Richter, M. Dominik, E. Roźniecka, M. Koba, P. Mikulic, W.J. Bock, M. Łoś, M. Śmietana, J. Niedziółka-Jönsson, Long-period fiber grating sensor for detection of viruses, *Sensors Actuators B Chem.* 250 (2017) 32–38, <https://doi.org/10.1016/j.snb.2017.04.148>.
- [19] F. Chiavaioli, P. Biswas, C. Trono, S. Jana, S. Bandyopadhyay, N. Basumallick, A. Giannetti, S. Tombelli, S. Bera, A. Mallick, F. Baldini, Sol-gel-based titania-silica thin film overlay for long period fiber grating-based biosensors, *Anal. Chem.* 87 (2015) 12024–12031, <https://doi.org/10.1021/acs.analchem.5b01841>.
- [20] P. Pilla, A. Sandomenico, V. Malachovská, A. Borriello, M. Giordano, A. Cutolo, M. Ruvo, A. Cusano, A protein-based biointerfacing route toward label-free immunoassays with long period gratings in transition mode, *Biosens. Bioelectron.* 31 (2012) 486–491, <https://doi.org/10.1016/j.bios.2011.11.022>.
- [21] K.H. Czarnecka, M. Dominik, M. Janczuk-Richter, J. Niedziółka-Jönsson, W.J. Bock, M. Śmietana, Specific detection of very low concentrations of DNA oligonucleotides with DNA-coated long-period grating biosensor, *Proc. SPIE – Int. Soc. Opt. Eng.* (2017), <https://doi.org/10.1117/12.2267411>.
- [22] X. Chen, L. Zhang, K. Zhou, E. Davies, K. Sugden, I. Bennion, M. Hughes, A. Hine, Real-time detection of DNA interactions with long-period fiber-grating-based biosensor, *Opt. Lett.* 32 (2007) 2541–2543, <https://doi.org/10.1364/OL.32.002541>.
- [23] S.A. Vasiliev, D. Varelas, H.G. Limberger, E.M. Dianov, R.P. Salathé, Postfabrication resonance peak positioning of long-period cladding-mode-coupled gratings, *Opt. Lett.* 21 (1996) 1830, <https://doi.org/10.1364/OL.21.001830>.
- [24] M. Śmietana, M. Koba, P. Mikulic, W.J. Bock, Measurements of reactive ion etching process effect using long-period fiber gratings, *Opt. Express* 22 (2014) 5986–5994, <https://doi.org/10.1364/OE.22.005986>.

-
- [25] M. Śmietana, M. Koba, P. Mikulic, W.J. Bock, Towards refractive index sensitivity of long-period gratings at level of tens of μm per refractive index unit: fiber cladding etching and nano-coating deposition, *Opt. Express* 24 (2016) 11897, <https://doi.org/10.1364/OE.24.011897>.
- [26] M. Dominik, A. Leśniewski, M. Janczuk, J. Niedziółka-Jönsson, M. Hołdyński, Ł. Wachnicki, M. Godlewski, W.J. Bock, M. Śmietana, Titanium oxide thin films obtained with physical and chemical vapour deposition methods for optical biosensing purposes, *Biosens. Bioelectron.* 93 (2017) 102–109, <https://doi.org/10.1016/j.bios.2016.09.079>.
- [27] M. Smietana, M. Koba, P. Mikulic, W.J. Bock, Combined plasma-based fiber etching and diamond-like carbon nanooverlay deposition for enhancing sensitivity of longperiod gratings, *J. Lightwave Technol.* 34 (2016) 4615–4619, <https://doi.org/10.1109/JLT.2016.2528411>.
- [28] P. Pilla, C. Trono, F. Baldini, F. Chiavaioli, M. Giordano, A. Cusano, Giant sensitivity of long period gratings in transition mode near the dispersion turning point: an integrated design approach, *Opt. Lett.* 37 (2012) 4152, <https://doi.org/10.1364/OL.37.004152>.
- [29] M. Śmietana, P. Mikulic, W.J. Bock, Nano-coated long-period gratings for detection of sub-nanometric changes in thin-film thickness, *Sensors Actuators A Phys.* 270 (2018) 79–83, <https://doi.org/10.1016/J.SNA.2017.12.052>.
- [30] S. Roh, T. Chung, B. Lee, Overview of the characteristics of micro- and nanostructured surface plasmon resonance sensors, *Sensors (Basel.)* 11 (2011) 1565–1588, <https://doi.org/10.3390/s110201565>.
- [31] B. Lee, S. Roh, H. Kim, J. Jung, Waveguide-based surface plasmon resonance sensor design, *Proc. SPIE* 7420 (2009), <https://doi.org/10.1117/12.826865.74200C-74200C-12>.
- [32] A. Eshaghi, A. Graeli, Optical and electrical properties of indium tin oxide (ITO) nanostructured thin films deposited on polycarbonate substrates “thickness effect, *Opt. – Int. J. Light Electron. Opt.* 125 (2014) 1478–1481, <https://doi.org/10.1016/J.IJLEO.2013.09.011>.
- [33] I. Del Villar, F.J. Arregui, I.R. Matias, a. Cusano, D. Paladino, a. Cutolo, Fringe generation with non-uniformly coated long-period fiber gratings, *Opt. Express* 15 (2007) 9326–9340, <https://doi.org/10.1364/OE.15.009326>.
- [34] G.T. Reed, C.E. Jason Png, Silicon optical modulators, *Mater. Today* 8 (2005) 40–50, [https://doi.org/10.1016/S1369-7021\(04\)00678-9](https://doi.org/10.1016/S1369-7021(04)00678-9).
- [35] J.G. Mendoza-Alvarez, F.D. Nunes, N.B. Patel, Refractive index dependence on free carriers for GaAs, *J. Appl. Phys.* 51 (1980) 4365–4367, <https://doi.org/10.1063/1.328298>.
-

- [36] X. Han, S.B. Mendes, Spectroelectrochemical properties of ultra-thin indium tin oxide films under electric potential modulation, *Thin Solid Films* 603 (2016) 230–237, <https://doi.org/10.1016/j.tsf.2016.02.018>.
- [37] S. Grimnes, Ø.G. Martinsen, S. Grimnes, Ø.G. Martinsen, *Electrodes, Bioimpedance Bioelectr. Basics*, Elsevier, 2015, pp. 179–254, <https://doi.org/10.1016/B978-0-12411470-8.00007-6>.
- [38] V. Lioubimov, A. Kolomenskii, A. Mershin, D.V. Nanopoulos, H. a Schuessler, Effect of varying electric potential on surface-plasmon resonance sensing, *Appl. Opt.* 43 (2004) 3426–3432, <https://doi.org/10.1364/AO.43.003426>.
- [39] S.A. Abayzeed, R.J. Smith, K.F. Webb, M.G. Somekh, C.W. See, Sensitive detection of voltage transients using differential intensity surface plasmon resonance system, *Opt. Express* 25 (2017) 31552, <https://doi.org/10.1364/OE.25.031552>.
- [40] M. Smietana, M. Sobaszek, B. Michalak, P. Niedzialkowski, W. Bialobrzaska, M. Koba, P. Sezemsky, V. Stranak, J. Karczewski, T. Ossowski, R. Bogdanowicz, Optical monitoring of electrochemical processes with ITO-based Lossy-mode resonance optical fiber sensor applied as an electrode, *J. Lightwave Technol.* 36 (2018) 954–960, <https://doi.org/10.1109/JLT.2018.2797083>.
- [41] G. Prampolini, P. Yu, S. Pizzanelli, I. Cacelli, F. Yang, J. Zhao, J. Wang, Structure and dynamics of ferrocyanide and ferricyanide anions in water and heavy water: an insight by MD simulations and 2D IR spectroscopy, *J. Phys. Chem. B* 118 (2014) 14899–14912, <https://doi.org/10.1021/jp511391b>.
- [42] B.-J. Hwang, H.-C. Chen, F.-D. Mai, H.-Y. Tsai, C.-P. Yang, J. Rick, Y.-C. Liu, Innovative strategy on hydrogen evolution reaction utilizing activated liquid water, *Sci. Rep.* 5 (2015) 16263, <https://doi.org/10.1038/srep16263>.

B3. Optical Monitoring of Electrochemical Processes with ITO-Based Lossy-Mode Resonance Optical Fiber Sensor Applied as an Electrode

Mateusz Smietana, Michał Sobaszek, Bartosz Michalak, Paweł Niedzialkowski, Wioleta Białobrzaska, Marcin Koba, Petr Sezemsky, Vitezslav Stranak, Jakub Karczewski, Tadeusz Ossowski, Robert Bogdanowicz, Optical Monitoring of Electrochemical Processes With ITO-Based Lossy-Mode Resonance Optical Fiber Sensor Applied as an Electrode, Journal of Lightwave Technology 36, (2018), 954-960.

Abstract

In this paper, we discuss the application of optical fiber sensors based on lossy-mode resonance (LMR) phenomenon for real-time optical monitoring of electrochemical processes. The sensors were obtained by a reactive high power impulse magnetron sputtering of indium tin oxide (ITO) on a 2.5 cm long core of polymer-clad silica fibers. The LMR effect made monitoring of changes in optical properties of both ITO and its surrounding medium possible. Moreover, since ITO is electrically conductive and electrochemically active, it was used as a working electrode in a three-electrode cyclic voltammetry setup. The investigations have shown that the sensor's optical response strongly depends on the potential applied to the sensor, as well as on electrochemical modification of its surface. The obtained LMR effect can be applied in parallel to electrochemical measurements for real-time optical monitoring of the electrode conditions and properties of the surrounding medium.

1. INTRODUCTION

Multi-domain sensing, which includes a combination of optical, electrical or mechanical effects, can offer the capability for simultaneous investigation of optical, electrical or mechanical properties of analyte in proximity of the sensor surface [1]. Moreover, the approach allows for the initiation of a specific process in one domain and at the same time monitoring of the process progress using the other domain.

Electrochemical (EC) processes are widely applied for electrical detection of a variety of organic compounds and heavy metals, as well as electrode surface treatment [2-4]. It has already been shown that EC processes can be simultaneously monitored optically using gold-coated glass electrodes. In such a configuration for the optimized gold film thickness, an optical effect, namely surface plasmon resonance (SPR), can also be obtained [5]. The SPR effect depends on the optical properties of a medium at the gold surface, and therefore makes real-time optical monitoring of the various biochemical processes taking place at the EC sensing electrode possible. These processes include thin biological film growth. The method was used to investigate electrical switching of DNA monolayers at the gold electrode [6]. The potential applied to the gold film attracted the intrinsically negatively charged DNA, which was either driven away from, or pulled towards the gold surface. SPR was also used for the real-time evaluation of live cancer cells in the EC setup [7]. Since SPR phenomenon employs light polarized in the plane of the surface, interrogation setups require light polarization control and mature EC-SPR setups are typically based on planar Kretschmann configuration, where gold-coated glass slides are used [8]. Few configurations have been reported where the sensor/electrode is based on an optical fiber, which offers a probe-like shape as is often expected [9]. Moreover, when biosensing applications of the gold-coated sensor are foreseen, its surface needs to be functionalized, which in the case of a gold surface is more complex than for, e.g., metal or semiconductor oxides [10]. Gold has no chemically reactive groups on its surface, which are required for attachment of organic compounds. Therefore, a specific gold surface modification is needed to form organic bridges that make interaction between the electrode and detected organic compound in the analyte possible [11]. Gold easily ties with sulfur and form one, two, or triple

bonds between them. However, this phenomenon significantly affects charge transfer between modified electrode and the analyte [12].

Since gold is not a perfect EC electrode material, other materials are intensively investigated for this purpose. When semiconductors are concerned, for an effective EC process the EC potential of reaction is expected to be between their conduction and valence band [13]. However, semiconductors barely satisfy the SPR conditions and thus other materials and sensing phenomena need to be sought for a multi-domain sensing application. It has been shown that simultaneous application of optical absorption measurements and EC methods make collection of enhanced data possible on, e.g., chemical reaction kinetics and dynamic concentration of a specific compound [14]. Since optical absorption is mainly analyzed via the analyte and the electrode, an optically transparent electrode material such as indium tin oxide (ITO) [15] or boron-doped diamond [16] is required.

ITO is known for its high optical transparency and low electrical resistivity [17]. Moreover, thanks to its band-gap, it is a good candidate for an EC electrode, as well as enabling it to be used for optical measurements. That is why ITO often substitutes gold electrodes wherever optical absorption at the electrode surface needs to be monitored during the EC process [15]. In contradiction to other transparent EC electrode materials, such as boron-doped diamond, thin ITO films can be deposited at relatively low temperatures on various substrates and shapes [18]. Plasma assisted deposition is often used for obtaining high quality ITO films [19]. The deposition process is typically followed by thermal post-processing at temperatures of about a few hundred degrees Celsius [20]. The main physical effect of the thermal annealing is to deliver the energy required for a crystallization process and to attain a favorable position of atoms forming the film. Also, another way of energy transfer to the film is possible when deposition using direct current magnetron sputtering at power range from 0.4 to 2.0 kW is applied. During such deposition the high power load provides a similar effect to annealing at temperatures of about 200 °C [21]. Ellmer et al. have attributed this behavior to energetic ions which occur in plasma discharges [22]. Energetic ions can be intensively generated during reactive high power impulse magnetron sputtering (R-HiPIMS). A high degree of ionization [23], which is controlled

by input plasma parameters, is one of the main benefits of HiPIMS discharges that usually improves the film quality [24].

Lossy-mode resonance (LMR) is a thin-film-based optical effect, which takes place when certain relations between electric permittivity of the film, substrate, and external medium are fulfilled, namely the real part of the film's electric permittivity must be positive and higher in magnitude than both the imaginary part of the thin film's permittivity and the permittivity of the analyte [25]. Any variation in optical properties (especially refractive index (RI)) of the analyte, have an influence on resonance conditions and thus can be detected. The effect has recently gained significant attention due to the possible relatively simple sensor fabrication process, the wide selection of thin film materials supporting the LMR and no need for the application of expensive or complex optical devices, such as lasers or polarizers [26]. Since in visible spectral range ITO shows relatively high RI ($n_D \sim 2$ RIU) and non-zero extinction coefficient corresponding to optical absorption, it has already been successfully applied for LMR-based sensing devices [27]. Applications of other thin films supporting the LMR effect such as diamond-like carbon [28], SiN_x [29], TiO_2 [30], and polymers [31] have also been reported, but among these materials only ITO offers low electrical resistivity and can be applied as an electrode material. To date, both the electrical conductivity of ITO and supported by its thin film LMR effect have been applied only for monitoring high voltage change in properties of an electro-optic material deposited on ITO surface [32] and for electro-polymerization of a chemical compound on ITO surface [33].

In this work, we discuss ITO-coated LMR optical fiber sensor used as a working electrode in cyclic voltammetry EC configuration. By adjusting the ITO properties, the LMR effect could be obtained and applied for optical monitoring of the EC processes.

2. EXPERIMENTAL DETAILS

The LMR structures were fabricated using approx. 15 cm long polymer-clad silica (PCS) fiber samples of 400/840 μm core/cladding diameter, where 2.5 length of polymer cladding was removed from the fiber central section [34]. Next, the electrically conductive and optically transparent ITO films were

deposited by R-HiPIMS of two perpendicularly oriented ITO targets (In_2O_3 - SnO_2 - 90/10 wt% and purity of 99.99%). The magnetron, whose axis was parallel to the substrate, was driven with dc-pulse modulated HiPIMS with the repetition frequency $f = 1$ kHz, duty cycle 10 % and the pulse width 100 μs . The mean discharge current was kept constant at 780 mA. The magnetron, whose axis was perpendicular to the substrate, was supplied by a RF source COMET Cito1310 (13.56 MHz, 300 W). The experiments were carried out at pressure $p = 1.0$ Pa in reactive N_2/Ar atmosphere, gas flows were 15 and 0.5–1.0 sccm for Ar and N_2 , respectively. The overlays were deposited on the fiber structures in a 2-step process, where between the processes the samples were flipped. Simultaneously, Si wafers were also coated with ITO for reference. Optical properties, i.e., RI (n) and extinction coefficient (k), as well as the thickness of the films deposited on reference Si wafers were measured with Jobin Yvon UVISEL spectroscopic ellipsometer, according to the procedure described in [35]. Next, the ITO samples were annealed (200 °C in air for 2 h) and both the fiber sample end-faces were mechanically polished before further optical testing.

To determine RI sensitivity of the fabricated ITO-based devices they were investigated in the air and mixtures of water/glycerin with RI from $n_D = 1.33$ to 1.43 RIU. The RI of the mixtures was measured using Rudolph J57AB refractometer. The optical transmission of the ITO-LMR structure was interrogated in range of $\lambda = 350$ –1050 nm using Ocean Optics HL-2000 white light source and USB4000 spectrometer. The optical transmission (T) in the specified spectral range was detected as counts in specified integration time (up to 100 ms) and presented in relation to normalized transmission for the setup with no sensing device installed (T_0). Numerical analysis of the ITO-LMR structure was performed according to the procedure described in [28].

Scanning electron microscope (SEM) analysis was done using FEI Quanta FEG 250 with beam accelerating voltage 15 kV and secondary electron Everhart-Thornley detector (SE-ETD) working in high vacuum mode ($p = 10^{-4}$ Pa).

Cyclic voltammetry (CV) measurements were performed in a three-electrode system where the ITO-LMR sensor, platinum wire and Ag/AgCl 0.1 M KCl electrodes were used as working (WE), counter (CE) and reference (REF) electrodes, respectively. The measurements were carried out in aqueous media

consisting of 5 mM $K_3[Fe(CN)_6]$ and 0.5 M Na_2SO_4 or in the 0.1 M phosphate buffer (PBS, pH = 7.02) solutions. The state of the electrodes was controlled by potentiostat galvanostat Autolab 204 N (Metrohm) supported by Nova 1.10 software. The cyclic voltammograms were recorded at a scan rate of 10 mVs^{-1} for ITO-LMR sensor and 100 mVs^{-1} for ITO films deposited on Si. Schematic representation of the investigated setup is shown in Fig. 1.

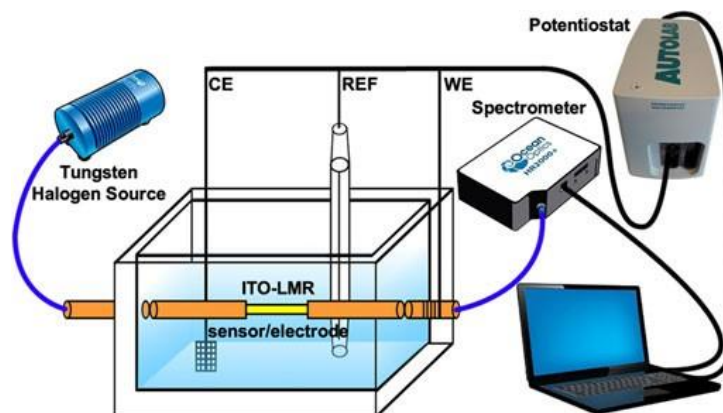


Fig. 1. Scheme of the combined EC and optical setup used in this experiment.

3. RESULTS AND DISCUSSION

Before the EC measurements, the ITO-LMR samples were tested in the optical setup to determine influence of the annealing process and external RI on their spectral response. It can be seen in Fig. 2 that all the resonances observed in the interrogated spectral range shift with external RI towards longer wavelength. The shift increases with wavelength. The annealing process, which is often applied to enhance or stabilize ITO properties, namely decrease both optical absorption and electrical resistivity, typically strongly modifies the properties of ITO, most likely due to the crystallization processes [35]. In our experiment, as a result of the process, the pattern was only slightly shifted towards shorter wavelengths. Moreover, the resonances shift less with RI than for the sample before the annealing. The effects correspond to some changes in optical properties of the ITO overlay with the annealing, namely a decrease in thickness and RI of the ITO film [36]. Nevertheless, the response is clearly visible for both annealed and non-annealed samples and the change in optical properties of the external medium can be easily noticed.

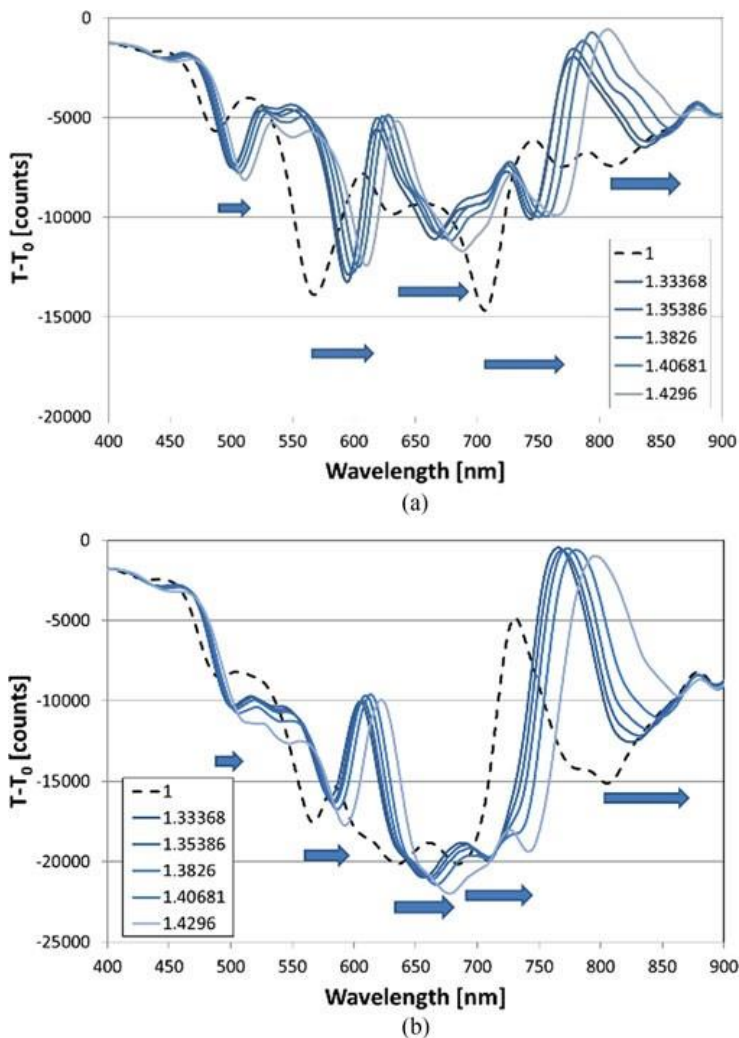


Fig. 2. Spectral response of the ITO-LMR sensor to changes in external RI for as deposited (a) and annealed (b) sample.

The influence of external RI and changes in the properties of the overlay on response of the ITO-LMR structure have been analysed numerically and the results are shown in Fig. 3. For the sake of calculations, optical properties of ITO received as a result of ellipsometric measurements of reference Si samples (as shown in Fig. 3(b)) were used. To determine thickness of the ITO overlay on fiber directly, we have made SEM analysis which results are shown in Fig. 4. The SEM analysis of the ITO thickness were possible just on short fragment of the cross-section (Fig. 4(c)) and the measured thickness (950 nm) was used for calculations. It must be noted that the results obtained numerically and experimentally correspond well qualitatively. Numerical

analysis assume uniform and well defined thickness of the ITO film around the fiber, where in reality it is not uniform, since the film was deposited with no rotation during the process. Non-uniform ITO distribution around the fiber may induce asymmetrical lossy mode coupling and thus less pronounced resonances are observed in the transmission spectrum. When the sample is annealed, the film properties change differently around the fiber, which on top of the resonance wavelength shift, make the resonance pattern look slightly different in selected spectral ranges. However, numerical analysis confirm that for LMR effect resonances observed at higher wavelength shift more with external RI than those at lower wavelength (Fig. 3(a)).

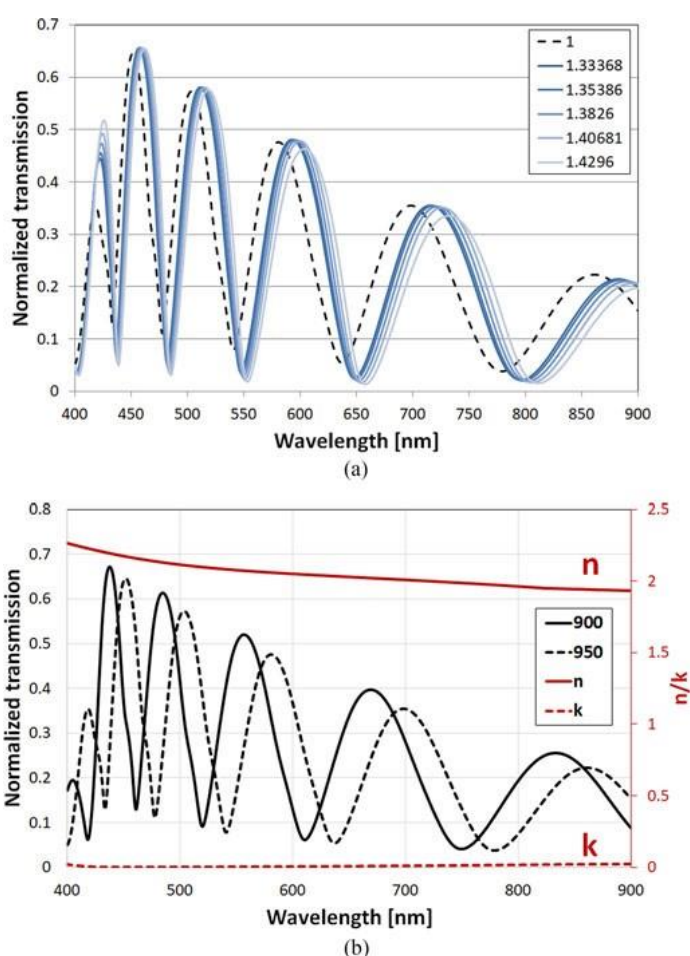


Fig. 3. Numerical analysis of the ITO-LMR sample when (a) increase in external RI and (b) decrease in thickness by 50 nm for external RI equal to 1 are considered. The n and k of ITO where assumed as shown in (b).

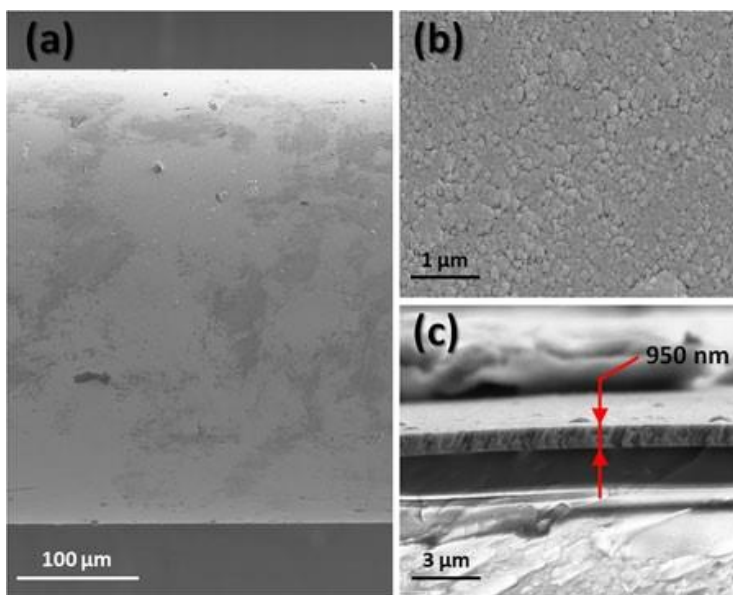


Fig. 4. SEM images of (a) section of the fiber coated with ITO, (b) ITO surface, and (c) fiber cross-section with indicated ITO overlay thickness.

Also a decrease in overlay thickness induces a shift of the spectrum towards shorter wavelength (Fig. 3(b)). As shown earlier, such modification might take place during the annealing [36]. The numerical results also here stays in agreement with experimental results where annealing induced wavelength shift towards the same direction.

The deposited ITO films are satisfactory for LMR effect, even with no annealing post-processing. This result is attributed to the unique advantages of R-HiPIMS discharge application. The R-HiPIMS process enables ionization of sputtered species on their passage from the target to the substrate. Our previous investigations have clearly shown that at the deposition pressure $0.5 \text{ Pa} < p < 1.0 \text{ Pa}$ collisions of the sputtered particles may be optimized [37]. The ITO films were deposited at pressures below 1.0 Pa, which makes the mean free path of particles in chamber comparable to the distance between target and the substrate. Hence, the sputtered particles having a Thompson energy distribution impinging the substrate without collision [37]. This results in their energy depletion and formation of surfaces with enhanced epitaxial crystallite growth. Here we observed the deposited crystalline ITO structure with small roughness (Fig. 4(b)). The crystalline structure, film density and surface roughness have an influence on optical, as well as electrical properties

of the deposited ITO. Generally, the RI of about $n_D \approx 2.2$ RIU was measured for crystalline films and a decrease was observed when the crystallinity was reduced. A higher RI of the ITO films is attained by enhanced material density, caused by the bombardment of energetic species during the deposition process. Hence, it is clear that application of R-HiPIMS is advantageous and lets the optical and electrical properties of deposited ITO films be tailored with no additional post-deposition annealing as required for other deposition methods [36].

Next, to estimate EC performance of the obtained ITO-coated electrodes, the reference samples were tested first in the CV setup. The ferrocyanide $[\text{Fe}(\text{CN})_6]^{3-/4-}$ (5 mM) in 0.5 M Na_2SO_4 and 0.5 M Na_2SO_4 were used here as a reduction/oxidation (redox) couple and working potential window test solutions, respectively. The measurements of ITO-coated Si wafer reference electrode are shown in Fig. 5. For this electrode electrochemical

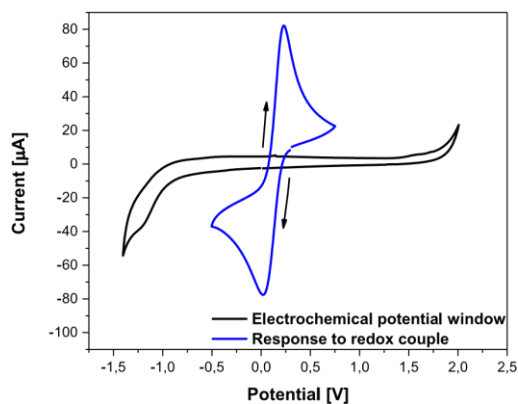


Fig. 5. CV recorded with a scan rate 100 mVs^{-1} on the ITO-coated Si reference wafer in 0.5 M Na_2SO_4 water solution (black) and with added to it 5 mM $[\text{Fe}(\text{CN})_6]^{3-/4-}$ (blue).

potential window ranges from -1 V to 1.75 V vs. Ag/AgCl 0.1 M KCl . This range is ca. -0.9 V wider than the window reported for standard gold electrodes thus enables enhanced EC detection of organic compounds [38]. The reduction/oxidation current peak separation in the potential domain reaches $\Delta E = 0.196 \text{ V}$, which indicates a quasi-reversible character of the reactions. For comparison, gold electrodes often show reduction and oxidation peaks at 0.6 and 0.85 V, respectively [8]. The absence of any visible peak of oxidation and reduction of the ITO electrode material in wide potential range is a meaningful advantage of this material over the gold electrode. These redox processes made on the gold electrode would have permanently modified it. The results directly indicate that the obtained ITO film can play the role of the EC active electrode.

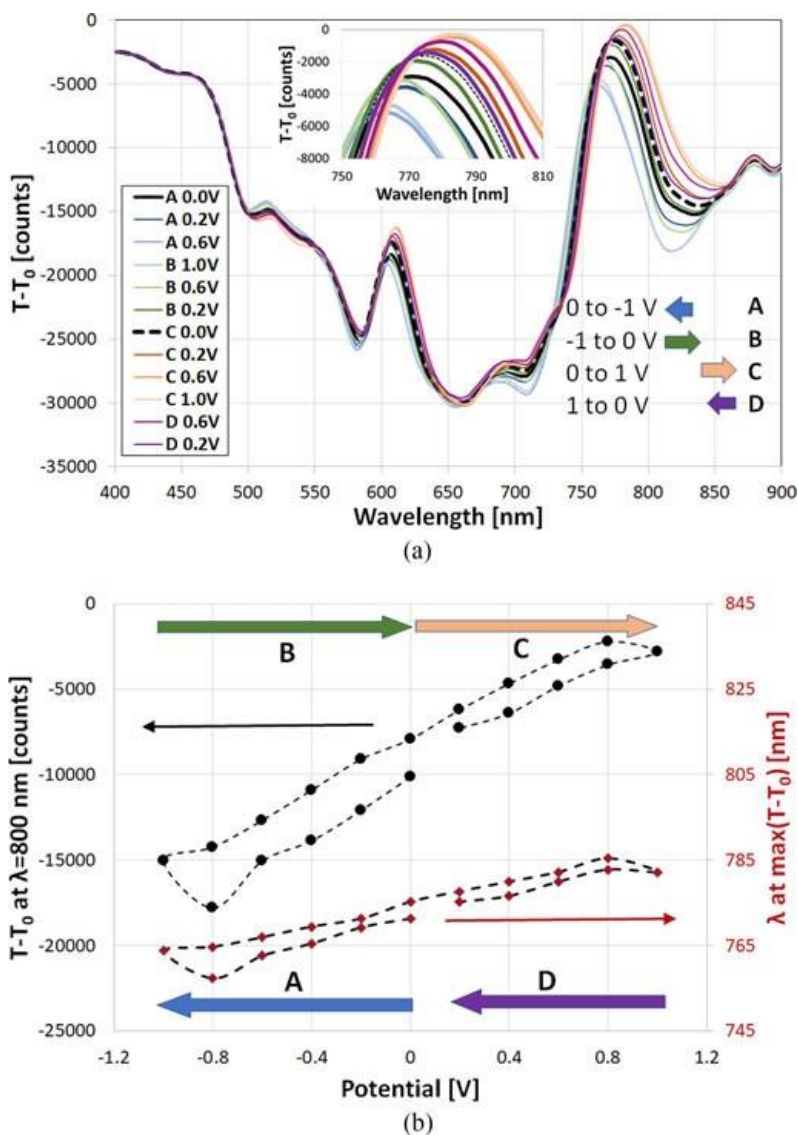


Fig. 6. Response of the ITO-LMR sensor to cycling potential between -1 and 1 V with a scan rate 10 mVs^{-1} in $0.5 \text{ M Na}_2\text{SO}_4$ solution containing $5 \text{ mM } [\text{Fe}(\text{CN})_6]^{3-/4-}$ where (a) shows the sensor's spectral response and (b) compares corresponding transmission changes at $\lambda = 800 \text{ nm}$ and transmission maximum's wavelength shift. Scan rate was set to 10 mVs^{-1} . An inset in (a) shows the investigated spectral range.

Combined EC and optical measurements using ITO-LMR electrode/sensor were performed next. In Fig. 6 the spectral response of the annealed ITO-LMR device to CV scanning potential in $[\text{Fe}(\text{CN})_6]^{3-/4-}$ redox complex is shown. Within one cycle the potential was first decreased to -1 V, then increased to 1 V and returned back to 0 V at a scan rate of 10 mVs^{-1} . It can be seen in Fig. 6(a)

that the resonances, especially at $\lambda \sim 580$ nm and ~ 820 nm strongly shift with the applied potential. The response, like in the case of RI variations, is greater with the wavelength. The resonances at higher wavelength correspond to higher order lossy modes [30]. What is more, referring to numerical analysis these two resonances may correspond to symmetrical lossy modes.

To analyze the response quantitatively, two parameters in the spectrum were taken into account, namely transmission at $\lambda = 800$ nm, which is on the resonance slope, and the wavelength corresponding to the maximum transmission in the spectrum ($\lambda = 750 - 800$ nm). Change of these parameters with the potential is shown in Fig. 6(b). Both of them follow the changes in the applied potential well. When the potential is negative, the resonances shift towards shorter wavelengths, and when it is positive, a red-shift of the resonance is observed. This red-shift of resonant wavelength corresponds to an increase of external RI close to the electrode surface (Fig. 2). Localized variation of solution density can be attributed to the relocations of negatively charged $[\text{Fe}(\text{CN})_6]^{3-/4-}$ ions attracted towards the positively biased ITO electrode. The reverse effect is observed at the electrode surface when the negative potential is applied, causing suppression of negative $[\text{Fe}(\text{CN})_6]^{3-/4-}$ ions [8, 39]. The shift of λ corresponding to the transmission maximum with cycling potential is meaningful and reaches over -12.5 nm/V. It can be then concluded that in these experimental conditions the potential applied to the ITO-LMR sensor/electrode corresponds to the increase in external RI at its surface. This effect is similar to that previously reported for SPR at gold electrodes, but makes application of transparent ITO electrode possible [5, 39].

Next, the possibility of optical monitoring of the ITO modification in the LMR setup was investigated. It is known that the presence of oxygen on the ITO electrode can improve its EC response [40]. By applying a high potential (from 0.3 to 2.0 V) an oxidation process was induced at the ITO-LMR electrode surface. In this case, a non-annealed ITO-LMR sample was used and its response was examined during ten consecutive CV cycles recorded for 0.1 M PBS solution (pH = 7.02) with the scan rate of 10 mVs⁻¹. In Fig. 7(a) the influence of both surface modification and scanning potential are observed in transmission response of the ITO-LMR sensor. As a result of subsequent CV scans, a clear decrease in current is also observed for the ITO-LMR electrode/sensor (Fig. 7(b)). This effect seems to result from the accumulation

of charge on the electrode's surface when it increases its resistivity. This phenomenon, on top of the potential cycling effect, is visible in Fig. 7(a) as a gradual build-up of the mean $T-T_0$ along with number of scans.

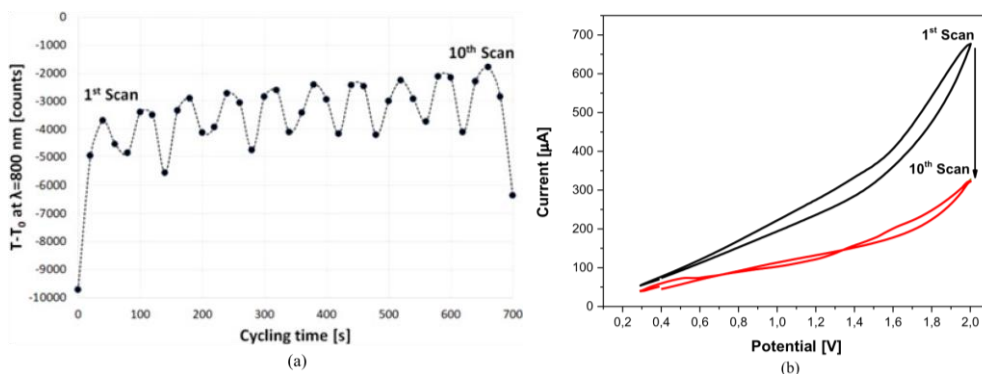


Fig. 7. The effect scanning process in 0.1 M PBS (pH = 7.02) where (a) shows change in transmission at $\lambda = 800$ nm acquired on average every 20 s and (b) change of current peaks during the cyclic voltammetry scans from 1 to 10 scan. Scan rate 10 mVs^{-1} and first measurement in (a) corresponds to 0.4 V.

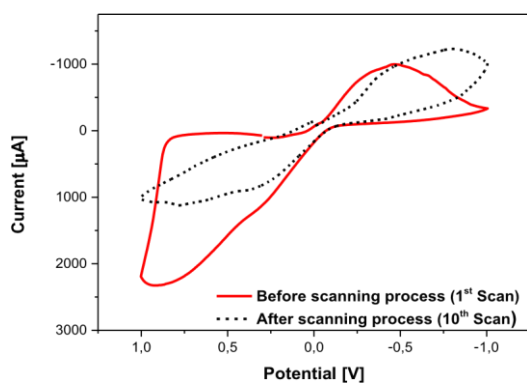


Fig. 8. CV recorded with a scan rate 10 mVs^{-1} on the ITO-LMR on not annealed sample in 0.5 M Na_2SO_4 containing 5 mM $[\text{Fe}(\text{CN})_6]^{3-/4-}$ before (red) and after (dotted) oxidation process.

To verify the oxidation effect on performance of the ITO-LMR electrode/sensor its CV response to $[\text{Fe}(\text{CN})_6]^{3-/4-}$ couple was recorded and compared to the one before the oxidation process. The results shown in Fig. 8 indicate that the responses are different than for the typical redox processes for this EC couple [41]. However, there is a noticeable difference in response before and after the oxidation process. After the oxidation process, the peak to peak (reduction to oxidation) separation is a bit narrower. This can be explained by an increase in electroactivity as a result of modification of the ITO surface and exposure of Sn-rich surface sites [40]. It is proven that the modification process of the

electrode can also be successfully monitored with the LMR approach. This powerful tool makes observation of any surface modification possible.

4. CONCLUSION

As a result of this study we have developed optical fiber sensors based on LMR effect supported by ITO thin overlay and used it for real-time optical monitoring of electrochemical processes. The high electrochemical and optical performance of ITO-LMR structure was achieved by its deposition with two unique perpendicularly oriented sputtering magnetrons, i.e., HiPIMS and continuous RF power guns, where no thermal post processing was required. A developed, highly conductive ITO overlay was deposited on optical fiber core and applied as a working electrode in cyclic voltammetry electrochemical setup. We have found that a change in potential applied to the ITO surface induces a significant change in the LMR response. The changes in optical transmission for the ITO-LMR sensor follow the straight progress in the electrochemical process. The sensor can then be optically interrogated by tracing the resonant power as well as the wavelength changes. The proposed novel sensing approach provides a promising strategy for both optical and electrochemical detection of modifications of ITO or changes taking place at its surface induced by various bio-compounds. Additionally, the monitoring of the bio-compound concentration is also possible. Due to the high optical transparency of ITO other techniques, such as absorption spectroscopy, can be additionally combined in the proposed setup.

References

- [1] E.Eltzov,S.Cosnier,andR.S.Marks,“Biosensorsbasedoncombinedoptical and electrochemical transduction for molecular diagnostics,” *Expert Rev. Mol. Diagnostics*, vol. 11, no. 5, pp. 533–546, Jun. 2011.
- [2] Y.-R. Kim et al., “Electrochemical detection of dopamine in the presence of ascorbic acid using graphene modified electrodes,” *Biosens. Bioelectron.*, vol. 25, no. 10, pp. 2366–2369, Jun. 2010.
- [3] K. Hashimoto, K. Ito, and Y. Ishimori, “Novel DNA sensor for electrochemical gene detection,” *Anal. Chim. Acta*, vol. 286, no. 2, pp. 219–224, Feb. 1994.

- [4] H. B. Suffredini, V. A. Pedrosa, L. Codognoto, S. A. S. Machado, R. C. Rocha-Filho, and L. A. Avaca, "Enhanced electrochemical response of boron-doped diamond electrodes brought on by a cathodic surface pretreatment," *Electrochim. Acta*, vol. 49, no. 22, pp. 4021–4026, Sep. 2004.
- [5] [5] V. Lioubimov, A. Kolomenskii, A. Mershin, D. V. Nanopoulos, and H. A. Schuessler, "Effect of varying electric potential on surface-plasmon resonance sensing," *Appl. Opt.*, vol. 43, no. 17, pp. 3426–3432, Jun. 2004.
- [6] X. Yang, Q. Wang, K. Wang, W. Tan, J. Yao, and H. Li, "Electrical switching of DNA monolayers investigated by surface plasmon resonance," *Langmuir*, vol. 22, no. 13, pp. 5654–5659, 2006.
- [7] C. Wu et al., "Real-time evaluation of live cancer cells by an *in situ* surface plasmon resonance and electrochemical study," *ACS Appl. Mater. Interfaces*, vol. 7, no. 44, pp. 24848–24854, Nov. 2015.
- [8] A. M. Lopatynskiy, O. G. Lopatynska, L. V. Poperenko, V. I. Chegel, and M. D. Guiver, "Factor of interfacial potential for the surface plasmonpolaritonresonancesensor response," *Semicond.Phys.QuantumElectron. Optoelectron.*, vol. 11, no. 4, pp. 329–336, 2008.
- [9] Y. Yuan et al., "Electrochemical surface plasmon resonance fiber-optic sensor: In situ detection of electroactive biofilms," *Anal. Chem.*, vol. 88, no. 15, pp. 7609–7616, Aug. 2016.
- [10] J. Lyskawa and D. Belanger, "Direct modification of a gold electrode with aminophenyl groups by electrochemical reduction of in situ generated aminophenyl monodiazonium cations," *Chem. Mater.*, vol. 18, no. 20, pp. 4755–4763, Oct. 2006.
- [11] K. Hashimoto, K. Ito, and Y. Ishimori, "Sequence-Specific gene detection with a gold electrode modified with DNA probes and an electrochemically active Dye," *Anal. Chem.*, vol. 66, no. 21, pp. 3830–3833, Nov. 1994.
- [12] H. Hakkinen, "The gold-sulfur interface at the nanoscale," *Nature Chem.*, vol. 4, no. 6, pp. 443–455, Jun. 2012.
- [13] S. Z. Karazhanov, P. Ravindran, P. Vajeeston, A. Ulyashin, T. G. Finstad, and H. Fjellvag, "Phase stability, electronic structure, and optical properties of indium oxide polytypes," *Phys. Rev. B*, vol. 76, no. 7, Aug. 2007, Art. no. 075129.
- [14] W. Kaim and J. Fiedler, "Spectroelectrochemistry: The best of two worlds," *Chem. Soc. Rev.*, vol. 38, no. 12, pp. 3373–3382, 2009.
- [15] J. Agrisuelas, D. Gimenez-Romero, J. J. Garcia-Jareno, and F. Vicente, "Vis/NIR spectroelectrochemical analysis of poly-(Azure A) on ITO electrode," *Electrochem. Commun.*, vol. 8, no. 4, pp. 549–553, Apr. 2006.

-
- [16] J. Stotter, J. Zak, Z. Behler, Y. Show, and G. M. Swain, "Optical and electrochemical properties of optically transparent, boron-doped diamond thin films deposited on quartz," *Anal. Chem.*, vol. 74, no. 23, pp. 5924–5930, Dec. 2002.
- [17] T. Minami, "Present status of transparent conducting oxide thin-film development for indium-tin-oxide (ITO) substitutes," *Thin Solid Films*, vol. 516, no. 17, pp. 5822–5828, 2008.
- [18] D. C. Paine, T. Whitson, D. Janiac, R. Beresford, C. O. Yang, and B. Lewis, "A study of low temperature crystallization of amorphous thin film indium–tin–oxide," *J. Appl. Phys.*, vol. 85, no. 12, pp. 8445–8450, May 1999.
- [19] M. Quaas, H. Steffen, R. Hippler, and H. Wulff, "The growth process of plasma-deposited ITO films investigated by grazing incidence X-ray techniques," *Surf. Sci.*, vol. 454, pp. 790–795, May 2000.
- [20] B. Szyszka et al., "Recent developments in the field of transparent conductive oxide films for spectral selective coatings, electronics and photovoltaics," *Curr. Appl. Phys.*, vol. 12, pp. S2–S11, Dec. 2012.
- [21] M. Huang, Z. Hameiri, A. G. Aberle, and T. Mueller, "Influence of discharge power and annealing temperature on the properties of indium tin oxide thin films prepared by pulsed-DC magnetron sputtering," *Vacuum*, vol. 121, pp. 187–193, Nov. 2015.
- [22] K. Ellmer and T. Welzel, "Reactive magnetron sputtering of transparent conductive oxide thin films: Role of energetic particle (ion) bombardment," *J. Mater. Res.*, vol. 27, no. 5, pp. 765–779, Mar. 2012.
- [23] V. Stranak et al., "Highly ionized physical vapor deposition plasma source working at very low pressure," *Appl. Phys. Lett.*, vol. 100, no. 14, Apr. 2012, Art. no. 141604.
- [24] V. Stranak, Z. Hubicka, M. Cada, S. Drache, M. Tichy, and R. Hippler, "Investigation of ionized metal flux in enhanced high power impulse magnetron sputtering discharges," *J. Appl. Phys.*, vol. 115, no. 15, Apr. 2014, Art. no. 153301.
- [25] I. D. Villar et al., "Design rules for lossy mode resonance based sensors," *Appl. Opt.*, vol. 51, no. 19, pp. 4298–4307, Jul. 2012.
- [26] I. D. Villar et al., "Optical sensors based on lossy-mode resonances," *Sens. Actuators B Chem.*, vol. 240, pp. 174–185, Mar. 2017.
- [27] C. R. Zamarrano, M. Hernaez, I. Del Villar, I. R. Matias, and F. J. Arregui, "Tunable humidity sensor based on ITO-coated optical fiber," *Sens. Actuators B Chem.*, vol. 146, no. 1, pp. 414–417, Apr. 2010.
- [28] M. Smietana, M. Dudek, M. Koba, and B. Michalak, "Influence of diamond-like carbon overlay properties on refractive index sensitivity of nano-coated optical fibres," *Phys. Status Solidi A*, vol. 210, no. 10, pp. 2100–2105, Oct. 2013.
-

- [29] B. Michalak, M. Koba, and M. Smietana, "Silicon nitride overlays deposited on optical fibers with RF PECVD method for sensing applications: Overlay uniformity aspects," *Acta Phys. Pol. A*, vol. 127, no. 6, pp. 1587–1591, Jun. 2015.
- [30] D. Burnat, M. Koba, Ł. Wachnicki, S. Gierałtowska, M. Godlewski, and M. Smietana, "Refractive index sensitivity of optical fiber lossy-mode resonance sensors based on atomic layer deposited TiOx thin overlay," vol. 9916, *Proc. SPIE*, 2016, Art. no. 99161G1.
- [31] C. R. Zamarreno, M. Hernáez, I. Del Villar, I. R. Matías, and F. J. Arregui, "Optical fiber pH sensor based on lossy-mode resonances by means of thin polymeric coatings," *Sens. Actuators B Chem.*, vol. 155, no. 1, pp. 290–297, Jul. 2011.
- [32] J. Ascorbe, J. M. Corres, F. J. Arregui, and I. R. Matías, "Optical fiber current transducer using lossy mode resonances for high voltage networks," *J. Lightw. Technol.*, vol. 33, no. 12, pp. 2504–2510, Jun. 2015.
- [33] M. Sobaszek et al., "Optical monitoring of thin film electropolymerization on surface of ITO-coated lossy-mode resonance sensor," *Proc. SPIE*, vol. 10323, 2017 pp. 103234W1.
- [34] M. Smietana, J. Szmids, M. Dudek, and P. Niedzielski, "Optical properties of diamond-like cladding for optical fibres," *Diamond Relat. Mater.*, vol. 13, no. 4, pp. 954–957, Apr. 2004.
- [35] M. Dominik et al., "Annealing of indium tin oxide (ITO) coated optical fibers for optical and electrochemical sensing purposes," *Proc. SPIE*, vol. 10175, 2016, Art. no. 10175151.
- [36] I. Del Villar, C. R. Zamarreno, M. Hernáez, P. Sanchez, F. J. Arregui, and I. R. Matias, "Generation of surface plasmon resonance and lossy mode resonance by thermal treatment of ITO thin-films," *Opt. Laser Technol.*, vol. 69, pp. 1–7, Jun. 2015.
- [37] V. Stranak et al., "Effect of mid-frequency discharge assistance on dual-high power impulse magnetron sputtering," *Surf. Coating Technol.*, vol. 206, no. 11, pp. 2801–2809, 2012.
- [38] J. D. Benck, B. A. Pinaud, Y. Gorlin, and T. F. Jaramillo, "Substrate selection for fundamental studies of electrocatalysts and photoelectrodes: Inert potential windows in acidic, neutral, and basic electrolyte," *PLOS One*, vol. 9, no. 10, Oct. 2014, Art. no. e107942.
- [39] A. Lopatynskiy, M. Guiver, and V. Chegel, "Surface plasmon resonance biomolecular recognition Nanosystem: Influence of the interfacial electrical potential," *J. Nanosci. Nanotechnol.*, vol. 14, no. 9, pp. 6559–6564, Sep. 2014.

-
- [40] M. Brumbach et al., “Surface composition and electrical and electrochemical properties of freshly deposited and acid-etched indium tin oxide electrodes,” *Langmuir*, vol. 23, no. 22, pp. 11089–11099, Oct. 2007.
- [41] I. Ashur and A. K. Jones, “Immobilization of azurin with retention of its native electrochemical properties at alkylsilane self-assembled monolayer modified indium tin oxide,” *Electrochim. Acta*, vol. 85, pp. 169–174, Dec. 2012.

© 2018 IEEE. Reprinted, with permission, from Mateusz Smietana et al., Optical Monitoring of Electrochemical Processes With ITO-Based Lossy-Mode Resonance Optical Fiber Sensor Applied as an Electrode, *Journal of Lightwave Technology*, Feb./2018.

B4. Study on Combined Optical and Electrochemical Analysis Using Indium-tin-oxide-coated Optical Fiber Sensor

Mateusz Smietana, Paweł Niedzialkowski, Wioleta Białobrzaska, Dariusz Burnat, Petr Sezemsky, Marcin Koba, Vitezslav Stranak, Katarzyna Siuzdak, Tadeusz Ossowski, Robert Bogdanowicz, Study on Combined Optical and Electrochemical Analysis Using Indium-tin-oxide-coated Optical Fiber Sensor, Electroanalysis 31, (2019), 398.

Republished with permission of John Wiley & Sons - Books; permission conveyed through Copyright Clearance Center, Inc.

Abstract

In this work an optical fiber sensor, where a lossy-mode resonance (LMR) effect was obtained due to indium tin oxide (ITO) thin overlay, has been simultaneously applied as a working electrode in a 3-electrode cyclic voltammetry electrochemical setup. Since LMR conditions highly depend on refractive index of a surrounding medium, an LMR-based sensor was applied for optical investigations of electrolyte's properties at the ITO surface. We have found that the optical response of the sensor highly depends on the applied potential and its changes, as well as the properties of the investigated electrolyte, i. e., its composition and presence of a redox probe. Both optical and electrochemical response of the ITO-LMR sensor to various concentrations of phosphate-buffered saline (PBS), NaCl and Na₂SO₄, as well as scan rate were investigated and discussed. We have found that the responses in optical and electrical domains differ significantly and may deliver supplementary information about the investigated analyte.

1. INTRODUCTION

Possibilities for multi-domain sensing, which may include simultaneous, e. g., optical, electrical or mechanical interrogation, has been intensively explored in the last decade [1-3]. Study in additional domains may enhance information about the investigated sample or provide confirmation of results received in the other domain. The later advantage may help to reduce the amount of false positive results. One of the domains may also be used to initiate certain phenomenon, where the monitoring of effects is provided in the other domain. As a successful multi-domain approach optical analysis using surface plasmon resonance (SPR) effect combined with electrochemical (EC) measurements can be pointed [4]. The EC-SPR systems typically employs a thin gold layer deposited on a glass slide, where the metal supports SPR effect and simultaneously plays a role of a working electrode in the EC setup. The EC-SPR concept has also been applied using gold-coated tilted fiber Bragg grating [5]. The application of optical fiber offers a probe-like sensor shape, which e. g., allows for its application in widely available standard cuvette-based EC setups or other sensing architectures [6].

Besides gold, there is a set of electrode materials that are used in EC analysis. The most popular thin film materials are boron-doped diamond (BDD), indium tin oxide (ITO), and fluorine-doped tin oxide (FTO), which in contrast to gold, are also optically transparent. Since BDD requires high temperature deposition, which may induce damage to temperature-sensitive substrate materials [7], the doped tin oxides are considered as much less temperature demanding. Furthermore, they are considered as universal materials for transparent EC electrodes, where additionally to EC measurements also optical transmission through the sample may be monitored (spectroelectrochemistry) and it can deliver additional information about the EC process [8]. Thin ITO films have similarly been applied for combined optical and EC analysis on planar and optical fiber sensing devices, but in this case ITO was applied mainly in order to initialize EC-induced polymerization of a compound necessary for further detection procedure [1]. Meanwhile, it has been found that when the potential is applied to the electrode in opto-EC setup and both optical and EC responses are investigated simultaneously, significantly more information can be received about the investigated medium than when the responses are studied separately [3, 9].

In our previous work we proposed a simple optical-fiber-based device where both optical and EC readouts are possible [10]. Such a sensor may be used for optical monitoring of EC processes taking place on its surface [11]. Unlike in other works employing ITO deposited on tip of optical fibers [1], here a 2–3 cm long cladding-stripped side surface of a multimode fiber core was coated. In such a structure at certain ITO thickness and with certain optical properties a lossy-mode resonance (LMR) can be seen in fiber transmission spectrum [12]. The LMR wavelength highly depends on the properties of ITO and external medium, i. e., its refractive index (RI), as well as any thin film formed on its surface. These advantages make application of the LMR-based structure in label-free biosensing possible [13]. When the device is supported by EC setup, it offers the capability of receiving enhanced information about the investigated analyte compared to simple optical interrogation. The analytes, when investigated in EC setups, are present in various electrolytes which are used as the main source of electrically conducting ionic species. For this purpose acids, bases, both organic and inorganic salts and buffered solutions are commonly diluted by aqueous and non-aqueous solutions. The concentration of these electrolytes is usually between 0.01 M and 1.0 M and is higher than the one of the investigated analyte [14]. The main role of the electrolyte is to lower the solution resistance between electrodes and to eliminate migration of the analyte to the working electrode [15, 16].

In this work we focus on the influence of EC stimulation, i. e., potential applied to the ITO-LMR sensor in 3-electrode cyclic voltammetry (CV) setup, on optical and EC responses received from the sensor. We used electrolytes containing several commonly applied inorganic salts to have a deeper understanding of the origin of the changes observed in both readouts. This work is of high importance when further dual-domain label-free biosensing with ITO-LMR device is considered.

2. EXPERIMENTAL

The experimental setup for combined optical and EC measurements has been reported in detail in [10]. The ITO-LMR sensors were based on approx. 15 cm-long polymer-clad silica fiber samples of 400/840 μm core/cladding diameter, where 2.5 cm long polymer cladding was removed from the fiber's central section. Next, ITO overlays were deposited on the fibers using standard planar magnetron with unbalanced magnetic field. The deposition system used

sputtering gun running in continuous RF power mode only and equipped with ITO target composed of In_2O_3 – SnO_2 90–10 wt% and with purity of 99.99 % employing a similar concept as in our previous work [17]. In this experiment, to increase RI sensitivity of the ITO-LMR sensor, the overlay thickness was reduced to observe the lowest possible order of LMR resonances [12]. The overlays were deposited in a 1 h-long process when the fiber samples were continuously rotated in the chamber to obtain uniform ITO deposition around the fiber. Next, both fiber end-faces were mechanically polished before optical testing in mixtures of water/glycerin with RI from $n_D = 1.33$ to 1.45 RIU. The RI of the mixtures was measured using Rudolph J57 refractometer. The optical transmission of the ITO-LMR sensor was observed in $\lambda = 350$ – 1050 nm using Ocean Optics HL-2000 white light source and Ocean Optics USB4000 spectrometer supported by a software continuously acquiring optical data. The optical power in the specified spectral range was detected as counts in 100 ms of integration time and presented in relation to normalized power transmitted in the system in which the fiber sensing device had no ITO overlay and the measurement was performed in standard conditions.

CV measurements in a 3-electrode configuration were performed with a Metrohm-Autolab PGSTAT 204 potentiostat-galvanostat supported by Nova 1.10 software. An ITO-LMR sensor was used as a working electrode, while platinum wire and silver-silver chloride electrode Ag/AgCl (0.1 M KCl) were used as auxiliary and reference electrodes, respectively. All potentials in the range from -1.0 to $+1.0$ V at a scan rate of 100 mV s^{-1} were applied versus the reference electrode at room temperature. A set of aqueous electrolytes was applied, i. e., 0.1 M and 0.01 M phosphate-buffered saline (PBS, pH = 7.0), 0.5 M and 0.05 M NaCl, 0.5 M and 0.05 M Na_2SO_4 . Measurements were also performed in reduction/oxidation (redox) probe-containing solution, i. e., 5 mM $\text{K}_3[\text{Fe}(\text{CN})_6]$ in 0.5 M Na_2SO_4 and additionally at scan rate 1 mV s^{-1} for PBS. The 0.1 M PBS was prepared according to the European Pharmacopoeia 5.0 by adding 35 g of Na_2HPO_4 to solution of 1.361 g of KH_2PO_4 and diluted in 1 l of deionized water. All chemicals used in the experiments were of analytical grade and used without further purification.

3. RESULTS AND DISCUSSION

3.1. RI Sensitivity of the ITO-LMR Sensor

The optical response of the ITO-LMR sensor to changes in external RI is presented in Figure 1. Compared to previously reported results 10, due to reduced thickness of ITO and more uniform deposition around the fiber obtained by introduction of fiber rotation during the process, a single and well-defined resonance was observed in the investigated spectral range. The RI sensitivity has also been increased significantly to approx. 325 nm/RIU in RI range $n_D = 1.333$ to 1.382 RIU. Typically applied electrolytes have their RI in this range.

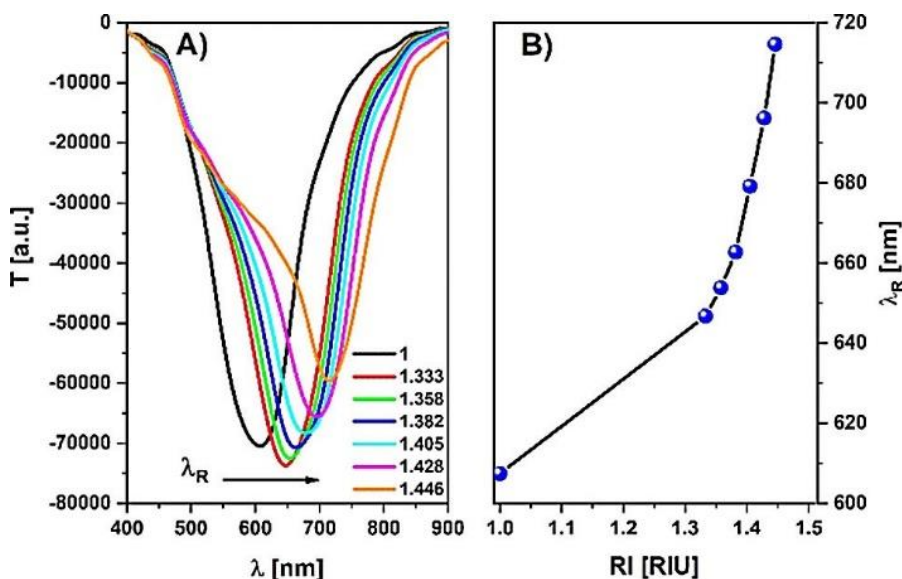


Figure 1. Optical response of the ITO-LMR sensor to changes in external RI, where (A) shows spectra and (B) corresponding resonance wavelengths.

3.2. EC Response of the ITO-LMR Sensor to Applied Potential in Various Electrolyte Solutions

CV response of the ITO-LMR sensors was studied in detail for applied potential in the range of -1.0 to 1.0 V and the following electrolytes: 0.1 M PBS, 0.5 M NaCl and 0.5 M Na₂SO₄. Next, the measurements were repeated in the same electrolytes, but each with ten-fold lower concentration. The EC responses for all the electrolytes are shown in Figure 2A to 2C. The CV when the redox probe was added to Na₂SO₄ is shown for comparison in Figure 2D.

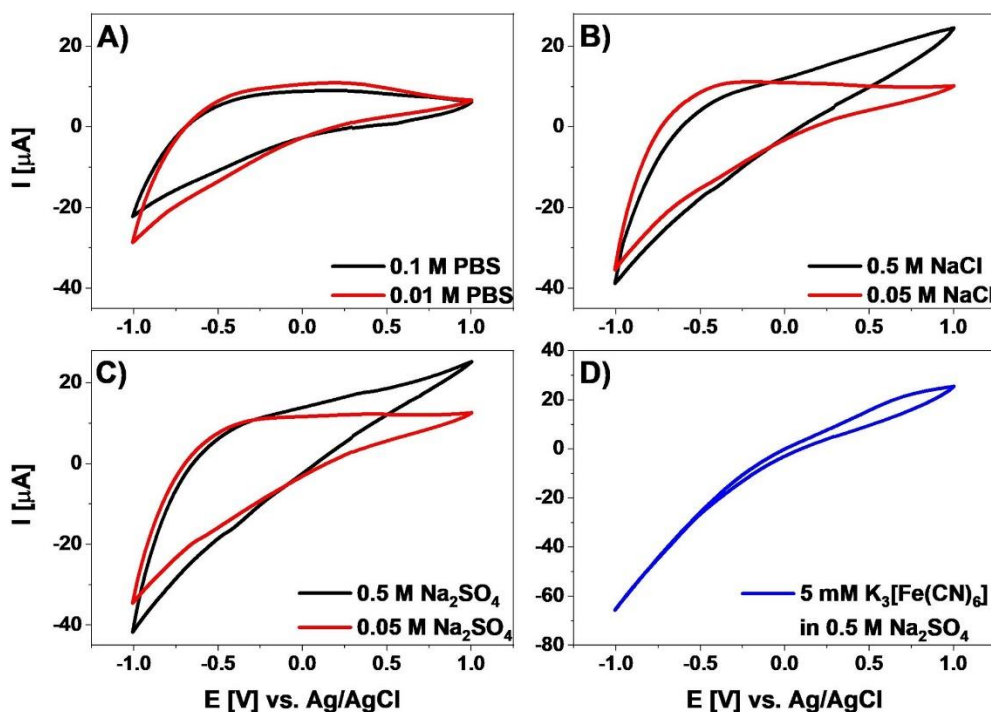


Figure 2. CVs recorded with the ITO-LMR sensor as a working electrode in various concentration of PBS (A), NaCl (B) and Na_2SO_4 (C). CV for electrolyte with redox probe is shown in (D), where different scale of current was used. Scan rate was set to 100 mV s^{-1} .

Upon positive potential change of the ITO-LMR sensor, its surface acquires positive charges. Cations near the surface respond to this charge by migrating away from the surface and anions migrate toward the electrode/electrolyte interface. This migration occurs until the equilibrium is achieved between the electrode's positive surface charge and the negative charge of the solution near the electrode. Because the movement of ions and electrons is indistinguishable, the result corresponds to a small, short-lived, non-faradaic current, called a charging current. When the electrode potential is changed, a transient current flows. CV curves recorded in PBS exhibit a very similar shape independently to its concentration (Figure 2A) and are similar to those obtained for lower concentrations of NaCl and Na_2SO_4 (Figure 2B and 2C). The comparison of results for 0.5 M NaCl and 0.05 M NaCl in turn indicates that the curves are very similar to these obtained in 0.05 M Na_2SO_4 and 0.5 M Na_2SO_4 , respectively. An increase in NaCl and Na_2SO_4 concentration is followed by an increase in the current when a positive potential is applied. The

explanation of this phenomenon is complex due to many factors affecting the EC process. The capacitance of the electrode which depends on the electrolyte properties, i. e., its pH, type of cation and anion species, and salt concentrations, should be mainly taken into consideration [18-20]. The electrolyte concentration has a significant influence on the mass transport of the analyte according to the Nerst-Planck equation. Additionally, the cationic mobility influence the ionic conductivity, efficient ion/charge diffusion/exchange and relaxation time [21].

In order to determine the EC behavior of the ITO-LMR sensor, the CVs were recorded in 0.5 M Na₂SO₄ solution containing 5 mM K₃Fe(CN)₆ as a redox probe. When the probe was present in the electrolyte, the characteristic for [Fe(CN)₆]^{3-/4-} reversible peaks of the reduction and oxidation processes are not observable within the potential range -1.0 to +1.0 V vs. Ag/AgCl (0.1 M KCl) [22] (Figure 2D). Such complete blocking behavior of obtained ITO-LMR sensor can indicate that there is an inappropriate alignment of levels of energy between ITO and ferriicyanide redox couple [23], as will be discussed later. According to Gerischer [24], as well as the Bard and Wrighton [25] models, there are thermodynamic criteria for the stability of semiconducting electrodes, based on the oxidative and reductive decomposition potentials and quasi Fermi levels of negative and positive charges at the electrodes' surfaces. Following the model assumptions, when the electrode is immersed in electrolyte containing redox species an electron transfer occurs from an occupied state of the semiconductor to an empty state in the redox system. The reverse process covering the injection of minority carriers from the redox system into the semiconductor is only possible with redox species, where standard potential is very close to the corresponding band of the semiconductor [26], as it is schematically shown in Figure 3. This means that the electron transfer is faster than any rearrangement of the solvent molecules and the rate of such process depends on the density of energy states at the electrode/electrolyte interface. Additionally, it should be noted that the dissolution of the electrode material characteristic for n-type conductivity, as it is in ITO-LMR sensor case, takes place when its formal oxidation potential E_{decomp} is lower than the edge of the valence band at the surface electrons. If the redox couple is present in the electrolyte with the formal reversible potential of the redox reaction (E_{rdx}), spontaneous oxidation of the

semiconductor by the electrolyte solution is possible when $E_{\text{decomp}} < E_{\text{rdx}}$. Those thermodynamic predictions, however, are limited because the electrode reactions are controlled by kinetics and the detailed relative position of energy states of both sides of the interface: electrode material and redox formal potential. As was emphasized above, the most efficient electron transfer is expected from the occupied states of the redox system to the valence band of the semiconductor when these energy states show good overlap. Thus, it is highly possible that the beneficial relation between energy bands of ITO-LMR sensor and redox species does not occur, thus no peak in CV curve is present, as happens in the plots shown in Figure 2D.

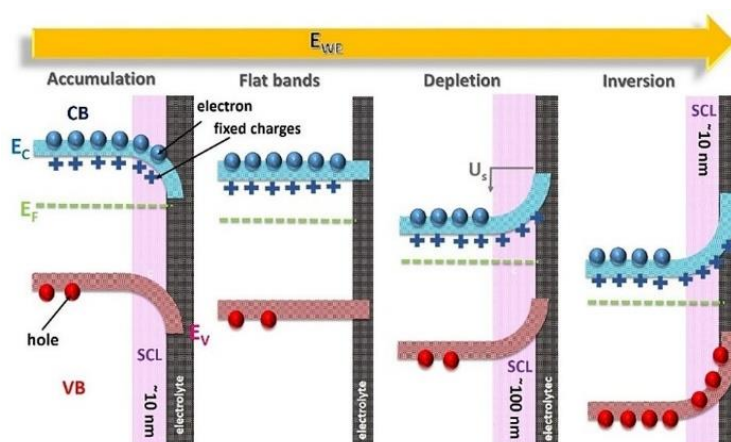


Figure 3. Band diagram at the electrode (ITO-LMR sensor) at different stages of polarization, i. e. applied potential. Injection of minority carriers (holes) from a redox system into the valence band of an n-type semiconductor (ITO) electrode and their subsequent recombination upon the anodic bias.

3.3. Optical Response of the ITO-LMR Sensor to Applied Potential in Various Electrolyte Solutions

The previously reported ITO-LMR sensor with thicker ITO showed the multiple resonances in the investigated spectral range [10]. Here, the probe with thinner ITO cladding exhibits single traced resonance, where the resonance wavelength clearly follows the changes in the applied potential. Optical responses for the sensor at the lowest and (-1.0 V) the highest (+1.0 V) applied potentials when Na_2SO_4 with $\text{K}_3[\text{Fe}(\text{CN})_6]$ and PBS were used as electrolytes are shown in Figure 4A and 4B, respectively. The

responses for these two solutions were selected to show how much the composition of the solution influences response of the ITO-LMR sensor to the applied potential. For both measurements all other experimental conditions were the same, i. e. the applied scan rate was 100 mV s^{-1} . The maximum shift in resonance wavelength induced by the applied potential for Na_2SO_4 with $\text{K}_3[\text{Fe}(\text{CN})_6]$ and PBS reaches 5 and 24 nm, respectively. Origins of the observed differences are discussed later in this section.

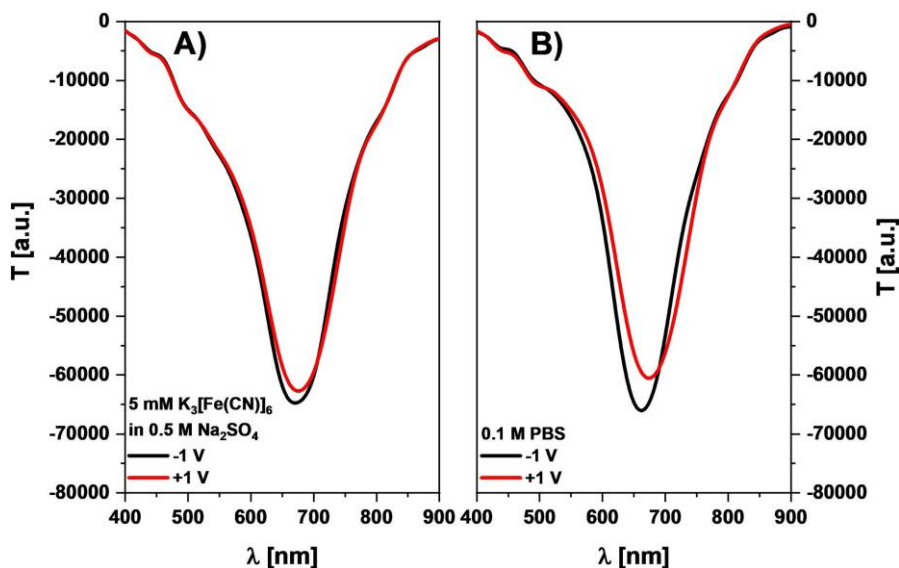


Figure 4. Optical spectrum of the ITO-LMR sensor at maximum (+1.0 V) and minimum (-1.0 V) applied potential when investigated in (A) Na_2SO_4 with $\text{K}_3[\text{Fe}(\text{CN})_6]$ redox probe and (B) PBS. Scan rate was set to 100 mV s^{-1} .

In Figure 5, the results of optical measurements (the trace of resonance wavelength – λ_R) are summarized for different potential and electrolytes. The measurements were recorded at the same time instances as the EC ones shown in Figure 2, but for optical measurements the results are more sparse due to integration and data processing time required by the optical setup. The character of both optical and EC results is very similar, i. e., the resonance shifts more when negative potential is applied and for the positive one the changes are less significant. The shift in resonance wavelength can be induced by the change in both optical properties of ITO and external RI (electrolyte) in proximity of ITO surface. Considering properties of ITO as an n-type semiconductor, when negative potential is applied, the charges are delivered to the film a decrease and increase of its real (n) and imaginary (k) RI part,

respectively [27, 28]. A decrease in n is followed by a negative shift of the resonance wavelength [29], as observed in Figure 5. Moreover, influence of external RI on the resonance wavelength may be taken into account. As shown in Figure 1, an increase in external RI is followed by a shift of the resonance towards longer wavelength. According to the reference measurements, the RI of the electrolytes varies and is equal to 1.33308 and 1.34334 RIU for 0.01 M PBS and 0.5 M Na_2SO_4 , respectively. For applied initially +0.3 V potential the resonance wavelength reached 671 and 662 nm for 0.01 M PBS and 0.5 M Na_2SO_4 , respectively. The RI may change with applied potential, i. e., the electrolyte may densify at the surface of the electrode what corresponds to the increase of its RI in short distance from the ITO surface. The magnitude of the changes correspond to the RI of the electrolyte, i. e., the range of wavelength where the resonance shift decreases with RI from 24 to 18 nm for the electrolyte with the lowest (Figure 5A) and the highest RI (Figure 5C), respectively. The only exception from this trend is when the redox probe is present in the electrolyte, as seen in Figure 5D. The possible reasons for this exceptions will be discussed later in this section.

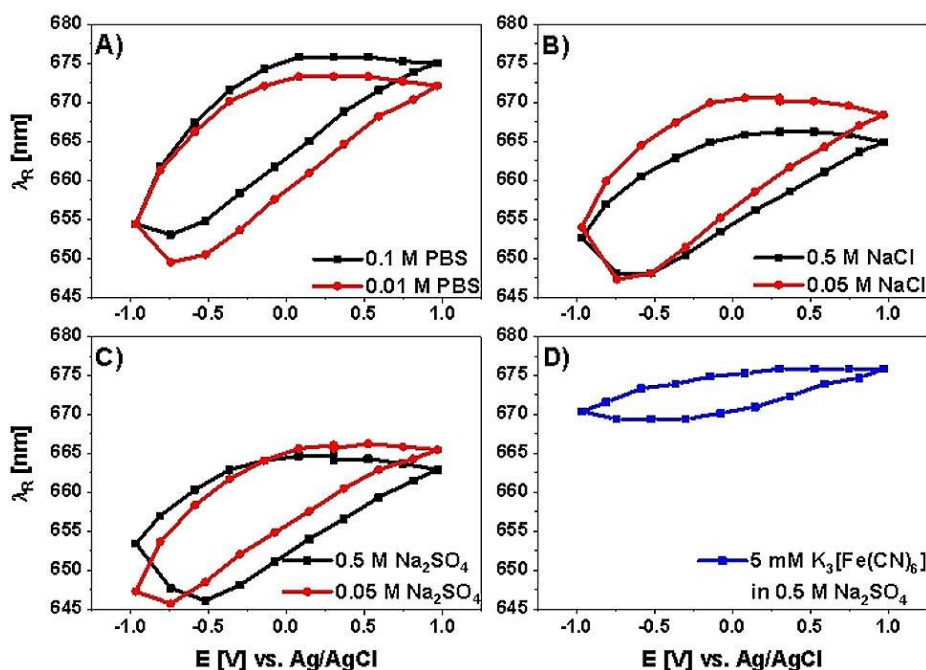


Figure 5. Influence of changes in potential in range from -1.0 to 1.0 V with a scan rate of 100 mV s^{-1} on resonance wavelength for the ITO-LMR sensor measured in various concentration of PBS (A), NaCl (B), and Na_2SO_4 (C). Corresponding results for Na_2SO_4 with a redox probe are shown in (D).

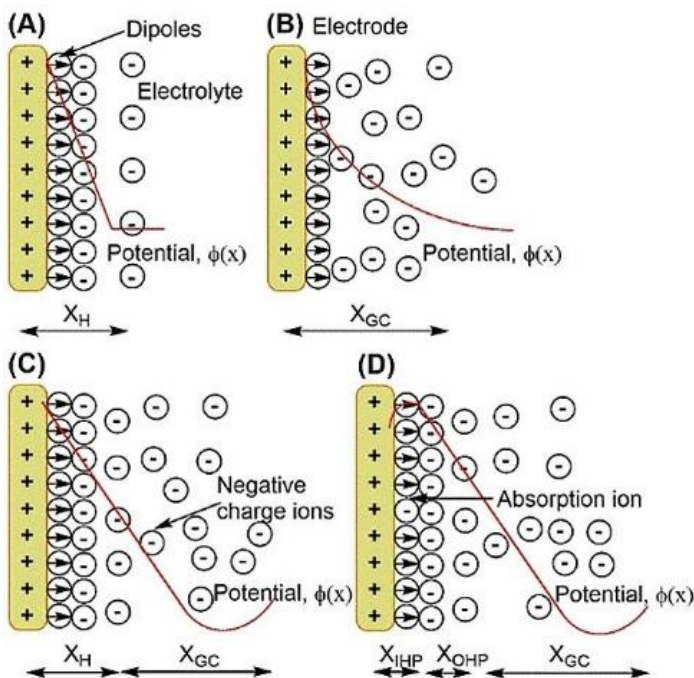


Figure 6. Schematics models of electrical double-layer according to Helmholtz (A), Gouy-Chapman (B), Stern (C), and Grahame (D).

The possible changes at the surface of the electrode can be explained by the EC theory. The electrical double layer is formed on the surface of electrode in consequence of interactions between positive and negative ions and the electrode surface (Figure 6). [30]. The thin layer of charge on the electrode surface is formed as a result of an excess or a deficiency of electrons [31]. The charge separation between the electrode surface and solution is known as an interfacial potential difference. This double-layer model has been described previously by Helmholtz, Gouy-Chapman, Stern and Grahame [30]. Historically the first model described by Helmholtz considers presence of two layers of opposite charge between the electrode surface and electrolyte interface as a result of electrostatic interaction [32]. The second model of electrical double-layer is the Gouy-Chapman model that includes the thermal motion of cations and anions near the charged electrode surface and is a consequences of diffusion and electrostatic forces [30]. Additionally, the Gouy-Chapman model assumes that the double-layer is not rigid between the electrode surface and electrolyte interface. The gradient concentration of ions occurs from the electrode surface to the solution due to thermal movement [30]. The third model, called as the Stern model, includes the

concepts of Helmholtz and Gouy-Chapman models. In these models, along with the distance from the electrode surface the electrical potential increases up to the rigid layer (Gouy-Chapman layer) and then potential decreases exponentially – so-called diffuse layer [30]. The last, Graham model of double-layer includes two region: inner Helmholtz plane (IHP) where the phenomena of absorption of ions occurs on the electrode surface and the outer Helmholtz plane (OHP) (Figure 6) and the diffusion region [33]. In this model the absorbed anions on the electrode surface partially leave the surface. Such anion behavior causes inversion of electrostatic potential between the OHP and IHP [30].

Influence of the potential scan rate on both EC and optical response was investigated next. The tests were performed in 0.1 M PBS at scan rates of 10 and 100 mV s^{-1} (Figure 7). For a lower scan rate, the diffusion layer will grow much further from the electrode in comparison to a fast scan approach [34]. In the consequence of thicker diffusion layer, flux to the electrode is smaller at 10 mV s^{-1} than in the case of 100 mV s^{-1} (Figure 7A). Because the current is proportional to the flux toward the electrode, at a higher scan rate an increased charging current is observed compared to CV recorded at very slow scan rates.

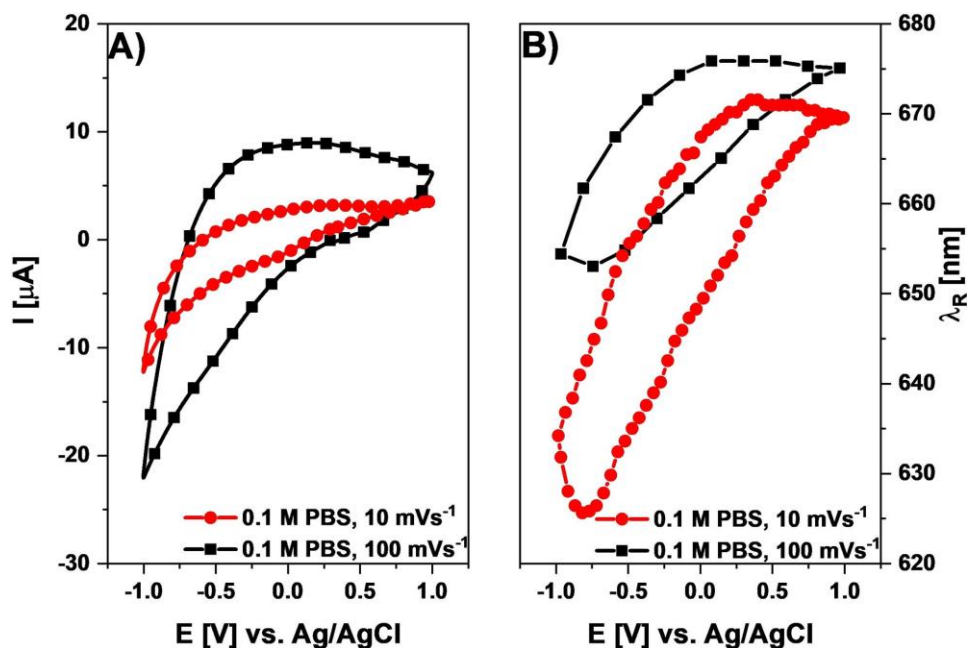


Figure 7. Electrochemical (A) and optical (B) response of the ITO-LMR sensor when investigated in 0.1 M PBS with a scan rate of 10 and 100 mV s^{-1} .

Differences in optical and EC response discussed in this paper can be explained considering described above models, i. e., changes of capacitance dependent on the composition of the electrolyte. The areal capacitance is calculated according to Equation 1, where C_a is an areal capacitance (F/cm^2), I is a current density (A/cm^2), v is a scan rate (A/s) and (V_2-V_1) is a potential window [35-37].

$$C_a = \frac{\int_{V_1}^{V_2} I(V)dV}{v(V_2 - V_1)} \quad (1)$$

Obtained calculation for the ITO-LMR sensor using CV indicate that in the case of PBS solution the capacitance is higher for less concentrated electrolyte (Table 1). In the case of the NaCl electrolytes the capacitances are very similar, while for the Na_2SO_4 solutions the capacitance is lower in less concentrated electrolyte. Moreover, the capacitance decreases with the scan rate reaching for ITO-LMR sensor and 0.1 M PBS solution $6.58 \text{ mF}/\text{cm}^2$ and $2.25 \text{ mF}/\text{cm}^2$ at scan rate 10 mV s^{-1} and 100 mV s^{-1} , respectively. This phenomenon results from the limited access of ions to the surface of the electrode at higher scan rates [38]. At lower scan rates ions present in the electrolyte had more time to easily access the electrode surface, than at a high scan rate [39]. The effect is clearly seen in optical response, where for the lower scan rate, the magnitude of changes is higher what corresponds to higher ion fluctuations at the ITO surface (Figure 7B).

Table 1. The capacitance of ITO-LMR sensor in various electrolytes.

Supporting electrolyte	Areal Capacitance (mF/cm^2)
0.1 M PBS	2.25
0.01 M PBS	2.57
0.5 M NaCl	2.98
0.05 M NaCl	2.93
0.5 M Na_2SO_4	3.12
0.05 M Na_2SO_4	2.90

The difference of response of the ITO-LMR sensor in different electrolytes seems to be also dependant on the size and concentration of cations and hydrated ions present in the electrolyte. The shape of CV curves and

capacitance is related to ionic mobility [38]. Due to the highest molar ionic conductivity, the highest capacitance is observed for H₂SO₄ electrolyte (Table 2). High ionic mobility and conductivity influence fast ion charge transfer, while the smaller hydration sphere radius caused ion adsorption on the electrode [21]. The biggest amount of ions in PBS, both cations - sodium and potassium and dihydrogen phosphate and hydrogen phosphate anions, reduces the value of capacitance. Additionally, the presence of these ions contribute to the lower capacitance for 0.1 M PBS electrolyte in comparison to 0.01 M PBS solution used as electrolyte.

Table 2. The properties of ions presence in supporting electrolytes based on [16, 21].

Ion	Ionic radius (Å)	Radius of hydrated sphere (Å)	Ionic mobility (10⁻⁸ m² s⁻¹ V⁻¹)	Molar ionic conductivity (mS m² mol⁻¹)
Na⁺	1.02	3.58	5.19	5.01
K⁺	1.38	3.31	7.62	7.35
Cl⁻	1.81	3.32	7.91	7.64
SO₄²⁻	2.30	3.79	8.29	16.00
H⁺	0.012	2.80	36.23	34.96

Influence of redox probe added to the electrolyte on the optical response must be finally discussed. It has been shown that its presence in the electrolyte highly increases the measured current (Figure 2D), where in turn it decreases the magnitude of potential-induced changes in the resonance wavelength (Figure 4A and 5D). When only the electrolyte is investigated, the character of shift is very similar to the case in which the RI is increased, namely the resonance shifts towards higher wavelengths and reduces its depth (Figure 1A and 4B). When the redox probe was added, the shift was smaller and occurred only in the resonance wavelength. It also needs to be noted that the resonance shifts toward higher wavelengths when the probe is added (Figure 5D). It may suggest that the probe molecules absorb to the surface of the electrode and despite better charge transfer at the sensor/electrolyte interface it keeps the ions away from the surface. Thus their fluctuations take place further from the surface of ITO, what limits their interactions with evanescent wave of light guided in the ITO-LMR sensor and results in low influence of the applied potential on the resonance wavelength shift.

4. CONCLUSIONS

In this work we discussed simultaneously acquired optical and electrochemical responses of ITO-coated optical fiber sensor. The working principle of the sensor was based on the lossy-mode resonance effect. Due to the tuning of ITO properties, the investigated ITO-LMR sensor offers a well-defined resonant response in the visible spectral range and reasonably high refractive index sensitivity reaching 325 nm/RIU in RI range typical for electrolytes widely used in electrochemistry. The influence of electrolyte composition, its concentration, and presence of redox probe, as well as potential scan rate has been considered and discussed according to electrochemical theory. We have shown that both electrochemical and optical responses of the sensor to the applied potential are similar in character, but optical readout may deliver supplementary information about the investigated liquid, i. e., molecules absorbed to the surface of the electrode, as observed when redox probe was applied, or clear response at low scan rate when the recorded current tends to be low. When the electrochemical response depends solely on the charge transfer at the ITO/electrolyte interface, optical response on top of charge-induced changes in optical properties of ITO also depends on composition of the electrolyte and its admixtures. We believe that the presented sensing concept can be successfully applied for label-free biosensing purposes where enhanced information about the analyte is received, especially when the current measured in electrochemical setup is low. What is more, optical response depends on properties of ITO, including its thickness, what may be found as an useful source of information when etching of the electrode is possible.

Acknowledgements

The authors gratefully acknowledge financial support for this work from National Science Centre (NCN), Poland under Grant No. 2014/14/E/ST7/00104 and National Centre for Science and Development Grant Techmatstrateg No. 347324. The support of NATO through the project SPS G5147 and the DS funds of the Faculty of Electronics, Telecommunications, and Informatics of the Gdansk University of Technology are also acknowledged.

References

- [1] E. Eltzov, S. Cosnier, R. S. Marks, *Expert Rev. Mol. Diagn.* 2011, 11, 533–546.
- [2] C. M. Hill, D. A. Clayton, S. Pan, *Phys. Chem. Chem. Phys.* 2013, 15, 20797–20807.
- [3] J. Juan-Cola's, S. Johnson, T. Krauss, J. Juan-Cola's, S. Johnson, T. F. Krauss, *Sensors* 2017, 17, 2047.
- [4] N.-F. Chiu, C.-D. Yang, C.-C. Chen, C.-T. Kuo, *Sens. Actuators B* 2018, 258, 981–990.
- [5] J. Lao, P. Sun, F. Liu, X. Zhang, C. Zhao, W. Mai, T. Guo, G. Xiao, J. Albert, *Light: Science & Applications* 2018, 7, 34.
- [6] K. Imai, T. Okazaki, N. Hata, S. Taguchi, K. Sugawara, H. Kuramitz, *Anal. Chem.* 2015, 87, 2375–2382.
- [7] R. Bogdanowicz, M. Sobaszek, M. Ficek, M. Gnyba, J. Ryl, K. Siuzdak, W. J. Bock, M. Smietana, *J. Opt. Soc. Korea* 2015, 19, 705–710.
- [8] O. Ordeig, P. Ortiz, X. Muñoz-Berbel, S. Demming, S. Büttgenbach, C. Fernández-Sánchez, A. Llobera, *Anal. Chem.* 2012, 84, 3546–53.
- [9] J. H. Ghithan, M. Moreno, G. Sombrio, R. Chauhan, M. G. O'Toole, S. B. Mendes, *Opt. Lett.* 2017, 42, 1205–1208.
- [10] M. Śmietana, M. Sobaszek, B. Michalak, P. Niedziałkowski, W. Białobrzeska, M. Koba, P. Sezemsky, V. Stranak, J. Karczewski, T. Ossowski, R. Bogdanowicz, *J. Lightwave Technol.* 2018, 36, 954–960.
- [11] R. Bogdanowicz, P. Niedziałkowski, M. Sobaszek, D. Burnat, W. Białobrzeska, Z. Cebula, P. Sezemsky, M. Koba, V. Stranak, T. Ossowski, M. Śmietana, *Sensors* 2018, 18, 1361.
- [12] I. D. Villar, C. R. Zamarreno, M. Hernaez, F. J. Arregui, I. R. Matias, *J. Lightwave Technol.* 2010, 28, 111–117.
- [13] F. Chiavaioli, P. Zubiato, I. Del Villar, C. R. Zamarreño, A. Giannetti, S. Tombelli, C. Trono, F. J. Arregui, I. R. Matias, F. Baldini, *ACS Sens.* 2018, 3, 936–943.
- [14] Z. Zainal, C. Y. Lee, M. Z. Hussein, A. Kassim, N. A. Yusof, *J. Photochem. Photobiol. A* 2005, 172, 316–321.
- [15] L. K. Morris, E. A. Abu, C. Bowman, C. E. Estridge, S. E. Andria, C. J. Seliskar, W. R. Heineman, *Electroanalysis* 2011, 23, 939–946.
- [16] N. G. Tsierekzos, U. Ritter, *Phys. Chem. Liq.* 2012, 50, 661–668.
- [17] V. Stranak, R. Bogdanowicz, P. Sezemsky, H. Wulff, A. Kruth, M. Smietana, J. Kratochvil, M. Cada, Z. Hubicka, *Surf. Coat. Technol.* 2018, 335, 126–133.
- [18] C. Xu, C. Wei, B. Li, F. Kang, Z. Guan, *J. Power Sources* 2011, 196, 7854–7859.
- [19] Y. Cai, Z. Qin, L. Chen, *Prog. Nat. Sci.: Materials International* 2011, 21, 460–466.

- [20] A. Qian, S. E. Hyeon, J. Y. Seo, C.-H. Chung, *Electrochim. Acta* 2018, 266, 86–93.
- [21] J. Zhu, Y. Xu, J. Wang, J. Lin, X. Sun, S. Mao, *Phys. Chem. Chem. Phys.* 2015, 17, 28666–28673.
- [22] M. Diaconu, A. Chira, L. Radu, *Thin Solid Films* 2014, 565, 84–88.
- [23] S. Umadevi, V. Ganesh, S. Berchmans, *RSC Adv.* 2014, 4, 16409–16417.
- [24] H. Gerischer, *J. Electroanal. Chem. Interfacial Electrochem.* 1977, 82, 133–143.
- [25] A. J. Bard, M. S. Wrighton, *J. Electrochem. Soc.* 1977, 124, 1706–1710.
- [26] R. Memming, *Semiconductor Electrochem.*, Wiley-VCH, Weinheim; New York, 1 edition. 2001.
- [27] Z. Ma, Z. Li, K. Liu, C. Ye, V. Sorger, *Nanophotonics* 2015, 4, 198–213.
- [28] X. Han, S. B. Mendes, *Thin Solid Films* 2016, 603, 230–237.
- [29] M. S´mietana, M. Dudek, M. Koba, B. Michalak, *physica status solidi* 2013, 210, 2100–2105.
- [30] M. S. Uddin, H. Tanaya Das, T. Maiyalagan, P. Elumalai, *Appl. Surf. Sci.* 2018, 449, 445–453.
- [31] M. Valizadeh Kiamahalleh, S. Hussein Sharifzein, G. Najafpour, S. Abdsata, Suranibuniran, *NANO* 2012, 07.
- [32] L. L. Zhang, X. S. Zhao, *Chem. Soc. Rev.* 2009, 38, 2520–2531.
- [33] M. Endo, T. Takeda, Y. J. Kim, K. Koshiba, K. Ishii, *Carbon letters* 2001, 1, 117–128.
- [34] D. A. C. Brownson, C. E. Banks, *The Handbook of Graphene Electrochemistry*, Springer, New York, 2014.
- [35] S. J. Patil, J. Park, D.-W. Lee, *IOP Conf. Ser.: Mater. Sci. Eng.* 2017, 282, 012004.
- [36] S. J. Patil, J. H. Kim, D. W. Lee, *J. Power Sources* 2017, 342, 652–665.
- [37] S. J. Patil, C. D. Lokhande, *Mater. Des.* 2015, 87, 939–948.
- [38] S. Ghosh, T. Mathews, B. Gupta, A. Das, N. Gopala Krishna, M. Kamruddin, *Nano-Structures & Nano-Objects* 2017, 10, 42–50; *Nano-Objects* 2017, 10, 42–50.
- [39] A. M. A. Paul, *ACS Omega* 2017, 2, 8039–8050.

B5. Enhancing electrochemical properties of an ITO-coated lossy-mode resonance optical fiber sensor by electrodeposition of PEDOT:PSS

Michał Sobaszek, Dariusz Burnat, Petr Sezemsky, Vitezslav Stranak, Robert Bogdanowicz, Marcin Koba, Katarzyna Siuzdak, Mateusz Smietana, Enhancing electrochemical properties of an ITO-coated lossy-mode resonance optical fiber sensor by electrodeposition of PEDOT:PSS, Optical Materials Express 9(7), (2019), 3069-3078.

© 2019 Optical Society of America. Users may use, reuse, and build upon the article, or use the article for text or data mining, so long as such uses are for non-commercial purposes and appropriate attribution is maintained. All other rights are reserved.

Abstract

A sensor working in multiple domains may offer enhanced information about the properties of an investigated analyte, including those containing biological species. It has already been shown that a dual-domain sensing capability, i.e., in optical and electrochemical domains, can be offered by lossy-mode resonance (LMR) sensors based on indium-tin-oxide (ITO) thin film. The spectral response of the LMR sensors depends on the refractive index (RI) at the ITO surface. In this work, we discuss a capability for enhancing the electrochemical properties of these sensors by electrodeposition of poly(3,4-ethylenedioxythiophene)–poly(4-styrenesulfonate) (PEDOT:PSS) on the ITO surface. This conjugated polymer shows high electrical conductivity, high optical transmittance, as well as good chemical stability, and thus can be used as a transparent electrode. We have found that the PEDOT:PSS deposition improves the reversibility of the electrochemical reduction/oxidation reactions by 2.5 times with no negative impact on LMR-based measurements of the RI of the analyte.

1. INTRODUCTION

In recent years, increasing demand for novel diagnostic and analytical methods capable of investigating various biological targets at ultralow quantities has been observed [1]. When the label-free sensing concept is considered, where no fluorescent marker is applied and just binding phenomena between a biological receptor and a target at the sensor surface are monitored, the targets can be investigated in their natural state, and without a requirement for their additional modification or amplification. In the case of optical sensors, the label-free sensing concept relies on monitoring changes in the refractive index (RI) in the vicinity of the sensor surface [2]. An increase in RI corresponds to an increase in density that is induced by biological binding events and can be monitored optically in real time [3].

Optical fiber sensors, due to their set of unique properties such as their small size, immunity to electromagnetic interference, and capability of multiparameter and remote sensing, have gathered significant attention of the scientific community. A number of optical fiber sensors capable of measurement of RI with high sensitivity have already been reported [4–6]. Due to their immunity to optical power fluctuations, sensors based on resonance effects such as surface plasmon resonance or lossy-mode resonance (LMR) [7–9] are desired. Among the advantages of LMR sensors is that many materials, which include metal and semiconductor oxides or nitrides, some carbon-based materials, as well as various polymers, can be used as thin films supporting the LMR effect [7, 10, 11]. An indium tin oxide (ITO) thin film deposited on fused silica glass may offer suitable properties for LMR observations. ITO is also well known for its low electrical resistivity, and due to its band-gap, it is often used as an electrochemical (EC) working electrode [12]. For this reason, ITO-based electrodes typically substitute those made of gold wherever optical absorption at the electrode surface needs to be monitored during the EC process [13]. In contrast to other transparent electrode materials, such as boron-doped diamond, thin ITO films can be deposited at a relatively low temperature on various substrates and shapes [14]. When ITO is used as an LMR-supporting thin film, a combined optical and EC analysis can be performed to deliver an enhanced set of data about the investigated analytes [3, 15, 16]. EC-enhanced optical measurements open up the possibility for detection of a variety of organic

compounds and heavy metals, but also allow for sensor surface treatment in the EC domain, followed by optical detection. It is worth noting that tuning the properties of ITO to allow both high-quality LMR and EC response to be achieved is still challenging. The most recent reports of the EC response to the presence of a reduction/oxidation (redox) probe in a solution are unsatisfactory, i.e., weakly defined reduction (I_{red}) and oxidation (I_{ox}) current peaks were recorded using an ITO-LMR sensor [3, 15, 16]. Moreover, the difference in potentials corresponding to these peaks (ΔE) is significantly higher than observed for other commercially available electrodes, including those based on ITO. These parameters, namely I_{red} , I_{ox} and ΔE are crucial when label-free sensing applications in the EC domain are considered [17].

In this work, we propose electropolymerization of a conducting polymer on the ITO-coated optical fiber. The approach makes it possible to improve the EC properties of the device when the LMR effect has already been achieved. Poly(3,4-ethylenedioxythiophene)–poly(4-styrenesulfonate) (PEDOT:PSS) was chosen for electropolymerization by means of chronoamperometry (CA), and its further investigations were done with cyclic voltammetry (CV). PEDOT:PSS is a conjugated polymer showing high electrical conductivity (up to 550 S cm^{-1}) and good chemical stability in a doped state [18]. When polymerized as a thin film, PEDOT:PSS can be used as a transparent electrode with optical transmittance reaching up to 80% [19]. What is more, PEDOT:PSS is often used in various EC biosensors targeted towards e.g., pesticides [20], glucose [21], ascorbic acid [22] and dopamine [23]. In this work, we particularly focus on the influence of PEDOT:PSS electropolymerization on optical and EC properties of the ITO-LMR optical fiber sensor.

2. EXPERIMENTAL

2.1. ITO-LMR sensor fabrication and optical testing

The LMR structures were fabricated using approx. 15 cm-long 400/840 μm core/cladding diameter polymer-clad silica fiber samples, where 2.5 cm of polymer cladding was removed from the fiber central section [15]. Next, the electrically conductive and optically transparent ITO films were deposited by reactive magnetron sputtering of the ITO target ($\text{In}_2\text{O}_3\text{--SnO}_2\text{—}90/10 \text{ wt } \%$ and a purity of 99.99%). The magnetron, whose axis was perpendicular to the

substrate, was supplied by a Cito1310 (13.56 MHz, 300 W) RF source (Comet AG, Flamatt, Switzerland). The experiments were carried out at pressure $p = 0.1$ Pa in an argon atmosphere. The fibers were rotated in the chamber during the process to uniformly cover with ITO the exposed fiber core section.

To determine the RI sensitivity of the fabricated ITO-LMR devices, they were investigated in mixtures of water/glycerine with different proportions of these components resulting in $n_D = 1.33$ – 1.45 RIU. Before immersing the sensors in subsequent mixtures their RI was measured using an AR200 automatic digital refractometer (Reichert Inc., Buffalo, NY, USA). The RI sensing studies were conducted without any applied bias potential. The optical transmission of the ITO-LMR structure was interrogated in the range $\lambda = 350$ – 1050 nm using a HL-2000 white light source and a USB4000 spectrometer (Ocean Optics, USA). The optical transmission (T_i) in the specified spectral range was measured as counts in the specified integration time (up to 100 ms) and referred to the transmission of the fiber without the ITO coating (T_0). The results were normalized and presented as $T = T_i/T_0$. The temperature of the solutions was stabilized at 25 °C.

For the combined optical and EC analysis, the ITO-LMR sensor was installed in the measurement setup to record the T_i during each stage of the EC processing [15]. The T_i was monitored and the data were acquired approx. every 2 s. For comparison of the results, the following parameters were selected: (1) LMR wavelength (λ_R), and (2) T at the slope of the resonance at the arbitrary chosen $\lambda = 700$ nm (T_{700}).

2.2. Electropolymerisation and EC setup

The CA processing and CV measurements were performed with a PalmSens Emstat 3+ potentiostat/galvanostat controlled by the PSTrace 5 software. We used the ITO-LMR sensor, a platinum wire, and Ag/AgCl/0.1 M KCl as the working (WE), counter (CE), and reference (REF) electrodes, respectively. The electropolymerization on ITO-LMR sensor was conducted by chronoamperometry by treated at constant potential 1.25 V vs. REF for 120 s in 0.1 M NaSO₄ containing 15 mM EDOT and 0.1 M PSS. The procedure allowed for electropolymerization of EDOT with a PSS counterion at the surface of the ITO-LMR sensor. The obtained at these conditions PEDOT:PSS

film thickness may reach up to 800 nm [24, 25]. The EC property, i.e., response to redox probes, before and after the electropolymerization was verified in 1 mM ferrocenedimethanol in 0.5 M Na₂SO₄ solution at a scan rate of 50 mV·s⁻¹. The measurement cell used for the optical-EC investigation of the optical fiber sensor is shown schematically in Fig. 1.

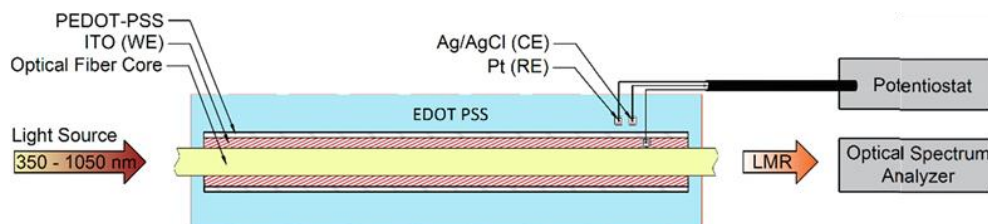


Fig. 1. Schematically shown experimental setup used for EDOT-PSS electropolymerization with optical monitoring of the ITO-LMR device.

The EC impedance spectroscopy (EIS) measurements were carried out to investigate process changes in space charge capacitance and resistance of charge transfer between the electrode and the electrolyte, whose detection is crucial. EIS is known for high precision and is frequently used to evaluate heterogeneous charge-transfer parameters and a double-layer structure [1]. During an EIS analysis, the impedance at a certain frequency (Z_i) is measured. When the WE is immersed in the electrolyte containing redox probe, it polarizes at the formal potential (E_f) of a particular redox reaction. The E_f , also known as the mid-peak potential, is defined as a half of the sum of the oxidation and reduction potential. For a reversible and diffusion-controlled redox reaction, at E_f the reduced and oxidized species diffuse at equal rates. Following that, EIS measurements were performed for ITO-coated and PEDOT:PSS-ITO-coated optical fiber structures at a determined E_f of ferrocenedimethanol redox reaction. The spectra were recorded in the frequency range 20 kHz – 0.1 Hz and with a 10 mV amplitude. The measured impedances were analyzed with an EIS Analyzer using an electric equivalent circuit (EEQC). The EEQC consists of different components, such as resistors, capacitors, a coil or Warburg elements of features that correspond to the real processes occurring at the electrode/electrolyte interface. In other words, the EEQC shows the same electrical response as the WE. A modified Powell algorithm [26] was used with an amplitude weighting r_a as in Eq. 1, where N is the number of points, M is the number of parameters, ω is the angular frequency, and $P_1 \dots P_M$ are model parameters. The r_c is defined as in

Eq. 2, where i corresponds to the measured values of impedance, and i_{calc} is attributed to the calculated values.

$$r_a = (\omega, P_1 \dots P_M) = r_c^2 / (N - M) \quad (1)$$

$$r_c^2 = \sum_{i=1}^N \frac{(Z'_i - Z'_{i_{\text{calc}}})^2 + (Z''_i - Z''_{i_{\text{calc}}})^2}{Z_i'^2 - Z_{i_{\text{calc}}}^2} \quad (2)$$

3. RESULT AND DISCUSSION

Before the EDOT-PSS electropolymerization, the response of the ITO-LMR sensor to the applied potential was verified. The attenuation band in the monitored spectrum is originated by a resonance effect. The LMR is dependent on the thin film thickness since the thickness determines propagation conditions for the lossy modes [27]. It can be seen in Fig. 2 that during CV measurements, the optical spectrum did not experience any significant alterations. The corresponding CV curve is shown in Fig. 4A. For a better insight, in Fig. 2C both the λ_R and T_{700} were plotted vs. the measurement number that corresponds to the applied potential. During the measurements, λ_R stayed almost constant, which means that there was no influence of the potential on the LMR. For the previously investigated ITO-LMR sensors [12–14], where ITO was deposited at a higher pressure, it was shown that the changes in applied potential had a significant impact on the LMR. The negligible influence observed here corresponds to the properties of the ITO coating deposited at a lower pressure, i.e., the ITO layer contains more crystalline forms, so its bandgap is different than for ITO deposited at a higher pressure [28]. Moreover, the lack of potential influence can be explained by a mismatch between energy levels for ITO and the ferrocenedimethanol redox probe [16]. The simultaneously recorded EC response for one of the cycles is shown in Fig. 4, and it will be discussed later together with the results obtained after the electropolymerization.

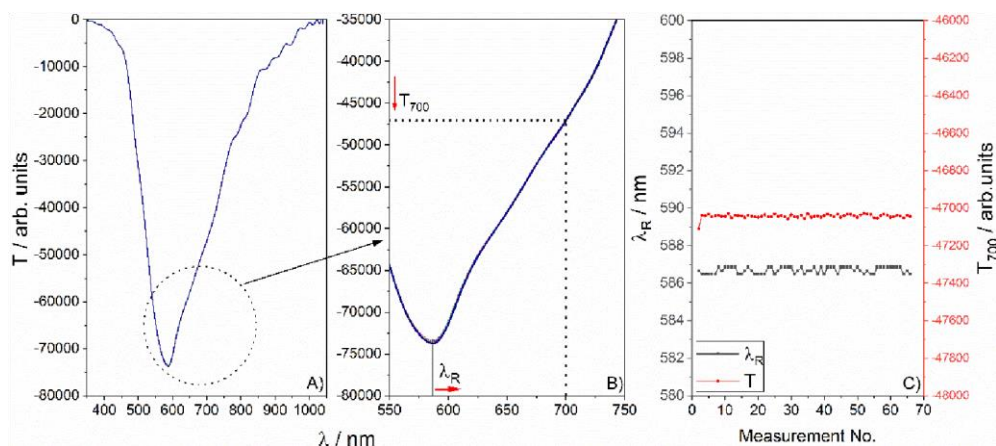


Fig. 2. Optical response of the ITO-LMR sensor to potential scanning (4 scans) with scan rate 50 mV/s in 1 mM ferrocenedimethanol in 0.1 M KCl, where (A) shows spectrum presented as $T = T_i - T_0$, where T_i and T_0 are the optical transmissions of the ITO coated and uncoated fiber respectively, (B) magnification of selected part of the spectrum with shown evolution of T_{700} and λ_R , and (C) resonance wavelength and T at $\lambda = 700$ nm for all the measurements.

Next, electropolymerization of EDOT was performed on the ITO-LMR sensor. Its optical response during the process is shown in Fig. 3. Significant alteration of the spectrum can be observed. The λ_R , initially at 578.56 nm, gradually shifts within 60 s (approx. 30 initial measurements) towards longer wavelengths reaching 594.73 nm ($\Delta\lambda_R = 16.17$ nm). The T_{700} follows the trend for λ_R . After the initial 60 s, a significantly lower influence of the process on the T_{700} was observed too (Fig. 3(C)). The results confirm the PEDOT:PSS film deposition on the ITO-LMR sensors, i.e., a direction of the shift corresponds to an increase in RI at the ITO surface, which is followed by deposition of the film [3]. It must be noted that mainly the right slope of the resonance is influenced by the deposition. The effect may be caused by non-uniform polymer deposition around the fiber, possibly induced by some distribution in the ITO resistivity. Non-uniform coating distribution around the fiber may induce asymmetrical mode coupling and thus less pronounced resonances are observed in the transmission spectrum [29].

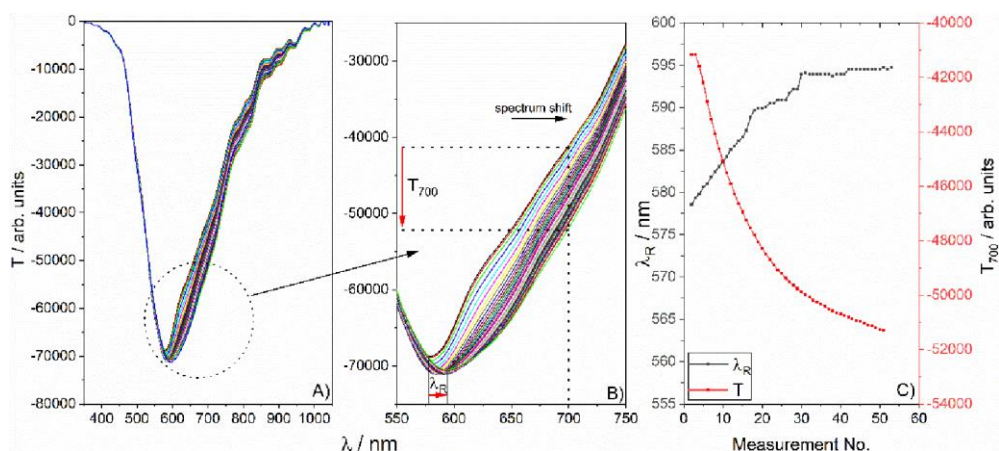


Fig. 3. Optical response of the ITO-LMR sensor to EDOT electropolymerization in 0.5 Na₂SO₄ at 1.25 V during a 120 s long process, where (A) shows the evolution of the spectrum, (B) magnification of selected part of the spectrum with shown evolution of T_{700} and λ_R , and (C) the shift of the resonance wavelength and T at $\lambda = 700$ nm.

CV is an EC technique often used for verification of changes at an electrode surface. PEDOT:PSS electrode typically exhibits wide potential range of c.a. 1-1.5 V, but it concerns the full range when this electrode works in a buffer solution. In the case of the electrode immersed in an electrolyte containing ferrocyanide redox probe, the difference between oxidation and reduction peaks reaches 450 mV or even 200 mV [30]. Low ΔE is attributed to improved conductivity and mass transfer between redox species and surface of the polymer electrode [31, 32]. Hence, the EC properties of the ITO-LMR sensor before and after electropolymerization were compared (Fig. 4(A)). For the sensor, prior to the electropolymerization, reversible reduction and oxidation peaks corresponding to one electron process are not well-defined, and $\Delta E = 510$ mV. As a result of the electropolymerization process, ΔE has been reduced by factor of 2.4, reaching $\Delta E = 210$ mV. A similar ΔE value is often achieved for glassy carbon, boron-doped diamond or gold electrodes [12, 33]. For commercially available ITO films deposited on glass slides, ΔE is close to 100 mV. It must also be emphasized that the polymer deposition resulted in better definition of both I_{ox} and I_{red} , which are higher for the sensor coated with PEDOT:PSS. The absolute values of the currents are nearly equal, which indicates a high reversibility of the redox reaction. The key EC parameters received from the CV curves are summarized in Table 1.

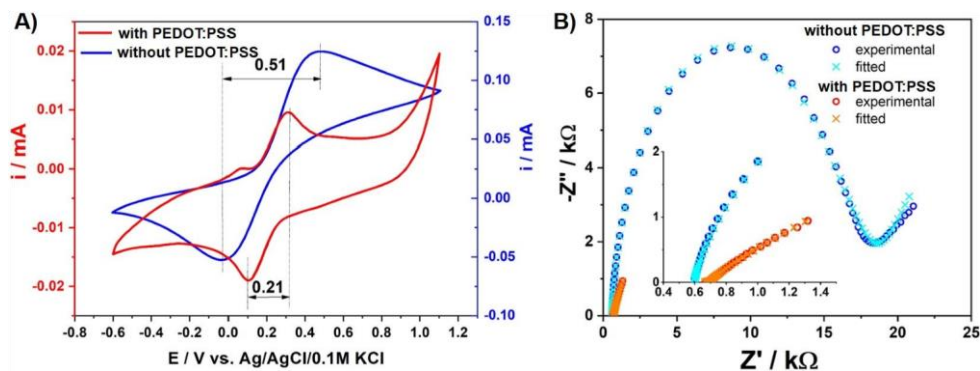


Fig. 4. (A) CV recorded in 1 mM ferrocenedimethanol in 0.1 M KCl with the ITO-LMR sensor before and after PEDOT:PSS deposition. The potential and currents corresponding to redox peaks are indicated in Table 1. (B) EIS response recorded at the redox formal potential for ITO-LMR sensor with and without PEDOT:PSS coating. The inset in (B) is a close-up of the initial part of the figure.

Additionally, at the E_f of the redox reaction, EIS was also recorded and presented in Fig. 4(B). When bare ITO was interfacing the electrolyte containing the redox probe, a semicircle initially with a 45° slope was observed. After deposition of the PEDOT:PSS, the response changed significantly and the overall impedance decreased. As already mentioned in the experimental section, to better understand the impedance data, EIS modelling was performed. The EEQC proposed for both cases is presented in Fig. 5. According to the applied EEQC including both of the electrode materials, goodness was at the level of 10^{-5} , whereas the error at each element value did not exceed several %, which is proof of the correctness of the designed circuit.

Table 1. Oxidation and reduction potentials and currents obtained for CV recorded in 1 mM ferrocenedimethanol in 0.1 M KCl with the ITO-LMR sensor before and after PEDOT:PSS deposition.

Sample	E_{ox} [V]	E_{red} [V]	$\Delta E = E_{ox} - E_{red}$ [V]	I_{ox} [μ A]	I_{red} [μ A]
ITO-LMR	0.485	-0.025	0.51	20	16
PEDOT:PSS/ITO-LMR	0.311	0.101	0.21	73	71

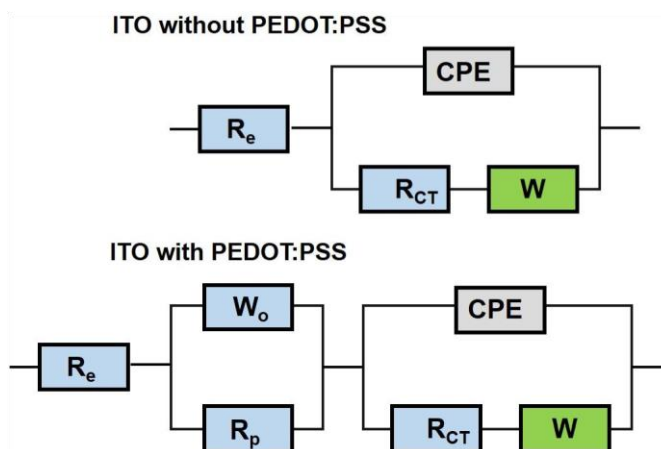


Fig. 5. The EEQC used for fitting of the EIS data received with and without PEDOT:PSS film.

The designed EEQC consists of the following components: i) resistances: R_e – attributed to the electrolyte resistance, R_p – the polymer resistance itself, R_{CT} – charge transfer resistance, ii) constant phase element (CPE) that models the behavior of a double layer, and iii) two Warburg-like components, which will be discussed later. Independently on the investigated working electrode, the electrolyte resistance is at the same level, and equals to 590 Ω and 667 Ω for ITO and ITO/PEDOT:PSS, respectively. The difference may result from some slight changes in the geometric arrangement of electrodes for both the cases, but it does not impact on the overall impedance value.

The CPE is attributed to the space charge capacitance, and its impedance is described by $Z = Q^{-1}(i\omega)^{-m}$, where Q is a CPE parameter, m is exponential and in both cases reaches c.a. 0.9. According to Bard et al. [34], for $m = 1$, it stands for an ideal capacitance, while for $m = 0.5$ indicates highly dispersed capacitance that is typical for porous electrodes. The Warburg component labelled as W represents the impedance of semi-infinite diffusion to/from a flat electrode. This component contributes equally to the real ($\text{Re}Z$) and imaginary ($\text{Im}Z$) parts of the impedance: $\text{Re}Z(\omega) = A_W/\omega^{0.5}$ and $\text{Im}Z(\omega) = -A_W/\omega^{0.5}$, where A_W is the Warburg coefficient.

In comparison to the bare ITO, for a PEDOT:PSS-coated substrate, the EEQC includes an additional section consisting of W_o and R_p , where they represent finite length diffusion at a reflective boundary and ω_{or} stands for the Warburg coefficient, whereas $W_{OC} = d/D^{0.5}$. The impedance of the W_o component is

given by Eq. 3. W_o is typically applied for modelling of diffusion processes occurring in a polymer matrix and sometimes is termed subdiffusion impedance [35].

$$Z_{W_o}(\omega) = \frac{\omega_{or}}{\sqrt{\omega}} (1 - j) \coth(W_{OC}\sqrt{j\omega}) \quad (3)$$

The difference between both of the electrode materials can be seen when the EEQC segment attributed to the charge transfer is considered. The values for those elements are listed in Table 2. The ITO/PEDOT:PSS electrode exhibits much higher capacitance and lower charge transfer resistance, while the Warburg diffusion is 2.6 times lower for the electrode coated with ITO only. The PEDOT:PSS film enhances the transfer of electric charges between the electrolyte and ITO. Therefore, the presence of PEDOT:PSS significantly enhances the EC response.

Table 2. The values of EEQC parameters responsible for charge transfer and diffusion.

Element / Unit	ITO	ITO/PEDOT:PSS
CPE / $\Omega^{-1}s^n$	$1.76 \times 10^{-5} (m = 0.86)$	$5 \times 10^{-4} (m = 0.91)$
R_1 / Ω	2608.2	1.5
$W / \Omega s^{-0.5}$	2399.8	912.7

The PEDOT:PSS/ITO-LMR sensor, simultaneously to EC interrogation, was again tested optically (Fig. 6). Afterwards, the film deposition alterations in the spectrum are more intense when compared to those before the deposition. Both the λ_R and T_{700} respond to the applied potential. The λ_R reaches its maximum and minimum for 0.1 V and 0.3 V applied potential, respectively, while the relation for T_{700} is inverted due to its location on the right slope of the resonance. This phenomenon can be explained by modulation of the RI of the ITO, which is an n-type semiconductor when charges are delivered, and changes in RI of the solution at the sensor surface when ions from the electrolyte are attracted or pushed away from the sensor surface [16]. After the PEDOT:PSS deposition, the charge transfers because of substantial resistances R and W decrease, as indicated in Table 2.

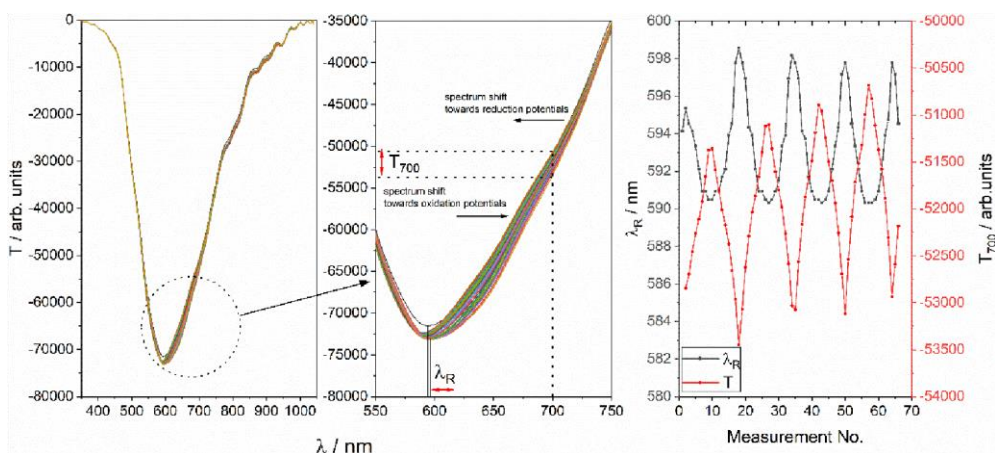


Fig. 6. Optical response of the PEDOT:PSS/ITO-LMR sensor to potential scanning (4 scans) at a rate of 50 mV/s in 1 mM ferrocenedimethanol in 0.1 M KCl, where (A) shows the evolution of the spectrum, (B) magnification of selected part of the spectrum with shown evolution of T_{700} and λ_R , and (C) the shift of resonance wavelength and T at $\lambda = 700$ nm.

Finally, the optical response to RI changes at the PEDOT:PSS/ITO-LMR sensor has been verified. For any label-free sensing applications, the sensor must be sensitive to RI changes at its surface. As shown in [15–16], ITO–LMR optical fiber sensors without additional coatings are suitable for this application. To preserve the possibility of multiple domain detection the optical response of the PEDOT:PSS/ITO-LMR sensor must not be disturbed. In Fig. 7(A), a well-defined LMR can be seen. It experiences a shift towards higher wavelengths when the RI increases. Referring to spectra presented above, measured in the electrolytes with redox probes or EDOT and PSS, the resonance is initially shifted towards shorter wavelengths due to the lower RI of the external medium. The significant response to RI after the electropolymerization proves that the PEDOT:PSS does not disturb the optical sensing effect, i.e., the surface is not blocked by the polymer films and does not prevent interactions with an external medium.

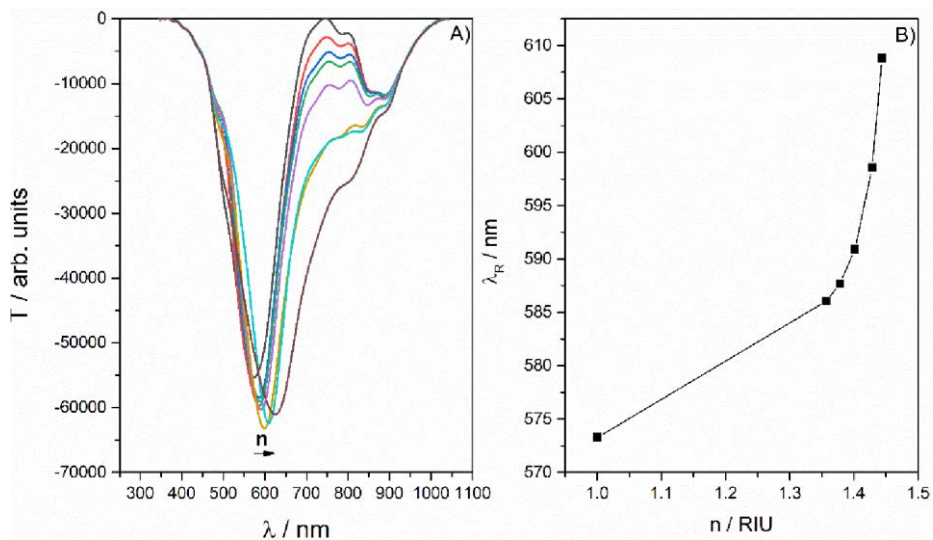


Fig. 7. Optical response of the PEDOT:PSS/ITO-LMR sensor to external RI (n), where (A) shows evolution of the spectrum, and (B) shift in the resonance wavelength.

4. CONCLUSION

We investigated the possibility to enhance the sensing properties of an ITO-LMR sensor by electropolymerization of PEDOT:PSS on ITO surface. As a result of the process the reduction-oxidation peak-to-peak separation was significantly reduced, and the current peaks became more pronounced. Most importantly, after the PEDOT:PSS deposition, the sensor still stayed sensitive to external refractive index. This fact allows such an approach to be considered as suitable for improving the properties of opto-electrochemical label-free sensors. The deposition of a conducting polymer like PEDOT:PSS is a low-cost solution to enhance the electrochemical properties of the ITO-LMR devices.

Funding

Narodowe Centrum Nauki (NCN) (2014/14/E/ST7/00104, 2016/21/B/ST7/01430); Narodowe Centrum Badań i Rozwoju (NCBR) (347324/12/NCBR/2017); North Atlantic Treaty Organization (NATO) (SPS G5147).

Disclosures

The authors declare that there are no conflicts of interest related to this article.

References

- [1] D. Nidzworski, K. Siuzdak, P. Niedziałkowski, R. Bogdanowicz, M. Sobaszek, J. Ryl, P. Weiher, M. Sawczak, E. Wnuk, W. A. Goddard, A. Jaramillo-Botero, and T. Ossowski, “A rapid-response ultrasensitive biosensor for influenza virus detection using antibody modified boron-doped diamond,” *Sci. Rep.* **7**(1), 15707 (2017).
- [2] J. E. Antonio-Lopez, J. J. Sanchez-Mondragon, P. LiKamWa, and D. A. May-Arrioja, “Fiber-optic sensor for liquid level measurement,” *Opt. Lett.* **36**(17), 3425–3427 (2011).
- [3] R. Bogdanowicz, P. Niedziałkowski, M. Sobaszek, D. Burnat, W. Białobrzeska, Z. Cebula, P. Sezemsky, M. Koba, V. Stranak, T. Ossowski, and M. Śmietana, “Optical Detection of Ketoprofen by Its Electropolymerization on an Indium Tin Oxide-Coated Optical Fiber Probe,” *Sensors* **18**(5), 1361 (2018).
- [4] D. K. C. Wu, B. T. Kuhlmeiy, and B. J. Eggleton, “Ultrasensitive photonic crystal fiber refractive index sensor,” *Opt. Lett.* **34**(3), 322–324 (2009).
- [5] M. Janik, A. K. Myśliwiec, M. Koba, A. Celebańska, W. J. Bock, and M. Śmietana, “Sensitivity Pattern of Femtosecond Laser Micromachined and Plasma-Processed In-Fiber Mach-Zehnder Interferometers, as Applied to Small-Scale Refractive Index Sensing,” *IEEE Sens. J.* **17**(11), 3316–3322 (2017).
- [6] M. Śmietana, M. Koba, P. Mikulic, and W. J. Bock, “Towards refractive index sensitivity of long-period gratings at level of tens of μm per refractive index unit: fiber cladding etching and nano-coating deposition,” *Opt. Express* **24**(11), 11897–11904 (2016).
- [7] I. D. Villar, C. R. Zamarreño, M. Hernaez, F. J. Arregui, and I. R. Matias, “Lossy Mode Resonance Generation With Indium-Tin-Oxide-Coated Optical Fibers for Sensing Applications,” *J. Lightwave Technol.* **28**(1), 111–117 (2010).
- [8] N. Paliwal and J. John, “Lossy Mode Resonance (LMR) Based Fiber Optic Sensors: A Review,” *IEEE Sens. J.* **15**(10), 5361–5371 (2015).
- [9] Q. Wang and W.-M. Zhao, “A comprehensive review of lossy mode resonance-based fiber optic sensors,” *Opt. Lasers Eng.* **100**, 47–60 (2018).
- [10] M. Śmietana, M. Dudek, M. Koba, and B. Michalak, “Influence of diamond-like carbon overlay properties on refractive index sensitivity of nano-coated optical fibres,” *Phys. Status Solidi A* **210**(10), 2100–2105 (2013).
- [11] K. Kosiol, M. Koba, M. Masiewicz, and M. Śmietana, “Tailoring properties of lossy-mode resonance optical fiber sensors with atomic layer deposition technique,” *Opt. Laser Technol.* **102**, 213–221 (2018).

- [12] J. Stotter, Y. Show, S. Wang, and G. Swain, "Comparison of the Electrical, Optical, and Electrochemical Properties of Diamond and Indium Tin Oxide Thin-Film Electrodes," *Chem. Mater.* **17**(19), 4880–4888 (2005).
- [13] J. Agrisuelas, D. Giménez-Romero, J. J. García-Jareño, and F. Vicente, "Vis/NIR spectroelectrochemical analysis of poly-(Azure A) on ITO electrode," *Electrochem. Commun.* **8**(4), 549–553 (2006).
- [14] D. C. Paine, T. Whitson, D. Janiac, R. Beresford, C. O. Yang, and B. Lewis, "A study of low temperature crystallization of amorphous thin film indium–tin–oxide," *J. Appl. Phys.* **85**(12), 8445–8450 (1999).
- [15] M. Śmietana, M. Sobaszek, B. Michalak, P. Niedziałkowski, W. Białobrzaska, M. Koba, P. Sezemsky, V. Stranak, J. Karczewski, T. Ossowski, and R. Bogdanowicz, "Optical Monitoring of Electrochemical Processes With ITO-Based Lossy-Mode Resonance Optical Fiber Sensor Applied as an Electrode," *J. Lightwave Technol.* **36**(4), 954–960 (2018).
- [16] 16. M. Śmietana, P. Niedziałkowski, W. Białobrzaska, D. Burnat, P. Sezemsky, M. Koba, V. Stranak, K. Siuzdak, T. Ossowski, and R. Bogdanowicz, "Study on Combined Optical and Electrochemical Analysis Using Indium-tin-oxidecoated Optical Fiber Sensor," *Electroanalysis* **31**(2), 398–404 (2019).
- [17] G. Li, Z. Li, X. You, J. Chen, and S. Tang, "A novel label-free and sensitive electrochemical biosensor for Hg²⁺ based on ligase-mediated formation of DNAzyme," *Talanta* **161**, 138–142 (2016).
- [18] L. A. A. Pettersson, F. Carlsson, O. Inganäs, and H. Arwin, "Spectroscopic ellipsometry studies of the optical properties of doped poly(3,4-ethylenedioxythiophene): an anisotropic metal," *Thin Solid Films* **313-314**, 356–361 (1998).
- [19] Y. Chen, K. S. Kang, K. J. Han, K. H. Yoo, and J. Kim, "Enhanced optical and electrical properties of PEDOT: PSS films by the addition of MWCNT-sorbitol," *Synth. Met.* **159**(17-18), 1701–1704 (2009).
- [20] G. Istamboulie, T. Sikora, E. Jubete, E. Ochoteco, J.-L. Marty, and T. Noguer, "Screen-printed poly(3,4ethylenedioxythiophene) (PEDOT): A new electrochemical mediator for acetylcholinesterase-based biosensors," *Talanta* **82**(3), 957–961 (2010).
- [21] J. Park, H. K. Kim, and Y. Son, "Glucose biosensor constructed from capped conducting microtubules of PEDOT," *Sens. Actuators, B* **133**(1), 244–250 (2008).
- [22] A. Bello, M. Giannetto, G. Mori, R. Seeber, F. Terzi, and C. Zanardi, "Optimization of the DPV potential waveform for determination of ascorbic acid on PEDOT-modified electrodes," *Sens. Actuators, B* **121**(2), 430–435 (2007).

-
- [23] K.-C. Lin, T.-H. Tsai, and S.-M. Chen, "Performing enzyme-free H₂O₂ biosensor and simultaneous determination for AA, DA, and UA by MWCNT–PEDOT film," *Biosens. Bioelectron.* **26**(2), 608–614 (2010).
- [24] B. Friedel, P. E. Keivanidis, T. J. K. Brenner, A. Abrusci, C. R. McNeill, R. H. Friend, and N. C. Greenham, "Effects of Layer Thickness and Annealing of PEDOT:PSS Layers in Organic Photodetectors," *Macromolecules* **42**(17), 6741–6747 (2009).
- [25] A. U. Palma-Cando, B. A. Frontana-Uribe, J. L. Maldonado, and M. R. Hernández, "Control of Thickness of PEDOT Electrodeposits on Glass/ITO Electrodes from Organic Solutions and its Use as Anode in Organic Solar Cells," *Procedia Chem.* **12**, 92–99 (2014).
- [26] L. Lu, B. H. Brown, D. C. Barber, and A. D. Leathard, "A fast parametric modelling algorithm with the Powell method," *Physiol. Meas.* **16**(3A), A39–A47 (1995).
- [27] I. Del Villar, M. Hernaez, C. R. Zamarreño, P. Sánchez, C. Fernández-Valdivielso, F. J. Arregui, and I. R. Matias, "Design rules for lossy mode resonance based sensors," *Appl. Opt.* **51**(19), 4298–4307 (2012).
- [28] L. Meng and M. P. dos Santos, "Properties of indium tin oxide (ITO) films prepared by r.f. reactive magnetron sputtering at different pressures," *Thin Solid Films* **303**(1-2), 151–155 (1997).
- [29] P. Zubiarte, C. R. Zamarreño, I. D. Villar, I. R. Matias, and F. J. Arregui, "Experimental Study and Sensing Applications of Polarization-Dependent Lossy Mode Resonances Generated by D-Shape Coated Optical Fibers," *J. Lightwave Technol.* **33**(12), 2412–2418 (2015).
- [30] F. Abd-Wahab, A. Guthoos, H. Farhana, W. Salim, and W. W. Amani, "Solid-State rGO-PEDOT:PSS Transducing Material for Cost-Effective Enzymatic Sensing," *Biosensors* **9**(1), 36 (2019).
- [31] Y. Hui, C. Bian, J. Wang, J. Tong, and S. Xia, "Comparison of Two Types of Overoxidized PEDOT Films and Their Application in Sensor Fabrication," *Sensors* **17**(3), 628 (2017).
- [32] A. Benoudjit, M. M. Bader, and W. W. A. W. Salim, "Study of electropolymerized PEDOT:PSS transducers for application as electrochemical sensors in aqueous media," *Sensing and Bio-sensing Research* **17**, 18–24 (2018).
- [33] G. M. Swain and R. Ramesham, "The electrochemical activity of boron-doped polycrystalline diamond thin film electrodes," *Anal. Chem.* **65**(4), 345–351 (1993).
- [34] A. J. Bard and L. R. Faulkner, *Electrochemical Methods: Fundamentals and Applications*, 2nd edition (Wiley, 2000).
- [35] E. Hernández-Balaguera, H. Vara, and J. L. Polo, "An electrochemical impedance study of anomalous diffusion in PEDOT-coated carbon microfiber electrodes for neural applications," *J. Electroanal. Chem.* **775**, 251–257 (2016).
-

B6. Optical fiber lossy-mode resonance sensors with doped tin oxides for optical working electrode monitoring in electrochemical systems

Dariusz Burnat, Marta Janczuk-Richter, Paweł Niedziałkowski, Wioleta Białobrzeska, Petr Sezemsky, Marcin Koba, Vitezslav Stranak, Robert Bogdanowicz, Tadeusz Ossowski, Joanna Niedziolka-Jönsson, Mateusz Smietana, Optical fiber lossy-mode resonance sensors with doped tin oxides for optical working electrode monitoring in electrochemical systems, Proceedings SPIE 11199, Seventh European Workshop on Optical Fibre Sensors, (2019), 111991O.

Abstract

This work discusses optical fiber sensors based on lossy-mode resonance (LMR) effect and their potential for simultaneous sensing in multiple domains, i.e., optical and electrochemical. As electrically conductive materials able to guide lossy modes, two doped tin oxides, i.e., fluorine doped tin oxide (FTO) and indium tin oxide (ITO) thin films were employed. Since the ITO-LMR sensor has already been discussed broader, this work focuses on properties of the FTO-LMR sensor and brief comparison of devices based on the two materials. In optical domain the sensitivity to surrounding medium refractive index was determined by immersing the sensors in solutions of different refractive index. Both the sensors showed sensitivity of 300 nm/RIU in a refractive index range of approx. 1.33–1.39 RIU. Electrochemical measurements were performed in 0.01 M phosphate-buffered saline (PBS, pH 7.0) to identify the influence of the applied potential on the optical response of both sensors. In applied potential from -1.0 V to 1.0 V the FTO-LMR sensor reached LMR shift of 31.3 nm compared to 23.8 nm of the ITO-LMR one.

1. INTRODUCTION

The fast developing area of sensors requires them to be reliable, have a long operating time, and above all, offer high sensitivity. The sensitivity and trust in results can be enhanced if acquired results are confirmed by simultaneous, independent, and made in the same place and time measurement based on different physical mechanism. Thus, multi-domain sensing techniques becoming more popular in recent years, especially in the biosensing area¹⁻³. This work is focused on optical fiber sensor which can be applied on top of optical interrogation also as a working electrode in electrochemical measurements.

The considered sensors for detection in optical domain employ lossy-mode resonance (LMR) effect. The main advantage of this type of sensor is its relatively uncomplicated, several-stage fabrication process^{4, 5}. An inherent element of the LMR sensor is an optical transparent thin film coating and the capability of this film for guiding lossy modes. The LMR occurs when there is a coupling between lossy mode and waveguide modes⁴. The following materials were primarily used as thin films up to the present moment: titanium oxide⁵, indium tin oxide (ITO)⁶, indium oxide⁴ and different polymers⁴. In terms of electrochemical domain the applied thin film material must be conductive. Thus, for simultaneous interrogation the optical fibers were coated with fluorine doped tin oxide (FTO) and ITO.

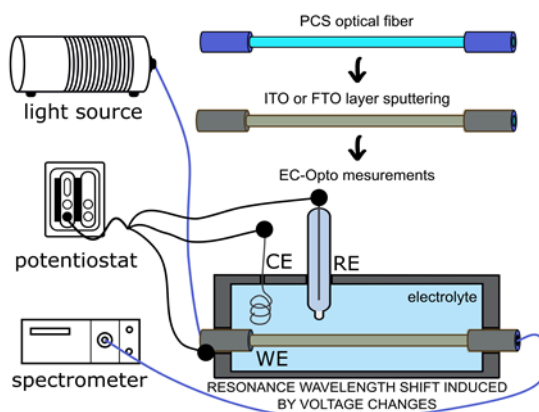


Figure 1. Schematic representation of the setup used for simultaneous optical and electrochemical measurements.

The ITO–LMR sensor was previously applied as a working electrode^{7, 8}. The aim of this work is to show possibility of employing the FTO–LMR sensor and compare properties of ITO- and FTO-based devices in terms of optical and electrochemical response. Comparing to ITO, FTO is less expensive and also more mechanically and chemically durable⁹, therefore it offers advantages highly desirable in sensing applications.

2. EXPERIMENTAL DETAILS

2.1. Thin films deposition

Investigated sensors were based on 400 μm core diameter polymer-clad silica optical fiber, where polymer cladding in the 2.5 cm-long central section of sample was mechanically removed and coated by FTO or ITO thin film. The thin films were deposited by magnetron sputtering method. The fiber samples placed in the ultra-high vacuum chamber were rotated during the process and exposed to sputter beam generated by RF driven sputtering gun equipped with 3 in. FTO (90:10 wt% $\text{SnO}_2\text{:SnF}_2$) or ITO (90:10 wt% $\text{In}_2\text{O}_3\text{:SnO}_2$) target. Deposition times were adjusted to obtain possibly the lowest order of resonance in the visible range and thus higher sensitivity⁶. The thickness and optical properties of thin films were measured using HORIBA Jobin Yvon UVISEL spectroscopic ellipsometer based on reference silicon wafers.

2.2. Optical measurements

After the deposition the FTO/ITO samples were tested in water/glycerin solutions to determine their sensitivity to external refractive index (RI) changes. The RIs of the solutions were measured by Rudolph J57AB refractometer. The samples were placed in the setup consisting of Ocean Optics HL-2000 white light source and Ocean Optics USB4000 spectrometer, and immersed in consecutive solutions. Recorded optical spectrum were presented in relation to the spectrum of the sample before FTO/ITO deposition ($T-T_0$).

2.3. Electrochemical measurements

The prepared FTO/ITO-LMR sensors were applied as a working electrode in 3-electrode cyclic voltammetry setup, where as an auxiliary and a reference electrode platinum wire and silver-silver chloride electrode Ag/AgCl (0.1 M KCl) were used, respectively. Electrochemical response of the sensors was

monitored using PalmSens EmStat3+ potentiostat in 0.01 M phosphate-buffered saline (PBS, pH = 7.0) and presented as cyclic voltammogram. Applied potentials changed in range from -1.0 V to 1.0 V with a scan rate of 100 mV/s.

3. RESULTS AND DISCUSSION

3.1. Refractive index sensitivity

The optical response of the FTO–LMR and ITO–LMR sensors in RI varying solution are presented in Figure 2. According to spectroscopic ellipsometry results the thickness of the FTO equals to 60 nm while the ITO thin film is much thicker and reaches 260 nm. In both cases well-defined peak can be observed, it indicates the LMR presence. In deionized water (1.333 RIU) minima were registered at 687.2 nm and 646.9 nm for the FTO–LMR and ITO–LMR sensors, respectively. With increasing RI of surrounding medium the resonance shifts toward longer wavelengths. The sensitivity increases with RI and is comparable for both sensors, reaching on average 275 nm/RIU (RI range: 1.333 – 1.391) and 325 nm/RIU (RI range: 1.333 – 1.382) for the FTO-LMR and ITO–LMR sensors, respectively.

3.2. Electrochemical results

Next, the response of the FTO-LMR sensor in electrochemical setup was considered. Increasing of the potential (Figure 3) leads to anions transfer toward the working electrode and thus build of double layer at FTO/PBS interface what is noticed as increase of capacitive current¹⁰. Due to electroactive species absence in the electrolyte no redox reaction was observed. Further potential changes towards negative values cause anions depletion in vicinity of the FTO-LMR sensor and current decrement. In comparison to the ITO-LMR sensor's response in the same conditions, i.e., the same electrolyte, its concentration, potentials applied, scan rate, and distance between electrodes, the magnitude of the capacitive current changes is less noticeable. This is a result of different materials – ITO and FTO – deposited on the fiber's core and their properties such as thickness¹¹, electrical conductivity, microstructure, electron-transfer kinetics¹². Nevertheless, both sensors show capability for working as electrodes in electrochemical systems.

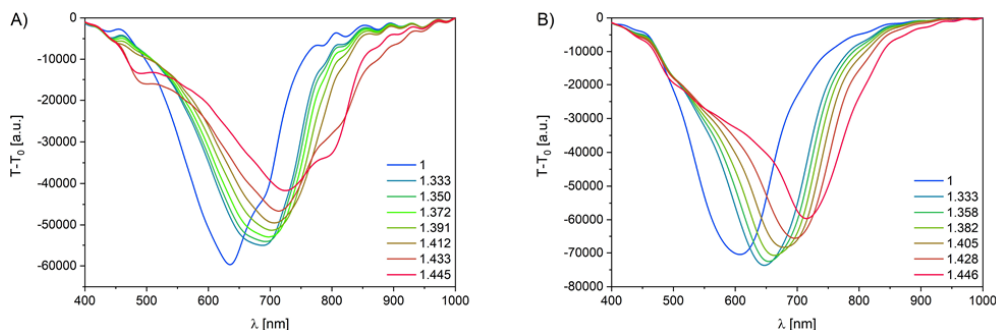


Figure 2. Optical spectra of the FTO-LMR (A) and ITO-LMR (B) sensors in surrounding media of different RI. The thickness of FTO and ITO thin films reached 60 nm and 250 nm, respectively.

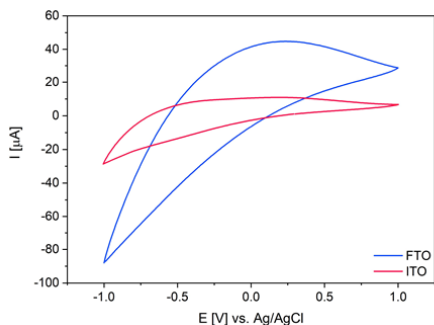


Figure 3. Cyclic voltammograms for FTO-LMR and ITO-LMR sensors as working electrodes.

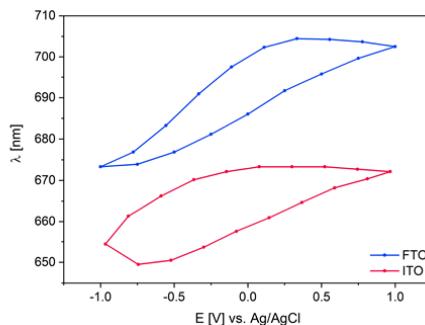


Figure 4. Evolution of LMR wavelength for the FTO-LMR and ITO-LMR sensors as a function of applied potential.

The influence of applied potential on the optical response of the sensors has also been investigated in parallel. The evolution of LMR wavelength with the potential is shown in Figure 4. The resonances appear at slightly different wavelengths, what is induced by different refractive indices and thicknesses of ITO and FTO. When the potential is applied, change in distribution of carriers in the film affects its refractive index, both its real and imagine part, hence the conditions for lossy modes guiding follow⁸. However, the formation of double layer in the sensors' vicinity is more evident. One can see that the LMRs' evolution in Figure 4 is very similar to the capacitive current evolution in Figure 3. As the FTO-LMR and ITO-LMR sensors are sensitive to RI the ions' transfer leads to changes of RI in the vicinity of the sensor¹³. Migration of anions causes the LMR shift toward longer wavelength, opposite to cations.

For the FTO-LMR sensor the LMR changes its wavelength from 673.3 nm to 704.5 nm which results in a 31.3 nm difference at a 132.9 μA change in the capacitive current. In the case of the ITO-LMR sensors the resonance wavelength difference is at 23.8 nm when the current change is lower and reaches 39.5 μA . Such limitation of LMR shift with simultaneous clear growth of capacitive current may occur due to blocking the sensor's surface by migrating ions and progressive increase of the ions does not change LMR conditions distinctly after a certain point.

4. CONCLUSIONS

In this work, we discussed dual domain, i.e., optical and electrochemical, performance of lossy-mode resonance optical fiber sensor supported by FTO thin film. The properties of the FTO-LMR sensor were compared to those of an ITO-LMR sensor offering similar optical response. The sensitivity to external medium refractive index was similar and reaches 300 nm/RIU (in RI range of approx.: 1.33–1.39 RIU). However, in case of the FTO the effect has been achieved for significantly thinner film and was sufficient for achieving well-defined resonance in the visible range. The sensors based on both tin oxide doped films are also applicable as an electrode in combined electrochemical measurements and allow for dual-domain sensing. The influence of changes in the potential on the LMR conditions was investigated. In comparison to the ITO-LMR sensor, in presented case, the FTO-LMR offered higher shift in LMR wavelength in the same range of applied potentials. The optical response of both FTO-LMR and ITO-LMR sensors corresponds primarily to the formation of a double layer at thin film/electrolyte interface.

Acknowledgements

This work was supported by the National Science Centre, Poland as a part of 2014/14/E/ST7/00104 project, the National Centre for Research and Development, Poland as a part of 347324/12/NCBR/2017 project, and the Polish National Agency for Academic Exchange within PPN/BIL/2018/1/00126 project.

References

- [1] Wang, X., Que, M., Chen, M., Han, X., Li, X., Pan, C. and Wang, Z. L., "Full Dynamic-Range Pressure Sensor Matrix Based on Optical and Electrical Dual-Mode Sensing," *Advanced Materials* 29(15), 1605817 (2017).
- [2] Huang, X., Yu, H., Liu, X., Jiang, Y., Yan, M., and Wu, D., "A dual-mode large-arrayed CMOS ISFET sensor for accurate and high-throughput pH sensing in biomedical diagnosis," *IEEE Transactions on Biomedical Engineering* 62(9), 2224-2233 (2015).
- [3] Juan-Colás, J., Johnson, S. and Krauss, T., "Dual-mode Electro-Optical techniques for biosensing applications: A Review," *Sensors* 17(9), 2047 (2017).
- [4] Del Villar, I., Hernaez, M., Zamarreño, C. R., Sánchez, P., Fernández-Valdivielso, C., Arregui, F. J. and Matias, I. R., "Design rules for lossy mode resonance based sensors," *Applied optics* 51(19), 4298-4307 (2012).
- [5] Burnat, D., Koba, M., Wachnicki, Ł., Gierałtowska, S., Godlewski, M. and Śmietana, M., "Refractive index sensitivity of optical fiber lossy-mode resonance sensors based on atomic layer deposited TiO₂ thin overlay," *Proc. SPIE* 9916, 99161G (2016).
- [6] Del Villar, I., Zamarreño, C. R., Hernaez, M., Arregui, F. J. and Matias, I. R., "Lossy mode resonance generation with indium-tin-oxide-coated optical fibers for sensing applications," *JLT* 28(1), 111-117 (2010).
- [7] Bogdanowicz, R., Niedziałkowski, P., Sobaszek, M., Burnat, D., Białobrzaska, W., Cebula, Z., Sezemsky, P., Koba, M., Stranak, V., Ossowski, T., and Śmietana, M., "Optical detection of ketoprofen by its electropolymerization on an indium tin oxide-coated optical fiber probe," *Sensors* 18(5), 1361 (2018).
- [8] Śmietana, M., Niedziałkowski, P., Białobrzaska, W., Burnat, D., Sezemsky, P., Koba, M., Stranak, V., Siuzdak, K., Ossowski, T. and Bogdanowicz, R., "Study on Combined Optical and Electrochemical Analysis Using Indium-tin-oxide-coated Optical Fiber Sensor," *Electroanalysis*, 31(2), 398-404 (2019).
- [9] Benck, J. D., Pinaud, B. A., Gorlin, Y. and Jaramillo, T. F., "Substrate selection for fundamental studies of electrocatalysts and photoelectrodes: inert potential windows in acidic, neutral, and basic electrolyte," *PLoS one* 9(10), e107942 (2014)
- [10] Morrison, S. R., [Electrochemistry at semiconductor and oxidized metal electrodes], Plenum Press, 56-72, 1980.
- [11] Zhao, R., Liu, J. and Gu, J., "The effects of electrode thickness on the electrochemical and thermal characteristics of lithium ion battery," *Applied Energy* 139, 220-229 (2015).

- [12] Zoski, C. G., (Ed.), [Handbook of electrochemistry], Elsevier, 111-114, 2006.
- [13] Janczuk-Richter, M., Piestrzyńska, M., Burnat, D., Sezemsky, P., Stranak, V., Bock, W. J., Bogdanowicz, R., Niedziółka-Jönsson, J. and Śmietana, M., "Optical investigations of electrochemical processes using a longperiod fiber grating functionalized by indium tin oxide," *Sens. and Act. B: Chemical*, 279, 223-229 (2019).

C1. Optical monitoring of thin film electro-polymerization on surface of ITO-coated lossy-mode resonance sensor

Michał Sobaszek, Magdalena Dominik, Dariusz Burnat, Robert Bogdanowicz, Vitezslav Stranak, Petr Sezemsky, Mateusz Smietana, Optical monitoring of thin film electro-polymerization on surface of ITO-coated lossy-mode resonance sensor, 2017 25TH INTERNATIONAL CONFERENCE ON OPTICAL FIBER SENSORS (OFS), Proceedings of SPIE 10323, (2017), UNSP 103234W.

Abstract

This work presents an optical fiber sensors based on lossy-mode resonance (LMR) phenomenon supported by indium tin oxide (ITO) thin overlay for investigation of electro-polymerization effect on ITO's surface. The ITO overlays were deposited on core of polymer-clad silica (PCS) fibers using reactive magnetron sputtering (RMS) method. Since ITO is electrically conductive and electrochemically active it can be used as a working electrode in 3-electrode cyclic voltammetry setup. For fixed potential applied to the electrode current flow decrease with time what corresponds to polymer layer formation on the ITO surface. Since LMR phenomenon depends on optical properties in proximity of the ITO surface, polymer layer formation can be monitored optically in real time. The electrodeposition process has been performed with Isatin which is a strong endogenous neurochemical regulator in humans as it is a metabolic derivative of adrenaline. It was found that optical detection of Isatin is possible in the proposed configuration.

1. INTRODUCTION

There are numbers of optical fiber sensors already developed for refractive index (RI) measurements¹⁻⁴. Recently, RI sensors based on electromagnetic resonance effect known as lossy-mode resonance (LMR) are extensively investigated^{2, 5-8}. These sensors often employ a multimode optical fiber, where cladding on its short length is replaced with a thin film⁹. The optical properties of the film must fulfill specific conditions to guide lossy modes, i.e., the real part of the film electric permittivity must be positive and higher in magnitude than both its own imaginary part and the permittivity of the external medium¹⁰. The advantage of LMR sensors include, e.g., no need of complex optical devices, such as lasers or polarizers, as well as a relatively simple design and capability for high RI sensitivity. In addition, many different materials such as metal or semiconductor oxides and nitrides or polymers can be used as thin films supporting the LMR phenomenon^{5, 7-9, 11}. One of the thin film material that satisfy conditions for LMR is indium tin oxide (ITO) deposited on fused silica glass. ITO film can be deposited with reactive magnetron sputtering (RMS) method¹². The RMS, which belongs to group of physical vapor deposition method, gives precise control over the thin films properties, is highly repeatable and can be used for deposition of a wide selection of metal alloy or compound with excellent adhesion and uniformity. Moreover, properties of ITO can be easy modified by changing flow rates of O₂ or Ar during sputtering, thus ITO films can be used as an effective and useful coating for optical fiber sensors, where its optical properties as well as thickness are crucial parameters for sensor performance^{2, 10}.

In this work we investigate possibility for optical Isatin detection when it electro-polymerizes on ITO surface. Isatin (1H-indole-2,3-dione) is a versatile heterocyclic compound and it is well known as one of the most important indole present in mammalian tissues and brain¹³. Isatin is a strong endogenous neurochemical regulator in humans as it is a metabolic derivative of adrenaline¹⁴. Control of the Isatin level in humans and rats urine can be used as marker for Parkinson's disease^{15, 16}. Furthermore, Isatin and its derivatives like Schiff and Mannich bases are widely used as antibacterial, antifungal and anti-HIV component¹⁷. That is why there is a high demand for its detection. In the measurement configuration, the ITO-based LMR sensor has been used as a working electrode in cyclic voltammetry (CV) 3-electrode configuration

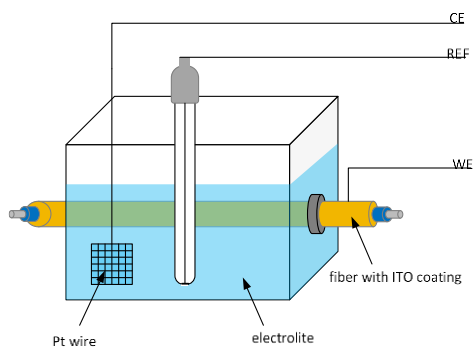


Fig. 1. Schematically shown cell allowing for combined electrochemical and optical measurements.

(Fig. 1). When constant potential is applied to the ITO-LMR sensor, the electropolymerization takes place and the effect can be monitored by observation of changes in the sensor optical transmission spectrum. According to our best knowledge, ITO-LMR sensor applied in electrochemical setup is shown for a first time.

2. EXPERIMENTAL DETAILS

2.1. Sensor fabrication

The LMR structures were fabricated using PCS fiber of 400/840 μm core/cladding diameter, where polymer cladding was removed on 2.5 cm length in the fiber central section. Next, ITO films were deposited using standard planar magnetrons with unbalanced magnetic field. The deposition system, arranged for deposition on fibers combined two perpendicularly oriented sputtering guns, i.e., one operating in mode of high power impulse (HiPIMS) and the second running in continuous RF power mode. Both the magnetron cathodes were equipped with ITO targets with composition $\text{In}_2\text{O}_3\text{-SnO}_2$ 90-10 wt% and 99.99% purity. Next, the ITO samples were annealed (200 $^\circ\text{C}$) in air for 2 h.

2.2. Electrochemical measurements and electro-polymerization

Test CV measurement was carried out at a scan rate of 50 mVs^{-1} in aqueous media consisting of 5 mM $\text{K}_3[\text{Fe}(\text{CN})_6]$ and 0.5 M K_2SO_4 . Next, chronoamperometry (CA) experiment was carried out at applied potential 1.2 V for 600 sec. in aqueous media consisting of 50 mM Isatin diluted in 0.1 M pH 7.0 phosphate buffer. Electrochemical cell used in the experiment consisted three electrode system, i.e., ITO-coated fiber, platinum wire and $\text{Ag}/\text{AgCl}/0.1$ KCl used as working, counter and reference electrodes,

respectively (Fig. 1). Moreover, we used Autolab 204N potentiostat/galvanostat and Nova 2.0 software for signal acquisition and processing, respectively.

2.3. Optical measurements

To determine RI sensitivity of the ITO-based devices the structures were investigated in air and in mixtures of water/glycerine with RI from $n_D = 1.33$ to 1.45 RI units (RIU). The RI of the mixtures was measured using Rudolph J57AB refractometer. The optical transmission of the LMR-ITO structure was observed in range of $\lambda = 340\text{--}1040$ nm using Ocean Optics HL-2000 white light source and Ocean Optics USB4000 spectrometer. The optical power (T) in the specified spectral range was detected as counts in 100 ms integration time and presented in relation to the power transmitted in the fiber structure for ITO thin film sample surrounded by air ($T-T_0$)/ T_0 .

3. RESULTS & DISCUSSION

In Fig. 2 spectral response of the LMR-ITO sensor is shown when it was immersed in various RI. It can be seen that the set of resonances shift with RI towards longer wavelengths (Fig. 2a) as it takes place in case of the LMR phenomenon². The sensitivity to RI increases rapidly when external RI exceeds ~ 1.45 RIU. When the results are referred to the spectrum recorded in air, not only spectral shift can be monitored by also a change in transmission at a certain wavelength.

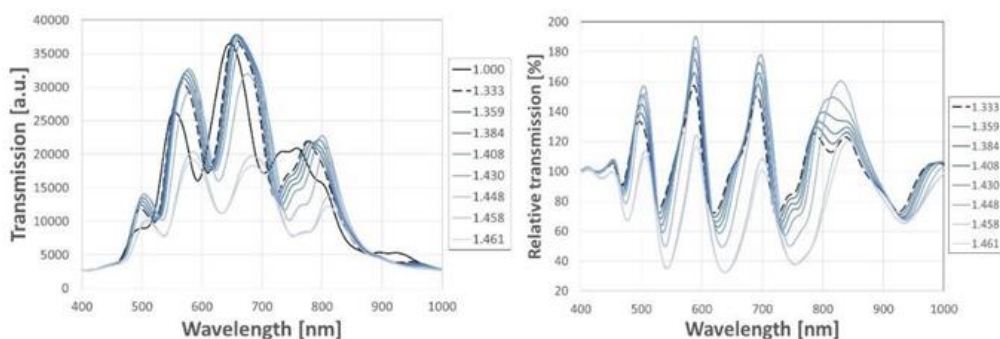


Fig. 2. Transmission changes induced by increase in external RI ($n_{ext} = 1 - 1.461$ RIU), where (a) shows spectra directly acquired from the spectrometer and (b) transmission changes referred to spectrum acquired for $n_{ext} = 1$.

CV is considered a very useful and easy method for investigating electrochemical properties of materials at interface being in contact with an electrolyte. Typically applied as a reference $\text{Fe}(\text{CN})_6^{3-/4-}$ redox system is sensitive to surface properties, such as density of electronic states near the formal potential. In Fig. 3a is shown electrochemical cycle recorded for LMR-ITO sensor investigated in 5 mM $\text{K}_3\text{Fe}(\text{CN})_6/0.5 \text{ M Na}_2\text{SO}_4$ vs. $\text{Ag}/\text{AgCl}/0.1 \text{ M KCl}$. The result proves that the ITO film deposited on optical sensor responds correctly in CV configuration. The recorded value of $\Delta E = 0.42 \text{ V}$ is relatively small, what is a very good result, especially taking into consideration fact that the deposition on substrate of cylindrical shape is challenging. Moreover, the ITO active surface on fiber is small comparing to widely used flat ITO samples deposited on glass plates. It is also worth noting that electrical parameters of ITO are strongly influenced by annealing temperature^{18, 19}.

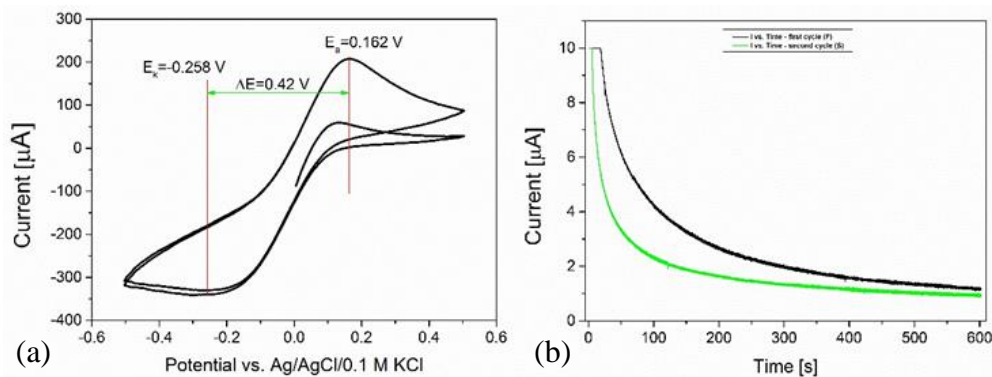


Fig. 3. Electrochemical measurements for (a) reference CV cycle and (b) chronoamperometry cycle resulting in Isatin electro-polymerization.

The electro-polymerization effect monitored electrically is shown in Fig. 3b. The chronoamperometry was carried out towards oxidation of Isatin what is effective at 1.2 V^{20} . Two cycles were performed where each took 600 sec. The difference in current decreasing in time is clearly seen between the first (F) and the second (S) cycle. During the first cycle a thin film formation process took place resulting in deposition of Isatin oxidation product at surface of the ITO electrode. The faster drop in current for the second cycle can be explain by already smaller active surface than for the first cycle. Furthermore, the effect of electro-polymerization can also be seen by changes in relative transmission (RT) (Fig. 4a). When RT values for selected wavelengths are discussed, it can be clearly seen that the LMR-ITO sensor also responds to

polymer layer formation on its surface (Fig. 4b). In optical response the biggest difference can be seen at initial stage of the process, where the RT drops rapidly as for measurements in high RI (Fig. 2b). The result proves that formation of thin polymer film on ITO surface takes place. When the electro-polymerization process continues, the spectrum also changes and the trend can be clearly seen at each stage of the process (Fig. 4b).

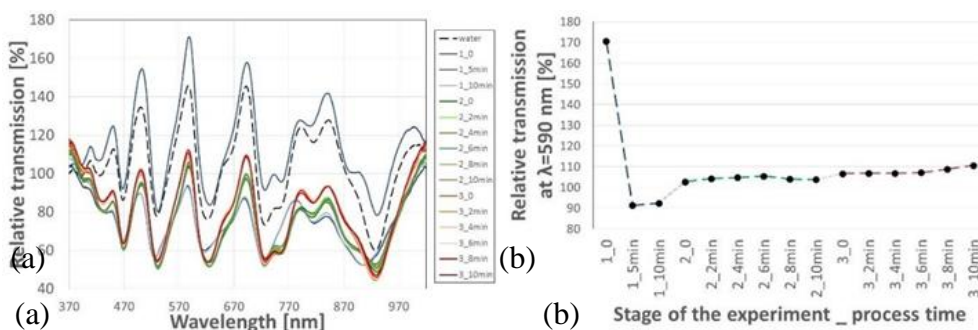


Fig. 4. Effect of the thin film electro-polymerization process on transmission of the sensor, where (a) shows transmission referred to response in air at different stage of the experiment and process time, and (b) shows changes at a selected wavelength.

4. CONCLUSIONS

As a result of this study we developed an optical fiber sensors based on LMR effect supported by ITO thin overlay for detection of Isatin, which is a strong endogenous neurochemical regulator in humans as well as a metabolic derivative of adrenaline. The high electrochemical and optical performance of ITO-based structure was achieved by its deposition with unique two perpendicularly oriented sputtering magnetrons, i.e., HiPIMS and continuous RF power guns. Since the highly conductive ITO overlay enables for effective electro-polymerization of Isatin with chronoamperometric method at the optical fibre surface, the significant change in lossy-mode resonance response has been recorded. The changes in relative transmission of LMR sensor follow straightly progress in polymer layer formation at the ITO surface. The proposed novel sensing approach provides a promising strategy for both optical and electrochemical detection of various bio-compounds and monitoring of their concentration.

Acknowledgements

This work was supported by the Polish National Science Centre (NCN) as a part of 2014/14/E/ST7/00104 project.

References

- [1] Smietana, M., Koba, M., Brzozowska, E., Krogulski, K., Nakonieczny, J., Wachnicki, L., Mikulic, P., Godlewski, M., Bock, W. J., "Label-free sensitivity of long-period gratings enhanced by atomic layer deposited TiO₂ nano-overlays," *Opt. Express* **23**(7), 8441 (2015).
- [2] Del Villar, I., Arregui, F.J., Zamarreño, C.R., Corres, J.M., Barriain, C., Goicoechea, J., Elosua, C., Hernaez, M., Rivero, P.J., et al., "Optical sensors based on lossy-mode resonances," *Sensors Actuators B Chem.* **240**, 174–185 (2017).
- [3] Smietana, M., Brabant, D., Bock, W.J., Mikulic, P., Eftimov T., "Refractive-index Sensing with Inline Core-cladding Intermodal Interferometer Based on Silicon Nitride Nano-coated Photonic Crystal Fiber," *J. Lightwave Technol.* **30**(8), 1185-1189 (2012).
- [4] Brzozowska, E., Śmietana, M., Koba, M., Górka, S., Pawlik, K., Gamian, A., Bock, W.J., "Recognition of bacterial lipopolysaccharide using bacteriophage-adhesin-coated long-period grating," *Biosens. Bioelectron.* **67**, 93-99 (2015).
- [5] Hernaez, M., Del Villar, I., Matias, I.R., Arregui, F.J., Zamarre, C.R., "Chemical Tunable humidity sensor based on ITO-coated optical fiber," *Sensors Actuators B Chem.* **146**, 414–417 (2010).
- [6] Zubiate, P., Zamarreño, C.R., Del Villar, I., Matias, I.R., Arregui, F., "Tunable optical fiber pH sensors based on TE and TM Lossy Mode Resonances (LMRs)," *Sensors Actuators B Chem.* **231**, 484–490 (2016).
- [7] Śmietana, M., Dudek, M., Koba, M., Michalak, B., "Influence of diamond-like carbon overlay properties on refractive index sensitivity of nanocoated optical fibres," *Phys. Status Solidi A* **2105**(10), 2100–2105 (2013).
- [8] Michalak, B., Koba, M., Śmietana, M., "Silicon Nitride Overlays Deposited on Optical Fibers with RF PECVD Method for Sensing Applications: Overlay Uniformity Aspects," *Acta Physica Polonica* **127**(6), 1587-1590 (2015).
- [9] Smietana, M., Szmiedt, J., Dudek, M., Niedzielski, P., "Optical properties of diamond-like cladding for optical fibres," *Diamond Relat. Mater.* **13**, 954-95 (2004)
- [10] Del Villar, I., Hernaez, M., Zamarreño, C.R., Sánchez, P., Fernández-Valdivielso, C., Arregui, F.J., Matias, I.R., "Design rules for lossy mode resonance based sensors," *Appl. Opt.* **51**(19), 4298 (2012).

-
- [11] Burnat, D., Koba, M., Wachnicki, Ł., Gierałowska, S., Godlewski, M., Śmietana, M., "Refractive index sensitivity of optical fiber lossy-mode resonance sensors based on atomic layer deposited TiO_x thin overlay," *Proc. SPIE* **9916**, 99161G (2016).
- [12] Mazur, M; Szymańska, M; Kalisz, M; Kaczmarek, D; Domaradzki, J., "Surface and mechanical characterization of ITO coatings prepared by microwave-assisted magnetron sputtering process," *Surf. Interface Anal.* **46**, 827–831 (2014).
- [13] Medvedev, A.E., Clow, A., Sandler, M., Glover, V., "Isatin: A link between natriuretic peptides and monoamines?," *Biochem. Pharmacol.* **52**(3), 385–391 (1996).
- [14] d'Ischia, M., Palumbo, A., Prota, G., "Adrenalin oxidation revisited. New products beyond the adrenochrome stage," *Tetrahedron* **44**(20), 6441–6446 (1988).
- [15] Medvedev, A., Crumeyrolle-Arias, M., Cardona, A., Sandler, M., Glover, V., "Natriuretic peptide interaction with [3H]isatin binding sites in rat brain," *Brain Res.* **1042**(2), 119–124 (2005).
- [16] Zhou, Y., Zhao, Z.-Q., Xie, J.-X., "Effects of isatin on rotational behavior and DA levels in caudate putamen in Parkinsonian rats," *Brain Res.* **917**(1), 127–132 (2001).
- [17] Goyal, R.N., Sangal, A., "Studies of the behavior of 5-hydroxyindole-3-acetamide at a solid electrode," *J. Electroanal. Chem.* **578**(2), 185–192 (2005).
- [18] Wu, W.-F., Chiou, B.-S., "Effect of annealing on electrical and optical properties of RF magnetron sputtered indium tin oxide films," *Appl. Surf. Sci.* **68**(4), 497–504 (1993).
- [19] Fallah, H.R., Ghasemi, M., Hassanzadeh, A., Steki, H., "The effect of annealing on structural, electrical and optical properties of nanostructured ITO films prepared by e-beam evaporation," *Mater. Res. Bull.* **42**(3), 487–496 (2007).
- [20] Diculescu, V.C., Kumbhat, S., Oliveira-Brett, A.M., "Electrochemical behaviour of isatin at a glassy carbon electrode," *Anal. Chim. Acta* **575**(2), 190–197 (2006).

C2. Optical Detection of Ketoprofen by Its Electropolymerization on an Indium Tin Oxide-Coated Optical Fiber Probe

Robert Bogdanowicz, Paweł Niedziałkowski, Michał Sobaszek, Dariusz Burnat, Wioleta Białobrzeska, Zofia Cebula, Petr Sezemsky, Marcin Koba, Vitezslav Stranak, Tadeusz Ossowski, Mateusz Smietana, Optical Detection of Ketoprofen by Its Electropolymerization on an Indium Tin Oxide-Coated Optical Fiber Probe, Sensors (Basel) 18(5), (2018), pii: E1361.

Abstract

In this work an application of optical fiber sensors for real-time optical monitoring of electrochemical deposition of ketoprofen during its anodic oxidation is discussed. The sensors were fabricated by reactive magnetron sputtering of indium tin oxide (ITO) on a 2.5 cm-long core of polymer-clad silica fibers. ITO tuned in optical properties and thickness allows for achieving a lossy-mode resonance (LMR) phenomenon and it can be simultaneously applied as an electrode in an electrochemical setup. The ITO-LMR electrode allows for optical monitoring of changes occurring at the electrode during electrochemical processing. The studies have shown that the ITO-LMR sensor's spectral response strongly depends on electrochemical modification of its surface by ketoprofen. The effect can be applied for real-time detection of ketoprofen. The obtained sensitivities reached over 1400 nm/M ($\text{nm}\cdot\text{mg}^{-1}\cdot\text{L}$) and 16,400 a.u./M ($\text{a.u.}\cdot\text{mg}^{-1}\cdot\text{L}$) for resonance wavelength and transmission shifts, respectively. The proposed method is a valuable alternative for the analysis of ketoprofen within the concentration range of 0.25–250 $\mu\text{g mL}^{-1}$, and allows for its determination at therapeutic and toxic levels. The proposed novel sensing approach provides a promising strategy for both optical and electrochemical detection of electrochemical modifications of ITO or its surface by various compounds.

1. INTRODUCTION

Demand for nonprescription drugs, such as 2-(3-benzoylphenyl)-propanoic acid (ketoprofen, KP) is expected to increase in the near future. KP is a nonsteroidal anti-inflammatory drug, widely used for the treatment of various kinds of pains, rheumatoid arthritis and osteoarthritis [1]. KP exhibits analgesic and antipyretic activity, which is mainly caused by the inhibition of prostaglandin synthesis by inhibiting cyclooxygenase [2]. The widespread and growing volume of human and veterinary prescriptions needs to be followed by the development of analytical techniques allowing for detection of KP traces in various biofluids or sludge water.

Several methods have already been reported for quantitative determination of KP, including liquid chromatography-mass spectrometry [3], UV-fluorescence [4], ion chromatography [5], flow injection with chemiluminescence [6], or electrochemical detection [7]. Both chromatographic and non-chromatographic techniques usually require rigorous sample preparation and expensive extraction methods (including solid-phase extraction) when real samples are considered. Mass spectrometry in turn requires analyte signal suppression or enhancement during electrospray ionization, especially for analysis of multi-compound samples. Application of all these methods is time-consuming and requires expensive and highly specialized setups which are only available in well-equipped research laboratories. Among other techniques, fluorescence at porous SnO₂ nanoparticles was applied for KP detection using combined ion chromatography with photodetection. The limit of detection (*LOD*) in human serum, urine, and canal water samples was 0.1 µg/kg, 0.5 µg/kg, and 0.39 µg/kg, respectively [5]. However, photometric UV and fluorescence-based methods commonly suffer from low sensitivity and selectivity, while the latter require specific chemicals or compounds (e.g., nanoparticles) in the detection procedure.

Electrochemical studies of KP have already been performed using the polarographic method [8, 9] or simultaneously cyclic voltammetry and coulometry techniques at the mercury dropping electrode surface [8, 10]. Kormosh et al. [11] developed ion-selective electrodes for potentiometric analysis of KP in piroxicam based on Rhodamine 6G in a membrane

plasticizer. The measurements of KP using direct current stripping voltammetry as well as spectrophotometric methods were also reported by Emara et al. [9]. With dropping mercury electrode and using different supporting electrolytes at different pH values it was possible to reach a *LOD* as low as $5.08 \times 10^{-4} \text{ ng mL}^{-1}$. A similar electrode was utilized by Ghoneim and Tawfik [10], and in a Britton-Robinson buffer (pH 2.0) the *LOD* was 0.10 ng mL^{-1} . Next, a setup containing glassy carbon (GC) electrode with multiwalled carbon nanotubes/ionic liquid/chitosan composite for covalent immobilization of the ibuprofen by specific aptamer was proposed [7].

It can be concluded that the electrochemical methods offer reliability and accuracy, enabling development of simple, rapid, and cost-effective approaches for the detection of electroactive compounds. However, electrodes for KP detection usually need complex pre-treatment in order to reach high repeatability and environmental stability. Furthermore, KP shows poor solubility in water, a tendency to adsorb and block electrodes, and a rapid metabolization to by-products [12]. Thus, conventional electrochemical assay procedures are not well-suited for this specific application.

To overcome the limitations listed above, we propose a novel approach for KP detection, where together with an electrochemical method an indium tin oxide (ITO)-coated optical fiber sensor is used. ITO is known for its high optical transparency and low electrical resistivity. Moreover, thanks to its band-gap, it is a good candidate for an electrochemical electrode, and it can be used for optical measurements as well. Contrary to other transparent electrode materials, such as boron-doped diamond, thin ITO films can be deposited at a relatively low temperature on various substrates and shapes [13]. Plasma-assisted deposition is often used for obtaining high quality ITO films. An ITO overlay was applied as a standard working electrode, where KP was electropolymerized with the cyclic voltammetry technique. Thanks to the adjustment of both ITO's electrochemical and optical properties, lossy-mode resonance (LMR) effect in optical fiber sensor can also be applied for KP detection. LMR is a thin-film-based optical effect, which takes place when a certain relation between electric permittivity of the film, substrate, and external medium is fulfilled, namely the real part of the film's electric permittivity must be positive and higher in magnitude than both the thin film's permittivity imaginary part and the permittivity of the analyte [14]. Any

variation in optical properties of the analyte, especially its refractive index (RI), has an influence on resonance conditions and can thus be detected. Since in visible spectral range ITO shows relatively high RI ($n_D \sim 2$ RIU) and non-zero extinction coefficient (corresponding to optical absorption), it has already been successfully applied in LMR-based sensing devices [15]. There have been reported applications of other thin films supporting the LMR effect such as diamond-like carbon [16], SiN_x [17], TiO_2 [18], and polymers [19], but among these materials only ITO offers low electrical resistivity and can be applied as an electrode material. Until now both the electrical conductivity of ITO and supported by its thin film LMR effect have been applied only with the purpose of inducing a high voltage change in properties of an electro-optic material deposited on ITO surface [20], and for electropolymerization of a chemical compound on the ITO surface [21]. As an alternative to the conventional assay procedures, the developed opto-electrochemical probe can offer a KP detection method free from pre-treatment of the electrode's surface, as well as prolonged analysis time and sophisticated experimental setup.

The application of opto-electrochemical probes is a novel approach. To the best of our knowledge, in this paper we discuss for the first time the application of LMR phenomenon at the ITO-coated optical fiber for electrochemically-induced KP detection. The developed opto-electrochemical probe offers capability for label-free KP detection with no need of the electrode's surface pre-treatment. Additionally, the GC electrode has been modified by KP for reference.

2. MATERIALS AND METHODS

KP (2-(3-benzoylphenyl) propionic acid) of purity greater than 98% was obtained from Cayman Company (Ann Arbor, MI, USA) and used without any further purification. A KP solution with a concentration of 2 mM was prepared in a 0.1 M phosphate buffer saline (pH = 7.0). Na_2SO_4 and $\text{K}_3[\text{Fe}(\text{CN})_6]$ were purchased from POCh (Gliwice, Poland).

2.1. ITO Optical Probe Fabrication and Testing

The LMR structures were fabricated using approx. 15 cm-long polymer-clad silica fiber samples of 400/840 μm core/cladding diameter, where 2.5 cm of polymer cladding was removed in the fiber central section [22]. Next, the electrically conductive and optically transparent ITO films were deposited by

reactive magnetron sputtering of ITO target ($\text{In}_2\text{O}_3\text{-SnO}_2$ —90/10 wt % and purity of 99.99%). The magnetron, whose axis was perpendicular to the substrate, was supplied by a Cito1310 (13.56 MHz, 300 W) RF source (Comet AG, Flamatt, Switzerland). The experiments were carried out at pressure $p = 1.0$ Pa in a reactive N_2/Ar atmosphere, gas flows were 15 and 0.5–1.0 sccm for Ar and N_2 , respectively. The overlays were deposited on fibers rotated in the chamber during the process. Simultaneously, Si wafers and glass slides were also coated for reference. Both of the end-faces of the fiber sample were mechanically polished before the optical testing.

To determine RI sensitivity of the fabricated ITO-LMR devices, they were investigated in the air and mixtures of water/glycerin with $n_D = 1.33$ –1.45 RIU. The RI of the mixtures was measured using an AR200 automatic digital refractometer (Reichert Inc., Buffalo, NY, USA). The optical transmission of the ITO-LMR structure was interrogated in the range of $\lambda = 350$ –1050 nm using an HL-2000 white light source (Ocean Optics Inc., Largo, FL, USA) and an Ocean Optics USB4000 spectrometer. The optical transmission (T) in the specified spectral range was detected as counts in specified integration time (up to 100 ms). The temperature of the solutions was stabilized at 25 °C to avoid thermal shift of the RI.

2.2. Electrochemical Setup and Electropolymerization of KP

Cyclic voltammetry measurements were performed with a PGSTAT204 potentiostat/galvanostat (Metrohm, Herisau, Switzerland) controlled by Nova 1.1 software, and using the ITO-LMR probe as a working electrode (WE), a platinum wire as counter electrode (CE), and an Ag/AgCl/0.1 M KCl as a reference electrode (REF). The ITO-LMR working electrode was electrochemically processed in 0.1 M phosphate buffer saline containing from 1×10^{-6} to 1×10^{-3} M of KP at scan rate $50 \text{ mV} \cdot \text{s}^{-1}$ for 6 cycles. The process allowed for anodic electrooxidation of KP in the potential ranging from 0.3 to 2.0 V vs. Ag/AgCl/0.1 M KCl electrode. The reference GC and ITO electrodes were processed under the same conditions as the ITO-LMR electrode, but for the GC electrode the modification took 10 cycles. Next, the electrodes were washed in water and methanol, and dried under a stream of air. The electrode examinations before and after modification with cyclic voltammetry were performed in 5 mM of $\text{K}_3[\text{Fe}(\text{CN})_6]$ in 0.5 M Na_2SO_4 solution at scan rate of

$100 \text{ mV}\cdot\text{s}^{-1}$. The setup used in this experiment is schematically shown in Figure 1.

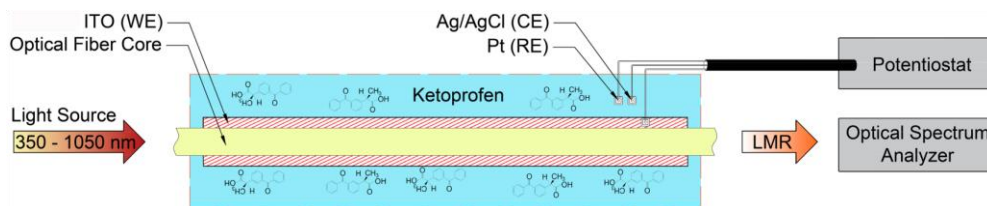


Figure 1. The schematic representation of the experimental setup with ITO-LMR probe used for combined optical and electrochemical KP detection. The electrodes were denoted as working (WE), reference (RE), and counter (CE).

2.3. X-ray Photoelectron Spectroscopy Surface Studies

X-ray Photoelectron Spectroscopy (XPS) studies were carried out using an ESCA300 XPS setup (Scienta Omicron GmbH, Taunusstein, Germany) with a high resolution spectrometer equipped with a monochromatic $K\alpha$ source. Measurements were done at 10 eV pass energy and 0.05 eV energy step size. A flood gun was used for charge compensation purpose. Finally, the calibration of XPS spectra was performed for carbon peak C1s at 284.6 eV [23, 24].

3. RESULTS AND DISCUSSION

3.1. The RI Sensitivity of the ITO-LMR Probe

First, the optical probes were studied in an optical setup only. This part of the experiment was done in order to estimate the sensitivity of the device to changes of optical properties at the ITO surface. The probes were installed in a setup allowing one to record the transmission spectra, while the sensor was consecutively immersed in different RI solutions. In Figure 2 a well-defined resonance can be seen that experiences a shift towards higher wavelengths when the external RI increases. It is worth noting that the applied ITO coatings provide relatively narrow resonance. The full width at half maximum (*FWHM*) obtained for the resonances is approx. 110 nm. When the probe is immersed in the higher RI, the *FWHM* of the resonance slightly increases. Based on the obtained results, two ways of sensor interrogation can be selected, namely tracking of resonance wavelength (λ_R) or monitoring transmission at discrete wavelength, the most effectively chosen at the

resonance slope. In the case of this experiment, the transmission was monitored at $\lambda = 600$ nm (T_{600}). Both the λ_R and T_{600} were plotted vs. RI in the inset of Figure 2. The shift is positive for both of the interrogation schema, but for tracking λ_R the dependence is less linear (the sensitivity increases with RI) than for the T_{600} .

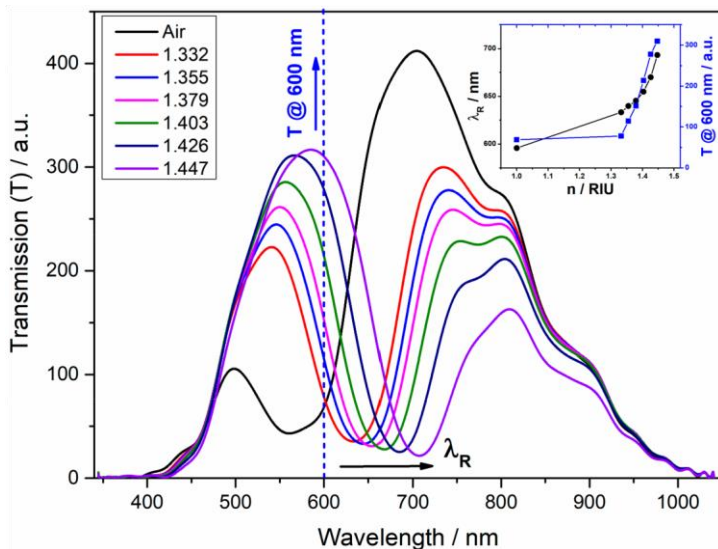


Figure 2. Spectral response of ITO-LMR probe to changes in external RI (n). The changes of resonance wavelength (λ_R) and transmission (T) at $\lambda = 600$ nm are shown in the inset.

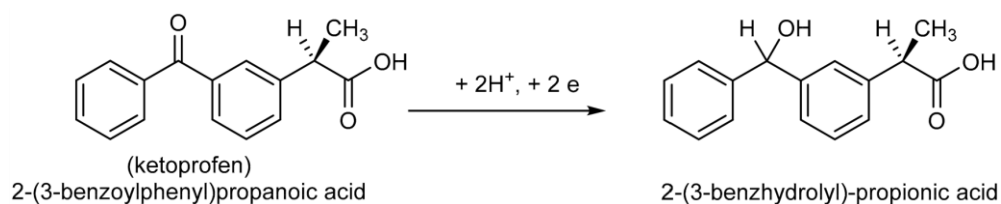
The measurements of reference Si samples allowed to estimate the thickness of the coating to 260 nm. According to theoretical studies [25], a low order LMR may be observed for such thickness of ITO. It is known that low order LMRs offer the highest sensitivity to changes in external RI [14], as well as changes in properties of a layer formed on the ITO surface [26].

The standard commercial ITO electrodes undergo thermal annealing to decrease both optical absorption and electrical resistivity, most likely due to the crystallization processes [27]. The LMR-satisfying properties of non-annealed, as fabricated ITO films are attributed to unique advantages of the applied discharge during deposition process. Our previous research clearly showed that optimization of the deposition pressure $0.5 \text{ Pa} < p < 1.0 \text{ Pa}$ induces collisions of the sputtered particles [28, 29]. The application of magnetron sputtering is advantageous and allows to tailor the optical and electrical properties of the deposited ITO films with no additional post-

deposition annealing as it is often required in case of other deposition methods [30].

3.2. Electrodeposition of KP on GC, ITO and ITO-LMR Electrodes

The electrochemical deposition of KP on GC, ITO and ITO-LMR electrodes was made by anodic oxidation. The redox behavior of KP molecule at the GC and ITO electrode has not been reported yet. However, the anodic oxidation of KP was observed at the boron doped diamond electrode. The current peak measured for this electrode during the electrodeposition processes is associated with the oxidation of carboxyl group in KP [31]. Moreover, the mechanism of the electrochemical reduction of KP have been until now examined only at the mercury electrode and requires transfer of two electrons. This reduction leads to formation of 2-(3-benzhydrolyl)-propionic acid [8] (Scheme 1). The mechanism of reduction of KP—benzophenone-3 has been described elsewhere [32].



Scheme 1. Chemical structure of KP and mechanism of its electrochemical reduction.

Anodic oxidation by electron transfer leads to deactivation of electrode surface and its modification by adsorption of oxidized polymeric products of the reaction. This effect has been used in this work for modification of different types of electrodes, i.e., GC, ITO, and ITO-LMR. It must be emphasized that only ITO-LMR electrode allows for simultaneous optical and electrochemical monitoring of the modification processes by KP.

The cyclic voltammetry is a very valuable and convenient tool to monitor the electrode surface properties before and after each step of modification [33]. The electrochemical responses of the bare GC, ITO and ITO-LMR electrodes were investigated in a solution of 0.5 M Na₂SO₄ containing 5 mM [Fe(CN)₆]^{3-/4-}. The comparison of cyclic voltammograms of modified and bare electrodes is presented in Figure 3. For the bare GC electrode, well-defined reversible redox peaks corresponding to one-electron reversible

reaction and the peak to peak separation value of 95 mV were reported [34]. This redox reaction of KP completely blocked the GC electrode after 10 scans. The current peak observed in the first scan (Figure 3a) can be attributed to the oxidation of carboxyl group of the KP [35]. The absence of any current for the GC electrode cycled in presence of KP suggests that KP-based layer was formed on the GC surface (Figure 3b). Polymerized KP film the most likely prevents from the penetration of the electroactive substance towards the electrode surface [36]. This phenomenon has been commonly observed for a series of compounds and different electrode material [37, 38].

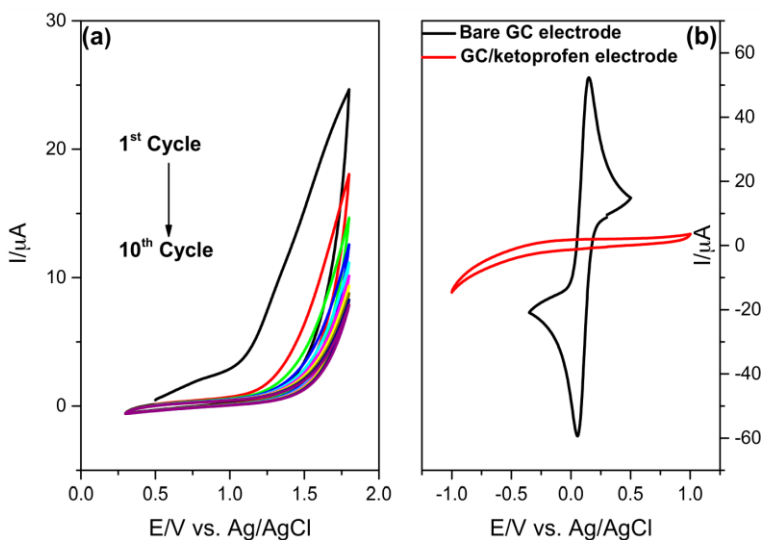


Figure 3. Cyclic voltammograms recorded for (a) GC electrode in 0.1 M phosphate buffer saline containing 2 mM of KP for 10 cycles, scan rate of $50 \text{ mV} \cdot \text{s}^{-1}$; and (b) bare GC and GC/KP electrode in 0.5 M Na_2SO_4 containing of 5 mM $[\text{Fe}(\text{CN})_6]^{3-/4-}$. The scan rate was set to $100 \text{ mV} \cdot \text{s}^{-1}$.

Next, a reference ITO electrode deposited on a glass slide underwent a similar modification procedure. In Figure 4a the cyclic voltammograms recorded for ITO electrode in 0.1 M phosphate buffer saline containing 2 mM of KP in 10 cycles are shown. For the bare ITO electrode a redox response with peak to peak potential separation reached 245 mV. Significant differences between the electrochemical response for bare and modified electrodes recorded in 0.5 M Na_2SO_4 solution containing 5 mM $[\text{Fe}(\text{CN})_6]^{3-/4-}$ were observed. The decrease in peak current and increase in peak to peak potential separation of up to 511 mV, indicate that the modification of the electrode surface by KP was effective (Figure 4b). This phenomenon also suggests that the surface of

the ITO electrode was blocked by KP, which is observed in the disappearance of the anodic and cathodic peak [39].

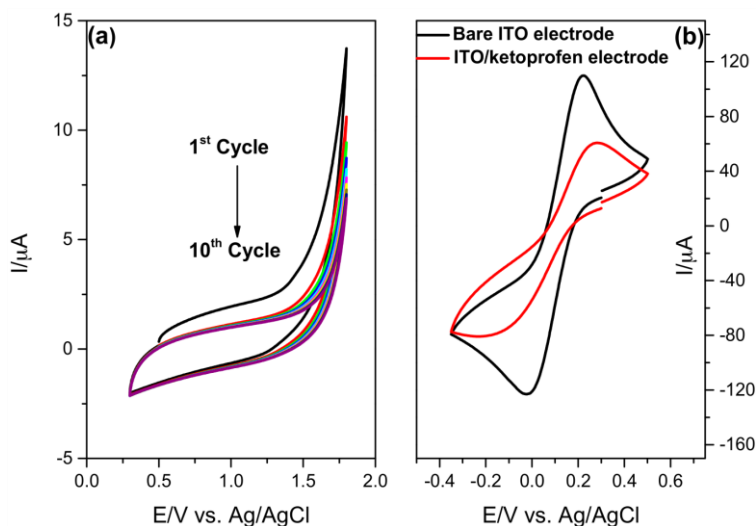


Figure 4. Cyclic voltammograms recorded for (a) ITO electrode in 0.1 M phosphate buffer saline containing 2 mM of KP (10 cycles, scan rate of $50 \text{ mV} \cdot \text{s}^{-1}$) and (b) ITO and ITO/KP electrode in 0.5 M Na_2SO_4 containing 5 mM $[\text{Fe}(\text{CN})_6]^{3-/4-}$, scan rate $100 \text{ mV} \cdot \text{s}^{-1}$.

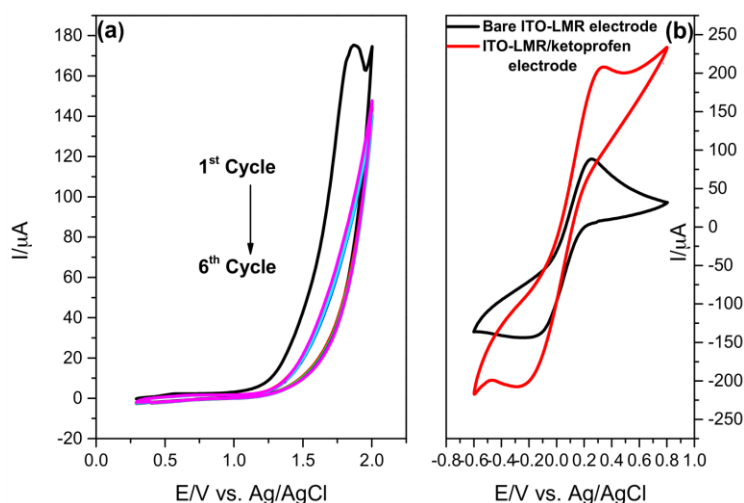


Figure 5. Cyclic voltammograms recorded for (a) ITO-LMR electrode in 0.1 M phosphate buffer saline containing 2 mM of KP for 6 cycles at scan rate of $50 \text{ mV} \cdot \text{s}^{-1}$; and (b) bare for and KP-modified ITO-LMR in 0.5 M Na_2SO_4 containing 5 mM $[\text{Fe}(\text{CN})_6]^{3-/4-}$, scan rate $100 \text{ mV} \cdot \text{s}^{-1}$.

The ITO-LMR probe was coated with KP during only six anodic oxidation cycles in the potential range from 0.3 to 2.0 V and with a scan rate of

50 mV·s⁻¹ (Figure 5a). After this process, the electrode was extensively washed with water and methanol. It is worth noting that for the modification by KP of GC and ITO electrodes, 10 cycles were applied. In the case of ITO-LMR electrode, six cycles were enough to completely cover the electrode. In Figure 5b the cyclic voltammetry response to 0.5 M Na₂SO₄ containing 5 mM [Fe(CN)₆]^{3-/4-} is shown for bare and KP-modified ITO-LMR electrode. Bare and modified ITO-LMR electrodes show redox responses with peak to peak potential separation reaching 419 mV and 628 mV, respectively. Moreover, for the KP-modified ITO-LMR electrode the redox current peaks significantly increased. This effect suggests that the electrode has a more developed active surface area than the one before modification [40]. This was only observed for anodic oxidation of KP on the ITO-LMR electrode. In the other cases, namely reference ITO and GC electrodes, the current peaks for redox couple decreased significantly as a result of modification by KP.

In Table 1 are summarized the electrochemical results obtained for the samples before and after KP modification. The peak splitting difference between bare ITO and ITO-LMR electrodes, i.e., ΔE reaching 245 mV and 419 mV, respectively, can originate from two effects. First, the ITO deposition on cylindrical shape, such as optical fiber, is more challenging than on a flat surface and has an impact on size, crystallinity and morphology of the electrode active surface. Second, the KP modifies the shape of the cyclic voltammetry curves and the peak to peak separations ΔE from 511 to 628 mV for ITO and ITO-LMR electrode, respectively. The diffusion of electrons through the KP is disturbed, revealing slightly reduced electrocatalytic activities, which can be attributed to its structural features and electrochemical properties.

Table 1. Electrochemical parameters of the reactions for [Fe(CN)₆]^{3-/4-} on the surface of bare and KP modified ITO electrodes.

Sample	<i>E</i> _{red} (mV)	<i>E</i> _{ox} (mV)	Δ <i>E</i> (mV)	<i>E</i> _{1/2} (mV)
Bare ITO electrode	-24	221	245	123
KP/ITO electrode	-230	281	511	230
Bare ITO-LMR electrode	-165	254	419	210
KP/ITO-LMR electrode	-285	343	628	314

3.3. XPS Studies of KP-Modified ITO Surface

High-resolution XPS spectra, analyzed within the energy range of C1s and O1s peaks, make it possible to verify successful KP modification of ITO surface at the level of 10^{-3} M. Survey of the XPS spectrum presented in Figure 6 reveals significant contribution from ITO background seen as tin, indium, and oxygen peaks, and smaller contribution from electropolymerized thin KP layer on ITO surface. The high-resolution XPS spectra were also acquired, in the energy range characteristic for C1s and O1s peaks. The high-resolution analysis allows for verification of successful KP modification of ITO surface at the level of 10^{-3} M. Recorded spectra with their deconvolution are shown in the inset of Figure 6 and extracted data are summarized in Table 2.

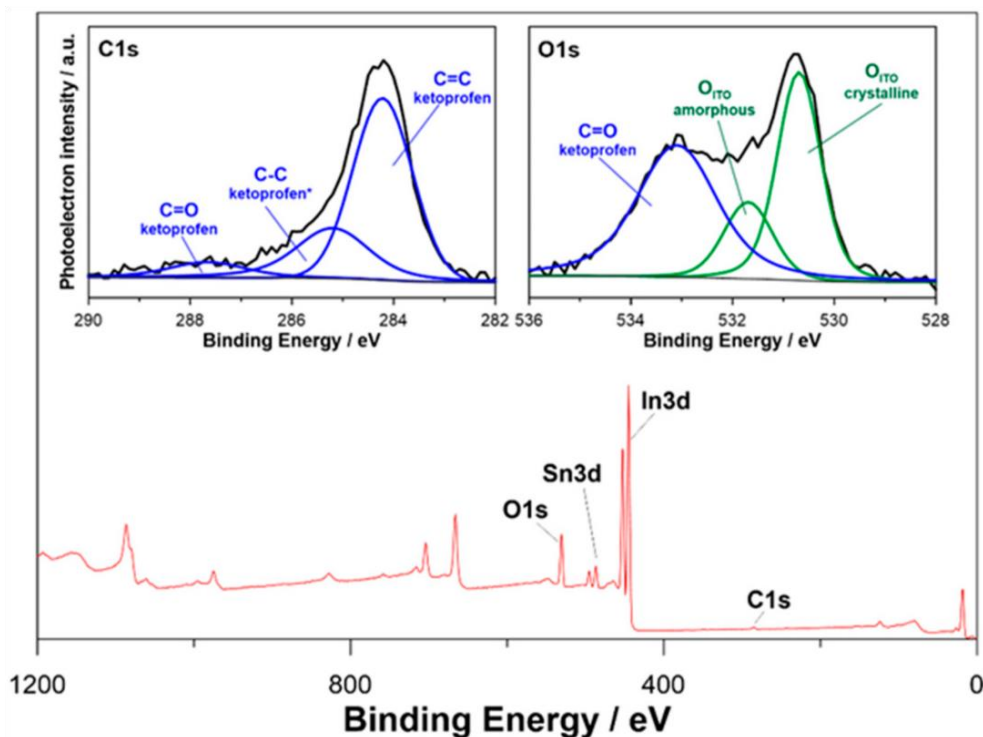


Figure 6. XPS survey spectrum and high-resolution XPS spectra registered for C1s and O1s energy range. Peaks underwent spectral deconvolution are superimposed with colors depending on their origination (blue for KP and green for ITO). The KP concentration was 1×10^{-3} M.

Table 2. Comparison of chemical composition of bare ITO and ITO/KP electrode.

XPS Photopeak	Chemical State	Binding Energy (eV)	Chemical Composition (at.%)	
			Bare ITO Electrode	ITO/KP Electrode
C1s	C = C	284.2	-	27.8
	C–C *	285.2	-	9.9
	C = O	287.7	-	4.3
O1s	ITO _{cryst}	530.7	40.5	13.6
	ITO _{amorph}	531.7	12.8	5.5
	C = O	533.1	-	17.3
In	ITO _{cryst}	444.1	29.8	9.8
	ITO _{amorph}	445.1	11.8	9.2
Sn	ITO _{cryst}	486.1	3.7	1.4
	ITO _{amorph}	487.0	1.4	1.2

* Indicates the influence of adventitious carbon in total chemical composition of C–C chemical state.

The C1s spectrum was deconvoluted with three peaks, each denoting a different chemical state of carbon. The primary component is located at +284.2 eV and is characteristic for aromatic C = C bonds in KP. The second and third type of interaction can be associated with aliphatic C–C and C = O bonds. Their energy shift versus the primary spectral component is +1.0 for C–C and +3.5 eV for C = O type of bonds and highly correlates with other results found in the literature [41-43]. Furthermore, the XPS analysis carried out within the O1s energy region confirmed the pronounced presence of peak located at 533.1 eV, which is characteristic for carbonyl bonds. Finally, the acquired C = C:C–C:C = O ratio of 6.5:2.8:1 corresponds to the known for KP 6:1:1. A slight excess of C–C contribution can be explained by the presence of adventitious carbon coming from sample storage in atmospheric conditions. The amount of adventitious carbon found at bare ITO electrode did not exceed 5 at.% and was excluded from further analysis.

We have also performed detailed XPS analysis of peaks located in In3d5 and Sn3d5 energy range. The results of the analysis were also summarized

in Table 2. According to literature survey, ITO analysis are typically based on spectral deconvolution using two sub-peaks—often ascribed to be contribution from crystalline and amorphous ITO. The observed peak shift between crystalline and amorphous phases—1.0 eV for In and 0.9 eV for Sn peaks—was found to stay in agreement with literature survey [44-46].

3.4. ITO-LMR-Based KP Electropolymerization Monitoring

The electrochemically-induced polymerization of KP was monitored optically using ITO-LMR probe. As shown in Figure 7, there were changes in the spectral response during cyclic voltammetry electropolymerization of KP for its two concentrations in the solution, i.e., the lowest and the highest. Obviously, for high KP concentration (1×10^{-3} M) results in electropolymerization of denser film which is followed by more pronounced changes in the optical spectrum (Figure 7B). Nevertheless, as low KP concentration as 1×10^{-6} M can be observed in optical response (Figure 7A). For all the applied concentrations, the most noticeable changes in the spectrum can be observed for the resonance at approx. $\lambda_R \sim 650$ nm, where a shift towards longer wavelengths takes place with the process progress. On top of tracking the resonant wavelength shift, in the discussed case also changes in T can be monitored at specific wavelength. For these resonance conditions, as previously when response to RI has been analyzed, we picked $\lambda = 600$ nm that is in the middle of the resonance slope. Due to the limited resolution of the spectrometer, T monitoring may deliver more accurate data than λ_R .

The saturation of KP polymerization process was noticed for the ITO-LMR probe during the second CV cycle. The scan rate was set to $100 \text{ mV} \cdot \text{s}^{-1}$ in the range 0–2 V what resulted in 40 s per one cycle. The full range optical transmission was recorded with integration time up to 100 ms for 3500 data set. Thus, the entire optical analysis took 6 minutes. However, the wavelength range could be limited to e.g., 50 nm (approx. 250 data points) resulting in 25 seconds-long analysis. Summarizing, the result of KP determination was achieved with response time below 1 minute with no additional pretreatment, labeling, or incubation required.

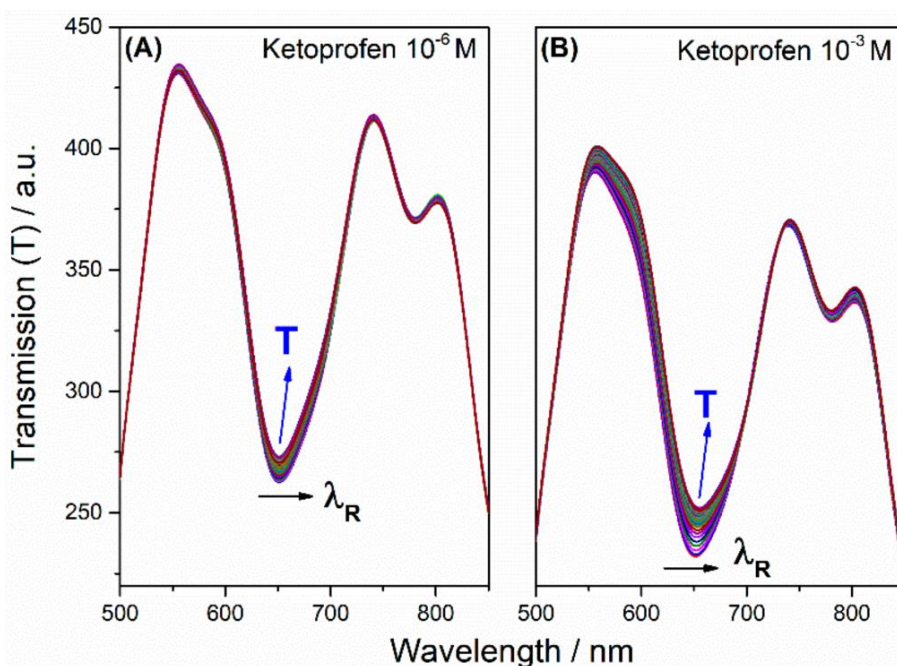


Figure 7. Changes in optical response of the ITO-LMR probe recorded during electropolymerization of KP on ITO surface for two KP concentrations, namely (A) 1×10^{-6} M and (B) 1×10^{-3} M.

Variations of the two parameters, namely λ_R and T versus progress in the electrodeposition process are shown for all the KP concentrations in Figure 8. As in the case of an increase in external RI, both of them increase with progress of the electrodeposition process. The effect can be explained as a mass transfer of KP, i.e., densification of the medium at the ITO surface, resulting in the growth of the KP polymer film. A similar shift has already been reported for aptamer immobilization or swelling of poly-acrylic acid (PAA) and polyallylamine hydrochloride (PAH) polymeric coatings on ITO deposited on a fiber [26, 47]. The increase in both parameters depends on the concentration of KP and surely has an impact on the thickness of the electrodeposited film. The effect of KP deposition on the electrode was revealed earlier by XPS studies (Figure 6) and recognized by a shift of peaks characteristic for aromatic C = C and aliphatic C–C and C = O bonds existing in this compound.

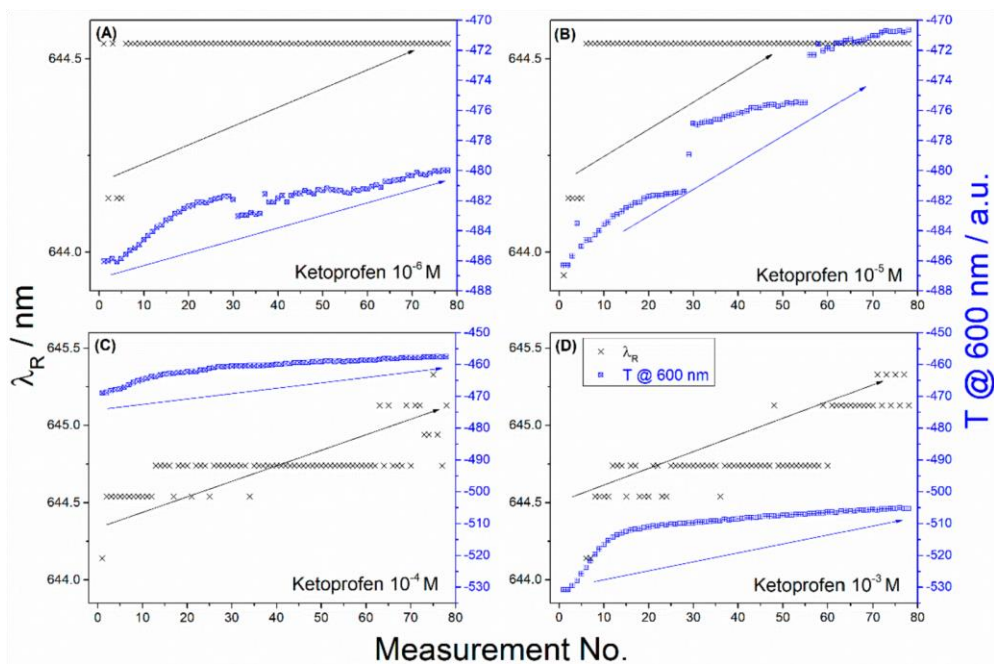


Figure 8. Change in resonance wavelengths (λ_R) { \times } and transmission (T) at 600 nm { \square } with progress of KP electropolymerization process on ITO-LMR probe for KP concentration (A) 1×10^{-6} M; (B) 1×10^{-5} M; (C) 1×10^{-4} M; and (D) 1×10^{-3} M.

The relative changes of λ_R and T at $\lambda = 600$ nm are summarized in Table 3 using data shown in Figure 8. The final values of the achieved parameters after 80 measurements (approx. 120 s) were plotted versus the KP concentration. It must be noted that both the parameters linearly depend on the concentration with an average correlation coefficient R^2 higher than 0.93. The sensitivities have been considered as ratios of the slopes reaching 1400.86 nm/M ($\text{nm} \cdot \text{mg}^{-1} \cdot \text{L}$) and $16,422.46$ a.u./M ($\text{a.u.} \cdot \text{mg}^{-1} \cdot \text{L}$) for resonance wavelengths (λ_R) and T , respectively. The calculated LOD of KP is 0.536 or 0.575 mM using λ_R and T , respectively. The application of enhanced resolution equipment and standardized solutions at lower concentration would allow us to enhance this value as well as the LOD . The KP detection experiments were performed three times using separately deposited ITO-LMR probes. They were used to determine 1 mM KP solution with an average RSD value 8.5%, which indicates the satisfactory reproducibility and repeatability of the approach.

Table 3. The relative changes of λ_R and T at 600 nm of ITO-LMR probe recorded vs. KP concentration.

KP Concentration	ΔT (a.u.)	$\Delta\lambda$ (nm)
1×10^{-3} M	255.2	1.98
1×10^{-4} M	123.2	0.99
1×10^{-5} M	113.9	0.6
1×10^{-6} M	60.4	0.4

Analytical capability for KP determination with bare ITO-LMR electrode and other previously used nanomaterials is compared in Table 4. It can be concluded that the measurements with the ITO-LMR probe offer competitive sensitivity mainly when higher KP concentrations are considered. At these conditions standard electrochemical sensors are not effective due to adsorption at the electrode surface. The sensing concept can be further developed towards detection of other polymerizing agents. Fabrication of such sensors can be easily scaled-up keeping physical homogeneity and electrochemical performance. Summarizing, the application of the ITO-LMR probe offers competitive response toward KP detection mainly when larger concentrations are considered and standard electrochemical sensors are oversaturated by adsorption. The sensing concept can be further developed for future studies of other polymerizing agents.

Table 4. Comparison of KP linear measurement range and LOD achieved with different methods.

Technique	Details	Linear Range	Limit of Detection	Reference
Adsorptive Stripping Square Wave	Mercury electrode	1×10^{-8} – 3×10^{-7} M	0.1 ng mL ⁻¹	[10]
LC-APCI-MS	Single Ion Monitoring mode (SIM)	100–500 ng/mL	1.0 ng/mL	[3]
IC-FLD	SnO ₂ nanoparticles	0.1 µg/kg	0.2–1.5 mg/kg	[5]
Differential Pulse Voltammetry	Aptamer and glassy carbon electrode	70 pM–6 µM	20 pM	[7]
Potentiometry	PVC electrode	0.0001–0.05 mol/L	6.3×10^{-5} mol/L	[11]
Microdialysis	Short polymeric columns (SPE)	25–5000 ng/mL	3 ng/mL	[48]
Flow injection	Flow injection with chemiluminescence	5.0×10^{-8} – 3.0×10^{-6} mol/L	2.0×10^{-8} mol/L	[6]
High-Performance Liquid Chromatography	Single-pass intestinal perfusion method	12.5–200 ng/mL	0.05 ng/mL	[49]
Rp-HPLC	PDA detector	872.5 nM	4.85 – 9.7×10^5	[7]
Differential Pulse Polarography	Dropping-mercury electrode	1×10^{-5} – 5×10^{-4} M	9.8×10^{-6} mol/L	[8]
Polarography	Dropping-mercury electrode	10^{-8} – 10^{-6} M	2.0×10^{-9} mol/L	[8]
Stripping voltammetry	Mercury electrode	1×10^{-8} – 1×10^{-7} M	2.0×10^{-9} mol/L	[9]
ITO-LMR probe	ITO electrode	1×10^{-6} – 1×10^{-3} M	0.5×10^{-3} mol/L	This work

4. CONCLUSIONS

In this study we have developed an optical fiber sensor based on the LMR effect supported by a thin ITO overlay and used it for real-time optical monitoring of electrochemical deposition of KP. The developed highly conductive ITO overlay was deposited on an optical fiber core and applied as a working electrode in cyclic voltammetry electrochemical setup. We have found that electrodeposition of KP on the ITO surface induces a significant change in the LMR response. The variation in optical transmission for the ITO-LMR sensor gradually follows the progress in the electrochemical deposition process. The sensor can be interrogated by tracing transmission at discrete wavelength as well as resonant wavelength shifts. Optical setup enables LMR monitoring of the KP concentration down to 1×10^{-6} M. Thus, the proposed method is a valuable alternative for the analysis of KP within the concentration range of 0.25–250 $\mu\text{g mL}^{-1}$, allowing its determination at therapeutic and toxic levels. The sensing concept can be applied for detection of various other pharmaceuticals, as well as organics or biocompounds that are capable for electropolymerization at ITO surface. It is worth noting that this effect was obtained at bare ITO electrodes fabricated by magnetron sputtering. This deposition method is known for scalability and thus is widely applied as an industrial technology for a wide range of applications. The obtained devices are cheap in large-scale production, disposable, and can be applied in low-power, portable point-of-care devices or microchips. Moreover, the probes can be interrogated with simplified and limited in wavelength range systems based on LED source and Si photodiode with a bandpass filter.

Author Contributions

R.B., P.N., M.S., V.S., T.O. and M.Ś. conceived and designed the experiments; D.B., W.B., Z.C. and P.S. performed the experiments; R.B., P.N. and M.Ś. analyzed the data; M.K. developed measurement setup elements and data acquisition and analysis tools; R.B., P.N. and M.Ś. wrote the paper.

Funding

This research was funded by NATO grant number SPS G5147, National Science Centre (NCN), Poland grant numbers 2014/14/E/ST7/00104 and

2016/21/B/ST7/01430, and Faculty of Electronics, Telecommunications and Informatics of the Gdansk University of Technology (DS funds).

Conflicts of Interest

The authors declare no conflict of interest.

References

- [1] Sakeena, M.H.F.; Yam, M.F.; Elrashid, S.M.; Munavvar, A.S.; Aznim, M.N. Anti-inflammatory and Analgesic Effects of Ketoprofen in Palm Oil Esters Nanoemulsion. *J. Oleo Sci.* **2010**, *59*, 667–671.
- [2] Asanuma, M.; Asanuma, S.N.; Gómez-Vargas, M.; Yamamoto, M.; Ogawa, N. Ketoprofen, a non-steroidal anti-inflammatory drug prevents the late-onset reduction of muscarinic receptors in gerbil hippocampus after transient forebrain ischemia. *Neurosci. Lett.* **1997**, *225*, 109–112.
- [3] Abdel-Hamid, M.E.; Novotny, L.; Hamza, H. Determination of diclofenac sodium, flufenamic acid, indomethacin and ketoprofen by LC-APCI-MS. *J. Pharm. Biomed. Anal.* **2001**, *24*, 587–594.
- [4] Patrolecco, L.; Ademollo, N.; Grenni, P.; Tolomei, A.; Barra Caracciolo, A.; Capri, S. Simultaneous determination of human pharmaceuticals in water samples by solid phase extraction and HPLC with UV-fluorescence detection. *Microchem. J.* **2013**, *107*, 165–171.
- [5] Muhammad, N.; Li, W.; Subhani, Q.; Wang, F.; Zhao, Y.-G.; Zhu, Y. Dual application of synthesized SnO₂ nanoparticles in ion chromatography for sensitive fluorescence determination of ketoprofen in human serum, urine, and canal water samples. *New J. Chem.* **2017**, *41*, 9321–9329.
- [6] Zhuang, Y.; Song, H. Sensitive determination of ketoprofen using flow injection with chemiluminescence detection. *J. Pharm. Biomed. Anal.* **2007**, *44*, 824–828.
- [7] Roushani, M.; Shahdost-fard, F. Covalent attachment of aptamer onto nanocomposite as a high performance electrochemical sensing platform: Fabrication of an ultra-sensitive ibuprofen electrochemical aptasensor. *Mater. Sci. Eng. C* **2016**, *68*, 128–135.
- [8] Amankwa, L.; Chatten, L.G. Electrochemical reduction of ketoprofen and its determination in pharmaceutical dosage forms by differential-pulse polarography. *Analyst* **1984**, *109*, 57–60.
- [9] Emara, K.M.; Ali, A.M.; Abo-El Maali, N. The polarographic behaviour of ketoprofen and assay of its capsules using spectrophotometric and voltammetric methods. *Talanta* **1994**, *41*, 639–645.

- [10] Ghoneim, M.M.; Tawfik, A. Voltammetric studies and assay of the anti-inflammatory drug ketoprofen in pharmaceutical formulation and human plasma at a mercury electrode. *Can. J. Chem.* **2003**, *81*, 889–896.
- [11] Kormosh, Z.; Hunka, I.; Bazel, Y.; Matviychuk, O. Potentiometric determination of ketoprofen and piroxicam at a new PVC electrode based on ion associates of Rhodamine 6G. *Mater. Sci. Eng. C* **2010**, *30*, 997–1002.
- [12] Cheng, Y.; Xu, T.; Fu, R. Polyamidoamine dendrimers used as solubility enhancers of ketoprofen. *Eur. J. Med. Chem.* **2005**, *40*, 1390–1393.
- [13] Paine, D.C.; Whitson, T.; Janiac, D.; Beresford, R.; Yang, C.O.; Lewis, B. A study of low temperature crystallization of amorphous thin film indium–tin–oxide. *J. Appl. Phys.* **1999**, *85*, 8445–8450.
- [14] Villar, I.D.; Hernaez, M.; Zamarreño, C.R.; Sánchez, P.; Fernández-Valdivielso, C.; Arregui, F.J.; Matias, I.R. Design rules for lossy mode resonance based sensors. *Appl. Opt.* **2012**, *51*, 4298–4307.
- [15] Zamarreño, C.R.; Hernaez, M.; Del Villar, I.; Matias, I.R.; Arregui, F.J. Tunable humidity sensor based on ITO-coated optical fiber. *Sens. Actuators B Chem.* **2010**, *146*, 414–417.
- [16] Śmietana, M.; Dudek, M.; Koba, M.; Michalak, B. Influence of diamond-like carbon overlay properties on refractive index sensitivity of nano-coated optical fibres. *Phys. Status Solidi A* **2013**, *210*, 2100–2105.
- [17] Michalak, B.; Koba, M.; Śmietana, M. Silicon Nitride Overlays Deposited on Optical Fibers with RF PECVD Method for Sensing Applications: Overlay Uniformity Aspects. *Acta Phys. Pol. A* **2015**, *127*, 1587–1591.
- [18] Burnat, D.; Koba, M.; Wachnicki, Ł.; Gieraltowska, S.; Godlewski, M.; Śmietana, M. Refractive index sensitivity of optical fiber lossy-mode resonance sensors based on atomic layer deposited TiO_x thin overlay. In Proceedings of the 6th European Workshop on Optical Fibre Sensors, Limerick, Ireland, 31 May–3 June 2016.
- [19] Zamarreño, C.R.; Hernaez, M.; Del Villar, I.; Matías, I.R.; Arregui, F.J. Optical fiber pH sensor based on lossy-mode resonances by means of thin polymeric coatings. *Sens. Actuators B Chem.* **2011**, *155*, 290–297.
- [20] Ascorbe, J.; Corres, J.M.; Arregui, F.J.; Matías, I.R. Optical Fiber Current Transducer Using Lossy Mode Resonances for High Voltage Networks. *J. Light. Technol.* **2015**, *33*, 2504–2510.

-
- [21] Sobaszek, M.; Dominik, M.; Burnat, D.; Bogdanowicz, R.; Stranak, V.; Sezemsky, P.; Śmietana, M. Optical monitoring of thin film electro-polymerization on surface of ITO-coated lossy-mode resonance sensor. In Proceedings of the 25th International Conference on Optical Fiber Sensors, Jeju, Korea, 24–28 April 2017.
- [22] Smietana, M.; Szmidt, J.; Dudek, M.; Niedzielski, P. Optical properties of diamond-like cladding for optical fibres. *Diam. Relat. Mater.* **2004**, *13*, 954–957.
- [23] Miller, D.J.; Biesinger, M.C.; McIntyre, N.S. Interactions of CO₂ and CO at fractional atmosphere pressures with iron and iron oxide surfaces: One possible mechanism for surface contamination? *Surf. Interface Anal.* **2002**, *33*, 299–305.
- [24] Wysocka, J.; Krakowiak, S.; Ryl, J. Evaluation of citric acid corrosion inhibition efficiency and passivation kinetics for aluminium alloys in alkaline media by means of dynamic impedance monitoring. *Electrochim. Acta* **2017**, *258*, 1463–1475.
- [25] Villar, I.D.; Zamarreño, C.R.; Sanchez, P.; Hernaez, M.; Valdivielso, C.F.; Arregui, F.J.; Matias, I.R. Generation of lossy mode resonances by deposition of high-refractive-index coatings on uncladded multimode optical fibers. *J. Opt.* **2010**, *12*, 095503.
- [26] Zubiate, P.; Zamarreño, C.R.; Sánchez, P.; Matias, I.R.; Arregui, F.J. High sensitive and selective C-reactive protein detection by means of lossy mode resonance based optical fiber devices. *Biosens. Bioelectron.* **2017**, *93*, 176–181.
- [27] Dominik, M.; Siuzdak, K.; Niedziałkowski, P.; Stranak, V.; Sezemsky, P.; Sobaszek, M.; Bogdanowicz, R.; Ossowski, T.; Śmietana, M. Annealing of indium tin oxide (ITO) coated optical fibers for optical and electrochemical sensing purposes. In Proceedings of the 2016 Electron Technology Conference, Wisla, Poland, 11–14 September 2016.
- [28] Śmietana, M.; Sobaszek, M.; Michalak, B.; Niedziałkowski, P.; Białobrzeska, W.; Koba, M.; Sezemsky, P.; Stranak, V.; Karczewski, J.; Ossowski, T.; et al. Optical Monitoring of Electrochemical Processes with ITO-Based Lossy-Mode Resonance Optical Fiber Sensor Applied as an Electrode. *J. Light. Technol.* **2018**, *36*, 954–960.
- [29] Stranak, V.; Bogdanowicz, R.; Sezemsky, P.; Wulff, H.; Kruth, A.; Smietana, M.; Kratochvil, J.; Cada, M.; Hubicka, Z. Towards high quality ITO coatings: The impact of nitrogen admixture in HiPIMS discharges. *Surf. Coat. Technol.* **2018**, *335*, 126–133.
- [30] Del Villar, I.; Zamarreño, C.R.; Hernaez, M.; Sanchez, P.; Arregui, F.J.; Matias, I.R. Generation of Surface Plasmon Resonance and Lossy Mode Resonance by thermal treatment of ITO thin-films. *Opt. Laser Technol.* **2015**, *69*, 1–7.
-

- [31] Feng, L.; Oturan, N.; Hullebusch, E.D.; van Esposito, G.; Oturan, M.A. Degradation of anti-inflammatory drug ketoprofen by electro-oxidation: Comparison of electro-Fenton and anodic oxidation processes. *Environ. Sci. Pollut. Res.* **2014**, *21*, 8406–8416.
- [32] Vidal, L.; Chisvert, A.; Canals, A.; Psillakis, E.; Lapkin, A.; Acosta, F.; Edler, K.J.; Holdaway, J.A.; Marken, F. Chemically surface-modified carbon nanoparticle carrier for phenolic pollutants: Extraction and electrochemical determination of benzophenone-3 and triclosan. *Anal. Chim. Acta* **2008**, *616*, 28–35.
- [33] Wu, B.; Zhao, N.; Hou, S.; Zhang, C. Electrochemical Synthesis of Polypyrrole, Reduced Graphene Oxide, and Gold Nanoparticles Composite and Its Application to Hydrogen Peroxide Biosensor. *Nanomaterials* **2016**, *6*.
- [34] Sun, Y.; Ren, Q.; Liu, X.; Zhao, S.; Qin, Y. A simple route to fabricate controllable and stable multilayered all-MWNTs films and their applications for the detection of NADH at low potentials. *Biosens. Bioelectron.* **2013**, *39*, 289–295.
- [35] Murugananthan, M.; Latha, S.S.; Bhaskar Raju, G.; Yoshihara, S. Anodic oxidation of ketoprofen—An anti-inflammatory drug using boron doped diamond and platinum electrodes. *J. Hazard. Mater.* **2010**, *180*, 753–758.
- [36] Yang, H.; Zhu, Y.; Chen, D.; Li, C.; Chen, S.; Ge, Z. Electrochemical biosensing platforms using poly-cyclodextrin and carbon nanotube composite. *Biosens. Bioelectron.* **2010**, *26*, 295–298.
- [37] Kannan, P.; Chen, H.; Lee, V.T.-W.; Kim, D.-H. Highly sensitive amperometric detection of bilirubin using enzyme and gold nanoparticles on sol–gel film modified electrode. *Talanta* **2011**, *86*, 400–407.
- [38] Oztekin, Y.; Tok, M.; Bilici, E.; Mikoliunaite, L.; Yazicigil, Z.; Ramanaviciene, A.; Ramanavicius, A. Copper nanoparticle modified carbon electrode for determination of dopamine. *Electrochim. Acta* **2012**, *76*, 201–207.
- [39] Radi, A.-E.; Muñoz-Berbel, X.; Lates, V.; Marty, J.-L. Label-free impedimetric immunosensor for sensitive detection of ochratoxin A. *Biosens. Bioelectron.* **2009**, *24*, 1888–1892.
- [40] Rahman, M.M.; Jeon, I.C. Studies of electrochemical behavior of SWNT-film electrodes. *J. Braz. Chem. Soc.* **2007**, *18*, 1150–1157.
- [41] Nikitin, L.N.; Vasil'kov, A.Y.; Banchemo, M.; Manna, L.; Naumkin, A.V.; Podshibikhin, V.L.; Abramchuk, S.S.; Buzin, M.I.; Korlyukov, A.A.; Khokhlov, A.R. Composite materials for medical purposes based on polyvinylpyrrolidone modified with ketoprofen and silver nanoparticles. *Russ. J. Phys. Chem. A* **2011**, *85*, 1190–1195.

-
- [42] Bosselmann, S.; Owens, D.E.; Kennedy, R.L.; Herpin, M.J.; Williams, R.O. Plasma deposited stability enhancement coating for amorphous ketoprofen. *Eur. J. Pharm. Biopharm.* **2011**, *78*, 67–74.
- [43] Zhuo, N.; Lan, Y.; Yang, W.; Yang, Z.; Li, X.; Zhou, X.; Liu, Y.; Shen, J.; Zhang, X. Adsorption of three selected pharmaceuticals and personal care products (PPCPs) onto MIL-101(Cr)/natural polymer composite beads. *Sep. Purif. Technol.* **2017**, *177*, 272–280.
- [44] Thøgersen, A.; Rein, M.; Monakhov, E.; Mayandi, J.; Diplas, S. Elemental distribution and oxygen deficiency of magnetron sputtered indium tin oxide films. *J. Appl. Phys.* **2011**, *109*, 113532.
- [45] Brumbach, M.; Veneman, P.A.; Marrikar, F.S.; Schulmeyer, T.; Simmonds, A.; Xia, W.; Lee, P.; Armstrong, N.R. Surface Composition and Electrical and Electrochemical Properties of Freshly Deposited and Acid-Etched Indium Tin Oxide Electrodes. *Langmuir* **2007**, *23*, 11089–11099.
- [46] Li, Y.; Zhao, G.; Zhi, X.; Zhu, T. Microfabrication and imaging XPS analysis of ITO thin films. *Surf. Interface Anal.* **2007**, *39*, 756–760.
- [47] Sanchez, P.; Zamarreño, C.R.; Hernaez, M.; Villar, I.D.; Fernandez-Valdivielso, C.; Matias, I.R.; Arregui, F.J. Lossy mode resonances toward the fabrication of optical fiber humidity sensors. *Meas. Sci. Technol.* **2012**, *23*, 014002.
- [48] Pickl, K.E.; Magnes, C.; Bodenlenz, M.; Pieber, T.R.; Sinner, F.M. Rapid online-SPE-MS/MS method for ketoprofen determination in dermal interstitial fluid samples from rats obtained by microdialysis or open-flow microperfusion. *J. Chromatogr. B* **2007**, *850*, 432–439.
- [49] Zakeri-Milani, P.; Barzegar-Jalali, M.; Tajerzadeh, H.; Azarmi, Y.; Valizadeh, H. Simultaneous determination of naproxen, ketoprofen and phenol red in samples from rat intestinal permeability studies: HPLC method development and validation. *J. Pharm. Biomed. Anal.* **2005**, *39*, 624–630.

C3. Combined optical and electrochemical analysis of protein binding with ITO-coated lossy-mode resonance sensor

Marcin Koba, Dariusz Burnat, Katarzyna Szot-Karpińska, Petr Sezemsky, Vitezslav Stranak, Robert Bogdanowicz, Joanna Niedziolka-Jönsson, Mateusz Smietana, Combined optical and electrochemical analysis of protein binding with ITO-coated lossy-mode resonance sensor, Proceedings SPIE 11199, Seventh European Workshop on Optical Fibre Sensors, (2019), 111991E.

Abstract

This work discusses indium tin oxide (ITO) coated optical fiber lossy-mode resonance (LMR) sensor working in an electrochemical setup for monitoring of protein binding to the sensor's surface. The binding mechanism has been observed simultaneously in optical and electrochemical domain. The combined measurement was enabled by the electrically conductive ITO overlay. In the experiment, biotin molecules have been used to test the collective optical and electrochemical setup and to illustrate the binding effect. It has been shown that the effect is observed in the investigated domains at applied potential, and the qualitative comparison shows high resemblance of the outcome.

1. INTRODUCTION

Recent years have opened many bio-oriented research programs especially in waste disposal and energy harvesting fields. There is a demand for emerging techniques which could give better understanding of the phenomena taking place in the investigated medium, and among them these employing multiple domains seem very promising. The techniques may combine voltammetry with optical measurements. The optical analyses are performed in ultraviolet, visible, and infrared light using various spectroscopic effects and procedures, e.g., Raman, absorption, or surface plasmon resonance (SPR). They all seem to be good candidates for supplementing electrochemistry (EC), and thus such opto-EC analysis gives two separate insights (in two different domains) into one phenomenon at the time. For example, SPR combined with EC (EC-SPR) was used to study conformational and electronic changes of purified *c-Cyts* protein¹ or to probe EC properties of polymer thin films². Nevertheless, given examples and most of the listed techniques are not well conditioned for EC measurements, especially when they require bulky optics and are not easily introduced into real-live environments and in situ measurement. Fiber-based SPR setups might be found as an exception from the mentioned drawbacks, as they are also well known for in situ measurements of various chemical and biological compounds, e.g., in the studies of EC properties of a living biofilm accompanied by in-situ redox transformation³. However, it must be mentioned that the presented structure, although compact, is technologically demanding and expensive. It requires fabrication of tilted fiber Bragg gratings and costly deposition of gold nanolayer.

In this work we investigate a fiber-based setup which takes advantage of the lossy-mode resonance (LMR) effect^{4, 5}. The LMR based sensors consist of a light guiding structure and thin film deposited on it. For the sensor to work, the overlay should satisfy certain conditions, i.e., the real part of its electrical permittivity must be positive and higher than the imaginary part of the film's permittivity and at the same time higher than the permittivity of the analyte and optical waveguide⁶. Such structure exhibits a resonance in wavelength domain and can echo variations in optical properties (particularly the refractive index (RI)) of the analyte by power and wavelength changes of this resonance. The proposed LMR based structure, first introduced in an EC setup in ⁷, is simple and inexpensive, its fabrication is generally based on a single

deposition process of a thin indium tin oxide (ITO) film. Some other thin films support the LMR effect, e.g., diamond-like carbon⁸ and polymers⁹, but among them only ITO exhibits low electrical resistivity and can be successfully used as a working electrode in an EC measurement, which has been shown in e.g.,^{10, 11}. In¹⁰, it has been shown that the optical response of the sensor highly depends on the applied potential and its changes, and on the properties of the investigated electrolyte. While in¹¹, an enhancement of EC response is induced by electrodeposition of PEDOT:PSS. The purpose of this paper is to present the possibility of using combined optical and EC analysis for monitoring of biomolecule (biotin) binding.

2. EXPERIMENTAL DETAILS

The experimental setup for combined optical and EC measurements has been reported in detail in⁷, and its schematic is shown in Figure 1.

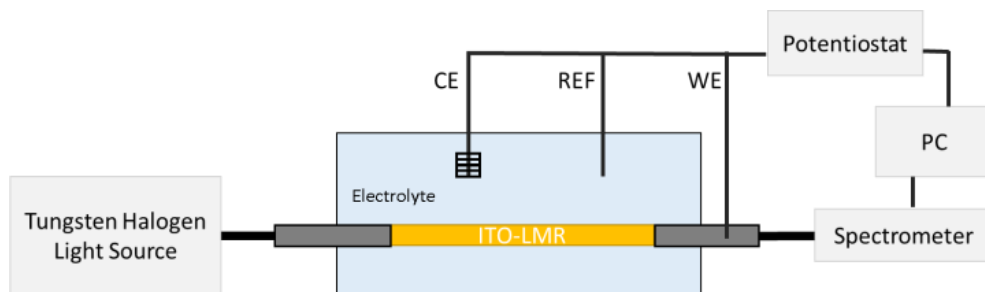


Figure 1. Scheme of an experimental setup. (CE – counter electrode, REF – reference electrode, WE – working electrode, PC – personal computer)

The ITO-LMR probes were based on approx. 15 cm-long polymer-clad silica (PCS) fiber samples of 400/840 μm core/cladding diameter, where 2.5 cm section of polymer cladding was removed from the central part of the fiber. Next, ITO films were deposited using standard planar magnetrons with unbalanced magnetic field. The deposition system used sputtering gun running in continuous RF power mode and equipped with ITO targets with composition $\text{In}_2\text{O}_3\text{-SnO}_2$ 90/10 wt% and 99.99% purity. The overlays were deposited at 0.5 Pa pressure in 1h-long process, where PCS samples were continuously rotated in the chamber to obtain uniform ITO deposition around the fiber. Next, both the fiber sample endfaces were mechanically polished before optical testing in mixtures of water/glycerin with refractive index (RI) from $n_D = 1.33$ to 1.43 RIU. The RI of the mixtures was measured using

Rudolph J57AB refractometer. The optical transmission of the ITO-LMR structure was observed in range of $\lambda = 350\text{--}1050$ nm using Ocean Optics HL-2000 white light source and Ocean Optics USB4000 spectrometer. The optical power (T) in the specified spectral range was detected as counts acquired during certain integration time slots and presented in relation to normalized power transmitted in the system for the fiber sensing device with no film at normal conditions (T_0).

EC cyclic voltammetry (CV) measurements in a 3-electrode configuration were performed in a custom-made cell with the PalmSens Emstat3+ potentiostat supported by PSTrace 5.4 software. ITO-LMR was used as working electrode (WE), while platinum wire and silver-silver chloride electrode Ag/AgCl (0.1 M KCl) were used as counter (CE) and reference (REF) electrodes, respectively. All the potentials in range from $E = -1.0$ to $+1.5$ V at a scan rate of $20\text{ mV}\cdot\text{s}^{-1}$ were applied versus the reference electrode at room temperature. A common phosphate-buffered saline (PBS, pH = 7.4) was used as an aqueous electrolyte. The experiment started with ITO surface silanization using 3-aminopropyltriethoxysilane (APTES) according to procedure given in ¹². After surface silanization, the reference measurement was performed in the PBS. Next, biotin (1 mg/mL in PBS) solution containing N-(3-Dimethylaminopropyl)-N'-ethylcarbodiimide (4 mg/ml in PBS) was added and the final measurement was again conducted in the PBS solution. The differential measurements, i.e., the ones in PBS before and after incubation in biotin, were considered. The chemical compounds used in the experiments were of analytical grade and used without any further purification.

3. RESULTS

Optical response of the LMR based optical sensor to variation of external RI is depicted in Fig 2(A). As expected in case of LMR sensors a separate minimum is evident and its corresponding wavelength exhibit redshift with increasing value of external RI. The change of RI was attained by diverse solutions of glycerin. For RI close to the water (1.333-1.356 RIU) the sensor exhibits sensitivity reaching ~ 320 nm/RIU, while in higher RI range (1.427-1.448 RIU) it increases up to ~ 820 nm/RIU.

After the solely optical characterization the sensor was integrated in EC setup, where it became a WE. Selected optical responses of the sensor in PBS to potential from 1.5 V to -1 V are shown in Figure 2(B). In this case the resonant minimum shifts towards shorter wavelength with decreasing potential. The spectrum, especially the resonance wavelength, experiences significant changes in potential range -1 V to 0.5 V and 1 V to -1 V for increasing and decreasing potential, respectively (Fig. 3(B)).

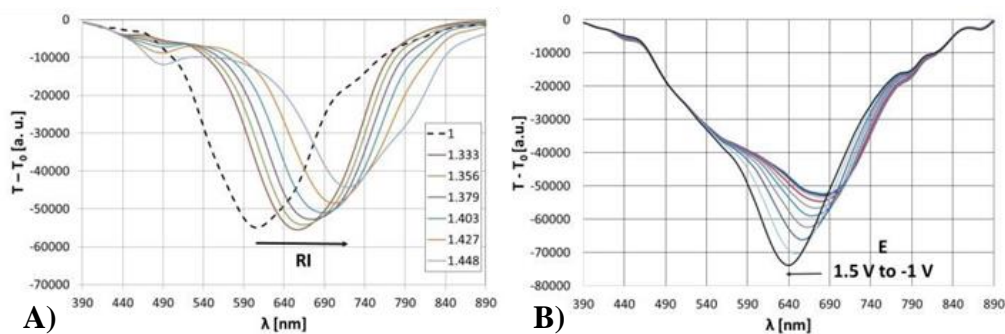
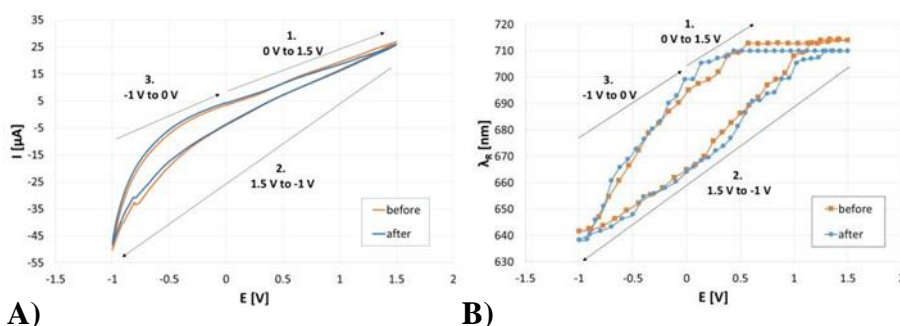


Figure 2. Optical response of the ITO-LMR probe to changes in external RI (A) and to potential applied to it in range 1.5 V to -1 V (B). In (B) the spectra correspond to selected measurements of section 2. in Fig. 3(B). The spectrum corresponding to $E = 0$ V is marked in red.

In Fig. 3(A), CV curves recorded in EC domain are shown before (orange curve) and after (blue curve) incubation in biotin. The potential during the experiment changes from 0 to 1.5 V (section 1), then from 1.5 V to -1 V (section 2) and finally from -1 V to 0 V (section 3). The curves exhibit slight changes induced by incubation in the protein-containing solution, especially observed at high positive and low negative potential range. The lower current values after biotin immobilization may be attributed to the blocking of the electrode's surface by formation of additional thin protein layer. The additional overlay acts as a charge barrier and causes lower charge exchange efficiency. Thus the differences of the curves before and after biotin immobilization.

Very similar behavior in optical domain has been recorded in parallel to the EC response (Fig. 3(B)). Here, a shift of the resonant wavelength corresponding to current change in CV is observed. When the potential increases, the optical response quickly saturates at about 0.5 V (before and after biotin immobilization) and stays roughly the same till 1.5 V. It responds

swiftly to potential direction change and leaves the saturated state just at ca. 1.25 V. As a result of processing with the protein the curve is shifted towards lower wavelengths. Since the saturation state values are stable they seem meaningful and noteworthy. In the high and low potential points the curves split. In optical domain by ca. 4.1 nm, and in electrical domain by ca. 1.1 μA . During the potential change the sensor experiences carrier fluctuations in the ITO layer. This is an origin of the resonance curve behavior in optical domain (Fig. 3(B)) and the direct resemblance to the CV characteristics (Fig. 3(A)). The flat sections for $E > 0.5$ V (Fig. 3(B)) correspond to carrier saturation in thin overlay and establishment of equilibrium of refractive index of ITO at this specific potential. The origin of the difference between before and after biotin immobilization comes from the fact that a thin biotin layer is formed on the ITO surface, and a compound ITO-biotin overlay is formed. The biotin modification changes the LMR conditions by influencing the thickness and the real and imaginary parts of the averaged RI of the overlay and consequently alters the overall sensor's response.



A) *Figure 3. (A) CVs recorded with the ITO-LMR sensor as a working electrode in PBS before and after incubation in biotin, and (B) corresponding results showing the influence of potential cycling between 1.5 and -1 V at a scan rate of 20 mVs⁻¹ on resonance wavelength of the ITO-LMR. Potential cycling direction has been marked.*

4. CONCLUSIONS

In this work we analyzed a protein binding with an LMR-based optical fiber sensor with ITO overlay working as an electrode. We investigated and analyzed the sensor's behavior before and after biotin incubation. We found that both optical and electrochemical responses reflect the fact of the molecules bonding. This is manifested by the change of current by 1 μA and

wavelength by 4 nm. The presented sensor in the proposed setup has never been used before for investigation of biomolecule binding mechanism, and although it is still under development it appears to be very promising for acquiring data of biological effects in the two domains.

Acknowledgments

This work was supported by the National Science Centre (NCN), Poland, as a part of 2014/14/E/ST7/00104 project, and the National Centre for Research and Development, Poland as a part of 347324/12/NCBR/2017 project.

References

- [1] Boussaad, S., Pean, J. and Tao, N. J. "High-resolution multiwavelength surface plasmon resonance spectroscopy for probing conformational and electronic changes in redox proteins," *Anal. Chem.* 72, 222-226 (2000).
- [2] Baba, A., Taranekar, P., Ponnampati, R. R., Knoll, W. and Advincula, R. C., "Electrochemical surface plasmon resonance and waveguide-enhanced glucose biosensing with N-Alkylaminated polypyrrole/glucose oxidase multilayers," *ACS Appl. Mater. Interfaces* 2, 2347-2354 (2010).
- [3] Yuan, Y., Guo, T., Qiu, X., Tang, J., Huang, Y., Zhuang, L., Zhou, S., Li, Z., Guan, B.-O., Zhang, X. and Albert, J., "Electrochemical surface plasmon resonance fiber-optic sensor: In situ detection of electroactive biofilms," *Anal. Chem.* 88, 7609-7616 (2016).
- [4] Kaura, D., Sharma, V. K. and Kapoor, A., "High sensitivity lossy mode resonance sensors," *Sensor. Actuat. BChem.* 198, 366-376 (2014).
- [5] Arregui, F. J., Del Villar, I., Corres, J. M., Goicoechea, J., Zamarreño, C. R., Elosua, C., Hernaez, M., Rivero, P. J., Socorro, A. B., Urrutia, A., Sanchez, P., Zubiate, P., Lopez, D., De Acha, N. and Matias, I. R., "Fiberoptic Lossy Mode Resonance Sensors," *Procedia Engineering* 87, 3-8 (2014).
- [6] Del Villar, I., Hernaez, M., Zamarreño, C. R., Sánchez, P., Fernández-Valdivielso, C., Arregui, F. J. and Matias, I. R., "Design rules for lossy mode resonance based sensors," *Appl. Opt.* 51, 4298-4307 (2012).
- [7] Smietana, M., Sobaszek, M., Michalak, B., Niedziałkowski, P., Białobrzeska, W., Koba, M., Sezemsky, P., Stranak, V., Karczewski, J., Ossowski, T. and Bogdanowicz, R., "Optical monitoring of electrochemical processes with ITO-based lossy-mode resonance optical fiber sensor applied as an electrode," *J. Lightwave Technol.* 36, 954-960 (2018).

-
- [8] Śmietana, M., Dudek, M., Koba, M. and Michalak, B., "Influence of diamond-like carbon overlay properties on refractive index sensitivity of nano-coated optical fibres," *Phys. Status Solidi A* 210, 2100-2105 (2013).
- [9] Zamarreño, C. R., Hernaez, M., Del Villar, I., Matias, I. R. and Arregui, F. J., "Optical fiber pH sensor based on lossy-mode resonances by means of thin polymeric coatings," *Sensor. Actuat. B-Chem.* 155, 290-297 (2011).
- [10] Śmietana, M., Niedziałkowski, P., Białobrzaska, W., Burnat, D., Sezemsky, P., Koba, M., Stranak, V., Siuzdak, K., Ossowski, T. and Bogdanowicz, R., "Study on Combined Optical and Electrochemical Analysis Using Indium-tin-oxide-coated Optical Fiber Sensor," *Electroanalysis* 31, 398 (2019).
- [11] Sobaszek, M., Burnat, D., Sezemsky, P., Stranak, V., Bogdanowicz, R., Koba, M., Siuzdak, K. and Śmietana, M., "Enhancing electrochemical properties of ITO-coated lossy-mode resonance optical fibre sensor by electrodeposition of PEDOT:PSS," *Optics Materials Express*, accepted for publication.
- [12] Piestrzyńska, M., Dominik, M., Kosiel, K., Janczuk-Richter, M., Szot-Karpińska, K., Brzozowska, E., Shao, L., Niedziółka-Jonsson, J., Bock, W. J. and Śmietana, M. "Ultrasensitive tantalum oxide nano-coated long-period gratings for detection of various biological targets," *Biosensors and Bioelectronics* 133, 8–15 (2019).

C4. Simultaneous optical and electrochemical label-free biosensing with ITO-coated lossy-mode resonance sensor

Mateusz Smietana, Marcin Koba, Petr Sezemsky, Katarzyna Szot-Karpinska, Dariusz Burnat, Vitezslav Stranak, Joanna Niedziolka-Jönsson, Robert Bogdanowicz, Simultaneous optical and electrochemical label-free biosensing with ITO-coated lossy-mode resonance sensor, Biosensors and Bioelectronics, 154, (2020), 112050.

Republished with permission of Elsevier Science & Technology Journals; permission conveyed through Copyright Clearance Center, Inc.

Abstract

In this work we discuss a new label-free biosensing device based on indium tin oxide (ITO) overlaid section of a multimode optical fiber fused silica core. The sensor has been used to optical measurements also simultaneously interrogated electrochemically (EC). Due to optimized thickness and optical properties of ITO film, a lossy-mode resonance (LMR) could be observed in the optical domain, where electrical properties of the film allowed for application of the sensor as a working electrode in an EC setup. It has been confirmed that the LMR response depends on optical properties of the external medium, as well as potential applied to the electrode during cyclic voltammetry. After the ITO surface functionalization with amine groups and covalently attached biotin, the device has been applied for label-free biosensing of avidin in both the domains simultaneously. On the example of biotin-avidin detection system it was demonstrated that when avidin concentration increases a decrease in current and increase in LMR wavelength shift were recorded in EC and optical domain, respectively. Both optical and EC responses follow the protein interaction process, and thus can be used as cross-verification of the readouts. Moreover, an extended information has been achieved comparing to solely EC interrogation, i.e., the grafting process of biotin and avidin was directly monitored optically displaying individual steps of an incubation procedure.

1. INTRODUCTION

Various biosensing instrumentations and procedures have been under intensive development in the recent years (Banica, 2012.). Combined efforts of both scientific and industrial communities are focused on improving functional properties of biosensors, mainly such as sensitivity, specificity, detection time, and cross-sensitivity, as well as reduction of sensor fabrication costs (Wongkaew et al., 2019). When high sensitivity is expected, the sensing instrumentation is often quite sophisticated and exceeds requirements as these for a simple strip test (Khoshbin et al., 2018). When detection time is crucial, such biological procedures as florescent labeling or biomaterial amplification can be pointed out as the most time-consuming (Truong et al., 2018; Kaczmarek et al., 2019; Zhuravskiy et al., 2018). That is why there is a significant interest in developing label-free biosensing methods where biological target is selectively recognized by receptor usually immobilized to the sensor's surface, and changes in density/mass at the surface are detected (Citartan et al., 2013).

The biosensors may be interrogated in many domains, which mainly include optical, electrical and mechanical (Juan-Colás, 2017). There are advantages of each of the interrogation schemes, e.g., when optical interrogation is employed, the biosensing procedure can be often monitored in a real time, when in turn electrochemical (EC) procedures are applied, a high sensitivity can be expected (Hill et al., 2013). For only a few sensors the interrogation in more than one domain is possible at the same time (Juan-Colás et al., 2017). The multi-domain sensing concept may allow for cross-verification of the readouts and reduce a number of false-positive results, enhance detection range or deliver more information about the analyzed biological target than when interrogated in a single domain. An example of successful multi-domain sensing includes readouts coming from surface plasmon resonance (SPR) effect together with EC response (EC-SPR). For this purposes gold-coated glass slides (Wu et al., 2015; Chiu et al., 2018) or fused silica-based optical fiber structures (Caucheteur et al., 2015) are typically used as sensors. While SPR empowers monitoring of changes of optical properties in proximity of the gold surface, the same gold film is used as an electrode, and thus it can be EC-modified or interrogated. The advantage of using optical fiber sensor over a glass slide include even more compact sensor size, more flexibility in the

electrode positioning in the tested solution, as well as immunity to electromagnetic interference, which may disturb the readout. Other multi-domain sensing concepts employ also EC-active, but optically transparent thin films. The requirements for such applications can be fulfilled, e.g., by some doped tin oxides, such as indium tin oxide (ITO) (Branch et al., 2017) or conductive carbon-based films, such as boron-doped diamond (Stotter et al., 2005). Due to the transparency, the electrode can also be interrogated optically in a broad spectral range. This makes it possible to gain more information about the investigated solution in comparison to single-domain analysis (Okazaki et al., 2018). In this case, EC is the most often applied method for sensor surface functionalization or modification, e.g., by electropolymerization (Eltzov et al., 2011; Konry et al., 2003). Both the combined sensing concepts, namely EC-SPR and spectroelectrochemistry are widely explored. Some other reported multi-domain label-free biosensing architectures combine EC with optical ring resonators (Juan-Colás et al., 2016), optical waveguides (Ghithan et al., 2017), localized SPR (Sannomiya et al., 2010), as well as micro-cantilever resonators with Raman spectroscopy (Park et al., 2014).

In this work we discuss the use of ITO-coated optical fibers for label-free opto-EC biosensing. Optical fiber sensors usually offer low limit of detection along with capability to investigate low volumes of analytes and needle-like shape of the sensor. On the other hand, the EC interrogation of the electrode at the sensor surface allows for reaching deeper insight into biochemical reactivity of target medium by investigating EC processes. EC additionally offers in parallel wide range of spatially localized electrografting reactions enabling site-selective control of the surface chemistry (e.g. antibody grafting, click-chemistry) for selective recognition of biocompounds. The optical biosensors offer capability for high-sensitivity analysis and scalable, low-cost manufacturing. Nevertheless, they offer limited ability to determine a single target without separation of possible interfering agents or additional information about its activity and interactions. Combining both optical and EC studies let to deliver additional quantitative information and unique insight into biochemical activity what is unreachable with optical detection alone. In this work optical properties and thickness of ITO film deposited on a short section of a multimode fused silica optical fiber core made appearing a lossy-

mode resonance (LMR) possible (Del Villar et al., 2012). The properties of the resonance observed in the fiber transmission spectrum depends on optical properties that include refractive index (RI) of medium surrounding the ITO film. The resonant effect obtained here for sensing purposes thanks to the ITO overlay, allows for focusing on resonance wavelength as a parameter, what mitigates error coming from optical power fluctuations. This differs our sensing concepts from many other concepts reported up to date employing ITO-coated optical fiber, where due to lack of resonance effect just absorption has been measured (Okazaki et al., 2018; Eltzov et al., 2011; Konry et al., 2003; Imai et al., 2015; Beam et al., 2009). When electrical potential is applied to the ITO film in EC setup, the properties of the resonance are influenced by composition of the electrolyte surrounding the sensor (Śmietana et al., 2018a, 2018b). For the ITO-coated optical sensor, the impact of EC-polymerized ketoprofen (Bogdanowicz et al., 2018) or PDOT:PSS (Sobaszek et al., 2019) on the transmitted optical spectrum has been already reported. In this work we discuss for the first time the results of dual-domain (optical and EC) label-free biosensing experiment based on ITO-LMR sensor. Comparing to other fiber-based sensor interrogated in multiple domains, such as fiber-grating-based devices (Caucheteur et al., 2015; Bogdanowicz et al., 2015; Janczuk-Richter et al., 2019), the approach stands out with simple and possible for mass production fabrication process.

2. EXPERIMENTAL DETAILS

2.1. Fabrication of the sensor

The sensor fabrication procedure has been described in details in (Niedziałkowski et al., 2019). Shortly, a 2.5 cm-long section of polymer-clad silica optical fiber core (400 μm core diameter) has been coated with ITO using RF magnetron sputtering. We used 3" ITO target ($\text{In}_2\text{O}_3\text{-SnO}_2$ - 90/10 wt% and purity of 99.99%) sputtered at 150 W in Ar atmosphere at pressure of 0.5 Pa. The fibers were located 20 cm away from the target surface and rotated during the deposition to maintain uniformity of the film around the fiber. Before further processing and measurements of the ITO-LMR sensors, the fiber end-faces were cleaved for efficient coupling with input and output fibers. The ITO thickness reached 350 nm and facilitated appearance

of the second order LMR in the investigated spectral range (Niedziałkowski et al., 2019).

2.2. Optical and electrochemical measurements

The transmission (T) of the sensor has been optically interrogated using USB4000 spectrometer and HL-2000 tungsten light source, both from Ocean Optics. The optical data acquisition and processing has been controlled using custom Matlab script allowing to save full available optical spectrum ($\lambda = 350\text{--}1050$ nm) approx. every 1.5 s. The integration time was set to 100 ms. Optical response of the ITO-LMR sensor to external RI has been investigated using water/glycerin solutions with RI varying from $n_D = 1.3330$ to 1.45 RIU. The RI of the solutions was each time verified using Reichert AR200 automatic refractometer.

Combined optical and EC responses were acquired using a custom-made measurement cell able to accommodate the ITO-LMR sensor that was electrically connected via copper tape away from the core section and sealed using two silicone gaskets (Niedziałkowski et al., 2019). The EC measurements were performed in controlled environment (temperature: 22 °C, humidity 45%) using PalmSens Emstat3+ potentiostat supported by a PStTrace 5.4 software and connected to three electrodes, namely the ITO-LMR sensor, an Ag/AgCl 0.1 M NaCl and a platinum wire. They were submerged in the measurement cell and used as a working (WE), reference (RE) and counter electrode (CE), respectively. During the experiments the electrodes were monitored for any contact between them. The cyclic voltammograms (CV) were recorded at 20 mV/s scan rate in the potential (E) ranging from -1 to 1.5 V. All the measurements were carried in phosphate buffered saline (PBS, pH 7.4) as well as PBS containing 1 mM 1,1-ferrocenedimethanol ($\text{Fc}(\text{CH}_2\text{OH})_2$) as a redox probe. Both, scan rate and the range of E were chosen as a result of our preliminary tests and found as the most suitable for simultaneous EC and optical detection. We are aware that the response from the redox probe used in this experiment can be also observed in a way narrower E range. However, the wide E window (from -1 V to 1.5 V) was intentionally applied to get more information from the experiment, such as how the changes in the E influence the optical response. It must also be mentioned that ITO electrodes are EC stable within the applied E range. PBS

tablets were bought from BioShop®Canada Inc., and contained 137 mM NaCl, 2.7 mM KCl, and 10 mM phosphate buffer, pH 7.4. Schematic representation of the applied measurement setup is shown in Fig. 1.

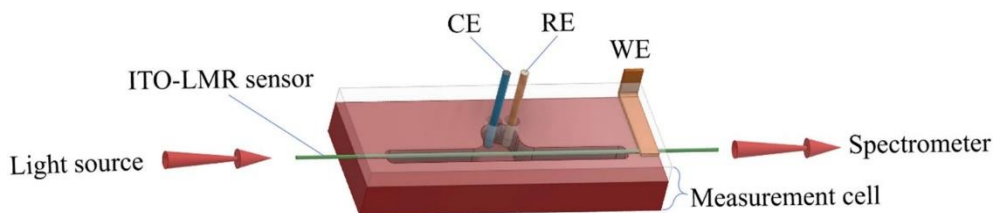


Fig. 1. Schematic representation of combined optical and electrochemical (EC) measurements performed with ITO-LMR sensor installed in a custom-made measurement cell. Instalments of reference (RE), counter (CE) and ITO-LMR sensor as a working electrode (WE) were marked. The sensor was connected to the potentiostat via copper tape and submerged in the electrolyte.

2.3. ITO surface functionalization and biosensing procedure

For the biosensing experiment we followed the procedure as the one for protein sensing described in detail in (Piestrzyńska et al., 2019). Shortly, a 30 μL of a silane precursor (3-aminopropyltriethoxysilane, APTES) and a 10 μL of catalyst (triethylamine) were used for functionalization. The fiber samples were exposed to the precursor and the catalyst vapors in a desiccator at room temperature for 2 h under argon atmosphere, and later cured for 48 h to form the amine layer (ITO-NH₂).

Next, a receptor - biotin (1 mg/mL in PBS) was chemically bonded to ITO-NH₂, like in (Dominik et al., 2017). The carboxylic group of biotin was activated in N-(3-dimethylaminopropyl)-N'-ethylcarbodiimide hydrochloride (EDC, 4 mg/mL in PBS) for 15 min. Later, the fiber samples with ITO-NH₂ on their surfaces were immersed in the solution of activated biotin and left for 30 min at room temperature, then thoroughly washed with PBS. This was followed by addition of target protein – avidin with different concentrations, i.e., 0.1 $\mu\text{g/mL}$, 1 $\mu\text{g/mL}$, 10 $\mu\text{g/mL}$, and 100 $\mu\text{g/mL}$, all in PBS. The biotin-terminated samples were immersed in solutions from the lowest to the highest avidin concentration, left for 30 min, then extensively washed with PBS, and finally measured in PBS.

3. RESULTS

3.1. ITO-LMR sensor parametrization

The ITO-LMR sensors revealed to be sensitive to external RI (n_{ext}) (Del Villar et al., 2012; Kosiel et al., 2018). As a result of increase in n_{ext} the resonance shifts towards longer wavelengths (Fig. 2(A)). A set of parameters can be investigated in the spectrum and used for quantitatively determining the RI sensitivity, i.e., shift of the resonance wavelength (λ_{R}) or T changes at a selected wavelength (Fig. 2(B)). In this work T at $\lambda = 630$ nm (T_{630}) has been chosen. Both parameters, namely λ_{R} and T_{630} changes significantly with n_{ext} . For the investigated case when the $d\lambda_{\text{R}}/dn_{\text{ext}}$ is considered, it increases from about 320 nm/RIU to 800 nm/RIU at 1.34 and 1.43 RIU, respectively. According to results of LMR-based biosensing experiment (Chiavaoli et al., 2018), such sensitivity makes it possible to monitor bio-overlay growth on the sensor's surface. When the precision in determination of λ_{R} is limited, as it is for simple spectrometers, the dT_{630}/dn_{ext} can be alternatively used. It offers higher resolution in identification of changes taking place at the ITO surface. One must be aware that when solely power-based interrogation is applied the result may be highly influenced by e.g. light source power fluctuations. That is why in this work, where possible, both parameters are discussed together. It facilitates identification of sources of errors more feasible than in case of single power interrogation. Moreover, as it will be shown in section 3.4, the identification of surface changes can be enhanced when additionally EC modulation is implemented.

Next, E has been applied to the ITO-LMR sensor when it was immersed in PBS. As shown in Fig. 3, the changes in E are followed by both λ_{R} and T_{630} . The changes in the optical response while sweeping the E are caused by variation in external RI of both the ITO overlay and the electrolyte in the closest vicinity of the ITO-LMR electrode. The applied E alternates the number of free carriers in the ITO overlay, and in agreement with the Drude-Lorentz model (Reed and Png, 2005) directly affects real part of RI (n), as well as in the imaginary part of RI (k) of thin ITO film (Han and Mendes, 2016). Since ITO is a n-type semiconductor, increase in number of free carriers takes place when negative E is applied, what decreases n and increases k (Li et al., 2017). Also, the double-layer formed on ITO after

immersion into the electrolyte will be rearranged by repelling and attracting counterions with the sweeping potential (Grimnes and Martinsen, 2015), what directly influences the external RI in the closest vicinity of ITO surface. Such a behavior for multi-domain measurements using ITO-coated long-period fiber grating (LPFG) was observed previously (Janczuk-Richter et al., 2019). Contrary to LPFG device, for the ITO-LMR sensor, which is as a way simpler device than ITO-LPFG, the optical changes are well visible both at the negative and the positive E . Moreover, a hysteresis for both the selected parameters can also be observed. In the applied E range, the λ_R alters by over 60 nm, what is comparable to the shift recorded during change in n_{ext} from 1.33 to 1.45 RIU. It can be clearly seen here that due to limited resolution of the used spectrometer in wavelength domain and high sensitivity in determining changes in T , tracing of T_{630} may offer more accurate readouts (smoother curves) than when shift in λ_R is analyzed.

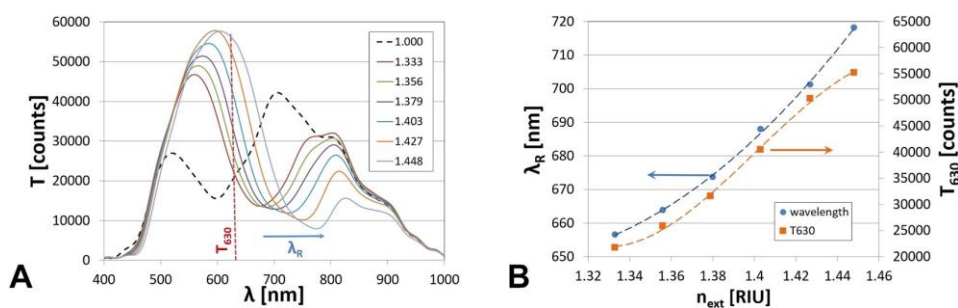


Fig. 2. Response of the ITO-LMR sensor to change in n_{ext} between 1 and 1.45 RIU, where (A) shows transmission (T) spectrum and (B) corresponding shift in resonance wavelength (λ_R) and transmission at $\lambda = 630$ nm (T_{630}) for measurements in various aqueous solutions.

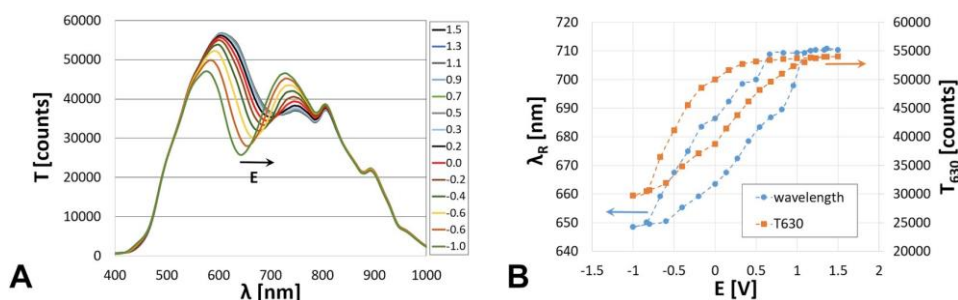


Fig. 3. Response of the ITO-LMR sensor to applied potential (E) varying between 1.5 V \rightarrow -1 V, where (A) shows transmission (T) spectrum and (B) corresponding shift in resonance wavelength (λ_R) and transmission at $\lambda = 630$ nm (T_{630}). PBS was used as an electrolyte and the scan rate was set to 20 mV/s.

3.2. Monitoring of biological binding events

Meaningful EC analysis done according to label-free biosensing concept is limited to the steps of the procedure, which follow those aiming to remove physically adsorbed biological material. When the results for these steps are compared, the only parameter influencing the measurement should be related to binding events on the sensor surface. At these steps PBS or more often other buffer solution containing redox probes are used as an electrolyte, which allow for comparing between the steps the current resulting from oxidation or reduction reactions taking place at surface of the electrode. The advantage of introducing optical domain in these measurements is capability for in-situ monitoring of the sensor surface during every step of the biosensing procedure, which also include incubation process.

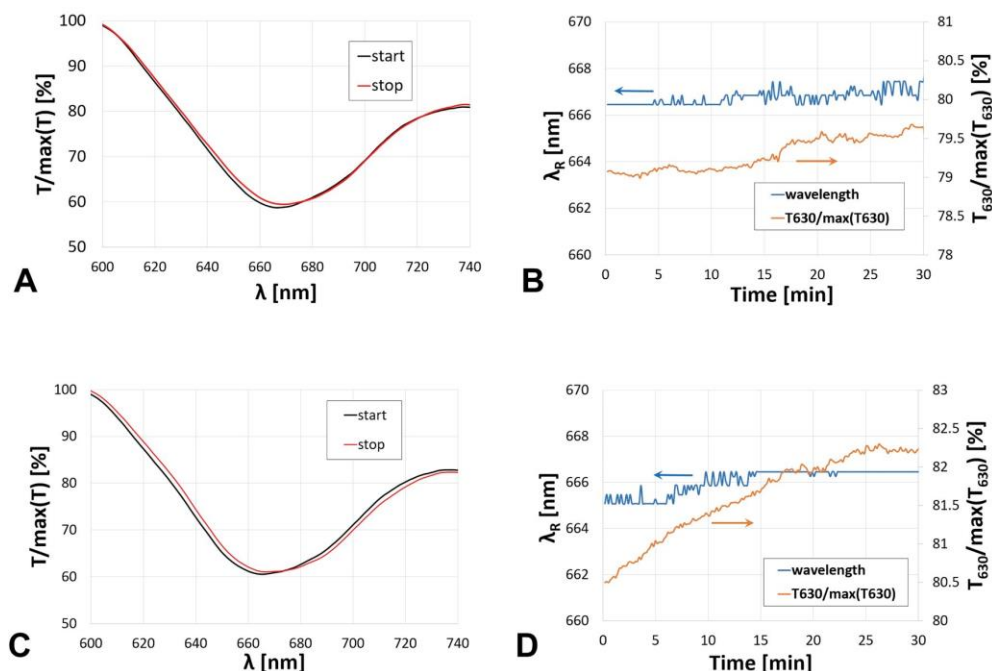


Fig. 4. Normalized initial (start) and final (stop) spectra acquired for 30 min-long incubation in 1 µg/mL (A) and 100 µg/mL (C) avidin solution. Evolution of the selected spectral parameters during the incubation is shown in (B) and (D) for 1 µg/mL and 100 µg/mL, respectively.

In Fig. 4, results of incubation monitoring at selected steps of the procedure are shown. For clearer presentation of the results the T_{630} has been normalized. In Fig. 4(A) and (C) initial (start) and final (stop) spectra recorded for two incubation steps (1 µg/mL and 100 µg/mL concentration of avidin,

respectively) were shown. Both the considered parameters, namely λ_R and $T_{630}/\max(T_{630})$ shift toward higher values with incubation time (Fig. 4(B) and (D)), what correspond to the increase in n_{ext} , or in other words densification of the medium in proximity of the sensor's surface. As well as in the case of above investigated influences of E and n_{ext} , changes in T_{630} can be better identified here. For incubation in the highest avidin concentration (100 $\mu\text{g}/\text{mL}$), the λ_R and $T_{630}/\max(T_{630})$ increase by about 0.5 nm and 2%, respectively (Fig. 4(D)). It can be clearly seen that in case of 100 $\mu\text{g}/\text{mL}$ avidin, the increase in λ_R and $T_{630}/\max(T_{630})$ saturates after incubation time of approx. 25 min. After extensive washing of the sensor in PBS the parameters, i.e., the λ_R and $T_{630}/\max(T_{630})$, were found to increase by about 1.4 nm and 1.7%. Drop in transmission indicate that an excess of avidin, which was only physically adsorbed to the surface, has been successively removed. Observation of only λ_R shift in may be misleading due to limited resolution in wavelength of the used spectrometer.

3.3. Detection in electrochemical domain

Fig. 5(A) depicts CV curves recorded in PBS and in presence of the redox probe ($\text{Fc}(\text{CH}_2\text{OH})_2$) after incubation in 1 $\mu\text{g}/\text{mL}$ and 10 $\mu\text{g}/\text{mL}$ of avidin followed by extensive washing in PBS. In presence of $\text{Fc}(\text{CH}_2\text{OH})_2$, two current peaks were recorded at E of about 0 V and 0.7 V that correspond to reduction and oxidation processes, respectively. As a result of incubation in the solutions containing biological compounds, a drop of current at $E > 0.5$ V was observed. The drop was detected for both PBS and $\text{Fc}(\text{CH}_2\text{OH})_2$. The CV curves recorded in PBS after sensor washing for all the steps of the experiment have been shown in Fig. 5(B). The decrease in current corresponds to elevated resistance of the interface, i.e., charge transfer blocking by the biomolecules immobilized at the functionalized ITO surface (Li et al., 2017).

ITO has been widely applied as an electrode material, especially when together with EC also spectrometric measurements are performed (Branch et al., 2017). In those measurements typically ITO-coated glass slides are used, where ITO is thermally annealed as a part of post-deposition procedure to improve electrical properties of the films (Del Villar et al., 2015). In case of ITO-coated fibers with polymer cladding the high-temperature annealing is

hardly possible due to low temperature resistance of the polymer. That is why the investigated ITO films may show slightly lower EC activity analyzed in presence of $\text{Fc}(\text{CH}_2\text{OH})_2$ than for commercially available ITO-coated glass slides (Niedziałkowski et al., 2019).

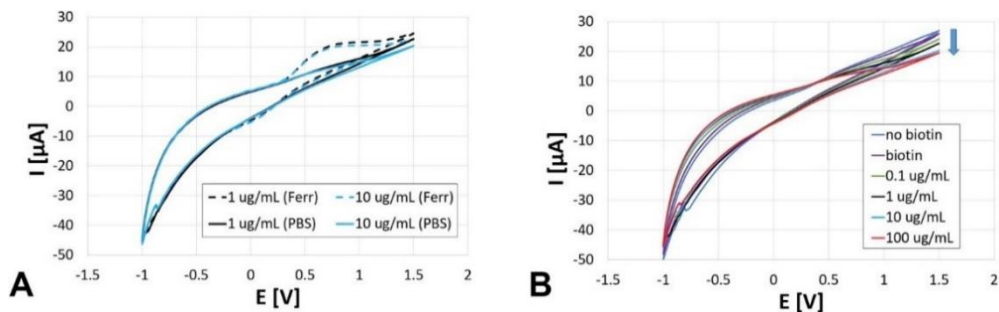


Fig. 5. CV curves recorded after incubation in solutions containing biological compounds and washing in PBS, where (A) shows results obtained in PBS and 1 mM $\text{Fc}(\text{CH}_2\text{OH})_2/\text{PBS}$ (Ferr) for two selected avidin concentrations and (B) shows results in PBS for all steps of the experiment. Arrow at $E = 1.5 \text{ V}$ in (B) shows the drop in current (I). Scan rate was set to 20 mV/s.

3.4. Detection in optical domain

Simultaneously to interrogation in electrochemical domain, the ITO-LMR sensor was interrogated optically. In contrast to CV measurements, the optical spectrum has been acquired approx. every 1.5 s. In Fig. 6(A) the evolution in time of λ_R , as well as corresponding E is show for each step of the experiment. The E -scan (from 1.5 V to -1 V and back to 1.5 V) took approx. 250 s and for comparison purposes evolution of the λ_R was shown in line for each step of the experiment. Similarly to results shown in Fig. 3, the λ_R changes significantly with E , but here additionally the shift depends on the step of the experiment, which in turn correspond to change in the bio-overlay properties (Fig. 6(A)). In general, the λ_R follows the E and its total shift, observed mainly when for $E < 0.5 \text{ V}$, increases from approx. 75 nm to 90 nm for initial measurement with no biotin attached and final step after incubation in 100 $\mu\text{g/mL}$ avidin solution, respectively. Moreover, when more biological film is grafted to the surface, the λ_R better follows the decrease in E . The mentioned above differences are attributed to changes in optical properties of ITO at the bio-overlay – ITO interface, as well as properties of the electrolyte at the electrolyte – bio-overlay interface. Increase in thickness and density of

the bio-overlay, where later corresponds to its RI, from electrical point of view can be interpreted as appearance of an insulating layer. When negative E is applied, the concentration of free charge carriers (electrons) in ITO increases, what is followed by decrease and increase in its n and k , respectively (Ma et al., 2015). These changes in optical properties of ITO make the LMR shift towards shorter wavelength and increase in its depth (Del Villar et al., 2012). When an insulating bio-overlay appears on the ITO surface, it increases resistance of the interface, but also induces accumulation of electrons in ITO at its interface with the bio-overlay. The accumulation additionally modifies the optical properties of ITO and enhances shift of λ_R at negative E . The difference between the $d\lambda_R/dE$ for decrease in E with grafting of the bio-overlay may in turn correspond to reduced double-layer i.e., lower capacitance of the electrolyte – bio-overlay interface, when biological film reduces/suppress interactions between ions in the electrolyte and the ITO surface. For quantitative determination of the sensor performance in optical domain, the λ_R at $E = -1$ V has been compared for different steps of the experiment (Fig. 6(B)). At low E values, the λ_R changes more and can be better identified than for higher values of E , where the resonance becomes shallow (Fig. 3(A)). It can be clearly seen that for the entire experiment, i.e. from the reference step before incubation in biotin up to the one for 100 $\mu\text{g/mL}$ concentration of avidin, the λ_R at $E = -1$ V decreases by over 17 nm, and its decrease is higher for the avidin concentration up to 1 $\mu\text{g/mL}$ than for its concentrations above. It must be noted that the shift is significantly greater than those measured during biosensing experiment based on LMR effect with no E -scanning applied (not shown here), where for the entire experiment the shift reached about 4 nm. When change in current at $E = 1.5$ V is compared to change in λ_R , the trends of readouts in optical and EC domains correspond to each other (Fig. 6(B)). The total current decreases in the whole biosensing experiment by 8 μA .

It must be noted that in this work we investigated response of the sensor to relatively high concentrations of analytes. Our aim was to more to show a novel sensing concept and its performance in broad range of analyte concentrations, than to focus on the sensor optimization towards reaching low limit of detection (LOD). It can be assumed that for the shown case the LOD corresponds with the lowest measured avidin concentration (0.1 $\mu\text{g/mL}$).

However, the *LOD* can be lowered when higher resolution in investigated sensing parameters is investigated in narrow range of negative *E*.

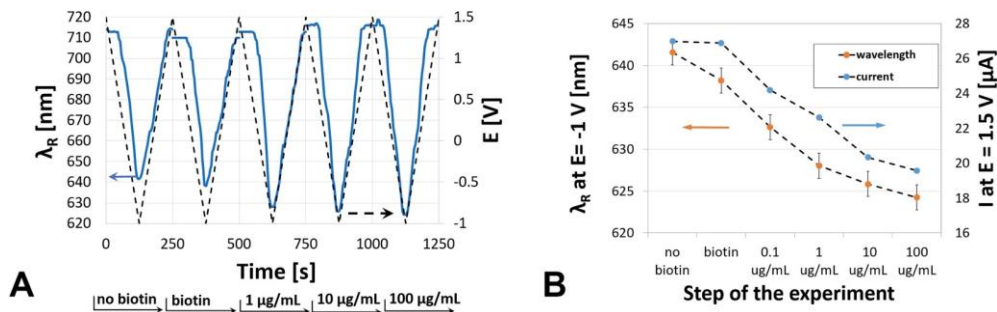


Fig. 6. (A) Influence of the *E* change on λ_R at different steps of the experiment performed in PBS. *E*-scan at each the experimental step took approx. 250 s and was set in line with other steps as indicated at the bottom of the plot. Optical (λ_R at *E* = -1 V) and electrochemical (*I* at *E* = 1.5 V) readouts for each step of the experiment were compared in (B).

4. CONCLUSION

In this paper we discuss for the first time the combined optical and electrochemical label-free biosensing based on resonant effect achieved for indium tin oxide thin film deposited on side surface of a multimode optical fiber core. In the optical domain, the measurements were based on the lossy-mode resonance effect. The electrical conductivity of the ITO overlay, in turn, made simultaneous use of the sensor as an electrode along with electrochemical investigation of its readout possible. In this work, the standard biotin-avidin biological complex was applied to verify functional properties of the sensor. While the sensor can be interrogated electrochemically only at certain steps of the experiment, which exclude incubation in liquids containing biological compounds, the LMR-based optical interrogation is possible in real-time during the entire biosensing procedure. When selected parameters of optical and electrochemical readouts are traced, the results of changes at the sensor's surface in both the domains correspond well to each other. Thus, we believe the second domain can be used to verify the results received in the first one. What is more, it has been found that the applied potential significantly enhances the optical readouts. The enhancement was achieved mainly at negative potentials applied to the electrode and corresponds to semiconducting character of the ITO film.

Small size of the ITO-LMR device, needle-like shape, which is common for electrochemical analysis, and capability for batch fabrication of the devices, can be pointed out as advantages of the proposed approach. Comparing to other opto-electrochemical sensing concepts, where metal film is used as an electrode, due to high transparency of ITO, also other spectroelectrochemical measurements can be additionally combined with the system and allow for even more in-depth analysis of a wider selection of biocompounds.

Declaration of competing interest

The authors declare that they have no known competing financial interests or personal relationships that could have appeared to influence the work reported in this paper.

Acknowledgement

This work was supported in Poland by the National Science Centre (NCN) under grant No. 2014/14/E/ST7/00104, the National Center for Research and Development (NCBiR) under grant No. 347324/12/NCBR/2017 and the National Agency for Academic Exchange (NAWA) under grant No. PPN/BIL/2018/1/00126. Support in optical measurements provided by Mr. Piotr Pardo is acknowledged.

References

- Beam, B.M., Armstrong, N.R., Mendes, B.S., 2009. An electroactive fiber optic chip for spectroelectrochemical characterization of ultra-thin redox-active films. *Analyst* 134 (3), 454–459.
- Bogdanowicz, R., Sobaszek, M., Ficek, M., Gnyba, M., Ryl, J., Siuzdak, K., Bock, W.J., Smietana, M., 2015. Opto-electrochemical sensing device based on long-period grating coated with boron-doped diamond thin film. *J. Opt. Soc. Korea* 19 (6), 705–710.
- Bogdanowicz, R., Niedziałkowski, P., Sobaszek, M., Burnat, D., Białobrzeska, W., Cebula, Z., Sezemsky, P., Koba, M., Stranak, V., Ossowski, T., Smietana, M., 2018. „Optical detection of ketoprofen by its electropolymerization on an indium tin oxide-coated optical fiber probe. *Sensors* 18 (5), 1361.
- Branch, S.D., Lines, A.M., Lynch, J., Bello, J.M., Heineman, W.R., Bryan, S.A., 2017. Optically transparent thin-film electrode chip for spectroelectrochemical sensing. *Anal. Chem.* 89 (14), 7324–7332.

- Caucheteur, C., Guo, T., Albert, J., 2015. Review of plasmonic fiber optic biochemical sensors: improving the limit of detection. *Anal. Bioanal. Chem.* 407 (14), 3883–3897.
- Chiavaioli, F., Zubiato, P., Del Villar, I., Zamarreno, C.R., Giannetti, A., Tombelli, S., Trono, C., Arregui, F.J., Matias, I.R., Baldini, F., 2018. Femtomolar detection by nanocoated fiber label-free biosensors. *ACS Sens.* 3 (5), 936–943.
- Chiu, N.-F., Yang, C.-D., Chen, C.-C., Kuo, C.-T., 2018. Stepwise control of reduction of graphene oxide and quantitative real-time evaluation of residual oxygen content using EC-SPR for a label-free electrochemical immunosensor. *Sensor. Actuator. B Chem.* 258, 981–990.
- Citartan, M., Gopinath, S.C., Tominaga, J., Tang, T.H., 2013. Label-free methods of reporting biomolecular interactions by optical biosensors. *Analyst* 138 (13), 3576–3592.
- Del Villar, I., Hernaez, M., Zamarreno, C.R., Sanchez, P., Fernandez-Valdivielso, C., Arregui, F.J., Matias, I.R., 2012. Design rules for lossy mode resonance based sensors. *Appl. Optic.* 51 (19), 4298–4307.
- Del Villar, I., Zamarreno, C.R., Hernaez, M., Sanchez, P., Arregui, F.J., Matias, I.R., 2015. Generation of surface plasmon resonance and lossy mode resonance by thermal treatment of ITO thin-films. *Optic Laser. Technol.* 69, 1–7.
- Dominik, M., Lesniewski, A., Janczuk, M., Niedziółka-Jonsson, J., Hołdyski, M., Wachnicki, Ł., Godlewski, M., Bock, W.J., Smietana, M., 2017. Titanium oxide thin films obtained with physical and chemical vapour deposition methods for optical biosensing purposes. *Biosens. Bioelectron.* 93, 102–109.
- Eltzov, E., Cosnier, S., Marks, R.S., 2011. Biosensors based on combined optical and electrochemical transduction for molecular diagnostics. *Expert Rev. Mol. Diagn.* 11 (5), 533–546.
- Ghithan, J.H., Moreno, M., Sombrio, G., Chauhan, R., O’Toole, M.G., Mendes, S.B., 2017. Influenza virus immunosensor with an electroactive optical waveguide under potential modulation. *Opt. Lett.* 42 (7), 1205–1208.
- Grimnes, S., Martinsen, Ø.G., 2015. *Bioimpedance and Bioelectricity Basics*. Elsevier, pp. 179–254.
- Han, X., Mendes, S.B., 2016. Spectroelectrochemical properties of ultra-thin indium tin oxide films under electric potential modulation. *Thin Solid Films* 603, 230–237.
- Hill, C.M., Clayton, D.A., Pan, S., 2013. Combined optical and electrochemical methods for studying electrochemistry at the single molecule and single particle level: recent progress and perspectives. *Phys. Chem. Chem. Phys.* 15, 20797–20807.

- Imai, K., Okazaki, T., Hata, N., Taguchi, S., Sugawara, K., Kuramitz, H., 2015. Simultaneous multiselective spectroelectrochemical fiber-optic sensor: demonstration of the concept using methylene blue and ferrocyanide. *Anal. Chem.* 87 (4), 2375–2382.
- Janczuk-Richter, M., Piestrzynska, M., Burnat, D., Sezemsky, P., Stranak, V., Bock, W.J., Bogdanowicz, R., Niedziółka-Jonsson, J., Smietana, M., 2019. Optical investigations of electrochemical processes using a long-period fiber grating functionalized by indium tin oxide. *Sensor. Actuator. B Chem.* 279, 223–229.
- Juan-Colas, J., Parkin, A., Dunn, K.E., Scullion, M.G., Krauss, T.F., Johnson, S.D., 2016. The electrophotonic silicon biosensor. *Nat. Commun.* 7, 12769.
- Juan-Colas, J., Johnson, S., Krauss, T.F., 2017. Dual-mode electro-optical techniques for biosensing applications: a review. *Sensors* 17 (9), 2047.
- Kaczmarek, J.A., Mitchell, J.A., Spence, M.A., Vongsouthi, V., Jackson, C.J., 2019. Structural and evolutionary approaches to the design and optimization of fluorescence-based small molecule biosensors. *Curr. Opin. Struct. Biol.* 57, 31–38.
- Khoshbin, Z., Housaindokht, M.R., Verdian, A., Bozorgmehr, M.R., 2018. Simultaneous detection and determination of mercury (II) and lead (II) ions through the achievement of novel functional nucleic acid-based biosensors. *Biosens. Bioelectron.* 116, 130–147.
- Konry, T., Novoa, A., Cosnier, S., Marks, R.S., 2003. Development of an “electroptode” immunosensor: indium tin oxide-coated optical fiber tips conjugated with an electropolymerized thin film with conjugated cholera toxin B subunit. *Anal. Chem.* 75 (11), 2633–2639.
- Kosiel, K., Koba, M., Masiewicz, M., Smietana, M., 2018. Tailoring properties of lossy-mode resonance optical fiber sensors with atomic layer deposition technique. *Optic Laser. Technol.* 102, 213–221.
- Li, C., Chen, X., Wang, N., Zhang, B., 2017. An ultrasensitive and label-free electrochemical DNA biosensor for detection of DNase I activity. *RSC Adv.* 7, 21666–21670.
- Ma, Z., Li, Z., Liu, K., Ye, C., Sorger, V.J., 2015. Indium-tin-oxide for high-performance electro-optic modulation. *Nanophotonics* 4, 198–213.
- Niedziółkowski, P., Białobrzaska, W., Burnat, D., Sezemsky, P., Stranak, V., Wulff, H., Ossowski, T., Bogdanowicz, R., Koba, M., Smietana, M., 2019. Electrochemical performance of indium-tin-oxide-coated lossy-mode resonance optical fiber sensor. *Sensor. Actuator. B Chem.* 301, 127043.
- Okazaki, T., Shiokawa, E., Orii, T., Yamamoto, T., Hata, N., Taguchi, A., Sugawara, K., Kuramitz, H., 2018. Simultaneous multiselective spectroelectrochemical fiber-optic sensor: sensing with an optically transparent electrode. *Anal. Chem.* 90 (4), 2440–2445.

- Park, J., Bang, D., Jang, K., Kim, E., Haam, S., Na, S., 2014. Multimodal label-free detection and discrimination for small molecules using a nanoporous resonator. *Nat. Commun.* 5, 3456.
- Piestrzynska, M., Dominik, M., Kosiel, K., Janczuk-Richter, M., Szot-Karpinska, K., Brzozowska, E., Shao, L., Niedziółka-Jonsson, J., Bock, W.J., Smietana, M., 2019. Ultrasensitive tantalum oxide nano-coated long-period gratings for detection of various biological targets. *Biosens. Bioelectron.* 133, 8–15.
- Reed, G.T., Png, C.E.J., 2005. Silicon optical modulators. *Mater. Today* 8, 40–50.
- Sannomiya, T., Dermutz, H., Hafner, C., Voros, J., Dahlin, A.B., 2010. Electrochemistry on a localized surface plasmon resonance sensor. *Langmuir* 26 (10), 7619–7626.
- Smietana, M., Niedziółkowski, P., Białobrzaska, W., Burnat, D., Sezemsky, P., Koba, M., Stranak, V., Siuzdak, K., Ossowski, T., Bogdanowicz, R., 2018a. Study on combined optical and electrochemical analysis using indium-tin-oxide-coated optical fiber sensor. *Electroanalysis* 31 (2), 392–404.
- Smietana, M., Sobaszek, M., Michalak, B., Niedziółkowski, P., Białobrzaska, W., Koba, M., Sezemsky, P., Stranak, V., Karczewski, J., Ossowski, T., Bogdanowicz, R., 2018b. Optical monitoring of electrochemical processes with ITO-based lossy-mode resonance optical fiber sensor applied as an electrode. *J. Lightwave Technol.* 36 (4), 954–960.
- Sobaszek, M., Burnat, D., Sezemsky, P., Stranak, V., Bogdanowicz, R., Koba, M., Siuzdak, K., Smietana, M., 2019. Enhancing electrochemical properties of ITO-coated lossy-mode resonance optical fiber sensor by electrodeposition of PEDOT: PSS. *Opt. Mater. Express* 9 (7), 3069–3078.
- Stotter, J., Show, Y., Wang, S., Swain, G., 2005. Comparison of the electrical, optical, and electrochemical properties of diamond and indium tin oxide thin-film electrodes. *Chem. Mater.* 17 (19), 4880–4888.
- Truong, J., Hsieh, Y.-F., Truong, L., Jia, G., Hammond, M.C., 2018. Designing fluorescent biosensors using circular permutations of riboswitches. *Methods* 143, 102–109.
- Wongkaew, N., Simsek, M., Griesche, C., Baeumner, A.J., 2019. Functional nanomaterials and nanostructures enhancing electrochemical biosensors and lab-on-a-chip performances: recent progress, applications, and future perspective. *Chem. Rev.* 119 (1), 120–194.
- Wu, C., ur Rehman, F., Li, J., Ye, J., Zhang, Y., Su, M., Jiang, H., Wang, X., 2015. Real-time evaluation of live cancer cells by an in situ surface plasmon resonance and electrochemical study. *ACS Appl. Mater. Interfaces* 7 (44), 24848–24854.

- Zhurauski, P., Arya, S.K., Jolly, P., Tiede, C., Tomlinson, D.C., Ferrigno, P.K., Estrela, P., 2018. Sensitive and selective Affirmer-functionalised interdigitated electrode-based capacitive biosensor for Her4 protein tumour biomarker detection. *Biosens. Bioelectron.* 108, 1–8.
- Banica, Florinel-Gabriel, 2012. *Chemical Sensors and Biosensors: Fundamentals and Applications*, 1 edition. Wiley.
- Juan-Colas, J., 2017. *Dual-Mode Electro-Photonic Silicon Biosensors*. Springer Theses, Springer.

C5. Electrochemically directed biofunctionalization of a lossy-mode resonance optical fiber sensor

Monika Janik, Paweł Niedziałkowski, Katarzyna Lechowicz, Marcin Koba, Petr Sezemsky, Vitezslav Stranak, Tadeusz Ossowski, Mateusz Smietana, Electrochemically directed biofunctionalization of lossy-mode resonance optical fiber sensor, Optics Express 28(11), (2020), 15934.

© 2019 Optical Society of America. Users may use, reuse, and build upon the article, or use the article for text or data mining, so long as such uses are for non-commercial purposes and appropriate attribution is maintained. All other rights are reserved.

Abstract

In this work, we present a direct electrochemical biofunctionalization of an indium-tin-oxide-coated lossy-mode resonance optical fiber sensor. The functionalization using a biotin derivative was performed by cyclic voltammetry in a 10 mM biotin hydrazide solution. All stages of the experiment were simultaneously verified with optical and electrochemical techniques. Performed measurements indicate the presence of a poly-biotin layer on the sensor's surface. Furthermore, dual-domain detection of 0.01 and 0.1 mg/mL of avidin confirms the sensor's viability for label-free detection.

1. INTRODUCTION

The recent advances in nanotechnology and photonics have opened the possibility to develop a new generation of flexible, portable, versatile, and high-performance optical fiber sensors, such as those based on lossy-mode resonance (LMR). Thanks to the flexibility and relatively high sensitivity this new approach has emerged in the last two decades and found numerous applications such as refractive index (RI) [1], voltage [2], pH [3], humidity [4], and chemical detection [5, 6]. Moreover, due to high RI sensitivity, numerous studies have been also reported on label-free biosensors based on the LMR effect [7, 8]. This optical effect takes place in the presence of a thin film on an optical fiber. However, specific conditions for the electric permittivity of the substrate (fiber), thin overlay, and external medium must be fulfilled. Generally, the real part of the film's permittivity must be positive and at the same time higher in magnitude than its imaginary part and the permittivity of the analyte [7]. Thus, to obtain the LMR an adequate material for fiber overlay needs to be chosen. Many thin-film materials when deposited on silica glass allows obtaining LMR. These materials, among others, include semiconductor and metal oxides or nitrides (indium-gallium-zinc oxide [9], silicon nitride [10], indium-tin-oxide (ITO) [11], fluorine-doped tin oxide (FTO) [12], tin oxide [13], zinc oxides [9, 14], indium oxide [15], titanium oxide [16], as well as hafnium, zirconium and tantalum oxides [17], diamond-like carbon films (DLC) [18] and various polymers [3]. Some of these materials, e.g., ITO [19–21] and FTO [12], thanks to their unique properties, such as good electrical conductivity and suitable bandgap [22], have already been reported as capable to work in two domains, where optical and electrochemical (EC) interrogations of the sensor were simultaneously possible. As multiple domain sensors, they provide enhanced information about the analyzed target, improve detection range, cross-verify measurements and thus reduce false-positive results. This, in turn, is very important during biosensing investigations where low limits of detection and high specificity are expected. However, label-free biosensing applications require chemical modification of the sensor's surfaces. A chemical functionalization is required to immobilize a receptor of interest on the sensor's surface enabling high binding selectivity of targeted biomaterial. In the majority of reports on non-metal coated biosensors,

poly(methylmethacrylate) polymeric (Eudragit L100) [13], (3-Aminopropyl)triethoxysilane (APTES) [23], or 3 (Triethoxysilyl)propylsuccinicanhydride (TESPSA) [24] depositions have been used to anchor biological molecule. Some of the silane compounds at the surface need to be additionally activated by a chemical coupling reaction with homo- or heterobifunctional cross-linker molecules that contain additional bioactive groups. Other reported approach employs a layer-by-layer coating of the LMR sensor's surface with oppositely charged polymers [25]. For example, to detect a C-reactive protein (CRP) [26], polymer bilayers containing Poly (allylamine) hydrochloride and Poly (sodium 4-styrenesulfonate) that are positively and negatively charged, respectively, have been used. After the formation of 4 bilayers a receptor i.e., DNA aptamer has been immobilized by electrostatic interactions as DNA is negatively charged. Although these chemical processes are essential for reaching selectivity of the sensors, a great majority of them is very time-consuming (from 2 to 4 h), require further modifications and curing of the deposited layer (from 2 to 48 h), and can induce a change in sensor properties, i.e., sensitivity and character of the spectral response of the sensor [24]. Moreover, due to the multiple steps, the processes may result in a lack of repeatability and stability.

Thus, where possible, other, simpler sensor surface biofunctionalization methods are highly expected. As one of them, EC-induced attachment of various compounds to the sensor's surfaces can be considered as a great alternative to chemical functionalization. The electropolymerization outstands other methods due to its easiness, precise positioning of the chosen compound, and short process time. Moreover, the electropolymerization is just a one-step process. However, the application of this method requires the surface of the sensor to be electrically conductive and EC-active. Electropolymerization has already been applied to ITO-LMR for its application in chemical sensing i.e., direct detection of Ketoprofen [27]. The process was conducted also to enhance the EC-activity of the sensor [28].

In this paper, we report a direct electrochemical ITO-LMR sensor's surface modification towards its application in label-free biosensing. We have used electropolymerized biotin hydrazide (BH) to form the receptor layer targeted towards selective dual-domain detection of avidin. The binding constant of the avidin-biotin formation complex ($K_a = 10^{15} \text{ M}^{-1}$) is considered as the

strongest non-covalent binding occurring in nature [29, 30]. Based on these interactions not only immunoenzymatic techniques have been developed [31], but it is also widely utilized to construct many sensors and immunosensors [32–35]. Therefore, applied surface modification greatly expands the application range of the dual-domain ITO-LMR biotin-functionalized sensor.

2. METHODOLOGY

2.1. Reagents

1,1'-Ferrocenedimethanol (Fc-(MeOH)₂), biotin hydrazide (BH), avidin, bovine serum albumin (BSA) were purchased from Sigma-Aldrich and used without further purification. K₃Fe(CN)₆, KCl, were purchased from POCh - Polish Chemical Reagents. 0.01 M Phosphate buffered saline (PBS) solution was obtained from Sigma-Aldrich by dissolving tablets in deionized water to obtain pH 7.4. Then the solution was adjusted to pH 7.0 with 0.1 M HCl using a glass electrode connected to pH meter.

2.2. ITO-LMR sensor fabrication

The ITO-LMR sensor is based on 15 cm long polymer-clad silica optical fiber, which had its 2.5 cm long cladding section removed in the middle part. The ITO thin film was deposited by magnetron sputtering in the ultra-high vacuum chamber. The magnetron was equipped with a 3-inch ITO target (In₂O₃:SnO₂ – 90:10 wt%) and supplied by COMET Cito1310 RF source (13.56 MHz, 150 W). The optical fiber sample was rotated during deposition to receive a homogenous coating around the fiber. The deposition at a pressure of 0.1 Pa and Ar flow of 26.4 sccm took 135 min. The sensors' fabrication was followed by optical and EC characterization as described in [23].

2.3. Electrochemical and optical setup

Cyclic voltammetry (CV) measurements were performed with a PalmSens EmStat 3+ potentiostat/galvanostat controlled by PSTrace 5.5 software using the ITO-LMR as a working electrode (WE). A platinum wire was used as a counter electrode (CE) and an Ag/AgCl/0.1 M KCl as a reference electrode (RE). The ITO-LMR electrode was EC-investigated both in 1 mM K₃Fe(CN)₆ in 0.1 M KCl and 1 mM Fc-(CH₂OH)₂ in 0.1 M KCl at scan rate 50 mV/s for 2 cycles in the potential ranging from -0.5 to 0.7 V. Each

cycle/scan is understood as applying the potential starting from 0 V \rightarrow 0.7 V \rightarrow 0 V \rightarrow -0.5 V \rightarrow 0 V and takes \sim 24 seconds.

Two redox couples – $\text{Fe}(\text{CN})_6^{3-/4-}$ and $\text{Fc}-(\text{CH}_2\text{OH})_2^{+/0}$ – were chosen due to their different sensitivity towards the surface and different EC behavior in the examined solution. $\text{Fe}(\text{CN})_6^{3-/4-}$ is a negatively charged, inner-sphere redox probe. The observed electron transfer reactivity in this redox probe significantly depends on preparation, modification, and coverage of the electrode surface [36, 37]. On the other hand, the $\text{Fc}-(\text{CH}_2\text{OH})_2^{+/0}$ is neutral, water-soluble redox couple, belonging to the outer-redox probe. This redox system was chosen due to the lack of any electrocatalytic activity and no adsorption processes observed during the electrochemical measurements [38]. The EC mechanism of both chosen redox couples was described in our previous work [19].

The optical response of the ITO-LMR sensor during the experiment has been interrogated in the spectral range from 350 to 1050 nm using USB4000 spectrometer and HL-2000 tungsten light source (Ocean Optics). The interrogation time was set to 4 ms. The optical data acquisition and processing have been controlled using in-house developed software. The schematic representation of the measurement setup used for the optical-EC investigation is shown in Fig. 1.

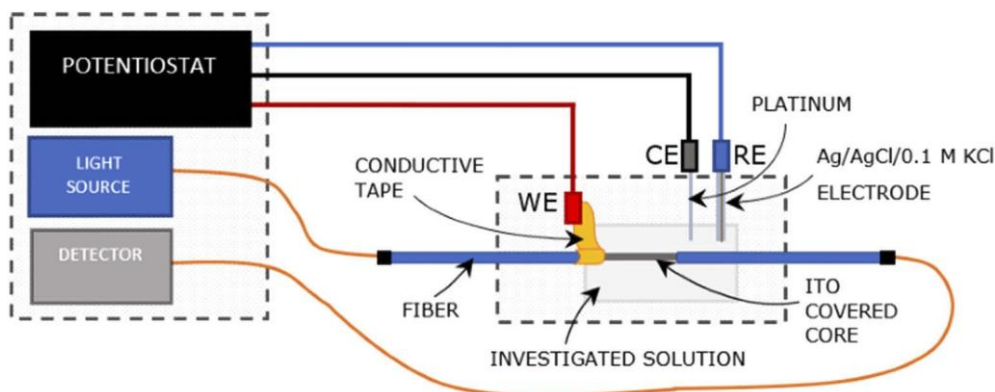


Fig. 1. Schematic representation of combined optical and EC measurements setup with ITO-LMR sensor subjected to the electropolymerization process. The electrodes were denoted as working (WE), reference (RE), and counter (CE) electrode.

2.4. Electropolymerization of biotin hydrazide

The electrodeposition was studied on bare ITO-LMR sensor used as a working electrode. To perform the electropolymerization process the fiber probe was immersed in 10 mM of BH in the 0.1 mM KCl solution and underwent 10 cycles performed in the potential range from 0 to 1.1 V at a scan rate of 50 mV/s (each scan followed the scheme 0 V \rightarrow 1.1 V \rightarrow 0 V). Each cycle took \sim 22 seconds, thus, the whole procedure was just \sim 3 min 40 sec long. The electropolymerization process was monitored by optical measurements as described in Section 2.3. After the functionalization the ITO-LMR was measured optically and EC in presence of 1 mM $K_3Fe(CN)_6$ in 0.1 M KCl at a scan rate of 50 mV/s for 2 cycles in the potential ranging from -0.5 to 0.7 V. Figure 2 presents a scheme of BH electropolymerization on the ITO surface and detection scheme of avidin.

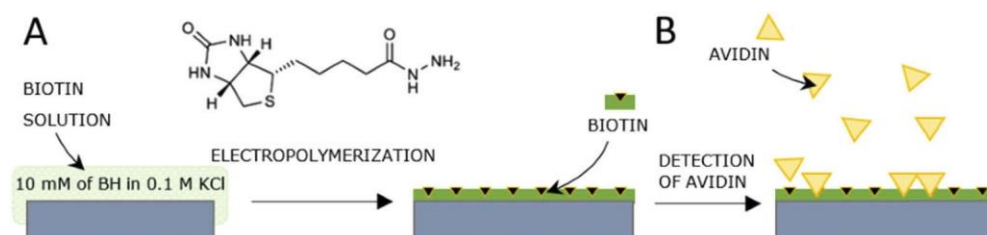


Fig. 2. Schematic representation of A) BH electropolymerization process, B) binding of avidin to the biotinylated ITO-LMR surface.

2.5. Avidin detection

The electropolymerization of biotin was followed by the detection of biotin specific glycoprotein – avidin, with two different concentrations, i.e., 0.01 mg/mL, 0.1 mg/mL dissolved in 0.01 M solution of PBS, pH 7.0. After the electropolymerization process, the electrode was immersed in 1% BSA in 0.01 M PBS, pH 7.0 for 30 minutes to block the nonspecific interactions. Next, the ITO-LMR poly-biotin-functionalized samples were incubated in consecutive solutions of avidin for 30 minutes. Then, the ITO-LMR electrode was extensively washed with water and PBS. Each step of the experiment was followed by optical and CV measurements in the presence of 1 mM $Fc-(CH_2OH)_2$ in 0.1 M KCl at a scan rate of 50 mV/s for 2 cycles in the potential ranging from -0.5 to 0.7 V.

3. RESULTS AND DISCUSSION

3.1. Electropolymerization of biotin hydrazide on the ITO-LMR electrode

The functionalization of the ITO-LMR sensor's surface was performed by the electropolymerization process following a modified procedure described in [39] to cover the ITO electrode by amino derivatives of biotin. The main advantage of the electropolymerization method is its easiness as well as time (~3 min 40 sec) and reagent saving in comparison to other chemical methods. The exact mechanism of the deposition of BH is unknown, however, two probable descriptions were proposed by Davis and co-workers [40]. The first mechanism is associated with the oxidation of carbazoyl group, whereas the second one suggests the formation of a radical cation upon oxidation of the hydrazide group [41].

Figure 3(a) presents the CVs obtained during the electropolymerization process. After the first scan, the anodic peak current significantly decreased. During the next 9 scans, the behavior followed the decreasing trend. It indicates the modification of the electrode surface. Similar electrochemical behavior was also observed during the modification of gold [40] and flat ITO electrode surfaces [39].

Like many other biological molecules, biotin does not undergo redox reaction and thus observation of current peaks in CV is not possible. That is why the additional redox couples present in the electrolyte are required to follow the changes occurring at the surface of the ITO electrode. To examine the EC immobilization of the biotin, the CV response was verified with the presence of $\text{Fe}(\text{CN})_6^{3-}$ and $\text{Fc}(\text{CH}_2\text{OH})_2^{+/0}$. The electrochemical properties of the ITO-LMR electrode before and after electropolymerization were investigated by cyclic CV performed in 1 mM $\text{Fe}(\text{CN})_6^{3-/4-}$ solution containing 0.1 M KCl. Figure 3(c) shows the CVs for the bare ITO-LMR probe before electropolymerization and the signal after the process. Two well-defined peaks are observed for the bare ITO-LMR electrode. The peak to peak separation (ΔE_p) is equal to 117 mV, the anodic peak current to cathodic peak current ratio (i_{pa}/i_{pc}) is equal 1, what indicates one electron *quasi*-reversible redox reaction. After the electropolymerization process, the anodic and cathodic peak currents decreased. ΔE_p for the poly-biotin-modified electrode

increased to 249 mV. It reveals that the electron transfer is blocked in comparison to the bare ITO-LMR electrode. Similar behavior was observed before using $\text{Fe}(\text{CN})_6^{3-/4-}$ as a redox couple [42]. This phenomenon clearly confirms that the ITO-LMR electrode was modified by biotin.

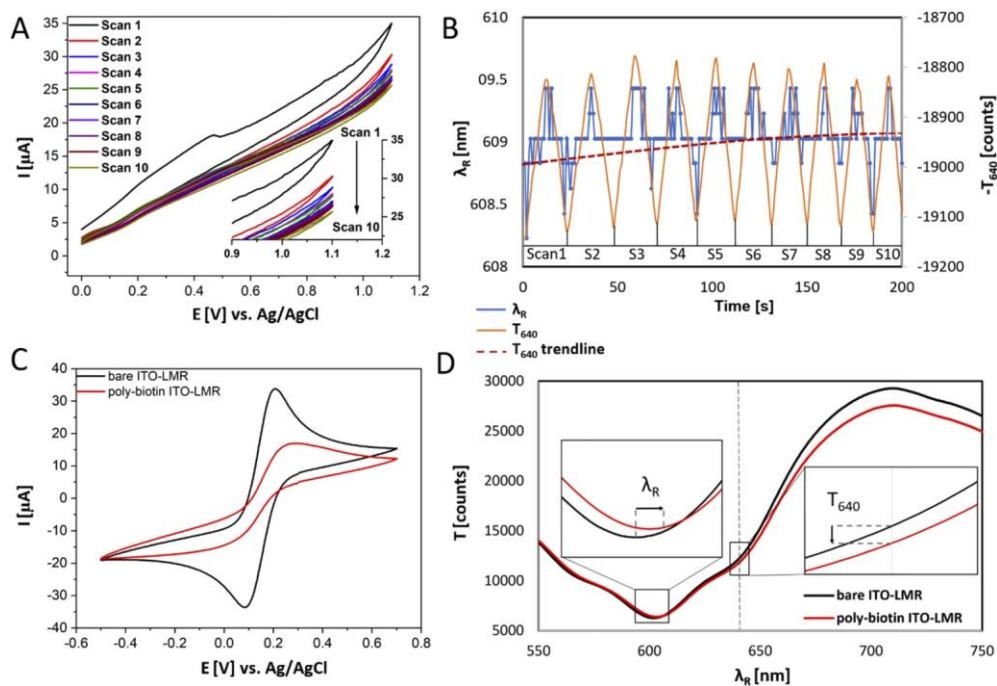


Fig. 3. A) CV scans recorded for the ITO-LMR sensor in 0.1 M KCl containing 10 mM of BH. The scan rate was 50 mV/s; B) Change in λ_R and T_{640} with the progress of the biotin electropolymerization process; (C) CV scans recorded before and after electropolymerization of biotin in the presence of $\text{K}_3\text{Fe}(\text{CN})_6$ in 0.1 M KCl. The scan rate was 50 mV/s; (D) Comparison of the ITO-LMR spectral response of the sensor in $\text{K}_3\text{Fe}(\text{CN})_6$ in 0.1 M KCl before and after the electropolymerization.

The electropolymerization process simultaneously to EC interrogation has been also monitored optically. Figure 3(b) shows the alterations in the optical spectrum during the BH deposition for selected spectral parameters, i.e. LMR wavelength (λ_R) and transmission at $\lambda = 640$ nm (T_{640}). The wavelength for transmission change analysis was selected in the middle of the resonance slope, where a noticeable variation could be observed. The main motivation of the choice was to match the wavelength of cheaper and widely available laser diodes possible to be applied as a light source when simple, solely power-based interrogation is considered. Furthermore, even though the change in terms of the amplitude is significant in other points, in these locations there is

no change in terms of the wavelength. In Fig. 3(d), a comparison of the full spectral response of the ITO-LMR sensor before and after the electropolymerization process is depicted. It is apparent that after the polymerization of BH a shift of λ_R towards longer wavelengths and a decrease in T_{640} took place. Due to low wavelength resolution of the spectrometer, we simultaneously traced changes in optical power T_{640} . Since the power resolution is higher it can be treated as a confirmation of a wavelength shift. Although the changes recorded for biotin deposition are close to the resolution of the spectrometer, we cannot expect any significant shifts. The biotin molecule with ~ 1.6 nm size and the RI close to the PBS buffer could not strongly affect the spectrum. On the other hand, such size is enough to change the conductivity of the ITO-LMR electrode. Thus, the spectral shift after biotin deposition is justified considering electrochemical measurements, where blocking of the surface by the biotin, traced as a decrease of anodic and cathodic peak currents, is indisputable (Fig. 3(c)).

3.2. Avidin detection using biotin-functionalized ITO-LMR electrode

To confirm the sensor's viability for label-free detection, the presence of the poly-biotin on the ITO-LMR surface, and stability of the surface's functionalization we performed a series of experiments for the selective immobilization of avidin. During the subsequent stages of electrode modification, both EC and optical measurements were performed. The CVs were obtained in 1 mM Fc-(CH₂OH)₂⁺⁰ solution containing 0.1 M KCl.

Figure 4(a) depicts CV curves recorded after incubation in BSA, 0.01 and 0.1 mg/mL of avidin, where each incubation was followed by an extensive washing in PBS and water. Therefore, the registered responses are induced only by interactions at the sensor's surface and were not disturbed by, e.g., RI changes in the volume. Right after the electropolymerization, the ITO-LMR electrode was immersed in a 1% BSA solution to block any nonspecific interactions on the surface. This caused a decrease in the current peak and increased ΔE_p from 220 to 270 mV. Next, the ITO-LMR electrode was incubated for 30 minutes in the 0.1 mg/mL of avidin. Although we could observe a decrease of the current peak after the incubation the shape of the obtained voltammograms was very similar to those after BSA. Additionally, the calculated value of ΔE_p was at the same level ~ 270 mV as for the previous

stage of the experiment. In contrast, the immersion of the ITO-LMR in the second concentration of avidin caused noticeable changes in CV decreasing the peak current and increasing ΔE_p to the value of ~ 250 mV.

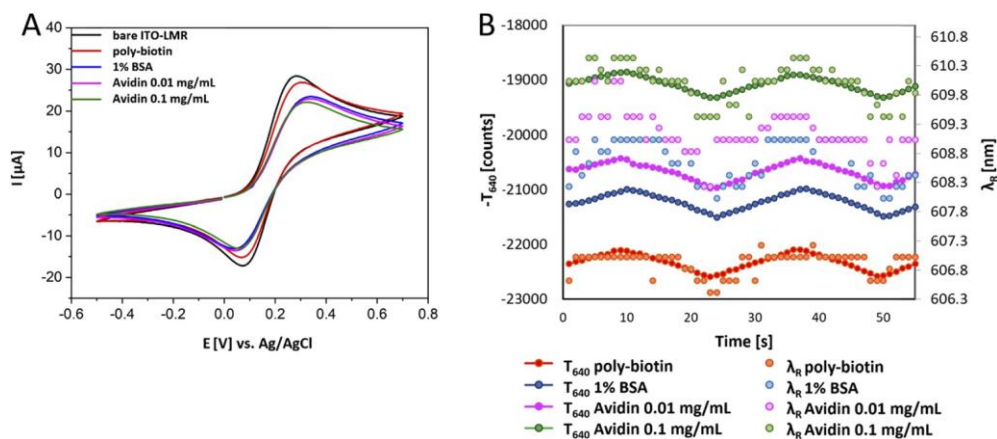


Fig. 4. A) CVs after each step of avidin detection in the presence of 1 mM $\text{Fc}-(\text{CH}_2\text{OH})_2$ in 0.1 M KCl , scan rate: 50 mV/s; (B) Corresponding change in ITO-LMR λ_R and T_{640} after each step of the avidin detection experiment.

Figure 4(b) shows the evolution of corresponding optical parameters, namely λ_R and T_{640} after each step of the experiment. The apparent shift towards longer wavelengths and decreases in transmission corresponds to an increase of the thickness and/or RI of the biological layer on the biotinylated ITO-LMR's surface. Starting from the formation of the BSA layer – the ~ 1 nm shift of λ_R can be noticed. Next, for the avidin molecule, we can observe further changes. It can be seen that the higher concentration of avidin, the bigger the LMR shift towards longer wavelengths is obtained. The most significant change of ~ 2 nm was observed for the 0.1 mg/mL concentration of avidin. All obtained results confirm avidin detection on the ITO-LMR sensor using both electrochemical and optical methods at the level from 0.01 to 0.1 mg/mL.

In this work we focused mainly on the optimization of the electropolymerization process, namely the number of scans, the range of the applied potential, and the concentration of the biotin hydrazide to obtain the effective biofunctionalization. Our aim was more to show a novel modification concept and its verification than to focus on a specific application, a broad range of concentrations or reaching a low limit of detection. Thus, the two avidin concentrations were used mainly to verify the

presence of the poly-biotin on the sensor's surface. It must be noted that this fast and efficient method is also very universal thanks to the presence of the biotin-avidin complex. Such a well-verified modification could be used in the future to detect any biotinylated molecule, such as antibodies, DNA aptamers, peptides, proteins, etc. Up to our best knowledge, there is no other report available on biotin hydrazide functionalization of the optical fiber sensor's surface, where the functionalization is verified optically and electrochemically.

The reported dual-domain system allows for gathering significantly more information on the investigated samples, unlike single domain investigation. Cross-verification of the obtained results is possible within one experiment. Since the sensitivity and its ranges for the two domains may be different, they can serve as a supplement to each other leading to significantly improved performance of the sensor. What is more, it also gives the capability to conduct a functionalization process, (namely the electropolymerization, as reported here) in one domain and monitor its progress using the other one. During label-free sensing with the support of theoretical simulations and knowledge about detected molecules, such as RI, estimation of the thickness and properties such as isoelectric point or permeability of the deposited layer are also possible.

4. CONCLUSIONS

In our work, we have demonstrated a simple, one-step method for direct electrochemical biofunctionalization of ITO-LMR sensor's surfaces. The modification was achieved by electropolymerization of 10 mM biotin hydrazide. The process was possible due to the electrical conductivity of the indium tin oxide film deposited on the multimode optical fiber core, which allowed to use the ITO probe as a working electrode. On the other hand, the lossy mode resonance effect enabled the parallel optical measurements. Both cyclic voltammetry experiments and optical measurements performed in the presence of two different redox couples confirmed the presence of poly-biotin film at the ITO-LMR sensor's surface. What is more, we demonstrated its viability for label-free sensing by detection of 0.01 and 0.1 mg/mL of avidin. The biotin-functionalized surface and its interaction with avidin – known from immunoenzymatic tests – can greatly expand the application range of the dual-domain ITO-LMR sensor. Except for the universal character of the reported

functionalization, the method outstands other techniques by its easiness (one-step process), repeatability, precise positioning of the compound, and short process time, which is lower than 4 minutes.

Funding

Narodowe Centrum Nauki (2014/14/E/ST7/00104); Narodowe Centrum Badań i Rozwoju (347324/12/NCBR/2017); Narodowa Agencja Wymiany Akademickiej (PPN/BIL/2018/1/00126).

Disclosures

The authors declare no conflicts of interest.

References

- [1] C. R. Zamarreño, M. Hernáez, I. Del Villar, C. Fernandez-Valdivielso, F. J. Arregui, and I. R. Matias, “Optical fiber pH sensor fabrication by means of indium tin oxide coated optical fiber refractometers,” *Phys. Status Solidi (c)* **7**(11–12), 2705–2707 (2010).
- [2] J. M. Corres, J. Ascorbe, F. J. Arregui, and I. R. Matias, “Tunable electro-optic wavelength filter based on lossy-guided mode resonances,” *Opt. Express* **21**(25), 31668 (2013).
- [3] C. R. Zamarreño, M. Hernáez, I. Del Villar, I. R. Matías, and F. J. Arregui, “Optical fiber pH sensor based on lossy-mode resonances by means of thin polymeric coatings,” *Sens. Actuators, B* **155**(1), 290–297 (2011).
- [4] C. R. Zamarreño, M. Hernaez, I. Del Villar, I. R. Matias, and F. J. Arregui, “Tunable humidity sensor based on ITO-coated optical fiber,” *Sens. Actuators, B* **146**(1), 414–417 (2010).
- [5] S. P. Usha, S. K. Mishra, and B. D. Gupta, “Fiber optic hydrogen sulfide gas sensors utilizing ZnO thin film/ZnO nanoparticles: A comparison of surface plasmon resonance and lossy mode resonance,” *Sens. Actuators, B* **218**, 196–204 (2015).
- [6] S. K. Mishra, S. P. Usha, and B. D. Gupta, “A lossy mode resonance-based fiber optic hydrogen gas sensor for room temperature using coatings of ITO thin film and nanoparticles,” *Meas. Sci. Technol.* **27**(4), 045103 (2016).
- [7] I. Del Villar, F. J. Arregui, C. R. Zamarreño, J. M. Corres, C. Bariain, J. Goicoechea, C. Elosua, M. Hernaez, P. J. Rivero, A. B. Socorro, A. Urrutia, P. Sanchez, P. Zubiate, D. Lopez, N. De Acha, J. Ascorbe, and I. R. Matias, “Optical sensors based on lossy-mode resonances,” *Sens. Actuators, B* **240**, 174–185 (2017).

- [8] Q. Wang and W. M. Zhao, “A comprehensive review of lossy mode resonance-based fiber optic sensors,” *Opt. Lasers Eng.* **100**(2018), 47–60 (2018).
- [9] A. Ozcariz, M. Dominik, M. Smietana, C. R. Zamarreño, I. Del Villar, and F. J. Arregui, “Lossy mode resonance optical sensors based on indium-gallium-zinc oxide thin film,” *Sens. Actuators, A* **290**, 20–27 (2019).
- [10] B. Michalak, M. Koba, and M. Śmietana, “Silicon nitride overlays deposited on optical fibers with RF PECVD method for sensing applications: Overlay uniformity aspects,” *Acta Phys. Pol. A* **127**(6), 1587–1591 (2015).
- [11] I. Del Villar, C. R. Zamarreño, M. Hernaez, F. J. Arregui, and I. R. Matias, “Lossy mode resonance generation with indium-tin-oxide-coated optical fibers for sensing applications,” *J. Lightwave Technol.* **28**(1), 111–117 (2010).
- [12] D. Burnat, M. Janczuk-Richter, P. Niedziałkowski, W. Białobrzaska, P. Sezemsky, M. Koba, V. Stranak, R. Bogdanowicz, T. Ossowski, J. Niedziółka-Jönsson, and M. Śmietana, “Optical fiber lossy-mode resonance sensors with doped tin oxides for optical working electrode monitoring in electrochemical systems,” in *Seventh European Workshop on Optical Fibre Sensors*, K. Kalli, G. Brambilla, and S. O. O’Keefe, eds. (SPIE, 2019), (111991O–1), p. 141.
- [13] F. Chiavaioli, P. Zubiate, I. Del Villar, C. R. Zamarreño, A. Giannetti, S. Tombelli, C. Trono, F. J. Arregui, I. R. Matias, and F. Baldini, “Femtomolar Detection by Nanocoated Fiber Label-Free Biosensors,” *ACS Sens.* **3**(5), 936–943 (2018).
- [14] S. P. Usha and B. D. Gupta, “Performance analysis of zinc oxide-implemented lossy mode resonance-based optical fiber refractive index sensor utilizing thin film/nanostructure,” *Appl. Opt.* **56**(20), 5716 (2017).
- [15] C. R. Zamarreño, P. Sanchez, M. Hernaez, I. Del Villar, C. Fernandez-Valdivielso, I. R. Matias, and F. J. Arregui, “Sensing properties of indium oxide coated optical fiber devices based on lossy mode resonances,” *IEEE Sens. J.* **12**(1), 151–155 (2012).
- [16] M. Hernaez, C. R. Zamarreño, I. Del Villar, I. R. Matias, and F. J. Arregui, “Lossy mode resonances supported by TiO₂-coated optical fibers,” *Procedia Eng.* **5**, 1099–1102 (2010).
- [17] K. Kosieli, M. Koba, M. Masiewicz, and M. Śmietana, “Tailoring properties of lossy-mode resonance optical fiber sensors with atomic layer deposition technique,” *Opt. Laser Technol.* **102**, 213–221 (2018).

-
- [18] M. Śmietana, M. Dudek, M. Koba, and B. Michalak, "Influence of diamond-like carbon overlay properties on refractive index sensitivity of nano-coated optical fibres," *Phys. Status Solidi A* **210**(10), 2100–2105 (2013).
- [19] P. Niedziałkowski, W. Białobrzeska, D. Burnat, P. Sezemsky, V. Stranak, H. Wulff, T. Ossowski, R. Bogdanowicz, M. Koba, and M. Śmietana, "Electrochemical performance of indium-tin-oxide-coated lossy-mode resonance optical fiber sensor," *Sens. Actuators, B* **301**(June), 127043 (2019).
- [20] M. Śmietana, M. Sobaszek, B. Michalak, P. Niedziałkowski, W. Białobrzeska, M. Koba, P. Sezemsky, V. Stranak, J. Karczewski, T. Ossowski, and R. Bogdanowicz, "Optical Monitoring of Electrochemical Processes with ITO-Based Lossy-Mode Resonance Optical Fiber Sensor Applied as an Electrode," *J. Lightwave Technol.* **36**(4), 954–960 (2018).
- [21] M. Śmietana, P. Niedziałkowski, W. Białobrzeska, D. Burnat, P. Sezemsky, M. Koba, V. Stranak, K. Siuzdak, T. Ossowski, and R. Bogdanowicz, "Study on Combined Optical and Electrochemical Analysis Using Indium-tin-oxide-coated Optical Fiber Sensor," *Electroanalysis* **31**(2), 398–404 (2019).
- [22] J. C. Manificier, "Thin metallic oxides as transparent conductors," *Thin Solid Films* **90**(3), 297–308 (1982).
- [23] M. Śmietana, M. Koba, P. Sezemsky, K. Szot-Karpińska, D. Burnat, V. Stranak, J. Niedziółka-Jönsson, and R. Bogdanowicz, "Simultaneous optical and electrochemical label-free biosensing with ITO-coated lossy-mode resonance sensor," *Biosens. Bioelectron.* **154**, 112050 (2020).
- [24] M. Piestrzyńska, M. Dominik, K. Kosił, M. Janczuk-Richter, K. Szot-Karpińska, E. Brzozowska, L. Shao, J. Niedziółka-Jonsson, W. J. Bock, and M. Śmietana, "Ultrasensitive tantalum oxide nano-coated long-period gratings for detection of various biological targets," *Biosens. Bioelectron.* **133**(March), 8–15 (2019).
- [25] L. Razquin, C. R. Zamarreno, F. J. Munoz, I. R. Matias, and F. J. Arregui, "Thrombin detection by means of an aptamer based sensitive coating fabricated onto LMR-based optical fiber refractometer," *Proc. IEEE Sensors* 3–6 (2012).
- [26] P. Zubiante, C. R. Zamarreño, P. Sánchez, I. R. Matias, and F. J. Arregui, "Biosensors and Bioelectronics High sensitive and selective C-reactive protein detection by means of lossy mode resonance based optical fiber devices," *Biosens. Bioelectron.* **93**, 176–181 (2017).
-

- [27] R. Bogdanowicz, P. Niedziałkowski, M. Sobaszek, D. Burnat, W. Białobrzeska, Z. Cebula, P. Sezemsky, M. Koba, V. Stranak, T. Ossowski, and M. Śmietana, “Optical detection of ketoprofen by its electropolymerization on an indium tin oxide-coated optical fiber probe,” *Sensors* **18**(5), 1361 (2018).
- [28] M. Sobaszek, D. Burnat, P. Sezemsky, V. Stranak, R. Bogdanowicz, M. Koba, K. Siuzdak, and M. Śmietana, “Enhancing electrochemical properties of an ITO-coated lossy-mode resonance optical fiber sensor by electrodeposition of PEDOT:PSS,” *Opt. Mater. Express* **9**(7), 3069 (2019).
- [29] N. Sugimoto, H. Kazuta, J. Zou, and D. Miyoshi, “A novel screening method for combinatorial chemistry for low affinity interactions,” *Chem. Commun.* **8**, 677–678 (1999).
- [30] O. Livnah, E. A. Bayer, M. Wilchek, and J. L. Sussman, “Three-dimensional structures of avidin and the avidin-biotin complex,” *Proc. Natl. Acad. Sci. U. S. A.* **90**(11), 5076–5080 (1993).
- [31] J. L. Guesdon, T. Ternynck, and S. Avrameas, “The use of avidin-biotin interaction in immunoenzymatic techniques,” *J. Histochem. Cytochem.* **27**(8), 1131–1139 (1979).
- [32] A. Jain and K. Cheng, “The principles and applications of avidin-based nanoparticles in drug delivery and diagnosis,” *J. Control. Release* **245**, 27–40 (2017).
- [33] C. Padeste, B. Steiger, A. Grubelnik, and L. Tiefenauer, “Redox labelled avidin for enzyme sensor architectures,” *Biosens. Bioelectron.* **19**(3), 239–247 (2003).
- [34] M. Wilchek and E. A. Bayer, “The avidin-biotin complex in bioanalytical applications,” *Anal. Biochem.* **171**(1), 1–32 (1988).
- [35] P. Pollheimer, B. Taskinen, A. Scherfler, S. Gusenkov, M. Creus, P. Wiesauer, D. Zauner, W. Schöffberger, C. Schwarzinger, A. Ebner, R. Tampé, H. Stutz, V. P. Hytönen, and H. J. Gruber, “Reversible biofunctionalization of surfaces with a switchable mutant of avidin,” *Bioconjug. Chem.* **24**(10), 1656–1668 (2013).
- [36] P. Chen, M. A. Fryling, and R. L. McCreery, “Electron Transfer Kinetics at Modified Carbon Electrode Surfaces: The Role of Specific Surface Site,” *Anal. Chem.* **67**(18), 3115–3122 (1995).
- [37] P. Chen and R. L. McCreery, “Control of Electron Transfer Kinetics at Glassy Carbon Electrodes by Specific Surface Modification,” *Anal. Chem.* **68**(22), 3958–3965 (1996).
- [38] R. L. McCreery, “Advanced Carbon Electrode Materials for Molecular Electrochemistry,” *Chem. Rev.* **108**(7), 2646–2687 (2008).
- [39] D. Yu and K. Kim, “Electrochemically directed modification of ITO electrodes and its feasibility for the immunosensor development,” *Bull. Korean Chem. Soc.* **30**(4), 955–958 (2009).

-
- [40] C. Brandon Davis, L. M. Shamansky, S. Rosenwald, J. K. Stuart, W. G. Kuhr, and S. A. Brazill, "Independently-addressable micron-sized biosensor elements," *Biosens. Bioelectron.* **18**(10), 1299–1307 (2003).
- [41] C. Rubio-González, M. T. Fernández-Abedul, and A. Costa-García, "Comparative electrochemical behaviour of biotin hydrazide and photobiotin. Importance in the development of biosensors," *Biosens. Bioelectron.* **14**(8-9), 729–735 (1999).
- [42] H. Kuramitz, K. Sugawara, and S. Tanaka, "Electrochemical sensing of avidin-biotin interaction using redox markers," *Electroanalysis* **12**(16), 1299–1303 (2000).

Other courses and experiences

- 2015 The Summer School of the Vacuum Society - Plasma Technologies and Processes
- 2016 Internship at the Institute of Physics in Greifswald (Germany; Institut für Physik - Universität Greifswald) – Preparation and analysis of thin films, plasma diagnostics
- 2016 Internship at the Institute of Microelectronics and Optoelectronics in Warsaw (Poland; Institute of Microelectronics and Optoelectronics, Warsaw University of Technology) – Preparation of the vacuum deposition system
- 2017 Internship at the Institute of Physics in Greifswald (Germany; Institut für Physik - Universität Greifswald) – Development of tool for reactive dusty plasma diagnostics
- 2019 The Summer School of the Vacuum Society – Systems for High and Ultrahigh Vacuum and Their Applications
- 2019 Internship at the Institute of Microelectronics and Optoelectronics in Warsaw (Poland; Institute of Microelectronics and Optoelectronics, Warsaw University of Technology) – Preparation of a vacuum system for plasma deposition, preparation and testing of bioactive sensors

Expertise

Operation of vacuum systems, various plasma discharge sources (surfatron, magnetron, hollow cathode) in different working modes, thin film deposition, surface treatment, surface analysis, optical measurements and plasma diagnostics

Computer oriented skills: Microsoft Office - advanced,
OriginPro - advanced,
programming in C++/C#, Arduino, MATLAB, and
web development (HTML, CSS, PHP, JavaScript)
- intermediate

English – fluent, TEOFL ITP certificate, level B2

Driving license

Awards

Bachelor studies graduated with honours
Master studies graduated with honours
Deans award for the outstanding research results in Master thesis

Publications out of the topic of the thesis

The following 3 publications do not serve as a base for this thesis as their topic does not concern sensor applications, although they utilize functional nanostructures:

Vitezslav Stranak, Jiri Kratochvil, Jiri Olejnicek, Petra Ksirova, **Petr Sezemsky**, Martin Cada, Zdenek Hubicka, Enhanced oxidation of TiO₂ films prepared by high power impulse magnetron sputtering running in metallic mode, *Journal of Applied Physics* 121, (2017), 171914.

<https://doi.org/10.1063/1.4977825>

(IF = 2.546)

Jiri Kratochvil, David Kahoun, Ondrej Kylian, Jan Sterba, Tereza Kretkova, Jaroslav Kousal, Jan Hanus, Jana Vaclova, Vadym Prysiashnyi, **Petr Sezemsky**, Pavla Fojtikova, Jaroslava Lieskovska, Helena Langhansova, Ivan Krakovsky, Vitezslav Stranak, Nitrogen enriched C:H:N:O thin films for improved antibiotics doping, *Applied Surface Science* 494, (2019), 301-308.

<https://doi.org/10.1016/j.apsusc.2019.07.135>

(IF = 6.707)

Jiri Kratochvil, Vadym Prysiashnyi, Filip Dycka, Ondrej Kylian, Peter Kus, **Petr Sezemsky**, Jan Sterba, Vitezslav Stranak, Gas aggregated Ag nanoparticles as the inorganic matrix for laser desorption/ionization mass spectrometry, *Applied Surface Science* 541, (2020), 148469.

<https://doi.org/10.1016/j.apsusc.2020.148469>

(IF = 6.707)

1. **Petr Sezemsky**, Zdenek Hubicka, Martin Cada, Rainer Hippler, Vitezslav Stranak, **Sobolewski probe method for diagnostics of reactive dusty plasma discharge**, “4th German-Czech Workshop on Nanomaterials”, May 10-11 (2018), České Budějovice, Czech Republic. (Talk)
2. **Petr Sezemsky**, Jiri Kratochvil, M. Smientana, Robert Bogdanowicz, Dariusz Burnat, Harm Wulff, Vitezslav Stranak, **Plasma-assisted deposition of thin ITO film for optical-fibre-based biosensors**, “28th Symposium on Plasma Physics and Technology (SPPT)”, June 18-21 (2018), Prague, Czech Republic. (Talk)
3. **Petr Sezemsky**, Jiri Kratochvil, Robert Bogdanowicz, Mateusz Smietana, Dariusz Burnat, Harm Wulff, Vitezslav Stranak, **Plasma-assisted deposition of thin ITO film for optical-fibre-based biosensors**, E-MRS Fall Meeting / Symposium C on Fabrication and characterization of emerging transparent conductive materials, September 16-19 2019, Warsaw, Poland. (Talk)
4. **Petr Sezemsky**, Vitezslav Stranak, Jiri Kratochvil, David Kahoun, Jaroslava Lieskovska, Jan Sterba, Ondrej Kylian, **Smart coatings for tailor-made multistage antibacterial action**, E-MRS Fall Meeting / Symposium V on Bioinspired and Biointegrated Materials as New Frontiers Nanomaterials, September 16-19 2019, Warsaw, Poland. (Invited talk)
5. **Petr Sezemsky**, Jiri Kratochvil, Robert Bogdanowicz, Mateusz Smietana, Dariusz Burnat, Harm Wulff, Vitezslav Stranak, **Plasma-assisted deposition of thin ITO film for optical-fibre-based biosensors**, Workshop on Plasma-Based Synthesis of Nanomaterials 10th - 11th of February 2020, Prague, Czech Republic. (Talk)
6. **Petr Sezemsky**, Jiri Kratochvil, Dariusz Burnat, Mateusz Smietana, Pawel Niedziałkowski, Robert Bogdanowicz, Harm Wulff, Vitezslav Stranak, **Optimization of ITO deposition process for electrochemically active LMR biosensors**, 5th German-Czech workshop on Nanomaterials, May 18 – 19, 2020, Dresden, Germany (Online talk)

© for non-published parts Petr Sezemský
sezemskypetr@gmail.com

Plasma-Assisted deposition of functional bio-active nanostructured films
Ph.D. Thesis Series, 2021, No. 19

All rights reserved
For non-commercial use only

Printed in the Czech Republic by Typodesign
Edition of 10 copies

University of South Bohemia in České Budějovice
Faculty of Science
Braníšovská 1760
CZ-37005 České Budějovice, Czech Republic

Phone: +420 387 776 201
www.prf.jcu.cz, e-mail: sekret-fpr@prf.jcu.cz